TriDurLE

National Center for Transportation Infrastructure Durability & Life-Extension

Project ID: 2021-SDSU-02

Repairable Precast Bridge Bents for Seismic Events

Final Report

by

Kallan Hart and Mostafa Tazarv

Department of Civil and Environmental Engineering
South Dakota State University
Brookings, South Dakota

for

September 6, 2022

ACKNOWLEDGEMENTS

DISCLAIMER

The contents of this report reflect the views of the authors, who are responsible for the facts and the accuracy of the information presented. This document is disseminated under the sponsorship of the Department of Transportation, University Transportation Centers Program, in the interest of information exchange. The U.S. Government assumes no liability for the contents or use thereof.

ABSTRACT

Bridges designed with current seismic codes exhibit large displacement capacities, and the bridge total collapse is prevented. However, damage of ductile members is allowed at this performance level. In reinforced concrete bridges excited by ground shaking, columns are the target ductile members in which concrete cover, core, and reinforcement may damage, and the column may not return to its original position. Minor damages are usually repaired but excessive damages such as core crushing, bar buckling, and/or bar fracture are hard to repair and will usually result in the column or bridge replacement. According to FHWA, approximately 25% of the US bridges require rehabilitation, repair, or total replacement. Furthermore, within the next 50 years, many bridges located in the 16 seismic prone states of the nation will experience large earthquakes that may cause significant damage. Induced seismic activities in formerly non-seismic states such as Oklahoma may also damage bridges with poor seismic detailing. Even though current practice is successful in attaining the no-collapse objective, a new design paradigm is needed to minimize bridge damage incorporating low- to no-damage techniques. The benefit can be enhanced if those low-damage technologies are combined with precast techniques to accelerate bridge construction. The main goal of the present study was to develop a new generation of bridge columns which are fully precast, low damage, and repairable through component replacement. To achieve the project objectives, 20 repairable precast detailing alternatives were developed then ranked using a 13-parameter rubric including design and construction considerations. Subsequently, top three candidates were selected, designed at 50% scale, and prepared for testing. The three precast columns incorporated different exposed fuses such as stainless-steel bars restrained against buckling and steel tendons, which are tension-only members. Advanced materials such as ultra-high performance concrete (UHPC) and self-centering mechanisms were utilized to reduce the column damage and residual displacements. A reference cast-in-place column (CIP) was included for comparison. The repairable precast bridge columns were tested twice under a slow cyclic loading. The columns were repaired only by replacing the exposed fuses and retested under the same loading. The repair of all three columns were overall feasible but the repair of the columns with exposed tendons were very easy, simple, and fast due to insignificant residual displacements. All precast columns exhibited displacement capacities comparable with or higher than CIP. Analytical modeling method were developed for repairable columns, which were reasonably accurate. Subsequently, a parametric study was conducted to better understand the behavior of repairable columns using different fuse materials. Finally, design and construction guidelines were proposed to facilitate the use of this new technology. Proof testing of the repair-by-replacement design concept, development of a new generation of rocking columns through external post-tensioning, and development of tendon-to-bar mechanical splices are the key outcomes of this study.

TABLE OF CONTENTS

ABBREVIATIONS

AASHTO	American Association of State Highway and Transportation Officials
ASTM	American Society of Testing and Materials
ABC	Accelerated Bridge Construction
ACI	American Concrete Institute
BRR	Buckling Restrained Reinforcement
CIP	Cast-in-Place
DOT	Department of Transportation
ECC	Engineered Cementitious Composite
FRP	Fiber Reinforced Polymer
ft	Feet
in.	Inch
kip	1000 pounds
ksi	kip per square inch
LSL	Lohr Structures Laboratory
MMFX	Micro-composite Multi-structural Formable
PCI	Precast Concrete Institute
SDSU	South Dakota State University
SMA	Shape Memory Alloy
SS	Stainless Steel
UHPC	Ultra-high Performance Concrete

LIST OF TABLES

LIST OF FIGURES

EXECUTIVE SUMMARY

ES.1 Introduction

Bridges designed with current seismic codes exhibit large displacement capacities, and the bridge total collapse is prevented. However, damage of ductile members is allowed at this performance level. In reinforced concrete (RC) bridges excited by ground shaking, columns are the target ductile members in which concrete cover, core, and reinforcement may damage, and the column may not return to its original position. Minor damages are usually repaired but excessive damages such as core crushing, bar buckling, and/or bar fracture are hard to repair and will usually result in the column or bridge replacement. According to FHWA, approximately 25% of the US bridges require rehabilitation, repair, or total replacement. Furthermore, within the next 50 years, many bridges located in the 16 seismic prone states of the nation will experience large earthquakes that may cause significant damage. Induced seismic activities in formerly non-seismic states such as Oklahoma may also damage bridges with poor seismic detailing. New detailing and enhanced materials are emerging to reduce the damage of RC bridge columns minimizing the need for repair or replacement after an event. Low- or no-damage detailing may be attractive to bridge owners in seismic regions due to a reduced cost associated with the repair or replacement of the bridge. Columns can be designed to be low damage using advanced materials and/or novel detailing.

The present work was carried out to advance the state-of-the-art column design with a new concept of repair-by-replacement methodology, such as those used in the car industry. The benefits can be maximized if accelerated bridge construction (ABC) detailing and advanced materials are incorporated in a repairable design.

ES.2 Objectives

The main objective of this study was to develop new details for RC bridge columns that are repairable through component replacement. To achieve this goal, advanced materials and ABC detailing were combined to develop feasible repairable alternatives. All repairable precast column alternatives were assessed through a 13-parameter evaluation method to select best details for experimental investigation. Of the top candidates, three repairable precast columns were selected, constructed, and tested and the results were compared with a reference cast-in-place (CIP) column. All specimens were half-scale and tested under a slow cyclic loading at the Lohr Structures Laboratory on the campus of South Dakota State University. Each column was tested twice under the same loading. In the second test of each specimen, the column exposed fuses were replaced to practice repair through replacement. Post-test and parametric analyses were performed to better understand the performance of repairable columns. Furthermore, design and construction guidelines were proposed for repairable precast bridge columns based on the findings of the study.

ES.3 Literature Review

Novel columns may improve the bridge seismic performance and lower its damage thus minimizing the repair need after an earthquake. The enhanced performance of a novel columns can be achieved using advanced materials and/or new detailing. Advanced materials for reinforced concrete bridges can improve column ductility, concrete confinement, and reduce cover spalling while novel column detailing

can minimize residual displacements and may further add to the displacement capacity. A review of past studies on advanced materials and novel bridge columns was performed.

ES.4 Repairable Column Alternative Development

In general, repairable columns envisioned in this project have bars that are exposed, accessible, and detachable using mechanical bar splices. If a type of steel bar is used in this detailing, it must be restrained against buckling to avoid low-cycle fatigue. BRR is a bar that is confined in a steel tube to minimize buckling, or a buckling restrained reinforcement. Alternative to BRR is a fuse with tension-only members such as steel tendons. Furthermore, the column diameter must be reduced in the plastic hinge region to accommodate the exposed fuses and couplers. The reduced section of a repairable column is called "neck region". All repairable columns that will be developed in this study are expected to be moment-resisting since the exposed bars are axial members forming a tension-compression couple. The shear forces associated with the moment will be resisted with either concrete components or an additional shear pin connection.

Any repairable column utilizing BRR in the neck region may be reinforced with different types of bars including black steel, stainless steel (SS), shape memory alloy (SMA), or Martensitic Micro-composite Formable Steel (MMFX). It may also be possible to use tendons (either steel, SMA, or fiber-reinforced polymer, FRP) instead of BRR to allow for a tension-only connection to prevent buckling. Furthermore, self-consolidating concrete (SCC), engineering cementitious composite (ECC), and ultra-high performance concrete (UHPC) may be used in the neck region in lieu of conventional concrete to reduce damage.

Based on the most feasible combination of advanced materials and novel column detailing, 20 new repairable bridge column alternatives were developed (**Fig. ES.1**). The alternative development was mainly based on the column detailing and their constitutive cementitious materials but not variations in exposed reinforcement (either BRR or tendons). Otherwise, the total number of repairable bridge columns would have exceeded 80.

NCHRP Report 864 (Saiidi et al., 2017) contains an evaluation method for novel bridge columns including plastic hinge damage, displacement capacity, residual displacement, design considerations, and construction and other considerations. This 13-parameter rating system was selected to assess the 20 repairable columns and to determine the top candidates for testing. **Table ES.1** presents a summary of assessment using the NCHRP method. For simplicity, all scores were converted to a five-star rating to determine the most viable alternatives. Some columns were rated better than others. However, it should be noted that all the proposed repairable columns will have a unique characteristic – repairability – which makes them better compared with conventional columns.

Figure ES.2 shows the top four repairable column alternatives based on the above rating system. Of the four alternatives, Column 1, which was ranked 2nd, was tested in a previous project by the research team (Sjurseth et al., 2022). Columns 3 and 15 (respectively ranked as 1st and 3rd) were selected for further experimental investigation in this project. Even though Column 19 rates as high as Column 15, the post-tensioning of Column 19 must be performed on site to connect the column to the footing. Nevertheless, the post-tensioning of Column 15 may be performed at the precast plant, which offers a better constructability and quality. Therefore, Column 19 was not included in the experimental study.
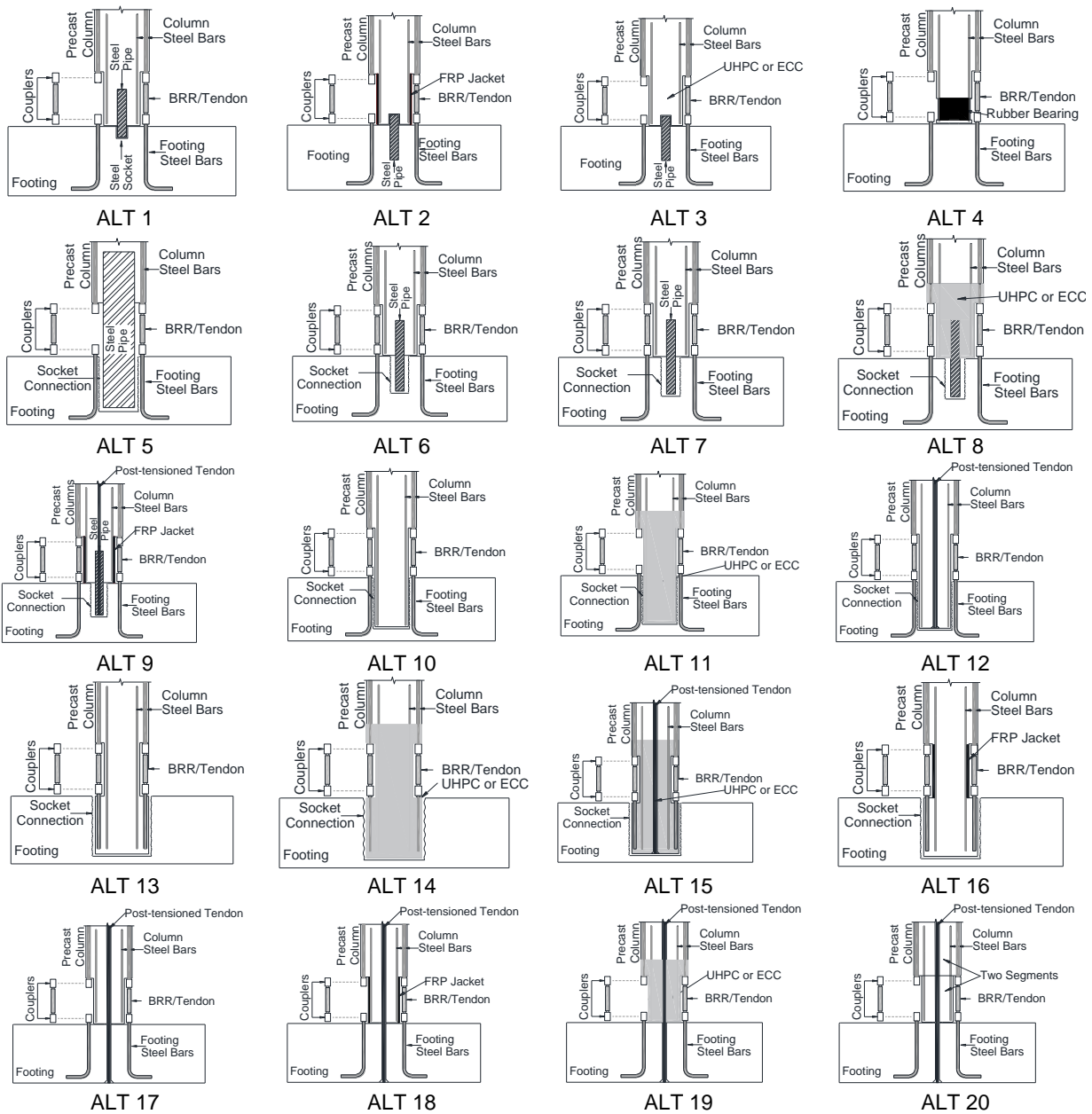
Figure ES.1. Twenty Detailing Alternatives for Repairable Precast Bridge Columns

Table ES.1. Repairable Column Ratings on Five-Star Scale

Column	Five-Star Rating (0-5)
1: Pipe-pin	3.19 ranked 2nd
2: Pipe-pin w/ FRP jacket	3.09
3: Pipe-pin w/ UHPC or ECC	3.26 ranked 1st
4: Rubber bearing	3.06
5: Large neck pipe-socket	2.99
6: Pipe-socket	2.92
7: Pipe-socket w/ FRP jacket	2.81
8: Pipe-socket w/ UHPC or ECC	2.99
9: Pipe-socket w/ post-tensioning	2.95
10: Neck-socket	2.92
11: Neck-socket w/ UHPC or ECC	2.95
12: Neck-socket w/ post-tensioning	2.95
13: Column-socket	3.06
14: Column-socket w/ UHPC or ECC	3.09
15: Column-socket w/ UHPC, post-tensioning	3.16 ranked 3rd
16: Column-socket w/ FRP jacket	2.95
17: Rocking	3.09
18: Rocking with FRP jacket	2.99
19: Rocking with UHPC or ECC	3.16 ranked 3rd
20: Segmental	2.95
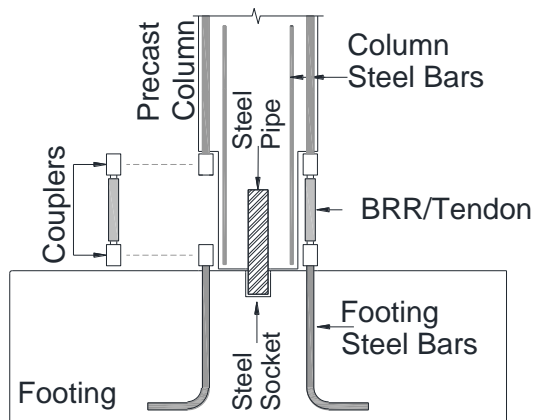
a) Column 1 – Ranked 2nd
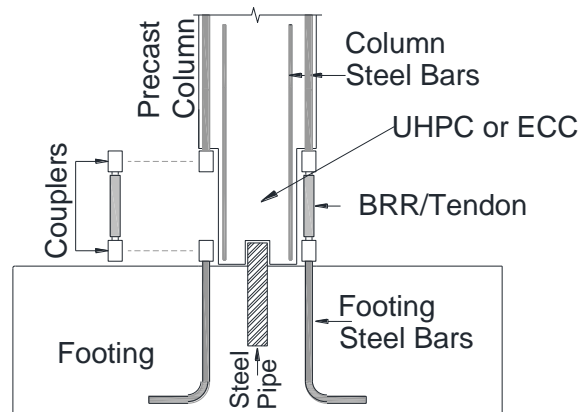
b) Column 3 – Ranked 1st
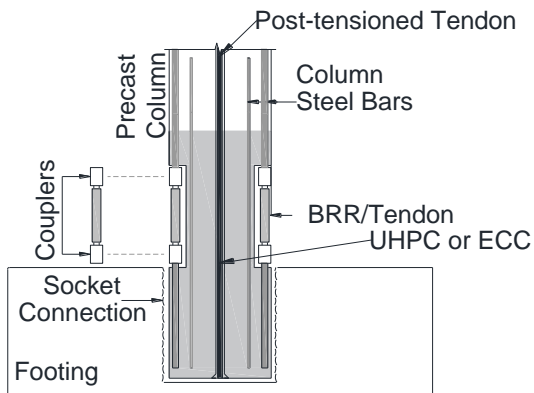
c) Column 15 – Ranked 3rd
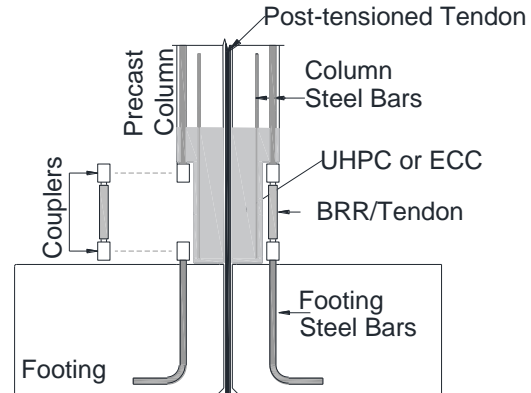
d) Column 19 – Ranked 3rd

Figure ES.2. Detailing of Top-Rated Repairable Columns

ES.5 Experimental Investigation

ES.5.1 Test Matrix

To evaluate the feasibility and seismic performance of the proposed repairable bridge columns, top three repairable columns were selected for proof testing. Furthermore, one reference cast-in-place column was included to serve as the benchmark model. **Figure ES.3** shows the column details selected for testing and **Table ES.2** presents the column test matrix. The four test specimens can be identified using a naming system including the column and connection type. The reference cast-in-place column is identified using the acronym "CIP". The name for the repairable columns starts with RPH referring to "repairable precast with headed longitudinal bars/couplers" followed by the connection type: "PC" for the column utilizing a pipe-pin connection at the column base with the pipe embedded in the column, "PF" for a pipe-pin connection with the pipe embedded in the footing, and "NP" for the column with no pin connection but instead using a socket connection. Later, a third term is added to each column "R", which indicates that the column is repaired by component replacement and retested to prove the proposed repair-by-replacement concept.

The CIP octagonal cross section was designed with a width of 24 in. (610 mm) and a height of 8 ft (2.44 m) from the top of the footing to the centerline of the applied lateral load resulting in an aspect ratio of 4. The CIP column model incorporated 10, No. 8 (Ø25-mm) longitudinal bars with No. 3 (Ø10-mm) transverse hoops spaced at 2 in. (51 mm) on center. The resulting longitudinal reinforcement ratio and transverse volumetric steel ratio were 1.66% and 2.0%, respectively. The column design axial load index was 5%, the design concrete compressive strength was 6,000 psi (41.4 MPa), and ASTM A706 bars were considered for all reinforcement. The column was designed to achieve a minimum displacement ductility capacity of 7 based on AASHTO SGS (2011).

A similar cross section to that of the CIP column was used in RPH-PC but a pipe-pin connection was devised between the precast column and footing to allow a large rotation at the column base while resisting plastic shear forces. In the neck region, a circular section with a reduced diameter was utilized to accommodate exposed reinforcement and connections. Stainless-steel bars were used instead of conventional black steel bars to improve the durability of the exposed components. Dowel bars matching the number and size of the exposed bars were extended out of the footing and the octagonal column to be connect to the exposed bars. Headed Reinforcement Corp. (HRC) 500 Series couplers were used in this precast column since they are detachable, reusable, and low profile. All bars were headed. The female portion of the coupler (the larger piece) was placed on the column/footing dowels and the male portion of the coupler was used on the exposed bar. Longitudinal bars in the RPH-PC column and footing were oversized to No. 10 (Ø32 mm) compared with the No. 8 (Ø25-mm) bars that were used in fuses. This was done to ensure that the bar yielding occurs within the fuses but not in the column/footing dowels. No. 8 (Ø25-mm) stainless-steel bars used as the exposed fuses were machined down from No. 10 (Ø32-mm) bars to match the CIP longitudinal reinforcement. In initial testing (fuses colored in yellow), the dog-bone length was 10.25 in. (260 mm) while the reduced diameter length was 5.125 in. (130 mm) in the second testing in which the column was repaired (fuses colored in green). Different fuse lengths were used to investigate their effects on the column overall ductility. A clear cover of 1 in. (25 mm) was used in the column.

Table ES.2. Column Test Matrix

Specimen Name	Exposed Reinforcement (Fuse) Type	Connection Type	Column Long. Reinforcement	Column Main Material	Additional Remarks
CIP	N/A	Monolithic	Black Steel	Conventional Concrete	Cast-in-place vertical construction
RPH-PC	Stainless Steel Bars Confined with Grouted Tubes	Pipe-Pin	Stainless Steel	SCC	Precast column seating on footing, column tested twice
RPH-PF	Steel Tendons	Inverted Pipe-Pin	Black Steel	UHPC	Precast column seating on footing, column tested twice
RPH-NP	Steel Tendons	Grouted Socket with no Pin	Black Steel	UHPC	Hybrid rocking precast column connected to footing via a socket connection, column tested twice

Note: SCC refers to self-consolidating concrete, and UHPC refers to ultra-high performance concrete.

a) CIP –Cast-in-Place Reference Column

b) RPH-PC w/ Pipe-pin Connection

c) RPH-PF w/ Inverted Pipe-pin Connection

d) RPH-NP w/ Grouted Socket Connection

Figure ES.3. Connection Details for Column Test Specimens

The detailing of RPH-PF was mostly the same as that of RPH-PC, but with some modifications based on lessons learned from the first repairable column testing (RPH-PC). The same geometry, cross section, and reinforcement as RPH-PC were used in the precast column, neck region, and cast-in-place footing. One major change in RPH-PF compared with RPH-PC was the use of UHPC in the column instead of SCC, which was done to reduce the column damage. Furthermore, conventional black steel was used in lieu of stainless steel since the effects of stainless-steel bars were already explored in RPH-PC. Despite attempts to eliminate buckling of BRR in RPH-PC, a major Z-shape bending occurred at high drift ratios outside BRR within the gap between the coupler and steel tube. To eliminate any type of buckling, a new bar-to-steel-tendon coupler was designed in collaboration with Headed Reinforcement Corp. in which the exposed fuses work in tension only in lieu of the tension-compression mechanism of BRR. The male portion of the HRC 500 couplers was redesigned to accommodate 0.6-in. (15-mm) diameter seven-wire steel tendon. Since the area of a 0.6-in. (15-mm) tendon is approximately one-third that of a 1-in. (25-mm) diameter bar used in BRR, the number of longitudinal reinforcing bars in RPH-PF was increased from 10 to 14 to better match the moment thus lateral force capacity of RPH-PC. Another detailing modification was that the pipe (now a solid steel shaft) in RPH-PF was embedded into the footing rather than the column as was the case in RPH-PC. This allowed for the steel socket to be inverted and placed in the column neck section, eliminating durability issues such as possible water buildup in the socket. Furthermore, the pipe cross section was changed from a circle to a solid square to better resist column torsion.

The cross-sectional properties, reinforcement, and cementitious materials of PRH-NP were the same as those of RPH-PF. UHPC was used for the entire precast column. Steel tendons were incorporated as tension-only fuses and no BRR was used. The column was fully precast and was connected to the footing using a grouted socket (pocket) connection. To accommodate the socket connection, the height of the footing was increased from 2 ft (610 mm) used in all other columns to 3 ft. (914 mm). The column height from the top of the footing to the centerline of the applied lateral load remained the same as other specimens, 8 ft. (2.44 m). Post-tensioning requirements of this hybrid rocking column were designed following recommendations from NCHRP Report 864 (Saiidi et al., 2017) in which the total tendon area must be greater than 0.4% of the gross cross-sectional area of the column and the initial tendon stress after all losses should be less than 30% of the tendon yield strength. These design values ensure that steel tendons do not yield, and that the column fails either by bar/fuse fracture or core concrete crushing. The final design resulted in 15, 0.5-in. (13-mm) diameter grade 270 (1862-MPa) seven-wire steel strands, each post-tensioned to no more than 60 ksi (414 MPa). A "DYWIDAG 19-0.5 Multiplane Anchorage MA" system was incorporated to anchor the 15 unbonded tendons, which were grouped and passed through the column cross section using a 3-in. (76-mm) plastic duct.

ES.5.2 Test Results

Figure ES.4 shows the damage of the plastic hinge region for CIP, RPH-PC, RPH-PF, and RPH-NP after the second pull of the 2.0% drift cycle. CIP and RPH-PC experienced some flexural cracks while no damage was observed in RPH-PF and RPH-NP. CIP was a conventional column thus the observed damage was typical. SCC was used in RPH-PC thus some cracks were expected. At the rocking face of RPH-PC, some spalling was observed mainly due to the use of the steel shims placed between the column and the steel baseplate at the rocking interface. Nevertheless, the apparent damage of RPH-PF and RPH-NP cast with UHPC was minimal at 2% drift ratios.

Figure ES.5 shows the damage of the four columns at 4% drift ratio, just prior to the repair (for the precast columns not CIP). CIP experienced a significant spalling. RPH-PC exhibited both flexural and shear cracks above the neck section, a minor Z-shape bending of BRR, and spalling of SCC at the column base. Nevertheless, RPH-PF showed no damage and RPH-NP exhibited minor flexural cracks in the neck section.

Figure ES.6 shows the plastic hinge damage of CIP, RPH-PC-R, RPH-PF-R, and RPH-NP-R at their failure. CIP exhibited extensive damage such as concrete crushing, and buckling and fracture of the longitudinal bars. Several cracks, spalling of SCC, and a Z-shape deformation of BRR were observed for RPH-PC-R. Nevertheless, the UHPC damage was minimal in RPH-PF-R and RPH-NP-R. RPH-PF-R had only a few cracks at the base of the column. RPH-NP-R had a few more flexural cracks than RPH-PF-R both on and above the neck section.
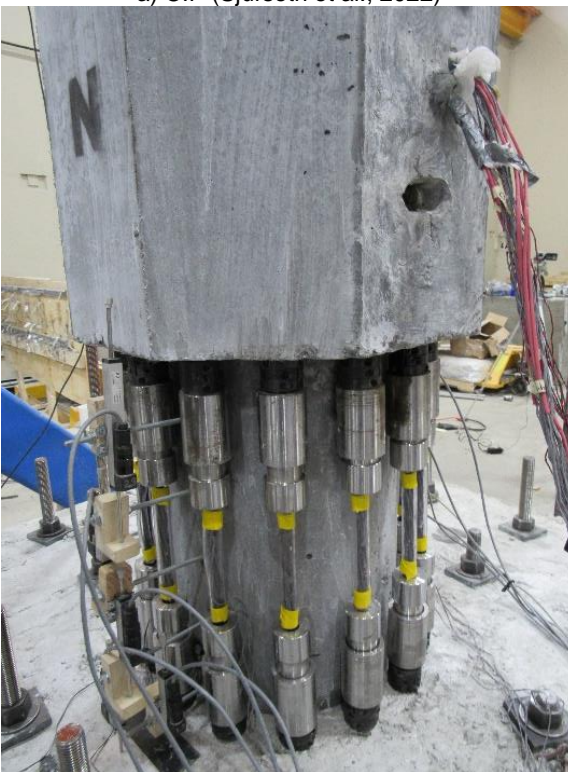
In terms of reparability, CIP could not be repaired at 10% drift due to the extent of the damage. The repair of RPH-PC was difficult due to the bending of column/footing dowel bars, the Z-shape deformation of BRR, and large residual displacements seen at high drifts. RPH-PF had insignificant residual displacements with no column/footing dowels bent thus it was very easy to repair. In fact, this column was repaired and prepared for retesting in less than two hours. The repair of RPH-NP was also simple and quick at 4% drift ratio; however, the repair might be slightly more challenging at very large drifts due to moderate level residual displacements. Nevertheless, at any residual displacements, the tendons can be cut to the appropriate lengths and installed. This is a significant enhancement of the repairability compared with RPH-PC where BRR lengths cannot be easily adjusted onsite (a portable heading machine is needed to head the ends of BRR onsite) and there is a small tolerance to install each BRR. Furthermore, tightening the coupler of the tendon-to-bars using simple tools (pipe wrenches) can generate a significant tensile force in tendons (e.g., 10 kips (44.5 kN) in RPH-PF) thus such fuses may serve as both the column longitudinal reinforcement and a recentering mechanism. This is a novel hybrid rocking connection in which post-tensioning is outside the column and fully accessible. This is a significant enhancement of durability compared to conventional rocking systems since post-tensioning of rocking columns in all past studies were internal with no to minimal accessibility for the inspection and maintenance. UHPC showed a superior performance compared with conventional concrete and SCC and is thus recommended for such repairable columns.

a) CIP (Sjurseth et al., 2022)

b) RPH-PC
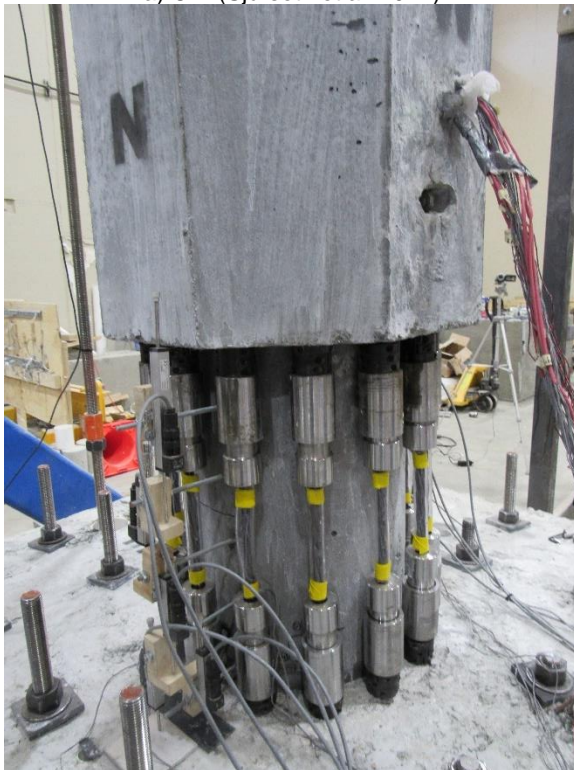
c) RPH-PF

d) RPH-NP

Figure ES.4. CIP, RPH-PC, RPH-PF, and RPH-NP Plastic Hinge Damage after 2% Drift Cycle

a) CIP (Sjurseth et al. 2022)
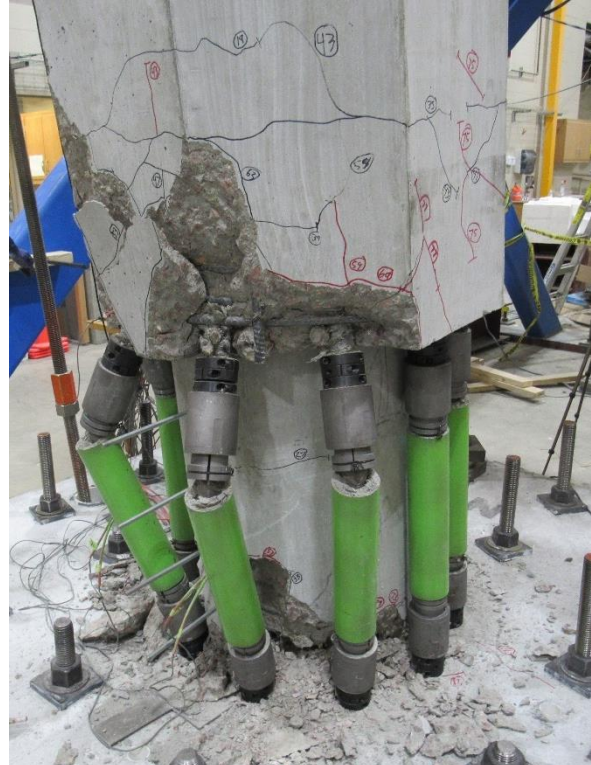
b) RPH-PC
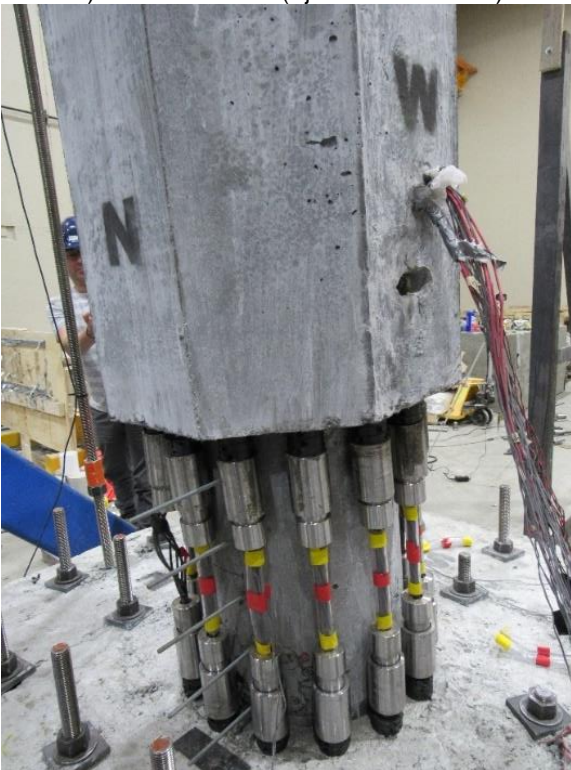
c) RPH-PF

d) RPH-NP

Figure ES.5. CIP, RPH-PC-R, RPH-PF-R, and RPH-NP-R Plastic Hinge Damage at 4%

a) CIP at 10% Drift (Sjurseth et al. 2022)

b) RPH-PC-R at 10% Drift

c) RPH-PF-R at 9% Drift

d) RPH-NP-R at 8% Drift

Figure ES.6. CIP, RPH-PC-R, RPH-PF-R, and RPH-NP-R Plastic Hinge Damage at Failure State

Figure ES.7 shows the lateral force-drift hysteretic curves for the three repairable columns including their repaired testing superimposed on the CIP response. RPH-PC and RPH-PC-R exhibited a lower initial stiffness compared with that of CIP, but similar force and displacement capacities were achieved. Note that RPH-PC did not fail but the test was stopped at 10% drift, where the CIP column failed. Even though no specific self-centering mechanism was used, RPH-PC and its repaired version, both with stainless-steel BRR, showed a moderate-level reduction (e.g., 44% at the last cycle) in residual displacements compared with CIP. However, the residual displacement reduction at high drifts was not sufficient to allow an easy BRR replacement. The column/footing dowels were also bent limiting the repair-by-replacement technique. Therefore, this column needs an alternative BRR such as SMA to minimize the dowel damage and residual displacement. The incorporation of tendon fuses might be another alternative.

RPH-PF and RPH-PF-R had a significantly lower initial stiffness, a slightly lower lateral strength, and a similar displacement capacity compared with CIP. Both RPH-PF and RPH-PF-R exhibited insignificant residual displacements throughout the entire testing allowing a simple and fast replacement of tendon fuses. The strong recentering behavior of this column proves that the external tendons can simultaneously serve as the column longitudinal reinforcement and rocking reinforcement. Therefore, RPH-PF detailing is a new generation of hybrid rocking columns in which rocking reinforcement is fully accessible. Note that exposing the tendons may cause durability issues. All exposed reinforcement should be protected against weather conditions. For example, stainless-steel bars must be used as column/footing dowels, and stainless-steel, galvanized, or epoxy-coated tendons (such as those used in cable-stayed bridges) should be incorporated as tendon fuses.

In RPH-NP and RPH-NP-R, the initial stiffness most closely matched that of CIP. Furthermore, this repairable column showed a 37% higher lateral strength, but a 14% lower displacement capacity compared with CIP. Despite the use of an established rocking system (internal post-tensioning) as well as the external tendon fuses, this column did not show insignificant residual displacements mainly due to the rebar hinge connection at the column base. Nevertheless, the repair at 4% drift ratio was relatively easy and fast since the new tendons were cut in length and installed even when the column had a residual drift ratio of 1.5%.

Figure ES.7d shows the average pushover envelopes for CIP and all repairable columns. The displacement ductility capacities of the three repaired precast columns were all significantly lower than that of CIP due to the reduced stiffness and delayed yielding. However, for novel columns, the drift capacity is often a better indicator of the column performance than the displacement ductility capacity. CIP failed by the longitudinal bar fracture at 8.96%. RPH-PC-R did not fail, since the test was stopped, but the column drift capacity was assumed to be 9.8%. RPH-PF-R failed by the tendon rupture at 8.9% drift ratio. RPH-NP-R failed by the neck bar rupture at 7.7% drift ratio. Therefore, the displacement capacity of RPH-PC-R was 9% higher than that of CIP and the displacement capacities of RPH-PF-R and RPH-NP-R were 0.6% and 14% lower than that of CIP, respectively. **Figure ES.7d** also includes the design level drift demand based on the AASHTO spectrum for Downtown Los Angeles, CA using the period of the CIP column. While all repairable columns were pushed well past the drift demand before repair and retesting, it may be noted that their reduced stiffness increases their period and thus likely increases their drift demand under the same design level earthquake. Further study such as shake table testing is needed to better understand the dynamic behavior of the proposed repairable columns.

Overall, all precast columns were repairable, especially those with tendon fuses, and were retested after being pushed well past the displacement demand of the CIP column with minimal damage.

a) CIP, RPH-PC, and RPH-PC-R

b) CIP, RPH-PF, and RPH-PF-R

c) CIP, RPH-NP, and RPH-NP-R

d) Backbone for All Columns
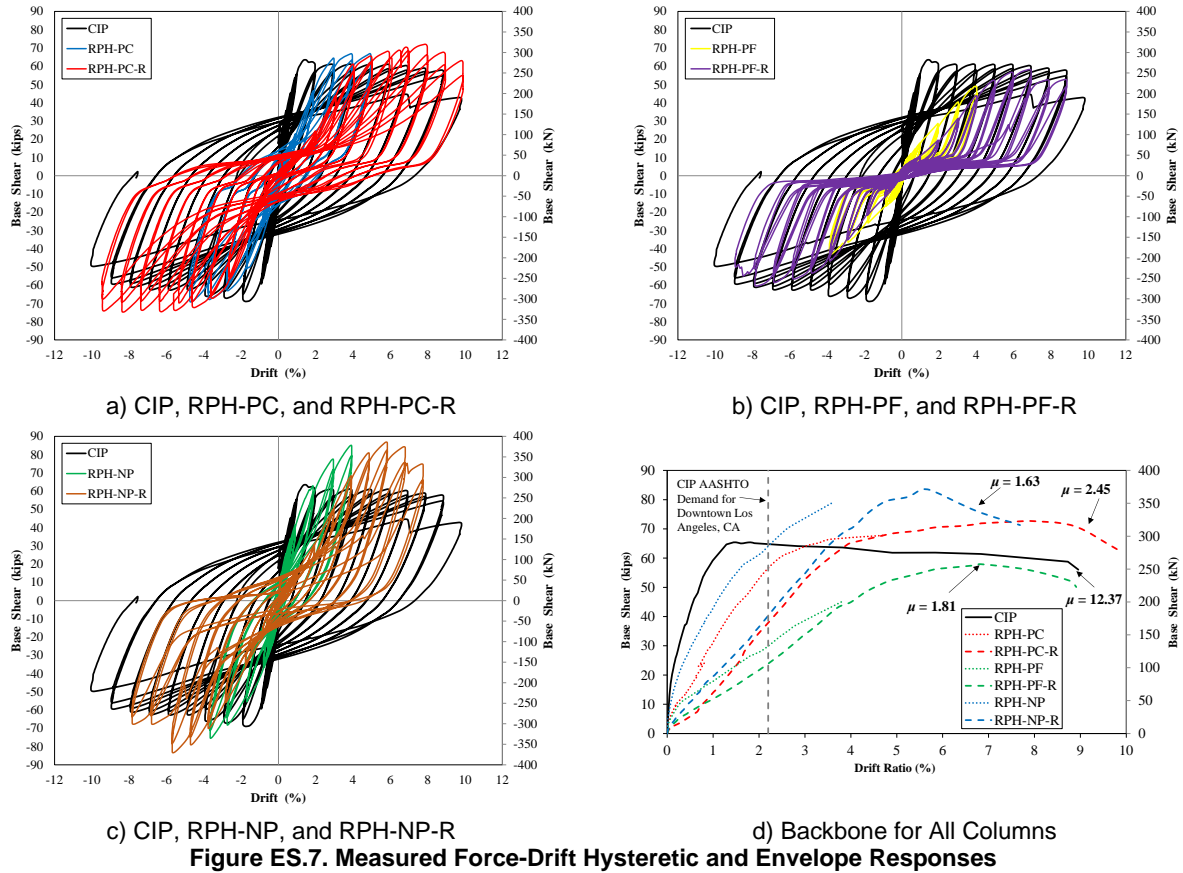
Figure ES.7. Measured Force-Drift Hysteretic and Envelope Responses

Figure ES.8 shows the measured residual versus peak drift relationships for the CIP and repairable columns. All columns had a negligible residual displacement up to 1% drift. Furthermore, RPH-PC and RPH-PF exhibited insignificant residual drifts up to 4.0% peak drift. The residual-peak drift relationships for RPH-PF-R and RPH-NP-R closely match those of their initial testing while RPH-PC-R experienced smaller residual drifts compared with its initial testing (RPH-PC). After their initial plateaus, it can be seen that the residual-peak drift response for RPH-PC-R and RPH-NP-R follows the same slope as CIP, while the response for RPH-PF-R increases at a much smaller rate.

Residual drifts less than 1% may be assumed insignificant after an earthquake (NCHRP 864). Overall, RPH-PF-R experienced the smallest residual drifts among all columns and stayed below the "1% residual drift" limit. Self-centering is a key parameter in the reparability of the proposed precast columns since a close-to-plumb position allows for a quick and easy replacement of the fuses.
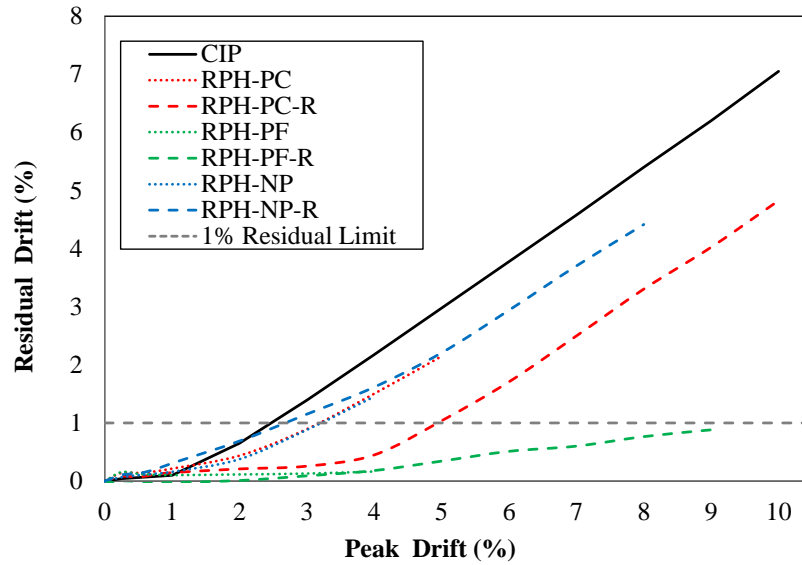
Figure ES.8. Measured CIP and Repairable Column Residual Drifts

ES.6 Analytical Investigation of Column Test Specimens

A general modeling methodology was developed for the repairable columns and was slightly modified per column specimen to accommodate different column details. A three-dimensional finite element model utilizing six degrees of freedom (DOFs) and a fiber-section was used to analyze the CIP, RPH-PC, RPH-PF, and RPH-NP columns. **Figure ES. 9** shows the CIP model and the general model developed for the repairable columns.
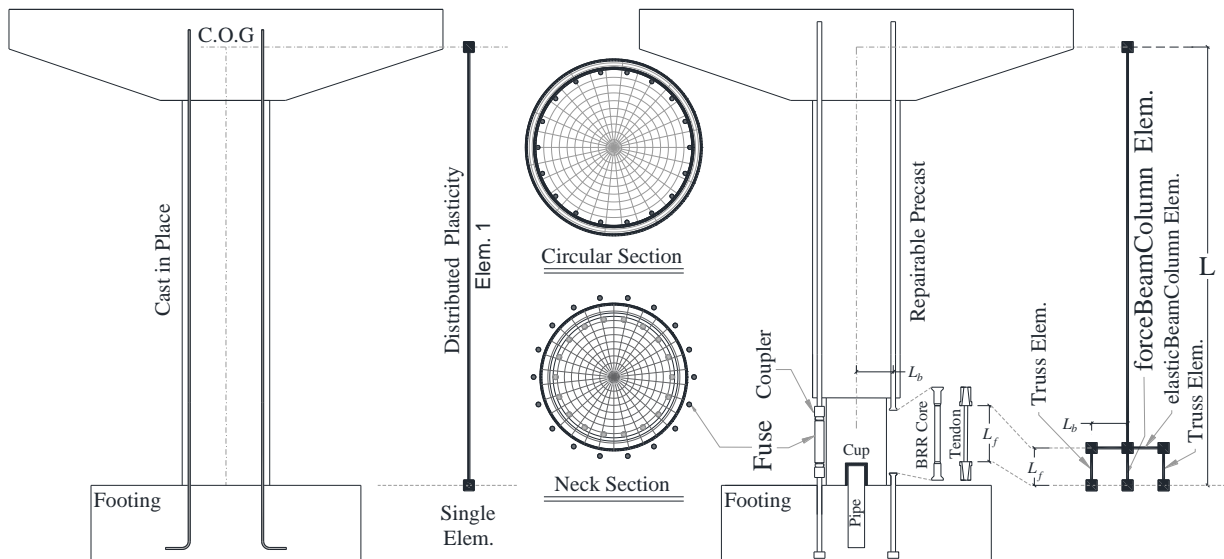
Figure ES.9. Cast-in-Place and Repairable Bridge Column Models

The fuses were simulated using "truss" elements spread radially around the center two "forceBeamColumn" elements. The truss elements had the length and sectional area of the fuses. The truss elements were connected to the column section using "elasticBeamColumn" elements. The core concrete properties were used to determine the modulus of elasticity used in the beam-column elements

while it was found that the cross section used to determine the area and moment of inertia could best be approximated using a rectangle with a width equal to one-tenth of the circumference of the column core and an arbitrary height.

Figure ES.10a shows the calculated and measured force-displacement relationships for the CIP column. The initial stiffness of the calculated and measured pushover curves matched well. Furthermore, there was only a 5.4% difference between the calculated (61.9 kips or 276 kN) and measured (65.4 kips or 291 kN) lateral strength of the column. The calculated drift capacity of CIP was 7.64%, which was 14.7% lower than the measured drift capacity of 8.96%. The model predicted that CIP failed by bar fracture, which was also observed in the column testing.

Figure ES.10b shows the calculated and measured force-drift relationships for RPH-PC with the long BRR (L_f of 11.25 in (286 mm) used in the first test). The initial calculated stiffness is slightly higher than the measured stiffness. The calculated peak lateral force was 64.0 kips (285 kN) while the measured lateral strength was 5.6% higher (67.8 kips or 302 kN). The first test of RPH-PC was stopped at a drift ratio of 5% to perform the fuse replacement. Nevertheless, the analytical model predicts that the failure is at 13.2% drift ratio due to a strength degradation. Overall, the analytical model for RPH-PC using the long fuses reasonably reproduced the behavior of RPH-PC up to 5% drift.

Figure ES.10c shows the calculated and measured force-drift relationships for both RPH-PF and RPH-PF-R. The same analytical model was used for both columns since no change to the fuse properties and geometries was made between the two tests. The average fuse length (L_f) was 13 in. (330 mm) but differed slightly between tendons due to a minor slipping of some wedges during installation and a minor difference in the column/footing dowel lengths. The calculated and measured initial stiffnesses were similar up to 5 kips (22 kN) after which the stiffness of the test specimens softened. The calculated peak lateral force was 56.8 kips (253 kN) while the measured lateral strength was slightly higher at 57.9 kips (258 kN), a 1.9% difference. The analytical model predicted the failure drift at 8.03% due to the rupture of the tendon fuses. RPH-PF-R failed at 8.91% drift ratio in the test, which is 9.9% higher than the calculated failure drift. Overall, the analytical model reproduced the behavior of the RPH-PF and RPH-PF-R columns with a reasonable accuracy.

The calculated and measured force-drift relationships for both RPH-NP and RPH-NP-R are shown in **Fig. ES5.10d**. Similar to RPH-PF, no change was made to the fuse properties and geometries between the two tests thus the same model was utilized for both columns. The average fuse length (L_f) was again 13 in. (330 mm) with a slight difference between tendons. It can be seen that the measured initial stiffness of the RPH-NP column matched well that of the analysis. The initial stiffness of RPH-NP-R was degraded between the two tests, mainly due to the UHPC and neck bar damage, which was not included in the analysis. The calculated peak lateral force was 83.0 kips (369 kN) while the measured lateral strength was 83.5 kips (371 kN), only a 0.6% difference. While the calculated stiffness and lateral load capacity of RPH-PF matched those of the testing, the calculated drift capacity was 9.59%, which was 25% higher than the measured drift capacity of 7.68%. The model predicts that the column fails by a tendon fuse rupture; however, the actual column failed by the strength degradation caused by the bar fracture in the rebar hinge connection. This is likely due to the large cracking of UHPC at the column-footing interface resulting in a high strain concentration at the rebar hinge, which would be very hard to simulate in software that assumes plane sections remain plane.

Overall, the models were able to replicate the force-displacement relationship of the columns with a reasonable accuracy. Further analyses are needed to include the material degradation between multiple testing of the same specimen.
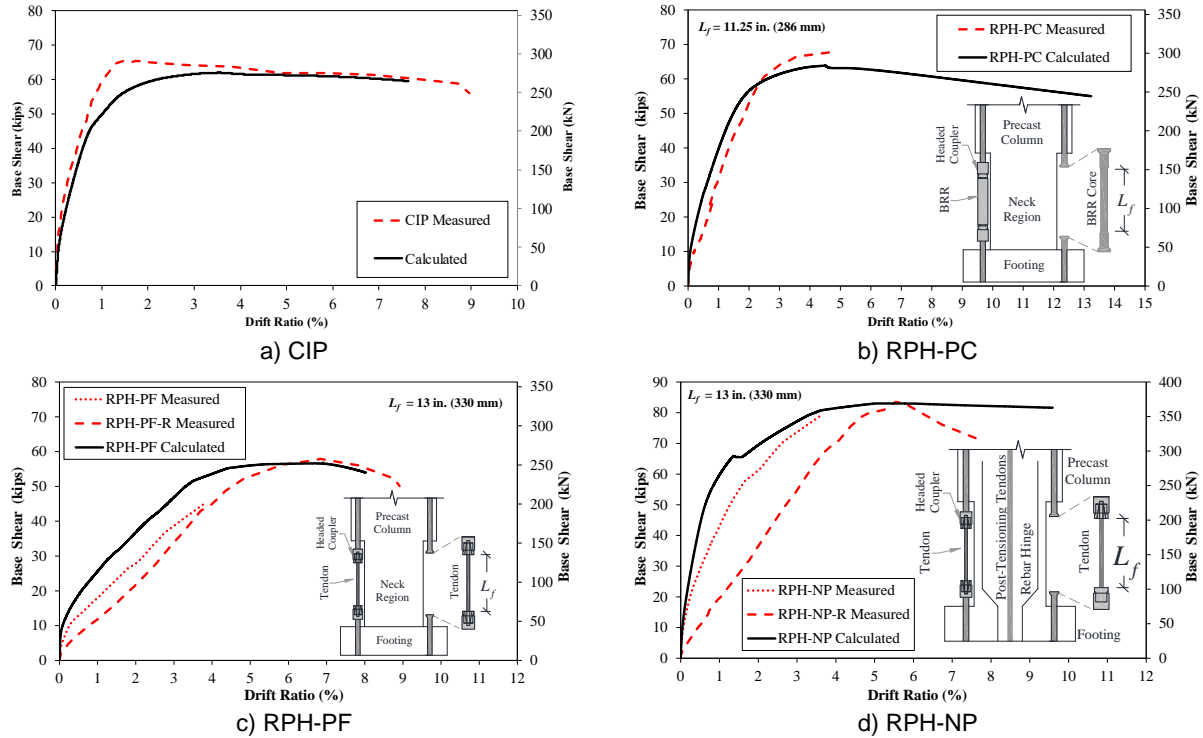
Figure ES.10. Calculated vs Measured Force-Drift Responses

ES.7 Parametric Investigation of Repairable Precast Columns

A parametric study was performed to investigate the effects of different variables on the force-displacement behavior of repairable columns. Four key variables were included in the parametric study including (a) three column aspect ratios (4, 6, and 8), (b) three column axial load indices (5%, 10%, and 15%), (c) three fuse types (stainless-steel bars, shape memory alloy bars, and steel tendons), and (d) three fuse lengths of $0.25L_p$, $0.5L_p$, and $0.75L_p$, where L_p is the analytical plastic hinge length of a corresponding CIP calculated according to AASHTO SGS (2011). A total of 81 repairable precast bridge columns were included in the study. Furthermore, 9 CIP columns with three ARs (of 4, 6, and 8) and three ALIs (of 5%, 10%, and 15%), all with a displacement ductility capacity of 7, were adopted from Sjurseth et al. (2022) and were included as the reference models. Only the CIP columns with the highest ductility were included since any repairable column matching or exceeding its corresponding CIP column's displacement capacity will of the interest. OpenSees (2016) was utilized in the analyses. The modeling methods for the repairable columns were the same as those used in the post-test model validation discussed earlier.

Figure ES.11 shows sample pushover results for CIP and repairable columns utilizing different fuse materials and lengths. Overall, the parametric study indicated that all three material types (SS, SMA, tendon) can be used as external fuses. The designer has the option to match the force and/or displacement capacity of RPH with its corresponding CIP column. The forces can be adjusted by the number or diameter of the fuses. Further, the displacement capacity can be adjusted by changing the fuse length. For example, a designer can increase the number of the 0.7-in. (Ø18-mm) diameter steel tendons with a fuse length of $0.75L_p$ to match the CIP force and displacement capacities.
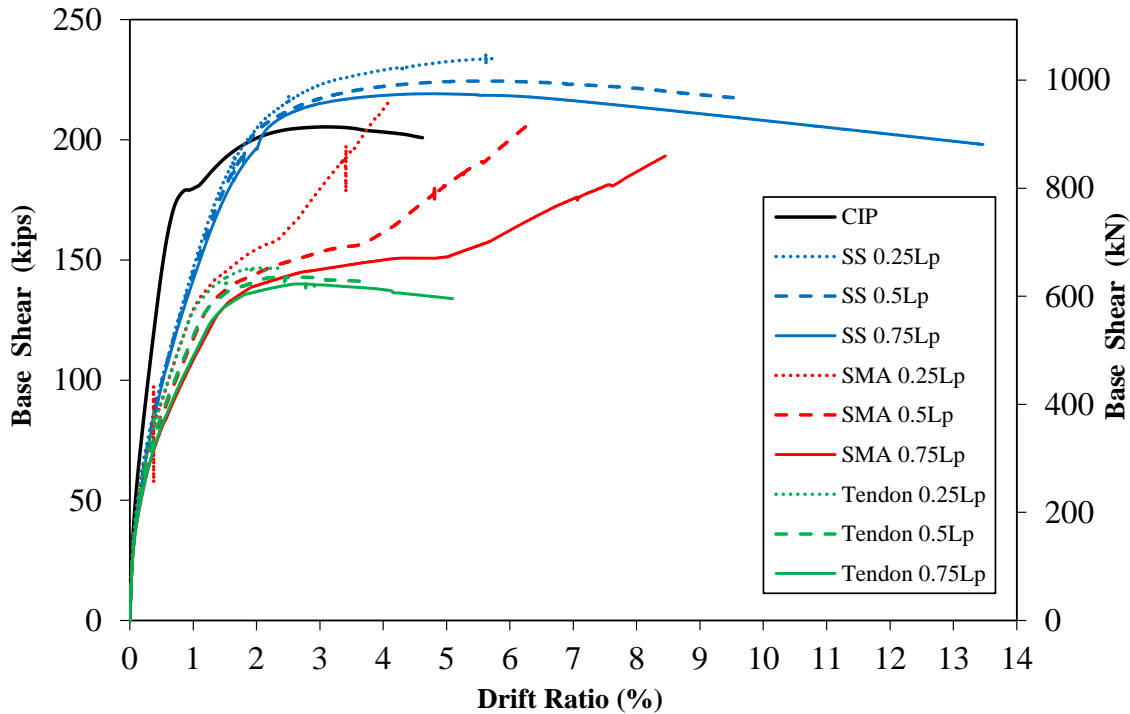
Figure ES.11. Pushover Analysis for RPH-AR4-ALI5

ES.8 Design and Construction Recommendations

General design and construction guidelines were proposed for repairable precast bridge columns based on the findings of the experimental and analytical studies to facilitate the use of these columns in future studies or field applications.

ES.9 Conclusions

The following conclusions were drawn based on the experimental and analytical investigations:

- The NCHRP 13-parameter rating system was found viable in identifying the best repairable bridge column detailing alternatives for testing. This rating system may be used for the development and evaluation of any new repairable column alternatives.

- CIP failed by the longitudinal bar fracture after extensive concrete spalling. The lateral strength of CIP was 65.4 kips (291 kN) with a drift capacity of 8.96%.

- Testing of RPH-PC-R was stopped at 10% drift to avoid setup damage, which was right before reaching the 15%-drop-in-force limit (as the failure point). SCC spalling was observed above the neck section mainly caused by compressive forces of BRR pressing clamping collars to SCC. Furthermore, a Z-shape bending of BRR was seen, which limited their replacement. The lateral strength of RPH-PC-R was 74.7 kips (332.3 kN), which was 14.2% higher than that of CIP. The drift capacity of RPH-PC-R was 9.80%, which was 9.3% higher than that of CIP.

- RPH-PF-R failed by the rupture of multiple tendon fuses with minimal UHPC damage. The lateral load capacity of RPH-PF-R was 59.8 kips (266 kN), which was 8.6% less than that of CIP. The drift capacity was 8.91%, which was very close to that of CIP.

- RPH-NP-R failed by the strength degradation mainly due to the rupture of neck bars at the rebar hinge. Minor UHPC spalling at the base of the column was observed. The lateral load capacity of RPH-NP-R was 86.9 kips (387 kN), which was 32.9% higher than that of CIP. The drift capacity of this column was 7.68%, which was 14.3% less than the CIP drift capacity.

- The Z-shape buckling of stainless-steel BRR used in the RPH-PC column made the repair by replacement very difficult. Furthermore, the column/footing dowels of RPH-PC were bent, and the column had some residual displacements which further complicated the placement of new BRR. Nevertheless, the incorporation of the steel tendons as the tension-only fuses in RPH-PF and PPH-NP eliminated any column/footing dowel damage and further helped with the recentering of the columns. Tendon fuse replacement was relatively quick and simple.

- No to minimal residual displacements are desired in any repairable column since the column should be close to its original position after the event easing the fuse replacement. All repairable columns showed smaller residual displacements compared with CIP. However, the residual displacement of RPH-PF was insignificant throughout the entire testing.

- A tendon fuse can double serve both as typical longitudinal reinforcement and self-centering reinforcement with an additional benefit of accessibility for inspection since they are exposed.

- Use of UHPC greatly reduced apparent cracking and spalling, even at the fuse failure.

- Overall, the proposed modeling methods for repairable columns can predict the column force-displacement relationship with a reasonable accuracy.

- Based on the 90 pushover parametric analyses, for a repairable column to surpass the displacement capacity of its corresponding CIP, the fuse length should be at least 25%, 50%, and 75% of the CIP analytical plastic hinge length using stainless-steel BRR, shape memory alloy BRR, and steel tendon fuse, respectively.

Overall, the proposed detailing alternatives for the three repairable columns were feasible since all columns were successfully repaired by fuse replacement and were retested. However, the repair-by-fuse-replacement is simple and easy if tension-only members are used as the external fuses. Furthermore, the three repairable columns exhibited comparable seismic performance compared with CIP with smaller residual displacements. Nevertheless, all repairable columns had lower initial stiffness compared with CIP and exhibited stiffness degradation between the two tests.

CHAPTER 1. INTRODUCTION

1.1 Introduction

Bridges designed with current seismic codes exhibit large displacement capacities, and the bridge total collapse is prevented. However, damage of ductile members is allowed at this performance level. In reinforced concrete (RC) bridges excited by ground shaking, columns are the target ductile members in which concrete cover, core, and reinforcement may damage, and the column may not return to its original position. Minor damages are usually repaired but excessive damages such as core crushing, bar buckling, and/or bar fracture are hard to repair and will usually result in the column or bridge replacement. According to FHWA, approximately 25% of the US bridges require rehabilitation, repair, or total replacement. Furthermore, within the next 50 years, many bridges located in the 16 seismic prone states of the nation will experience large earthquakes that may cause significant damage. Induced seismic activities in formerly non-seismic states such as Oklahoma may also damage bridges with poor seismic detailing. New detailing and enhanced materials are emerging to reduce the damage of RC bridge columns minimizing the need for repair or replacement after an event. Low- or no-damage detailing may be attractive to bridge owners in seismic regions due to a reduced cost associated with the repair or replacement of the bridge. Columns can be designed to be low damage using advanced materials and/or novel detailing.

Advanced materials such as ultra-high performance concrete (UHPC) and engineered cementitious composites (ECC) may be used in place of conventional concrete to provide some tensile capacity and to reduce cracking and spalling of concrete. Incorporation of different reinforcement such as stainless steel (SS) or micro-composite multi-structural formable (MMFX) steel may increase the strength and overall stiffness of the RC column while reducing reinforcement corrosion. The use of shape memory alloy (SMA) bars may eliminate residual displacements by providing recentering. Furthermore, fiber reinforced polymer (FRP) wraps can reduce concrete damage by providing a significant confinement.

A few accelerated bridge construction (ABC) details have been proof tested in laboratories and found suitable for bridge columns located in high-seismic regions of the nation: pocket connections, mechanical bar splice connections, and grouted duct connections. In a pocket connection, also known as socket connection, a fully precast column can be secured in a large void in the column adjoining member and then be grouted. A type of mechanical bar splice, e.g., grouted, is used in mechanically spliced columns. In a grouted duct connection, column longitudinal bars are extended out of the column, are placed in individual ducts, and then are grouted. Columns can be axially pre-stressed or post-tensioned to reduce residual displacements, which is called a rocking mechanism. When another type of reinforcement is used in addition to the tensioning reinforcement, the combined system is called a hybrid rocking column.

It is feasible to combine the innovative detailing such as ABC with advanced materials to expedite construction, provide additional ductility to RC columns, and reduce column damage. For example, a precast column utilizing pocket connection and a rubber bearing in the plastic hinge region will exhibit no damage and will have higher displacement capacity.

The present work is to advance the state-of-the-art column design with a new concept of repair-by-replacement methodology, such as those used in the car industry. It might also be possible to expose column bars for a quick replacement after an event. The benefits can be maximized if ABC detailing and advanced materials are incorporated in a repairable design.

1.2 Objective and Scope

The main objective of this study is to develop new details for RC bridge columns that are repairable through component replacement. To achieve this goal, advanced materials and ABC detailing are combined to develop feasible repairable alternatives. All repairable precast column alternatives are assessed through a 13-parameter evaluation method to select best details for experimental investigation. Of the top candidates, three repairable precast columns will be selected, constructed, and tested and the results are compared with a reference cast-in-place (CIP) column. All specimens will be half-scale and tested under a slow cyclic loading at the Lohr Structures Laboratory on the campus of South Dakota State University. Each column is tested twice under the same loading. In the second test of each specimen, the column exposed fuses are replaced to practice repair through replacement. Post-test and parametric analyses will be performed to better understand the performance of repairable columns. Furthermore, design and construction guidelines are proposed for repairable precast bridge columns based on the findings of the study.

1.3 Document Outline

Chapter 1, the present chapter, consists of an introduction, scope of work, and a document outline. A literature review is included in Chapter 2 including studies on both advanced materials and low-damage bridge columns. Chapter 3 discusses the development of 20 repairable column alternatives and a rating system to evaluate them for further investigation. Experimental investigation of the four, half-scale bridge columns is discussed in Chapter 4. Furthermore, Chapter 5 includes the analytical investigation of the repairable precast column test specimens. A parametric study was carried out in Chapter 6. Chapter 7 provides design and construction recommendations for repairable columns. Chapter 7 provides a summary and conclusions of the experimental and analytical investigations for the project.

CHAPTER 2. LITERATURE REVIEW

2.1 Introduction

Novel columns may improve the bridge seismic performance and lower its damage thus minimizing the repair need after an earthquake. The enhanced performance of a novel columns can be achieved using advanced materials and/or new detailing. Advanced materials for reinforced concrete bridges can improve column ductility, concrete confinement, and reduce cover spalling while novel column detailing can minimize residual displacements and may further add to the displacement capacity. This chapter presents a review of past studies on advanced materials and novel bridge columns.

2.2 Advanced Materials

Advanced materials can be utilized in the design of concrete bridge columns to improve performance, to reduce damage, and/or to increase concrete confinement. Advanced materials included in this review are ultra-high performance concrete (UHPC), engineered cementitious composite (ECC), fiber reinforced polymer (FRP), and shape memory alloy (SMA).

2.2.1 Study by Cruz Noguez and Saiidi (2012)

Cruz Noguez and Saiidi (2012) tested a 25%-scale, four span bridge constructed with advanced materials under shake table. A two-column bent was built with nickel-titanium (NiTi) SMA as longitudinal bars and ECC in the plastic hinge region (**Fig. 2.1a**). The second two-column bent was constructed with conventional concrete and a rocking mechanism. The third bent incorporated an elastomeric pad in the plastic hinge. In these columns the longitudinal bars were extended through the rubber pad, which was shimmed to prevent buckling. A steel pipe was included in the pad to take shear forces. Concrete blocks and lead pallets totaling 180 kips were placed on the post-tensioned bridge deck to provide an axial load and the bridge was subjected to increasing amplitudes of the 1994 Northridge earthquake record in the longitudinal direction.

a) Column Detailing
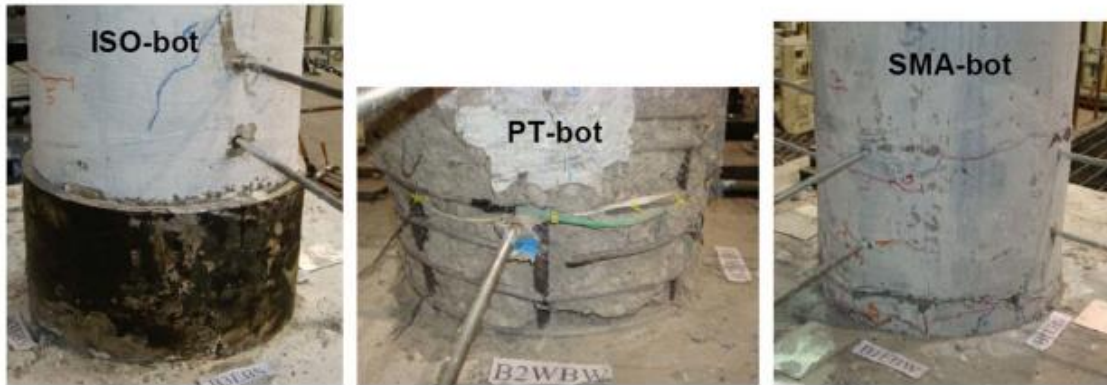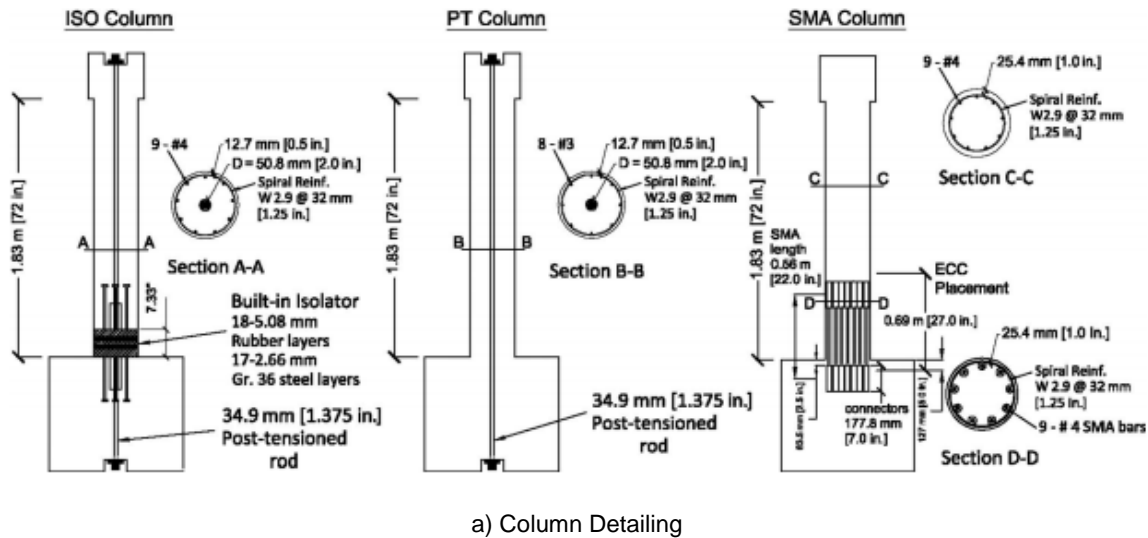
b) Column Damage
Figure 2.1. Column Detailing and Damage (Noguez and Saiidi, 2012)

Results of the testing indicated that all three bridge bents had high displacement capacities and negligible residual displacements. The bent incorporating the elastomeric pads reached the highest displacement, and a minimal damage was reported in the plastic hinge region of either the elastomeric pad bent or the bent incorporating SMA bars and ECC (**Fig. 2.1b**). All three columns exhibited high levels of damage in the hinge region at the column-cap beam interface, indicating the need to use the same design and materials at both the top and bottom of the columns. The post-tensioned bent without the rubber pad had low residual displacement due to its self-centering capability but the conventional concrete of this column exhibited a significant damage including hoop fracture. Overall, the test results showed that the incorporation of the advanced materials in two out of the three bents improved the bridge performance by allowing for the bridge to remain in service after the design level earthquake.

2.2.2 Study by Finnsson (2013)

Finnsson (2013) studied the use of hybrid fiber-reinforced concrete (HyFRC) shells to aid in the seismic capacity of unbonded pre-tensioned bridge columns. Two specimens were constructed and tested under cyclic loading with a 200-kip (890-kN) horizontal actuator and a constant axial load of 159 kips (707 kN). The columns were constructed with precast HyFRC shells within the plastic hinge region which were then filled with conventional concrete and pretensioned using eight steel strands (**Fig. 2.2**). The strands were

unbonded over the center 50% of the column length using plastic sleeves and prestressed to approximately 14.4 kips (64 kN). Columns were connected to the footings using grouted socket connections. In one column, stainless steel (SS) bars were used as longitudinal reinforcement in lieu of conventional steel bars.
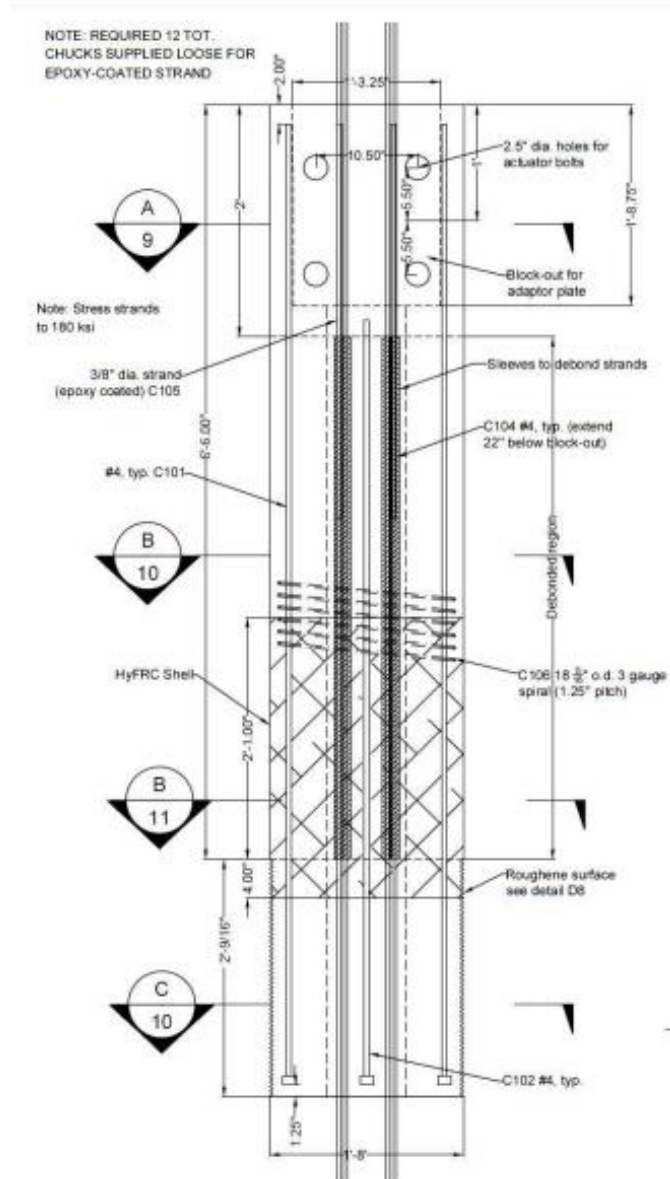
Figure 2.2. Column Detailing by Finnsson (2013)

The results of cyclic testing indicated that HyFRC in the plastic hinge region delayed both spalling and bar buckling when compared with columns with similar detailing but without HyFRC tested by Davis et al (2012). Both columns were more ductile than the reference columns with limited strength degradation and damage at higher drifts (**Fig. 2.3**). No residual displacement was recorded in the columns up to a drift ratio of 5% at which the prestressing strands yielded, and bond slip began was significant. The column constructed with stainless steel longitudinal bars slightly dissipated more energy than the conventional steel column and bar fracture was delayed.

Figure 2.3. Column Performance by Finnsson (2013)

2.2.3 Study by Motaref et al. (2014)

Motaref (2014) studied the use of different advanced materials in the plastic hinge region of segmental bridge columns. Five one-third scale columns were constructed, each with a base segment attached to the footing with normal bars to provide a higher energy dissipation capacity. A conventional concrete column was used as reference while other columns included a rubber elastomeric bearing pad, ECC, and a carbon fiber reinforced polymer (CFRP) wrap. The reference column was repaired with a CFRP wrap after the first test and resubjected to the same loading. All the columns were post-tensioned to create a recentering effect and to provide continuity between the column segments, and were then subjected to an increasing amplitudes of the Sylmar earthquake record (**Fig. 2.4a**) on shake tables at the University of Nevada, Reno.
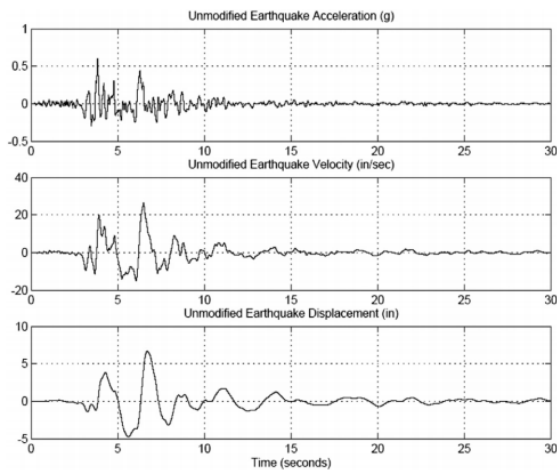
a) Sylmar Station Time History   b) Column Damage
Figure 2.4. Earthquake Time History and Column Damage by Motaref et al. (2014)

It was found that residual drifts were minimal in all columns due to the unbonded post-tensioning system. All columns incorporating advanced materials outperformed the reference column in terms of damage (**Fig. 2.4b**), energy dissipation, and displacement capacity. The primary form of damage was cover spalling which was reduced in the ECC column when compared to the others. Use of CFRP jacketing significantly improved confinement in the plastic hinge area and the rubber bearing increased the natural period of the column while reducing damage. Overall, all three types of advanced materials significantly improved the seismic performance of the columns.

2.2.4 Study by Nakashoji and Saiidi (2014)

Nakashoji and Saiidi (2014) tested three, 30%-scale square bridge columns in which one was a reference cast-in-place (CIP) column and two were novel columns. The novel columns incorporated SMA bars in the plastic hinge region coupled to the main longitudinal steel bars (**Fig. 2.5a**) using headed couplers, and ECC was used on the entire column length. The columns were tested under an increasing cyclic lateral loading using a 220-kip (979-kN) actuator and 140 kips (623 kN) axial load were applied. ECC was removed after testing to determine if any damage occurred to the couplers or SMA bars.

a) SMA Bar (middle) Coupled to Conventional Steel Bars (at Ends)
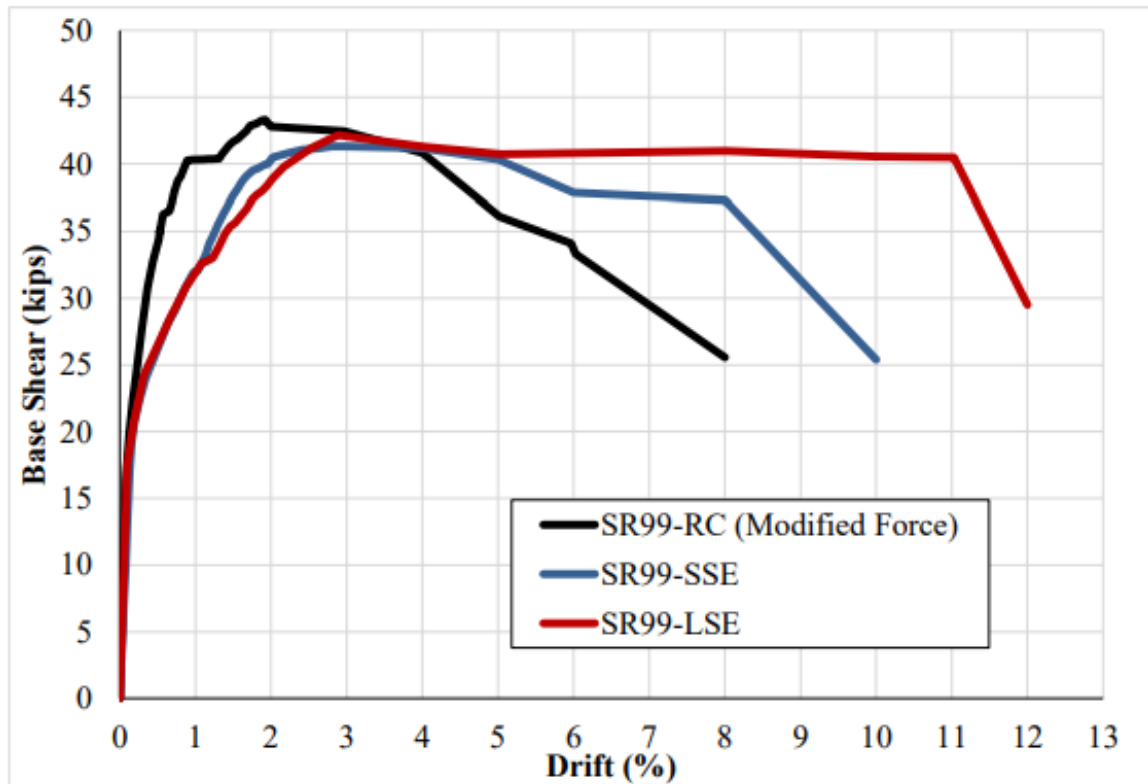
b) Force–Displacement Relationship

Figure 2.5. SMA Coupled Rebar and Force-Displacement Relationship (Nakashoji and Saiidi, 2014)

Flexural cracks were observed and comparable for all three columns up to a drift ratio of 2%. Spalling of the CIP column occurred from 4% drift onward while use of ECC in the two novel columns significantly reduced cover damage. A large crack at the base of each ECC column was seen, which was repairable. The CIP column and one of the novel columns experienced bar fracture at 8% drift; however, testing of

the novel column continued since there was minimal drop in the lateral strength. ECC seemed to increase the column confinement (by minimal cover spalling) as there was limited bar buckling in the two ECC columns compared with CIP. No damage was observed to the headed couplers and they proved to be a viable option to reduce costs by only using SMA bars in a small portion of the column. Overall, the two novel columns exhibited a higher drift capacity (**Fig. 2.5b**), lower residual drift, and lower damage than the CIP column due to the incorporation of ECC and SMA bars.

2.2.5 Study by Panagiotou et al. (2015)

Panagiotou (2014) tested two bridge columns constructed with highly flowable hybrid fiber reinforced concrete (HYFRC) and novel longitudinal reinforcement. The reinforcing bars of the first column were unbonded with tape near the bottom of the column and within the top of the footing to allow the column to rock. The second column was constructed with stainless steel longitudinal bars and an additional portion of HYFRC cast into the footing beneath the column to provide continuity of concrete properties (**Fig. 2.6a**). The specimens were tested unidirectionally under a cyclic lateral load reversal and a constant vertical axial load of 100 kips (445 kN).
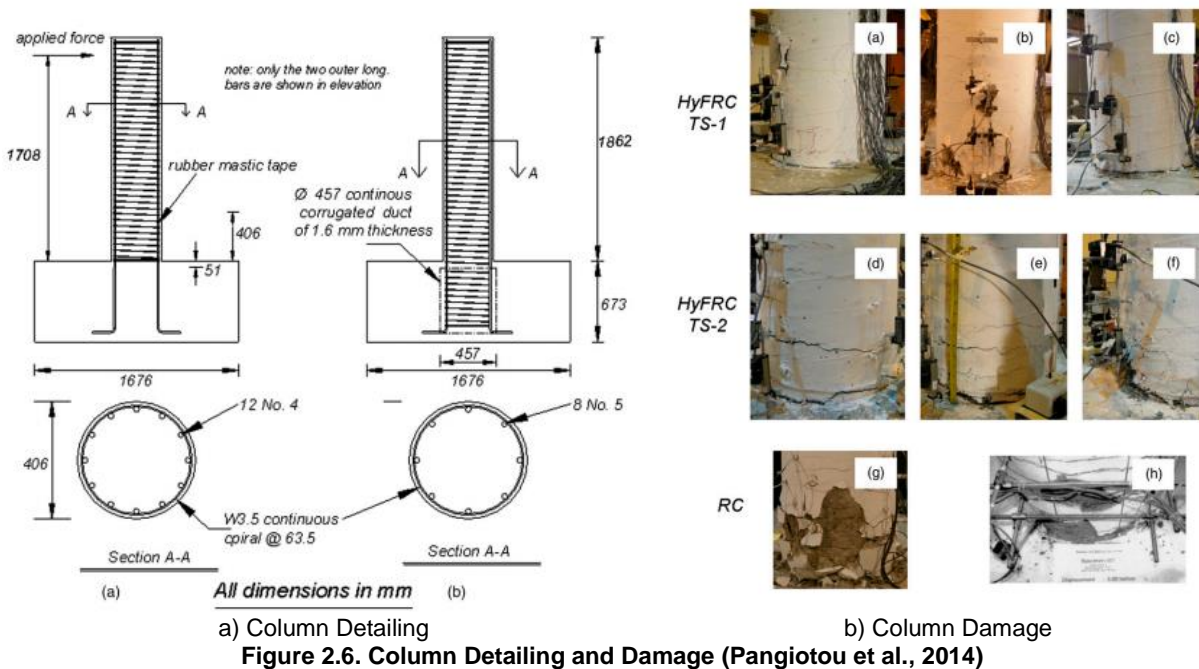
a) Column Detailing   b) Column Damage
Figure 2.6. Column Detailing and Damage (Pangiotou et al., 2014)

The two HYFRC columns were compared with a conventional reference column constructed by Terzic and Stojadinovic (2010) with an identical detailing except a larger transverse reinforcement ratio was used. Both specimens exhibited a reduced spalling (**Fig. 2.6b**) when compared to the reference column with an increase in the lateral strength. Stainless steel longitudinal rebar in the second column did not rupture until a drift ratio of 9.5% while bar fracture was reported in the first column at a drift ratio of 6%.

2.2.6 Study by Ibrahim et al. (2016)

Ibrahim (2016) considered the combination of steel and FRP reinforcement for square concrete bridge columns. Two conventional reference columns, one with a lower longitudinal reinforcement ratio and an added basalt FRP (BFRP) jacket, were constructed as well as five FRP steel-reinforced concrete (FSRC) columns. The FSRC columns were constructed with differing combinations and detailing of steel and BFRP bars (**Fig. 2.7**), some with additional roughening to increase bond strength with the concrete, as

well as BFRP jackets. The columns were subject to a constant axial load of 9 kips (40 kN) and a reversed cyclic loading sequence using a 157-kip (700-kN) actuator.
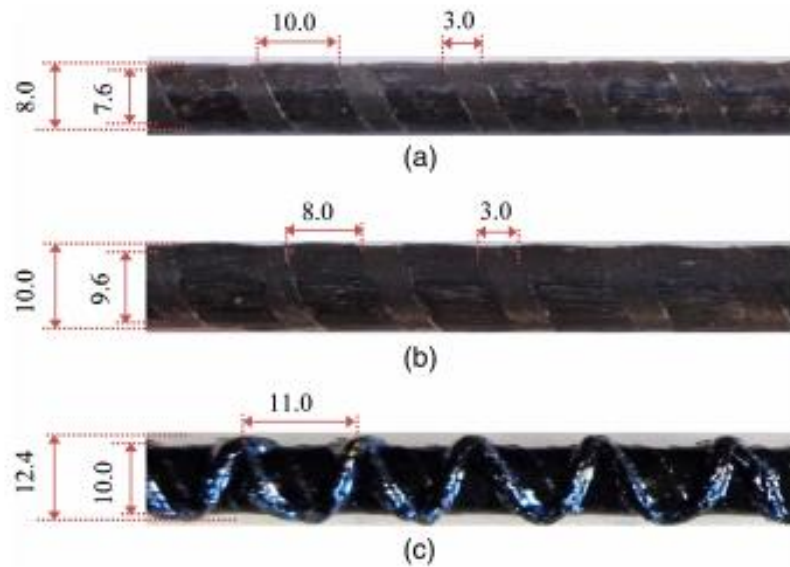
a) Smoothed and Roughened BFRP Bars
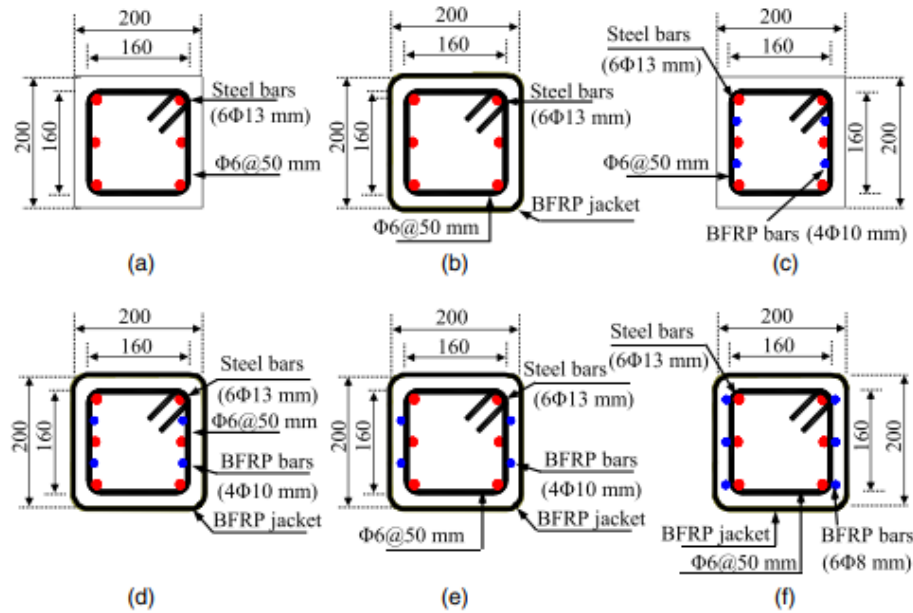
b) Column Cross Sections

Figure 2.7. BFRP Bars and Column Cross Sections (Ibrahim et al., 2016)

Analysis of test data indicated that FRP reinforcement and jacketing had no noticeable effect on the initial stiffness of the columns; however, the residual displacement decreased by up to 30%. Columns with roughened BFRP reinforcement failed through rupture of the bars at high strength while smooth BFRP reinforced columns failed at a smaller force and ductility due to local bond-slip failure. Overall, FRP jacketing added a significant confinement to the columns while the use of BFRP reinforcing bars needs to be further studied.

9

2.2.7 Study by Zhang et al. (2019)

Zhang et al. (2019) tested three bridge columns with polypropylene fiber reinforced ECC (PP-ECC) jackets with different thicknesses in the plastic hinge region. The PP-ECC was limited to the cover concrete due to the high cost of ECC as well as evidence indicating that ECC in the core has a lower effect on the column ductility than the cover. Two of the 1/5th-scale columns incorporated precast PP-ECC jackets with thicknesses of 50 mm and 100 mm up to a height of 1.33 times the width of the square cross section while a third column was cast with a full PP-ECC plastic hinge. PP-ECC was additionally extended 100 mm into the footing while conventional concrete was utilized for the remaining portion of the columns and footings. All columns were tested under a constant axial load of 20 kN and in flexure using a cyclic loading in the horizontal direction.
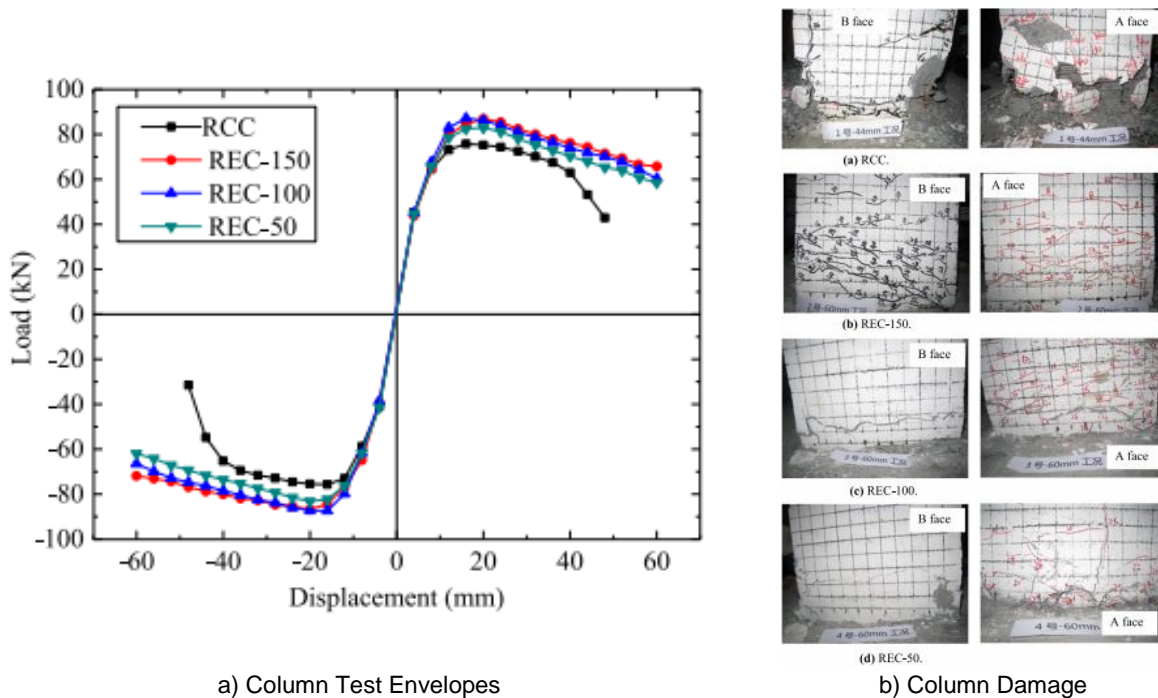
a) Column Test Envelopes   b) Column Damage
Figure 2.8. Column Test Envelopes and Damage (Zhang et al., 2019)

The displacement capacity was increased in the novel columns when compared with the reference column (**Fig. 2.8a**) while the initial stiffness was reduced as the thickness of the PP-ECC jackets was increased. Spalling within the plastic hinge region of the three PP-ECC columns was significantly reduced when compared to a reference cast-in-place column (**Fig. 2.8b**). Cracking was limited to the PP-ECC region while some expansion of the PP-ECC jackets was noted due to crushing of the conventional concrete used in the core. Altogether, the differing thickness of the PP-ECC jackets had little effects on the displacement or ultimate strength of the columns while the volume of PP-ECC used could be decreased up to 44% to lower construction costs.

2.2.8 Study by Alian Amiri (2020)

Alian Amiri (2020) tested bridge columns using high strength MMFX steel bars. Six columns were tested. The first three columns constructed using conventional Grade 60 (413-MPa) steel bars with differing transverse reinforcement ratios and some bar debonding at the column-footing interface. Other three columns utilized grade 100 (690-MPa) Chrome 9100 bars from MMFX conforming to ASTM A1035 with identical detailing to each of the respective first three columns. The columns were shake

table tested under both short- and long-term duration records from the 2011 Tohoku Japan earthquake and the 1999 Kocaeli Turkey earthquake with a constant axial load of 80 kips (356 kN).
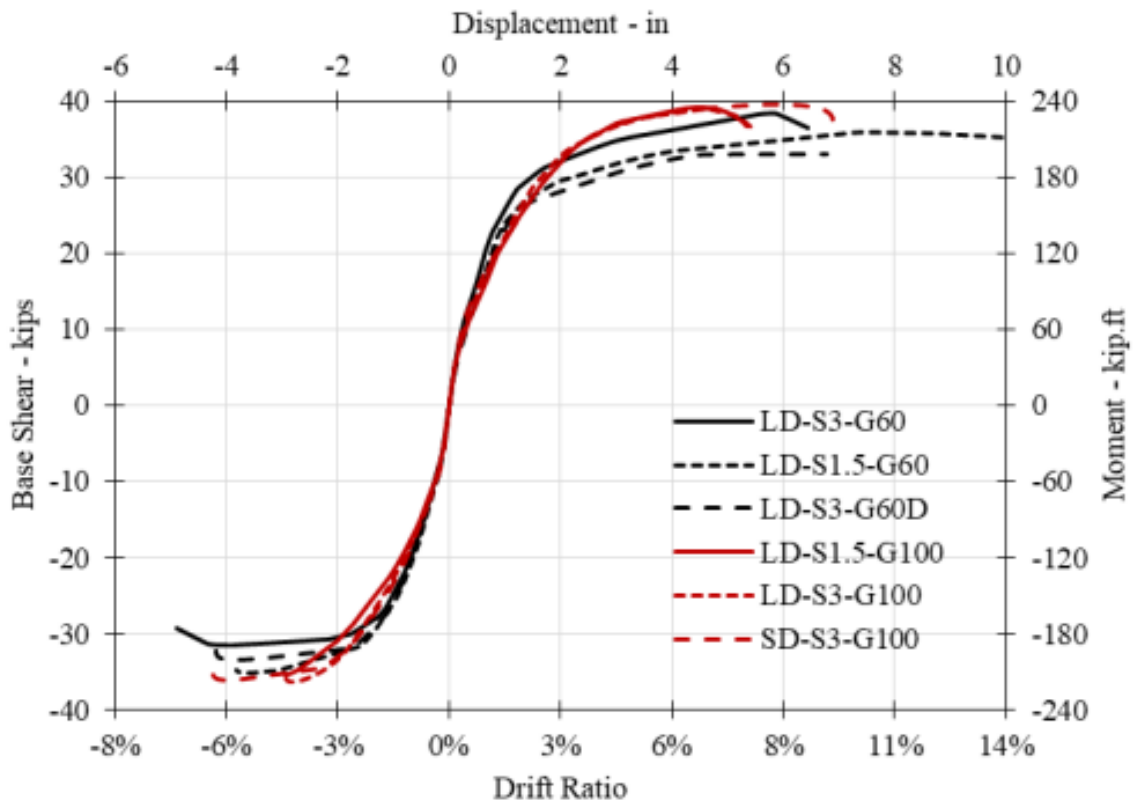
Figure 2.9. Column envelopes by Alian Amiri (2020)

Damage between the two sets of columns was similar and was confined to the plastic hinge regions of each specimen. Higher shear stresses were recorded in the columns with MMFX steel as well as higher number of inclined shear cracks. The conventional steel columns failed by bar buckling followed by bar rupture while the MMFX columns had a greater buckling resistance and failed by bar fracture. While smaller tie spacing and debonding of bars at the column-footing interface increased displacement capacity in the conventional columns, there was no apparent effect of using high strength steel. The columns with MMFX steel rebar had a higher yield displacement and similar force capacity to the conventional columns (**Fig. 2.9**), but they showed a lower displacement capacity than reference columns. All columns failed under 100% of the ground motion. The study recommends more testing with MMFX bars before field applications in seismic regions.

2.3 Novel Bridge Columns

Novel column detailing may also be utilized to reduce damage and residual displacement in the event of an earthquake. The following studies incorporated advanced detailing in their design and/or used advanced materials to improve column seismic performance.

2.3.1 Study by ElGawady and Sha'lan (2011)

ElGawady and Sha'lan (2011) investigated the seismic behavior of self-centering bridge bents constructed with precast concrete-filled fiber tubes (CFFT). Five, two-column bents were constructed and tested under cyclic loading including a reference CIP bent and four precast post-tensioned (PPT) bents of CFFT segments stacked and connected with a post-tensioning force of 33.9 kips (151 kN). The PPT-CFFT columns were constructed using varying numbers of segments, steel angles at the base as external energy dissipaters, and/or neoprene pads at the column-footing and column-cap beam interface as shown in **Fig. 2.10**.
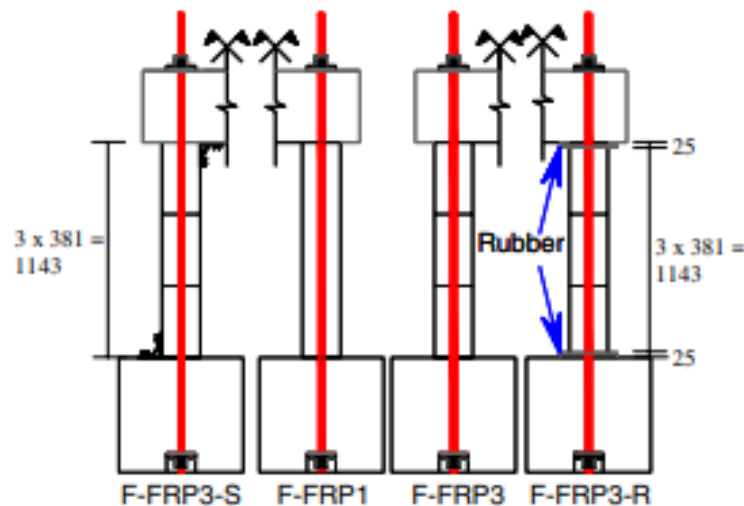
Figure 2.10. Column Models by ElGawady and Sha'lan (2011)

All four of the PPT-CFFT columns showed higher drift capacities and significantly lower residual drifts than the reference column due to the restoring force from the rocking mechanism. Damage was concentrated within the tubes and between the column and footing as rocking occurred at higher drift ratios. Including neoprene pads at the column joints greatly reduced the initial stiffness and force capacity while increasing the displacement capacity. Differing numbers of CFFT segments had a little effect on either the force or displacement capacities. The incorporation of steel angles as external energy dissipaters increased the viscous damping of the specimens but also resulted in higher residual strains.

2.3.2 Study by Guo et al. (2016)

Guo et al. (2016) tested the combination of aluminum external energy dissipaters and glass fiber-reinforced polymer (GFRP) jackets on self-centering precast concrete (SCPC) bridge piers. One reinforced concrete (RC) reference column and three 1/3-scale precast specimens were tested under a cyclic loading up to 4% drift ratio with an axial load of 27 kips (120 kN). Two of the precast columns incorporated GFRP jackets of different lengths in the plastic hinge area while the third was not constructed with a jacket (**Fig. 2.11a**). All three columns were post-tensioned to 22.5 (100 kN) using two basalt fiber-reinforced polymer (BFRP) tendons and utilized external energy dissipaters (**Fig. 2.11b**) in the form of "dog-boned" (reduced diameter) aluminum bars restrained against buckling inside confining tubes filled with epoxy. Aluminum bars with modified properties were used to prevent corrosion as the

energy dissipaters were incorporated outside of the column to allow for replacement after a seismic event. The columns were initially tested without the energy dissipaters and with differing post-tensioning forces.

Test number	Specimen	Height of GFRP jacket (mm)	F_0 (kN)	Type of tendons	Energy dissipaters	ED position	ED diameter (mm)[a]	ED length (mm)[b]
1	SC-1	500	120	BFRP	NA	NA	NA	NA
2			220					
3			220		Four aluminum bars	East and west	15	100
4			220		Four aluminum bars	North and south	15	100
5			220		Four aluminum bars	East and west	15	200
6	SC-2	300	120	BFRP	NA	NA	NA	NA
7			220					
8			120	Steel strands				
9			220					
10			220	BFRP	Four aluminum bars	East and west	15	100
11			220		Four aluminum bars	North and south	15	100
12			220		Four aluminum bars	East and west	12	100
13	SC-3	NA	220	BFRP	NA	NA	NA	NA
14			220	Steel strands				
15	RC	NA	220	NA	16 longitudinal steel rebars	NA	NA	NA

Note: NA = not available.
[a]Diameter of the weakened part of the aluminum bar.
[b]Length of the weakened part of the aluminum bar.

a) Column Test Matrix
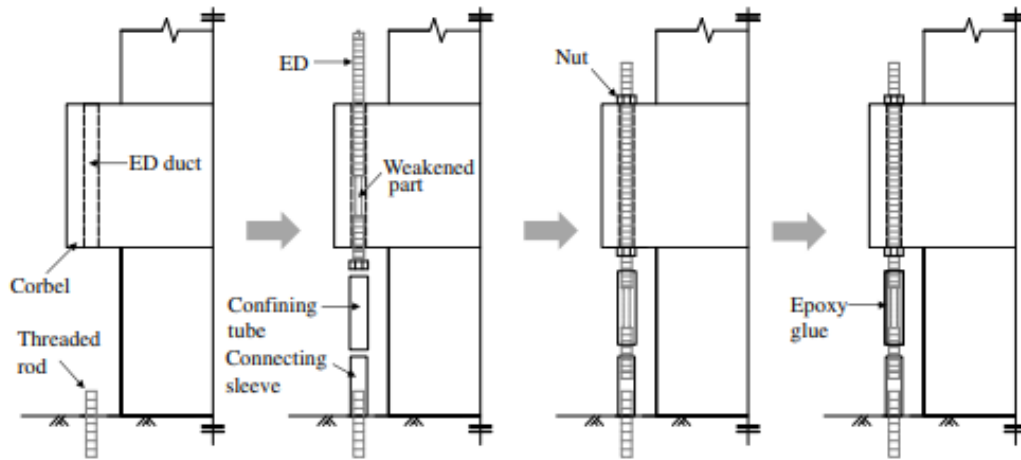
b) External Energy Dissipater Detailing
Figure 2.11. Column Matrix and Detailing (Guo et al., 2016)

Evaluation of the hysteretic results indicated that addition of the energy dissipaters changed the shape of the plots from bilinear to flag while the initial stiffness was also increased. A small amount of slip was recorded between the columns and the footing which added to the horizontal displacement. The use of shorter external energy dissipaters increased plastic strains in the aluminum bars and caused them to rupture at earlier drifts. The use of GFRP jacketing eliminated cracking and spalling of concrete when compared to the column without GFRP while the jacketing also added to the energy dissipation of the specimens. The higher post-tensioning force was also found to increase the initial stiffness and lower the residual drift when compared to the reference column. Overall, the SCPC piers showed desirable self-centering and energy dissipation characteristics and may be suitable for moderate to large earthquakes.

2.3.3 Study by Ichikawa et al. (2016)

Ichikawa et al. (2016) tested three columns under orbital bilateral cyclic loading to investigate the use of post-tensioning combined with UHPC in the plastic hinge region. The first two square specimens were identical and constructed with UHPC jackets in the plastic hinge region filled with conventional concrete

while the third column was similar in detailing except that the UHPC jackets were constructed in sections, left hollow rather than filled with concrete, and post-tensioned together (**Fig. 2.12a**). A constant axial load of 19.4 (86.1 kN) was applied and two of the columns were loaded in a circular orbit at increasing drift ratios while the second of the two non-tensioned columns was loaded in a hybrid test setup to simulate the acceleration record of the 1995 Kobe, Japan earthquake.

a) Column Detailing
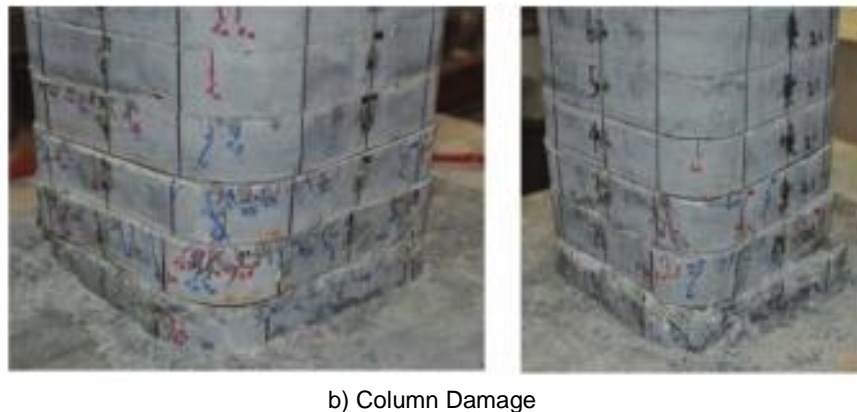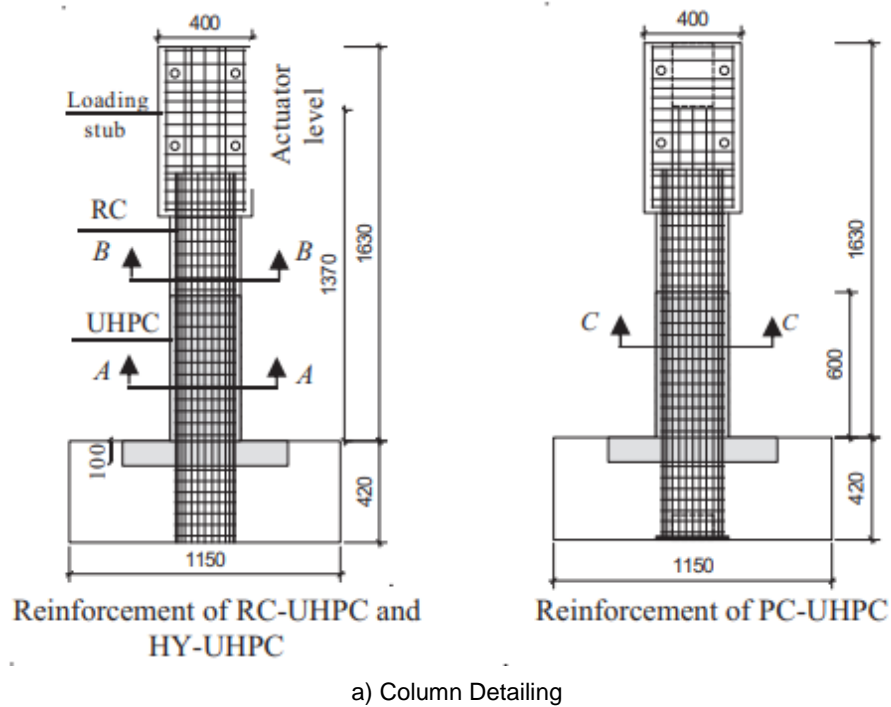
b) Column Damage

Figure 2.12. Column Detailing and Damage (Ichikawa et al., 2016)

Twisting was observed in the two columns tested with the circular orbit (**Fig. 2.12b**). However, limited spalling or concrete crushing was observed in either specimen. Rocking was observed between the segments of the post-tensioned column as well as greater levels of torsion, which resulted in residual twisting between segments. The post-tensioning bar in the segmental column yielded at a drift ratio of 3.5% at which point there was a significant loss in tension force. Less damage was observed in the segmental column as well as lower levels of energy dissipation. The column tested under the Kobe earthquake acceleration record reached higher drift ratios due to the non-circular testing cycles, and the failure occurred in the form of crushing of UHPC in the plastic hinge region.

2.3.4 Study by White and Palermo (2016)

White and Palermo (2016) utilized different precast connections in three half-scale concrete bridge columns. The column-to-footing connections included an emulative socket connection, a non-emulative socket connection incorporating post-tensioning, and a non-emulative coupled connection utilizing energy dissipators in the form of grade 300 steel bars in the plastic hinge region covered with grout (**Fig. 2.13a**). The two non-emulative columns were designed to rock at the base. The non-emulative socket column was a previously tested specimen that had been repaired using FRP wrap while the coupled column was designed to be repaired by removing the grout and replacing the energy dissipators which were connected to the column and footing using threaded couplers. The columns were tested under a quasi-static bilateral loading (**Fig. 2.13b**) to a displacement at which the non-emulative coupled column was repaired.

a) Connection Detailing

Drift Cycles (%)	
Uniaxial	Biaxial
0.25	0.33
0.35	0.46
0.50	0.65
0.75	0.98
1.00	1.30
1.50	1.95
2.00	2.60
2.50	3.25
3.00	3.90
4.00	5.20
5.00	6.50
6.00	7.80

b) Biaxial Loading Protocol
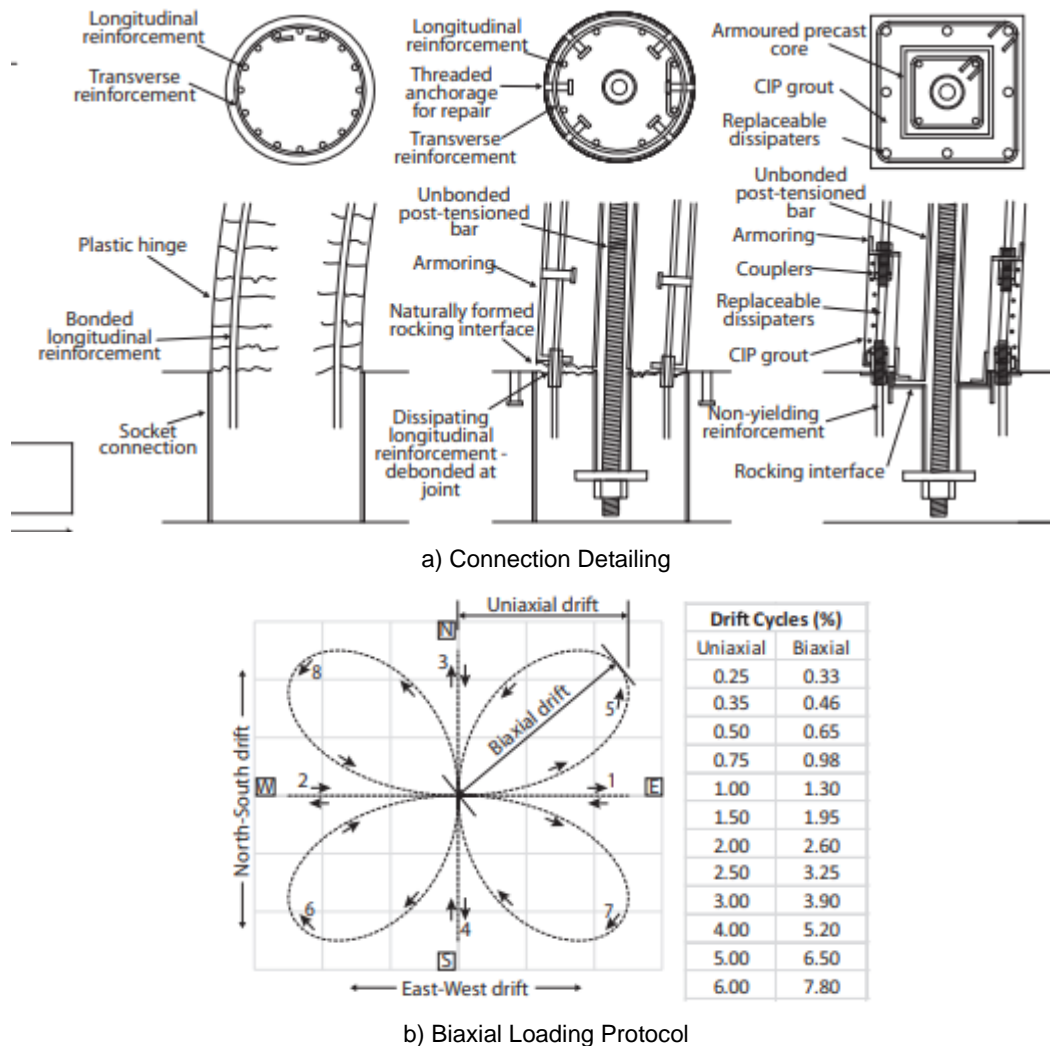
Figure 2.13. Connection Detailing and Biaxial Loading Protocol (White and Palermo, 2016)

Significant damage occurred in the emulative socket connection column while the damage was significantly reduced in the two non-emulative connection columns. All spalling in the coupled column occurred in the grouted region and a higher energy was dissipated in the two socket connection columns. The emulative socket connection column had comparable performance to that of a conventional cast-in-place column. Residual drift was limited in the two non-emulative columns due to the rocking mechanism. Residual drifts were slightly higher than expected in the coupled column due to an

unintentional bonding between the column and footing. Further, a premature failure of the energy dissipators in the repaired column was observed due to a design error as well as difficulties with realigning the replacement energy dissipators.

2.3.5 Study by Tazarv and Saiidi (2016)

Tazarv and Saiidi (2016) tested three half-scale column models using low damage materials and precast connections. All three columns were precast with hollow cores which were then filled with self-consolidating concrete (SCC) after column erection. The first column was connected to the footing by extending the column longitudinal rebar into a series of corrugated ducts which were then filled with UHPC. The second column incorporated debonded longitudinal rebar with an unbonded length of 11 in. (280 mm) within a pedestal. The column was connected to the pedestal using grouted couplers. The connection details for the third column were the same as the first column with UHPC filled ducts. Nevertheless, SMA bars were used in the plastic hinge region and connected to the steel longitudinal bars with headed couplers. Furthermore, ECC was used to construct the lower 3 ft (914 mm) of the column shell. A 220-kip (979-kN) actuator was used to test the columns under a slow reversed cyclic loading with an axial load index of 10%.
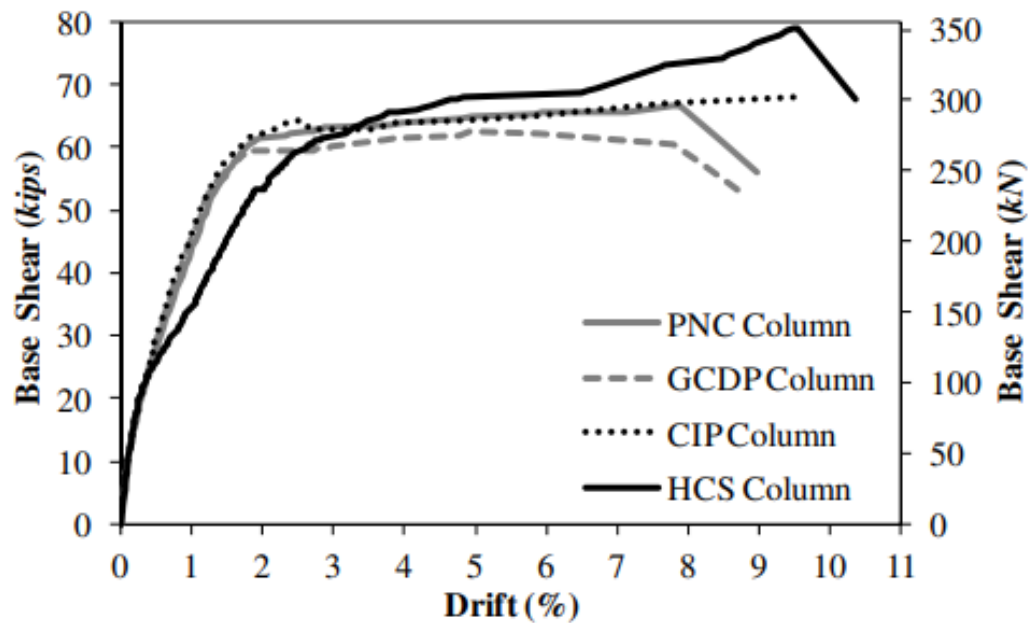
Figure 2.14. Column Test Envelopes (Tazarv and Saiidi, 2016)

Bar fracture was the failure mode for all three columns with no column-to-footing connection damage. No bar pullout was observed in any of the couplers or UHPC filled ducts while it was found that UHPC had up to 8 times the bond strength of conventional concrete. The first two columns incorporating conventional steel longitudinal bar, which failed at slightly lower drift ratios than the reference CIP column (**Fig. 2.14**), while the third column with SMA and ECC had a higher displacement capacity than the reference column, and substantially lower residual displacements. Overall, it was determined that these precast column connections were viable alternatives to conventional construction methods and the incorporation of advanced materials such as ECC, UHPC, and SMA bars significantly enhanced the seismic performance of the columns.

16

2.3.6 Study by Wang et al. (2018)

Wang et al. (2018) tested the self-centering capability of three, 1/3-scale precast segmental post-tensioned bridge columns constructed with UHPC. The square columns were constructed using three hollow UHPC segments in addition to a cap beam and footing. Eight steel cables were post-tensioned to a force of 89.9 kips (400 kN) while eight mild steel bars unbonded near the footing were added in UHPC grout filled ducts to promote energy dissipation in addition to the 32 longitudinal steel bars (**Fig. 2.15**). The second column incorporated an increased post-tensioning force while the third column was constructed with additional energy dissipators. Lateral cyclic loading was applied using a horizontal actuator in addition to a 224.8-kip (1000-kN) applied axial load.
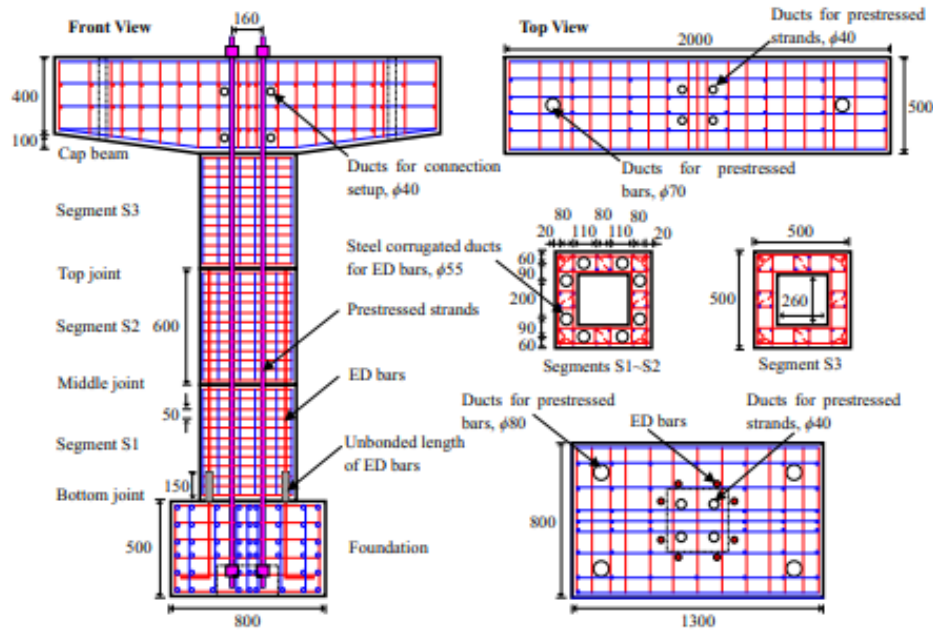
Figure 2.15. Segmental Column Detailing (Wang et al., 2018)

All three columns reached a drift ratio of at least 8% before fracture of their energy dissipators. No flexural or shear cracks were observed in UHPC of any of the columns; however, spalling was seen between the segments at higher drift ratios due to non-uniformity in the concrete surfaces. Slight sliding and uplift were recorded at the lowest joint, but this movement was reduced in the column with the increased post-tensioning force. Increasing the post-tensioning forces increased the overall ductility of the columns while additional energy dissipators decreased the ductility and significantly increased residual drifts.

2.3.7 Study by Mashal and Palermo (2019)

Mashal and Palermo (2019) tested a half-scale bridge column specimen with dissipative controlled rocking (DCR) connection utilizing post-tensioning and external energy dissipators. External metallic mini-dissipators of two different types were mounted to the column using steel brackets (**Fig. 2.16**). An initial post-tensioning force of 28.1 kips (125 kN) was applied to the threaded post-tensioning bars within the column using hydraulic jacks. A vertical 87.7-kip (390-kN) gravity load was applied with a vertical ram while a horizontal ram was used to displace the column laterally under a unidirectional quasi-static cyclic loading protocol.

Figure 2.16. Column with External Energy Dissipaters (Mashal and Palermo, 2019)

A gap was immediately noticed at the rocking interface at a drift ratio of 0.25%. No damage or strength degradation were observed up to a drift ratio of 3.0% at which point the test was stopped. There was significantly less damage in the DCR connection bridge bent than a comparison bent utilizing grouted socket and grouted duct connections. Residual displacement was also negligible in the DCR bent.

2.3.8 Study by Varela and Saiidi (2019)

Varela and Saiidi (2019) performed a shake table study on a ¼-scale, 2-span bridge model designed for disassembly. Novel materials and advanced precast connections were utilized to allow for quick construction as well as sustainable disassembly at the end of the bridge life without need for conventional demolition. Three, two-column bridge bents were constructed. One utilizing Copper-Aluminum-Manganese (CAM) SMA bars and ECC plastic hinges (EPH), one with Nickel-Titanium (NiTi) SMA bars and rubber plastic hinges (RPH), and another with NiTi SMA bars with EPH (**Fig. 2.17a**). The superstructure consisted of an RC deck and beams which were connected to the bents using pipe-pin connections to eliminate moments and allow for disassembly. The columns were wrapped in CFRP tubing while the SMA bars were connected to the main longitudinal reinforcement using threaded couplers. An axial load between 40 and 46 kips (177.9 and 204.6 kN) was applied to each column using RC blocks and the self-weight of the deck while the bridge was subject to increasing scaled amplitudes of

the Rinaldi earthquake record in the transverse direction. After initial testing, the bridge was disassembled, inspected, and reassembled for additional testing.
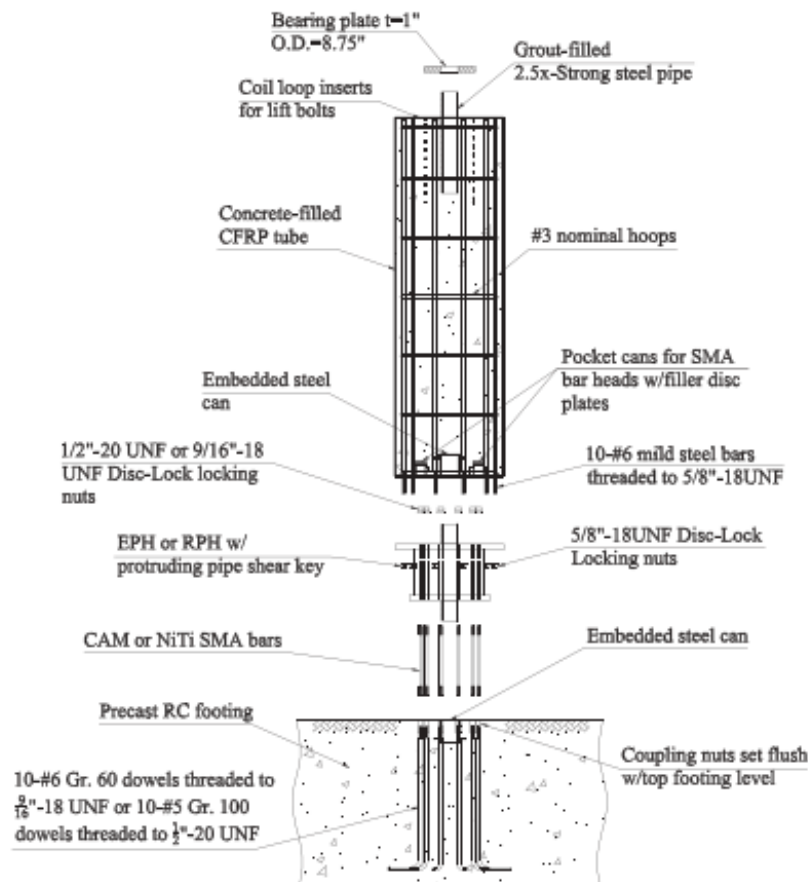
a) Column Detailing
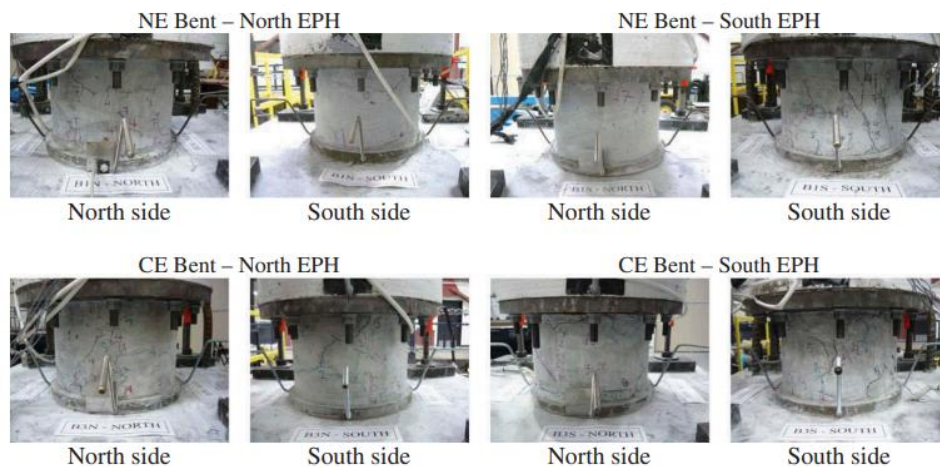
b) Column Damage

Figure 2.17. Column Detailing and Damage (Varela and Saiidi 2019)

Minimal damage was observed in the plastic hinges of the three bents (**Fig. 2.17b**) at drift ratios exceeding 6%. The column adjoining members remained elastic and damage free. Residual drifts remained under 0.4% and overall bent hysteretic behaviors were flag shaped due to the self-centering capability of the SMA bars. Rocking occurred at the footings and the segments of the columns which elongated the period of the bridge model and increased the displacement capacity. Disassembly and reconstruction of the bridge bents were successful in which the initial stiffness increased, and residual drifts decreased in the second set of testing. SMA bars fractured in two of the three bents during the last two runs. Overall, detailing for disassembly of bridge columns in seismic areas was proved feasible but further testing and development of design guidelines was necessary before implementation in the field.

2.3.9 Study by Han et al. (2019)

Han et al. (2019) investigated the combination of replaceable external energy dissipators and unbonded post-tensioning tendons. Three, 1/3-scale double column bridge bents were designed, constructed, and tested under a cyclic lateral loading. An axial load of 194.8 kips (866.4 kN) was applied. The bents incorporated reduced cross sections in the plastic hinge region which were encased with steel tubing as well as steel pipes as shear pin connections and steel plates at the column-footing and column-cap beam interfaces (**Fig. 2.18a**). The first column did not include external energy dissipators while the second and third columns included external "dog-boned" mild reinforcing bars and external buckling-restrained plates in the plastic hinge region respectively which were connected to the main longitudinal reinforcement. Each column in the bents was post-tensioned using four unbonded steel tendons with a total force of 94.4 kips (420 kN).
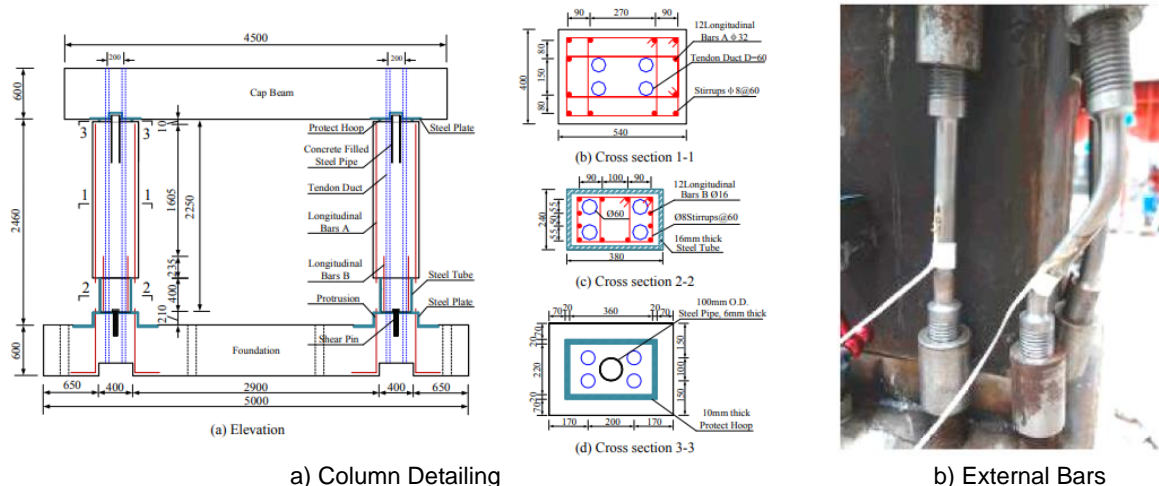
a) Column Detailing   b) External Bars
Figure 2.18. Column Detailing and Energy Dissipater Damage (Han et al., 2019)

Openings were recorded for all three bridge bents due to rocking at the column-footing connections; however, they were closed after each cycle due to the self-centering tendency of the columns. Only minor flexural cracks were seen in the specimens. The columns with external energy dissipators failed due to bar buckling (**Fig. 2.18b**) and plate rupture, respectively. The mild steel bars were not restrained against buckling and thus the third column had a better energy dissipation and self-centering capability than the second column while the first bent showed the lowest energy dissipation. All three bents had low residual drifts less than 1%, and the columns with external energy dissipators showed a higher lateral force capacity. It was also noted that an increase in post-tensioning force increases the lateral strength of the bents as well as the self-centering capacity.

2.3.10 Study by Jia et al. (2020)

Jia et al. (2019) studied the use of elastomeric pads as energy dissipaters in precast bridge columns. Four, 1/4-scaled bridge columns were constructed including a cast-in-place (CIP) column, a typical precast column with a grouted duct connection, and two precast columns using grouted duct connections and laminated and single-layer elastomeric pads, respectively (**Fig. 2.19a**). An additional steel pipe was included in the laminated elastomeric pad column to resist shear forces. For the three precast columns, longitudinal reinforcement was extended into corrugated metal ducts in the footing and filled with grout. The columns were tested under a quasi-static cyclic load with a constant axial load of 80.9 kips (360 kN).

a) Column Detailing
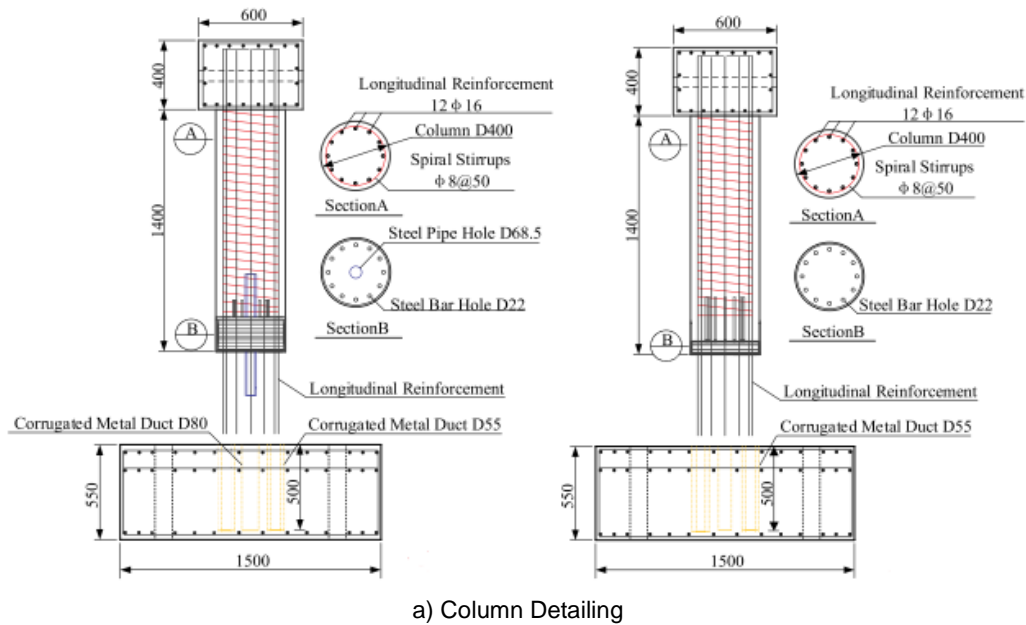
b) Column Damage

Figure 2.19. Column Damage and Cross Sections (Jia et al., 2016)

The use of elastomeric pads in the plastic hinge region significantly reduced concrete cover cracking and spalling (**Fig. 2.19b**). The pads also increased the energy dissipation through yielding of the unbonded portion of the rebars rather than concrete crushing as in the other two columns. Torsional deformation was noted in the rubber bearings which may have caused an uneven loading of the reinforcing bars, but no permanent damage was observed in the rubber. While the single-layer pad column exhibited better initial energy dissipation than laminated pad column, the pad dilated due to the alternating compressive forces. This column also had a lower initial stiffness and failed earlier due to a shorter debonding length of the bars. Meanwhile, the laminated pad column exhibited fewer and shorter cover cracks and had a smaller initial stiffness when compared to other columns. The grouted duct column without an elastomeric pad also proved to be a reliable alternative to the CIP column as it had similar seismic performance.

21

2.3.11 Study by Tazarv et al. (2020)

Tazarv et al. (2020) experimentally tested four, half-scale precast beam-column specimens under cyclic loading. The special moment resisting frame (SMRF) connections were designed using "strong column – weak beam" methodology to achieve a large displacement capacity. Exposed buckling restrained reinforcement (BRR) fuses were used as external energy dissipaters while a steel pipe and cup were incorporated to act as a shear pin at the beam-column interface (**Fig. 2.20a**). BRR fuses were connected to the main longitudinal reinforcement of the beam using headed mechanical bar splices for quick replacement. The column axial load was 68 kips (302 kN). Both unreduced and reduced diameter (dog-bone) steel bars were used in BRR. Each BRR was replaced with a similar conventional steel or SMA fuses after initial testing of each specimen.
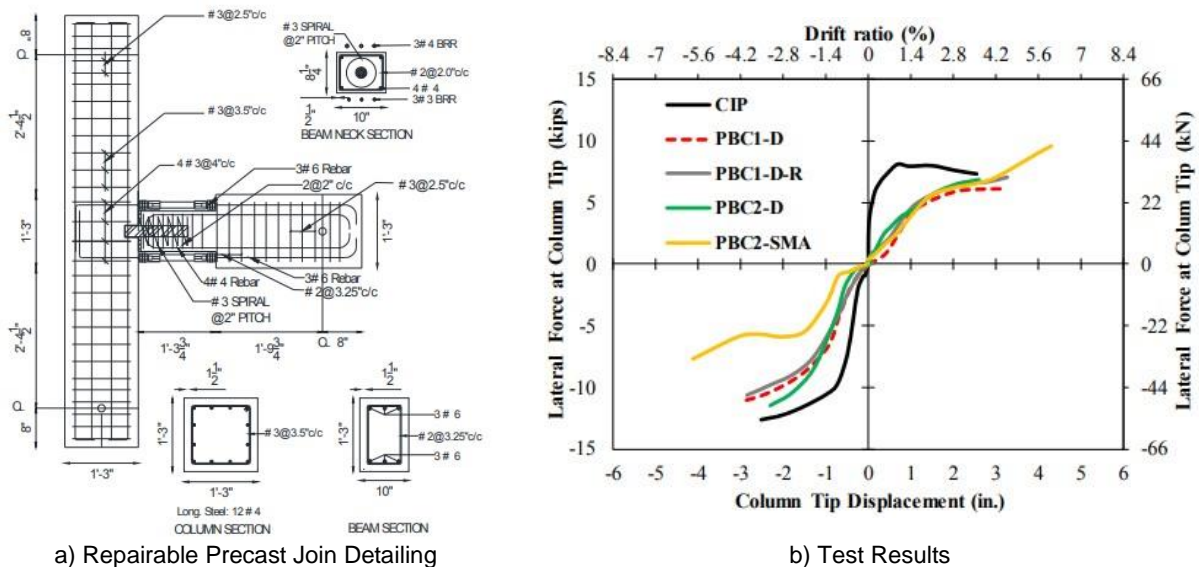
a) Repairable Precast Join Detailing   b) Test Results
Figure 2.20. Repairable Precast Beam-Column Joint detailing and Test Results (Tazarv et al., 2020)

It was determined that all four precast specimens achieved higher displacement capacities than the reference cast in place (CIP) connection (**Fig. 2.20b**) with only slightly lower recorded lateral load resistances due to reduced geometry in the beam neck. In the first beam with minimal longitudinal bars, the damage within the plastic hinge region was significant but purely cosmetic. However, in the second beam with a higher steel reinforcement, the damage was insignificant and limited to the replaceable BRR. Force displacement behavior remained relatively unchanged before and after beam repair while residual displacement was reduced, with SMA BRR providing the lowest residual displacements. CIP showed 3.6% drift capacity while the precast specimen with SMA BRR, the only specimen that was pushed to failure, exhibited more than 6% drift capacity. Overall, it was concluded that a precast building incorporating the proposed connection detailing will have significantly higher displacement capacities than conventional CIP buildings, without the need for costly building replacement. The damage will be minimal and limited to the exposed BRR, which can be easily replaced after an event.

2.3.12 Study by Pantelides and Thapa (2021)

Pantelides and Thapa (2021) explored the use of post-tensioning and external energy dissipators in a 42%-scaled precast two-column bridge bent. Steel chairs were utilized to hold external energy dissipators in the form of eight threaded bolts acting as stretch length anchors (SLA) between the column and footing and column and cap beam (**Fig. 2.21a**). Use of the steel chairs ensures that the SLAs act only in tension. Unbonded No. 8 (25-mm) threaded bars were passed through PVC within the column cross section and

post-tensioned to provide a recentering force. A 240-kip (1068-kN) actuator was used to apply a lateral cyclic quasi-static load to the bent while a 136-kip (605-kN) axial load was applied vertically.
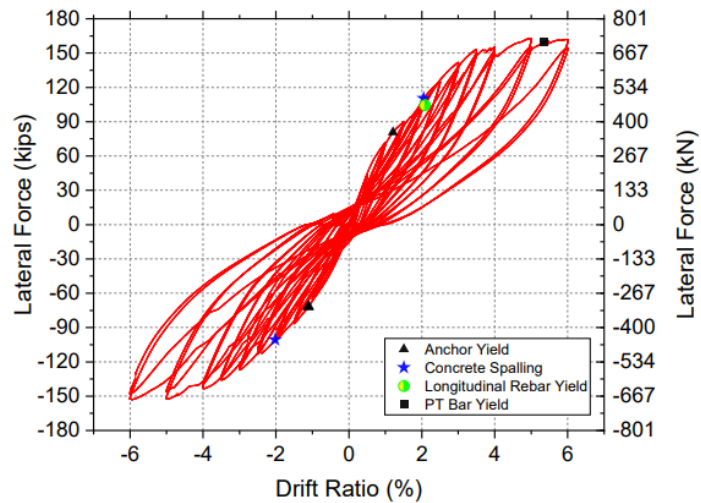
a) External Energy Dissipator   b) Force-Displacement Hysteresis

Figure 2.21. External Energy Dissipator and Force-Displacement Hysteresis (Pantelides and Thapa, 2021)

The bridge bent was tested up to a lateral drift ratio of 6% at which point the post-tensioning bars within the columns yielded (**Fig. 2.21b**). Yielding of the SLAs occurred at 1.1% drift followed by the longitudinal bar yielding and concrete spalling at 2.0% drift. Limited concrete damage occurred due to the rocking of the columns. The SLAs were easily removed after testing, proving that repair is possible. An average residual drift of 1.05% between the positive and negative directions was observed due to the rocking. Overall, no significant damage was observed during testing and the combination of post-tensioning and SLAs was proven to provide adequate energy dissipation and recentering capabilities.

2.4 Novel Column Design Recommendations

A few national documents exist on the design and construction of precast and/or novel bridge columns. National Cooperative Highway Research Program (NCHRP) report 935 (Saiidi et al., 2020) proposed seismic specifications for accelerated bridge construction (ABC) of bents. The report focuses on pocket/socket, grouted duct, and mechanical bar coupler connections. Pocket/socket connections are developed by inserting either exposed longitudinal rebar or a fully precast column into a pocket in the footing or cap beam and filling it with grout. Grouted duct connections similarly connect bridge components by grouting exposed rebar into corrugated metal ducts that have been cast into the adjoining member. In a mechanically spliced bridge column, the column bars are connected to the column adjoining member bars using a type of bar coupler. NCHRP report 864 on the seismic evaluation of bridge columns with energy dissipating mechanisms (Saiidi et al., 2017) evaluates the use of new materials and techniques to improve seismic performance of reinforced concrete bridge columns. SMA bars, ECC, FRP, UHPC, rubber pad, and rocking mechanisms were included. Thirty-nine novel columns were developed including advanced materials and/or novel techniques. New rating rubrics were developed to evaluate any novel bridge column. Design and construction guidelines were developed for three of the 39 columns: SMA-reinforced ECC column, SMA-reinforced FRP-confined column, and FRP-confined hybrid rocking column.

23

2.5 References

Alian Amiri, S.M. (2020). "Performance of Reinforced Concrete Bridge Columns with Various Reinforcement Details Subject to Long-duration Earthquakes." PhD Dissertation, University of Nevada, Reno, 289 pp.

Cruz Noguez, C.A. and Saiidi, M.S. (2012). "Shake-table Studies of a Four-span Bridge Model with Advanced Materials." Journal of Structural Engineering, Vol. 138, No. 2, pp.183-192.

Davis, P.M., Janes, T.M, Haraldsson, O.S, Eberhard, M.O., and Stanton, J.F. (2012). "Unbonded Pretensioned Columns for Accelerated Bridge Construction in Seismic Regions." Journal of Bridge Engineering, Vol. 22, No. 5: 04017003.

ElGawady, M.A., and Sha'lan, A. (2011) "Seismic Behavior of Self-centering Precast Segmental Bridge Bents." Journal of Bridge Engineering, Vol. 16, No. 3, pp. 328-339.

Finnsson, G. "Unbonded Pre-tensioned Bridge Columns with Hybrid Fiber-reinforced Concrete Shells." University of Washington, 2013.

Guo, T., Cao, Z., Xu, Z. and Lu, S., (2016). "Cyclic Load Tests on Self-centering Concrete Pier with External Dissipators and Enhanced durability." Journal of Structural Engineering, Vol. 142, No. 1, 04015088.

Han, Q., Jia, Z., Xu, K., Zhou, Y. and Du, X., (2019). "Hysteretic Behavior Investigation of Self-centering Double-column Rocking Piers for Seismic Resilience." Engineering Structures, Vol. 188, pp. 218-232.

Ibrahim, A.M., Wu, Z., Fahmy, M.F. and Kamal, D., (2016). "Experimental Study on Cyclic Response of Concrete Bridge Columns Reinforced by Steel and Basalt FRP Reinforcements." Journal of Composites for Construction Vol. 20, No. 3, p.04015062.

Ichikawa, S., Matsuzaki, H., Moustafa, A., ElGawady, M.A. and Kawashima, K., (2016). "Seismic-resistant Bridge Columns with Ultrahigh-performance Concrete Segments." Journal of Bridge Engineering, Vol. 21, No. 9, p.04016049.

Jia, J., Zhang, K., Saiidi, M.S., Guo, Y., Wu, S., Bi, K. and Du, X., (2020). "Seismic Evaluation of Precast Bridge Columns with Built-in Elastomeric Pads." Soil Dynamics and Earthquake Engineering, Vol. 128, p.105868.

Mashal, M. and Palermo, A., (2019). "Low-damage Seismic Design for Accelerated Bridge Construction." Journal of Bridge Engineering, Vol. 24, No. 2, p.04019066.

Motaref, S., Saiidi, M.S. and Sanders, D., (2014). "Shake Table Studies of Energy-dissipating Segmental Bridge Columns." Journal of Bridge Engineering, Vol. 19, No 2, pp. 186-199.

Nakashoji, B. and Saiidi, M.S., (2014). "Seismic Performance of Square Nickel-Titanium Reinforced ECC Columns with Headed Couplers." Rep. No. CCEER-14-05, Center for Civil Engineering Earthquake Research, Dept. of Civil and Environmental Engineering, Univ. of Nevada, Reno, NV.

Panagiotou, M., Trono, W., Jen, G., Kumar, P., and Ostertag, C.P., (2015). "Experimental Seismic Response of Hybrid Fiber-reinforced Concrete Bridge Columns with Novel Longitudinal Reinforcement Detailing." Journal of Bridge Engineering, Vol. 20, No. 7, p.04014090.

Pantelides, C.P. and Thapa, D., (2021). "Self-centering Bridge Bent for Accelerated Bridge Construction." MPC-21-436. North Dakota State University - Upper Great Plains Transportation Institute, Fargo: Mountain-Plains Consortium.

Saiidi, M.S., Tazarv, M., Varela, S., Bennion, S., Marsh, M.L., Ghorbani, I., Murphy, T.M. (2017). "Seismic Evaluation of Bridge Columns with Energy Dissipating Mechanisms, Volume 1: Research Overview and Volume 2: Guidelines," National Academies of Sciences, Engineering, and Medicine, NCHRP Report No. 864, Washington, DC: The National Academies Press, 344 pp.

Saiidi, M.S., Mehraein, M., Shrestha, G., Jordan, E., Itani, A., Tazarv, M., Sanders, D., Murphy, T.M., Reno, M.L., and Pohll, M.N. (2020). "Proposed AASHTO Seismic Specifications for ABC Column Connections," National Academies of Sciences, Engineering, and Medicine, NCHRP Report No. 935, Washington, DC: The National Academies Press, 354 pp.

Tazarv, M., Boudaqa, A., and Tuhin, I. (2020). "Repairable Precast Moment-Resisting Buildings: Part I—Experimental Investigations." ACI Structural Journal, Vol. 117, No. 6, pp. 147-160.

Tazarv, M. and Saiid, M.S., (2016). "Low-damage Precast Columns for Accelerated Bridge Construction in High Seismic Zones." Journal of Bridge Engineering, Vol. 21, No. 3, p.04015056.

Terzic, V., and Stojadinovic, B. (2010). "Post-earthquake Traffic Capacity of Modern Bridges in California." California. Dept. of Transportation. Division of Research and Innovation Report No. CA/PEER/2010-103.

Varela, S., and Saiidi, M.S. (2019). "Experimental Study on Seismically Resilient Two-span Bridge Models Designed for Disassembly." Journal of Earthquake Engineering, Vol. 23, No. 1, pp.72-111.

Wang, J., Wang, Z., Tang, Y., Liu, T. and Zhang, J. (2018). "Cyclic Loading Test of Self-centering Precast Segmental Unbonded Posttensioned UHPFRC Bridge Columns." Bulletin of Earthquake Engineering, Vol. 16, No. 11, pp. 5227-5255.

White, S., and Palermo, A. (2016). "Quasi-static Testing of Posttensioned Nonemulative Column-footing Connections for Bridge Piers." Journal of Bridge Engineering, Vol. 21, No. 6, p.04016025.

Zhang, R., Meng, Q., Shui, Q., He, W., Chen, K., Liang, M. and Sun, Z. (2019). "Cyclic Response of RC Composite Bridge Columns with Precast PP-ECC Jackets in the Region of Plastic Hinges." Composite Structures, Vol. 221, p.110844.

CHAPTER 3. DEVELOPMENT OF REPAIRABLE PRECAST BRIDGE COLUMN ALTERNATIVES

3.1 Introduction

The previous chapter gave an overview of past studies on novel materials and the performance of bridge columns incorporating those materials and/or new detailing. The repairable precast beam-column connections developed by Tazarv et al. (2020) was also discussed in Chapter 2. Inspired by this study, this chapter is to develop feasible repairable connections for bridge columns. Advanced materials and precast connections were combined to obtain the most feasible repairable precast column alternatives. A rating system to evaluate the design, construction, and performance of each alternative, the proposed repairable details, and the top candidates for experimental investigation are discussed herein.

3.2 Novel Column Evaluation

NCHRP Report 864 (Saiidi et al., 2017) contains an evaluation method for novel bridge columns (**Fig. 3.1**) including plastic hinge damage, displacement capacity, residual displacement, design considerations, and construction and other considerations. **Table 3.1** presents a 13-parameter rating system to assess any novel bridge column.

3.3 Development of Repairable Precast Bridge Column Detailing Alternatives

In general, repairable columns envisioned in this project have bars that are exposed, accessible, and detachable using mechanical bar splices. If a type of steel bar is used in this detailing, it must be restrained against buckling to avoid low-cycle fatigue. BRR is a bar that is confined in a steel tube to minimize buckling, or a buckling restrained reinforcement. Alternative to BRR is a fuse with tension-only members such as steel tendons. Furthermore, the column diameter must be reduced in the plastic hinge region to accommodate the exposed fuses and couplers. The reduced section of a repairable column is called "neck region". All repairable columns that will be developed in this study are expected to be moment-resisting since the exposed bars are axial members forming a tension-compression couple. The shear forces associated with the moment will be resisted with either concrete components or an additional shear pin connection.

Any repairable column utilizing BRR in the neck region may be reinforced with different types of bars including black steel, stainless steel (SS), shape memory alloy (SMA), or Martensitic Micro-composite Formable Steel (MMFX). It may also be possible to use tendons (either steel, SMA, or fiber-reinforced polymer, FRP) instead of BRR to allow for a tension-only connection to prevent buckling. Furthermore, self-consolidating concrete (SCC), engineering cementitious composite (ECC), and ultra-high performance concrete (UHPC) may be used in the neck region in lieu of conventional concrete to reduce damage.

Based on the most feasible combination of advanced materials and novel column detailing, 20 new repairable bridge column alternatives were developed. The alternative development was mainly based on the column detailing and their constitutive cementitious materials but not variations in exposed reinforcement (either BRR or tendons). Otherwise, the total number of repairable bridge columns would have exceeded 80. The 20 repairable column alternatives and their overall rating based on the NCHRP 864 evaluation method (Sec. 3.2) for novel columns are discussed in this section.

Goal: Minimize Bridge Column Damage and Enhance Serviceability after Earthquakes

Plastic Hinge Damage:
- Severe
- Moderate
- Low
- None

Displacement Capacity:
- Low Disp. Capacity
- Normal Disp. Capacity
- High Disp. Capacity

Residual Displacement:
- High Residual Displacement
- Moderate Residual Displacement
- Low Residual Displacement

Design Considerations:
- Proof Tests
- Analysis Tool Availability
- Design Guideline Availability
- Past Field Application

Construction and other Considerations:
- Initial Cost
- Material Limitations
- Ease of Construction
- Inspectability
- Maintenance
- Post-Earthquake Repair Need
- System Performance

"Owner" is the bridge owner who can be a federal or state/county/city agency, a private company, or an individual

Evaluate/Rate:
- Quantitative Evaluation by Designer/Developer
- Star-Based Rating for Owner
  ★★★★☆

[Flowchart boxes: Seismic Performance → Plastic Hinge Damage / Displacement Capacity / Residual Displacement → Try a Novel Column → Design Considerations / Construction and other Considerations → Evaluate/Rate → Owner Approval → No / Yes → Select the Novel Column]

Figure 3.1. Evaluation Flowchart for Novel Bridge Columns (NCHRP 864, 2017)

Table 3.1. General Quantification of Novel Column Evaluation Parameters (NCHRP 864, 2017)

Parameter	Quantification (deduction[a] form unity unless stated otherwise)	Weight
	Seismic Performance	
Plastic Hinge Damage	Based on demands on column materials and engineering judgement comment on the score as: 1.0 for no-damage, 0.75 for low damage, 0.25 for moderate damage, 0.0 for severe damage,	1.0
Displacement Capacity	1.0 for high displacement capacity: $\mu_c \geq 5$ 0.5 for normal displacement capacity: $3 \leq \mu_c < 5$ 0.0 for low displacement capacity: $\mu_c < 3$	1.0
Residual Displacement	1.0 for low residual displacement: $\delta_r \leq 1.0\%$ 0.5 for moderate residual displacement: $1.0\% < \delta_r \leq 1.5\%$ 0.0 for high residual displacement: $\delta_r > 1.5\%$	1.0
	Design Considerations	
Proof Test	1.0 when laboratory test data is available, 0.0 when there is no test data,	1.0
Analysis Tools	1.0 when material models and all analysis tools are available for accurate estimation of demands and capacities, Penalize by a factor of 0.25 when more information is needed for accurate estimation of demands and capacities (e.g., UHPC steel-confined properties are unknown).	0.75
Guidelines Readiness	1.0 when sufficient number of test data leading to development of design guideline, or a design guideline is available, Penalize for other conditions as: -0.25 when the concept was tested, but there are no guidelines, -0.50 when there is no concept test and there are no guidelines.	0.25
Field Application	1.0 when novel system has been used in actual bridges, 0.0 when there is no field application.	0.25
	Construction and other Considerations	
Initial Cost	Estimate the cost then the ratio of the RC column cost to the novel column cost will be the score but not to exceed 1.	0.25
Material Limitation	A novel column cannot be used in an environment where its constituents have significant limitations in that environment (e.g. rubber in cold weather).	Pass/Fail[b]
Constructability	1.0 when construction of a novel column is similar to conventional column construction, Penalize by a factor of 0.25 when construction of a novel column is tedious, requires skilled labor, and needs special tools (e.g. post-tensioning or coupler installation).	1.0
Inspectability	1.0 when inspection of a novel column is similar to conventional column inspection, Penalize by a factor of 0.25 when a novel column constituents require special inspection program or tighter schedule (e.g. corrosion of steel tendons).	0.75
Maintenance	1.0 when maintenance of a novel column is similar to conventional column maintenance, Penalize by a factor of 0.25 when a novel column constituents require special maintenance program (e.g. providing UV protection for exposed FRP).	0.75
System Performance	1.0 when overall performance of a novel bridge is similar to the conventional bridge performance, Penalize by a factor of 0.25 when a novel column constituents impose extra design considerations on other bridge elements (e.g. increase in seat width when rubber pad is used).	1.0

Note: [a] Deductions are additive for each parameter. Post-earthquake repair is needed when column is built with materials susceptible to damage. This parameter is implicit in the plastic hinge damage. μ_c is the displacement ductility capacity and δ_r is the residual drift ratio.

[b] The evaluation process shall be stopped, and the column shall be prohibited for field application if the bridge column incorporates a material that does not meet the minimum requirements due to the bridge site environment

3.3.1 Repairable Column 1: Pipe-Pin Connection

Figure 3.2 shows the detailing of proposed repairable Column 1. In this detailing, the column is precast with a steel socket to be matched with a steel pipe embedded in the footing. When the column is set, the exposed reinforcement can be attached using bar couplers. As discussed above, the exposed reinforcements in this and all following repairable columns can be constructed with bars or tendons, each with a different material (e.g., steel, SMA). The exposed reinforcement will generate bending moments through a tension-compression mechanism and the pipe-pin connection (the interaction between the steel socket and pipe) will resist the plastic shear forces while allowing rotation at the column base. **Table 3.2** presents a summary of column evaluation using the NCHRP method. The justification for each parameter is provided in the table. For example, when conventional materials are used, some damage may occur in the column especially within the neck region thus a 0.25 reduction (1.0 – 0.25 = 0.75) was included for the "plastic hinge damage" parameter. A soft start may also occur due to a possible gap between the pipe and socket in the pipe-pin connection, lowering the overall stiffness. Therefore, a 0.5 penalty was included for the "system performance" item.

Figure 3.2. Repairable Column 1 Detailing

Table 3.2. Evaluation of Repairable Column 1

Parameter	Description (score reduction value)	Wt.	Score	Weighted Score
Seismic Performance				
Plastic Hinge Damage	Low damage expected (-0.25)	1.0	0.75	0.75
Displacement Capacity	High displacement capacity expected	1.0	1.0	1.0
Residual Displacement	Some residual displacement possible, may be eliminated if use SMA bars (-0.5)	1.0	0.5	0.5
Design Considerations				
Proof Test	No lab data available (-1.0)	1.0	0	0
Analysis Tools	Modeling available	0.75	1.0	0.75
Guideline Readiness	Concept tested, no guidelines (-0.25)	0.25	0.75	0.1875
Field Application	No previous field application (-1.0)	0.25	0	0
Construction and other Considerations				
Initial Cost	Higher cost than CIP (pipe and BRR) (-0.25)	0.25	0.75	0.1875
Material Limitation **Pass/Fail** (rubber in cold, etc.)	No material limitations	N/A		Pass
Constructability	Special field construction (coupler/footing bar installation) (-0.25)	1.0	0.75	0.75
Inspectability	Additional BRR inspection (-0.25)	0.75	0.75	0.5625
Maintenance	Additional maintenance (BRR exposed) (-0.25)	0.75	0.75	0.5625
System Performance	Soft start possible (-0.5)	1.0	0.5	0.5
Total				5.75

3.3.2 Repairable Column 2: Pipe-Pin Connection with FRP Jacket in Neck Region

Figure 3.3 shows the detailing of repairable Column 2, which in general is the same as the connection detailing of Column 1. The only difference is the incorporation of a FRP jacket at the neck region to reduce concrete damage by providing significant confinement. Note that Columns 1 & 2 may allow for a full deconstruction of the bent after completing the bridge service life (e.g., 75 years) since all components can be detached.

Table 3.3 presents a summary of Column 2 evaluation using the NCHRP method. The justification for each parameter is provided in the table. For example, FRP will add to the initial costs of the bridge thus a 0.5 reduction factor was included for this parameter. Furthermore, the use of FRP will add additional inspection and treatment requirements thus a 0.5 penalty was included for the "Maintenance". A possible soft start thus reduction in the bridge stiffness is expected in this detailing. Therefore, a 0.5 reduction was included for the "system performance" criterion.

Figure 3.3. Repairable Column 2 Detailing

Table 3.3. Evaluation of Repairable Column 2

Parameter	Description (score reduction value)	Wt.	Score	Weighted Score
Seismic Performance				
Plastic Hinge Damage	No/very low damage expected	1.0	1.0	1.0
Displacement Capacity	High displacement capacity expected	1.0	1.0	1.0
Residual Displacement	Some residual displacement possible, may be eliminated if use SMA bars (-0.5)	1.0	0.5	0.5
Design Considerations				
Proof Test	No lab data available (-1.0)	1.0	0	0
Analysis Tools	Modeling available	0.75	1.0	0.75
Guideline Readiness	Concept tested, no guidelines (-0.25)	0.25	0.75	0.1875
Field Application	No previous field application (-1.0)	0.25	0	0
Construction and other Considerations				
Initial Cost	Higher cost than CIP (pipe and BRR, FRP) (-0.5)	0.25	0.5	0.125
Material Limitation **Pass/Fail** (rubber in cold, etc.)	No material limitations	N/A		Pass
Constructability	Special field construction (coupler/footing bar installation) (-0.25)	1.0	0.75	0.75
Inspectability	Additional BRR inspection, FRP inspection (-0.5)	0.75	0.5	0.375
Maintenance	Additional maintenance (BRR exposed, FRP) (-0.5)	0.75	0.5	0.375
System Performance	Soft start possible (-0.5)	1.0	0.5	0.5
Total				5.5625

3.3.3 Repairable Column 3: Pipe-Pin Connection with UHPC or ECC in Plastic Hinge Region

Figure 3.4 shows the detailing of repairable Column 3, which in general is the same as the connection detailing of Columns 1 and 2. The only difference is the addition of UHPC or ECC in the plastic hinge region to reduce concrete damage. Column 3 allows full deconstruction of the bent after completing the bridge service life (e.g., 75 years) since all components can be detached.

Table 3.4 presents a summary of the evaluation of Column 3 using the NCHRP method. The justification for each parameter is provided in the table. For example, UHPC will greatly add to the initial costs of the bridge thus a 0.75 reduction was included for this parameter. A possible soft start leads to a 0.5 reduction in the system performance for this column.

Figure 3.4. Repairable Column 3 Detailing

Table 3.4. Evaluation of Repairable Column 3

Parameter	Description (score reduction value)	Wt.	Score	Weighted Score
Seismic Performance				
Plastic Hinge Damage	No/very low damage expected	1.0	1.0	1.0
Displacement Capacity	High displacement capacity expected	1.0	1.0	1.0
Residual Displacement	Some residual displacement possible, may be eliminated if use SMA bars (-0.5)	1.0	0.5	0.5
Design Considerations				
Proof Test	No lab data available (-1.0)	1.0	0	0
Analysis Tools	Modeling available	0.75	1.0	0.75
Guideline Readiness	Concept tested, no guidelines (-0.25)	0.25	0.75	0.1875
Field Application	No previous field application (-1.0)	0.25	0	0
Construction and other Considerations				
Initial Cost	High cost due to UHPC (Pipe and BRR, UHPC/ECC) (-0.75)	0.25	0.25	0.0625
Material Limitation **Pass/Fail** (rubber in cold, etc.)	No material limitations	N/A		Pass
Constructability	Special field construction (coupler/footing bar installation) (-0.25)	1.0	0.75	0.75
Inspectability	Additional BRR inspection (-0.25)	0.75	0.75	0.5625
Maintenance	Additional maintenance (BRR exposed) (-0.25)	0.75	0.75	0.5625
System Performance	Soft start possible (-0.5)	1.0	0.5	0.5
Total				5.875

3.3.4 Repairable Column 4: Rubber Bearing

Figure 3.5 includes the detailing of repairable Column 4 which includes a rubber bearing at the column base to eliminate damage and to provide a high displacement capacity. Column 4 also allows for full deconstruction after the bent life.

Table 3.5 presents a summary of the evaluation of Column 4 according to the NCHRP method. The use of rubber bearing leads to a deduction in the constructability, inspectability, and maintenance in the field. The rubber bearing also leads to a full deduction in the system performance due to the low stiffness of the bearing.

Figure 3.5. Repairable Column 4 Detailing

Table 3.5. Evaluation of Repairable Column 4

Parameter	Description (score reduction value)	Wt.	Score	Weighted Score
Seismic Performance				
Plastic Hinge Damage	No/very low damage expected	1.0	1.0	1.0
Displacement Capacity	High displacement capacity expected	1.0	1.0	1.0
Residual Displacement	Low residual displacement expected	1.0	1.0	1.0
Design Considerations				
Proof Test	No lab data available (-1.0)	1.0	0	0
Analysis Tools	Modeling available	0.75	1.0	0.75
Guideline Readiness	Concept tested, no guidelines (-0.25)	0.25	0.75	0.1875
Field Application	No previous field application (-1.0)	0.25	0	0
Construction and other Considerations				
Initial Cost	Higher cost than CIP (Pipe and BRR, bearing) (-0.5)	0.25	0.5	0.125
Material Limitation **Pass/Fail** (rubber in cold, etc.)	Rubber bearing may not be viable in cold weather.	N/A		Pass (Fail in cold climates)
Constructability	Special field construction (coupler/ footing bar installation, bearing installation) (-0.5)	1.0	0.5	0.5
Inspectability	Additional BRR inspection, bearing inspection (-0.5)	0.75	0.5	0.375
Maintenance	Additional maintenance (BRR exposed, bearing) (-0.5)	0.75	0.5	0.375
System Performance	Very soft due to rubber bearing (-1.0)	1.0	0	0
Total				5.5125

3.3.5 Repairable Column 5: Oversized Pipe-Socket Connection

Figure 3.6 shows the detailing of repairable Column 5 which utilizes a large steel pipe as the neck section which is grouted into a socket connection in the footing. This column is not deconstructable at the end of its service life and requires demolition. The pipe will likely reduce damage in the plastic hinge of the column but may cause a higher damage further up in the column. **Table 3.6** presents a summary of the evaluation of Column 5 using the NCHRP method. The steel pipe will add some costs to the column (a 0.5 penalty) but will reduce the displacement capacity, leading to a deduction of 0.5 for this parameter. The column grouting also adds an additional field construction step which adds an additional deduction of 0.25 to the 0.25 penalty already included for the installation of the BRR or tendons.

Figure 3.6. Repairable Column 5 Detailing

Table 3.6. Evaluation of Repairable Column 5

Parameter	Description (score reduction value)	Wt.	Score	Weighted Score
Seismic Performance				
Plastic Hinge Damage	No damage expected	1.0	1.0	1.0
Displacement Capacity	Lower displ. capacity than other alternatives (pipe is stiff) (-0.5)	1.0	0.5	0.5
Residual Displacement	Some residual displacement possible, may be eliminated if use SMA bars (-0.5)	1.0	0.5	0.5
Design Considerations				
Proof Test	No lab data available (-1.0)	1.0	0	0
Analysis Tools	Modeling available	0.75	1.0	0.75
Guideline Readiness	Concept tested, no guidelines (-0.25)	0.25	0.75	0.1875
Field Application	No previous field application (-1.0)	0.25	0	0
Construction and other Considerations				
Initial Cost	Higher cost than CIP, (BRR, Large pipe) (-0.75)	0.25	0.25	0.0625
Material Limitation **Pass/Fail** (rubber in cold, etc.)	No material limitations	N/A		Pass
Constructability	Special field construction (coupler/footing bar installation, grout socket) (-0.5)	1.0	0.5	0.5
Inspectability	Additional BRR inspection (-0.25)	0.75	0.75	0.5625
Maintenance	Additional maintenance (BRR exposed) (-0.25)	0.75	0.75	0.5625
System Performance	No soft start, still worse than CIP (-0.25)	1.0	0.75	0.75
Total				5.375

3.3.6 Repairable Column 6: Pipe-Socket Connection

Figure 3.7 shows the detailing of repairable Column 6, which has a similar grouted socket connection as repairable column 5, but instead grouts a small shear pipe into the socket rather than a large pipe. This will slightly improve the displacement capacity from the previous column but will still not be able to be deconstructed at the end of its service life. There may also be more construction tolerance in the connection than the pipe-pin connection used in the first three repairable columns. **Table 3.7** presents the NCHRP evaluation for Column 6. There is a 0.5 deduction for the displacement capacity since the pipe does not allow the column to rotate at the base like in the pipe-pin columns. This will likely also lead to high residual displacements. The grouting of the socket connection similarly adds an additional construction step with a 0.25 deduction for constructability similar to that in Column 5.

Figure 3.7. Repairable Column 6 Detailing

Table 3.7. Evaluation of Repairable Column 6

Parameter	Description (score reduction value)	Wt.	Score	Weighted Score
Seismic Performance				
Plastic Hinge Damage	Low damage expected (-0.25)	1.0	0.75	0.75
Displacement Capacity	Lower displ. capacity than pipe-pin (-0.5)	1.0	0.5	0.5
Residual Displacement	Some residual displacement possible, may be eliminated if use SMA bars (-0.5)	1.0	0.5	0.5
Design Considerations				
Proof Test	No lab data available (-1.0)	1.0	0	0
Analysis Tools	Modeling available	0.75	1.0	0.75
Guideline Readiness	Concept tested, no guidelines (-0.25)	0.25	0.75	0.1875
Field Application	No previous field application (-1.0)	0.25	0	0
Construction and other Considerations				
Initial Cost	Higher cost than CIP (pipe and BRR) (-0.25)	0.25	0.75	0.1875
Material Limitation **Pass/Fail** (rubber in cold, etc.)	No material limitations	N/A		Pass
Constructability	Special field construction (coupler/footing bar installation, grout socket) (-0.5)	1.0	0.5	0.5
Inspectability	Additional BRR inspection (-0.25)	0.75	0.75	0.5625
Maintenance	Additional maintenance (BRR exposed) (-0.25)	0.75	0.75	0.5625
System Performance	No soft start, still worse than CIP (-0.25)	1.0	0.75	0.75
Total				5.25

3.3.7 Repairable Column 7: Pipe-Socket Connection with FRP Jacket in Neck Region

Figure 3.8 shows the detailing of repairable Column 7, which uses the same connection detail as repairable Column 8 but with an FRP jacket to the neck region as was the case for repairable Column 2. This FRP jacket will increase concrete confinement, which in turn increases the displacement capacity of the column as well as reduces concrete damage in the plastic hinge region. The evaluation of Column 7 is presented in **Table 3.8** using the NCHRP method. The FRP will add to the initial costs of the bridge, thus a 0.5 reduction was included for this parameter while also adding additional maintenance and inspection steps. Residual displacement is likely for this connection detail, thus a 0.5 reduction was included for that category.

Figure 3.8. Repairable Column 7 Detailing

Table 3.8. Evaluation of Repairable Column 7

Parameter	Description (score reduction value)	Wt.	Score	Weighted Score
Seismic Performance				
Plastic Hinge Damage	No/very low damage expected	1.0	1.0	1.0
Displacement Capacity	Lower displ. capacity than pipe-pin (-0.5)	1.0	0.5	0.5
Residual Displacement	Some residual displacement possible, may be eliminated if use SMA bars (-0.5)	1.0	0.5	0.5
Design Considerations				
Proof Test	No lab data available (-1.0)	1.0	0	0
Analysis Tools	Modeling available	0.75	1.0	0.75
Guideline Readiness	Concept tested, no guidelines (-0.25)	0.25	0.75	0.1875
Field Application	No previous field application (-1.0)	0.25	0	0
Construction and other Considerations				
Initial Cost	Higher cost than CIP (pipe and BRR, FRP) (-0.5)	0.25	0.5	0.125
Material Limitation **Pass/Fail** (rubber in cold, etc.)	No material limitations	N/A		Pass
Constructability	Special field construction (coupler/footing bar installation, grout socket) (-0.5)	1.0	0.5	0.5
Inspectability	Additional inspection (BRR, FRP) (-0.5)	0.75	0.5	0.375
Maintenance	Additional maintenance (BRR exposed, FRP) (-0.5)	0.75	0.5	0.375
System Performance	No soft start, still worse than CIP (-0.25)	1.0	0.75	0.75
Total				5.0625

3.3.8 Repairable Column 8: Pipe-Socket Connection with UHPC/ECC in Plastic Hinge Region

The detailing of repairable Column 8 is shown in **Fig. 3.9**, which is the same as the previous two columns but incorporating UHPC or ECC in the plastic hinge region to reduce damage. The column is not able to be deconstructed at the end of service life due to the connection detailing. **Table 3.9** presents a summary of the Column 8 evaluation using the NCHRP method. The UHPC will greatly add to the costs so a reduction score of 0.5 was included. Residual displacement is also still likely in this alternative so a 0.5 deduction was added to the residual displacement category.

Figure 3.9. Repairable Column 8 Detailing

Table 3.9. Evaluation of Repairable Column 8

Parameter	Description (score reduction value)	Wt.	Score	Weighted Score
Seismic Performance				
Plastic Hinge Damage	No/very low damage expected	1.0	1.0	1.0
Displacement Capacity	Lower displ. capacity than pipe-pin (-0.5)	1.0	0.5	0.5
Residual Displacement	Some residual displacement possible, may be eliminated if use SMA bars (-0.5)	1.0	0.5	0.5
Design Considerations				
Proof Test	No lab data available (-1.0)	1.0	0	0
Analysis Tools	Modeling available	0.75	1.0	0.75
Guideline Readiness	Concept tested, no guidelines (-0.25)	0.25	0.75	0.1875
Field Application	No previous field application (-1.0)	0.25	0	0
Construction and other Considerations				
Initial Cost	Higher cost than CIP (pipe and BRR, UHPC) (-0.75)	0.25	0.25	0.0625
Material Limitation **Pass/Fail** (rubber in cold, etc.)	No material limitations	N/A		Pass
Constructability	Special field construction (coupler/footing bar installation, grout socket) (-0.5)	1.0	0.5	0.5
Inspectability	Additional inspection (BRR) (-0.25)	0.75	0.75	0.5625
Maintenance	Additional maintenance (BRR exposed) (-0.25)	0.75	0.75	0.5625
System Performance	No soft start, still worse than CIP (-0.25)	1.0	0.75	0.75
Total				5.375

3.3.9 Repairable Column 9: Pipe-Socket Connection with Post-Tensioning

Figure 3.10 shows the detailing of repairable Column 9, which has post-tensioning tendons to help reduce residual displacements, thus the rating for this parameter is increased when compared to previous alternatives. The connection detailing is the same as the previous pipe-socket columns which will not allow for deconstruction at the end of the bridge life. **Table 3.10** summarizes the NCHRP method rating for Column 9 with a justification provided for each parameter. The post-tensioning tendons will add to the bridge cost and will add additional construction, inspection, and maintenance steps. Thus, a 0.5 deduction was included to each of these parameters. The stiffness of the column is still high due to the steel pipe, and thus the displacement capacity deduction is the same as the previous pipe-socket columns.

Figure 3.10. Repairable Column 9 Detailing

Table 3.10. Evaluation of Repairable Column 9

Parameter	Description (score reduction value)	Wt.	Score	Weighted Score
Seismic Performance				
Plastic Hinge Damage	Low damage expected (-0.25)	1.0	0.75	0.75
Displacement Capacity	Lower displ. capacity than pipe-pin (-0.5)	1.0	0.5	0.5
Residual Displacement	Low residual displacement expected (tendon recenters)	1.0	1.0	1.0
Design Considerations				
Proof Test	No lab data available (-1.0)	1.0	0	0
Analysis Tools	Modeling available	0.75	1.0	0.75
Guideline Readiness	Concept tested, no guidelines (-0.25)	0.25	0.75	0.1875
Field Application	No previous field application (-1.0)	0.25	0	0
Construction and other Considerations				
Initial Cost	Higher cost than CIP (tendons and pipe) (-0.25)	0.25	0.5	0.125
Material Limitation **Pass/Fail** (rubber in cold, etc.)	No material limitations	N/A		Pass
Constructability	Special field construction (coupler/footing bar, grout socket) (-0.5)	1.0	0.5	0.5
Inspectability	Additional inspection (BRR, tendon) (-0.5)	0.75	0.5	0.375
Maintenance	Additional maintenance (BRR exposed, tendon) (-0.5W)	0.75	0.5	0.375
System Performance	No soft start, still worse than CIP (-0.25)	1.0	0.75	0.75
Total				5.3125

3.3.10 Repairable Column 10: Neck-Socket Connection

Figure 3.11 illustrates the detailing of repairable Column 10, which also uses a grouted socket connection but instead inserts the entire neck section into the socket. This will require demolition of the column after its service life. **Table 3.11** summarizes the NCHRP method rating for Column 10. A 0.5 deduction was included for the additional construction step included with the column grouting. There is also likely to be a higher residual displacement and damage, thus a deduction was included for each of those parameters. Like all previous columns, SMA or tendon fuses may be used to increase the displacement capacity and to reduce the residual displacement, if needed.
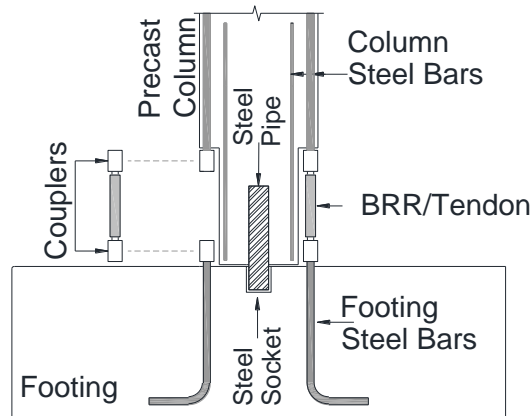

Figure 3.11. Repairable Column 10 Detailing

Table 3.11. Evaluation of Repairable Column 10

Parameter	Description (score reduction value)	Wt.	Score	Weighted Score
Seismic Performance				
Plastic Hinge Damage	Low damage expected (-0.25)	1.0	0.75	0.75
Displacement Capacity	Lower displ. capacity than pipe-pin (-0.5)	1.0	0.5	0.5
Residual Displacement	Some residual displacement possible, may be eliminated if use SMA bars (-0.5)	1.0	0.5	0.5
Design Considerations				
Proof Test	No lab data available (-1.0)	1.0	0	0
Analysis Tools	Modeling available	0.75	1.0	0.75
Guideline Readiness	Concept tested, no guidelines (-0.25)	0.25	0.75	0.1875
Field Application	No previous field application (-1.0)	0.25	0	0
Construction and other Considerations				
Initial Cost	Higher cost than CIP (BRR) (-0.25)	0.25	0.75	0.1875
Material Limitation **Pass/Fail** (rubber in cold, etc.)	No material limitations	N/A		Pass
Constructability	Special field construction (coupler/footing bar installation, grout socket) (-0.5)	1.0	0.5	0.5
Inspectability	Additional BRR inspection (-0.25)	0.75	0.75	0.5625
Maintenance	Additional maintenance (BRR exposed) (-0.25)	0.75	0.75	0.5625
System Performance	No soft start, still worse than CIP (-0.25)	1.0	0.75	0.75
Total				5.25

3.3.11 Repairable Column 11: Neck-Socket Connection with UHPC or ECC in Neck Region

Figure 3.12 shows the detailing of repairable Column 11, which in general is the same as the connection detailing of Column 11. The only difference is the incorporation of UHPC or ECC in the plastic hinge region to reduce damage. Note that Columns 11 does not allow for deconstruction at the end of its service life. **Table 3.12** presents a summary of the evaluation for Column 11. A justification for each parameter and a deduction were included when needed. UHPC will reduce damage but will greatly add to the column costs so a deduction score of 1.0 was included associated with the costs. An additional deduction of 0.25 was also included to the score for constructability due to the steps involved with grouting in the connection. This adds to the additional steps already required to insert the fuse reinforcement.
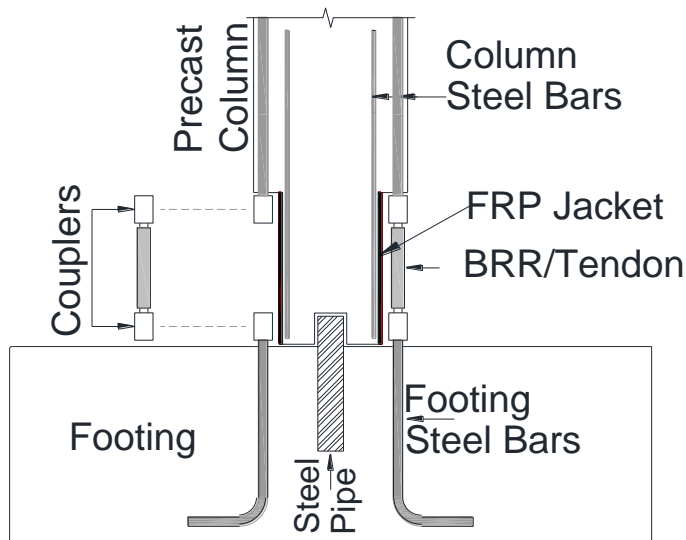

Figure 3.12. Repairable Column 11 Detailing

Table 3.12. Evaluation of Repairable Column 11

Parameter	Description (score reduction value)	Wt.	Score	Weighted Score
Seismic Performance				
Plastic Hinge Damage	No/very low damage expected	1.0	1.0	1.0
Displacement Capacity	Lower displ. capacity than pipe-pin (-0.5)	1.0	0.5	0.5
Residual Displacement	Some residual displacement possible, may be eliminated if use SMA bars (-0.5)	1.0	0.5	0.5
Design Considerations				
Proof Test	No lab data available (-1.0)	1.0	0	0
Analysis Tools	Modeling available	0.75	1.0	0.75
Guideline Readiness	Concept tested, no guidelines (-0.25)	0.25	0.75	0.1875
Field Application	No previous field application (-1.0)	0.25	0	0
Construction and other Considerations				
Initial Cost	High cost due to UHPC/ECC, more UHPC used than other options (-0.1)	0.25	0	0
Material Limitation **Pass/Fail** (rubber in cold, etc.)	No material limitations	N/A		Pass
Constructability	Special field construction (coupler/footing bar installation, grout socket) (-0.5)	1.0	0.5	0.5
Inspectability	Additional BRR inspection (-0.25)	0.75	0.75	0.5625
Maintenance	Additional maintenance (BRR exposed) (-0.25)	0.75	0.75	0.5625
System Performance	No soft start, still worse than CIP (-0.25)	1.0	0.75	0.75
Total				5.3125

3.3.12 Repairable Column 12: Neck-Socket Connection with Post-Tensioning

Figure 3.13 shows the detailing of repairable Column 12, which uses the same neck-socket connection as the previous column but utilizing post-tensioning tendons to help reduce residual displacements. The deductions to each individual rating parameter are included in **Table 3.13**. The column deconstruction is not possible while grouting requires an additional construction step. A deduction score of 0.5 was taken out for column inspectability and maintenance due to the additional column components included with the post-tensioning. Some damage is still expected while the displacement capacity is slightly lower than other columns due to the stiffness of this connection type.
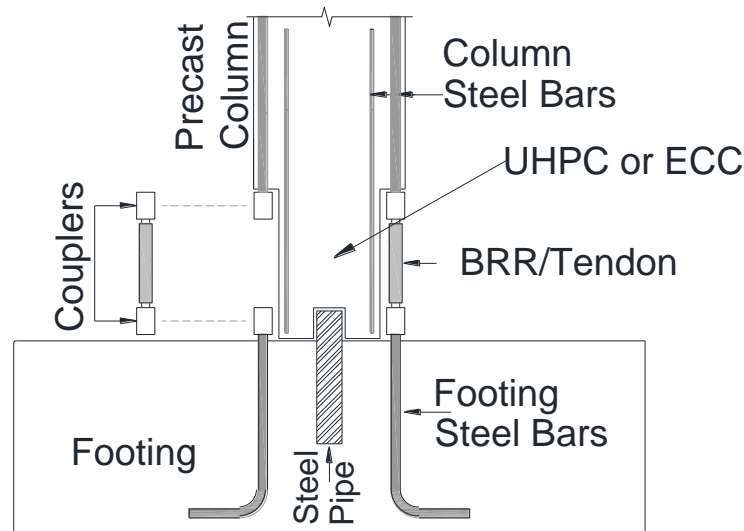
Figure 3.13. Repairable Column 12 Detailing

Table 3.13. Evaluation of Repairable Column 12

Parameter	Description (score reduction value)	Wt.	Score	Weighted Score
Seismic Performance				
Plastic Hinge Damage	Low damage expected (-0.25)	1.0	0.75	0.75
Displacement Capacity	Lower displ. capacity than pipe-pin (-0.5)	1.0	0.5	0.5
Residual Displacement	Low residual displacement expected (tendon recenters)	1.0	1.0	1.0
Design Considerations				
Proof Test	No lab data available (-1.0)	1.0	0	0
Analysis Tools	Modeling available	0.75	1.0	0.75
Guideline Readiness	Concept tested, no guidelines (-0.25)	0.25	0.75	0.1875
Field Application	No previous field application (-1.0)	0.25	0	0
Construction and other Considerations				
Initial Cost	Higher cost than CIP (BRR, tendons) (-0.25)	0.5	0.5	0.125
Material Limitation **Pass/Fail** (rubber in cold, etc.)	No material limitations	N/A		Pass
Constructability	Special field construction (coupler/footing bar, grout socket) (-0.5)	1.0	0.5	0.5
Inspectability	Additional inspection (BRR, tendon) (-0.5)	0.75	0.5	0.375
Maintenance	Additional maintenance (BRR exposed, tendon) (-0.5)	0.75	0.5	0.375
System Performance	No soft start, still worse than CIP (-0.25)	1.0	0.75	0.75
Total				5.3125

3.3.13 Repairable Column 13: Column-Socket Connection

Figure 3.14 shows the detailing of repairable Column 13, which is similar to the previous neck-socket connections except that the full column is now inserted into the socket rather than just the neck. This allows for the BRR or tendon fuses to be installed before the column is shipped and thus reduces the number of special construction steps. The column is not able to be deconstructed due to grouting of the socket connection. The rating of Column 13 is presented in **Table 3.14** based on the NCHRP method presented earlier in this chapter. A deduction of 0.25 is included for grouting of the column but no deduction is required for fuse installation in the field. The damage is also likely to be slightly higher and the displacement capacity slightly lower than for other columns with similar detailing, thus an appropriate deduction score was included for each parameter.
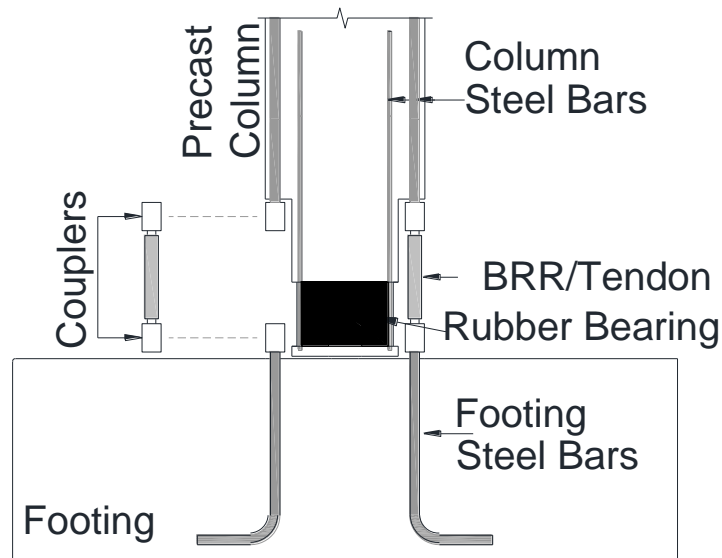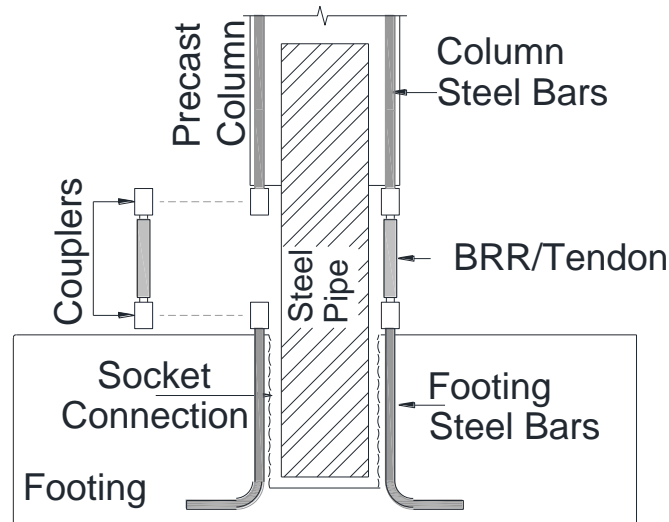

Figure 3.14. Repairable Column 13 Detailing

Table 3.14. Evaluation of Repairable Column 13

Parameter	Description (score reduction value)	Wt.	Score	Weighted Score
Seismic Performance				
Plastic Hinge Damage	Low damage expected (-0.25)	1.0	0.75	0.75
Displacement Capacity	Lower displ. capacity than pipe-pin (-0.5)	1.0	0.5	0.5
Residual Displacement	Some residual displacement possible, may be eliminated if use SMA bars (-0.5)	1.0	0.5	0.5
Design Considerations				
Proof Test	No lab data available (-1.0)	1.0	0	0
Analysis Tools	Modeling available	0.75	1.0	0.75
Guideline Readiness	Concept tested, no guidelines (-0.25)	0.25	0.75	0.1875
Field Application	No previous field application (-1.0)	0.25	0	0
Construction and other Considerations				
Initial Cost	Higher cost than CIP (BRR) (-0.25)	0.25	0.75	0.1875
Material Limitation **Pass/Fail** (rubber in cold, etc.)	No material limitations	N/A		Pass
Constructability	Special field construction (Grout socket) (-0.25)	1.0	0.75	0.75
Inspectability	Additional BRR inspection (-0.25)	0.75	0.75	0.5625
Maintenance	Additional maintenance (BRR exposed) (-0.25)	0.75	0.75	0.5625
System Performance	No soft start, still worse than CIP (-0.25)	1.0	0.75	0.75
Total				5.5

3.3.14 Repairable Column 14: Column-Socket Connection with UHPC or ECC in Plastic Hinge Region

Figure 3.15 shows the detailing of repairable Column 14 which uses the same column-socket connection as the previous column but utilizing UHPC or ECC in the plastic hinge region. This will help reducing damage and will allow for fuse installation before the column is shipped, but the column will not be able to be deconstructed at the end of its service life. **Table 3.15** presents a summary of Column 14 evaluation. UHPC will significantly add to the overall cost of the column, so a high deduction was included. There is also a 0.25 reduction for the grouting of the column as well as some reductions in displacement capacity and residual displacement. However, these parameters may be improved with the use of advanced material fuses like SMA or tendons.
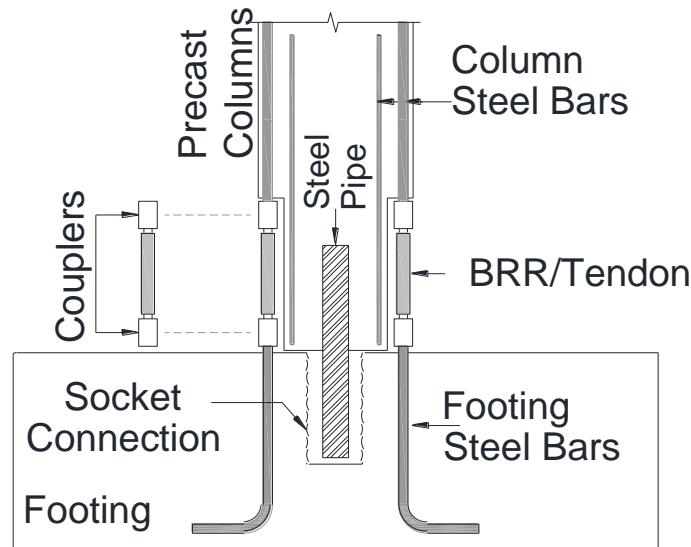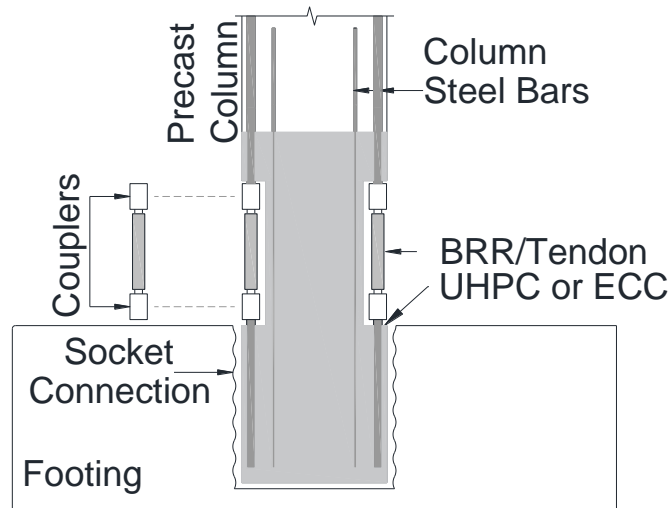

Figure 3.15. Repairable Column 14 Detailing

Table 3.15. Evaluation of Repairable Column 14

Parameter	Description (score reduction value)	Wt.	Score	Weighted Score
Seismic Performance				
Plastic Hinge Damage	No/very low damage expected	1.0	1.0	1.0
Displacement Capacity	Lower displ. capacity than pipe-pin (-0.5)	1.0	0.5	0.5
Residual Displacement	Some residual displacement possible, may be eliminated if use SMA bars (-0.5)	1.0	0.5	0.5
Design Considerations				
Proof Test	No lab data available (-1.0)	1.0	0	0
Analysis Tools	Modeling available	0.75	1.0	0.75
Guideline Readiness	Concept tested, no guidelines (-0.25)	0.25	0.75	0.1875
Field Application	No previous field application (-1.0)	0.25	0	0
Construction and other Considerations				
Initial Cost	High cost due to UHPC/ECC, more UHPC used than other options (-1.0)	0.25	0	0
Material Limitation **Pass/Fail** (rubber in cold, etc.)	No material limitations	N/A		Pass
Constructability	Special field construction (Grout socket) (-0.25)	1.0	0.75	0.75
Inspectability	Additional BRR inspection (-0.25)	0.75	0.75	0.5625
Maintenance	Additional maintenance (BRR exposed) (-0.25W)	0.75	0.75	0.5625
System Performance	No soft start, still worse than CIP (-0.25)	1.0	0.75	0.75
Total				5.5625

3.3.15 Repairable Column 15: Column-Socket Connection with Post-Tensioning and UHPC or ECC in plastic hinge region

Figure 3.16 shows the detailing of repairable Column 15 which has post-tensioning tendons and grouted column-socket connection. The rocking mechanism will reduce the residual displacement. Furthermore, UHPC or ECC is also used in the plastic hinge region of this column to reduce damage. **Table 3.16** presents a summary of Column 15 evaluation using the NCHRP method. Post-tensioning of this column alternative may be performed at the precast plant in addition to installation of BRR, thus the only deduction to constructability comes from the grouting of the connection. There is; however, an additional deduction in inspectability and maintenance as well as a significant deduction to the cost parameter due to use of UHPC and inclusion of the post-tensioning tendons.
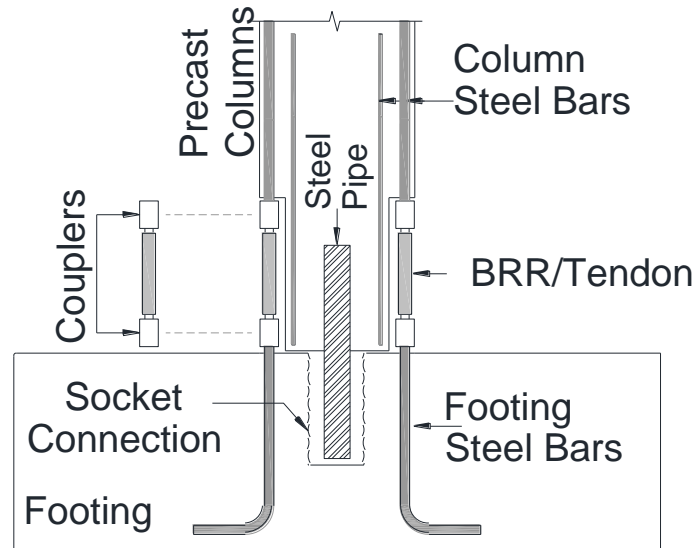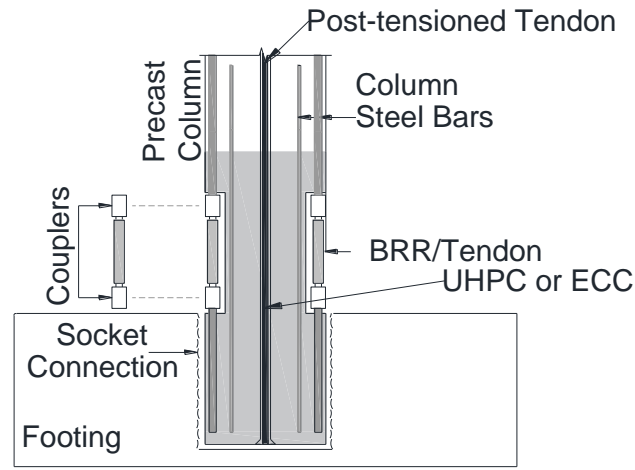

Figure 3.16. Repairable Column 15 Detailing

Table 3.16. Evaluation of Repairable Column 15

Parameter	Description (score reduction value)	Wt.	Score	Weighted Score
Seismic Performance				
Plastic Hinge Damage	No damage expected	1.0	1.0	1.0
Displacement Capacity	Lower displ. capacity than pipe-pin (-0.5)	1.0	0.5	0.5
Residual Displacement	Low residual displacement expected (tendon recenters)	1.0	1.0	1.0
Design Considerations				
Proof Test	No lab data available (-1.0)	1.0	0	0
Analysis Tools	Modeling available	0.75	1.0	0.75
Guideline Readiness	Concept tested, no guidelines (-0.25)	0.25	0.75	0.1875
Field Application	No previous field application (-1.0)	0.25	0	0
Construction and other Considerations				
Initial Cost	Higher cost than CIP (tendons, UHPC, BRR) (-1.0)	0.25	0	0
Material Limitation **Pass/Fail** (rubber in cold, etc.)	No material limitations	N/A		Pass
Constructability	Special field construction (grout socket) (-0.25)	1.0	0.75	0.75
Inspectability	Additional inspection (BRR, tendon) (-0.5)	0.75	0.5	0.375
Maintenance	Additional maintenance (BRR exposed, tendon) (-0.5)	0.75	0.5	0.375
System Performance	No soft start, still worse than CIP (-0.25)	1.0	0.75	0.75
Total				5.6875

3.3.16 Repairable Column 16: Column-Socket Connection with FRP Jacket in Neck Region

Column 16, which is shown in **Fig. 3.17**, includes an FRP jacket in the neck region to reduce damage as well as the same column-socket connection of the previous couple of repairable column alternatives. None of the grouted socket connection columns can be deconstructed at the end of their service life and thus may be less attractive to potential bridge owners. **Table 3.17** presents a summary of the evaluation for Column 16. The FRP jacket will add to the overall column cost despite increasing the displacement capacity through an increased concrete confinement as well as reducing damage. There is also additional inspection and maintenance included with the FRP jacketing.
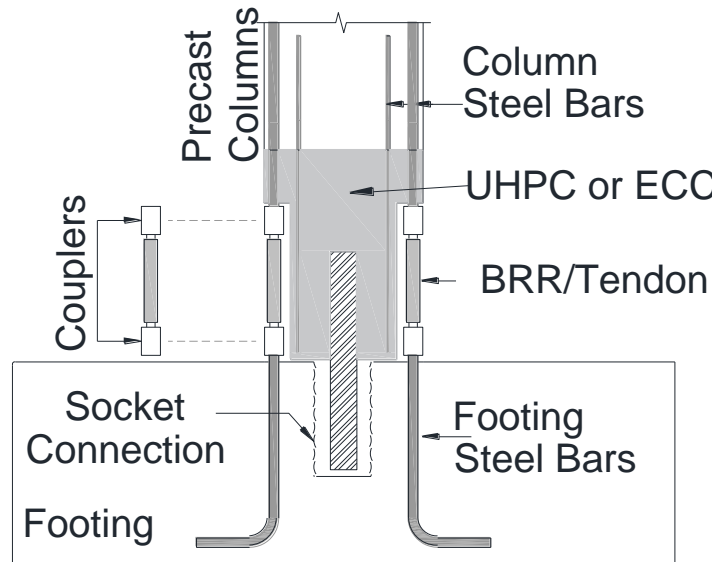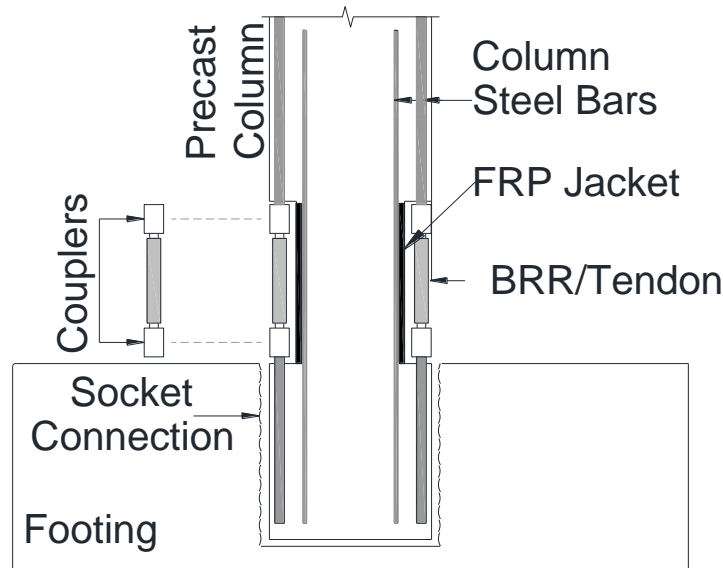

Figure 3.17. Repairable Column 16 Detailing

Table 3.17. Evaluation of Repairable Column 16

Parameter	Description (score reduction value)	Wt.	Score	Weighted Score
Seismic Performance				
Plastic Hinge Damage	No/very low damage expected	1.0	1.0	1.0
Displacement Capacity	Lower displ. capacity than pipe-pin (-0.5)	1.0	0.5	0.5
Residual Displacement	Some residual displacement possible, may be eliminated if use SMA bars (-0.5)	1.0	0.5	0.5
Design Considerations				
Proof Test	No lab data available (-1.0)	1.0	0	0
Analysis Tools	Modeling available	0.75	1.0	0.75
Guideline Readiness	Concept tested, no guidelines (-0.25)	0.25	0.75	0.1875
Field Application	No previous field application (-1.0)	0.25	0	0
Construction and other Considerations				
Initial Cost	Higher cost than CIP (BRR, FRP) (-0.5)	0.25	0.5	0.125
Material Limitation **Pass/Fail** (rubber in cold, etc.)	No material limitations	N/A		Pass
Constructability	Special field construction (Grout socket) (-0.25)	1.0	0.75	0.75
Inspectability	Additional inspection (BRR, FRP) (-0.25)	0.75	0.5	0.375
Maintenance	Additional maintenance (BRR, FRP exposed) (-0.25)	0.75	0.5	0.375
System Performance	No soft start, still worse than CIP (-0.25)	1.0	0.75	0.75
Total				5.3125

3.3.17 Repairable Column 17: Rocking Column

Column 17, which is a rocking column, is shown in **Fig. 3.18**. The rocking column does not include any special connection detailing other than post-tensioning tendons which provide sufficient force to recenter the column. This type of column may be deconstructed at the end of the bridge life due to the non-permanent nature of the connections. **Table 3.18** presents a summary of the Column 17 evaluation. The post-tensioning tendons will increase the cost of the column and add to construction, inspection, and maintenance steps, but will significantly reduce the residual displacement. The column is also likely to have a high displacement capacity.
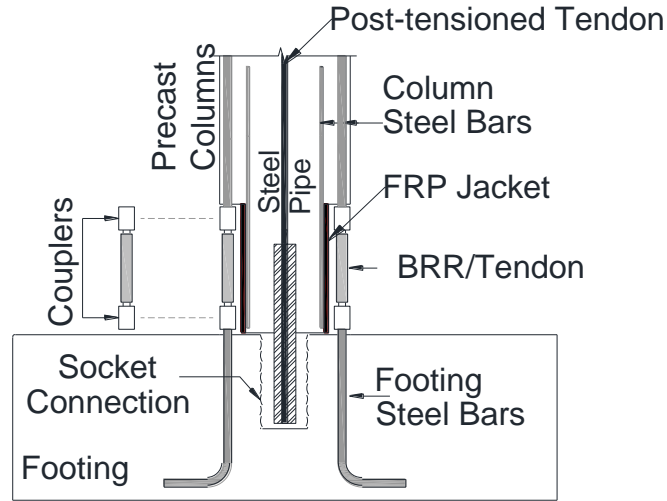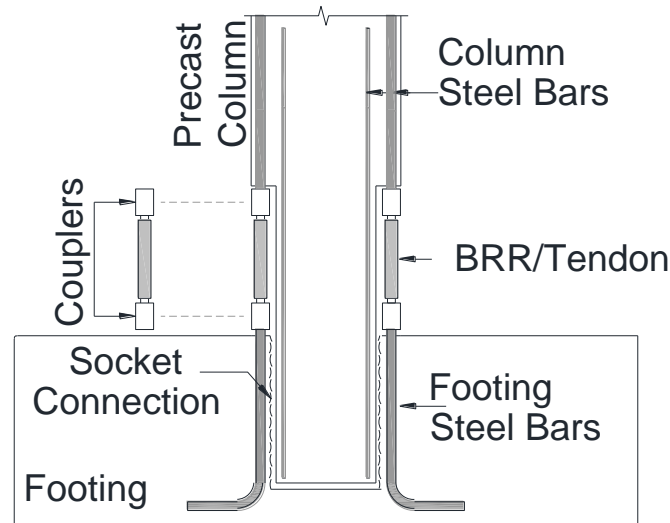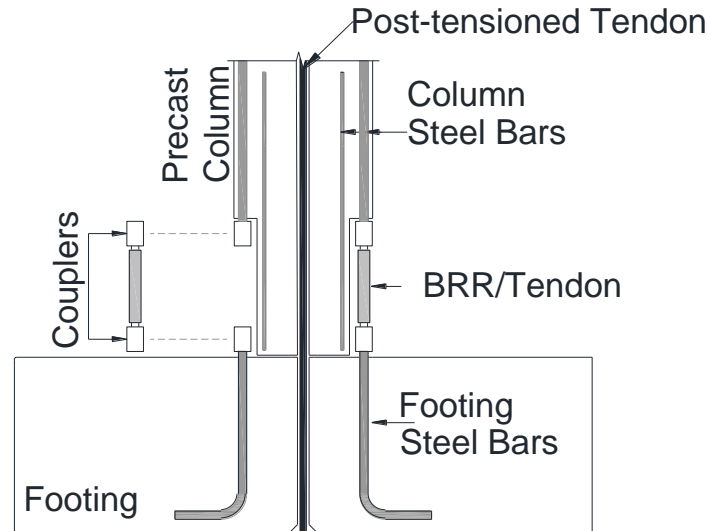

Figure 3.18. Repairable Column 17 Detailing

Table 3.18. Evaluation of Repairable Column 17

Parameter	Description (score reduction value)	Wt.	Score	Weighted Score
Seismic Performance				
Plastic Hinge Damage	Low damage expected (-0.25)	1.0	0.75	0.75
Displacement Capacity	High displacement capacity expected	1.0	1.0	1.0
Residual Displacement	No/very low residual displacement expected.	1.0	1.0	1.0
Design Considerations				
Proof Test	No lab data available (-1.0)	1.0	0	0
Analysis Tools	Modeling available	0.75	1.0	0.75
Guideline Readiness	Concept tested, no guidelines (-0.25)	0.25	0.75	0.1875
Field Application	No previous field application (-1.0)	0.25	0	0
Construction and other Considerations				
Initial Cost	Higher cost than CIP (BRR, tendon) (-0.5)	0.25	0.5	0.125
Material Limitation **Pass/Fail** (rubber in cold, etc.)	No material limitations	N/A		Pass
Constructability	Special field construction (coupler/footing bar installation, post-tensioning) (-0.5)	1.0	0.5	0.5
Inspectability	Additional inspection (BRR, tendon) (-0.5)	0.75	0.5	0.375
Maintenance	Additional maintenance (BRR exposed, tendon) (-0.5)	0.75	0.5	0.375
System Performance	Soft start not likely, sliding possible (-0.5)	1.0	0.5	0.5
Total				5.5625

3.3.18 Repairable Column 18: Rocking with FRP Jacket in the Neck Region

Figure 3.19 shows the detailing of repairable Column 18, which is the same as the previous column but includes an FRP jacket in the neck region. This column will also be deconstructable and is likely to see a low damage with high displacement capacity and low residual drift. The evaluation of the column is presented in **Table 3.19**. The post-tensioning tendons will add an additional construction step while both the tendons and the FRP jacketing will require additional inspection and maintenance, leading to deductions in each of the appropriate categories.
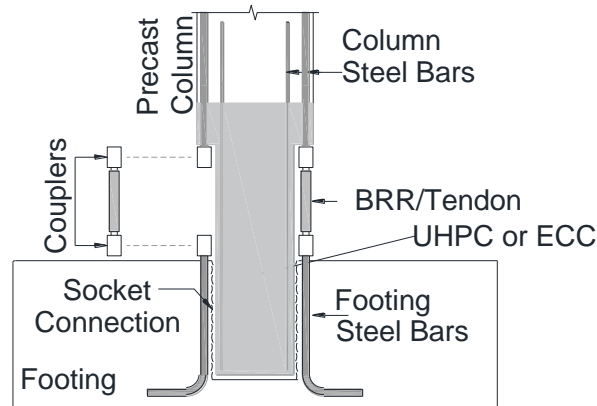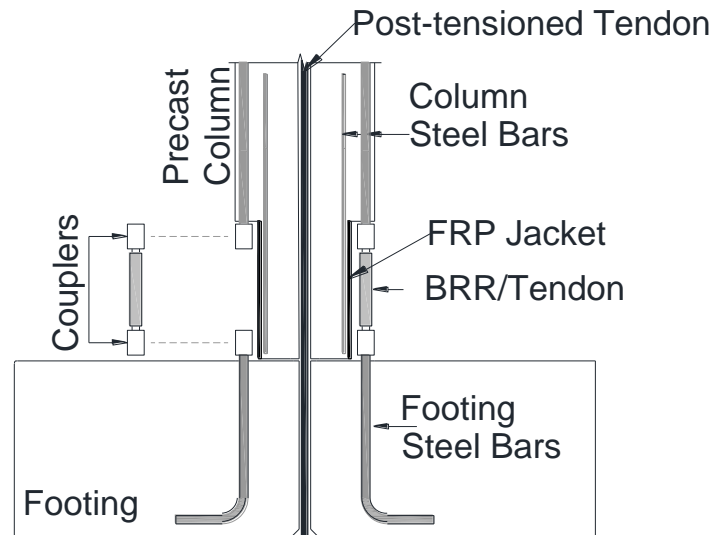
Figure 3.19. Repairable Column 18 Detailing

Table 3.19. Evaluation of Repairable Column 18

Parameter	Description (score reduction value)	Wt.	Score	Weighted Score
Seismic Performance				
Plastic Hinge Damage	No damage expected	1.0	1.0	1.0
Displacement Capacity	High displacement capacity expected	1.0	1.0	1.0
Residual Displacement	No/very low residual displacement expected.	1.0	1.0	1.0
Design Considerations				
Proof Test	No lab data available (-1.0)	1.0	0	0
Analysis Tools	Modeling available	0.75	1.0	0.75
Guideline Readiness	Concept tested, no guidelines (-0.25)	0.25	0.75	0.1875
Field Application	No previous field application (-1.0)	0.25	0	0
Construction and other Considerations				
Initial Cost	Higher cost than CIP (BRR, FRP, tendon) (-0.75)	0.25	0.25	0.0625
Material Limitation **Pass/Fail** (rubber in cold, etc.)	No material limitations	N/A		Pass
Constructability	Special field construction (coupler installation, post-tensioning) (-0.5)	1.0	0.5	0.5
Inspectability	Additional inspection (BRR, tendon, FRP) (-0.75)	0.75	0.25	0.1875
Maintenance	Additional maintenance (BRR exposed, tendon, FRP) (-0.75)	0.75	0.25	0.1875
System Performance	Soft start not likely, sliding possible (-0.5)	1.0	0.5	0.5
Total				5.375

3.3.19 Repairable Column 19: Rocking with UHPC/ECC in Plastic Hinge region

Figure 3.20 shows the detailing of repairable Column 19, which is a rocking column utilizing UHPC or ECC in the plastic hinge region. This column is likely to achieve a high displacement capacity as well as low residual displacement and damage. The column is also deconstructable at the end of service life. **Table 3.20** includes the rating of Column 19 as well as justification for each point deduction. UHPC and tendons will greatly add to the column costs, thus a full deduction was included. The post-tensioning tendons will also require additional construction, inspection, and maintenance steps.
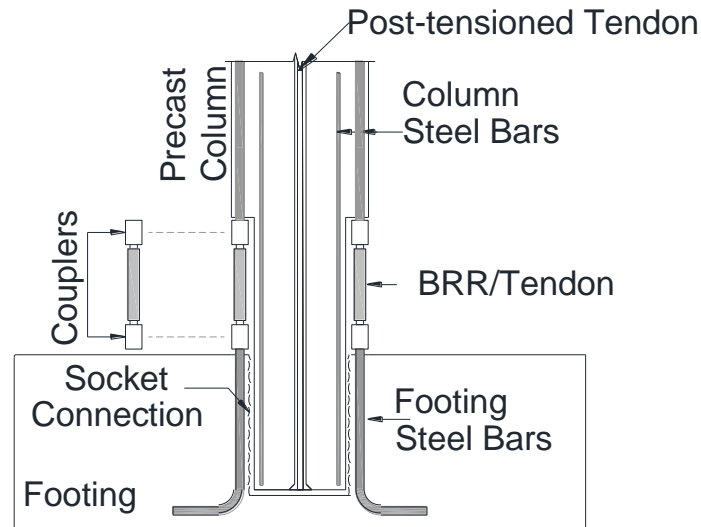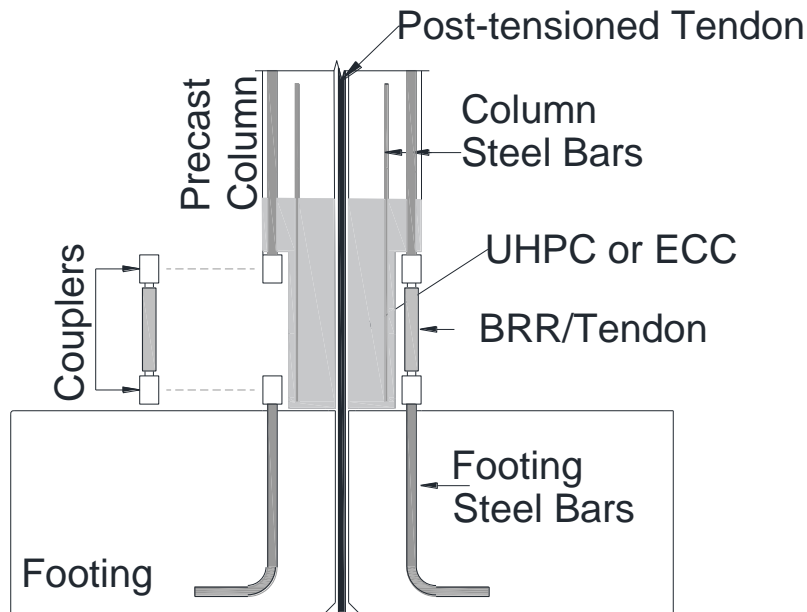

Figure 3.20. Repairable Column 19 Detailing

Table 3.20. Evaluation of Repairable Column 19

Parameter	Description (score reduction value)	Wt.	Score	Weighted Score
Seismic Performance				
Plastic Hinge Damage	No damage expected	1.0	1.0	1.0
Displacement Capacity	High displacement capacity expected	1.0	1.0	1.0
Residual Displacement	No/very low residual displacement expected.	1.0	1.0	1.0
Design Considerations				
Proof Test	No lab data available (-1.0)	1.0	0	0
Analysis Tools	Modeling available	0.75	1.0	0.75
Guideline Readiness	Concept tested, no guidelines (-0.25)	0.25	0.75	0.1875
Field Application	No previous field application (-1.0)	0.25	0	0
Construction and other Considerations				
Initial Cost	Higher cost than CIP (BRR, UHPC, tendon) (-1.0)	0.25	0	0
Material Limitation **Pass/Fail** (rubber in cold, etc.)	No material limitations	N/A		Pass
Constructability	Special field construction (coupler installation, post-tensioning) (-0.5)	1.0	0.5	0.5
Inspectability	Additional inspection (BRR, tendon) (-0.5)	0.75	0.5	0.375
Maintenance	Additional maintenance (BRR exposed, tendon) (-0.5)	0.75	0.5	0.375
System Performance	Soft start not likely, sliding possible (-0.5)	1.0	0.5	0.5
Total				5.6875

3.3.21 Repairable Column 20: Segmental

Figure 3.21 shows the detailing of the last repairable column alternative, Column 20, which is similar to the previous rocking columns but is constructed in two separate pieces, the neck and the main column section. This may allow for easier casting at the precast plant due to simplicity in the formwork but may make field construction more difficult. **Table 3.21** includes the evaluation of Column 20, with deductions for constructability, inspection, and maintenance due to the inclusion of the two separate segments and post-tensioning tendons. The necessary construction tolerances due to the separate neck section also likely will make field construction especially more difficult than previous column alternatives.
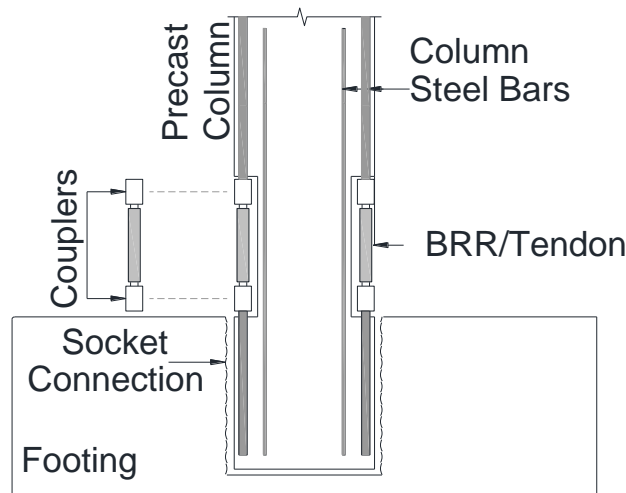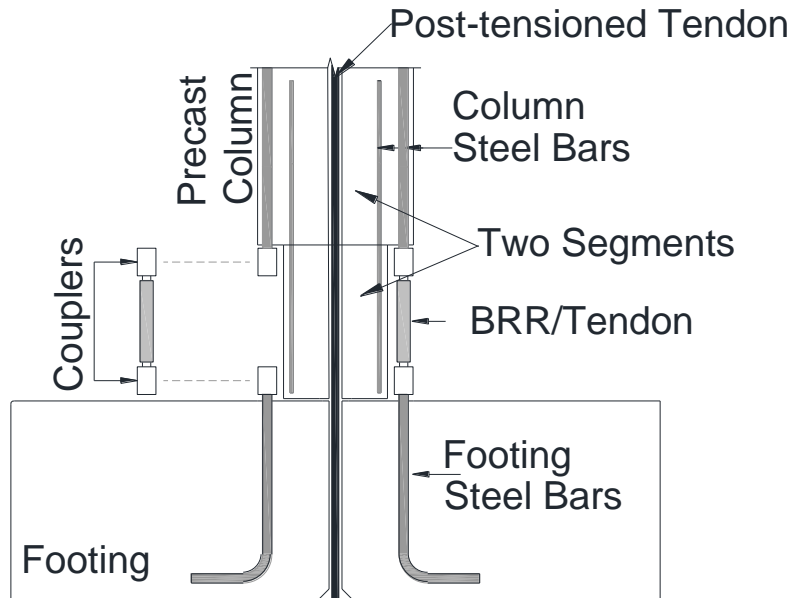

Figure 3.21. Repairable Column 20 Detailing

Table 3.21. Evaluation of Repairable Column 20

Parameter	Description (score reduction value)	Wt.	Score	Weighted Score
Seismic Performance				
Plastic Hinge Damage	Some damage possible (-0.25)	1.0	0.75	0.75
Displacement Capacity	High displacement capacity expected	1.0	1.0	1.0
Residual Displacement	No/very low residual displacement expected.	1.0	1.0	1.0
Design Considerations				
Proof Test	No lab data available (-1.0)	1.0	0	0
Analysis Tools	Modeling available	0.75	1.0	0.75
Guideline Readiness	Concept tested, no guidelines (-0.25)	0.25	0.75	0.1875
Field Application	No previous field application (-1.0)	0.25	0	0
Construction and other Considerations				
Initial Cost	Higher cost than CIP (BRR, tendon) (-0.5)	0.25	0.5	0.125
Material Limitation **Pass/Fail** (rubber in cold, etc.)	No material limitations	N/A		Pass
Constructability	Special field construction (coupler installation, post-tensioning, additional segment) (-0.75)	1.0	0.25	0.25
Inspectability	Additional inspection (BRR, tendon) (-0.5W)	0.75	0.5	0.375
Maintenance	Additional maintenance (BRR exposed, tendon) (-0.5)	0.75	0.5	0.375
System Performance	Soft start not likely, sliding possible (-0.5)	1.0	0.5	0.5
Total				5.3125

3.4 Summary of Evaluation for Repairable Columns

Conventional concrete, ECC, and/or UHPC combined with precast connections and rocking detailing results in 20 new feasible columns that can be repaired after an event through replacement of exposed bars. The 20 repairable column alternatives were evaluated using the NCHRP rating system, with a total weighted score of 9.0. For simplicity, all scores were converted to a five-star rating (**Table 3.22**) to determine the most viable alternatives. Some columns were rated better than others. However, it should be noted that all the proposed repairable columns will have a unique characteristic – repairability – which makes them better compared with conventional columns.

Table 3.22. Repairable Column Ratings on Five-Star Scale

Column	Five-Star Rating (0-5)
1: Pipe-pin	3.19
2: Pipe-pin w/ FRP jacket	3.09
3: Pipe-pin w/ UHPC or ECC	3.26
4: Rubber bearing	3.06
5: Large neck pipe-socket	2.99
6: Pipe-socket	2.92
7: Pipe-socket w/ FRP jacket	2.81
8: Pipe-socket w/ UHPC or ECC	2.99
9: Pipe-socket w/ post-tensioning	2.95
10: Neck-socket	2.92
11: Neck-socket w/ UHPC or ECC	2.95
12: Neck-socket w/ post-tensioning	2.95
13: Column-socket	3.06
14: Column-socket w/ UHPC or ECC	3.09
15: Column-socket w/ UHPC, post-tensioning	3.16
16: Column-socket w/ FRP jacket	2.95
17: Rocking	3.09
18: Rocking with FRP jacket	2.99
19: Rocking with UHPC or ECC	3.16
20: Segmental	2.95

3.5 Proposed Alternatives for Experimental Studies

Figure 3.22 shows the top four repairable column alternatives based on the rating system presented in the previous section, and **Table 3.23** presents the rating for these columns. Of the four alternatives, Column 1, which was ranked 2nd, was tested in a previous project by the research team (Sjurseth et al., 2022). Columns 3 and 15 (respectively ranked as 1st and 3rd) were selected for further experimental investigation in this project. Even though Column 19 rates as high as Column 15, the post-tensioning of Column 19 must be performed on site to connect the column to the footing. Nevertheless, the post-tensioning of Column 15 may be performed at the precast plant, which offers a better constructability and quality.

a) Column 1 – Ranked 2nd

b) Column 3 – Ranked 1st

c) Column 15 – Ranked 3rd

d) Column 19 – Ranked 3rd
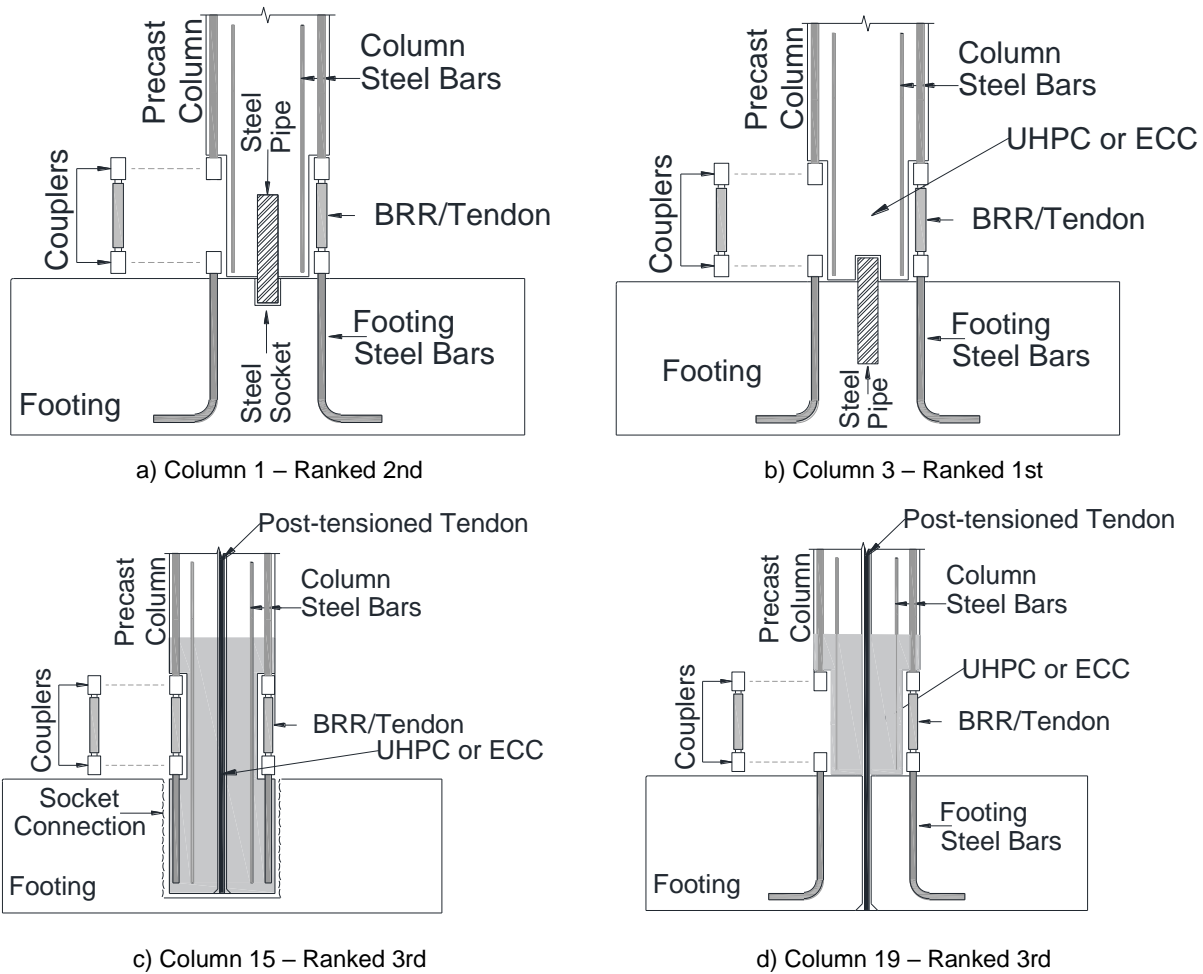
Figure 3.22. Detailing of Top-Rated Repairable Columns

Table 3.23. Top Four Repairable Column Alternatives

Rank	Column	Rating (0-5)
1	3: Pipe-pin w/ UHPC or ECC	3.26
2	1: Pipe-pin	3.19
3	15: Column socket w/ UHPC, post-tensioning 19: Rocking w/ UHPC	3.16

3.6 References

Saiidi, M.S., Tazarv, M., Varela, S., Bennion, S., Marsh, M.L., Ghorbani, I., Murphy, T.M. (2017). "Seismic Evaluation of Bridge Columns with Energy Dissipating Mechanisms, Volume 1: Research Overview and Volume 2: Guidelines," National Academies of Sciences, Engineering, and Medicine, NCHRP Report No. 864, Washington, DC: The National Academies Press, 344 pp.

Sjurseth, T., Greeneway, E., Hart, K., LaVoy, M., Tazarv, M., and Wehbe, N. (2022). "Mechanically Spliced Precast Bridge Columns," North Dakota State University - Upper Great Plains Transportation Institute, Fargo: Mountain-Plains Consortium (MPC), MPC Report No. 22-451, 359 pp.

Tazarv, M., Boudaqa, A., and Tuhin, I. (2020). "Repairable Precast Moment-Resisting Buildings: Part I—Experimental Investigations." ACI Structural Journal, Vol. 117, No. 6, pp. 147-160.

CHAPTER 4. EXPERIMENTAL INVESTIGATION ON REPAIRABLE PRECAST BRIDGE COLUMNS

4.1 Introduction

Bridge columns in high-seismic regions are expected to experience large displacement demands and should be designed to exhibit displacement capacities exceeding the demands. For reinforced concrete (RC) bridge columns, ductility is usually provided through confinement. Concrete spalling and reinforcement yielding are expected under moderate-level earthquakes and more severe damage such as core concrete crushing or bar buckling/fracture may be seen under strong earthquakes. Low- to no-damage details are emerging to minimize column damage. Nevertheless, development of novel details that allow repair of RC bridge columns through component replacement is an emerging field and is the focus of this study.

Precast bridge columns incorporating advanced materials and/or innovative detailing may allow for repair of columns through component replacement similar to how we repair a car. Twenty repairable details were developed for bridge columns in the previous chapter and top candidates were determined. An experimental investigation was performed at the Lohr Structures Laboratory (LSL) on the campus of South Dakota State University (SDSU) to determine the seismic performance of the top-rated repairable bridge columns. This chapter discusses the experimental study including the test matrix, design and construction of the test specimens, test setup, instrumentation plan, loading protocol, and test results.

4.2 Test Matrix

To evaluate the feasibility and seismic performance of the proposed repairable bridge columns, top three repairable columns from the previous chapter (**Fig. 3.22**) were selected for proof testing. Furthermore, one reference cast-in-place column was included to serve as the benchmark model. **Figure 4.1** shows the column details selected for testing and **Table 4.1** presents the column test matrix. The four test specimens can be identified using a naming system including the column and connection type. The reference cast-in-place column is identified using the acronym "CIP". The name for the repairable columns starts with RPH referring to "repairable precast with headed longitudinal bars/couplers" followed by the connection type: "PC" for the column utilizing a pipe-pin connection at the column base with the pipe embedded in the column, "PF" for a pipe-pin connection with the pipe embedded in the footing, and "NP" for the column with no pin connection but instead using a socket connection. Later, a third term is added to each column "R", which indicates that the column is repaired by component replacement and retested to prove the proposed repair-by-replacement concept.

Note that Column No. 19, which was jointly rated as the top third repairable column, was not included in the experimental study due to a budget constraint. Furthermore, CIP and RPH-PC were tested by the research team but in another study (Sjurseth et al., 2022) and are included herein for completeness.

Table 4.1. Column Test Matrix

Specimen Name	Exposed Reinforcement (Fuse) Type	Connection Type	Column Long. Reinforcement	Column Main Material	Additional Remarks
CIP	N/A	Monolithic	Black Steel	Conventional Concrete	Cast-in-place vertical construction
RPH-PC	Stainless Steel Bars Confined with Grouted Tubes	Pipe-Pin	Stainless Steel	SCC	Precast column seating on footing, column tested twice
RPH-PF	Steel Tendons	Inverted Pipe-Pin	Black Steel	UHPC	Precast column seating on footing, column tested twice
RPH-NP	Steel Tendons	Grouted Socket with no Pin	Black Steel	UHPC	Hybrid rocking precast column connected to footing via a socket connection, column tested twice

Note: SCC refers to self-consolidating concrete, and UHPC refers to ultra-high performance concrete.

a) CIP –Cast-in-Place Reference Column

b) RPH-PC w/ Pipe-pin Connection

c) RPH-PF w/ Inverted Pipe-pin Connection

d) RPH-NP w/ Grouted Socket Connection

Figure 4.1. Connection Details for Column Test Specimens

4.3 Design and Construction of Column Test Specimens

A summary of the design and construction of the test specimens is presented in this section.

4.3.1 CIP Column Model

A CIP column from a recent experimental study (Sjurseth et al., 2022) at SDSU was used as the reference column for this project. The CIP column geometry was determined based on the findings from another study at SDSU (LaVoy, 2020) that analytically found that coupler effects were more noticeable in columns with low aspect ratios, low axial loads, and high displacement capacities. The coupler effect was the highest for a column with an aspect ratio (the ratio of the column height to the column diameter) of 4, an axial load index (the ratio of the column axial load to the product of concrete strength and the column cross-sectional area) of 5%, and a displacement ductility capacity of seven. These properties were used in the design of CIP (Sjurseth et al., 2022). While circular RC columns are more common and have the most desirable seismic performance due to the highest confinement, an octagonal cross section with a circular bar arrangement was selected to allow for a horizontal pour at a precast plant.

The prototype conventional CIP column was designed based on AASHTO SGS (2011). A half-scale model of the prototype column was constructed due to size limitations in the laboratory. The scaling of the column properties was based on the recommendations by Krawinkler and Moncarz (1982).

The octagonal cross section was designed with a width of 24 in. (610 mm) and a height of 8 ft (2.44 m) from the top of the footing to the centerline of the applied lateral load resulting in an aspect ratio of 4. The CIP column model incorporated 10, No. 8 (Ø25-mm) longitudinal bars with No. 3 (Ø10-mm) transverse hoops spaced at 2 in. (51 mm) on center. The resulting longitudinal reinforcement ratio and transverse volumetric steel ratio were 1.66% and 2.0%, respectively. **Figure 4.2** shows the CIP column detailing. The column design axial load index was 5%, the design concrete compressive strength was 6,000 psi (41.4 MPa), and ASTM A706 bars were assumed for all reinforcement. The column was designed to achieve a minimum displacement ductility capacity of 7 based on AASHTO SGS (2011).

The upper 24 in. (610 mm) of the column section was changed to a square cross section to accommodate the hydraulic actuator which was fixed to the column using four high-strength threaded rods each passing through a PVC pipe in the head of the column. The CIP column was constructed monolithically in LSL at SDSU. The specimen was constructed vertically by first pouring the footing with the column cage embedded before casting the remainder of the column (**Fig. 4.3**). The concrete mix design was based on a precast plant mix by Gage Brothers Concrete Products in Sioux Falls, SD, at which the precast columns were constructed. This mix design, which had a target compressive strength of 6,000 psi (41.4 MPa), was provided to a local ready mix concrete company for the column pour.
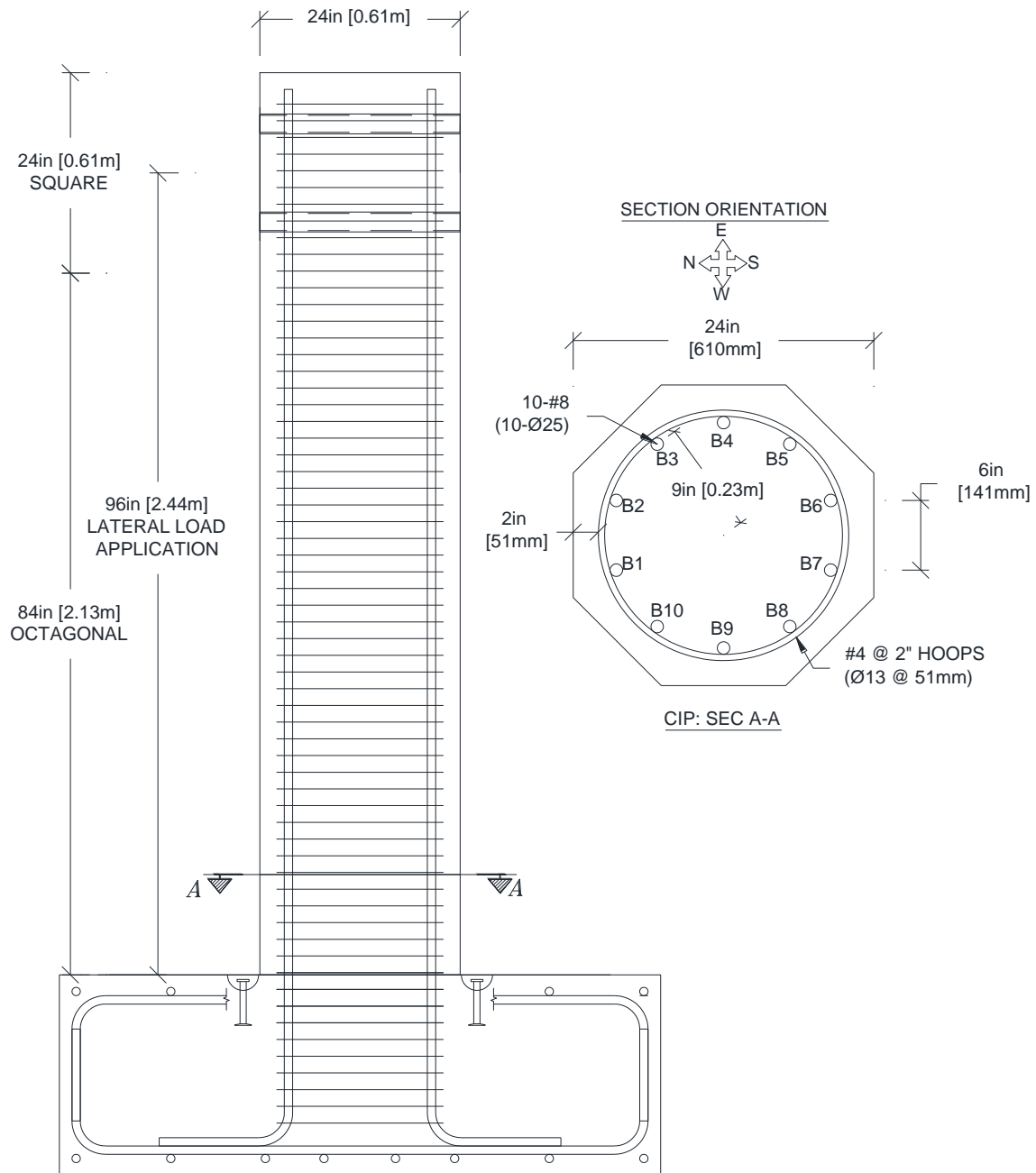
Figure 4.2. Reinforcement Detailing of CIP Column (Sjurseth et al., 2022)
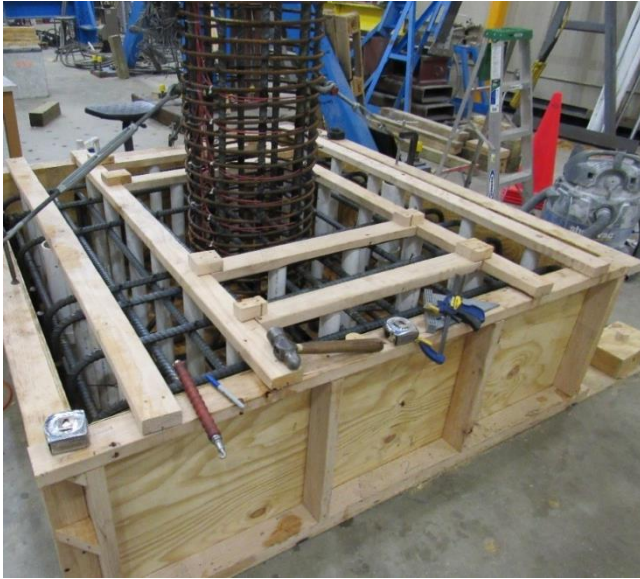
a) Before Pour   b) After Pour

Figure 4.3. Construction of CIP Footing (Sjurseth et al., 2022)

a) During Pour   b) After Pour

Figure 4.4. Construction of CIP Column (Sjurseth et al., 2022)

4.3.2. RPH-PC Column Model

Figure 4.5 shows the detailing of the repairable precast column with the pipe embedded in the column (RPH-PC). A similar cross section to that of the CIP column was used but a pipe-pin connection was devised between the precast column and footing to allow a large rotation at the column base while resisting plastic shear forces. A circular section with a reduced diameter was utilized at the column base to accommodate exposed reinforcement and connections. This reduced section is referred to as the "neck" hereafter. Note that similar to CIP, RPH-PC was constructed and tested by the research team under another project (Sjurseth et al., 2022).

Stainless steel bars were used instead of conventional black steel bars to improve the durability of the exposed components. Dowel bars matching the number and size of the exposed bars were extended out of the footing and the octagonal column to be connect to the exposed bars. Headed Reinforcement Corp. (HRC) 500 Series couplers were used in this precast column since they are detachable, reusable, and low profile. All bars were headed. The female portion of the coupler (the larger piece) was placed on the column/footing dowels and the male portion of the coupler was used on the exposed bar.

Longitudinal bars in the RPH-PC column and footing were oversized to No. 10 ($\emptyset$32 mm) compared with the No. 8 ($\emptyset$25 mm) bars that were used in fuses. This was done to ensure that the bar yielding occurs within the fuses but not in the column/footing dowels. No. 8 ($\emptyset$25 mm) stainless steel bars used as the exposed fuses were machined down from No. 10 ($\emptyset$32 mm) bars (**Fig. 4.6a**) to match the CIP longitudinal reinforcement (**Fig. 4.2**). In initial testing (fuses colored in yellow), the "dog-boned" length was 10.25 in. (260 mm) while the reduced diameter length was 5.125 in. (130 mm) in the second testing in which the column was repaired (fuses colored in green). Different fuse lengths were used to investigate their effects on the column overall ductility. A clear cover of 1 in. (25 mm) was used in the column.
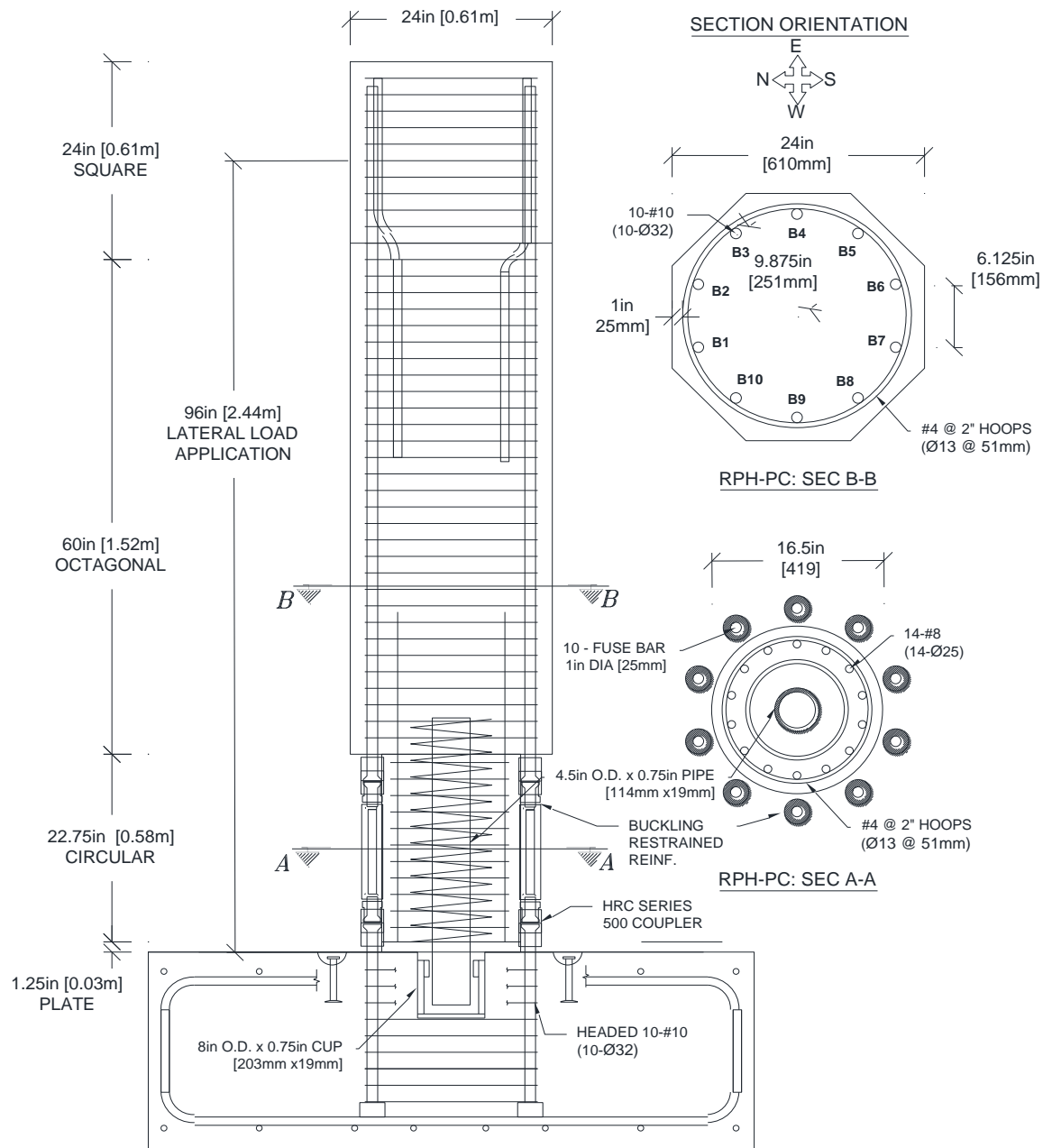
Figure 4.5. Reinforcement Detailing of RPH-PC Column

The exposed fuses were designed to resist buckling, and are referred to as "buckling restrained reinforcement, BRR" hereafter. As discussed earlier, the core reinforcement in BRR was No. 8 (Ø25 mm) stainless steel bar (**Fig. 4.6a**), which was machined from a larger bar. To prevent buckling, the core bar was placed inside a steel tube (**Fig. 4.6b**) then was filled with a high-strength non-shrink grout, "1428 HP" (**Fig. 4.6c**). The design of BRR was based on a previous study at SDSU (Boudaqa at al., 2017).

a) Dog-boned Fuse Bars and Couplers

b) Fuse Bars and Steel Tubes

c) BRR Grout Pour Setup

Figure 4.6. Construction of BRR used in RPH-PC

The neck section was designed assuming a secondary moment occurs in the opposite direction of the main column moment due to the lateral force against the pin connection. A moment-curvature analysis was performed in OpenSees (2016) using the 16.5-in. (419-mm) diameter neck cross section with No. 8 (Ø25-mm) longitudinal bars outside the section to simulate BRR. The resulting maximum moment was divided by the column length to determine the corresponding lateral force at the column base which was then multiplied by the length of the neck, 24 in. (610 mm), to determine the maximum neck moment. The neck moment was further increased by 20% including the material overstrength and then was used to design the longitudinal reinforcement of the neck. Thus, the neck was designed to experience minimal damage. The neck design resulted in 14 No. 8 (Ø25-mm) black steel bars as the neck longitudinal bars and No. 4 (Ø13 mm) transverse hoops spaced at 2 in. (51 mm). Note that the neck reinforcement were inside the section and were different from the exposed fuses, BRR.

A steel pipe and its matching steel socket (or cup) were utilized to resist shear forces of the moment-resisting connection. The pipe-pin connection was designed using the recommendations of Zaghi and Saiidi (2010). In this design, the reference lateral load capacity was taken as the lesser of the pure shear capacity of the in-filled (including the concrete within the pipe) steel pipe and the moment capacity of the pipe times its plastic hinge length. The neck had a shear reinforcement matching the column transvers reinforcement. An additional 10-in. (254-mm) O.D. No. 3 (Ø10-mm) spiral was incorporated in the neck section to provide further confinement around the steel pipe. To determine the shear capacity of the neck section, the shear capacity of the concrete in the neck, both sets of transverse reinforcement, and the pipe (determined using the ultimate moment capacity of the pipe) were included. The steel socket (cup) within the footing was assumed to have a significant shear capacity due to the large amount of concrete and reinforcement within the footing. It was found that the shear capacity of the in-filled pipe governed the design. In summary, the pipe-pin connection consisted of a 4.5 in. (114 mm) O.D. x 0.75 in. (19 mm) wall steel pipe which protruded into the neck section by 6.625 in. (168 mm). A 0.5-in. (13-mm) plate was

welded to the base of an 8 in. (203 mm) O.D. x 0.75 in. (19 mm) wall steel tube to provide a socket (cup) for the pipe to be inserted into. An additional 6.5 in. (165 mm) O.D. x 0.625 in. (16 mm) wall tube of length 2 in. (51 mm) was welded inside the upper portion of the larger cup to provide a contact surface for the pipe, simulating a pin connection (no moment) allowing the column to rotate.

A 1.25-in. (32-mm) thick steel plate with a diameter matching that of the neck section was placed between the column and footing to prevent concrete crushing at the rocking interface during testing. The plate had a 6-in. (152-mm) diameter hole at the center to allow for the pipe to pass through the cup embedded in the footing.

The precast RPH-PC specimen was built by Gage Brothers Concrete Products in Sioux Falls, SD, and the footing was constructed at SDSU. The construction sequence for RPH-PC was as follows:

- Cast the column with SCC at a precast plant with female portion of couplers on headed longitudinal bars (**Fig. 4.7**),
- Cast footing with normal concrete at SDSU with female portion of couplers on headed longitudinal bars (**Fig. 4.8**),
- Construct the BRR fuses at SDSU (**Fig. 4.6**),
- Erect and install the column (**Fig. 4.9**),
- Insert the fuses, tighten the couplers, and add clamping collars to prevent buckling of the column/footing dowels beyond the coupler (**Fig. 4.10**).

a) Column Cage   b) Concrete Pouring
Figure 4.7. Casting of RPH-PC Column

a) Footing Cage

b) Footing after Casting

Figure 4.8. Casting of RPH-PC Footing

a) Inserting Steel Pipe into Steel Can

b) Lowering Column

Figure 4.9. Erecting RPH-PC Column
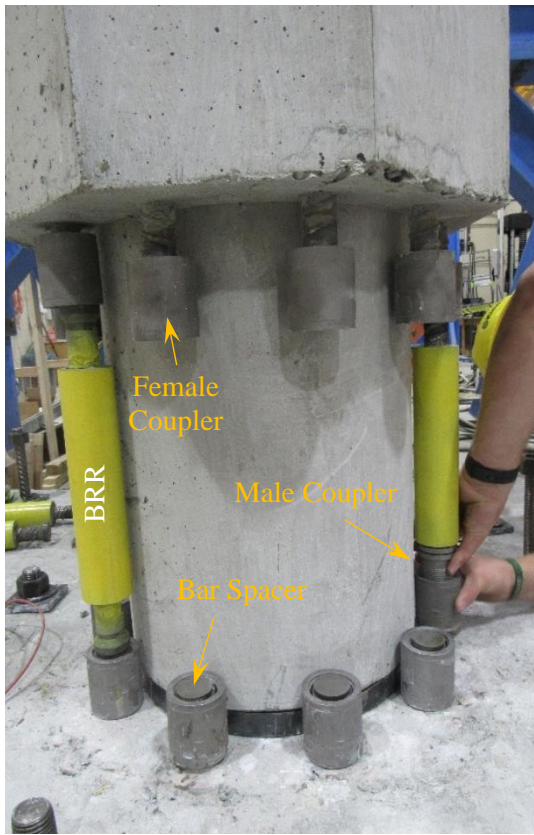
a) Inserting Fuses   c) Clamping Collars and Shims

Figure 4.10. RPH-PC BRR Fuse Installation

The longitudinal bars were extended out of both the footing and the main column cross section with a length of 3.375 in. (86 mm). After securing the column, there was a dowel head-to-head distance of 17.25 in. (438 mm). When the 17-in. (432-mm) long fuses were inserted, a total gap of 0.25 in. (6 mm) between the bar heads was observed. This gap was closed by inserting circular 0.125 in. (3 mm) spacers between the bar heads (**Fig. 4.10a**). The couplers were first tightened by hand before using a pipe wrench. The gap between the female portion of the couplers and the footing/column was closed using 1.325 in. (34 mm) bore clamping collars as well as steel washers (**Fig. 4.10c**). A slight gap between the base of the column and the steel plate was noticed on the southeast corner of the column and was filled by inserting rectangular 16-gauge (1.59 mm) steel shims. BRR limits the space to connect the coupler pieces. HRC 500 series couplers offers two male options of solid and split. The split male couplers were selected in this study to overcome the tight space issues imposed by BRR (**Fig. 4.10c**).

4.3.3. RPH-PF Column Model

After testing RPH-PC, the remaining top two column alternatives from **Chapter 3** were constructed at a precast plant, Gage Brothers, and assembled and tested at SDSU. Column alternative 3 was named RPH-PF, a repairable precast column with headed couplers and a pipe embedded in the footing. The detailing of RPH-PF (**Fig. 4.11**) was mostly the same as that of RPH-PC, but with some modifications based on lessons learned from the first repairable column testing (RPH-PC). The same geometry, cross section, and reinforcement as RPH-PC were used in the precast column, neck region, and cast-in-place footing. The clear cover in column was 1 in. (25 mm).
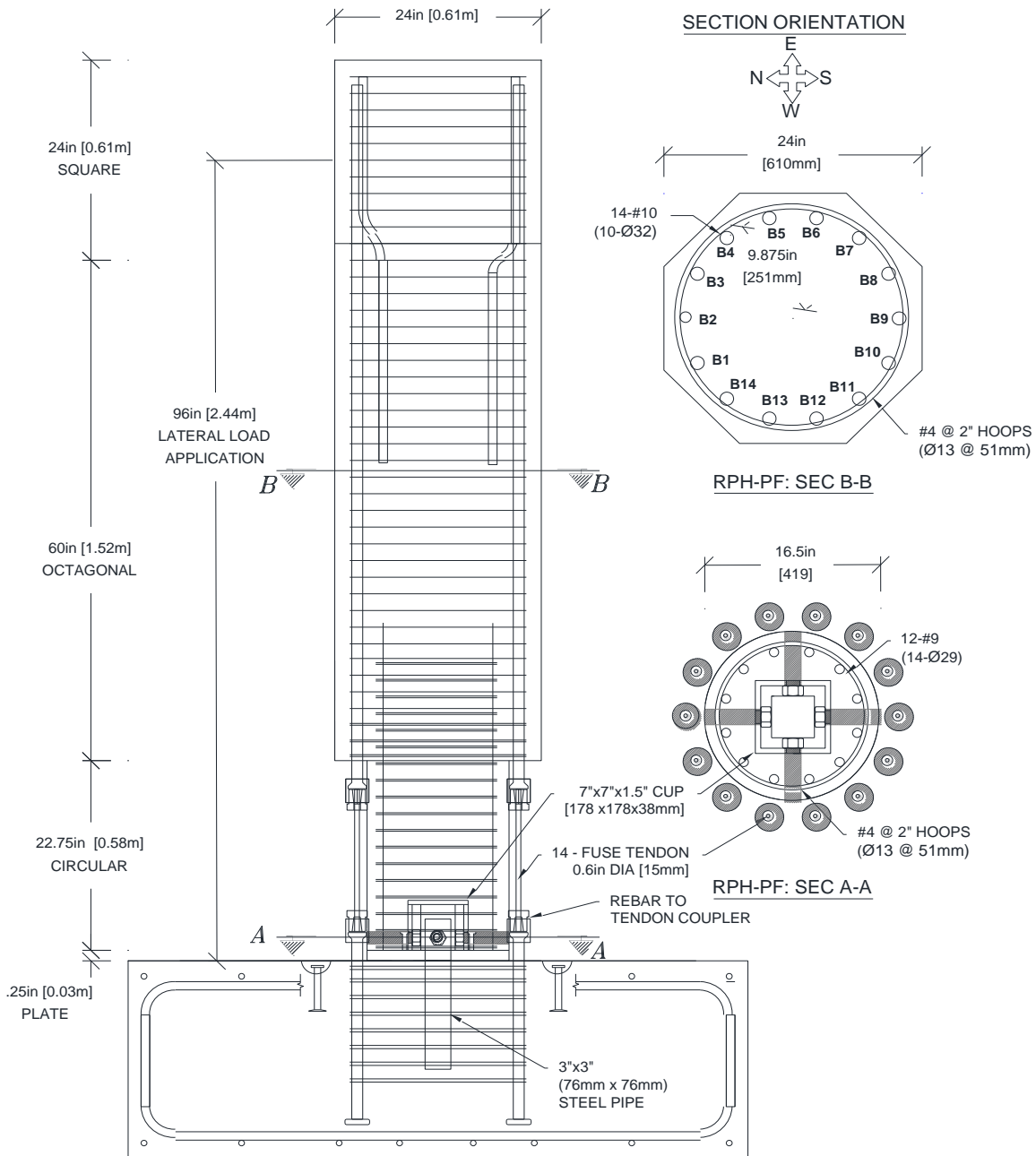
Figure 4.11. Reinforcement Detailing of RPH-PF Column

One major change in RPH-PF compared with RPH-PC was the use of UHPC in the column instead of SCC, which was done to reduce the apparent concrete damage. Furthermore, conventional black steel was used in lieu of stainless steel since the effects of stainless-steel bars were already explored in RPH-PC. Despite attempts to eliminate buckling of BRR in RPH-PC, a major Z-shape buckling occurred at high drift ratios outside BRR within the gap between the coupler and steel tube. To eliminate any type of buckling, a new bar-to-steel-tendon coupler was designed in collaboration with Headed Reinforcement Corp. in which the exposed fuses work in tension only in lieu of the tension-compression mechanism of BRR. The male portion of the HRC 500 couplers was redesigned to accommodate 0.6-in. (15-mm) diameter seven-wire steel tendon (**Fig. 4.12**). Since the area of a 0.6-in. (15-mm) tendon is approximately one-third that of a 1-in. (25-mm) diameter bar used in BRR, the number of longitudinal reinforcing bars in RPH-PF was increased from 10 to 14 to better match the moment thus lateral force capacity of RPH-PC.

Another detailing modification was that the pipe (now a solid steel shaft) in RPH-PF was embedded into the footing rather than the column as was the case in RPH-PC. This allowed for the steel socket to be inverted and placed in the column neck section, eliminating durability issues such as possible water buildup in the socket. Furthermore, the pipe cross section was changed from a circle to a solid square to better resist column torsion. The steel shaft was also designed using the recommendations of Zaghi and Saiidi (2010). However, to reduce the size of the steel socket within the neck, a solid 3-in. (76.2-mm) square steel tube was used in lieu of a hollow pipe filled with concrete as in RPH-PC. The shear capacity of the shaft governed the design.

a) Tendon Coupler Components

b) Steel Tendon and Couplers
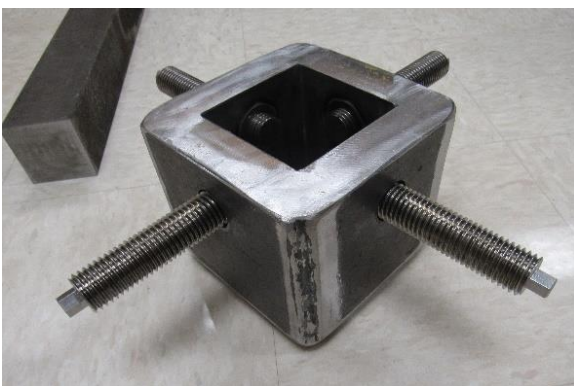
c) Solid Steel Pipe and Socket

b) Steel Plate with Shear Pins

Figure 4.12. RPH-PF Column Components

Rather than using steel shims to fill the gap between the pipe and socket (cup), the square cup in RPH-PF (**Fig. 4.12**) was designed to accommodate bolts and marching nuts to close the gap. High-strength 1.125-in. (29-mm) diameter steel nuts were welded to the 1-in. (25-mm) thick walls of the cup. An additional 0.5-in. (13-mm) thick steel plate was welded to the outside of each face of the cup to provide an additional bearing surface for the nuts, with a 1.325-in. (34-mm) diameter hole cut to allow the steel rod to pass through. The 1.125-in. (29-mm) high-strength steel rods were machined on one end to create a 0.5-in. (13-mm) socket head, allowing them to be screwed into place without the loss of concrete cover that would have been required if a bolt with a larger head was used. To allow for the threaded rods to pass through the neck section, it was necessary to rearrange the longitudinal bars within the neck. The overall area of the reinforcement was kept the same as RPH-PC, but the bars were increased in size to No. 9 (Ø29mm) with the quantity reduced from 14 to 12. To increase the effect of confinement within the neck, double No. 4 (Ø13 mm) transverse hoops were used, with the spacing remaining at 2 in. (51 mm). The first three levels of hoops in the main octagonal cross section were also changed to double hoops to eliminate the large spalling observed on the south face of RPH-PC. Finally, the hole in the 1.25 in (32 mm) thick steel plate was also changed from circular to a square with 4-in. (102-mm) side dimensions (**Fig. 4.12d**). Four shear studs were welded to the plate, and the plate was placed at the column base prior to pour. The plate was used at the rocking interface to reduce concrete damage at large displacements.

The RPH-PF specimen was built by Gage Brothers in Sioux Falls, SD, while the footing was constructed at SDSU. The construction sequence for RPH-PF was as follows:

- Cast the column with UHPC at the precast plant with the female portion of couplers on the headed longitudinal bars (**Fig. 4.13**),
- Cast footing with normal concrete at SDSU with the female portion of couplers on headed longitudinal bars (**Fig. 4.14**),
- Erect and install the column (**Fig. 4.15**),
- Insert the tendons, tighten the couplers, and add clamping collars to prevent buckling of the bars above the coupler (**Fig. 4.16**).

a) Column Cage   b) UHPC Pouring

Figure 4.13. Casting of RPH-PF Column

| a) Footing Cage | b) Footing after Casting and Before Concrete Grinding |

Figure 4.14. Casting of RPH-PF Footing

Steel Base Plate

Solid Steel Shaft

| a) Inserting Solid Steel into Steel Socket | b) Tightening Shear Pin Threaded Rods |

Figure 4.15. Erecting RPH-PF Column
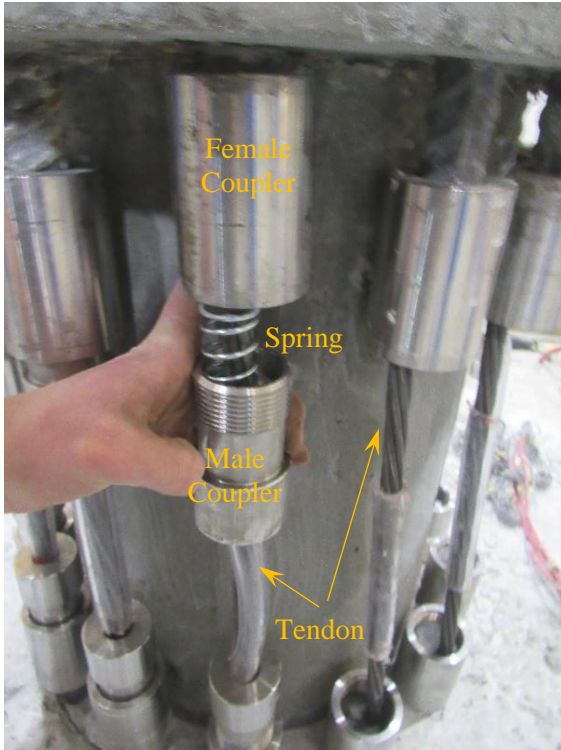
a) Inserting Fuses   b) Full Installation with Clamping Collars

Figure 4.16. RPH-PF Tendon Fuse Installation

The longitudinal bars were extended out of both the footing and precast column with a length of 3.375 in. (86 mm), resulting in a head-to-head distance of 17.25 in. (438 mm). The steel tendons were cut with a length of approximately 15 in. (318 mm) to ensure a gap of at least 2 in. (50.8 mm) between the ends of the tendons and bar heads which would prevent buckling of the tendons at high drift ratios and allow for adequate clearance during installation. The tendons were covered in plastic tubes as a safety measure in the case of tendon rupture during crack marking. The couplers were first tightened by hand then using a pipe wrench which resulted in tendon tensile forces of 10 kips (44.5 kN) based on strain gauge data. The remaining gap between the female portion of the couplers and the footing/column was closed using 1.325-in. (34-mm) bore clamping collars similar to what was done in RPH-PC. A small gap was left above the clamping collars rather than completely filling it with steel washers to prevent any concrete spalling.

4.3.4. RPH-NP Column Model

The repairable design concept of Column No. 15 from **Chapter 3**, which was a hybrid rocking column with replaceable fuses, was included in the test program as the repairable precast column with no shear pin (RPH-NP). **Figure 4.17** shows the hybrid rocking column detailing. The cross-sectional properties, reinforcement, and cementitious materials of PRH-NP were the same as those of RPH-PF. UHPC was used for the entire precast column. Steel tendons were incorporated as tension-only fuses and no BRR was used. The column was fully precast and was connected to the footing using a grouted socket (pocket) connection. To accommodate the socket connection, the height of the footing was increased from 2 ft (610 mm) used in all other columns to 3 ft. (914 mm). The column height from the top of the footing to the centerline of the applied lateral load remained the same as other specimens, 8 ft. (2.44 m).
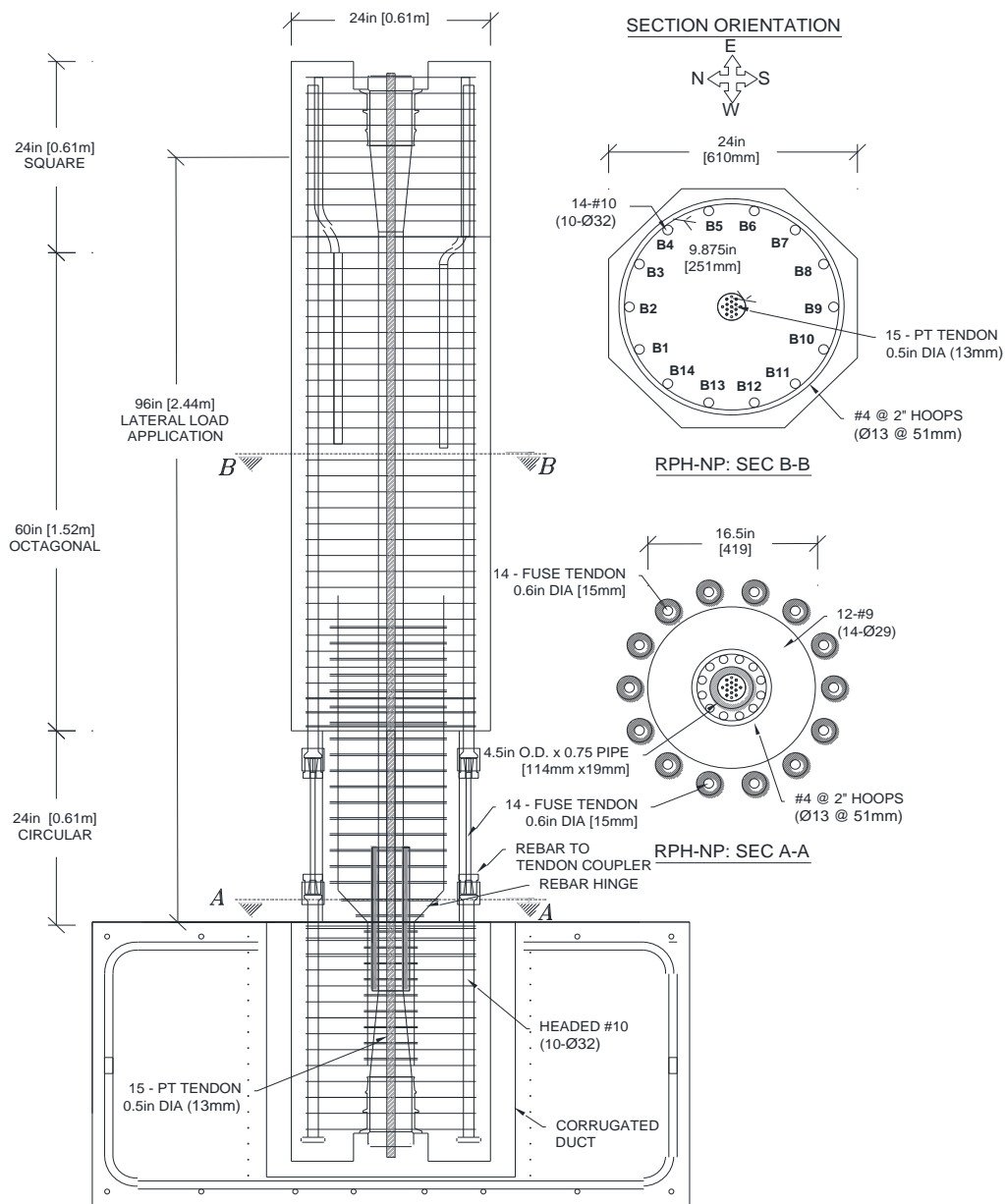
Figure 4.17. Reinforcement Detailing of RPH-NP Column

The grouted socket connection of RPH-NP was designed based on recommendations by NCHRP Report 935 (Saiidi et al., 2020). The socket was constructed using a 30-in. (762-mm) diameter steel corrugated duct conforming to ASTM A760. The duct was capped at the bottom using a thin piece of sheet metal and rested on the bottom layer of footing reinforcement. The 32-in. (813-mm) deep socket was then surrounded by No. 4 (Ø13 mm) transverse hoops spaced at 2 in. (51 mm) and eight No. 4 (Ø13 mm) steel bars placed diagonally to reinforce the socket at the four corners of the footing, in addition to the top layer of reinforcing mesh. Bars in the top layer of mesh that would otherwise intersect the socket had to be cut and bent.

To make the whole column precast, an additional octagonal cross section with dimensions matching the upper octagonal section was added below the circular neck section with a length of 30 in. (762 mm). The lower octagonal portion of the column was inserted into the socket connection (duct) providing 2 in. (51 mm) of gap underneath the column and 3 in. (76 mm) of gap surrounding the column to allow for grout to pass through. The detailing of the main longitudinal and transverse reinforcement was kept the same as the upper portion of the column, with the first three layers of hoops below the neck as double hoops. HRC Series 555 head bars were incorporated at the column base to allow for sufficient embedment length.

Post-tensioning requirements of the hybrid rocking column were designed following recommendations from NCHRP Report 864 (Saiidi et al., 2017) in which the total tendon area must be greater than 0.4% of the gross cross-sectional area of the column and the initial tendon stress after all losses should be less than 30% of the tendon yield strength. These design values ensure that steel tendons do not yield, and that the column fails either by bar/fuse fracture or core concrete crushing. The final design resulted in 15, 0.5-in. (13-mm) diameter grade 270 (1862-MPa) seven-wire steel strands, each post-tensioned to no more than 60 ksi (414 MPa). A "DYWIDAG 19-0.5 Multiplane Anchorage MA" system was incorporated to anchor the 15 unbonded tendons, which were grouped and passed through the column cross section using a 3-in. (76-mm) plastic duct.

Reinforcement of the neck section was kept the same as RPH-PF, with 12, No. 9 (Ø29mm) longitudinal bars and No. 4 (Ø13 mm) double hoops spaced at 2 in. (51 mm). With the neck longitudinal bars extending into the lower portion of the column (since the column was now to be connected to the footing through the socket connection), it was necessary to reduce the moment caused by the neck longitudinal bars. In this project, it was decided to use a rebar hinge to minimize the contribution of the neck bars to the overall moment capacity of the column. The rebar hinge was created by bending the neck bars towards the center of the column at the interface of the neck section and the lower octagonal cross section (or footing surface, **Fig. 4.18**). The double No. 4 (Ø13 mm) hoops then continued below the rebar hinge at a smaller diameter toward the bottom tendon anchorage.

With the neck bars bent at the base of the neck section, a steel pipe was added to ensure that the column does not fail in shear. The pipe was designed to match the 4.5-in. (114-mm) O.D. x 0.75-in. (19-mm) wall steel pipe used in RPH-PC. The 18-in. (457-mm) long pipe was placed against the edge of the lower anchoring system, matching the 3-in. (76-mm) inner diameter of the tendon duct, and extending into the neck section by approximately 9.375 in. (238 mm).

a) Post-Tensioning Duct, Rebar Hinge, and Longitudinal Headed Bars

b) Post-Tensioning Anchorage System

c) Neck Cage with Rebar Hinge and Post-Tensioning Duct
Figure 4.18. RPH-NP Column Components

Similar to other precast columns, the RPH-PC specimen was built by Gage Brothers in Sioux Falls, SD, while the footing was constructed at SDSU. The construction sequence for RPH-NP was as follows:

- Cast the column with UHPC at the precast plant with the female portion of couplers on the headed longitudinal bars (**Fig. 4.19**),
- Cast footing with normal concrete at SDSU with the female portion of couplers on the headed longitudinal bars (**Fig. 4.20**),
- Insert the post-tensioning tendons then tension the tendons at the precast plant (**Fig. 4.21**),
- Secure the column in the footing then grout the corrugated duct of the socket connection (**Fig. 4.22**),
- Insert the fuse tendons, tighten the couplers, and add clamping collars to prevent buckling of the bars above and below the couplers (**Fig. 4.23**).

a) Upper Column Cage

b) Lower Column Cage

c) UHPC Pouring

Figure 4.19. Casting of RPH-NP Column

a) Footing Cage

b) Footing after Casting

Figure 4.20. Casting of RPH-NP Footing

a) Steel Tendons

b) Hydraulic Ram

Figure 4.21. Post-Tensioning RPH-NP Column at Precast Plant

a) Inserting Column into Footing Socket

b) Grouting Footing Socket

Figure 4.22. Erecting RPH-NP Column

| a) Cutting Steel Tendons to be Used as Fuses | b) Tendon Fuses and Couplers Installed |
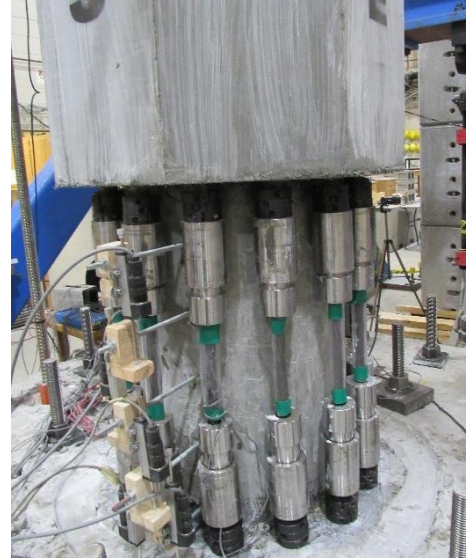
Figure 4.23. RPH-NP Tendon Fuse Installation

Post-tensioning was performed at the precast plant 3-days after the column pour with UHPC. A hydraulic ram was used to tension each of the 15 tendons in a circular pattern (**Fig. 4.21**). Strands were laid out before being inserted into the PT duct to ensure that no tendon twisting occurred. Five strain gauges were placed on five tendons, one per tendon, near the base of the column to record strain data both during the post-tensioning and column testing. Column UHPC strength on the day of post-tensioning was 14,655 psi (101 MPa). Strands were stressed to no more than 60 ksi (414 MPa), approximately equivalent to 25% of the tendon yield strength.

Before erection, the post-tensioning strain gauges were inserted into a plastic tube to allow them to extend out of the socket and a foam recess was used to cover the PT anchorage at the base of the column so that no grout would flow up into the PT duct. The column was erected by lowering the base into the corrugated socket and inserting shims to ensure adequate spacing for grout to flow (**Fig. 4.22**). H.R. Meadows 1428 HP non-shrink grout was mixed to a plastic consistency to ensure high strength and poured into the socket. After curing, a lower strength grout was used to level out the footing surface strictly for aesthetic purposes.

The longitudinal bars were extended out of the footing and the precast column with a length of 3.375 in. (86 mm), which was the same as the other two repairable columns. Tendons were inserted with the same process as RPH-PF before addition of the clamping collars. Some grinding of concrete around the base of the circular neck section was necessary to allow for the couplers to adequately slide and rotate for tendon installation due to leakage of UHPC during the pour.

4.4 Test Setup, Instrumentation, and Loading Protocol

The test setup, instrumentation, and loading protocol of the column test specimens are discussed herein.

4.4.1 Test Setup

A test setup with a cantilever configuration was utilized to laterally test columns in this project (**Fig. 4.24).** A series of four concrete reaction blocks, 3 x 5 x 8-ft (0.91 x 1.52 x 2.44-m) were stacked and post-tensioned to the lab strong floor. A 328-kip (1460-kN) hydraulic actuator was mounted between the reaction blocks and the head of the column to apply the horizontal displacements while high-strength threaded rods and two hollow core jacks were used to apply the axial load between the footing and a spreader beam mounted on the top of the column in a self-reacting mechanism.
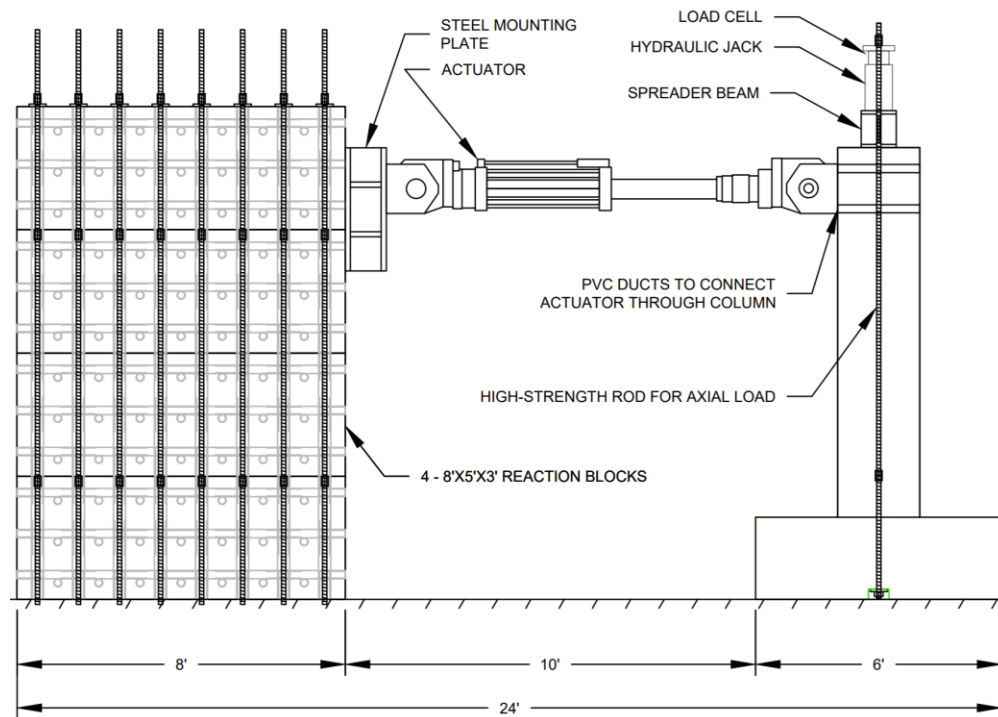
a) Column Test Setup Elevation View
Figure 4.24. Column Test Setup

b) Photograph of Column Test Setup
Figure 4.24. Continued

4.4.2 Instrumentation

Test data was recorded using various instruments and sensors. Strain gauges were installed on the longitudinal and transverse reinforcement at various levels within the footing and column cross sections. Concrete strain gauges were also utilized in a circular pattern at the base of the three repairable columns to evaluate concrete stresses at the column rocking interface. **Figure 4.25** shows the strain gauge plan used in the CIP column and **Fig. 4.26** shows the typical strain gauge plan used for the repairable columns. **Table 4.2** presents the strain gauge schedule for the column models. Note in RPH-NP, five strain gauges were placed on post-tensioning tendons at the column base. Three string potentiometers were used to measure the horizontal displacements and rotations of the column head as indicated in **Fig. 4.27** and the actuator load cell measured the lateral load. Rotations and curvatures were measured within the plastic hinge region using linear variable displacement transducers (LVDTs) on the north and south faces of the column (**Fig 4.27**). An additional LVDT was mounted at the base of the RPH-PC column to record lateral slippage due to a possible gap between the pipe and socket in the pipe-pin connections. However, this LVDT was not used in other repairable columns due to no/minimal gap. A 100-kip (445-kN) load cell was placed above each of the hollow-core jacks to measure the column axial load during testing. The axial load was adjusted between test runs at each drift ratio to achieve a constant target axial load of 155 kips (689 kN). This target axial load corresponds to an axial load index of approximately 5% for a design concrete strength of 6,000 psi (41.4 MPa). The actual index varied due to differences in concrete strength on the test day, especially with the use of UHPC in last two test specimens. All instrumentation was connected to a 128-channel data acquisition system using a sampling rate of 10 Hz.
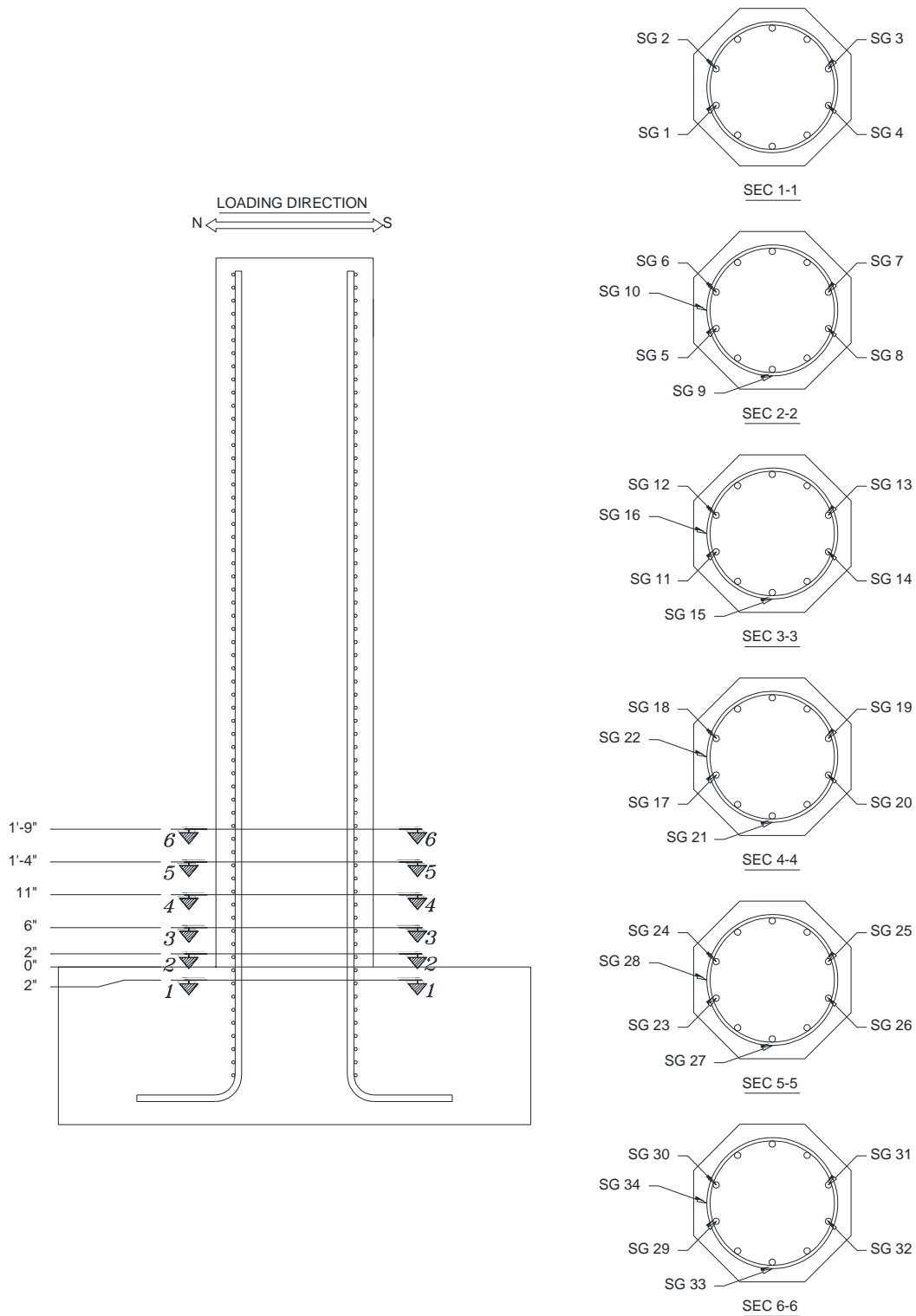
Figure 4.25. Strain Gauge Plan Used in Cast-in-place Column
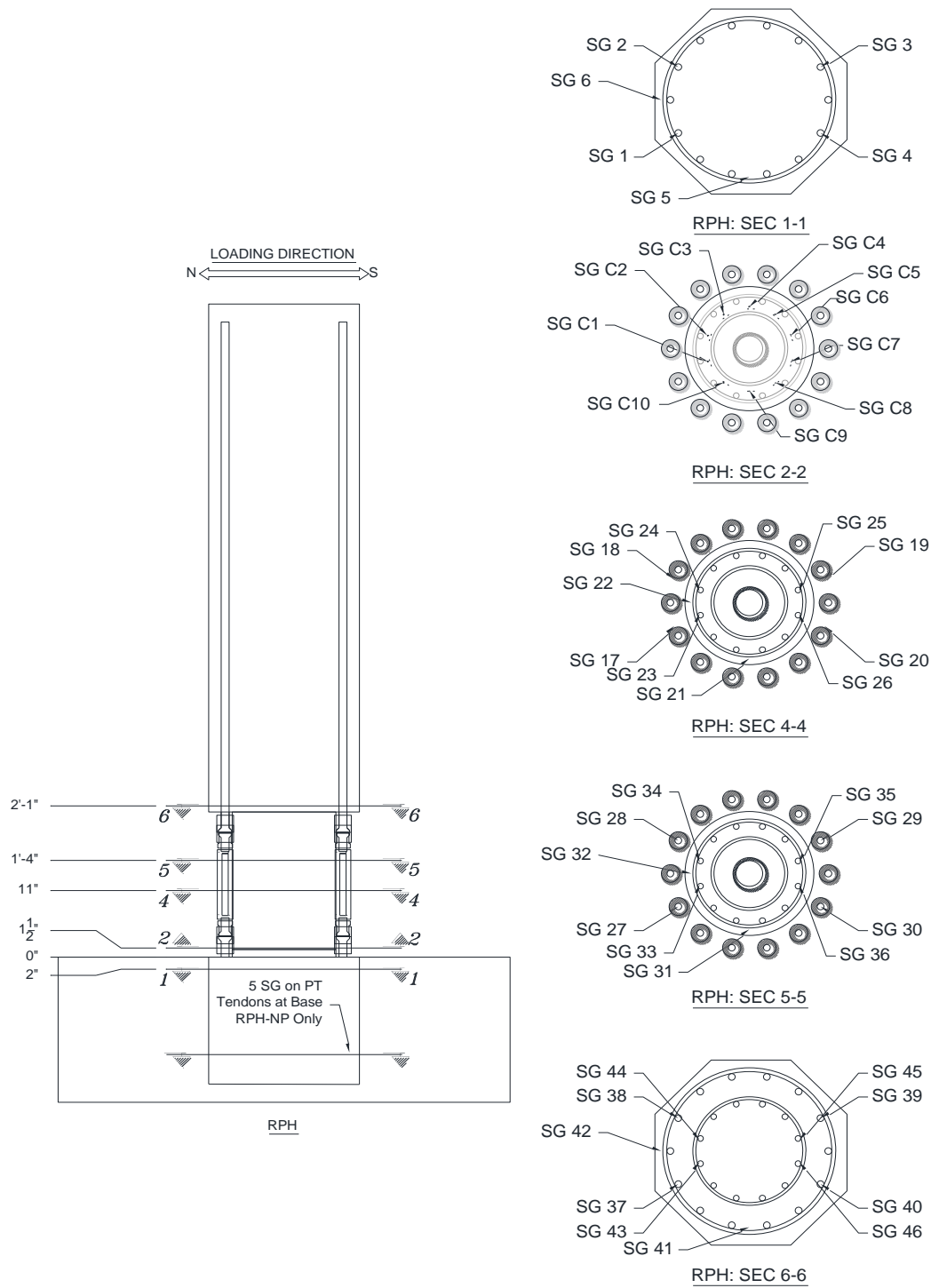
Figure 4.26. Typical Strain Gauge Plan Used in Repairable Precast Columns

Table 4.2. Column Model Strain Gauge Placement Schedule

Column	Sections Where Strain Gages Were Placed					
	SEC 1-1	SEC 2-2	SEC 3-3	SEC 4-4	SEC 5-5	SEC 6-6
CIP	X	X	X	X	X	X
RPH-PC	X	Conc. SG	No SG	X	X	X
RPH-PF	X	Conc. SG	No SG	X	X	X
RPH-NP*	X	Conc. SG	No SG	X	X	X

Note: "X" indicates that strain gauges were placed in column cross sections shown in Fig. 4.25 & 4.26.

* In RPH-NP, five strain gauges were placed on post-tensioning tendons at the column base.
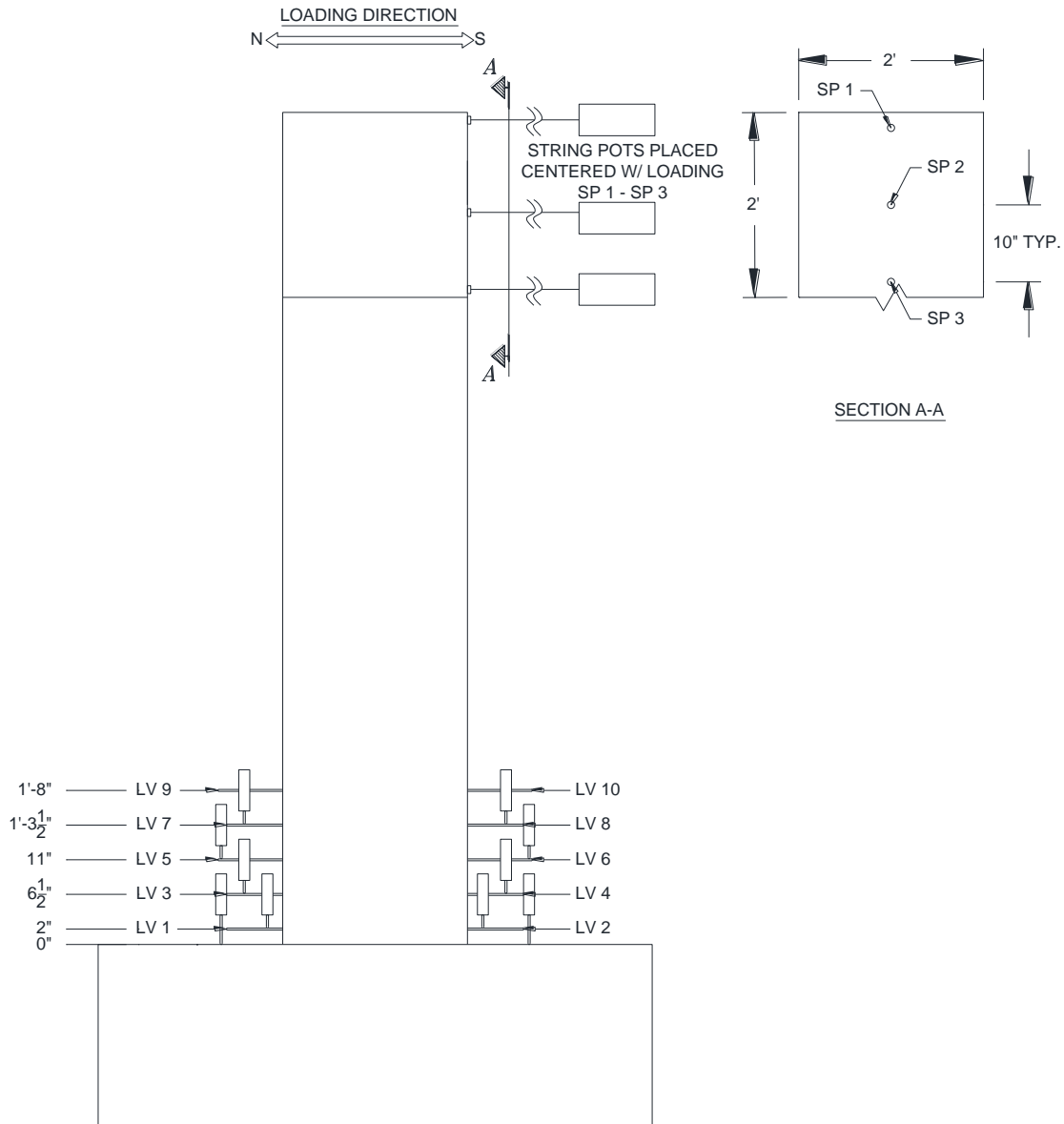
Figure 4.27. Typical LVDT and String Potentiometer Locations Used in Column Models

4.4.3 Loading Protocol

The column specimens were tested under an increasing cyclic drift-based lateral loading protocol conforming to ACI 374.2R-13 (2013). **Figure 4.28** shows the column loading regime. Drift is the ratio of the column lateral displacement to the column height. The columns were subject to two cycles of each drift ratio in both the push and pull directions. Initial cycles with drift ratios from 0.25% to 2% used a displacement rate of 3.0 in./min (76.2 mm/min) to record the yield point of the columns after which the rate was increased to 30 in./min (762 mm/min). These displacement rates were estimated based on ASTM E8 strain rate limits for steel bar tensile testing.
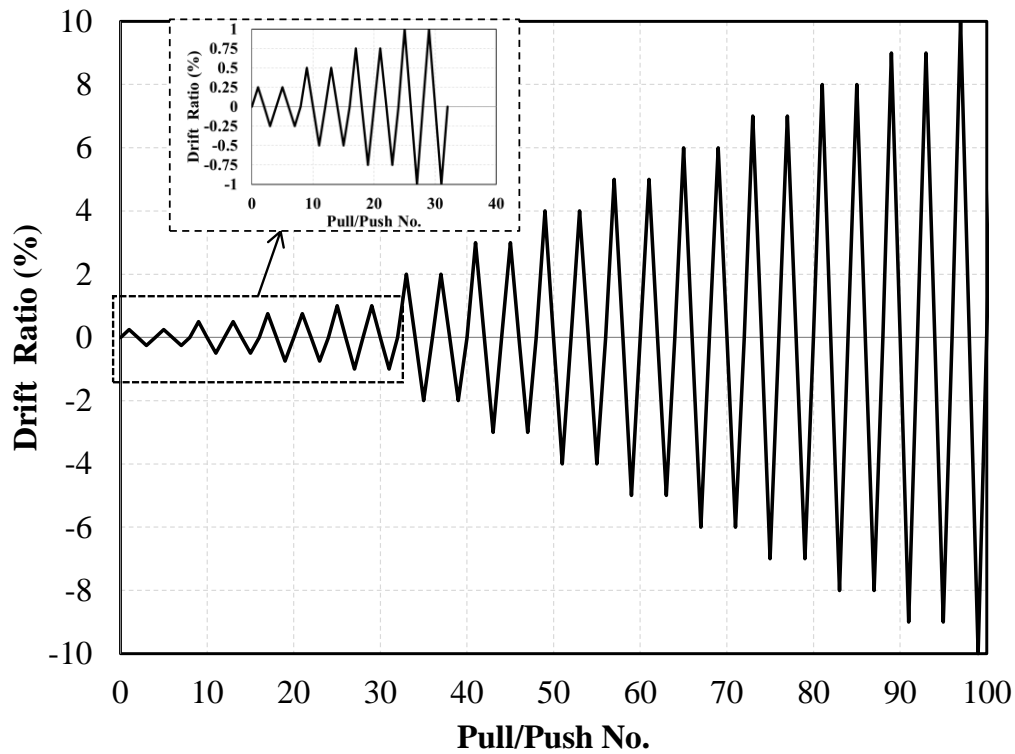
Figure 4.28. Typical Loading Protocol Used for Column Testing

4.5 Test Results

The testing of the CIP reference column and three repairable precast columns was performed at LSL on the campus of SDSU. Constitutive material properties for each column were also obtained. This section presents the results of the material and column tests.

4.5.1 Material Properties

Materials utilized in the construction of the CIP and repairable columns included conventional ready-mix concrete, SCC, UHCP, non-shrink grout, stainless and conventional steel bars, and steel tendons. The measured mechanical properties of each of these materials are presented herein. Testing of each material followed standard ASTM procedures when applicable.

4.5.1.1 Conventional Concrete

Conventional concrete from a local ready-mix plant was used in construction of all column footings as well as the CIP column. ASTM C39/C39M testing protocol was used to measure the compressive strength of standard 6-in. (152-mm) diameter cylinder samples with a height of 12 in. (305 mm). **Table 4.3** presents the measured concrete strength at 7-day, 28-day (when applicable), and the column test day.

4.5.1.2 Self Consolidating Concrete

The precast RPH-PC column was poured using SCC as it is a typical material in the precast industry. Standard samples with identical dimensions as those for the conventional concrete were taken and tested according to the same ASTM standard. **Table 4.3** presents a summary of SCC strength at different days.

4.5.1.3 Ultra-High Performance Concrete

UHPC was used in the construction of the RPH-PF and RPH-NP column specimens. The mix, designed by Gage Brothers, utilized a specific ratio of sand, cementitious material, water, and high-range water reducer. Samples were taken using 3-in. (152-mm) diameter cylinders with a height of 6 in. (305 mm). This sampling size is common for UHPC due to its high strength and limitations of compressive machines. A diamond saw blade was used to cut a small slice off of either end of the cylinders after stripping to provide a flat surface for compressive testing since typical rubber pads and steel caps are not used for the UHPC testing. A summary of UHPC compressive strength is reported in **Table 4.3**. Due to time limitations in finishing the experimental part, the columns were tested prior to 28 days. Columns RPH-PF and RPH-PF-R were tested 9 days after both the column and footing pour and columns RPH-NP and RPH-NP-R were tested 16 days and 17 days after the column and footing pour, respectively. This resulted in a small variation of UHPC strength between 7 days and the RPH-PF test day. Note that "-R" in the column naming indicates that the column was repaired and retested.

4.5.1.4 Non-Shrink Grout

High-strength non-shrink grout was used in BRR fuses of RPH-PC as well as the grouted socket connection of RPH-NP. W. R. Meadows 1428 HP grout was used for both applications. Two-inch (51-mm) cube samples were collected for each grout type following ASTM C109/C109M and their compressive strengths were determined using ASTCM C109/C109M. **Table 4.3** presents a summary of the measured grout compressive strength. Columns RPH-NP and RPH-NP-R were respectively tested 3 days and 4 days after the socket grout pour, resulting in a lack of 7-day and 28-day strength data in the table.

Table 4.3. Measured Compressive Strength of Cementitious Materials Used in Column Models

Material	Element	Measured at	CIP	RPH Column Models, psi (MPa) PC	PC-R	PF	PF-R	NP	NP-R
Conventional, SCC, and UHPC Concrete*	Footing	7-Day	3670 (25.3)	5954 (41.1)		6524 (45.0)		6524 (45.0)	
		28-Day	4620 (31.9)	6894 (47.5)		N/A		N/A	
		Test Day	4920 (33.9)	7421 (51.2)	7250 (50.0)	6515 (44.9)		6617 (45.6)	6631 (45.7)
	Column	7-Day	3360 (23.2)	9161 (63.2)		14655 (101)		14655 (101)	
		28-Day	4010 (27.6)	10189 (70.3)		N/A		N/A	
		Test Day	4300 (29.6)	10699 (73.8)	10597 (73.1)	14533 (100.2)		15068 (103.9)	15144 (104.4)
Grout	BRR and Socket	7-Day	N/A	6132 (42.3)	6132 (42.3)			N/A	
		28-Day	N/A	N/A	N/A	N/A		N/A	
		Test Day	N/A	7055 (48.7)	7568 (52.2)			6845 (47.2)	7460 (51.4)

* Conventional concrete was used in the CIP column and all footings. SCC was used in the RPH-PC column and UHPC was used in the RPH-PF and RPH-NP columns.

4.5.1.4 Reinforcing Steel Bars

Both conventional black steel bars conforming to ASTM A706 Grade 60 (414 MPa) and stainless-steel bars conforming to ASTM A955 Grade 60 (414 MPa) were used in this project. The reference CIP column was reinforced longitudinally using No. 8 (Ø25-mm) conventional steel bars. The three repairable columns were reinforced longitudinally using No. 10 (Ø25-mm) bars (stainless steel in RPH-PC; conventional black steel in RPH-PF and RPH-NP) while the BRR fuse in RPH-PC were dog-boned stainless steel with a diameter of 1.0 in. (25 mm.) to match the CIP column bar area. All specimens were reinforced transversely with No. 4 (Ø13-mm) hoops at 2 in. (51 mm.) pitch. ASTM E8 was followed for tensile testing of all bars. **Table 4.4** presents the measured average tensile properties for all steel bars used in this project.

Table 4.4. Measured Strength of Reinforcing Steel Bars Used in Column Models

Bar	Column Model	Bar Size	ASTM Type	Yield Strength, f_y ksi (MPa)	Ultimate Strength, f_u ksi (MPa)	Post-Yield Stiffness, E_{sh} ksi (MPa)	Ultimate Stain, ε_u (%)*
Long. Bars	CIP	No. 8 (Ø25)	A706 Gr. 60	69.3 (478)	97.4 (672)	853 (5880)	12.0
	RPH-PC	No. 10 (Ø32)	A955 Gr. 60	90.4 (623)	113.4 (782)	930 (6415)	16.6
	RPH-PF	No. 10 (Ø32)	A706 Gr. 60	67.1 (463)	105.5 (727)	1125 (7756)	11.7
	RPH-NP	No. 10 (Ø32)	A706 Gr. 60	67.1 (463)	105.5 (727)	1125 (7756)	11.7
Tendons as Fuses	RPH-PF and RPH-NP**	0.6 in. (Ø15)	A416 Gr. 270	284 (1958)	306.5 (2113)	863 (5950)	6.2
Hoops	CIP	No. 4 (Ø13)	A706 Gr. 60	66.6 (459)	102.1 (704)	1873 (12910)	9.9
	Repairable Precast	No. 4 (Ø13)	A706 Gr. 60	65.3 (450)	100.7 (694)	2567 (17700)	9.8

* Strain at the peak stress
** Post-tensioning tendons in RPH-NP were not tested. See ASTM A416 for strength values.
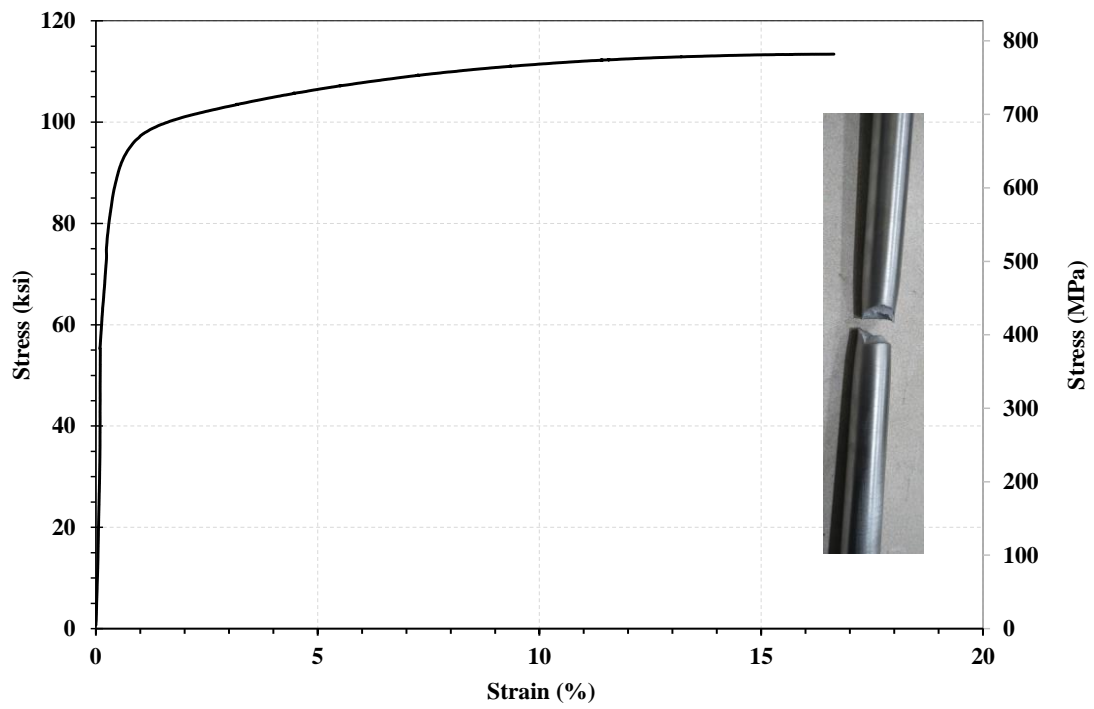
Figure 4.29. Tensile Test Results for 1.0 in. (25-mm) Dog-Bone from No. 10 (Ø32) Stainless Steel Bar
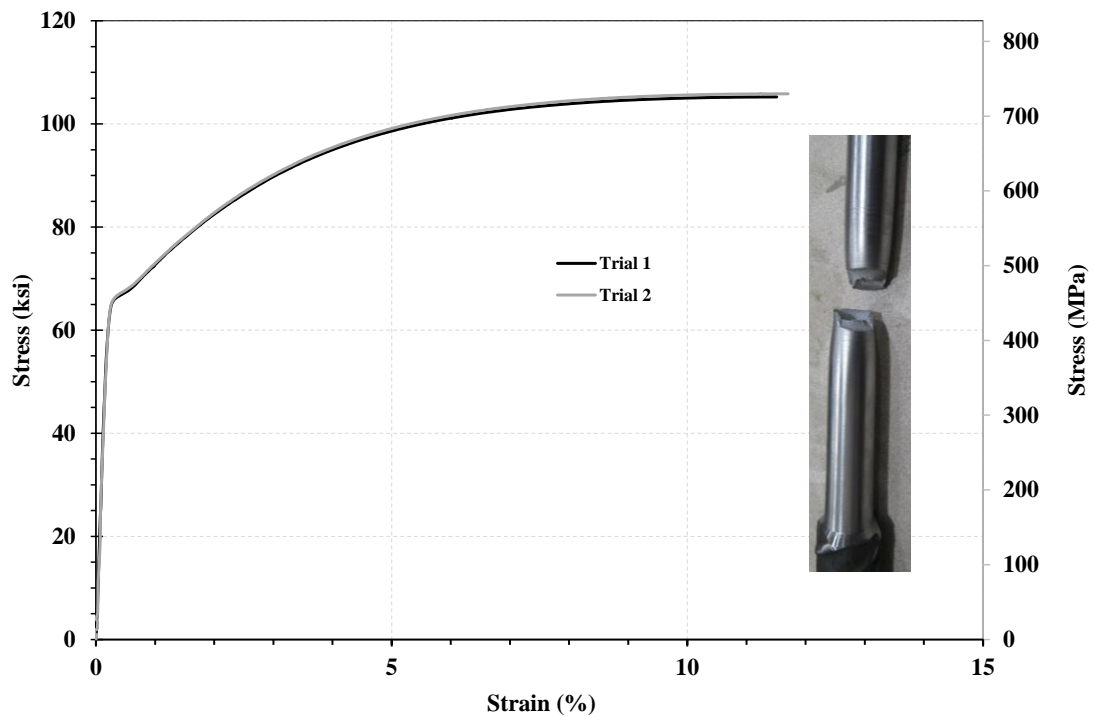
Figure 4.30. Tensile Test Results for 1.0 in. (25-mm) Dog-Bone from No. 10 (Ø32) Conventional Steel Bar

4.5.1.5 Steel Tendons

Steel tendons were utilized both in the post-tensioning of column RPH-NP and as a substitute for the BRR fuses in the columns RPH-PF and RPH-NP. Tendons conforming to ASTM A416 Grade 270 (1862 MPa) with a diameter of 0.5 in. (12.7 mm) were used for the post-tensioning of RPH-NP and with a diameter of 0.6 in. (15.24 mm) for the exposed fuses in RPH-PC and RPH-NP. Only tendons used in fuses were tested in which the core wire (the middle of the seven wires) was extracted and tested. Each wire had approximately a diameter of 0.2 in. (5 mm).
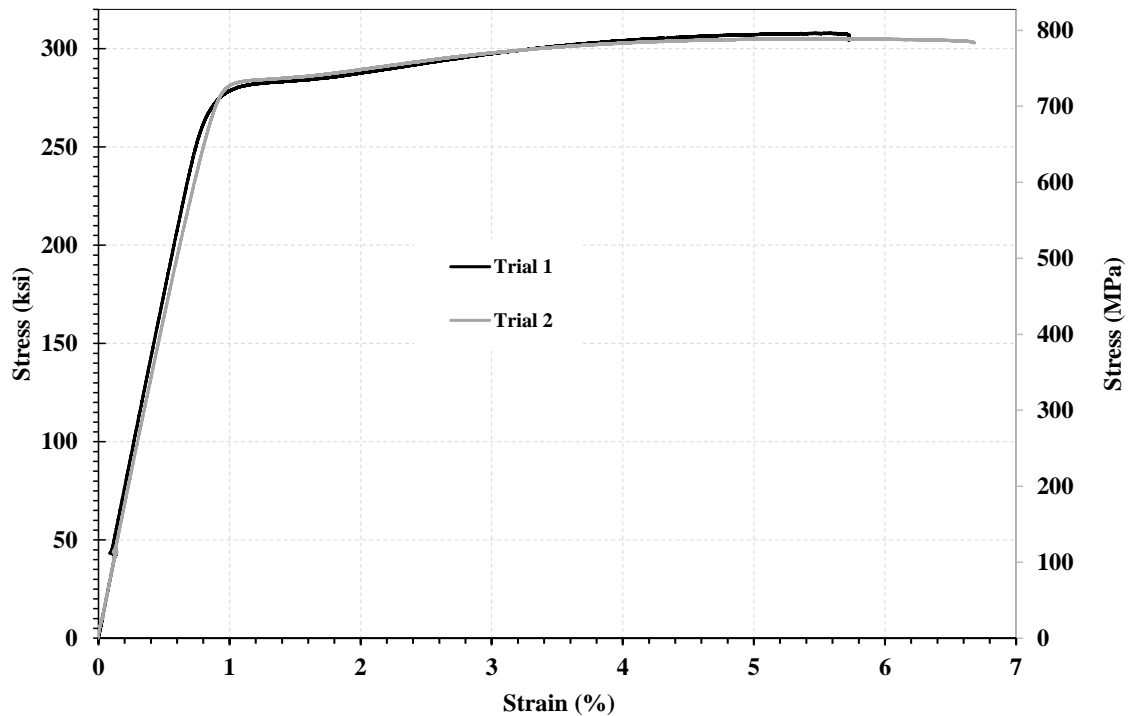
Figure 4.31. Tensile Test Results for 0.6-in. (15.24) Diameter Gr. 270 (1862-MPa) Steel Tendon

4.5.2 CIP Column Results

The CIP column from a previous study at SDSU performed by Sjurseth et al. (2022) was used as the reference model to assess the performance of the three repairable specimens. The column was tested under slow increasing cyclic loading protocol until failure. This section discusses the test results of the CIP column.

4.5.2.1 Observed Damage

All columns were tested horizontally using a hydraulic actuator in the north-south direction. Pushing refers to displacing the column from the north to south while pulling refers to the opposite direction (**Fig. 4.24**). A summary of the CIP damage observed for each cycle is presented in **Table 4.5** and **Fig. 4.32** to **4.57** show the plastic hinge damage after the second cycle of each drift level. Longitudinal bar buckling followed by bar fracture above the column-footing interface was the mode of failure for the CIP column.

Table 4.5. Summary of Damage in CIP (Sjurseth et al., 2022)

Drift Ratio, %	Observed Damage
+0.25	• Minor flexural cracks
-0.25	• Minor flexural cracks
+0.50	• Flexural and inclined cracks
-0.50	• Flexural and inclined cracks • Cracking at column base
+0.75	• Flexural Cracks • Bar Yielding
-0.75	• Flexural Cracks • Bar Yielding
+1.00	• Vertical, flexural, and inclined cracks
-1.00	• Vertical, flexural, and inclined cracks
+2.00	• Vertical, flexural, and inclined cracks • Initiation of spalling on South face of column
-2.00	• Vertical, flexural, and inclined cracks • Initiation of spalling on North face of column
+3.00	• Widening of cracks
-3.00	• Widening of cracks
+4.00	• Extensive concrete spalling
-4.00	• Extensive concrete spalling
+5.00	• Widening of cracks
-5.00	• Transverse bars exposed on South face of column
+6.00	• Transverse bars exposed on North face of column
-6.00	• Several transverse bars exposed on South face of column
+7.00	• Several transverse bars exposed on North face of column • Longitudinal bar exposed on North face of column
-7.00	• Longitudinal bar exposed on South face of column
+8.00	• No further damage
-8.00	• No further damage
+9.00	• Longitudinal bar buckled on South face of column
-9.00	• Longitudinal bar buckled on North face of column
+10.00	• Longitudinal bar rupture on North face of column
-10.00	• No further damage

Note: Positive drifts were based on displacements away from the reaction blocks (north to south)

84

a) North-West Side   b) South-East Side

Figure 4.32. CIP Column Plastic Hinge Damage, Second Push of 0.25% Drift Cycle (Sjurseth et al., 2022)

a) North-West Side   b) South-East Side

Figure 4.33. CIP Column Plastic Hinge Damage, Second Pull of 0.25% Drift Cycle (Sjurseth et al., 2022)

a) North-West Side   b) South-East Side

Figure 4.34. CIP Column Plastic Hinge Damage, Second Push of 0.5% Drift Cycle (Sjurseth et al., 2022)
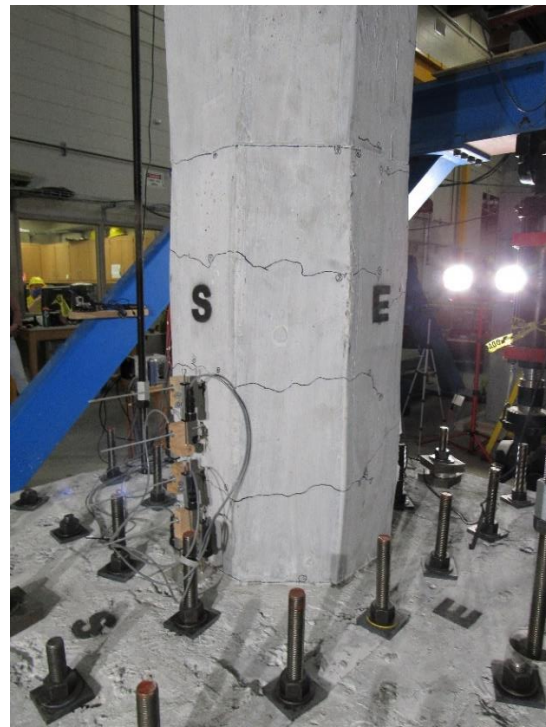
a) North-West Side   b) South-East Side

Figure 4.35. CIP Column Plastic Hinge Damage, Second Pull of 0.5% Drift Cycle (Sjurseth et al., 2022)

a) North-West Side   b) South-East Side

Figure 4.36. CIP Column Plastic Hinge Damage, Second Push of 0.75% Drift Cycle (Sjurseth et al., 2022)
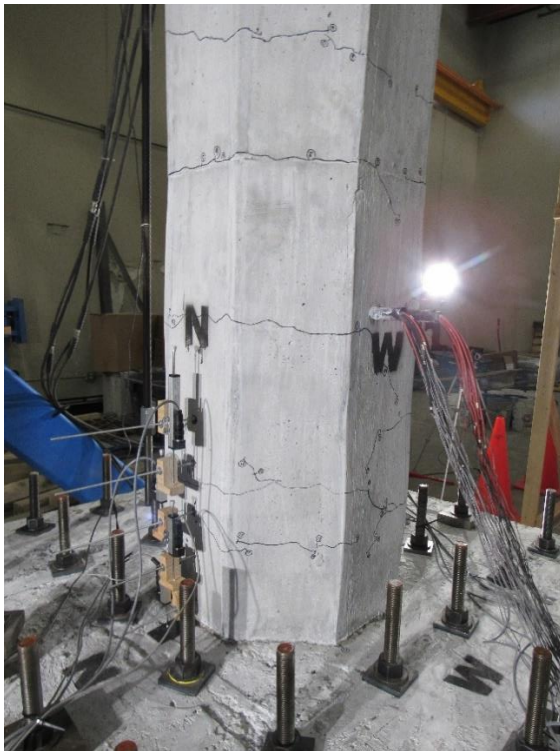
a) North-West Side   b) South-East Side

Figure 4.37 CIP Column Plastic Hinge Damage, Second Pull of 0.75% Drift Cycle (Sjurseth et al., 2022)
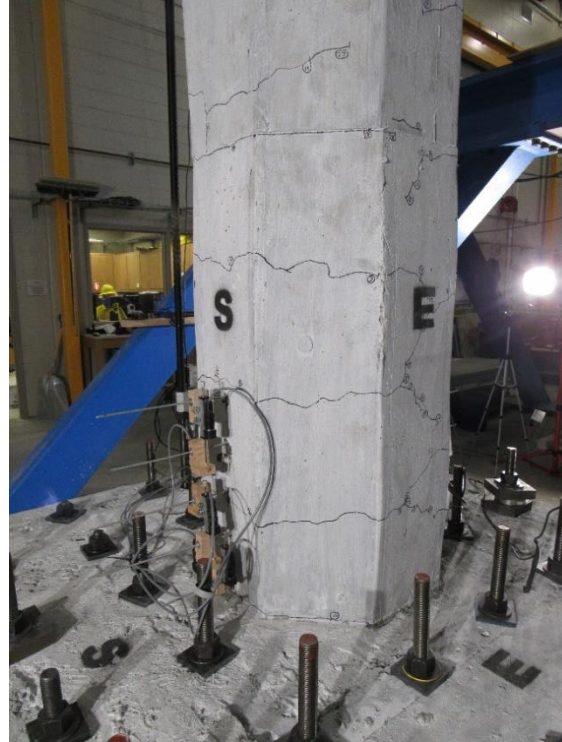
a) North-West Side   b) South-East Side
Figure 4.38. CIP Column Plastic Hinge Damage, Second Push of 1.0% Drift Cycle (Sjurseth et al., 2022)
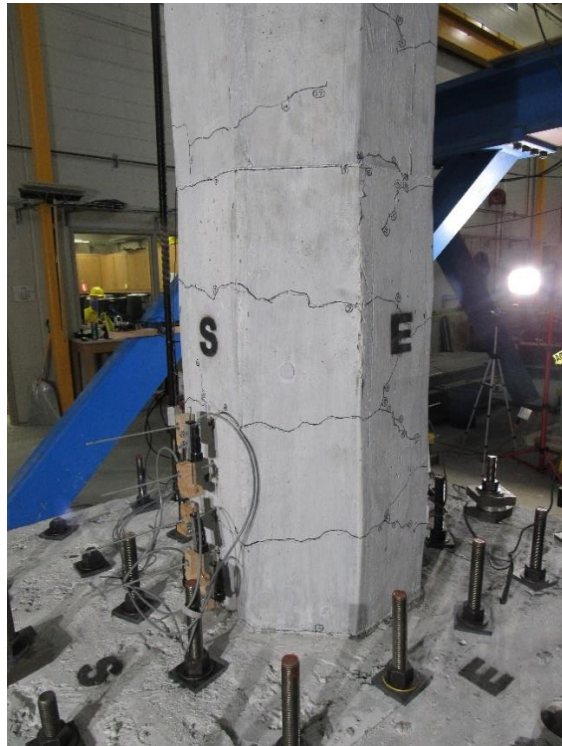
a) North-West Side   b) South-East Side
Figure 4.39. CIP Column Plastic Hinge Damage, Second Pull of 1.0% Drift Cycle (Sjurseth et al., 2022)

a) North-West Side
b) South-East Side
Figure 4.40. CIP Column Plastic Hinge Damage, Second Push of 2.0% Drift Cycle (Sjurseth et al., 2022)
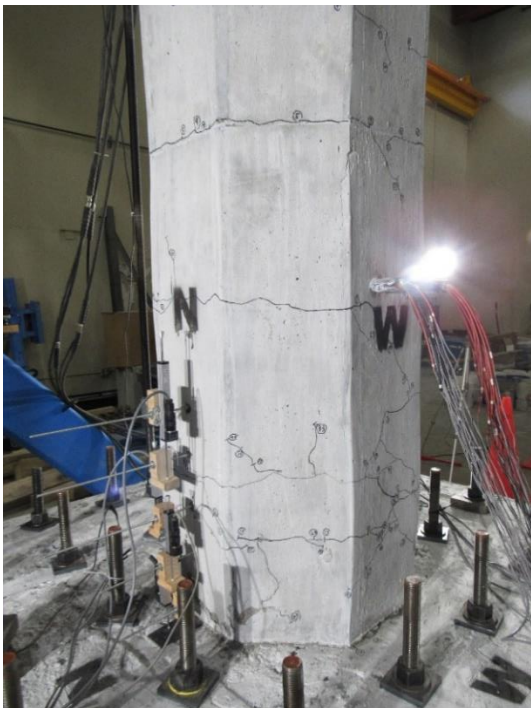
a) North-West Side
b) South-East Side
Figure 4.41. CIP Column Plastic Hinge Damage, Second Pull of 2.0% Drift Cycle (Sjurseth et al., 2022)

a) North-West Side   b) South-East Side

Figure 4.42. CIP Column Plastic Hinge Damage, Second Push of 3.0% Drift Cycle (Sjurseth et al., 2022)
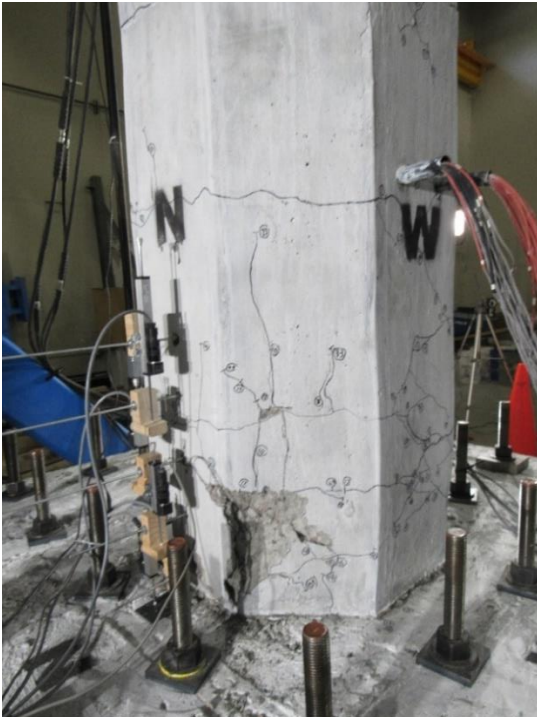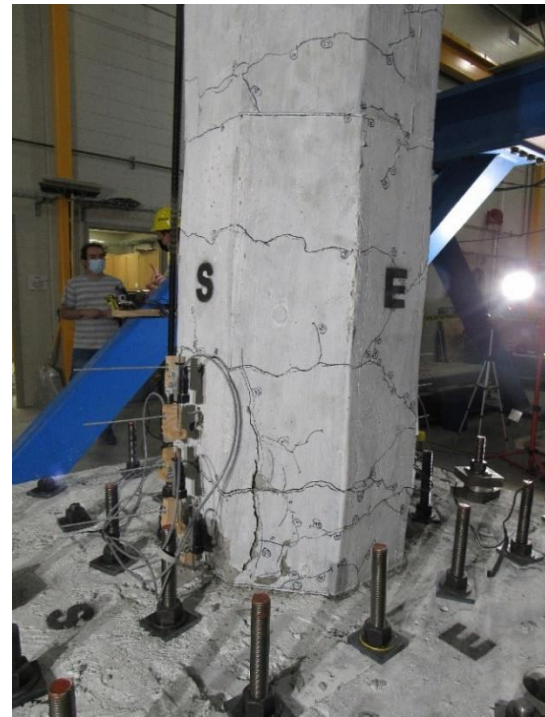
a) North-West Side   b) South-East Side

Figure 4.43. CIP Column Plastic Hinge Damage, Second Pull of 3.0% Drift Cycle (Sjurseth et al., 2022)

a) North-West Side   b) South-East Side

Figure 4.44. CIP Column Plastic Hinge Damage, Second Push of 4.0% Drift Cycle (Sjurseth et al., 2022)

a) North-West Side   b) South-East Side

Figure 4.45. CIP Column Plastic Hinge Damage, Second Pull of 4.0% Drift Cycle (Sjurseth et al., 2022)

a) North-West Side   b) South-East Side

Figure 4.46. CIP Column Plastic Hinge Damage, Second Push of 5.0% Drift Cycle (Sjurseth et al., 2022)

a) North-West Side   b) South-East Side

Figure 4.47. CIP Column Plastic Hinge Damage, Second Pull of 5.0% Drift Cycle (Sjurseth et al., 2022)

a) North-West Side   b) South-East Side

Figure 4.48. CIP Column Plastic Hinge Damage, Second Push of 6.0% Drift Cycle (Sjurseth et al., 2022)

a) North-West Side   b) South-East Side

Figure 4.49. CIP Column Plastic Hinge Damage, Second Pull of 6.0% Drift Cycle (Sjurseth et al., 2022)

a) North-West Side | b) South-East Side

Figure 4.50. CIP Column Plastic Hinge Damage, Second Push of 7.0% Drift Cycle (Sjurseth et al., 2022)

a) North-West Side | b) South-East Side

Figure 4.51 CIP Column Plastic Hinge Damage, Second Pull of 7.0% Drift Cycle (Sjurseth et al., 2022)

a) North-West Side   b) South-East Side
Figure 4.52. CIP Column Plastic Hinge Damage, Second Push of 8.0% Drift Cycle (Sjurseth et al., 2022)

a) North-West Side   b) South-East Side
Figure 4.53. CIP Column Plastic Hinge Damage, Second Pull of 8.0% Drift Cycle (Sjurseth et al., 2022)
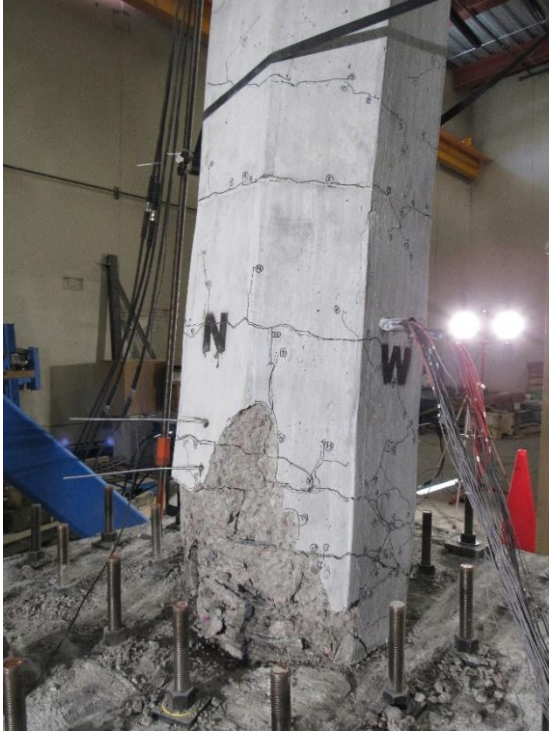
a) North-West Side   b) South-East Side

Figure 4.54. CIP Column Plastic Hinge Damage, Second Push of 9.0% Drift Cycle (Sjurseth et al., 2022)
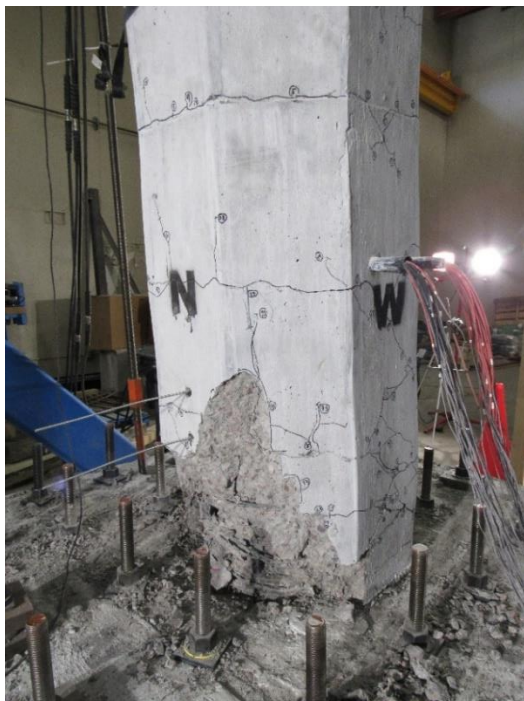
a) North-West Side   b) South-East Side

Figure 4.55. CIP Column Plastic Hinge Damage, Second Pull of 9.0% Drift Cycle (Sjurseth et al., 2022)
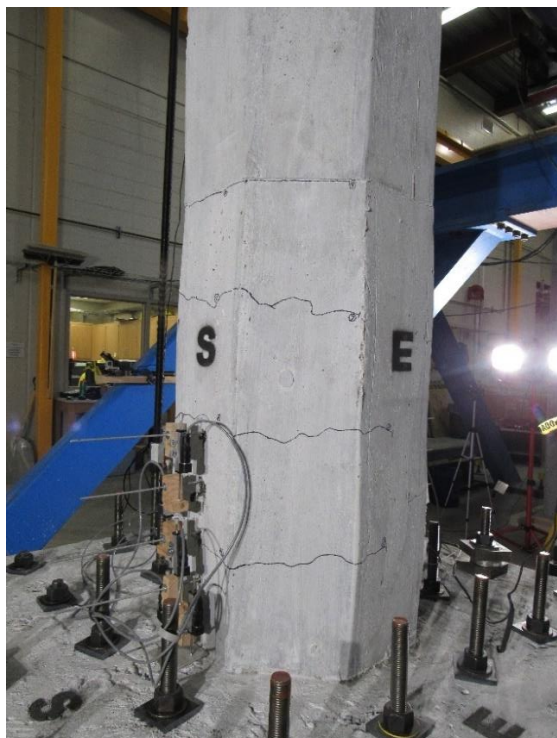
a) North-West Side b) South-East Side

Figure 4.56. CIP Column Plastic Hinge Damage, Second Push of 10% Drift Cycle (Sjurseth et al., 2022)
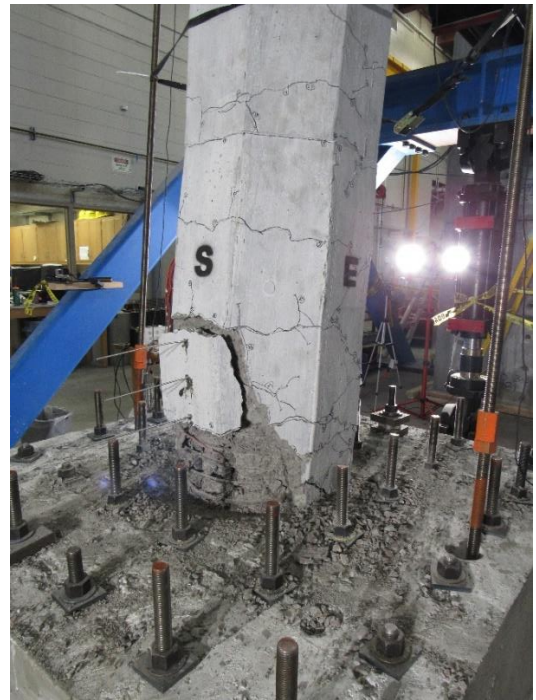
a) North-West Side b) South-East Side

Figure 4.57. CIP Column Plastic Hinge Damage, Second Pull of 10% Drift Cycle (Sjurseth et al., 2022)

4.5.2.2 Force-Displacement Relationship

Figure 4.58 shows the measured lateral force-drift hysteretic and envelope responses of CIP. The longitudinal bars in CIP yielded at 0.47% drift ratio in the push direction under a corresponding lateral load of 37.5 kips (166.9 kN) and at 0.44% drift ratio in the pull direction at a corresponding lateral load of 38.8 kips (172.6 kN).
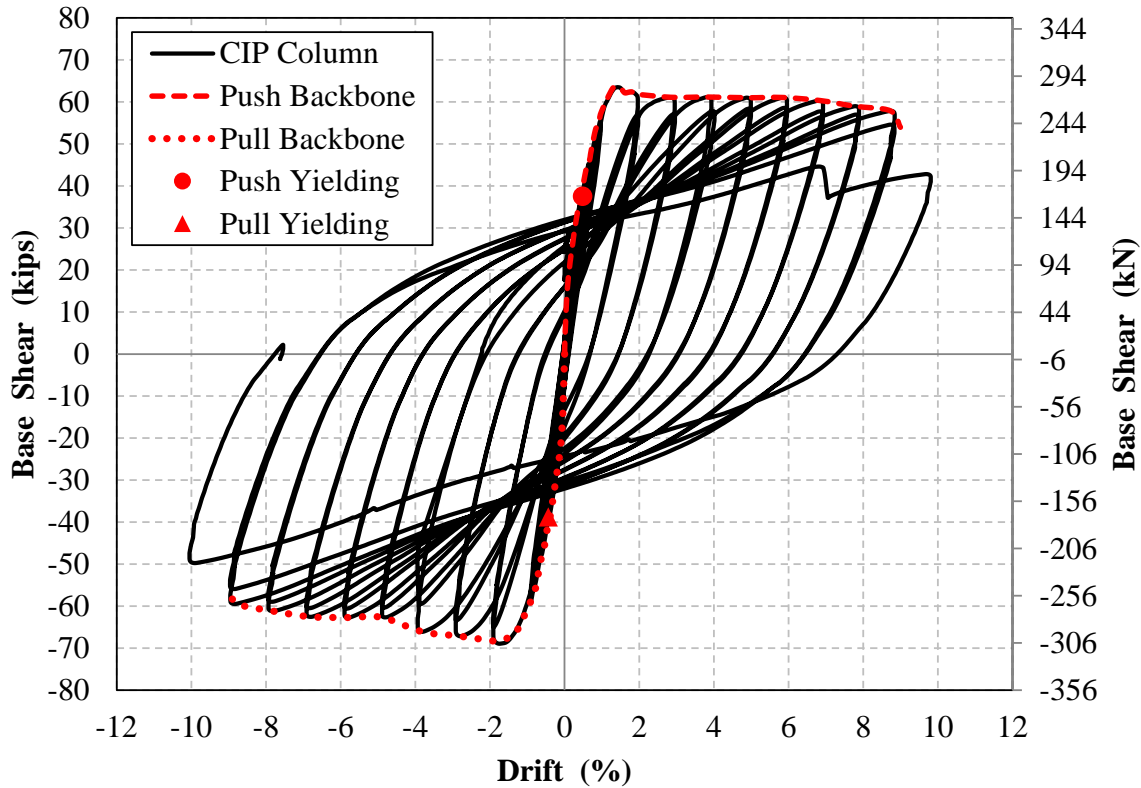
Figure 4.58. Measured CIP Column Force-Drift Hysteretic and Envelope Responses (Sjurseth et al., 2022)

Figure 4.59 shows the average envelope for the push and pull directions. The average yield drift ratio of 0.45% occurred at a lateral force of 38.2 kips (169.9 kN). The column envelope was ended after a drop of 15% in the lateral load resisting capacity after the peak baseshear. The ultimate drift of the CIP column was 8.96% under this consideration. The displacement ductility capacity, according to AASHTO SGS (2011), is defined as the ratio of the ultimate displacement to the effective yield displacement. **Figure 4.59** shows the idealized curve for the CIP column. The effective yield drift ratio was 0.72% at a lateral force of 61.9 kips (275.3 kN) resulting in a displacement ductility capacity (μ) of 12.37.
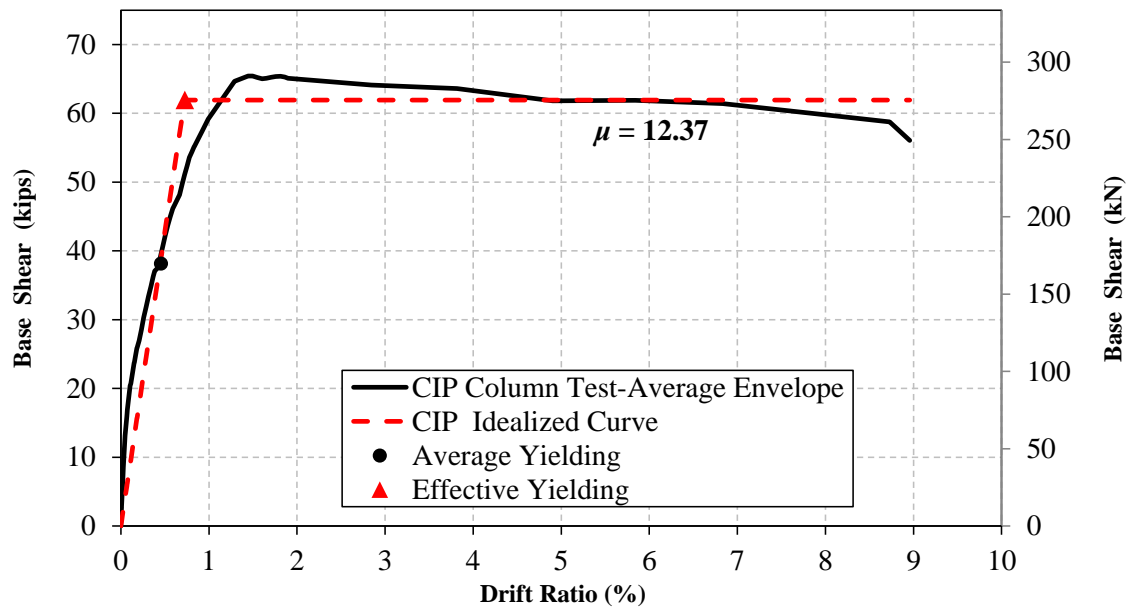
Figure 4.59. Measured CIP Column Average Force-Drift Envelope and Idealized Curve (Sjurseth et al., 2022)

4.5.2.3 Strain Profiles

Thirty-four strain gauges were installed on the CIP reinforcing steel bars at six levels of the column height. **Figures 4.60** to **4.63** show the maximum measured tensile strain along the column height for Bars B1, B2, B6, and B7. Bar number can be found in **Fig. 4.2**. The measured strains were higher near the base of the column and decreased along the column height. The strain on the reinforcing hoops was also monitored. The yield strain for the hoops in CIP was 0.23% while maximum measured strain in the hoops was 2.96% and occurred in a hoop near the base of the column inside the footing.
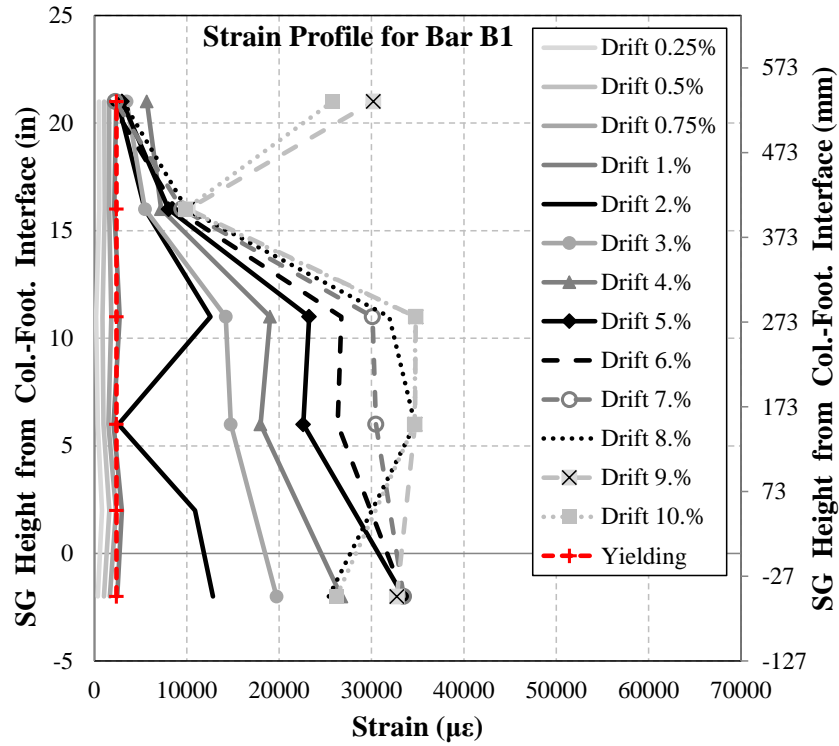
Figure 4.60. Measured Strain Profile for CIP Column Bar B1 (Sjurseth et al., 2022)
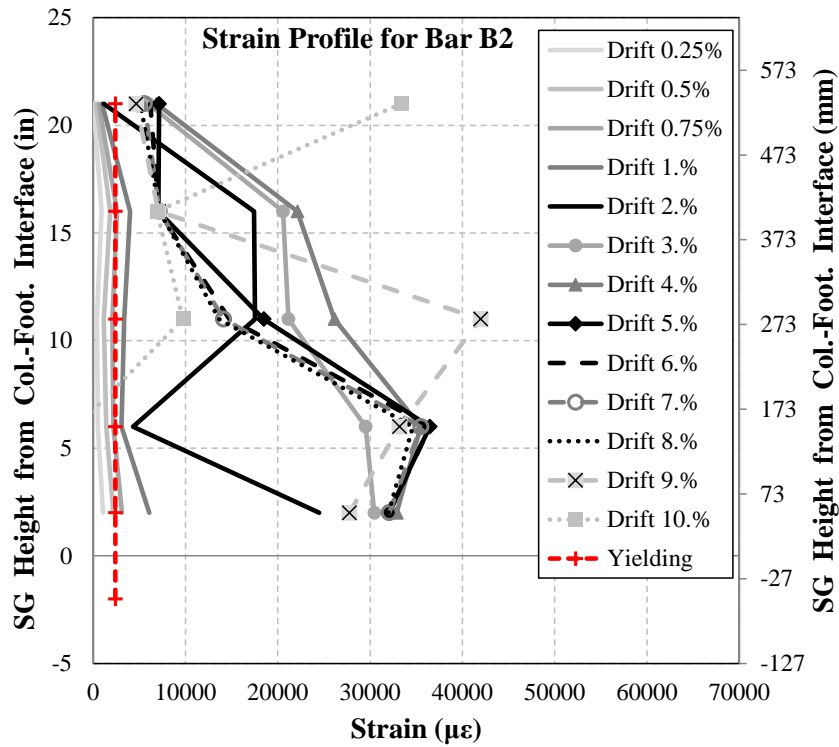
Figure 4.61. Measured Strain Profile for CIP Column Bar B2 (Sjurseth et al., 2022)
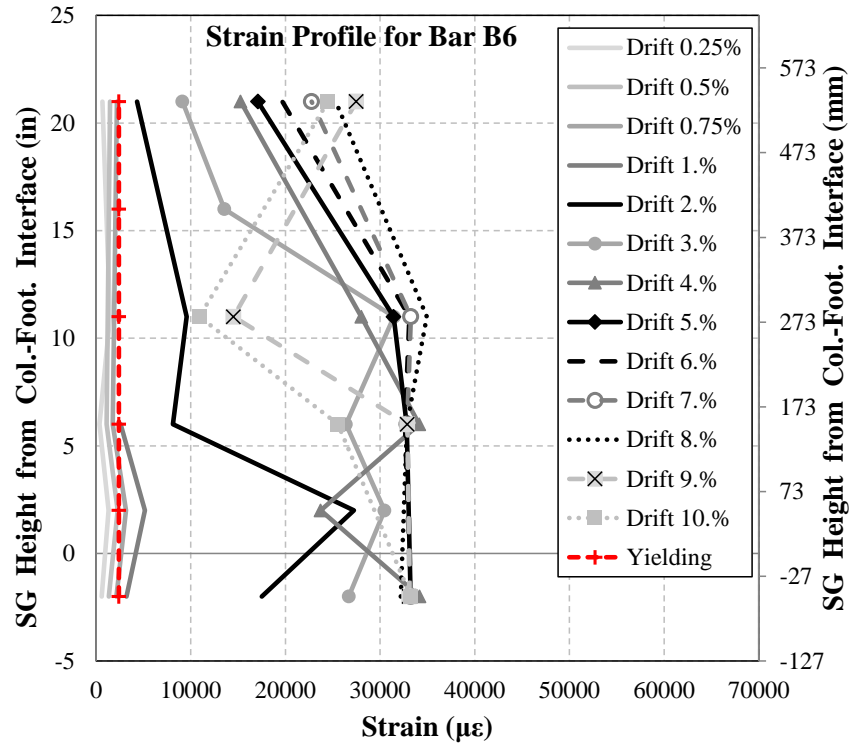
Figure 4.62. Measured Strain Profile for CIP Column Bar B6 (Sjurseth et al., 2022)
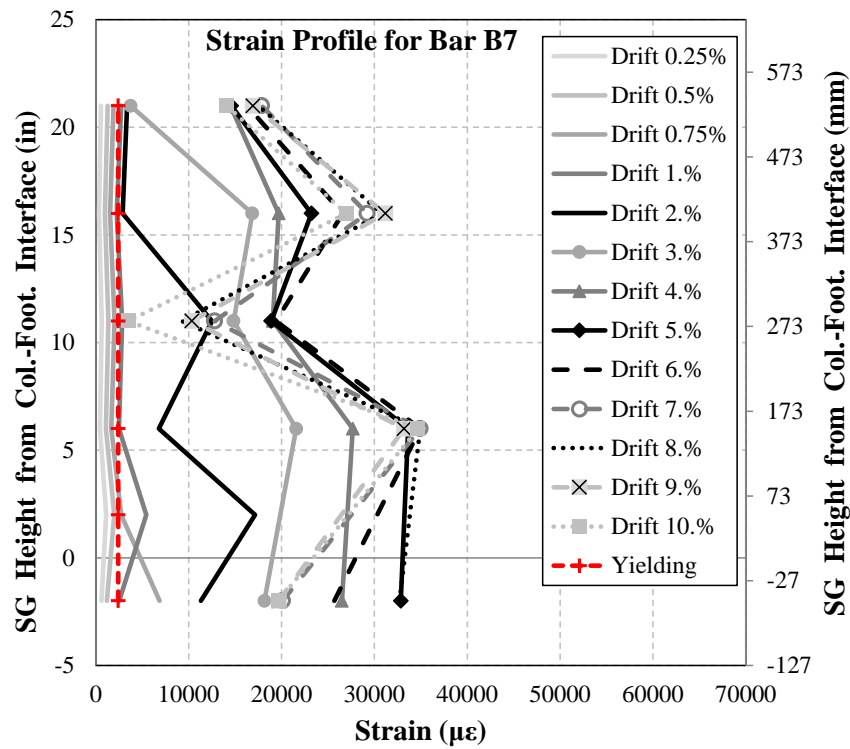
Figure 4.63. Measured Strain Profile for CIP Column Bar B7 (Sjurseth et al., 2022)

4.5.2.4 Measured Rotation and Curvature

LVDTs were installed in the loading plane on the north and south faces of the column to determine rotations and curvatures along the length of the plastic hinge. The instrumentation schedule for CIP was shown in **Fig. 4.27**. Rotations (θ) and curvatures (φ) were calculated according to the following equations:

$$\theta = \frac{\Delta L_L - \Delta L_R}{D + d_L + d_R} \tag{4-1}$$

$$\varphi = \frac{\theta}{h} \tag{4-2}$$

where ΔL_L and ΔL_R refer to the measured relative displacements at the left and right sides of the column in the loading direction, respectively. D is the diameter of the column, and d_L and d_R are the distances of the left and right LVDTs from the north and south faces of the column, respectively. The variable h refers to the relative height of the LVDTs.

Figure 4.64 shows the curvature profile along the height of the CIP column from drift ratios of 0.25% to 4.0%. The highest curvatures were measured at the base of the column.
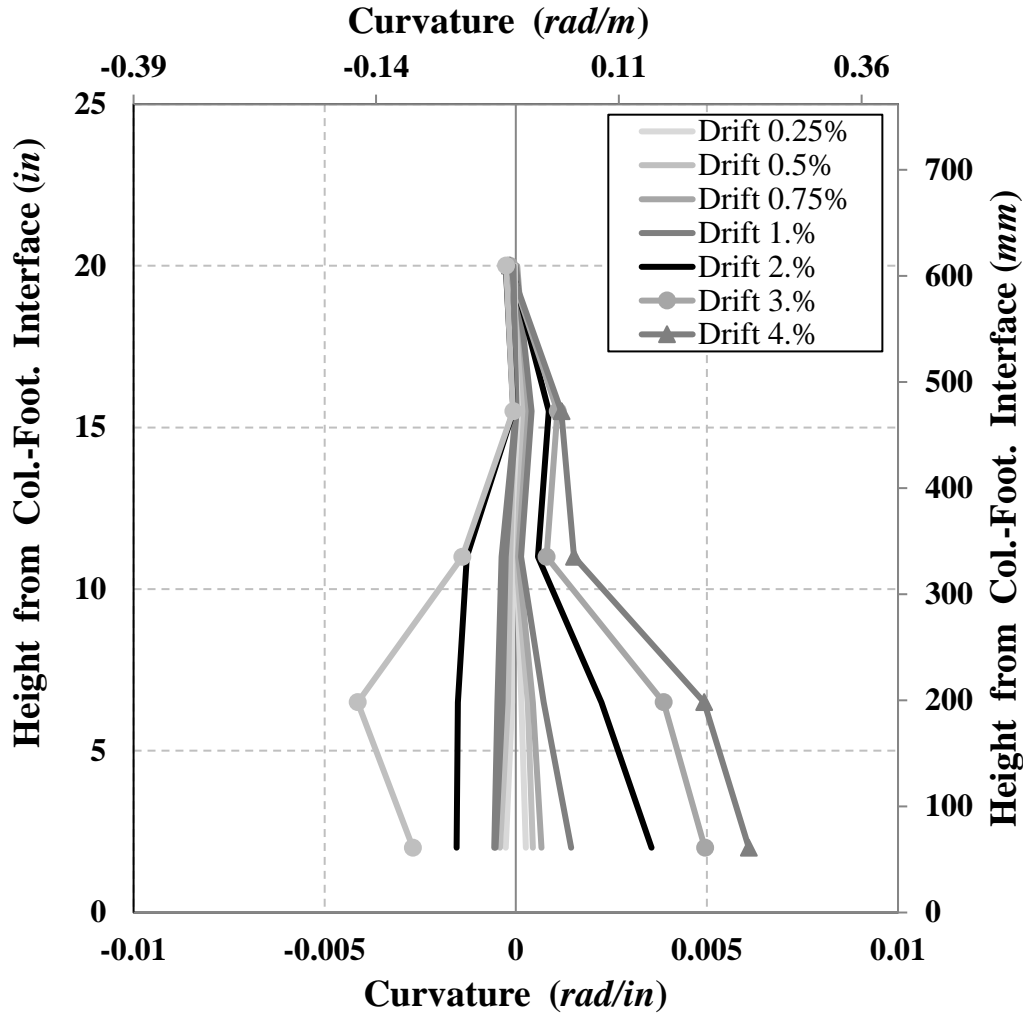
Figure 4.64. Measured Curvature Profile for CIP Column (Sjurseth et al., 2022)

4.5.2.5 Energy Dissipation

The dissipated energy of a column under cyclic loading is defined as the cumulative area under the loops of the force-displacement hysteresis. **Figure 4.65** shows the measured cumulative energy dissipation of the CIP column at each drift ratio. CIP dissipated a total of 8,041 kip-in. (908.5 kN-m) energy.
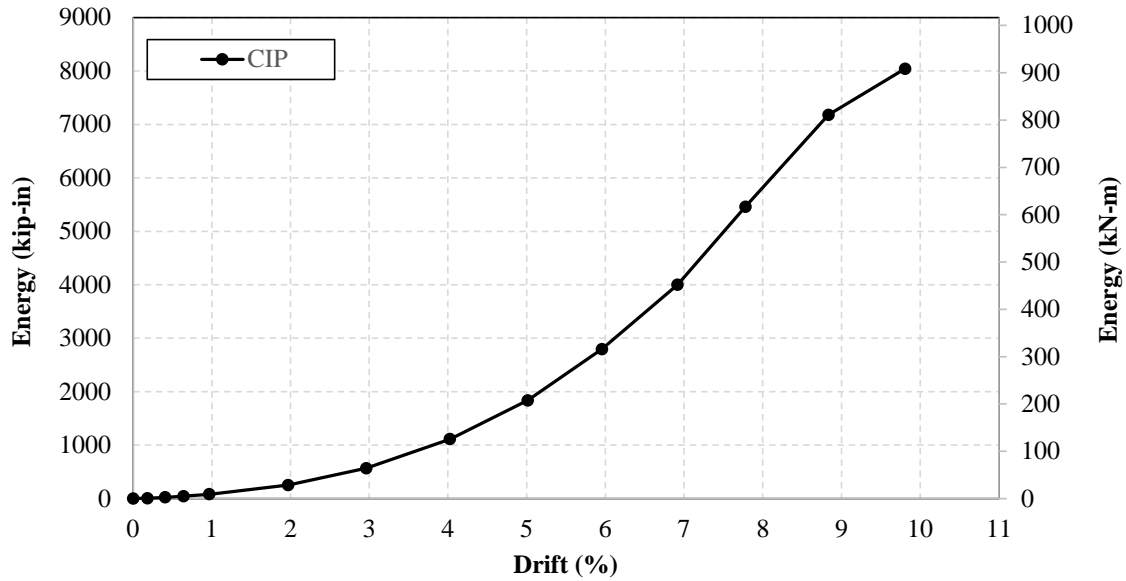
Figure 4.65. Measured Energy Dissipation for CIP Column (Sjurseth et al., 2022)

4.5.3 RPH-PC Column Results

The performance of the RPH-PC repairable precast column is presented in this section. RPH-PC was tested twice, once using a buckling restrained reinforcement with long fuse length (colored in yellow), and once using another set of BRR with a shorter "dog-boned" length (green BRR). The second test was to prove that the column repair through replacement of exposed BRR is feasible. To differentiate the results of two tests on the same column, the precast column specimen in the first test is named "RPH-PC" and the repaired column is labeled as "RPH-PC-R". The fuse length in RPH-PC was 10.25 in. (260 mm) and was 5.13 in. (130 mm) in RPH-PC-R.

4.5.3.1 RPH-PC Observed Damage

The same testing procedure that was used for the CIP column was followed for RPH-PC; however, the test was stopped at 5% drift ratio. After the repair, RPH-PC-R was tested to failure. A summary of the observed damage is presented in **Table 4.6** and **Figures 4.66** to **4.80** show the observed damage of RPH-PC at each drift cycle.

Only one minor flexural crack was observed during the first cycle of 0.25% drift ratio (**Fig. 4.67**). Additional minor flexural cracks were noticed in the neck section during the first cycle of 0.5% drift ratio (**Fig. 4.68**). Flexural cracks continued to form during the cycles at 0.75% and 1.0% drift ratios as well as some minor vertical cracks at the location of the inserted shims near the base of the column (**Fig 4.72**). Yielding of the longitudinal bars within the BRR fuses didn't occur until the first cycle of 2.0% drift ratio at which both bars B1 and B2 yielded in the push direction and both bars B6 and B7 yielded in the pull direction. Cover spalling at the base of the column was also initiated in both directions during the 2% drift ratio cycles while minor buckling of the BRR fuses between the couplers and steel tubes was observed (**Fig. 4.74**). During the first push at 3% drift ratio, cover concrete began to spall above the neck region at the point where the longitudinal bars enter the octagonal cross section due to compressive stresses as the concrete pressed against the clamping collars that were used to prevent buckling in the exposed portion of the rebar (**Fig. 4.76**). Cone-shape failure of the grout inside the BRR steel tubes was also observed at 3% drift ratio. A Z-shape buckling of the BRR fuses (not the fuse itself but bending of the exposed bars at the ends) continued to worsen during the 4% and 5% drift ratio cycles (**Fig. 4.78-4.80**). The RPH-PC column test was stopped at 5% drift ratio to perform the repair, which was done by only replacing BRR.

Table 4.6. Summary of Damage in RPH-PC

Drift Ratio, %	Observed Damage
+0.25	• One minor flexural crack above neck section
-0.25	• No further damage
+0.50	• Minor flexural cracks in neck section
-0.50	• No further damage
+0.75	• Large flexural crack above neck section
-0.75	• Short vertical cracks at column base above shims
+1.00	• Flexural cracks, vertical cracks above shims
-1.00	• Flexural cracks, vertical cracks above shims
+2.00	• Bar yielding in BRR fuses • Flexural and inclined cracks, vertical cracks at base • Initiation of spalling at column base on South face • Minor buckling of BRR between coupler and steel tube on South side
-2.00	• Bar yielding in BRR fuses • Flexural and inclined cracks, vertical cracks at base • Initiation of spalling at column base on North face • Minor buckling of BRR between coupler and steel tube on North side
+3.00	• Crushing of grout inside BRR • Flexural, inclined, vertical cracks • Initiation of spalling above neck region on South face
-3.00	• Crushing of grout inside BRR • Flexural, inclined, vertical cracks
+4.00	• Large spalling above neck region on South face • Large buckling of BRR
-4.00	• Large buckling of BRR
+5.00	• Very large buckling of BRR on South side
-5.00	• Large buckling of BRR on North side

Note: Positive drifts were based on displacements away from the reaction blocks (north to south)

a) North-West Side   b) South-East Side
Figure 4.66. RPH-PC Column Plastic Hinge Damage, Second Push of 0.25% Drift Cycle
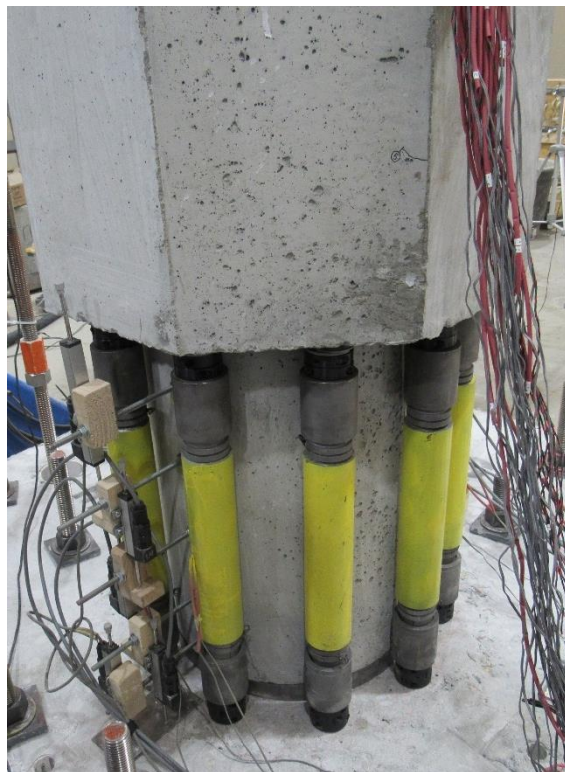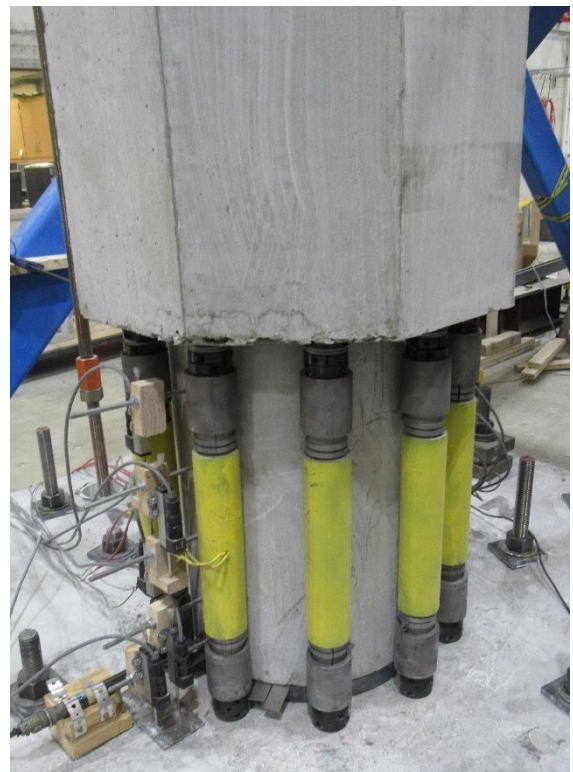
a) North-West Side   b) South-East Side
Figure 4.67. RPH-PC Column Plastic Hinge Damage, Second Pull of 0.25% Drift Cycle

a) North-West Side   b) South-East Side

Figure 4.68. RPH-PC Column Plastic Hinge Damage, Second Push of 0.50% Drift Cycle

a) North-West Side   b) South-East Side

Figure 4.69. RPH-PC Column Plastic Hinge Damage, Second Pull of 0.50% Drift Cycle
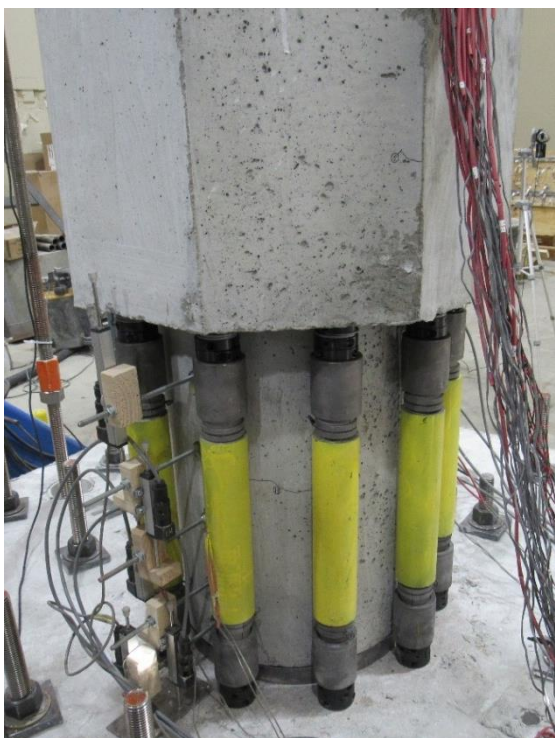
a) North-West Side   b) South-East Side
Figure 4.70. RPH-PC Column Plastic Hinge Damage, Second Push of 0.75% Drift Cycle

a) North-West Side   b) South-East Side
Figure 4.71. RPH-PC Column Plastic Hinge Damage, Second Pull of 0.75% Drift Cycle

a) North-West Side b) South-East Side

Figure 4.72. RPH-PC Column Plastic Hinge Damage, Second Push of 1.0% Drift Cycle

a) North-West Side b) South-East Side

Figure 4.73. RPH-PC Column Plastic Hinge Damage, Second Pull of 1.0% Drift Cycle

a) North-West Side   b) South-East Side

Figure 4.74. RPH-PC Column Plastic Hinge Damage, Second Push of 2.0% Drift Cycle

a) North-West Side   b) South-East Side

Figure 4.75. RPH-PC Column Plastic Hinge Damage, Second Pull of 2.0% Drift Cycle

a) North-West Side   b) South-East Side

Figure 4.76. RPH-PC Column Plastic Hinge Damage, Second Push of 3.0% Drift Cycle

a) North-West Side   b) South Side

Figure 4.77. RPH-PC Column Plastic Hinge Damage, Second Pull of 3.0% Drift Cycle

a) North-West Side   b) South Side

Figure 4.78. RPH-PC Column Plastic Hinge Damage, Second Push of 4.0% Drift Cycle

a) North-West Side   b) South Side

Figure 4.79. RPH-PC Column Plastic Hinge Damage, Second Pull of 4.0% Drift Cycle

a) North Side – At Push

b) South Side – At Push

c) North-West Side – At Pull

d) South-East Side – At Pull

Figure 4.80. RPH-PC Column Plastic Hinge Damage, Second 5.0% Drift Cycle

4.5.3.2 Repair of RPH-PC Column

Testing of RPH-PC was ended after two cycles of 5% drift ratio at which the clamping collars and steel washers were removed. The couplers were then unscrewed and the BRR fuses were removed. As the portion of the longitudinal bars protruding from the footing and octagonal cross section (footing/column dowels) had also buckled significantly, the new fuses could not be torqued in place until the bars were straightened. This was performed by first removing the fuses on the south side of the column then using the hydraulic actuator to push the column and straighten out the bars on the north side. The process was repeated by removing the fuses on the north side, reinserting the old fuses on the south side, and pulling the column with the actuator to straighten the bars on the south side. As this method obviously is not possible in the field, a method of straightening the bars or preventing the protruded portions from buckling must be devised. One option is to use steel tendons since they are tension-only members. Another option is to use recentering materials such as shape memory alloys.

After the bars were straightened, new fuses with a shorter dog-bone length of 5.128 in. (130 mm) were inserted and tightened into place using pipe wrenches. The clamping collars were replaced but a small gap was left between the uppermost clamping collar on each bar and the lower concrete face of the octagonal cross section to prevent further spalling that was observed during the first round of testing on the south face of the column above the neck section (**Fig. 4.81**). The shims that had been placed in the gap between the bottom of the column and steel plate were not utilized in RPH-PC-R as they had only added to the damage at the column-plate interface of RPH-PC. Any spalled concrete was removed, and dust was vacuumed from the footing and column before the second set of testing was performed. **Figure 4.81** shows the damage after cleanup and before starting the second round of testing.
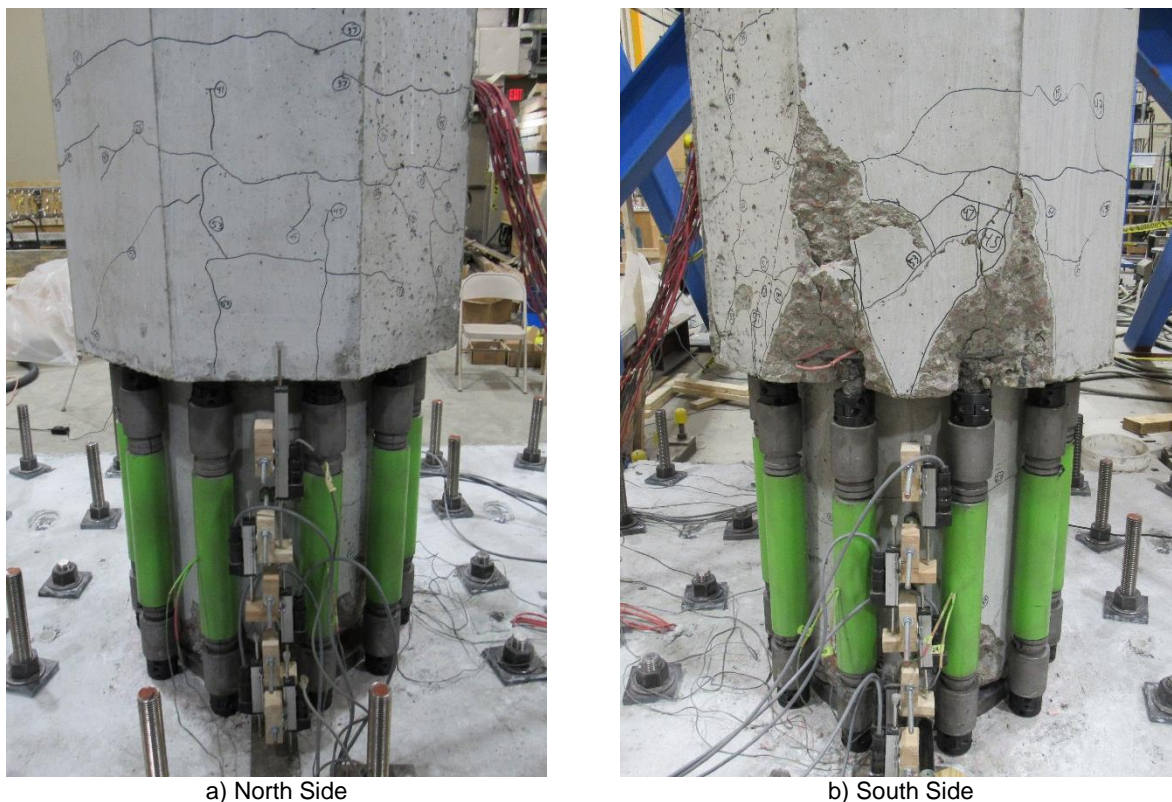
a) North Side   b) South Side
Figure 4.81. RPH-PC-R Column Plastic Hinge Damage before Retesting

114

4.5.3.3 RPH-PC-R Observed Damage

The second set of testing of the RPH-PC column, RPH-PC-R, was performed by following the same loading protocol of the original test but was continued to failure. **Table 4.7** presents a summary of the observed damage of RPH-PC-R and **Fig. 4.82-4.107** show the observed damage of RPH-PC-R. New cracks were marked in red in RPH-PC-R for the ease of damage identification.

No additional damage was observed in RPH-PC-R until the first cycle of 1.0% drift ratio when a small, vertical crack was spotted above the neck section on the north face (**Fig. 4.88-4.89**). Minor Z-shape buckling of BRR between the couplers and steel tubes became noticeable during the cycles at 2.0% drift ratio (**Fig. 4.90-4.91**). Bar yielding within the BRR fuses occurred during the first cycle of 3.0% drift ratio when bar B1 yielded in the push direction and bar B6 yielded in the pull direction (**Fig. 4.92-4.93**). Buckling of BRR continued to worsen until shallow conical failure of the grout at the ends of the BRR steel tubes was observed during the 5% drift cycles (**Fig. 4.96-4.97**). Spalling at the column base and above the column neck section worsened at the 6% and 7% drift cycles (**Fig. 4.98-4.101**). The Z-shape buckling of BRR and spalling at the column base continued at higher drifts. RPH-PC-R did not fail; however, the test was stopped at 10% drift ratio to match the failure point of CIP.

After column disassembly, no sign of damage to the pipe-pin connection (neither the pipe nor the housing socket) was observed. This indicates that the design of pipe-pin connection discussed in **Sec. 4.3.2** was successful. Furthermore, no significant damage of the neck beside the spalling at the rocking face was observed. The neck design was overall acceptable but the damage at the rocking face should be minimized in future applications. One option is to use UHPC.

Table 4.7. Summary of Damage in RPH-PC-R

Drift Ratio, %	Observed Damage
Beginning of Test	• Significant concrete spalling at column base on North and South faces • Significant spalling above neck region on South face
+0.25	• No further damage
-0.25	• No further damage
+0.50	• No further damage
-0.50	• No further damage
+0.75	• No further damage
-0.75	• No further damage
+1.00	• Small, inclined crack above neck section on North face
-1.00	• No further damage
+2.00	• Minor buckling of BRR between coupler and steel tube on South side • Vertical crack at column base on East face
-2.00	• Minor buckling of BRR between coupler and steel tube on North side • Vertical crack at column base on West face
+3.00	• Bar yielding in BRR fuses on North side • Vertical cracking on North face
-3.00	• Bar yielding in BRR fuses on South side
+4.00	• Buckling of BRR on South side worsens
-4.00	• Buckling of BRR on North side worsens
+5.00	• Grout crushing inside BRR tubes on South side
-5.00	• Grout crushing inside BRR tubes on North side
+6.00	• Further spalling above neck region on South face
-6.00	• No further damage
+7.00	• Further spalling above neck region and at column base on South face
-7.00	• Spalling above neck region on North face
+8.00	• Further buckling of BRR on South side
-8.00	• Further buckling of BRR on North side
+9.00	• Extreme buckling of BRR and spalling at column base on South side • Initiation of strength reduction in push direction
-9.00	• Extreme buckling of BRR and spalling at column base on North side
+10.00	• No further damage
-10.00	• No further damage

Note: Positive drifts were based on displacements away from the reaction blocks (north to south)
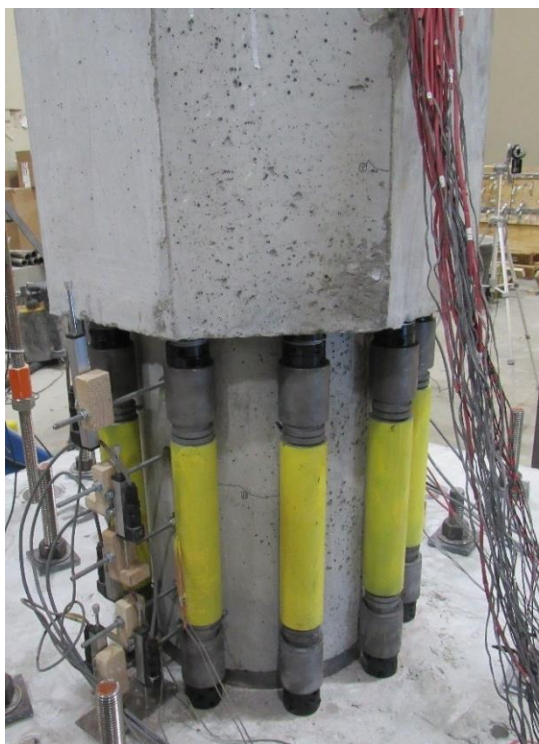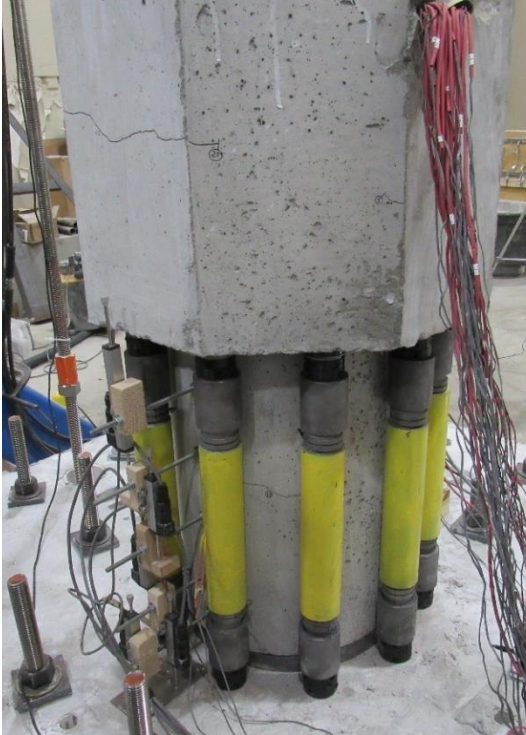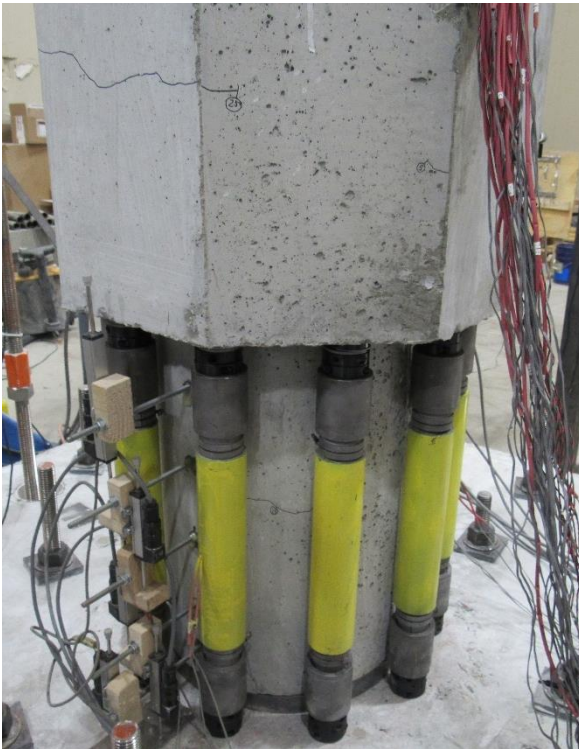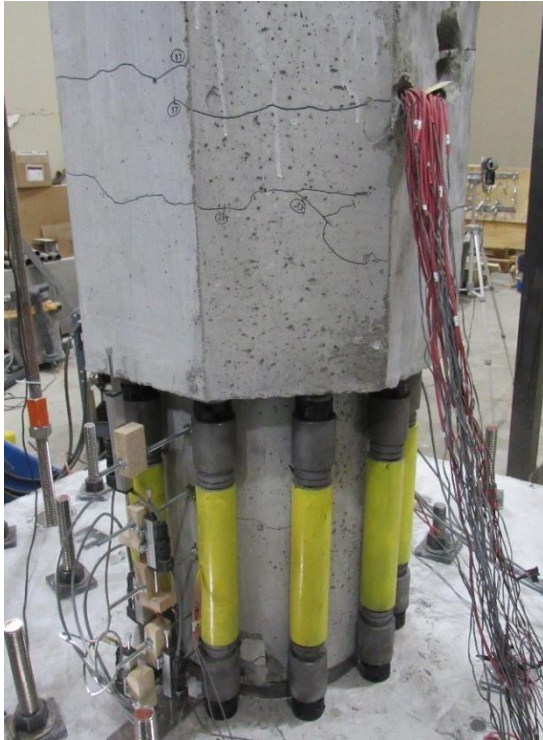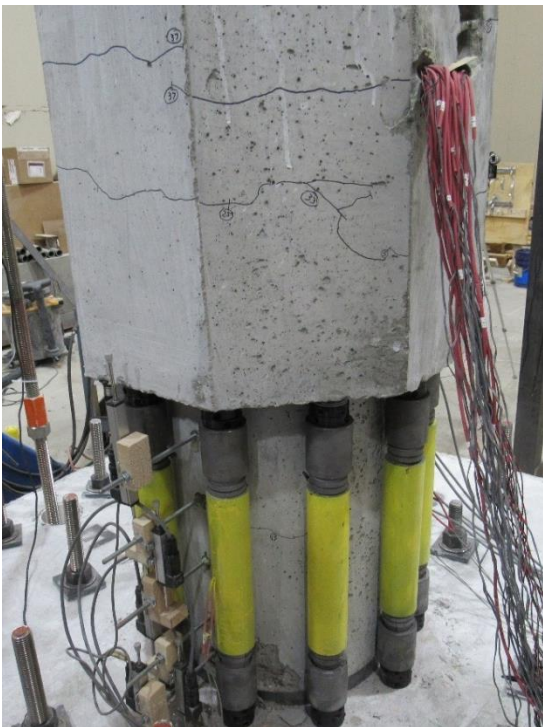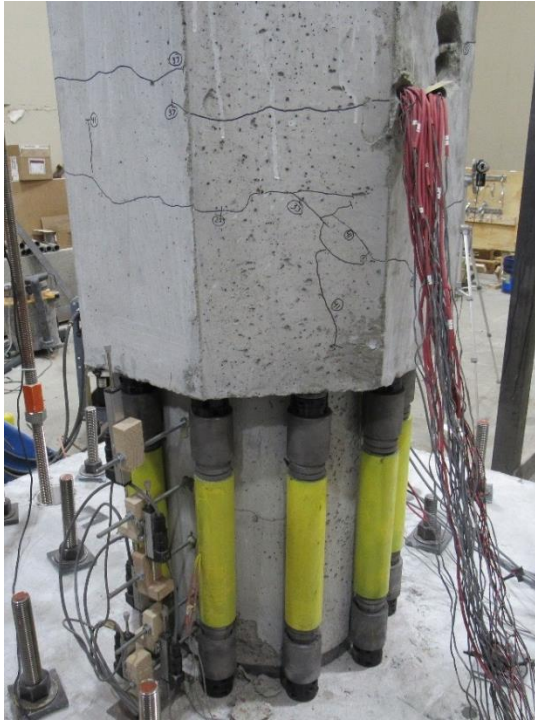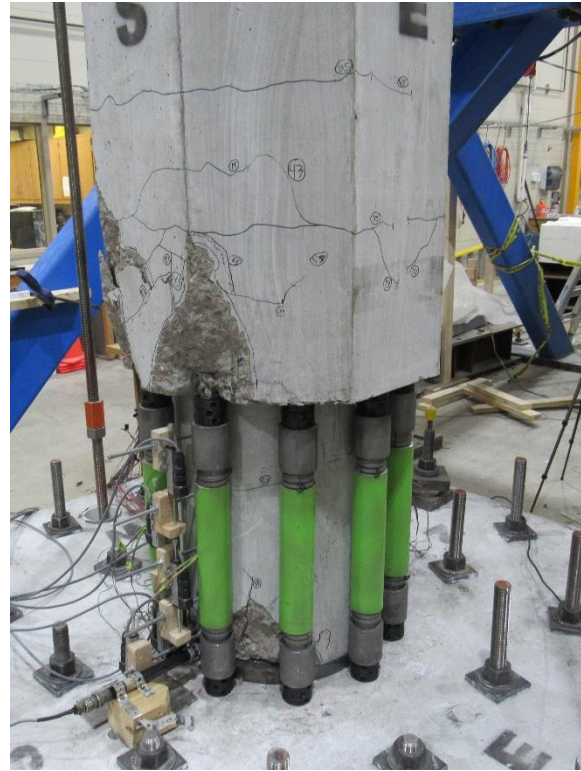
a) North-West Side   b) South-East Side

Figure 4.82. RPH-PC-R Column Plastic Hinge Damage, Second Push of 0.25% Drift Cycle
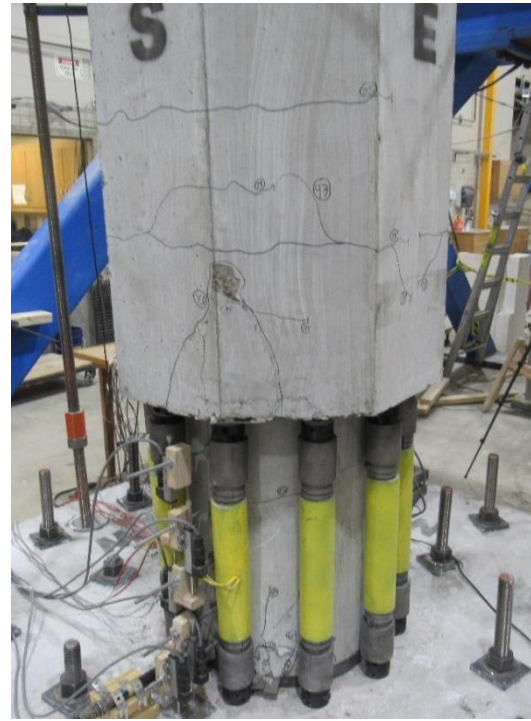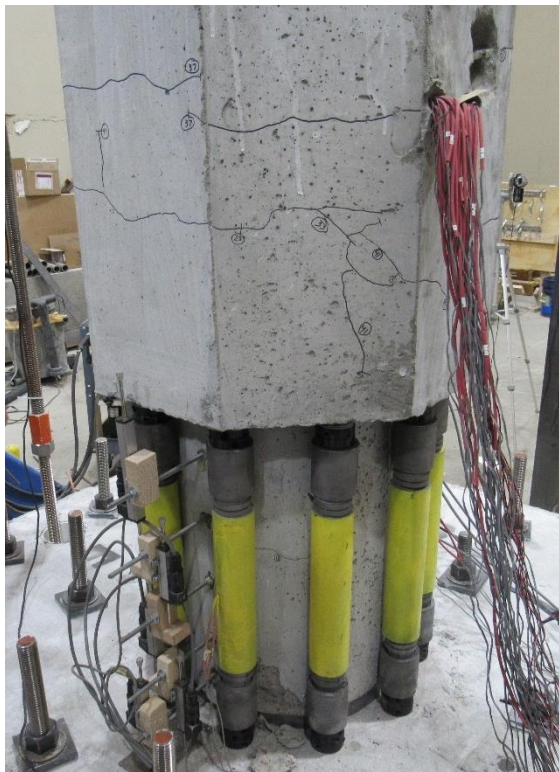

a) North-West Side   b) South-East Side

Figure 4.83. RPH-PC-R Column Plastic Hinge Damage, Second Pull of 0.25% Drift Cycle
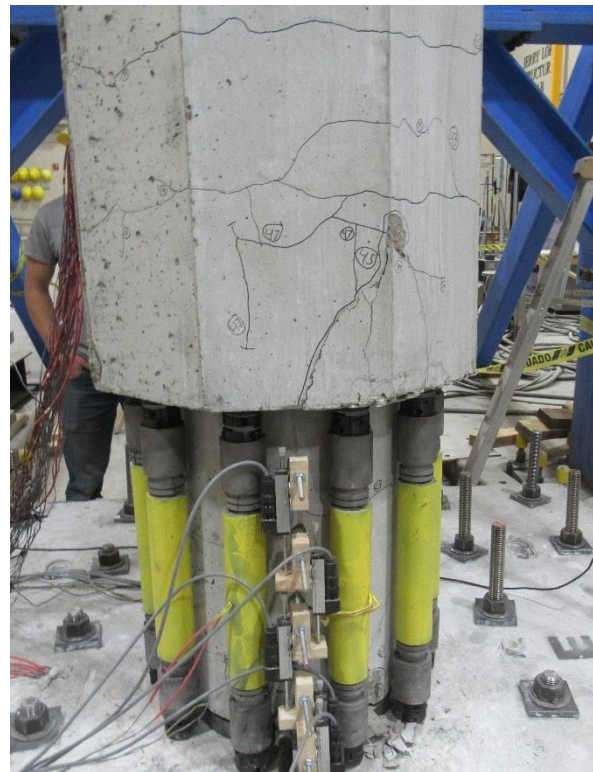
117

a) North-West Side   b) South-East Side
Figure 4.84. RPH-PC-R Column Plastic Hinge Damage, Second Push of 0.50% Drift Cycle
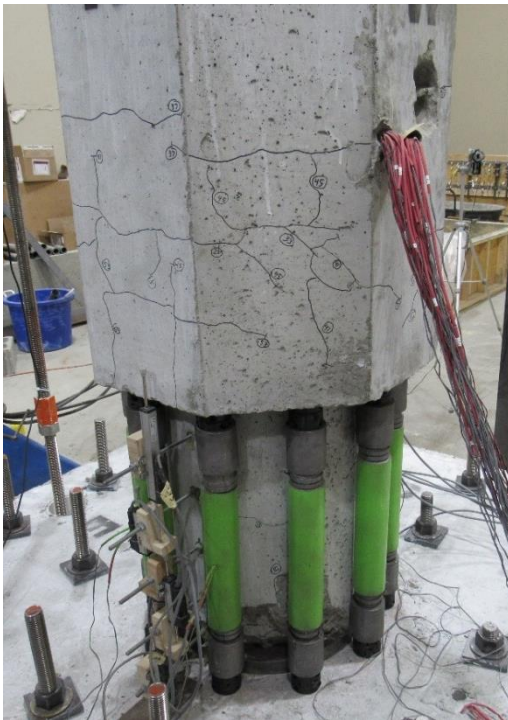
a) North-West Side   b) South-East Side
Figure 4.85. RPH-PC-R Column Plastic Hinge Damage, Second Pull of 0.50% Drift Cycle
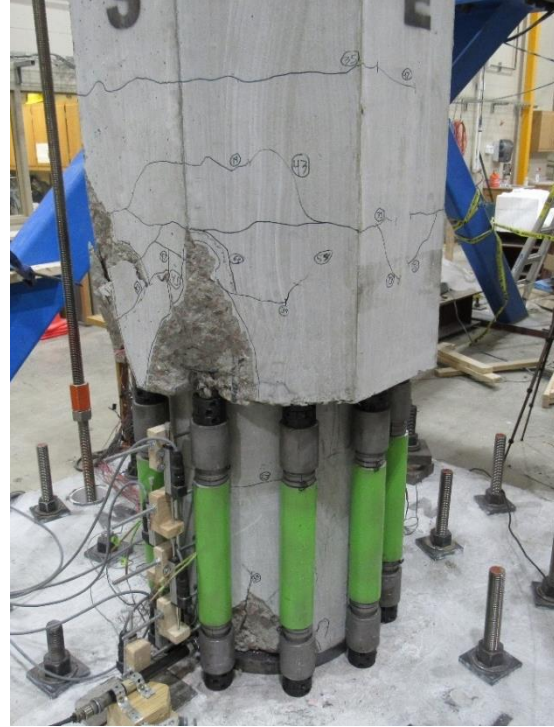
a) North-West Side b) South-East Side

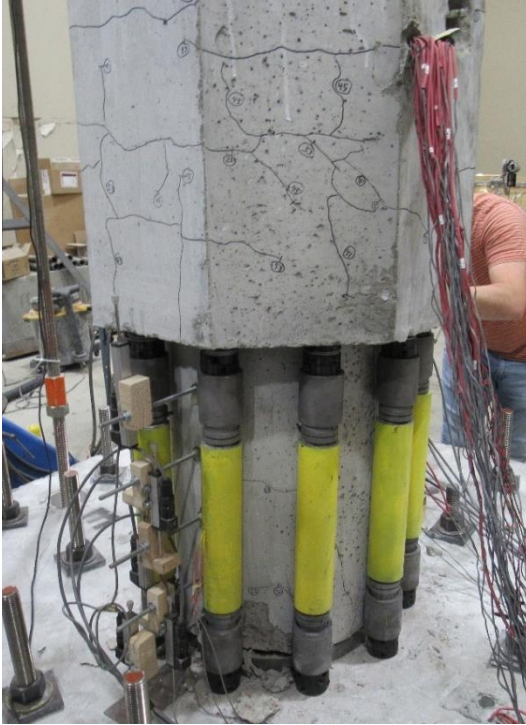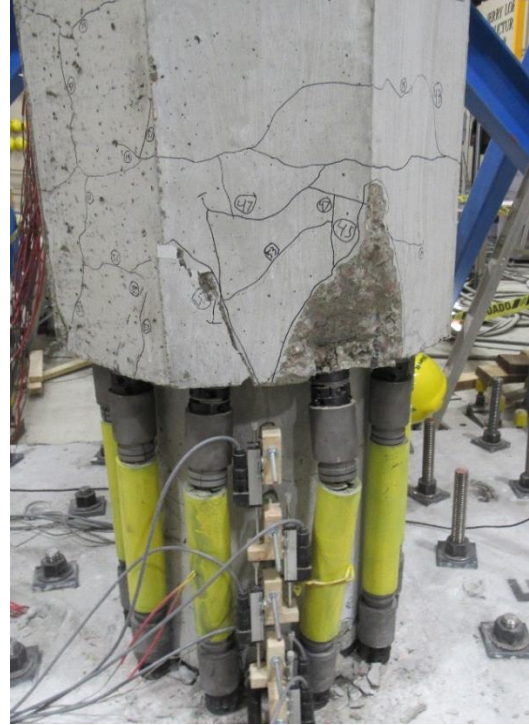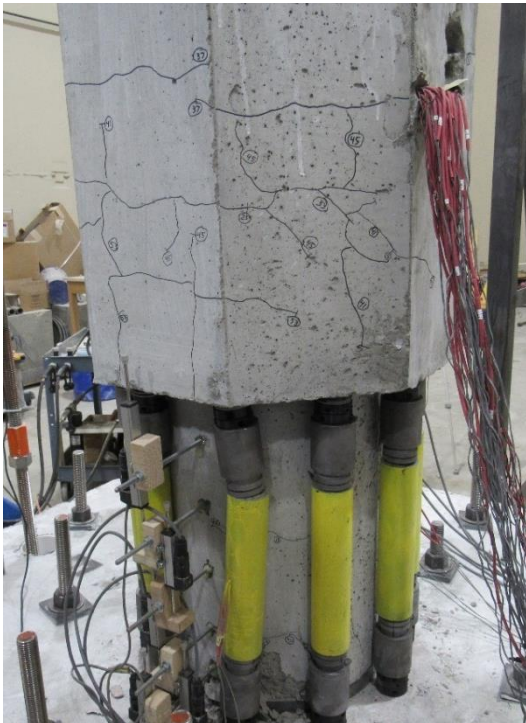**Figure 4.86. RPH-PC-R Column Plastic Hinge Damage, Second Push of 0.75% Drift Cycle**

a) North-West Side b) South-East Side

Figure 4.87. RPH-PC-R Column Plastic Hinge Damage, Second Pull of 0.75% Drift Cycle
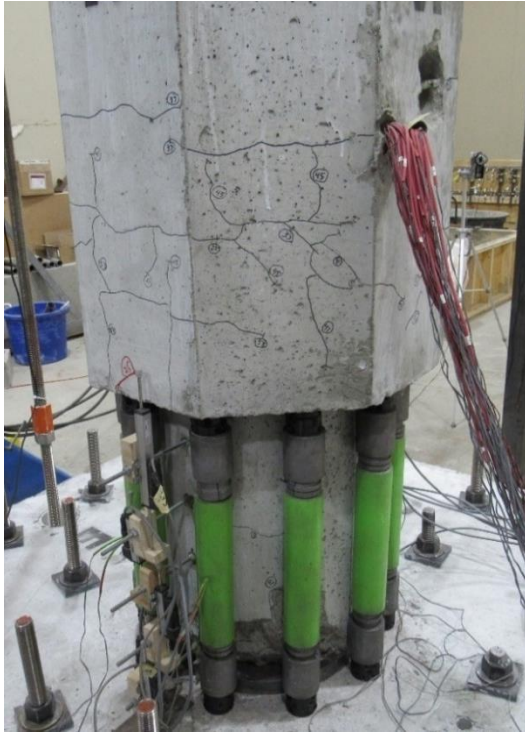
a) North-West Side   b) South-East Side
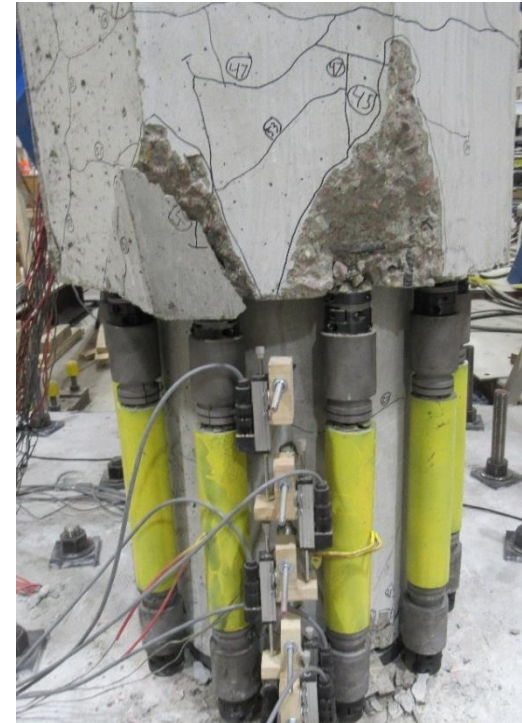**Figure 4.88. RPH-PC-R Column Plastic Hinge Damage, Second Push of 1.0% Drift Cycle**
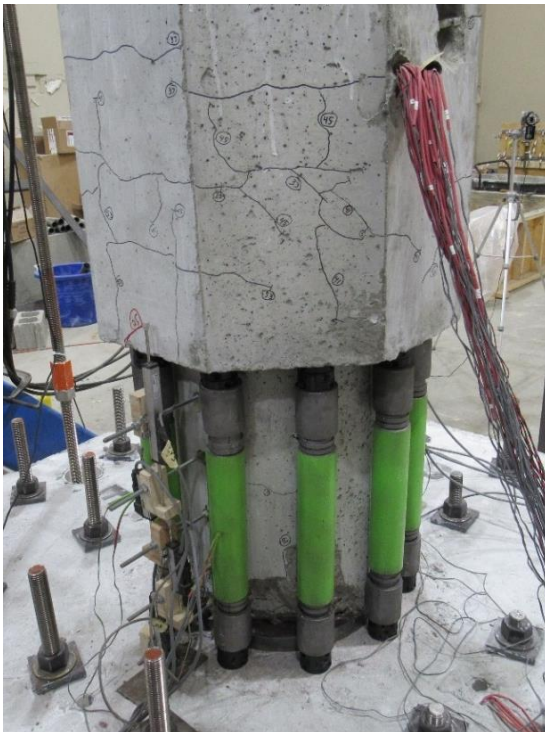
a) North-West Side   b) South-East Side
Figure 4.89. RPH-PC-R Column Plastic Hinge Damage, Second Pull of 1.0% Drift Cycle

120

a) North-West Side   b) South-East Side
Figure 4.90. RPH-PC-R Column Plastic Hinge Damage, Second Push of 2.0% Drift Cycle
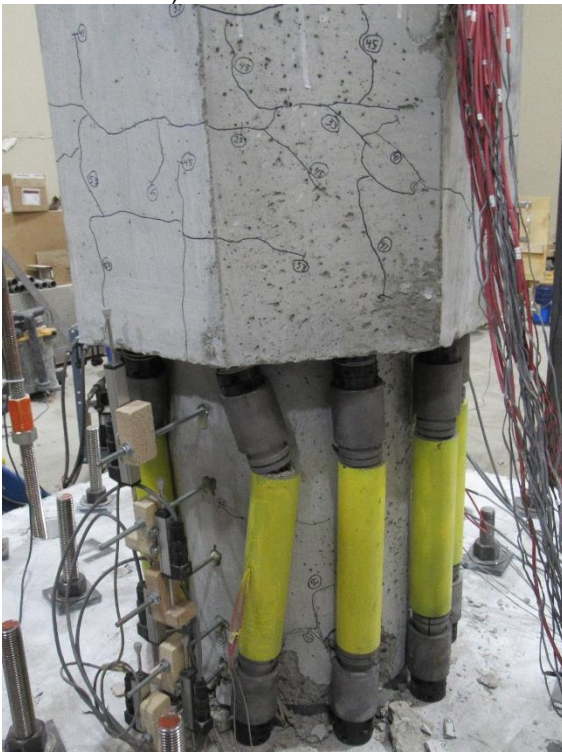

a) North-West Side   b) South-East Side
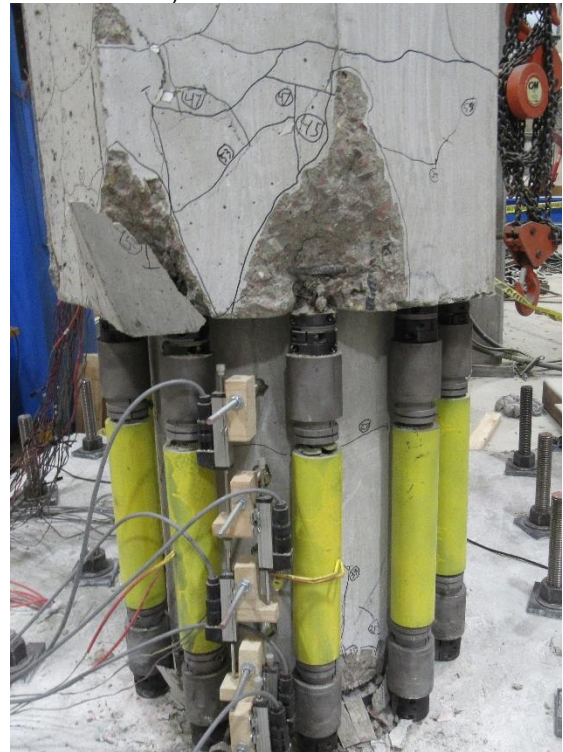**Figure 4.91. RPH-PC-R Column Plastic Hinge Damage, Second Pull of 2.0% Drift Cycle**

a) North-West Side   b) South-East Side
Figure 4.92. RPH-PC-R Column Plastic Hinge Damage, Second Push of 3.0% Drift Cycle
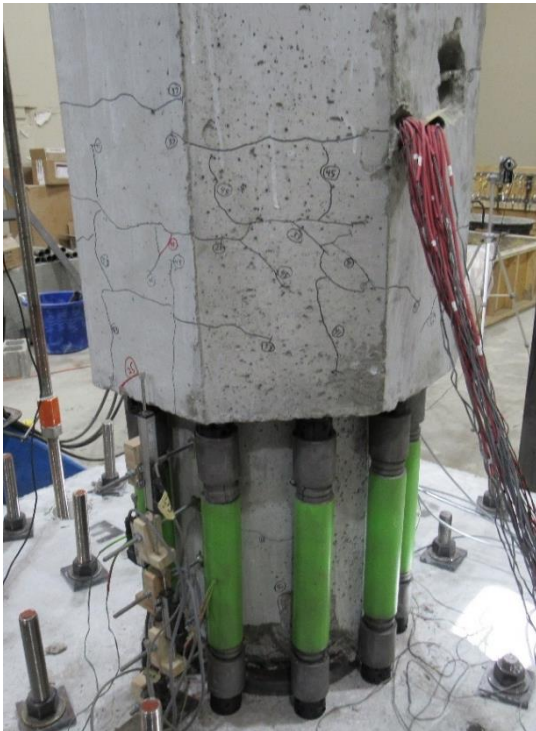
a) North-West Side   b) South-East Side
Figure 4.93. RPH-PC-R Column Plastic Hinge Damage, Second Pull of 3.0% Drift Cycle

a) North-West Side b) South-East Side

Figure 4.94. RPH-PC-R Column Plastic Hinge Damage, Second Push of 4.0% Drift Cycle

a) North-West Side b) South-East Side

Figure 4.95. RPH-PC-R Column Plastic Hinge Damage, Second Pull of 4.0% Drift Cycle

a) North-West Side   b) South-East Side

Figure 4.96. RPH-PC-R Column Plastic Hinge Damage, Second Push of 5.0% Drift Cycle
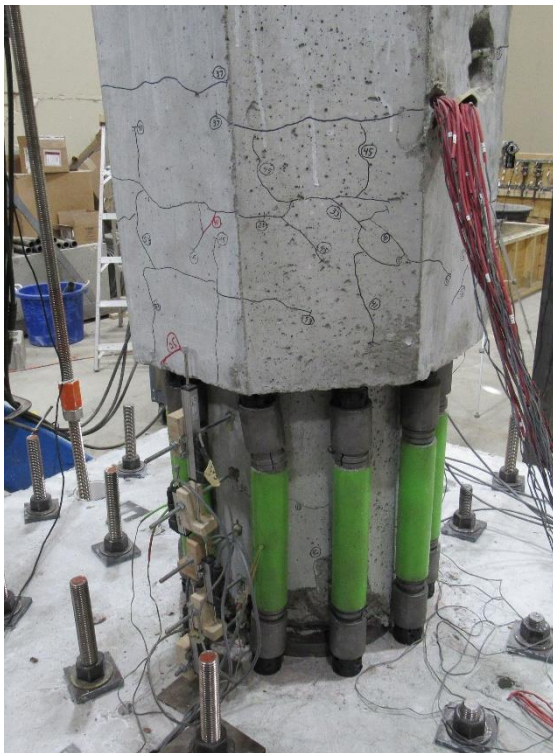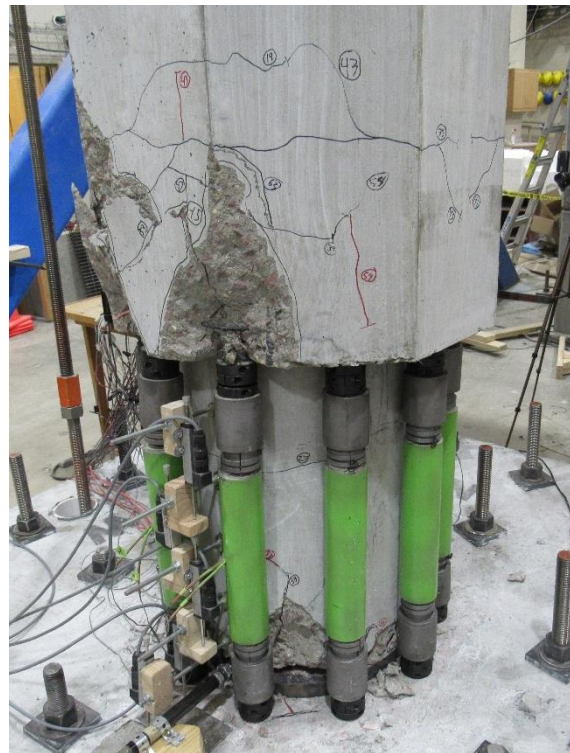
a) North-West Side   b) South-East Side

Figure 4.97. RPH-PC-R Column Plastic Hinge Damage, Second Pull of 5.0% Drift Cycle
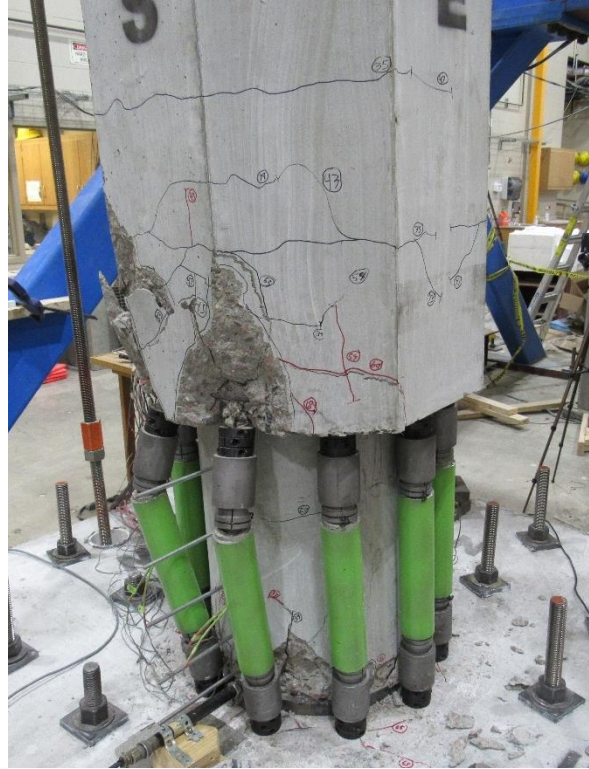
a) North-West Side   b) South-East Side

Figure 4.98. RPH-PC-R Column Plastic Hinge Damage, Second Push of 6.0% Drift Cycle
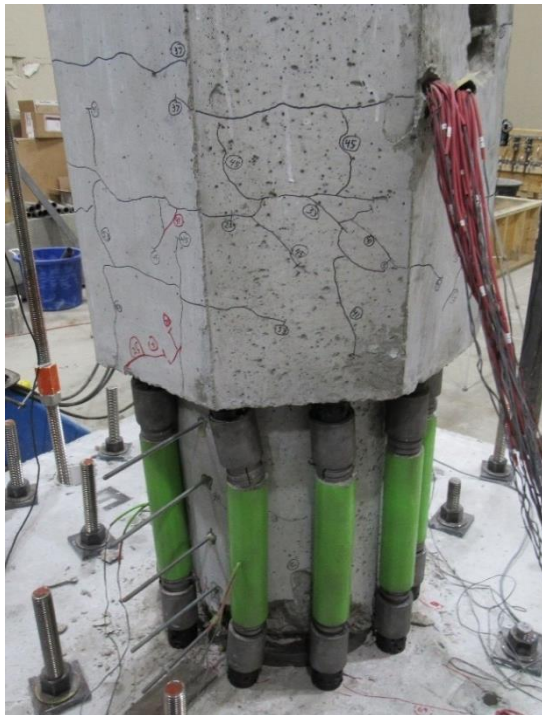
a) North-West Side   b) South-East Side

Figure 4.99 RPH-PC-R Column Plastic Hinge Damage, Second Pull of 6.0% Drift Cycle
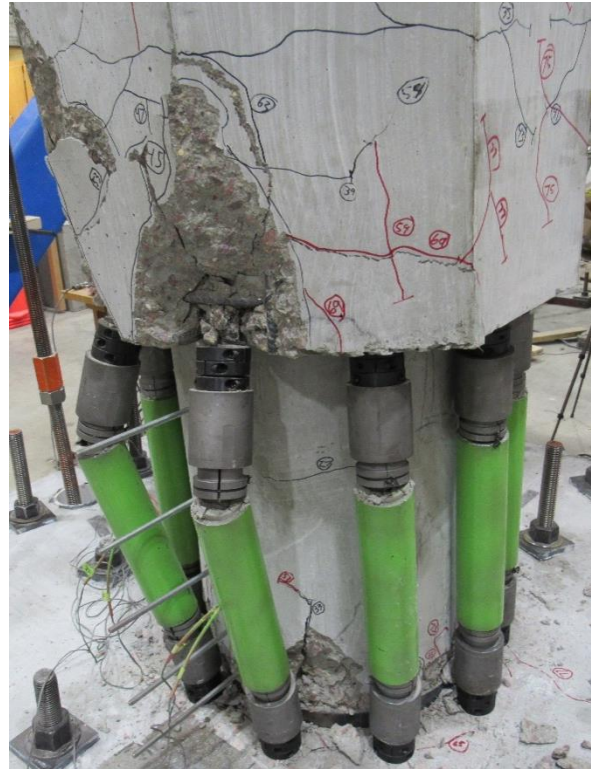
a) North-West Side   b) South-East Side

Figure 4.100. RPH-PC-R Column Plastic Hinge Damage, Second Push of 7.0% Drift Cycle

a) North-West Side   b) South-East Side

Figure 4.101. RPH-PC-R Column Plastic Hinge Damage, Second Pull of 7.0% Drift Cycle
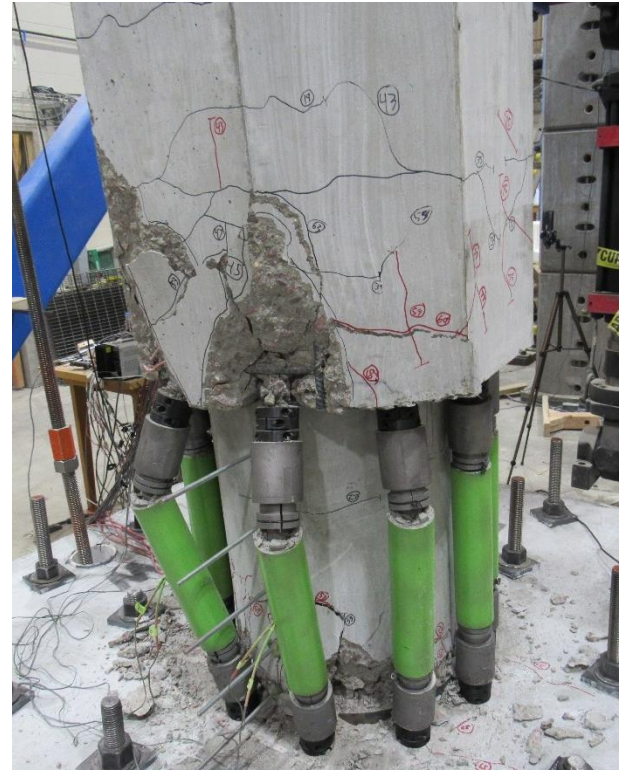
a) North-West Side   b) South-East Side
Figure 4.102. RPH-PC-R Column Plastic Hinge Damage, Second Push of 8.0% Drift Cycle

a) North-West Side   b) South-East Side
Figure 4.103. RPH-PC-R Column Plastic Hinge Damage, Second Pull of 8.0% Drift Cycle
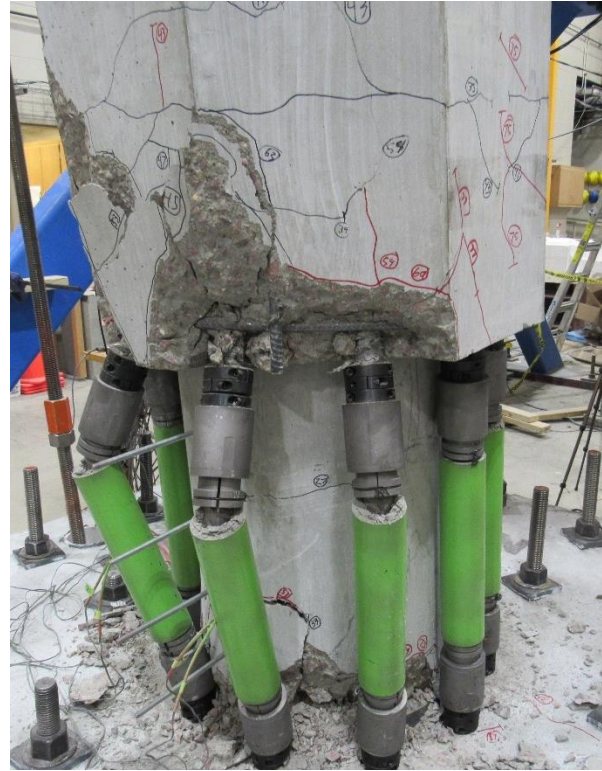
a) North-West Side   b) South-East Side
Figure 4.104. RPH-PC-R Column Plastic Hinge Damage, Second Push of 9.0% Drift Cycle

a) North-West Side   b) South Side
Figure 4.105. RPH-PC-R Column Plastic Hinge Damage, Second Pull of 9.0% Drift Cycle

128
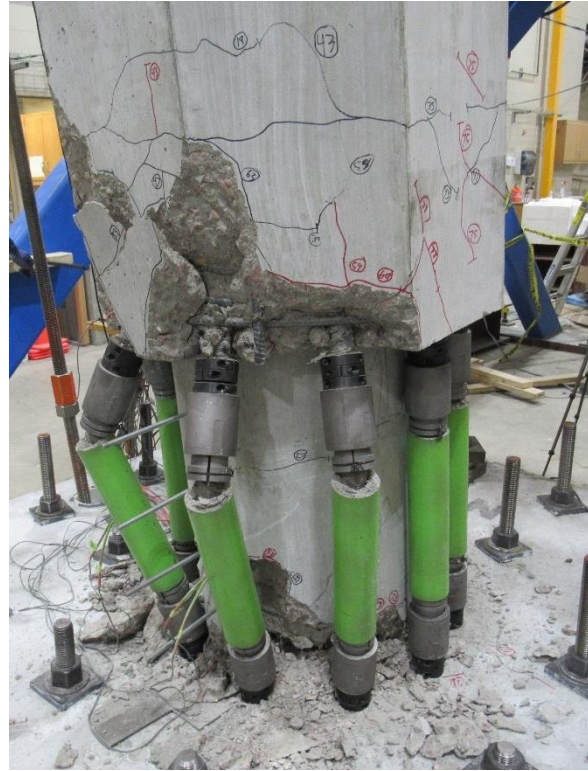
a) North-West Side   b) South-East Side

Figure 4.106. RPH-PC-R Column Plastic Hinge Damage, Second Push of 10.0% Drift Cycle

a) North-West Side   b) South-East Side

Figure 4.107. RPH-PC-R Column Plastic Hinge Damage, Second Pull of 10.0% Drift Cycle

4.5.3.4 RPH-PC Force-Displacement Relationship

Figure 4.108 shows the measured force-drift hysteretic and envelope responses of RPH-PC. Note that this test was stopped at 5% drift ratio to replace the BRR fuses. The maximum lateral load of 69.2 kips (308 kN) occurred in the pull direction at 5% drift. The column had a slightly higher stiffness and lateral load in the pull direction. The longitudinal bars yielded within the BRR fuses in the push direction at a drift ratio of 1.60% and a corresponding lateral load of 40.1 kips (178.44 kN), and in the pull direction at a drift ratio of 1.35% and a lateral load of 46.6 kips (207.3 kN).
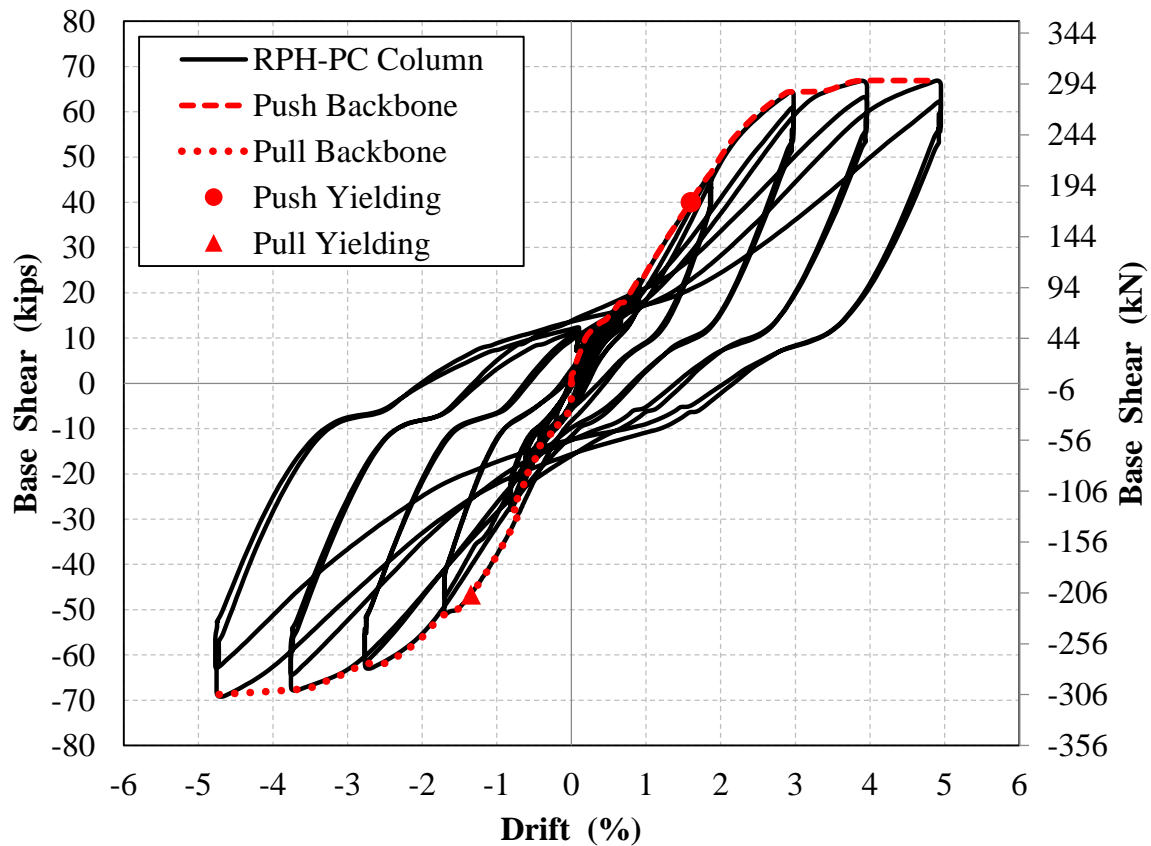
Figure 4.108. Measured RPH-PC Column Force-Drift Hysteretic and Envelope Responses

130

Figure 4.109 shows the average envelope of the push and pull directions for RPH-PC. The average yield drift ratio was 1.47% corresponding to a lateral force of 43.0 kips (191.3 kN). No sign of failure was observed at 5% drift where the test was stopped for the repair thus no idealization of the response was carried out for RPH-PC.
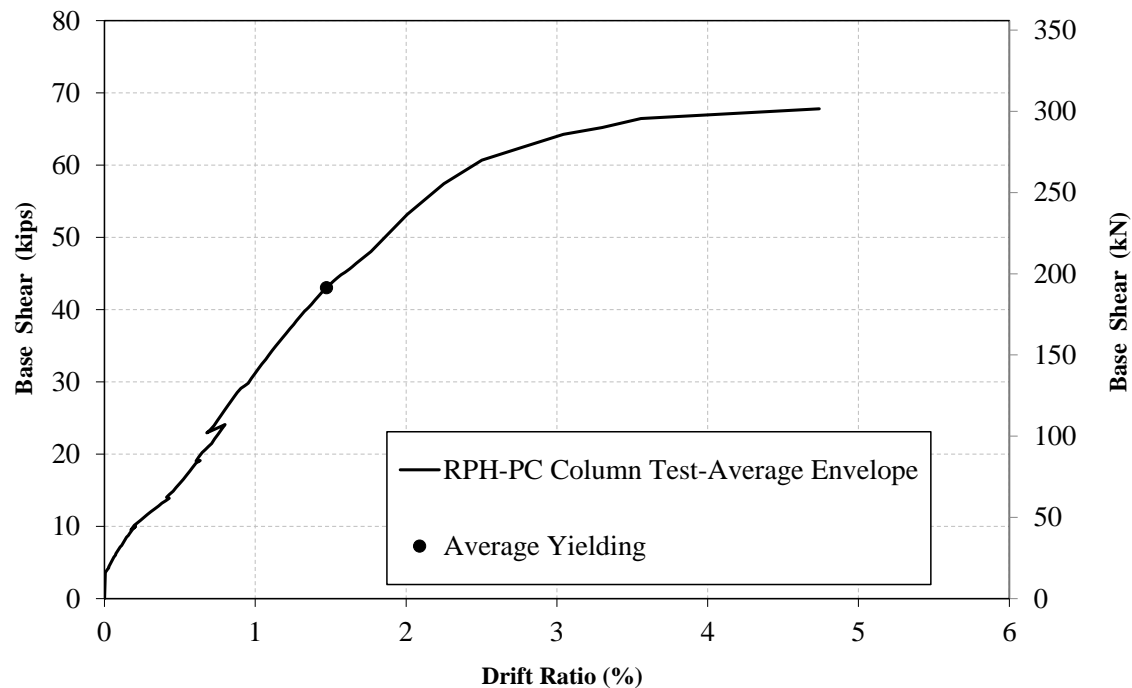
Figure 4.109. Measured RPH-PC Column Average Push/Pull Force-Drift Envelope

4.5.3.5 RPH-PC-R Force-Displacement Relationship

Figure 4.110 shows the measured lateral force-drift hysteretic and envelope responses from the repaired RPH-PC, or RHP-PC-R, up to 10% drift ratio. Even though a strength degradation can be seen after 8% drift ratio in the push direction, the force drop did not meet the 15% criterion for column failure. Nevertheless, the test was stopped at 10% drift ratio to avoid any setup damage. Furthermore, the CIP column failed at 10% drift ratio thus it was not necessary to exceed this drift limit. The maximum lateral load of 74.7 kips (332.3 kN) occurred in the pull direction at a drift ratio of 8.31%. The column was softer in the push direction mainly due to the spalling above the neck region on the south face of the column. The longitudinal bars within the BRR fuses yielded in the push direction at a drift ratio of 3.06% and a corresponding load of 43.8 kips (195.8 kN), and in the pull direction during the first 3% drift cycle but at a drift ratio of 2.0% and a lateral load of 44.0 kips (195.7 kN).

Figure 4.111 includes the average envelope of the push and pull directions for the RPH-PC-R column. The average yield drift ratio was 2.53% at a lateral load of 43.7 kips (194.3 kN). The idealized curve is also included in the figure. The effective yield point was at 4.0% drift ratio with a lateral load of 69.3 kips (308.3 kN). The drift capacity of the column was 9.80% (where the test was stopped). The resulting displacement ductility capacity is 2.45 for the RPH-PC-R column. It should be noted that for novel columns the displacement ductility capacity is not a good indicator for the design since the yield displacement is not a typical value. The drift ratio is a better design parameter. It is evident that the RPH-PC-R column exhibited a higher drift ratio capacity compared with the CIP column (9.80% vs. 8.96%).
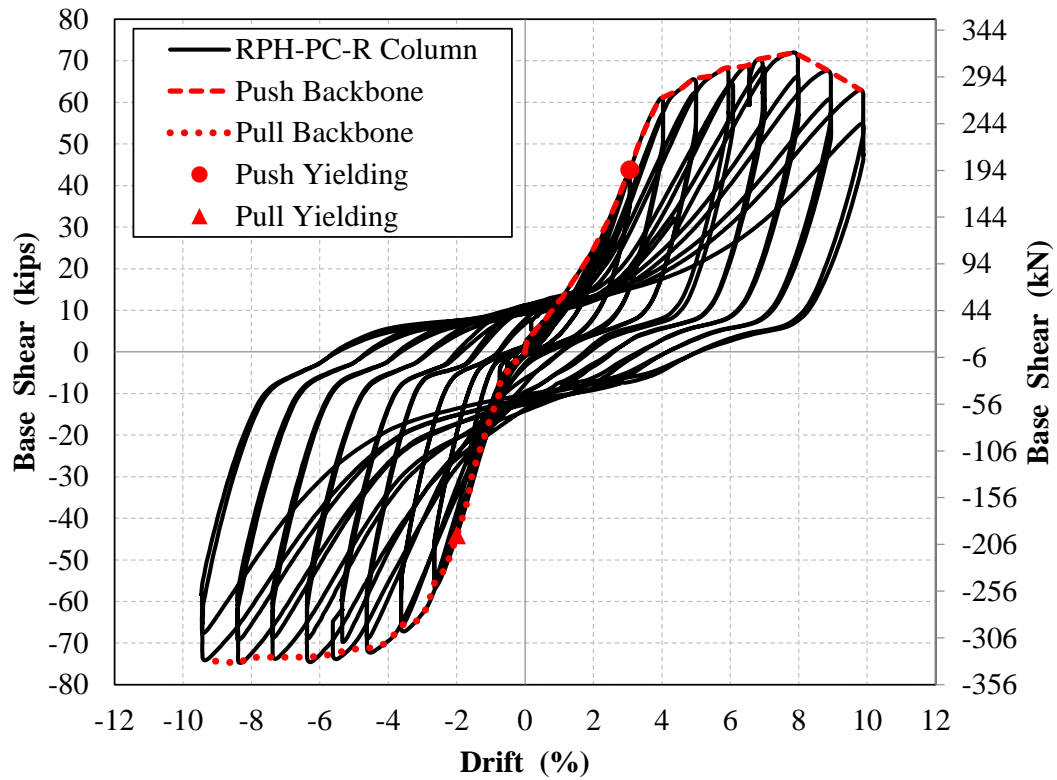
Figure 4.110. Measured RPH-PC-R Column Force-Drift Hysteretic and Envelope Responses
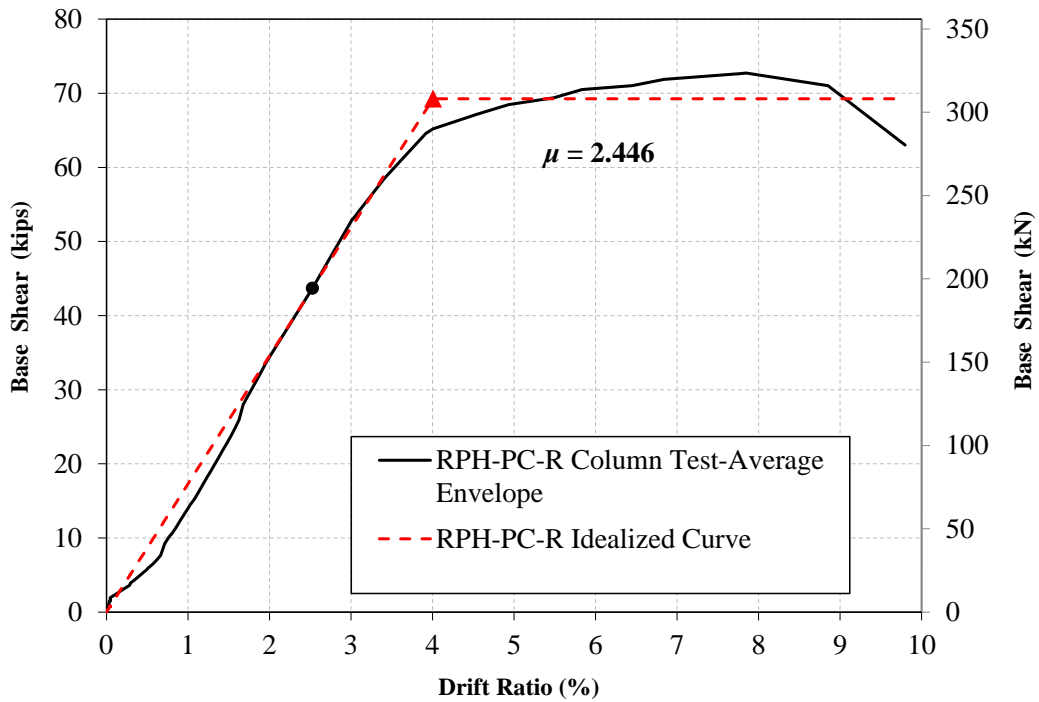
Figure 4.111. Measured RPH-PC-R Column Average Push/Pull Force-Drift Envelope and Idealized Curve

Figure 4.112 compares the average backbones of RPH-PC, RPH-PC-R, and CIP. The initial stiffness of both RPH-PC and RPH-PC-R was lower than CIP since the repairable column had a smaller neck section and a modular bar connection. The initial stiffness of RPH-PC-R was the lowest. The "dog-bone" length of the BRR in RPH-PC was 10.25 in. (260 mm) while the length was shortened to 5.125 in. (130 mm) in RPH-PC-R. This would be expected to result in a higher stiffness for the repaired column; however, the initial stiffness of RPH-PC-R decreased between the first and second sets of testing mainly due to the concrete damage at the column base and above the neck region.

The best performance of a repairable column in terms of initial stiffness would be that the stiffness of the column remains the same before and after replacement of BRR. To achieve this performance in future applications, the concrete damage should be minimized. Some options are to use UHPC and tension-only fuses to avoid concrete and bar damages.
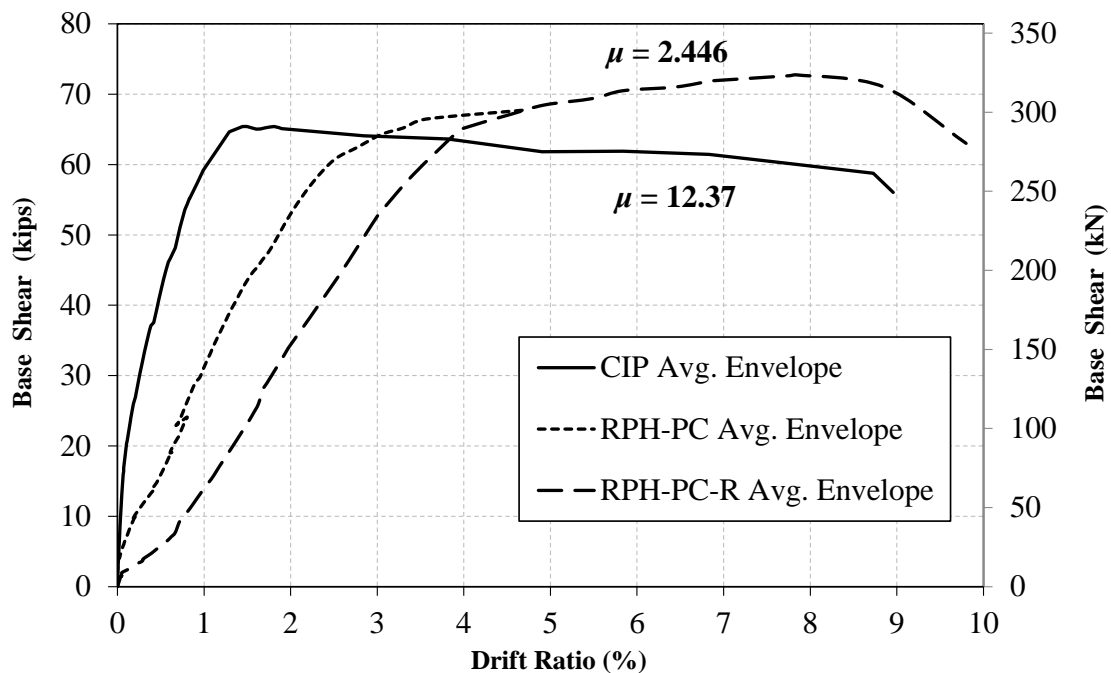
Figure 4.112. Measured Force-Drift Response of CIP, RPH-PC, and RPH-PC-R Columns

4.5.3.6 RPH-PC Strain Profiles

Forty-six steel strain gauges were installed on the RPH-PC column at five levels along the column height. Four of these levels included strain gauges on the longitudinal bars within the neck section. **Figures 4.113** to **4.116** show the measured strain profiles for Bars B1, B2, B6, and B7. The middle two levels of strain gauges were placed along the dog-bone region of the stainless-steel bars within BRR.

The strain profiles of the four bars were relatively uniform up to the yielding of the BRR bars after which the profiles show higher strains at the center two levels within the BRR fuses. The longitudinal bars outside BRR (column and footing dowels) slightly yielded or did not yield at all due to the higher bar cross-sectional area outside of the dog-bone region (dowels were No. 10 (Ø32 mm) while dog-bone fuses where machined down to No. 8 (Ø25 mm)). Strain for the transverse reinforcement was also monitored. The yield strain for the hoops in RPH-PC was 0.23% while the maximum measured strain was 0.42% recorded at a hoop in the center of the neck section. Furthermore, the strain data shows that the steel bars that were used to reinforce the neck in the longitudinal direction remained linear elastic during the entire testing indicating a successful design for the neck itself.

The maximum compressive strains during each drift cycle were also recorded for completeness (**Fig. 4.117-4.120**). The compressive strains in bars B1 and B2 (column north face) were concentrated within BRR at 16 in. (406 mm) height. The compressive strains in bars B6 and B7 (column south face); however, were concentrated above and below the neck section of the column. Compressive strain in bar B6 occurred at 25 in. (635 mm) height where significant spalling had occurred, allowing the bars to buckle.

It should be noted that all strain gauges were placed on the outermost face of the bars to record maximum tensile strains. In compression; however, the bars on either side of the column did not buckle in the same direction. For example, the north bars buckled sideways towards the east and west directions. This may have had an impact on the compressive strain readings. Overall, BRR could resist large compressive strains and stresses, well beyond the yielding. Therefore, the design of BRR was successful but the Z-shape buckling of BRR remains the main concern which will make the repair-by-replacement impractical in real applications.

Figure 4.113. Measured Tensile Strain Profile for RPH-PC Column Bar B1

Figure 4.114. Measured Tensile Strain Profile for RPH-PC Column Bar B2

135
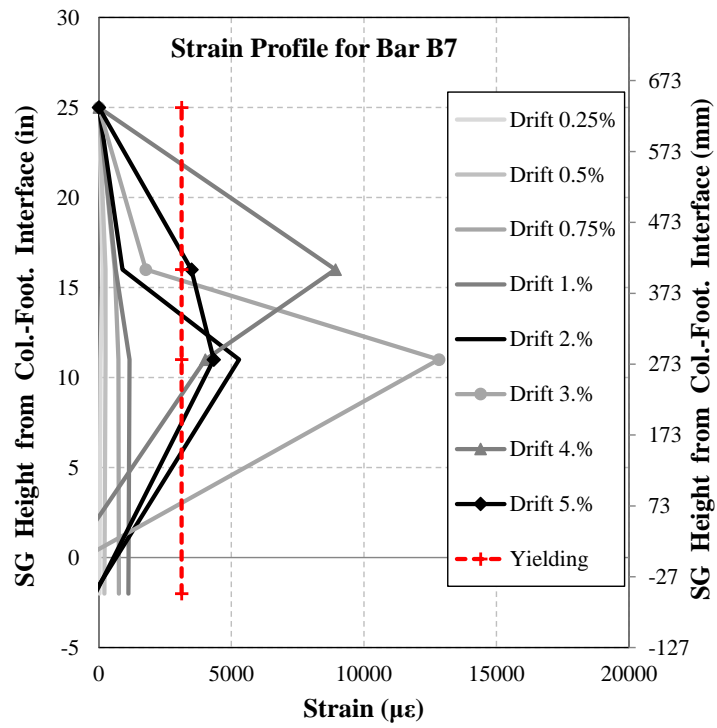
Figure 4.115. Measured Tensile Strain Profile for RPH-PC Column Bar B6

Figure 4.116. Measured Tensile Strain Profile for RPH-PC Column Bar B7

Figure 4.117. Measured Compressive Strain Profile for RPH-PC Column Bar B1
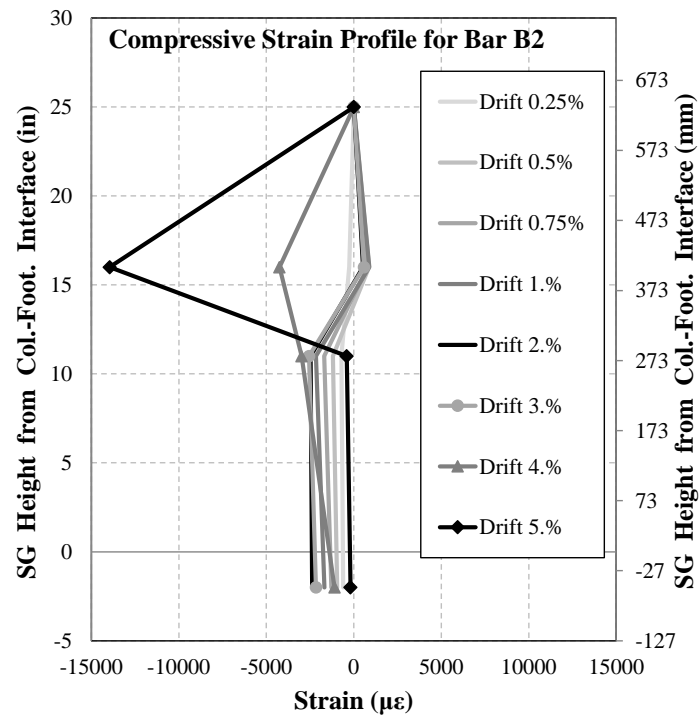
Figure 4.118. Measured Compressive Strain Profile for RPH-PC Column Bar B2

137
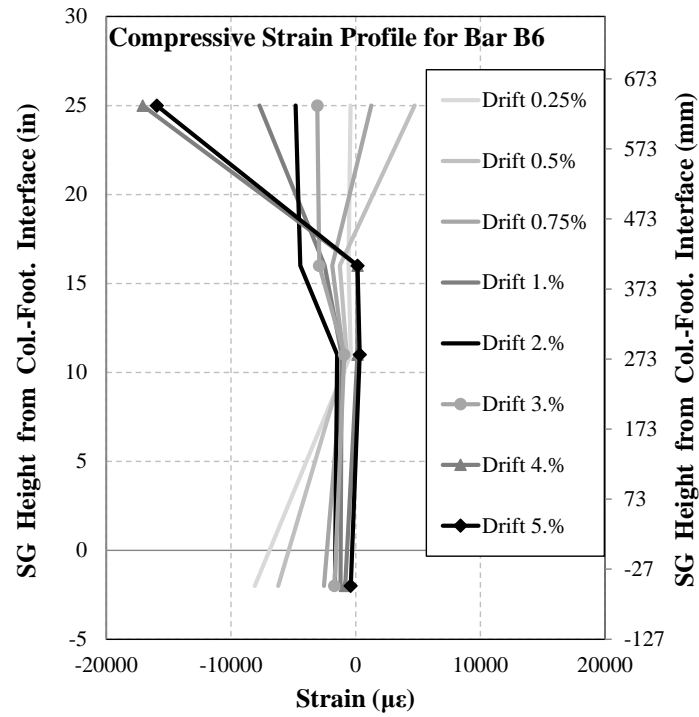
Figure 4.119. Measured Compressive Strain Profile for RPH-PC Column Bar B6
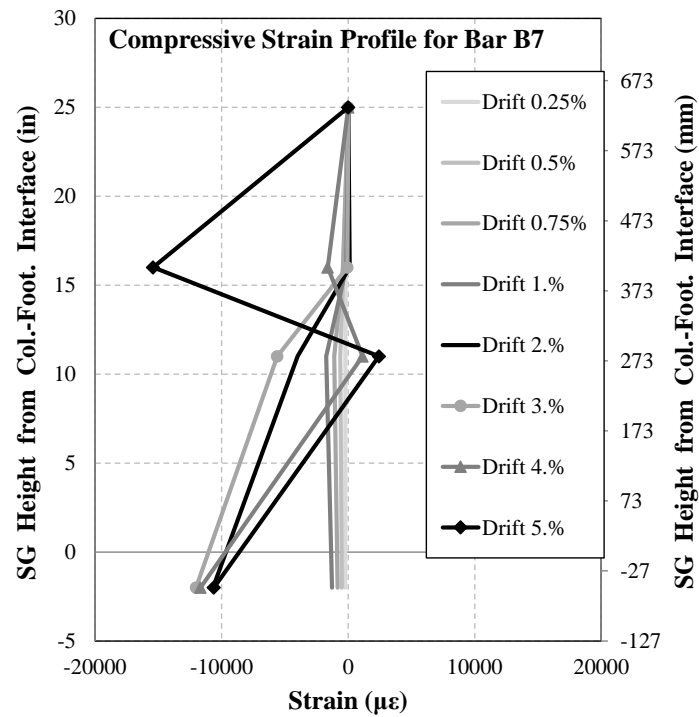
Figure 4.120. Measured Compressive Strain Profile for RPH-PC Column Bar B7

Strain profiles along the No. 8 (14-Ø25 mm) conventional steel bars in the neck section were also recorded to validate the neck section design (**Fig. 4.122-4.125**). The neck bars were numbered in the same way as the main column bars, with bars N1 and N2 corresponding to bars B1 and B2 and following in a clockwise direction (**Fig 4.121**). Bars N8 and N9 then correspond to bars B6 and B7, respectively. Strains in all bars except for bar N8 were well below the yield point, indicating a successful neck design. The values read at 16 in. (406 mm) height on bar N8 were more than a power of ten higher than all other values, and it is likely that the strain gauge at that level malfunctioned.

SECTION ORIENTATION
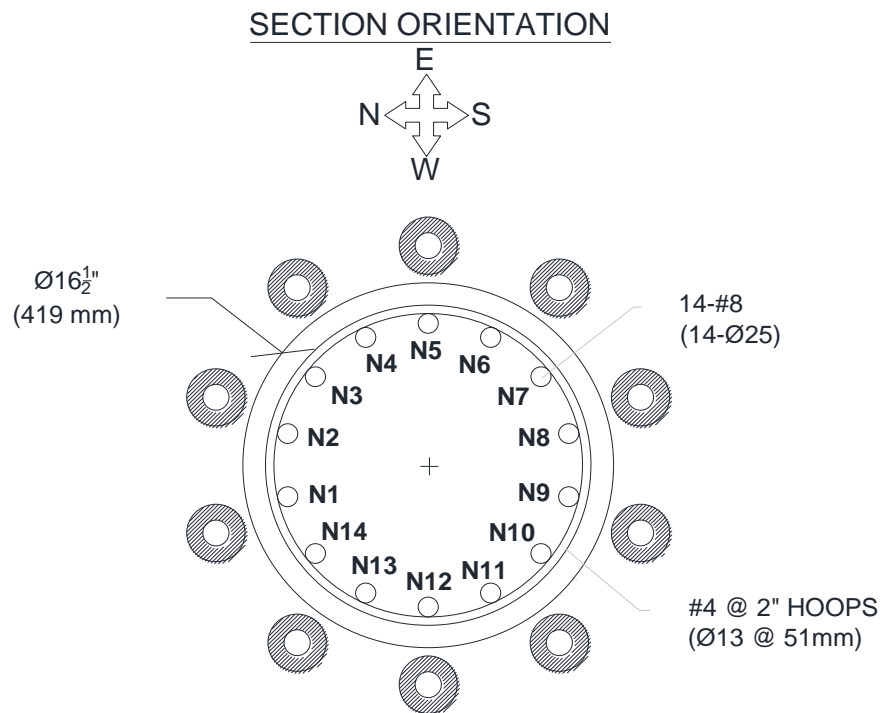
Figure 4.121. Numbering System for RPH-PC Neck Bars
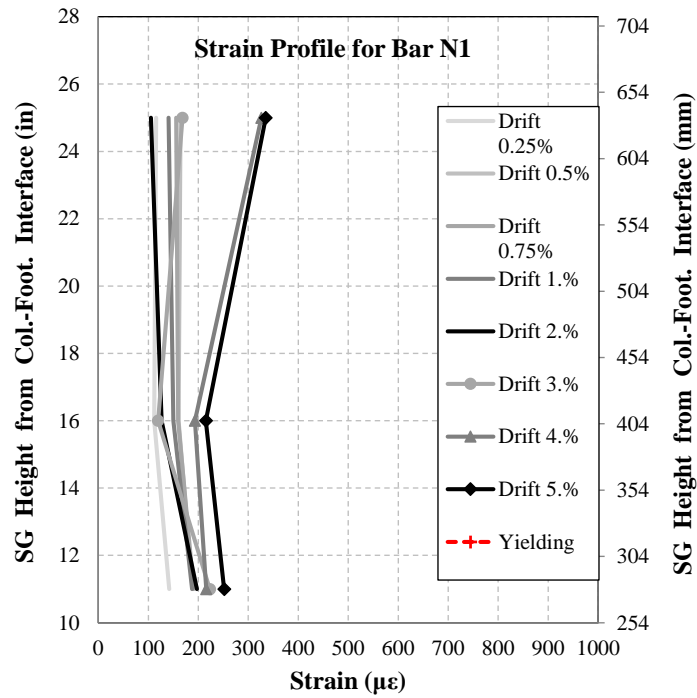
Figure 4.122. Measured Strain Profile for RPH-PC Column Neck Bar N1
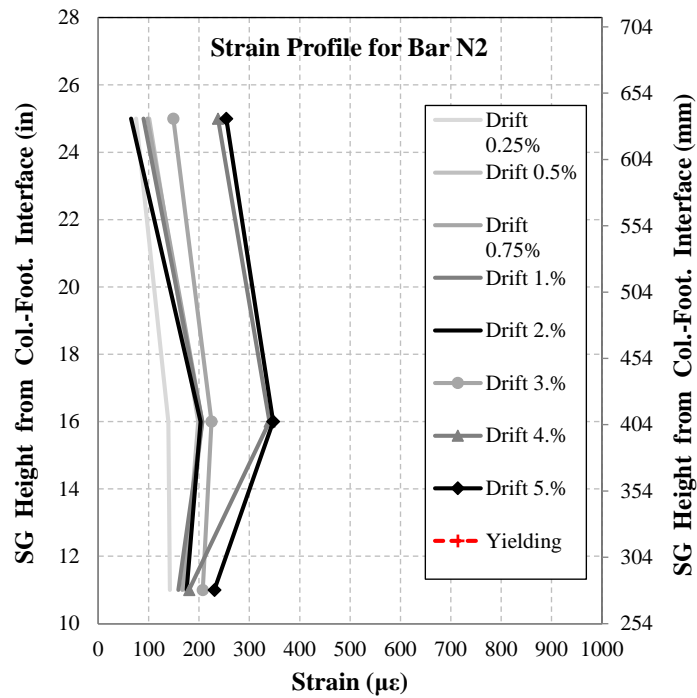
Figure 4.123. Measured Strain Profile for RPH-PC Column Neck Bar N2

140
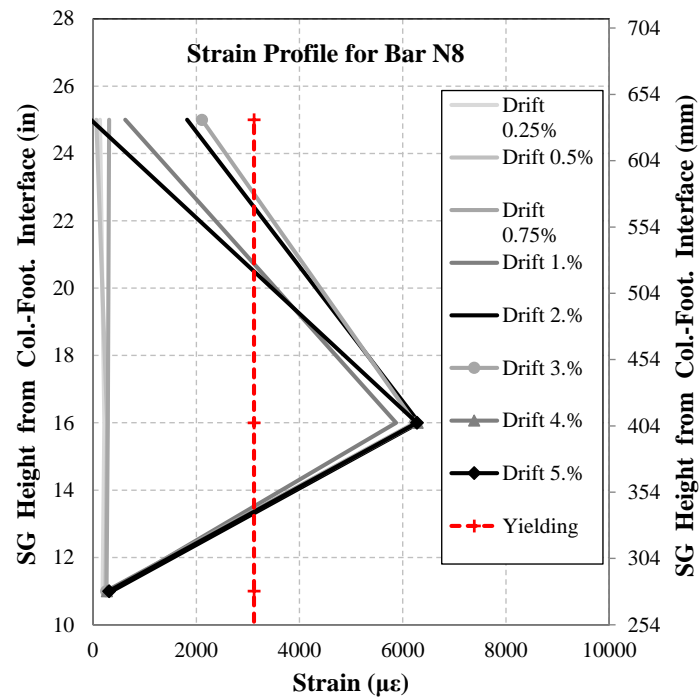
Figure 4.124. Measured Strain Profile for RPH-PC Column Neck Bar N8
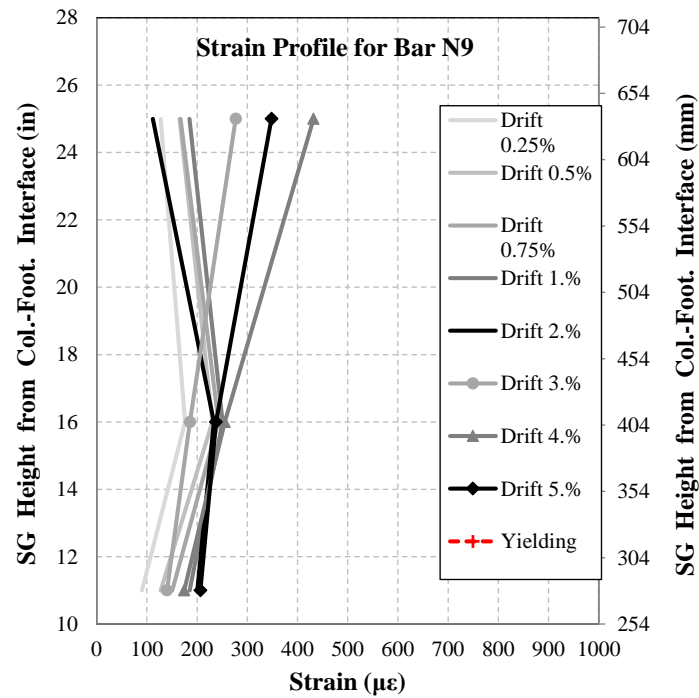
Figure 4.125. Measured Strain Profile for RPH-PC Column Neck Bar N9

Concrete strain gauges were installed along the perimeter of the base of the column, just inside the transverse reinforcement cage, to measure the strains in the core concrete. Concrete strain gauges were numbered following the same pattern as the main longitudinal bars, with a concrete strain gauge numbered to match each bar number (**Fig. 4.126**).
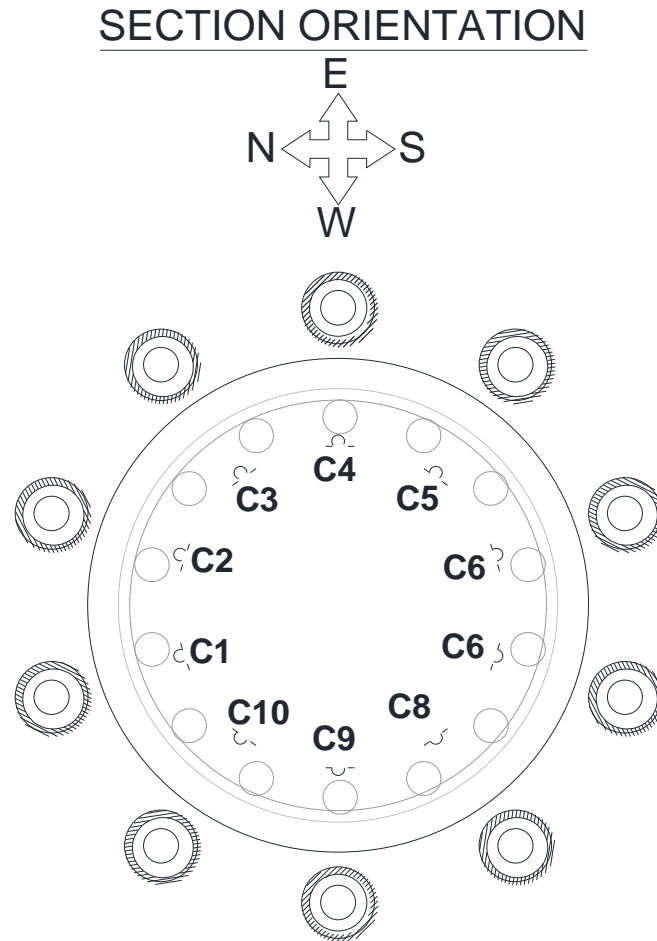
Figure 4.126. Numbering System for RPH-PC Concrete Strain Gauges in Neck Section

Figures 4.127 and **4.128** show the measured concrete compressive and tensile strain profiles for RPH-PC with positive values representing tensile strains and negative values representing compressive strains. In general, the maximum strains were concentrated near the north and south faces of the column. Strain gauges C1 and C10 on the north face of the column experienced both the highest compressive and tensile strains. At higher drifts, some gauges read only compressive strains throughout the entire cycle, indicating some crushing of surrounding concrete. While strain gauges C1 and C10 read values exceeding the cover strain capacity, values did not reach the strain capacity of the core concrete.

Figures 4.129 to **4.132** show the strain profiles along the east and west faces of the column during both push and pull cycles. Overall, it can be observed that during push cycles the gauges on the north side experienced tensile strains while the gauges on the south experienced compressive strains. The opposite can be said during pull cycles. The concrete strain gauges also recorded higher compressive strains than tensile strains, following the expected behavior of conventional concrete which has relatively low tensile capacity.
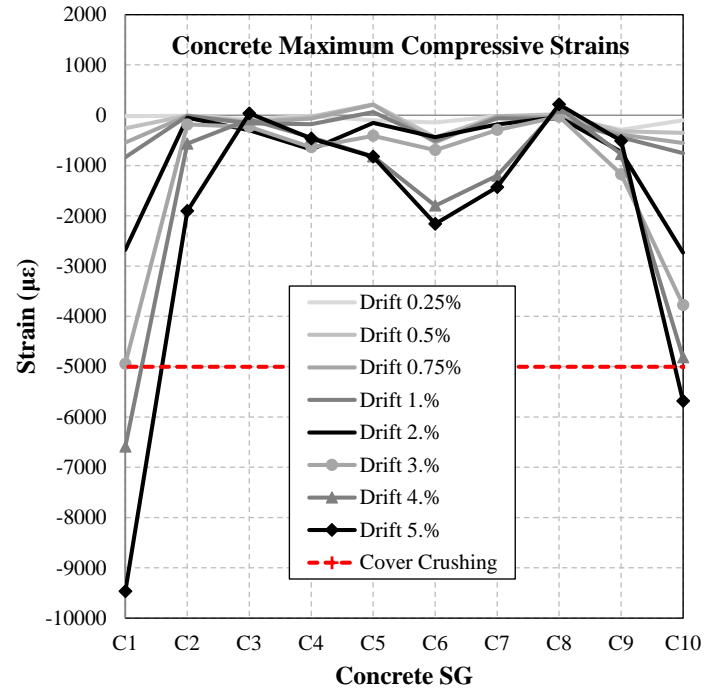
Figure 4.127. Measured Concrete Compressive Strain Profile for RPH-PC
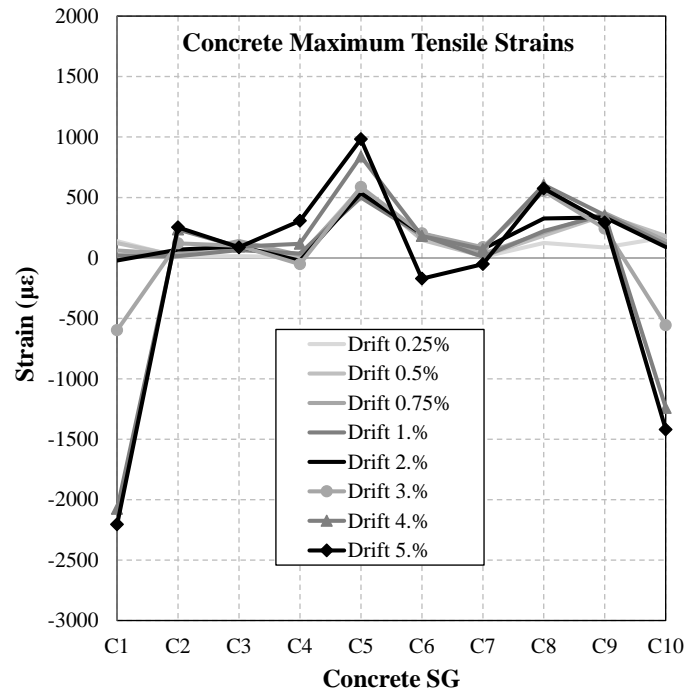
Figure 4.128. Measured Concrete Tensile Strain Profile for RPH-PC

143
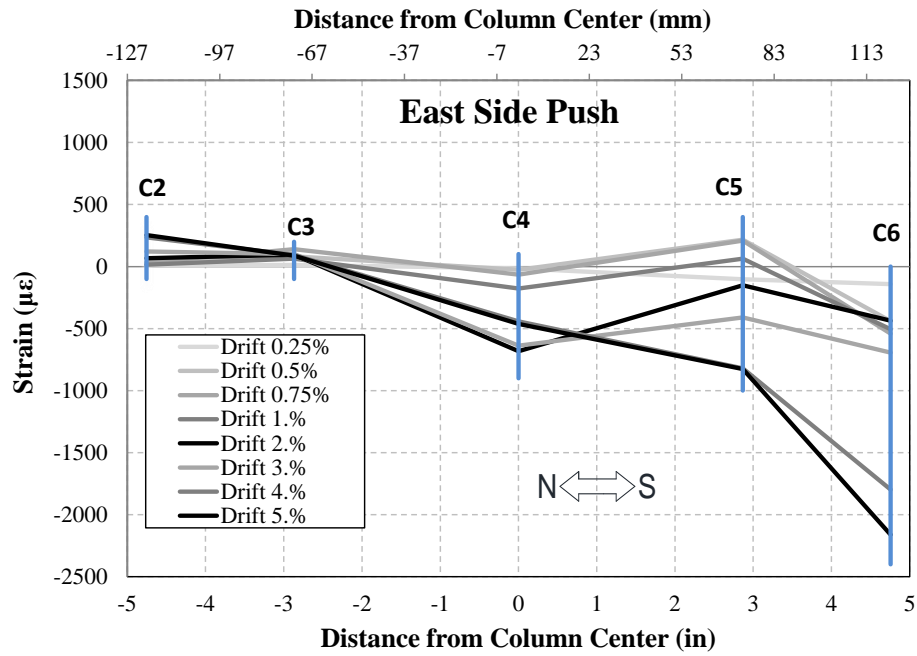
Figure 4.129. Measured Concrete Strain Profile for RPH-PC East Face During Push Cycles
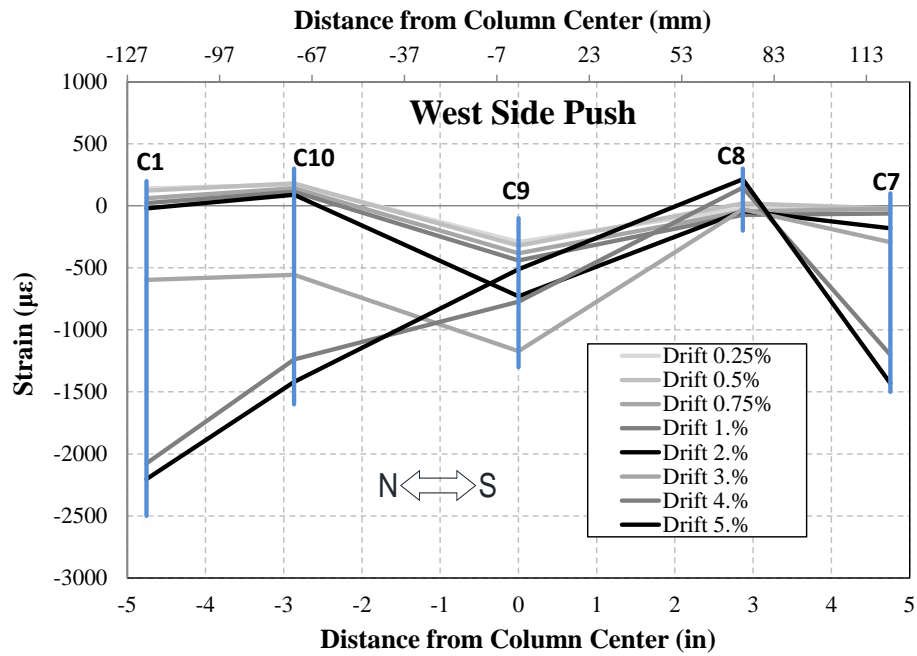
Figure 4.130. Measured Concrete Strain Profile for RPH-PC West Face During Push Cycles

144
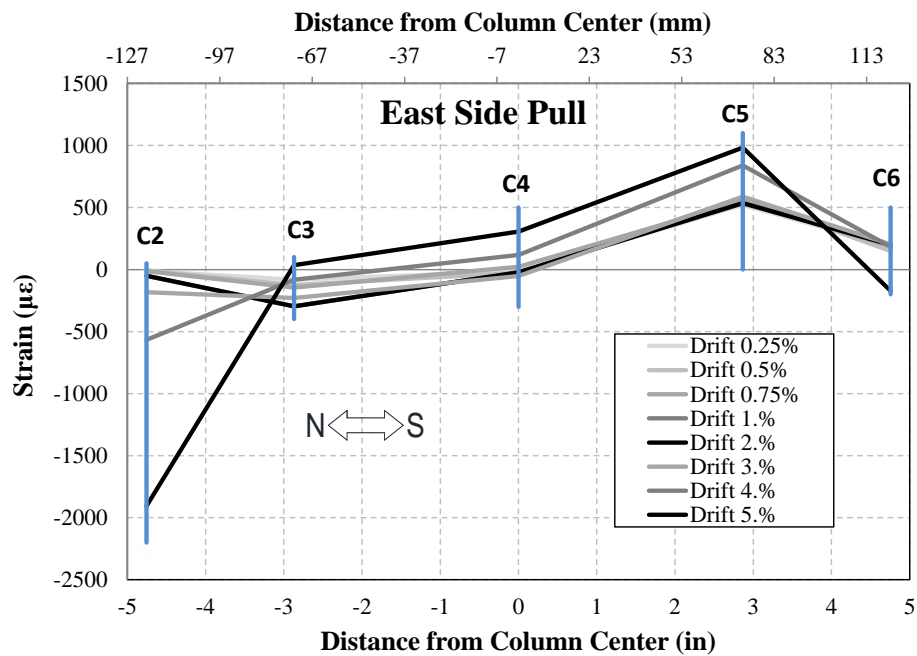
Figure 4.131. Measured Concrete Strain Profile for RPH-PC East Face During Pull Cycles
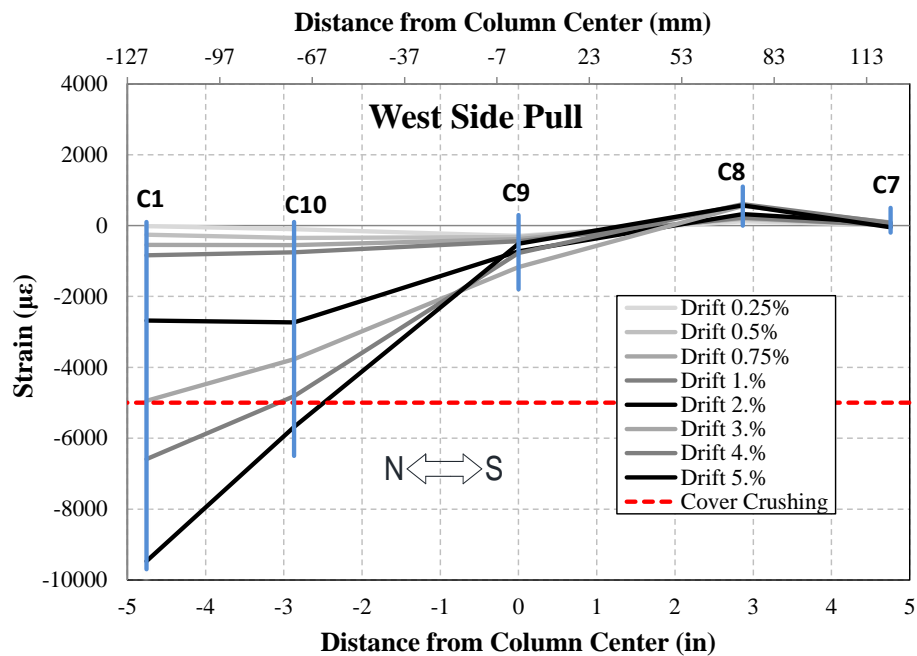
Figure 4.132. Measured Concrete Strain Profile for RPH-PC West Face During Pull Cycles

145

4.5.3.7 RPH-PC-R Strain Profiles

Figures 4.133-4.136 show the measured strain profiles for Bars B1, B2, B6, and B7 in RPH-PC-R. Strain at the middle two levels was recorded with new strain gauges since BRR were replaced between the two tests.

The strain profiles of the four bars for the repaired testing once again showed that the strain was concentrated within BRR (the center two levels of strain gauges). The maximum measured strain for the transverse reinforcement was 0.80% recorded at a hoop in the center of the neck section and was slightly higher the yield strain of 0.23% for the hoops.

Compressive strain profiles were also recorded for RPH-PC-R as shown in Fig. **4.137-4.140**. Compressive strains were concentrated outside of BRR in the footing and the precast column section while strains within BRR at the middle two strain gauge levels often remained positive during high drift ratios. Buckling of BRR once again may have played a role in any compressive strain discrepancies, depending on the direction of the buckling and placement of the strain gauges.
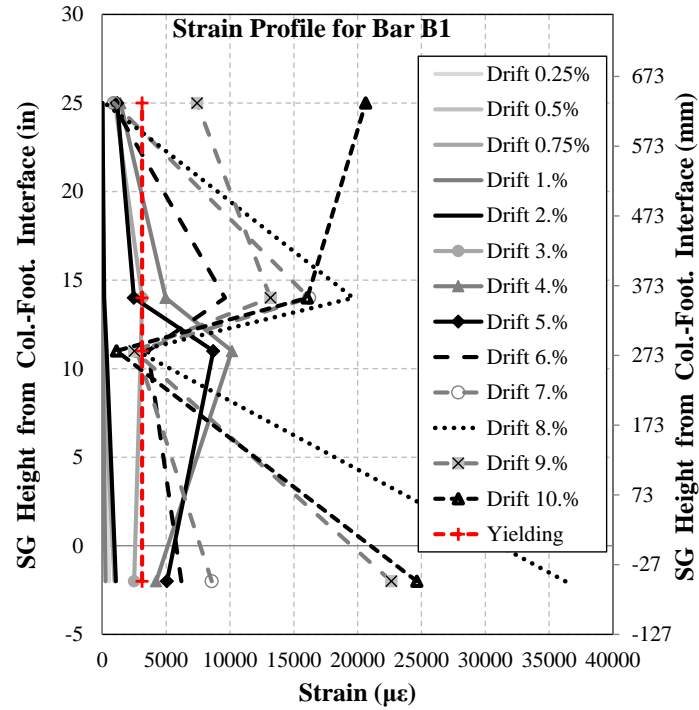
Figure 4.133. Measured Tensile Strain Profile for RPH-PC-R Column Bar B1
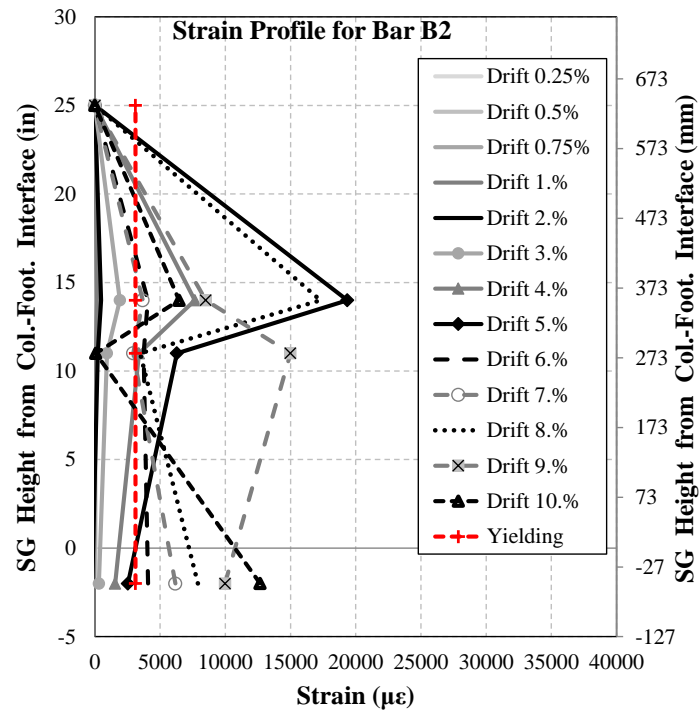
Figure 4.134. Measured Tensile Strain Profile for RPH-PC-R Column Bar B2

147
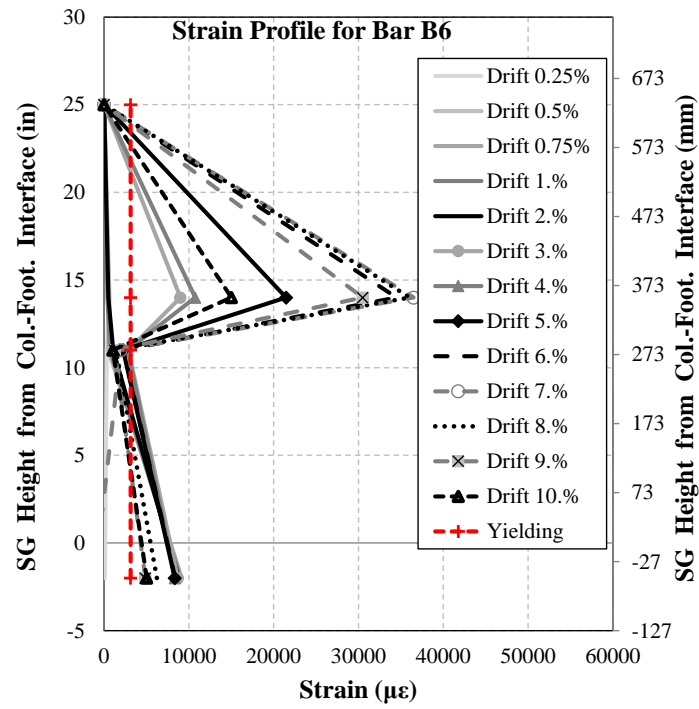
Figure 4.135. Measured Tensile Strain Profile for RPH-PC-R Column Bar B6
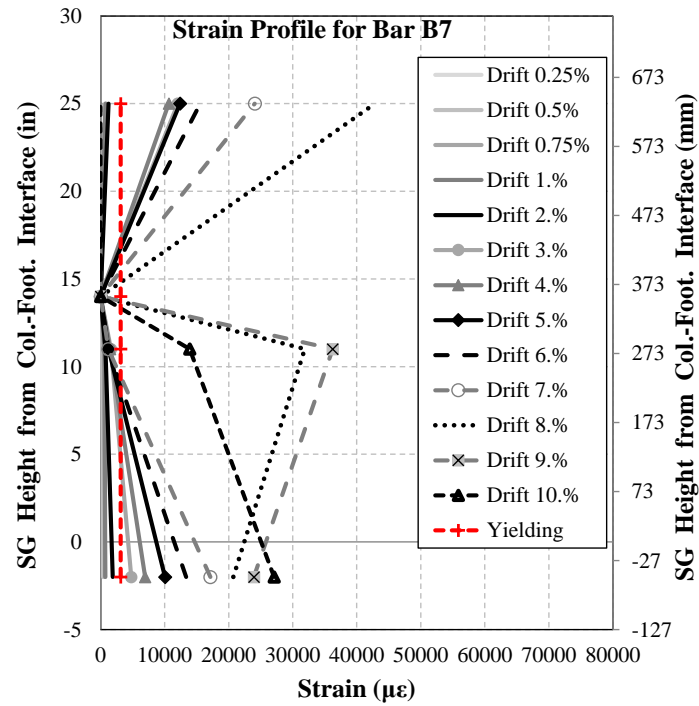
Figure 4.136. Measured Tensile Strain Profile for RPH-PC-R Column Bar B7
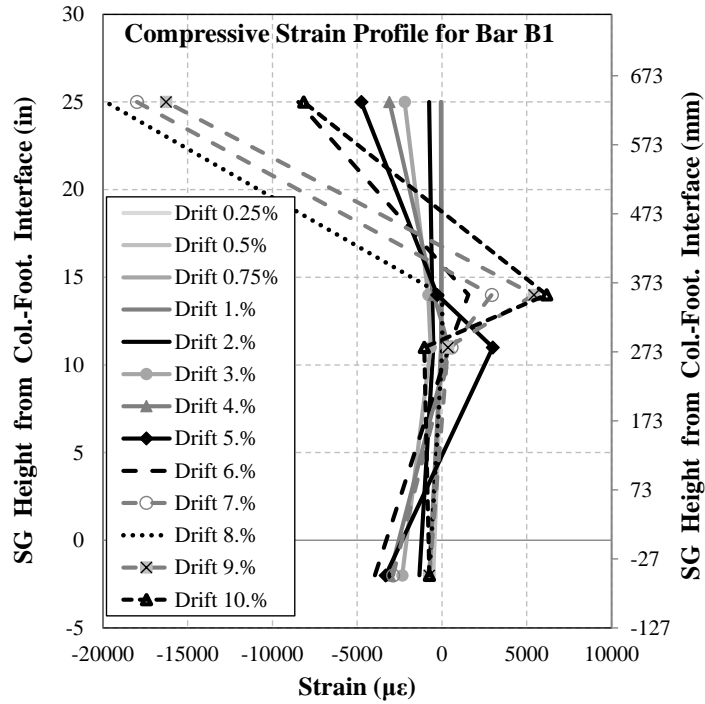
Figure 4.137. Measured Compressive Strain Profile for RPH-PC-R Column Bar B1
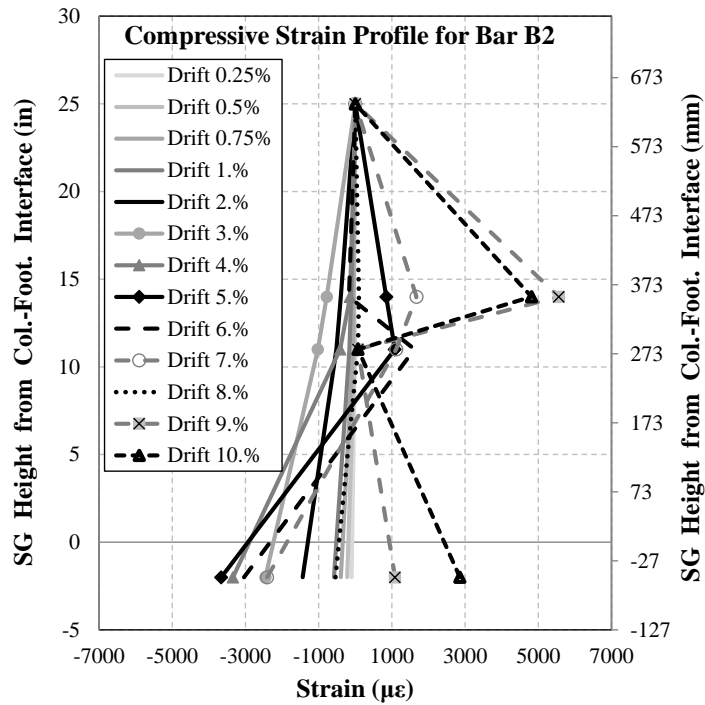
Figure 4.138. Measured Compressive Strain Profile for RPH-PC-R Column Bar B2

149
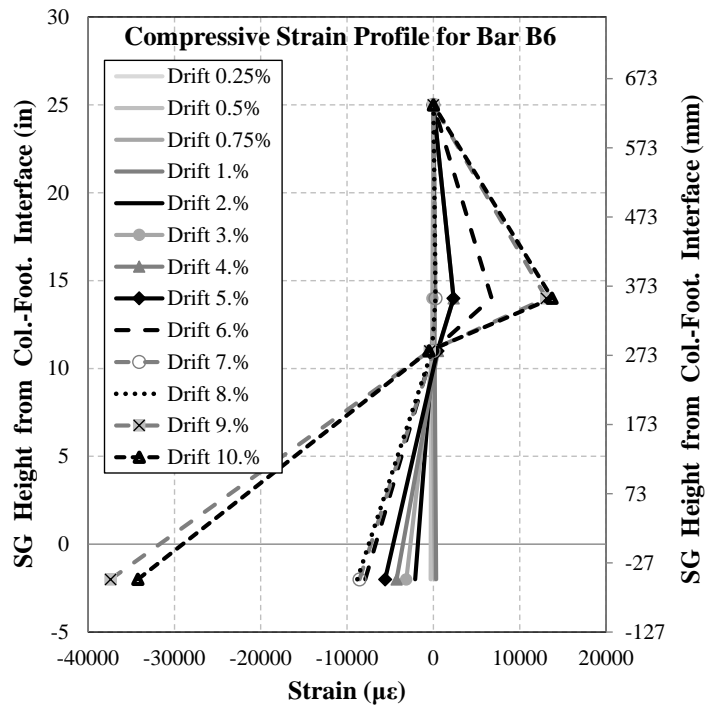
Figure 4.139. Measured Compressive Strain Profile for RPH-PC-R Column Bar B6
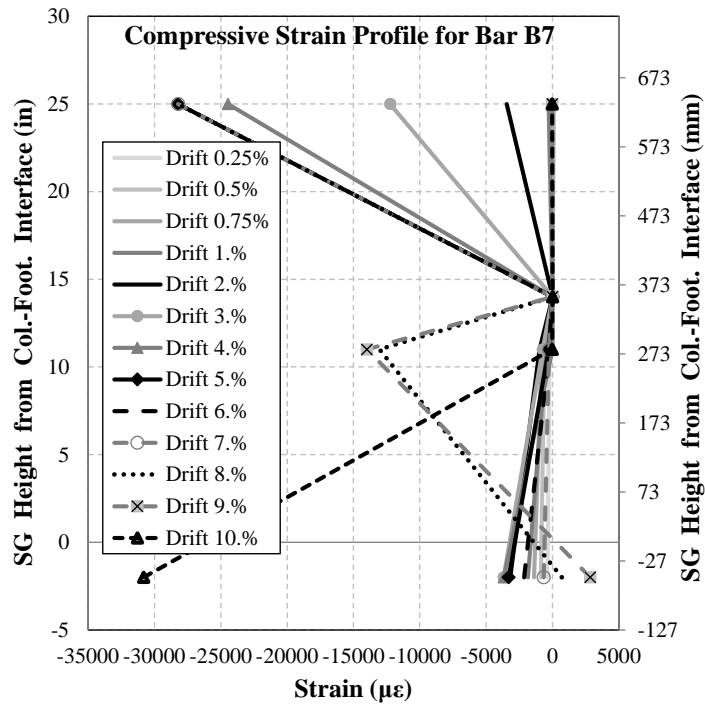
Figure 4.140. Measured Compressive Strain Profile for RPH-PC-R Column Bar B7

150

Neck bar strain gauge profiles for RPH-PC-R (**Fig. 4.141 - 4.144**) once again indicated that the neck longitudinal reinforcement remained linear elastic. All strains remained well below the yield point of the bars except for the center level in bar N8, which recorded strains above the yield point during the entirety of the test, validating the design of the neck section. This is the same strain gauge that recorded high strains during initial testing of RPH-PC, likely due to a malfunction and not actual yielding of the bar.

Figures 4.145 and **4.146** show the measured concrete compressive and tensile strain profiles for RPH-PC-R with positive values representing tensile strains and negative values representing compressive strains. Strains often remained positive at high drift ratios, likely due to the extensive spalling at the column face which left some of the strain gauges exposed. Only concrete strain gauge C2 experienced compressive strains above the strain capacity of the cover concrete.

Figures 4.147 to **4.149** show the strain profiles along the east and west faces of the column during both push and pull cycles. Strain gauges on the north side experienced tensile strains and gauges on the south experienced compressive strains during push cycles, while the opposite is true during pull cycles. All gauges recorded higher tensile strains during testing of RPH-PC-R than during testing of RPH-PC, while compressive strains were also lower, once again due to extensive spalling during the initial round of testing.
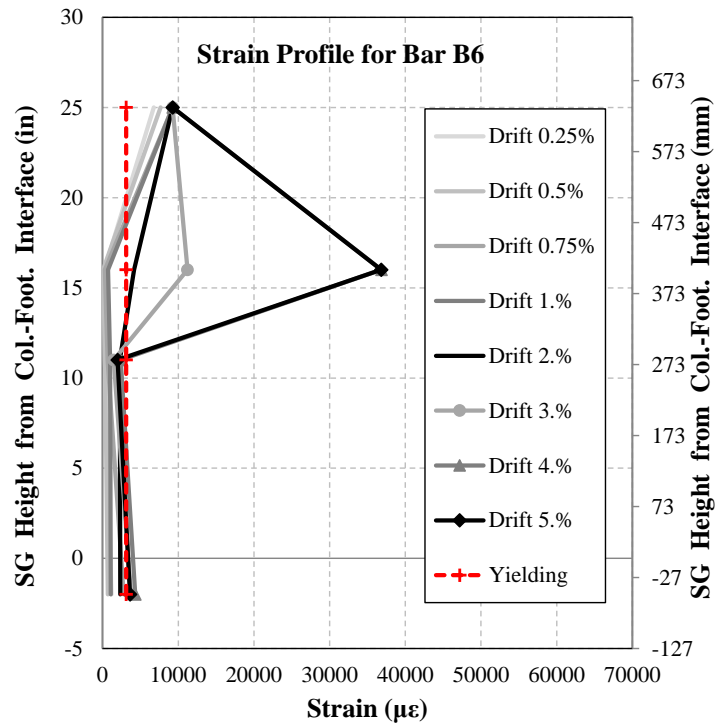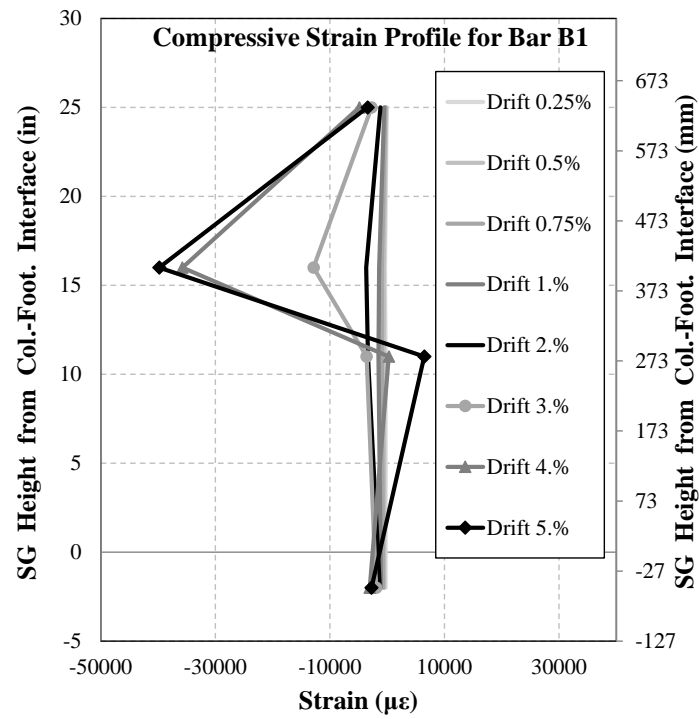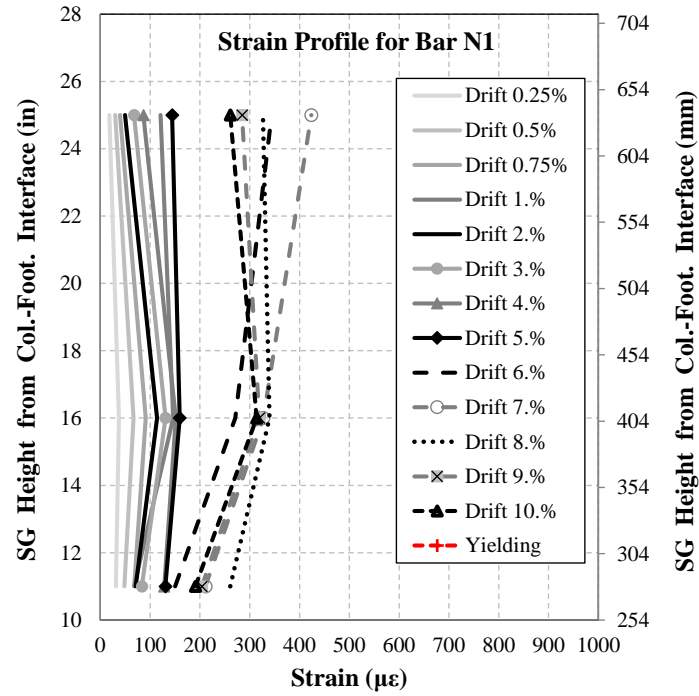
Figure 4.141. Measured Strain Profile for RPH-PC-R Column Neck Bar N1
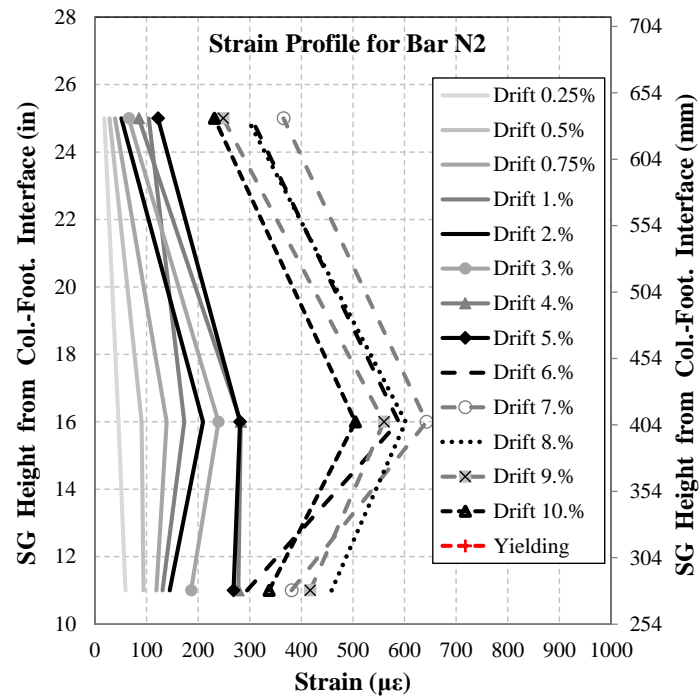
Figure 4.142. Measured Strain Profile for RPH-PC-R Column Neck Bar N2
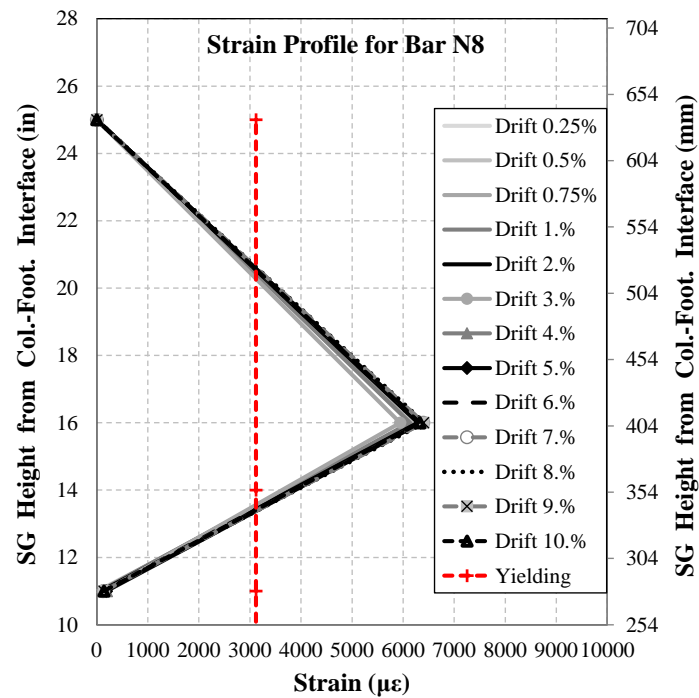
Figure 4.143. Measured Strain Profile for RPH-PC-R Column Neck Bar N8
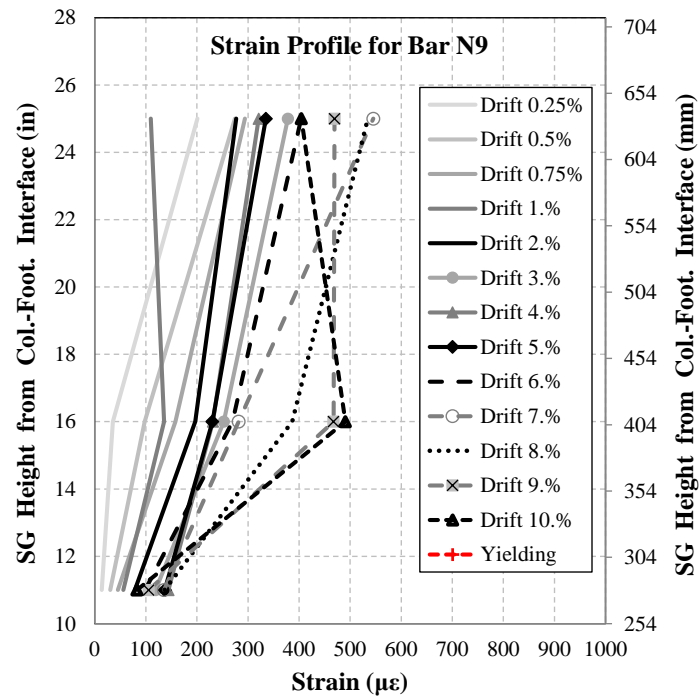
Figure 4.144. Measured Strain Profile for RPH-PC-R Column Neck Bar N9
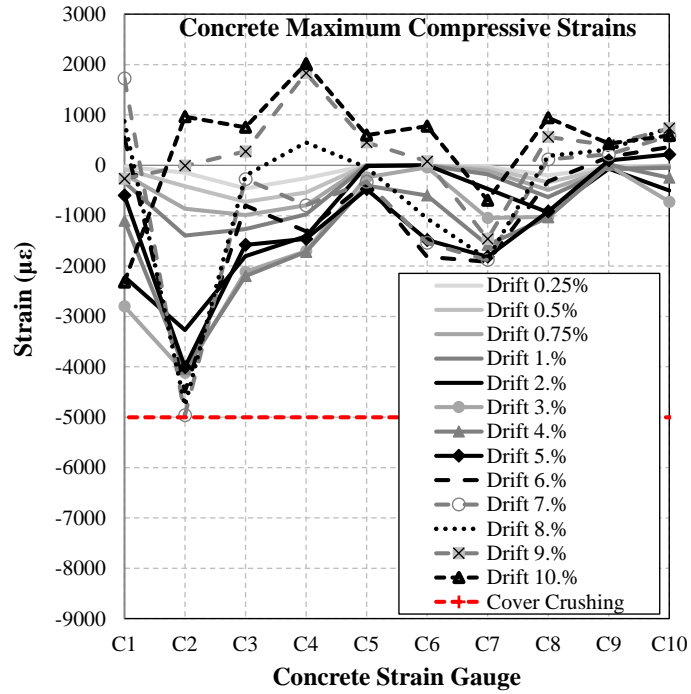
Figure 4.145. Measured Concrete Compressive Strain Profile for RPH-PC-R
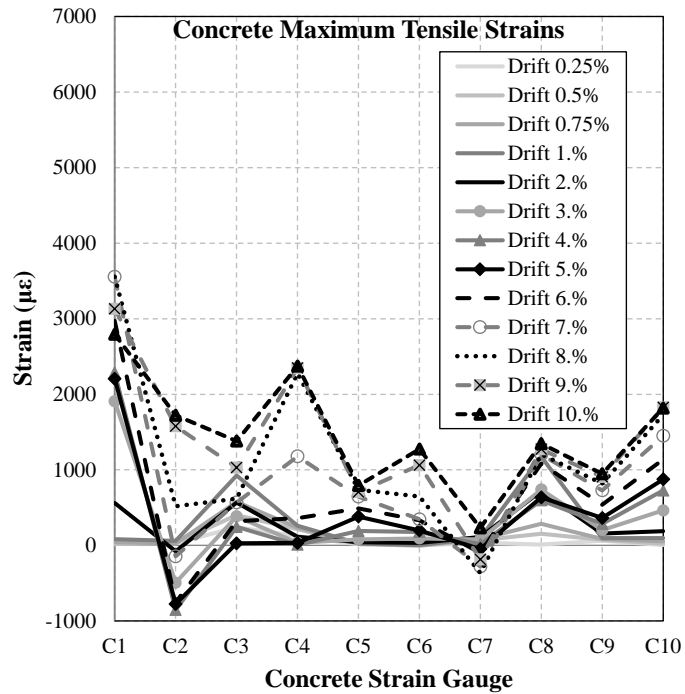
Figure 4.146. Measured Concrete Tensile Strain Profile for RPH-PC-R

154

a) East Face

b) West Face
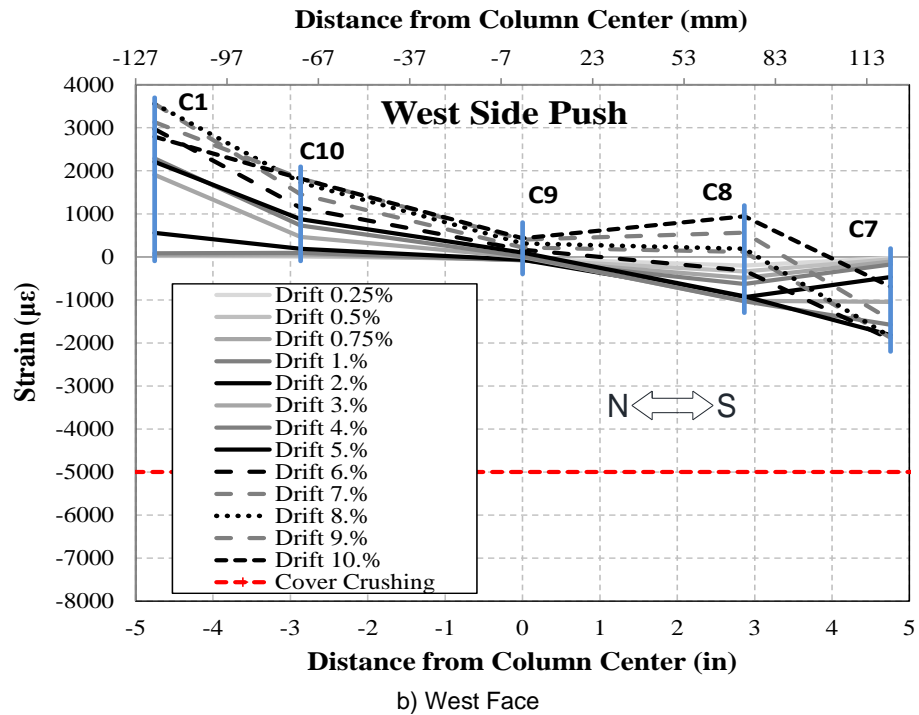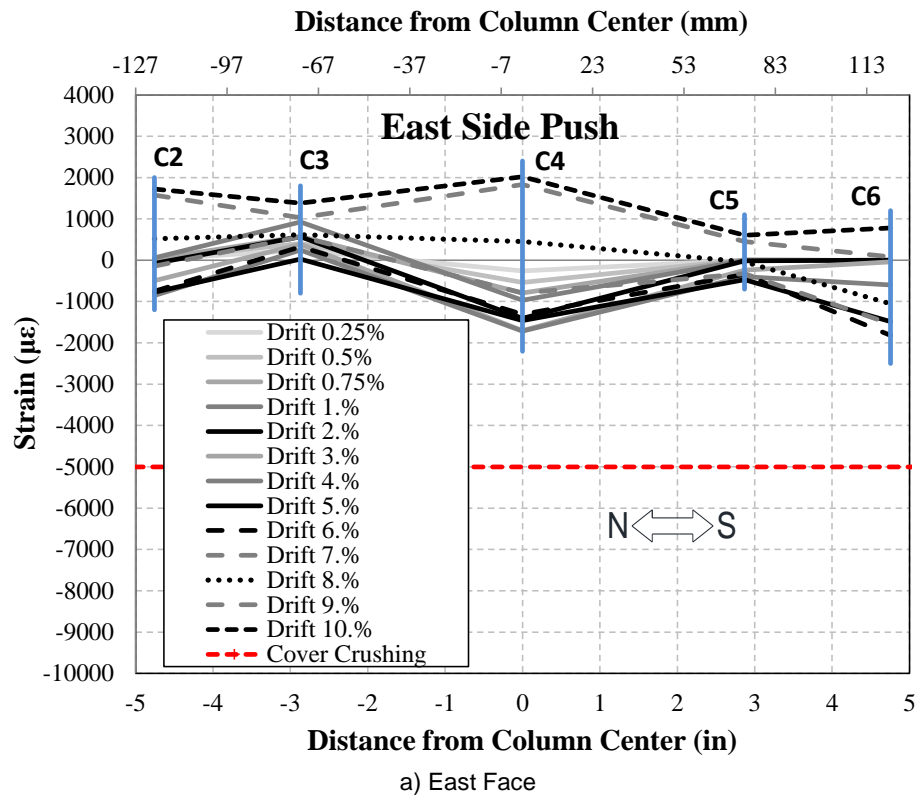
Figure 4.147. Measured Concrete Strain Profile for RPH-PC-R During Push Cycles

155

a) East Face

b) West Face
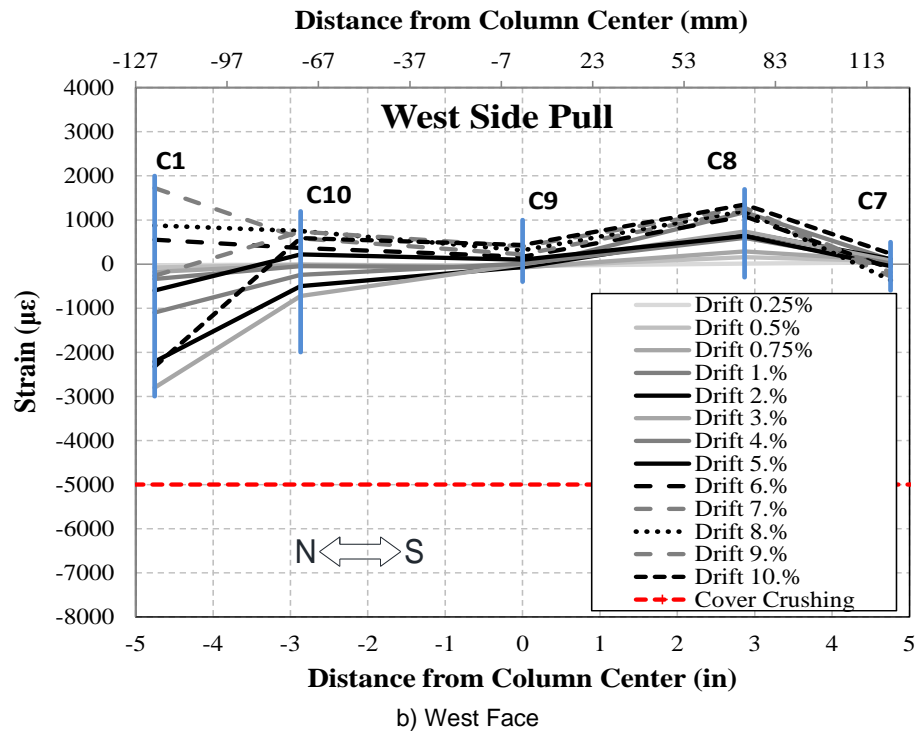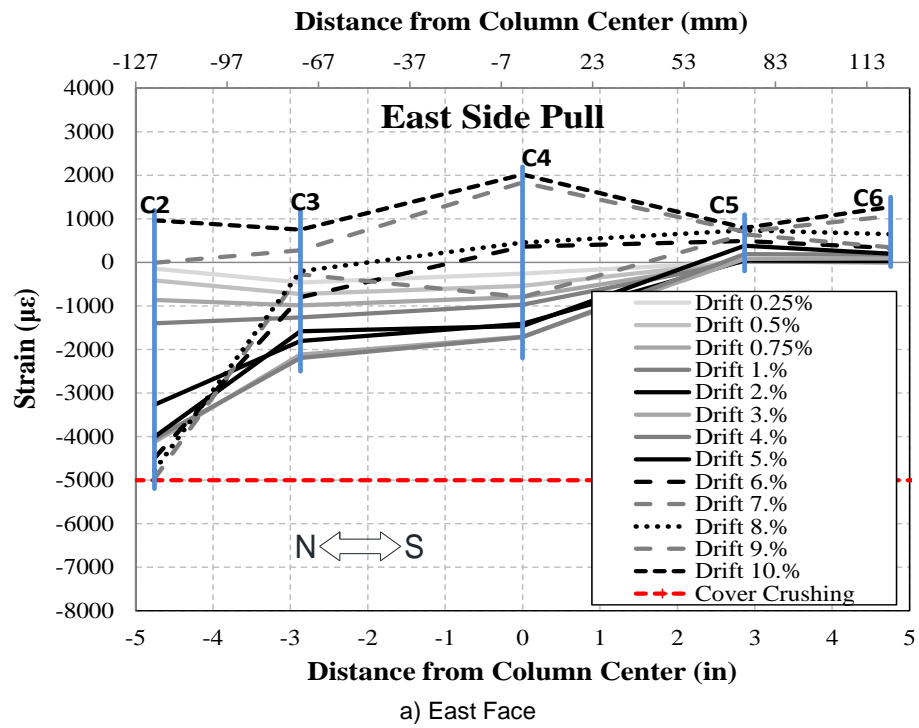
Figure 4.148. Measured Concrete Strain Profile for RPH-PC-R During Pull Cycles

4.5.3.8 RPH-PC Measured Rotation and Curvature

Rotations and curvatures were recorded and determined in the same manner as CIP. **Figure 4.149** shows the measured curvature profile for RPH-PC from drift ratios of 0.25% to 4.0%. The highest curvature was concentrated at the base of the column due to the rocking allowed by the pipe-pin connection. Curvatures at the second level were slightly higher than the first.
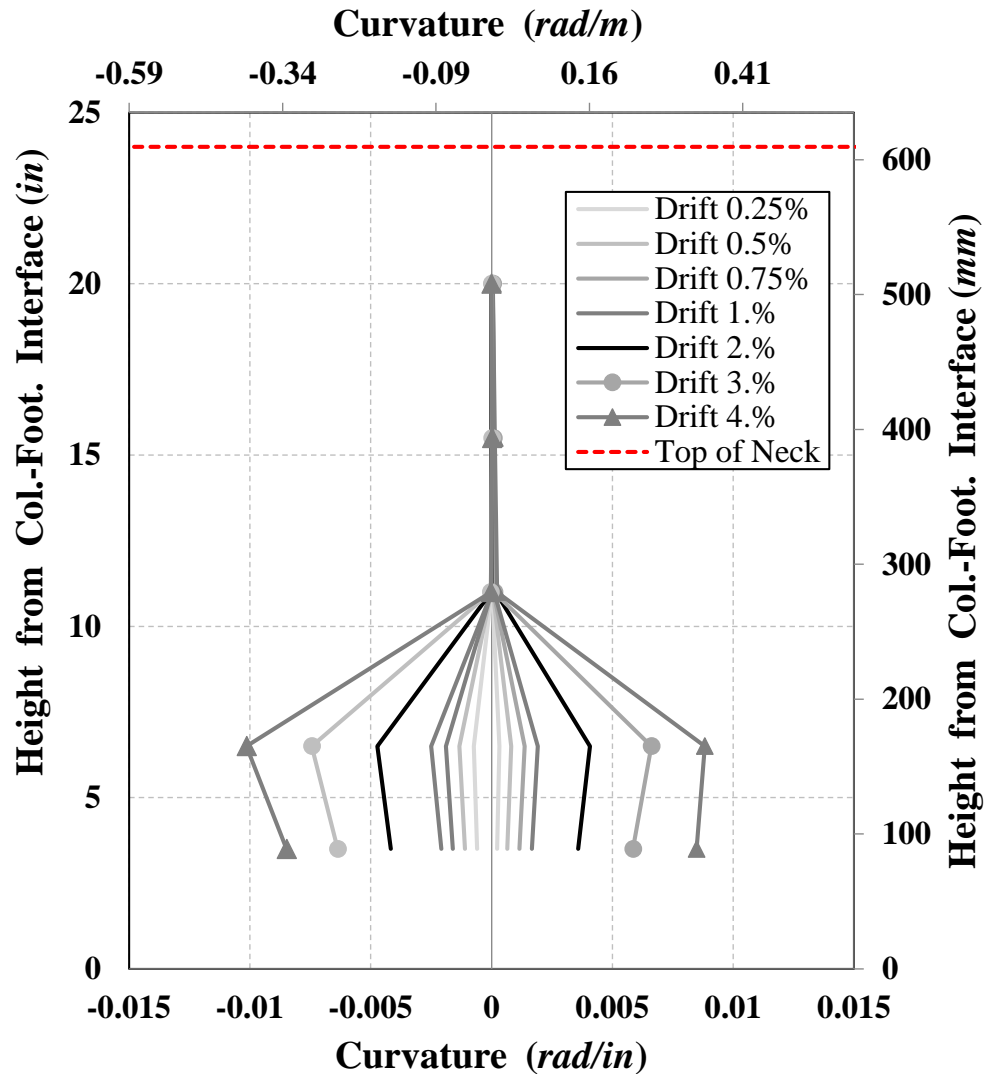
Figure 4.149. Measured Curvature Profile for RPH-PC Column

4.5.3.9 RPH-PC-R Measured Rotation and Curvature

Figure 4.150 shows the measured curvature profile for the RPH-PC-R column from drift ratios of 0.25% to 4.0%. The highest curvature was concentrated at the base of the column while the first level showed higher strains. Overall, RPH-PC and RPH-PC-R showed a similar curvature profile.
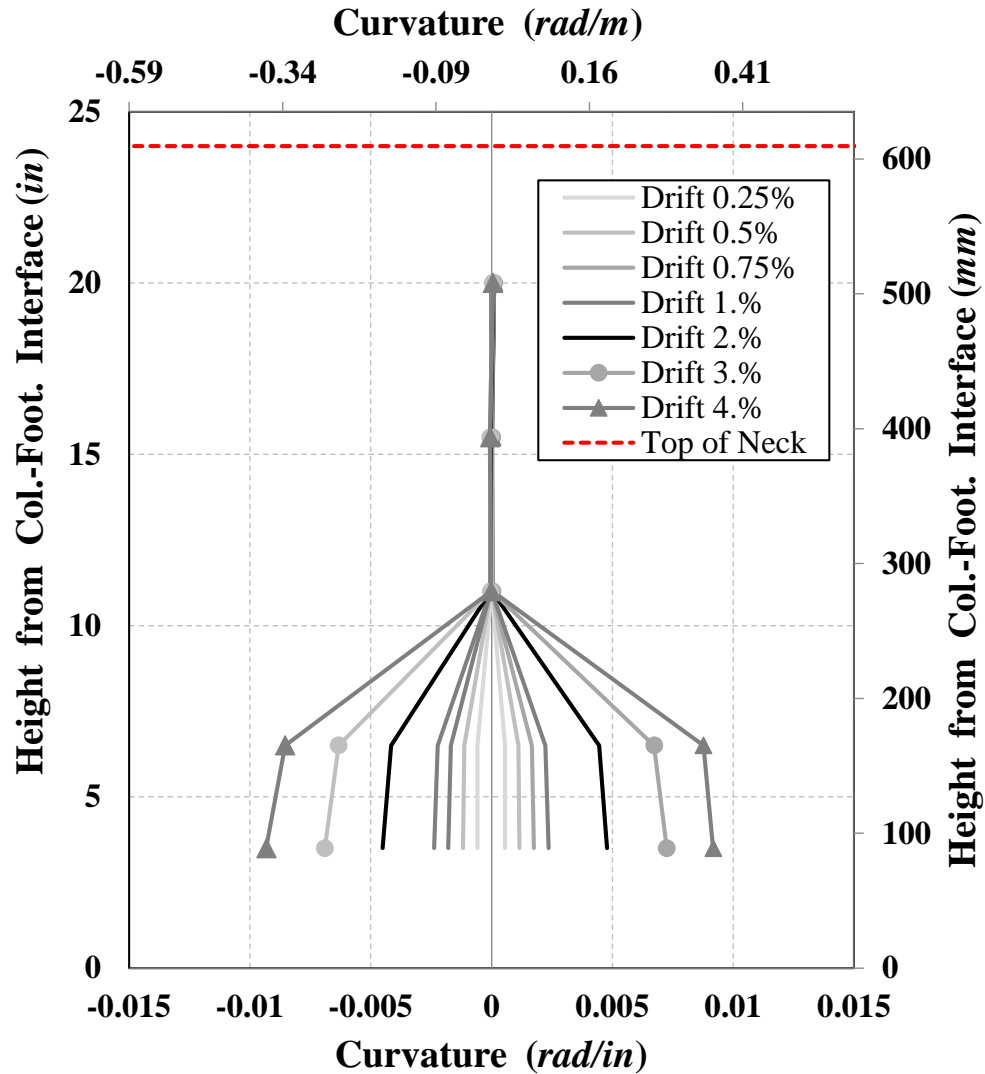
Figure 4.150. Measured Curvature Profile for RPH-PC-R Column

4.5.3.10 RHP-PC Energy Dissipation

The cumulative energy dissipation for RPH-PC is shown in **Fig. 4.152** for drift ratios of 0.25% until 5.0% when the test was stopped. The dissipated energy is negligible until 1.0% drift ratio. After bars yielded during the 2.0% drift runs, the width of the hysteretic loops slowly began to increase, resulting in a higher dissipated energy. RPH-PC dissipated a total of 1,024 kip-in. (116 kN-m) energy at 5.0% drift ratio.
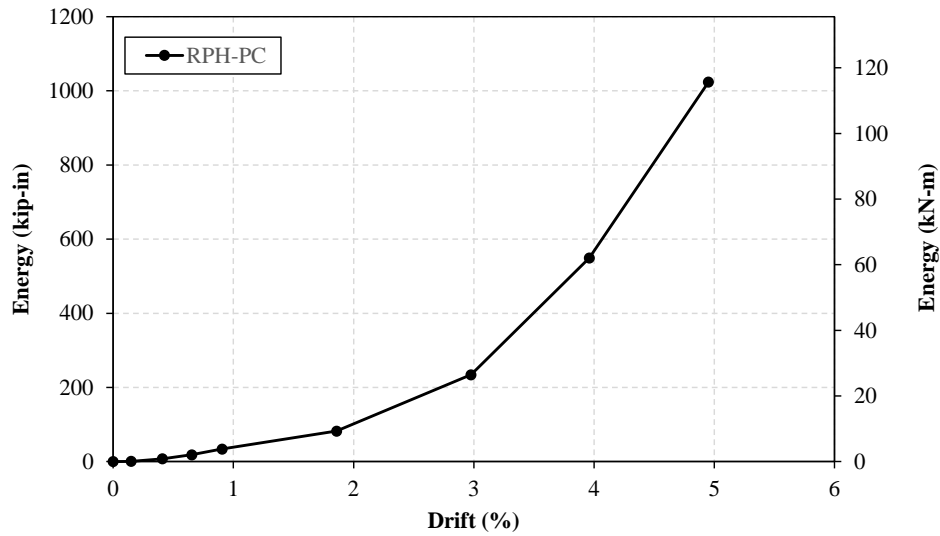
Figure 4.151. Measured Energy Dissipation for RPH-PC Column

4.5.3.11 RPH-PC-R Energy Dissipation

The cumulative energy dissipation for the RPH-PC-R column is shown in **Fig. 4.153**. The dissipated energy is low up to 3.0% drift ratio where BRR yielded. RPH-PC-R dissipated a total of 4,171 kip-in. (471 kN-m) energy at 10.0% drift ratio.
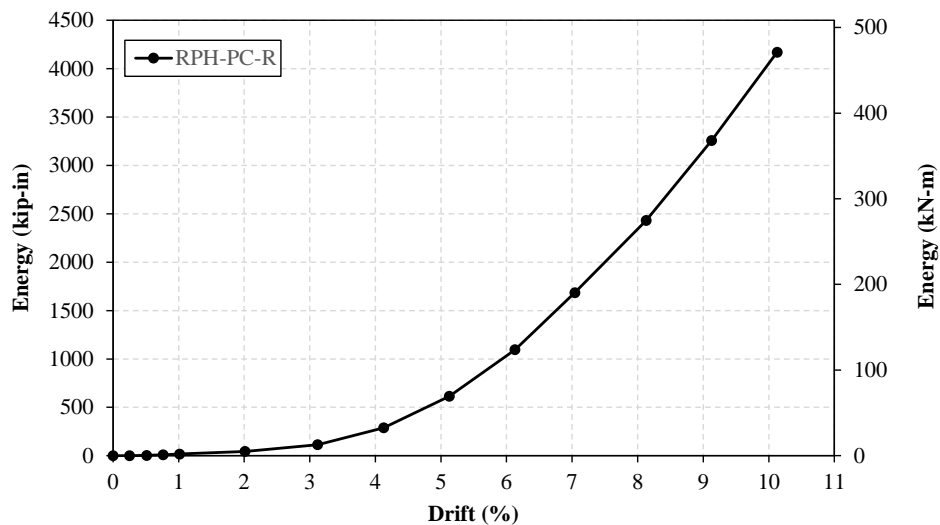
Figure 4.152. Measured Energy Dissipation for RPH-PC-R Column

159

4.5.4 RPH-PF Column Results

The following section discusses the performance of the RPH-PF column. RPH-PF was tested twice in the same day. Tendons were utilized as the external fuses in lieu of BRR. To differentiate between the two tests, the original specimen is named "RPH-PF" while the repaired column is named "RPH-PF-R". Yellow tapes were placed on the plastic tubing to identify RPH-PF while an additional piece of red tape was added for the RPH-PF-R test. Note that the transparent plastic tube was used to prevent any damage if tendons rupture during testing or specimen inspections.

4.5.4.1 RPH-PF Observed Damage

Testing of RPH-PF followed the same testing procedure utilized in the previous columns up to a drift ratio of 4%, at which the test was stopped to repair this column. While RPH-PC was tested up to 5%, the testing of RPH-PF was stopped at a lower drift cycle as a precaution to avoid concrete damages seen in RPH-PC. Nevertheless, UHPC was used in RPH-PF and the damage of this column, as will be discussed herein, was insignificantly. A summary of the column observed damage is presented in **Table 4.8** and **Fig. 4.153** to **4.165** show the observed damage of RPH-PF at each drift cycle. Only one minor flexural crack was observed throughout the first sixteen runs and was likely attributed to erection since it was noticed after the first cycle at 0.25% drift and was above the neck section (**Fig. 4.153**). The RPH-PF column, like RPH-PC, was designed to rock at the base, thus uplift due to this rocking began at 0.75% drift (**Fig. 4.157**). Some minor vertical compression cracks were marked during the 2.0% drift cycles as well as a minor flexural crack originating at the PVC used to house the threaded rods for the steel socket (cup) (**Fig. 4.161**). The uplift due to the column rocking was originally observed between the steel plate and footing but some separation between the steel plate and column was also seen during the pull of 2.0% drift (**Fig. 4.161**). Minor spalling occurred at the column base at 3.0% drift (**Fig. 4.163**). The gap between the steel plate and column continued to increase (**Fig. 4.165**) until rupture of one of the steel shear studs (of the steel base plate, four studs embedded in UHPC) heard at 4.0% drift, allowing the column and plate to fully separate. No yielding of the tendon fuses occurred during this testing; however, slight tendon buckling was seen at the beginning of higher drift ratios (**Fig. 4.165**). Note buckling of tendons was desired as a tension-only member. As the column was pushed or pulled past the vertical position, buckling of the extreme tendons could be seen before a minor popping noise as the wedges within the couplers released and allowed the tendons to straighten. During some drift ratios, the wedges did not slip resulting in the buckling of the tendons.

Table 4.8. Summary of Damage in RPH-PC

Drift Ratio, %	Observed Damage
+0.25	• One minor flexural crack above neck section, likely due to erection
-0.25	• No further damage
+0.50	• No further damage
-0.50	• No further damage
+0.75	• Rocking and uplift of plate begins to be noticeable
-0.75	• No further damage
+1.00	• No further damage
-1.00	• No further damage
+2.00	• Very short, horizontal crack near PVC for threaded rod • Short, inclined crack at column base
-2.00	• Some separation between steel plate and column noticeable • Short, vertical cracks at column base
+3.00	• Minor concrete spalling at column base
-3.00	• Minor concrete spalling at column base
+4.00	• Gap between column and plate increases • Gap between plate and footing increases
-4.00	• Loud pop heard, steel baseplate at the column end separated from the column

Note: Positive drifts were based on displacements away from the reaction blocks (north to south)
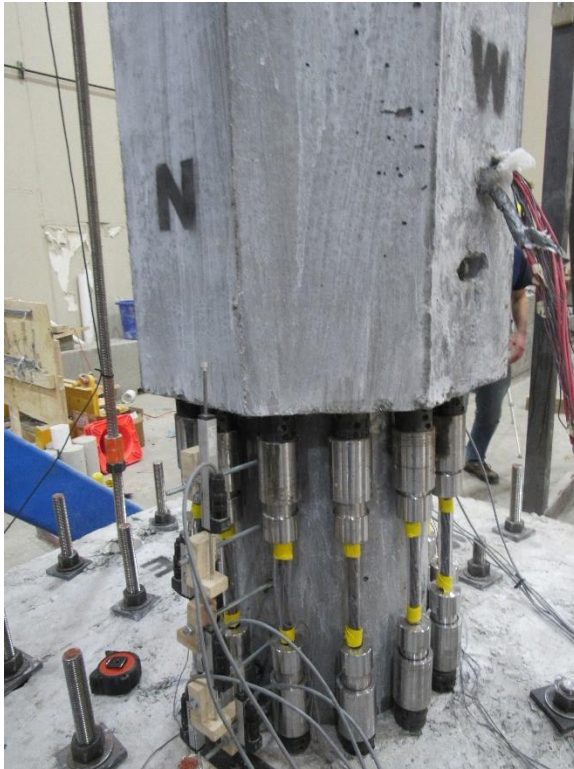
a) North-West Side

b) South-East Side

Figure 4.153. RPH-PF Column Plastic Hinge Damage, Second Push of 0.25% Drift Cycle

a) North-West Side

b) South-East Side

Figure 4.154. RPH-PF Column Plastic Hinge Damage, Second Pull of 0.25% Drift Cycle

a) North-West Side   b) South-East Side
Figure 4.155. RPH-PF Column Plastic Hinge Damage, Second Push of 0.50% Drift Cycle

a) North-West Side   b) South-East Side
Figure 4.156. RPH-PF Column Plastic Hinge Damage, Second Pull of 0.50% Drift Cycle

a) North-West Side   b) South-East Side

Figure 4.157. RPH-PF Column Plastic Hinge Damage, Second Push of 0.75% Drift Cycle

a) North-West Side   b) South-East Side

Figure 4.158. RPH-PF Column Plastic Hinge Damage, Second Pull of 0.75% Drift Cycle

a) North-West Side   b) South-East Side

Figure 4.159. RPH-PF Column Plastic Hinge Damage, Second Push of 1.0% Drift Cycle

a) North-West Side   b) South-East Side

Figure 4.160. RPH-PF Column Plastic Hinge Damage, Second Pull of 1.0% Drift Cycle

a) North-West Side

b) South-East Side

Figure 4.161. RPH-PF Column Plastic Hinge Damage, Second Push of 2.0% Drift Cycle

a) North-West Side

b) South-East Side

Figure 4.162. RPH-PF Column Plastic Hinge Damage, Second Pull of 2.0% Drift Cycle

a) North-West Side

b) South-East Side

Figure 4.163. RPH-PF Column Plastic Hinge Damage, Second Push of 3.0% Drift Cycle

a) North-West Side

b) South-East Side

Figure 4.164. RPH-PF Column Plastic Hinge Damage, Second Pull of 3.0% Drift Cycle

a) North-West Side – At Push

b) South-East Side – At Push

c) North-West Side – At Pull

d) South-East Side – At Pull

Figure 4.165. RPH-PF Column Plastic Hinge Damage, Second 4.0% Drift Cycle

4.5.4.2 Repair of RPH-PF Column

Testing of the RPH-PF was ended after two cycles of 4% drift ratio. Subsequently, the clamping collars and tendons were removed. No buckling of the main longitudinal reinforcement extending out of the octagonal cross section and footing (column/footing dowels) was observed (**Fig. 4.166**). This was a performance enhancement compared with RPH-PC in which column/footing dowels were bend and had to be straightened by pushing the column back and forth. In RPH-PF, the repair was very easy and relatively quick since column had insignificant residual displacements after 4% drift cycles and tendons were cut using a hand grinder and replaced using pipe wrenches. The repair was performed in less than 2 hours with a team of 3 individuals including installing new strain gauges on the tendon fuses and clamping collars.

During the repair, it was observed in a few couplers that wedges had set tightly against the tendons and the couplers could not be removed by hand. To facilitate the replacement, the tendons were cut, and the male couplers were removed then screwed into a spare female coupler to prevent damage to the threads. It was then possible to strike the exposed end of the cut tendon against the concrete strong floor to unset the wedges and remove the pieces of tendon.

Prior to tightening the new tendons, pressurized air was used to remove any dust inside the couplers that may make screwing them together difficult. After the tendon replacement, concrete dust was vacuumed from the column and footing. New tendons in the same length as those utilized in the original test were inserted using the same wedges and couplers. In summary, the tendon replacement was relatively simple and quick, and no other column components were replaced/repaired.
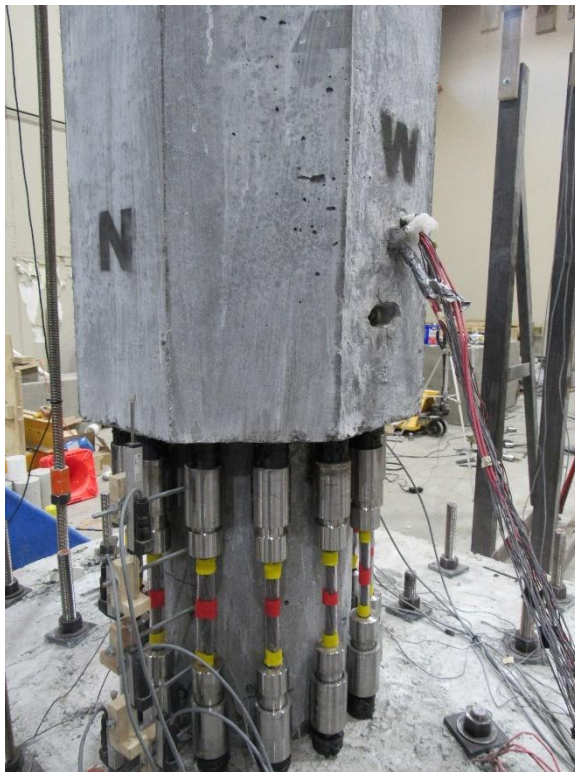
a) North-West Side   b) South-East Side
Figure 4.166. RPH-PF-R Column Plastic Hinge Damage before Retesting

4.5.4.3 RPH-PF-R Observed Damage

The testing of RPH-PF-R followed the same cyclic loading protocol as the original test and was continued to failure. **Table 4.9** presents a summary of the observed damage of RPH-PF-R and **Fig. 4.167-4.190** show the observed damage of RPH-PF-R. New cracks were marked in red. No additional damage occurred in RPH-PC-R up to a drift ratio of 1.0% when a small, inclined crack was found. At 2% drift, the gap between the column and the steel baseplate was noted (**Fig. 4.175**) as the plate and column had separated at the end of the last test. Some tendons buckled at 4.0% drift with some minor cracking and spalling (**Fig. 4.179**). At 5.0% drift, extreme tendons on both the North and South faces yielded (**Fig. 4.181**). The gap between the column and steel baseplate continued to widen while minor spalling occurred at the column base on the opposite side during the cycles of 6.0% and 7.0%. At the first push to 8.0%, the tendon corresponding to bar No. 3 ruptured (**Fig. 4.187-4.188**). The test was stopped at a drift ratio of 9.0% after the tendons corresponding to bars No. 8 and 10 ruptured during the first pull cycle with a significant drop in the lateral force resistance.

After testing, the tendon fuses were removed, and the column was disassembled. Very minor damage to the steel pipe and steel cup was observed; however, it was not possible to unscrew the threaded rods in the North-South sides of the steel cup, possibly due to thread damage during the testing. It was observed that only one of the steel shear studs on the steel plate had sheared off, and the other three pulled out from the UHPC. No significant damage to the column itself was noted and it was determined that the repair of the base of the column, which experienced pullout of the shear studs, could easily be performed with grout. Thus, the RPH-PF column was saved for future repair and testing.

Table 4.9. Summary of Damage in RPH-PF-R

Drift Ratio, %	Observed Damage
Beginning of Test	• Minor cracks and spalling at column base • Plate and column are separated
+0.25	• No further damage
-0.25	• No further damage
+0.50	• No further damage
-0.50	• No further damage
+0.75	• No further damage
-0.75	• No further damage
+1.00	• Small, inclined crack above neck section on North face
-1.00	• No further damage
+2.00	• Gap between column and steel plate is noticeable
-2.00	• Gap between column and steel plate is noticeable, still slight gap between plate and footing
+3.00	• No further damage
-3.00	• No further damage
+4.00	• Tendon on South side begins to buckle, but wedge pops out and allows tendon to straighten
-4.00	• Inclined flexural crack above neck section on South face • Further vertical cracks and minor spalling at column base
+5.00	• Yielding of tendon on North side
-5.00	• Yielding of tendon on South side
+6.00	• Gap between column and plate exceeds 0.5 in. (13 mm)
-6.00	• Gap between column and plate exceeds 0.5 in. (13 mm) • Inclined flexural cracks in neck section
+7.00	• Further spalling above neck region and at column base on South face
-7.00	• Tendon on North side buckles before wedge pops
+8.00	• Tendon on North side ruptures • Further minor spalling at column base
-8.00	• Gap between column and plate reaches 1 in. (25 mm) • Ruptured tendon buckles and strands separate
+9.00	• Further minor spalling
-9.00	• Two tendons on South side rupture

Note: Positive drifts were based on displacements away from the reaction blocks (North to South)
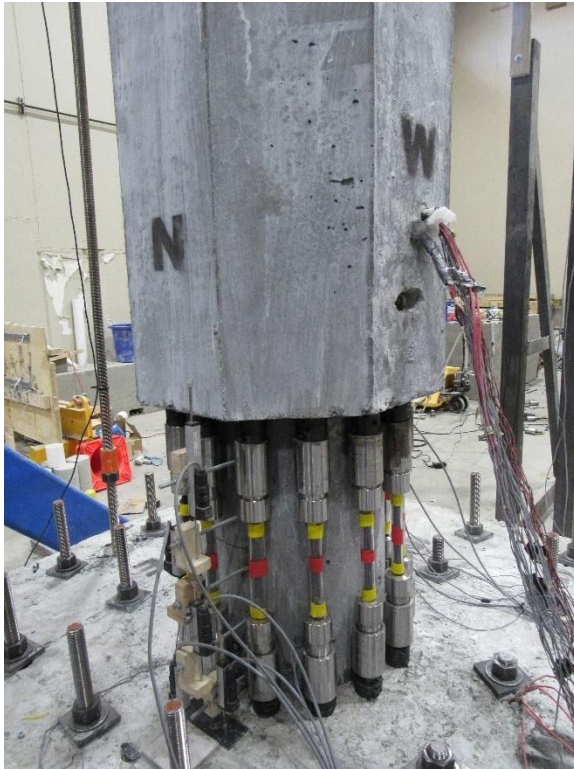
a) North-West Side   b) South-East Side

Figure 4.167. RPH-PF-R Column Plastic Hinge Damage, Second Push of 0.25% Drift Cycle
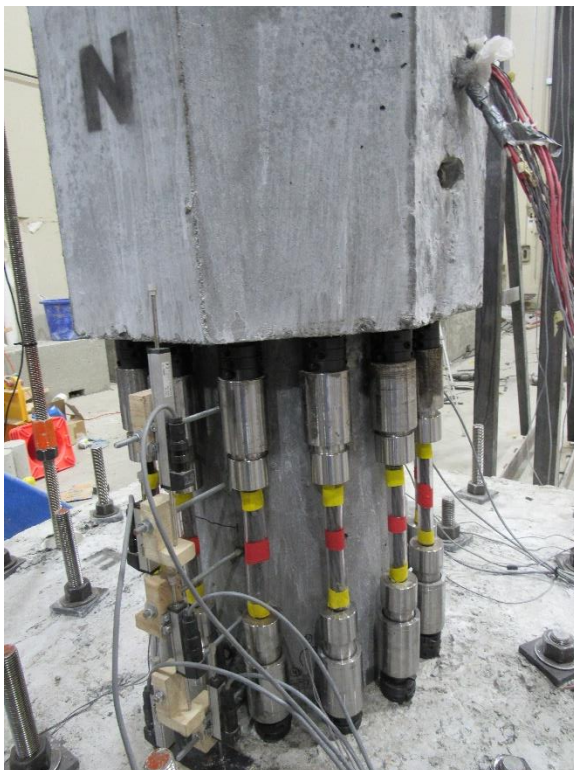
a) North-West Side   b) South-East Side

Figure 4.168. RPH-PF-R Column Plastic Hinge Damage, Second Pull of 0.25% Drift Cycle

a) North-West Side

b) South-East Side

Figure 4.169. RPH-PF-R Column Plastic Hinge Damage, Second Push of 0.50% Drift Cycle
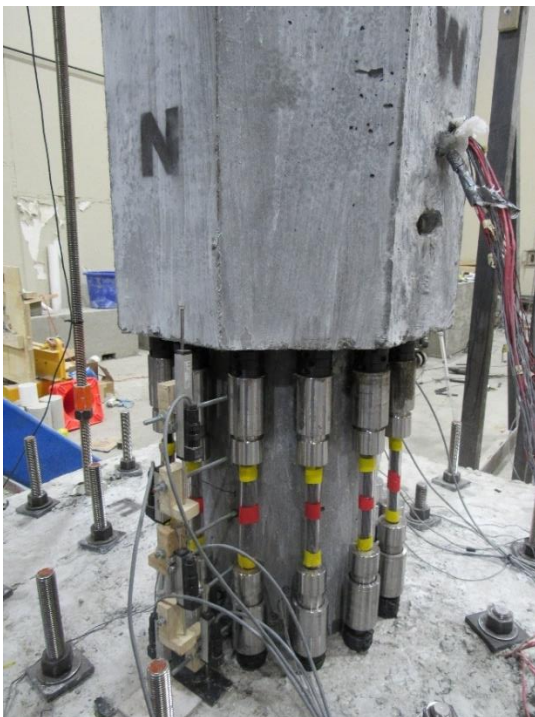
a) North-West Side

b) South-East Side

Figure 4.170. RPH-PF-R Column Plastic Hinge Damage, Second Pull of 0.50% Drift Cycle
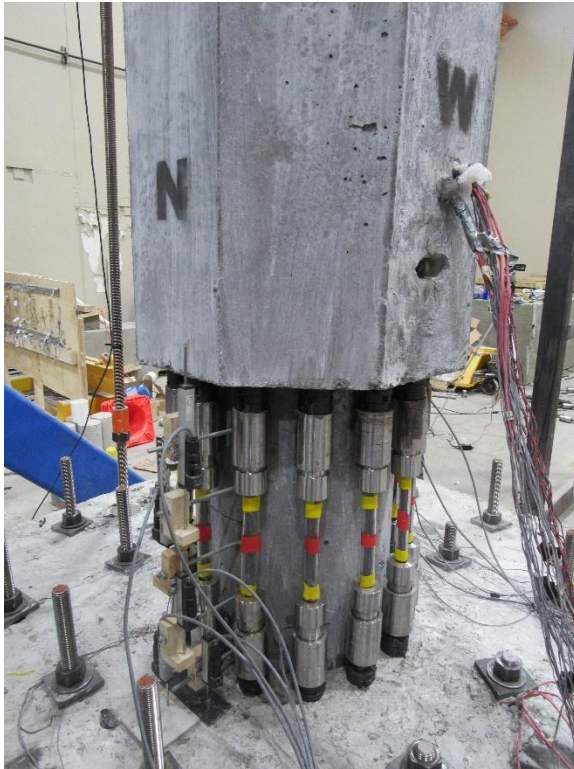
a) North-West Side b) South-East Side
Figure 4.171. RPH-PF-R Column Plastic Hinge Damage, Second Push of 0.75% Drift Cycle
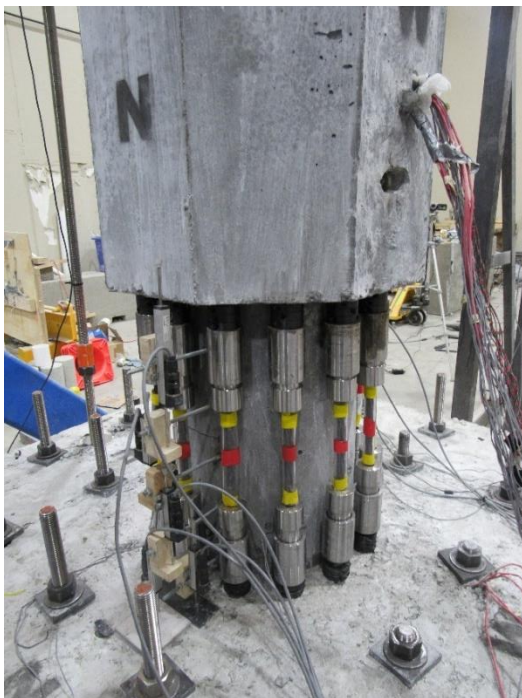
a) North-West Side b) South-East Side
Figure 4.172. RPH-PF-R Column Plastic Hinge Damage, Second Pull of 0.75% Drift Cycle

172
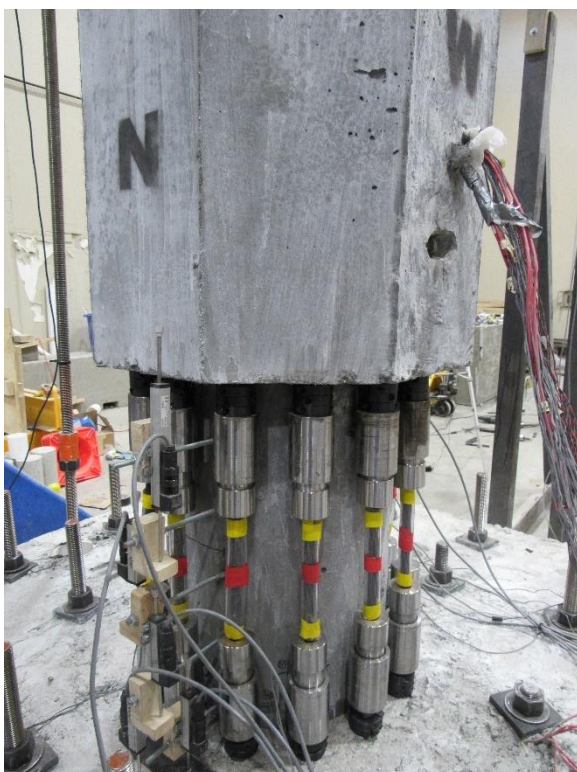
a) North-West Side

b) South-East Side

Figure 4.173. RPH-PF-R Column Plastic Hinge Damage, Second Push of 1.0% Drift Cycle
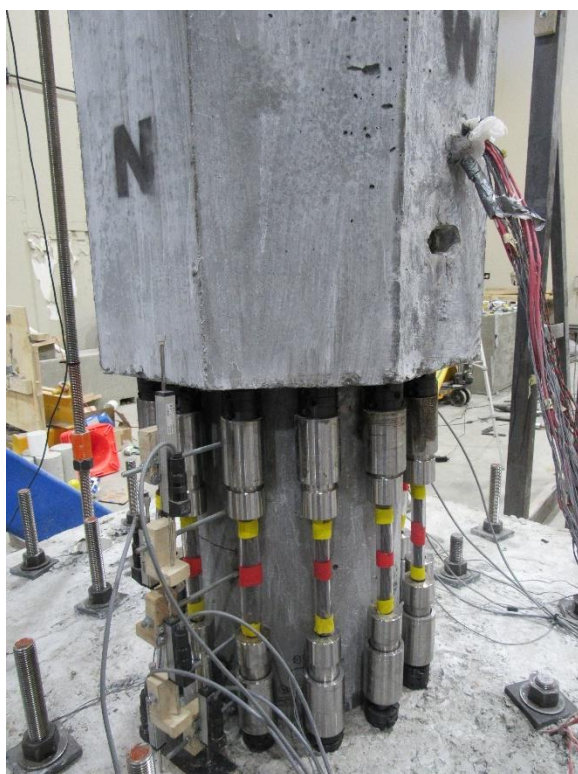
a) North-West Side

b) South-East Side

Figure 4.174. RPH-PF-R Column Plastic Hinge Damage, Second Pull of 1.0% Drift Cycle

173
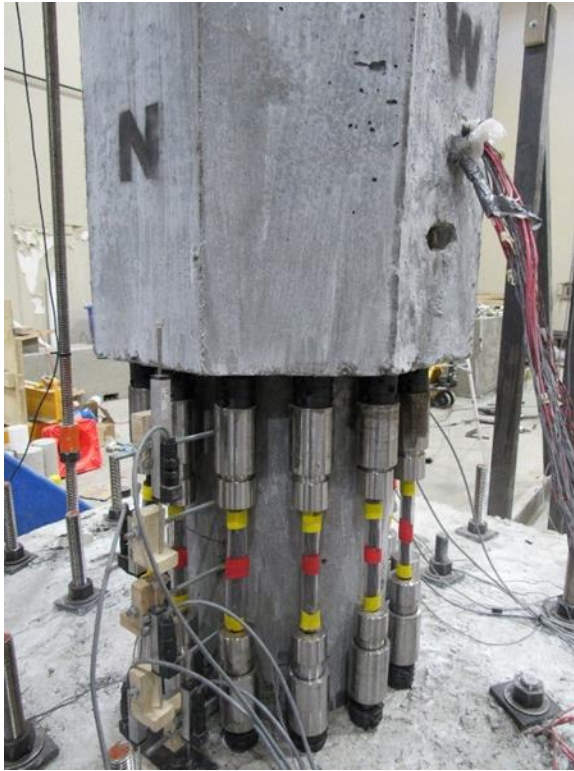
a) North-West Side

b) South-East Side

Figure 4.175. RPH-PF-R Column Plastic Hinge Damage, Second Push of 2.0% Drift Cycle
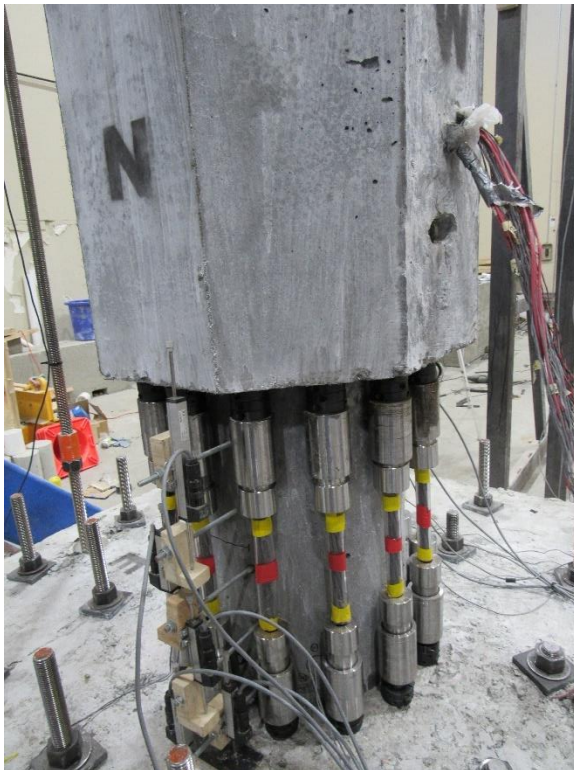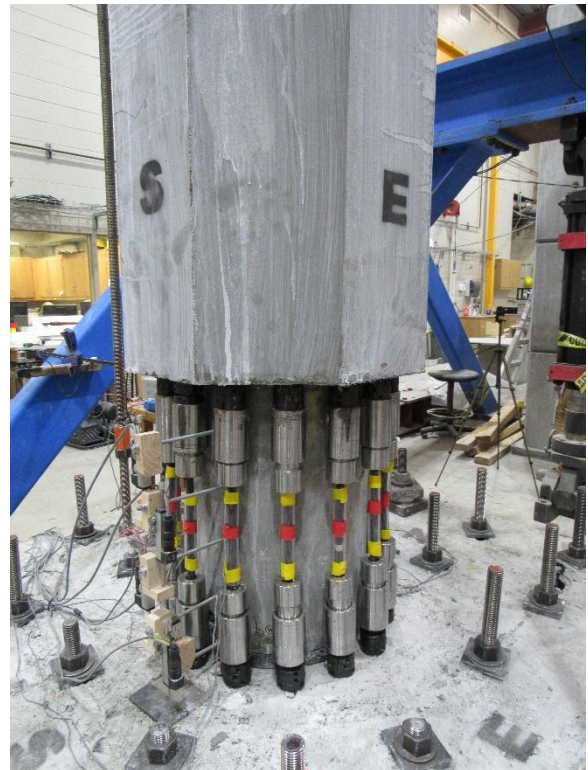
a) North-West Side

b) South-East Side

Figure 4.176. RPH-PF-R Column Plastic Hinge Damage, Second Pull of 2.0% Drift Cycle
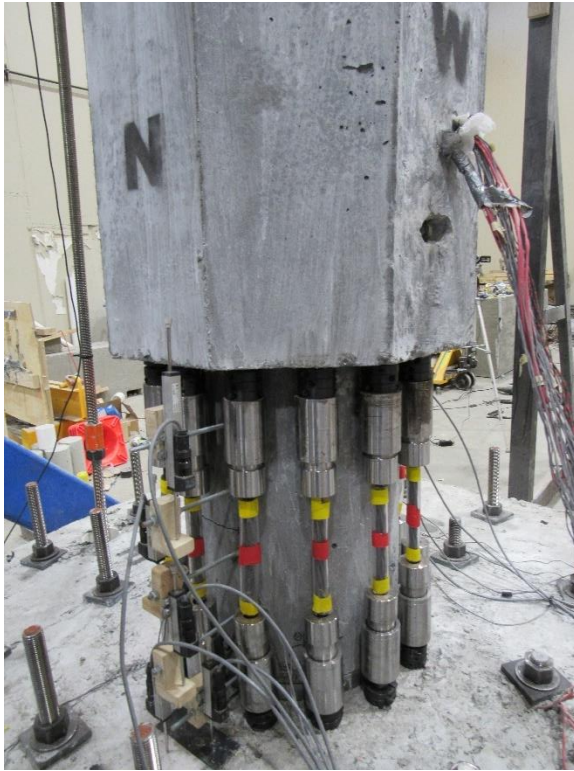
a) North-West Side
b) South-East Side
Figure 4.177. RPH-PF-R Column Plastic Hinge Damage, Second Push of 3.0% Drift Cycle
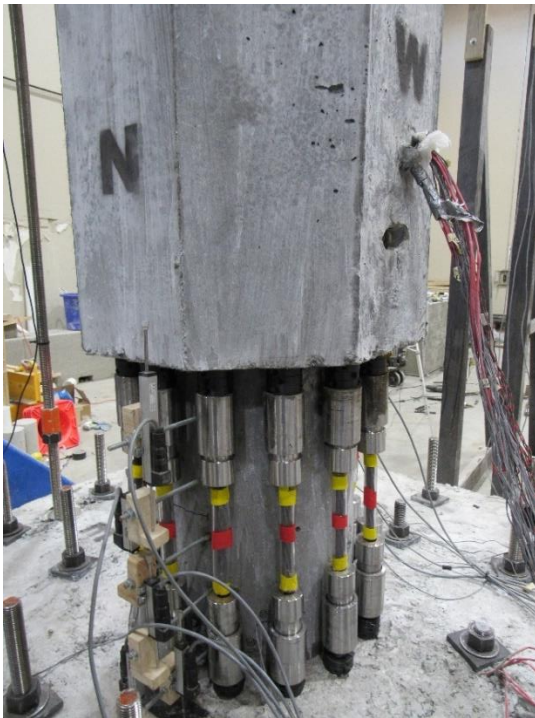
a) North-West Side
b) South-East Side
Figure 4.178. RPH-PF-R Column Plastic Hinge Damage, Second Pull of 3.0% Drift Cycle
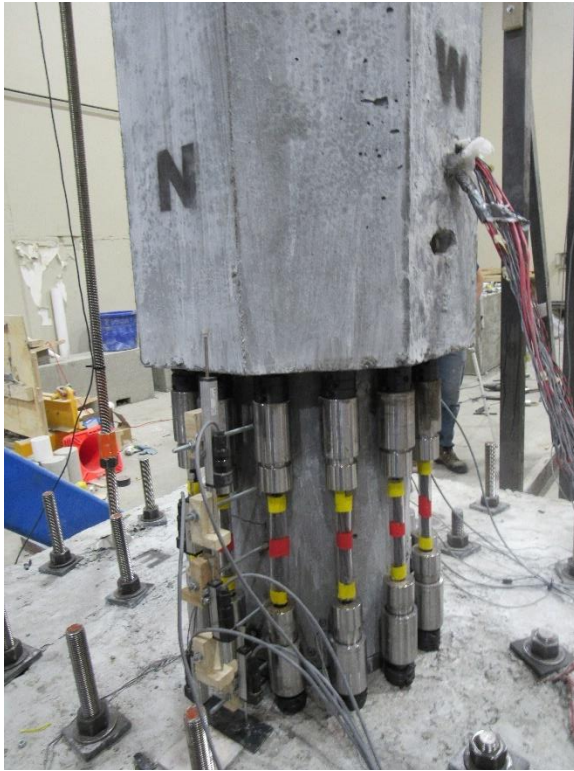
a) North-West Side   b) South-East Side
Figure 4.179. RPH-PF-R Column Plastic Hinge Damage, Second Push of 4.0% Drift Cycle
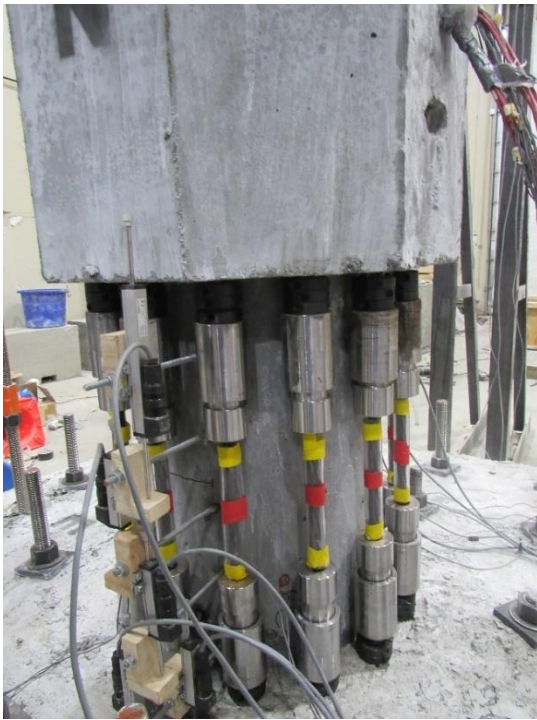
a) North-West Side   b) South-East Side
Figure 4.180. RPH-PF-R Column Plastic Hinge Damage, Second Pull of 4.0% Drift Cycle
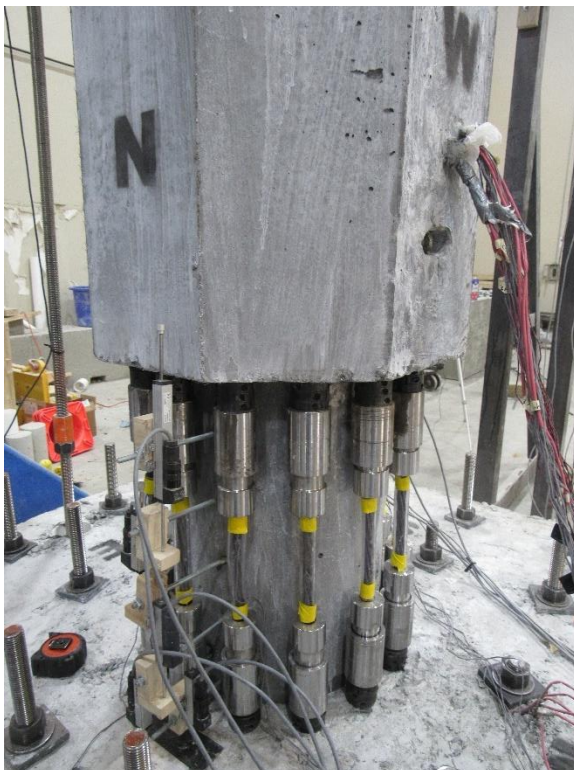
176
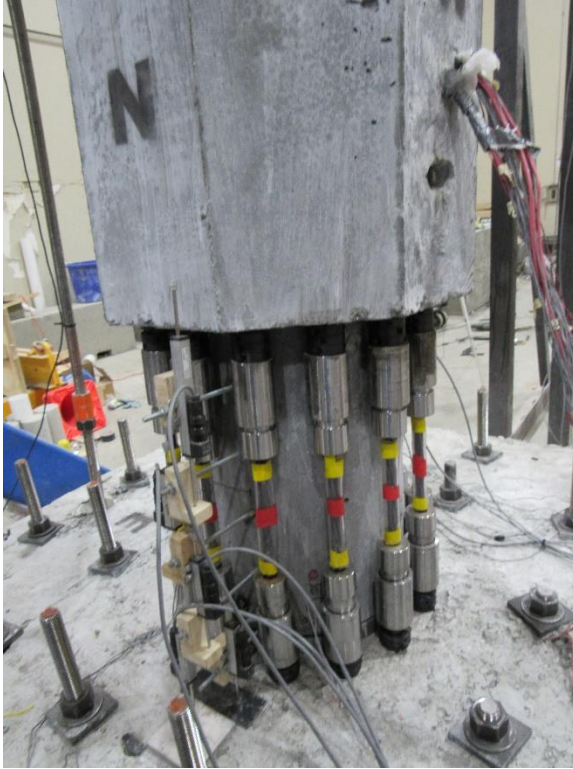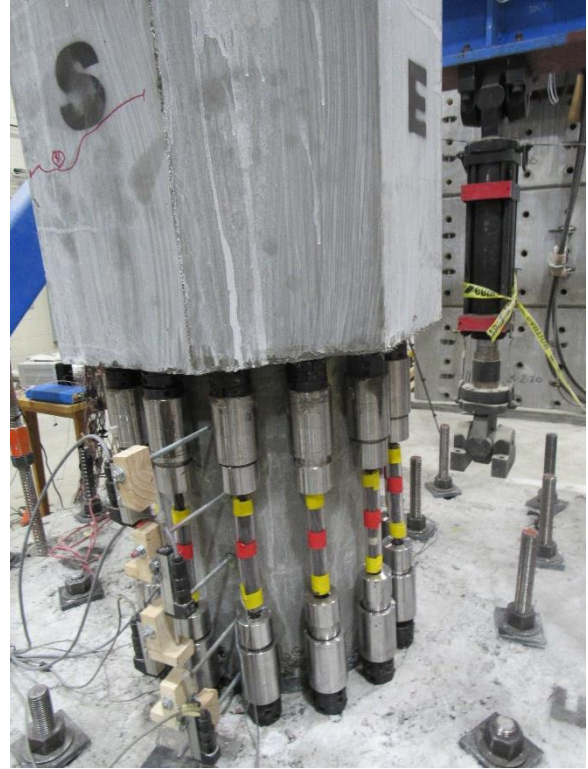
a) North-West Side   b) South-East Side

Figure 4.181. RPH-PF-R Column Plastic Hinge Damage, Second Push of 5.0% Drift Cycle

a) North-West Side   b) South-East Side

Figure 4.182. RPH-PF-R Column Plastic Hinge Damage, Second Pull of 5.0% Drift Cycle
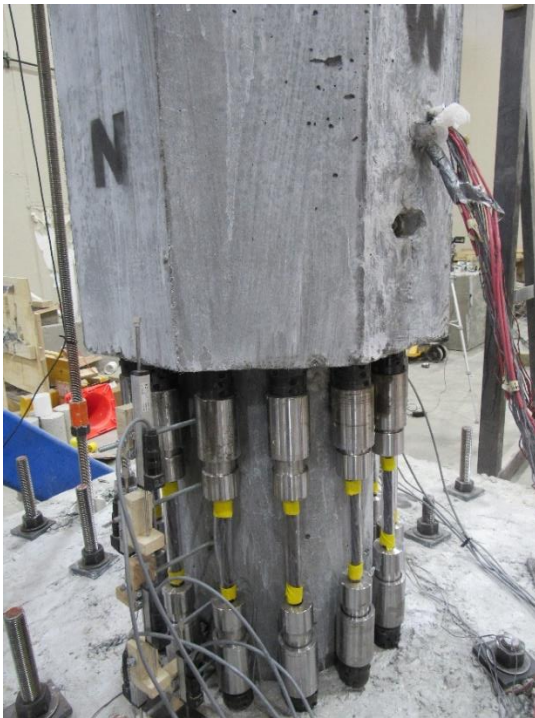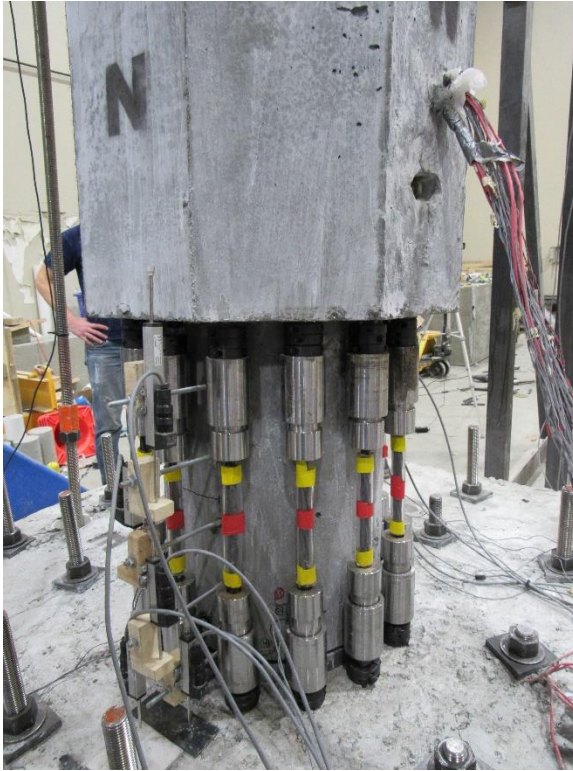
a) North-West Side   b) South-East Side
Figure 4.183. RPH-PF-R Column Plastic Hinge Damage, Second Push of 6.0% Drift Cycle
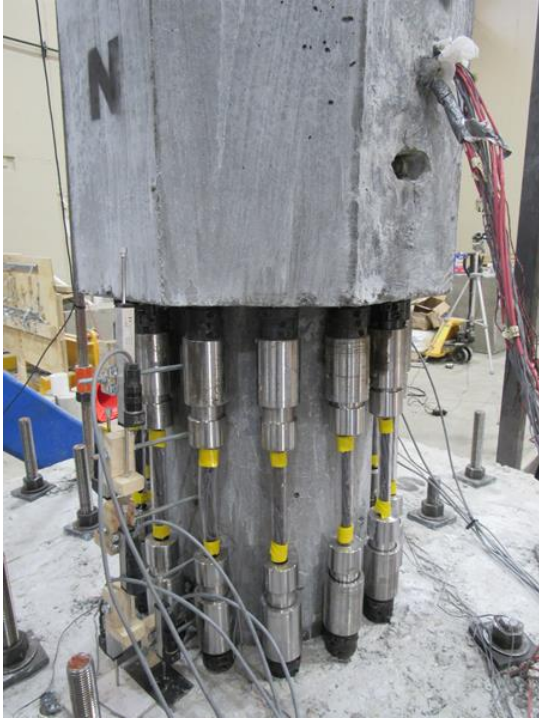

a) North-West Side   b) South-East Side
Figure 4.184. RPH-PF-R Column Plastic Hinge Damage, Second Pull of 6.0% Drift Cycle
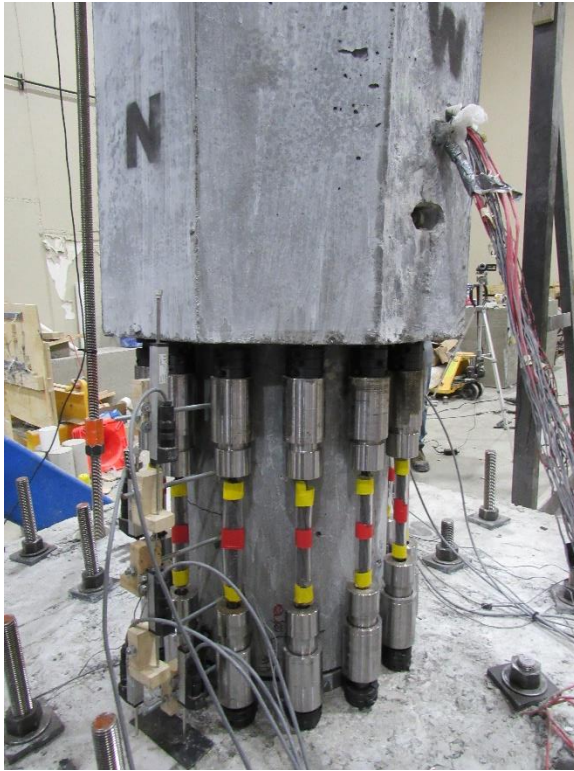
a) North-West Side   b) South-East Side

Figure 4.185. RPH-PF-R Column Plastic Hinge Damage, Second Push of 7.0% Drift Cycle
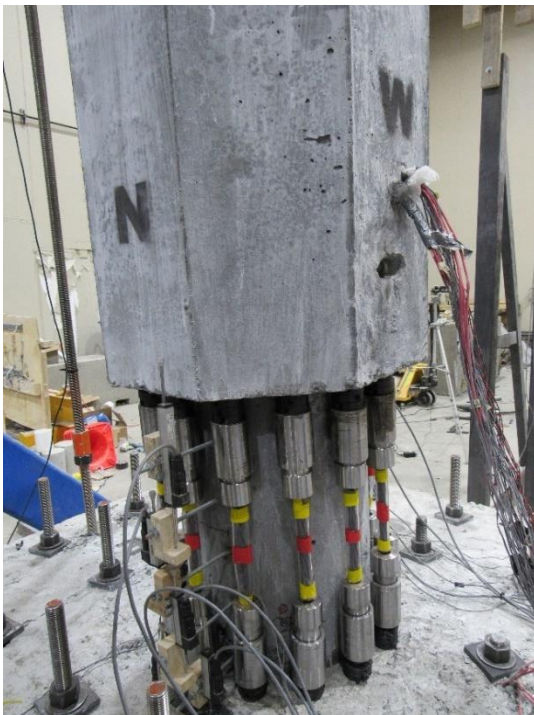
a) North-West Side   b) South-East Side

Figure 4.186. RPH-PF-R Column Plastic Hinge Damage, Second Pull of 7.0% Drift Cycle
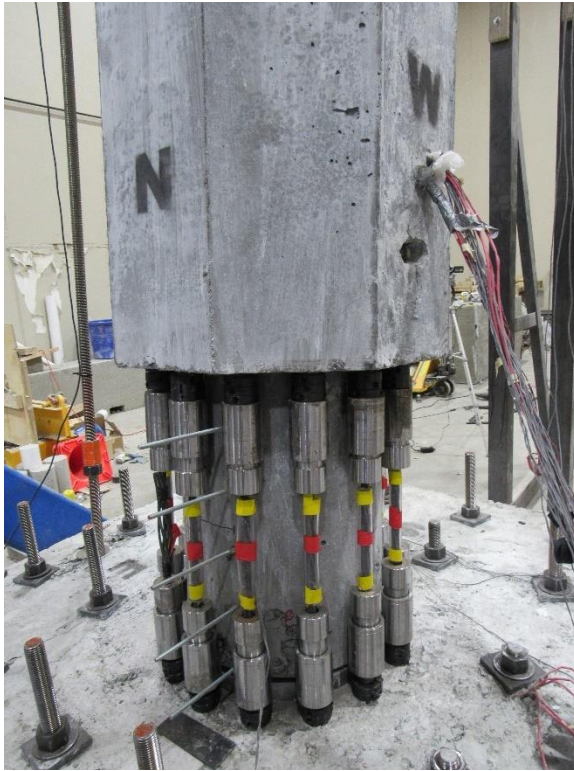
a) North-West Side

b) South-East Side

Figure 4.187. RPH-PF-R Column Plastic Hinge Damage, Second Push of 8.0% Drift Cycle
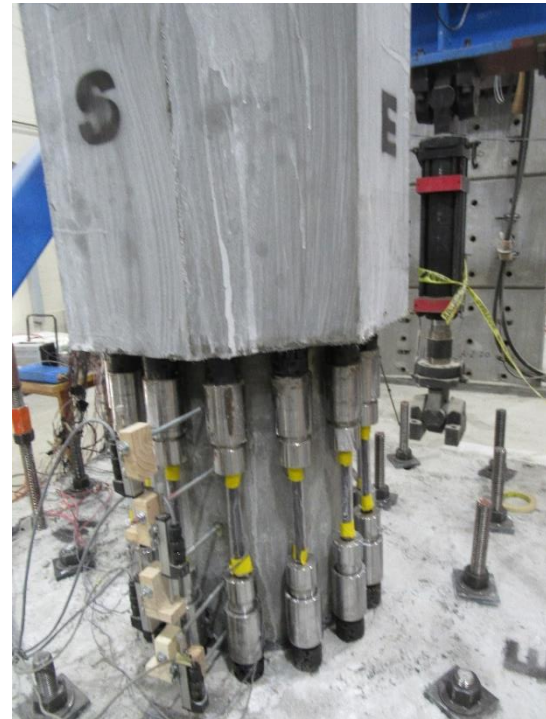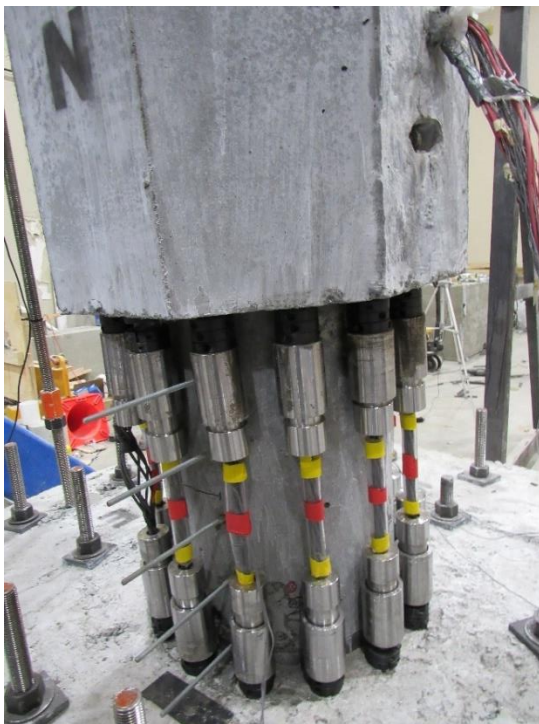

a) North-West Side

b) South-East Side

Figure 4.188. RPH-PF-R Column Plastic Hinge Damage, Second Pull of 8.0% Drift Cycle
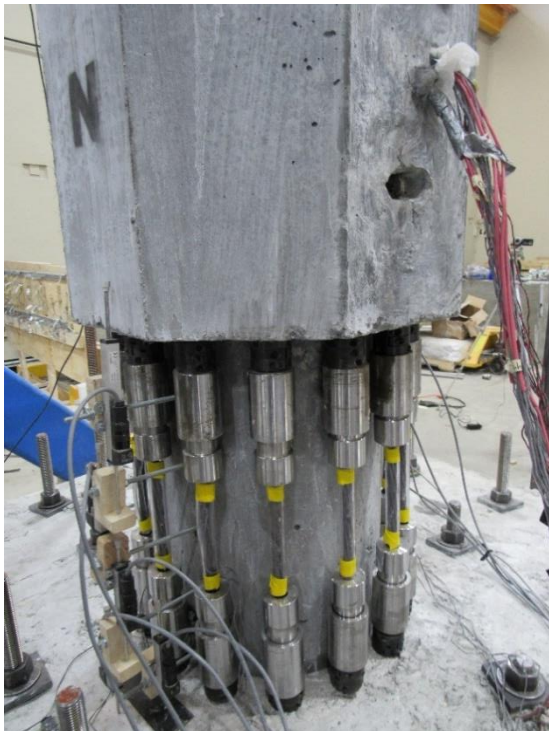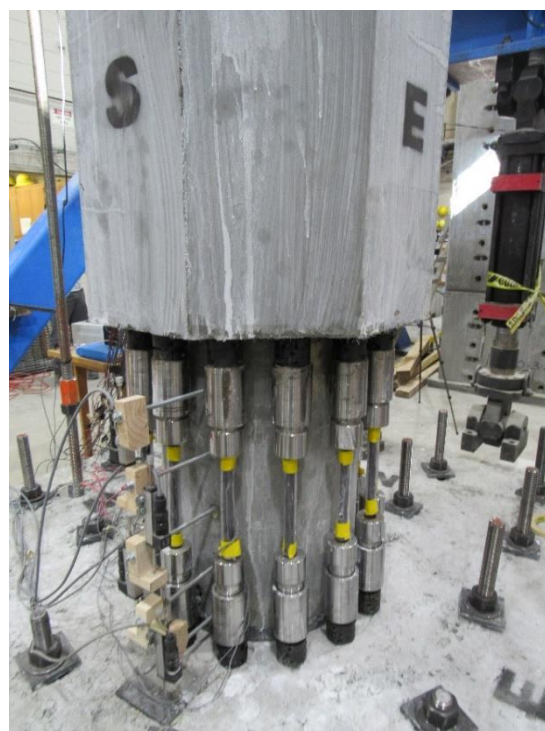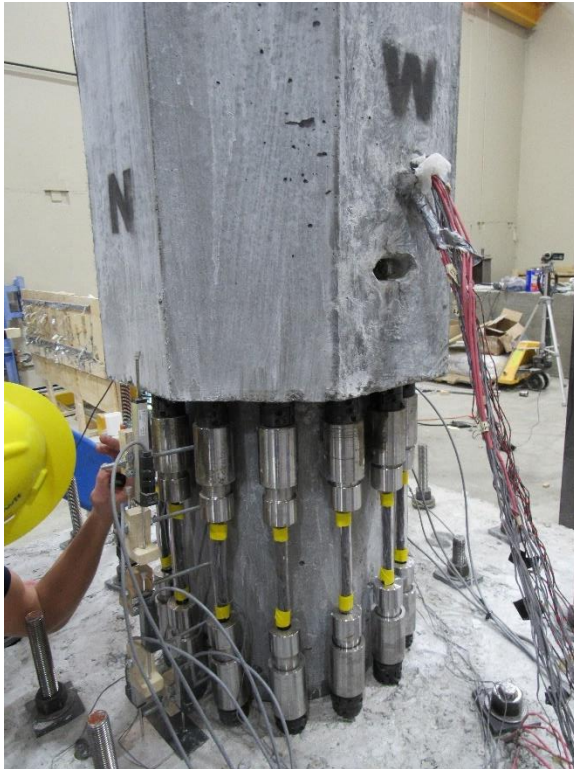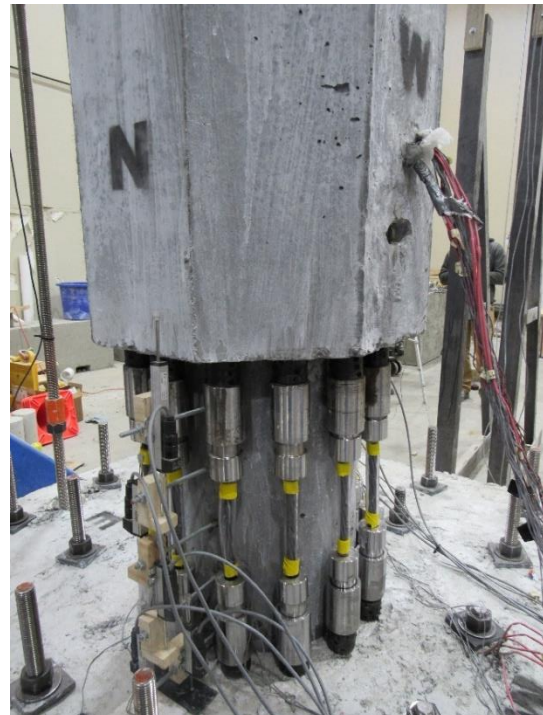
a) North-West Side b) South-East Side
Figure 4.189. RPH-PF-R Column Plastic Hinge Damage, Second Push of 9.0% Drift Cycle
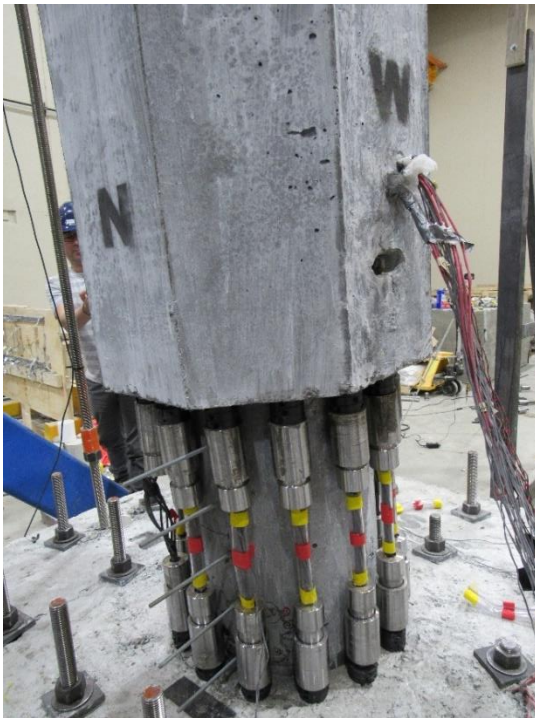
a) North-West Side b) South-East Side
Figure 4.190. RPH-PF-R Column Plastic Hinge Damage, First Pull of 9.0% Drift Cycle

181

4.5.4.4 RPH-PF Force-Displacement Relationship

Figure 4.191 shows the measured force-drift hysteretic and envelope responses of RPH-PF. This test was stopped at 4.0% drift ratio to replace the tendon fuses. A maximum lateral load of 49.0 kips (218 kN) was recorded in the push direction at 3.99% drift when the test was stopped. The column had a slightly higher initial stiffness in the pull direction but with a lower lateral force capacity. No yielding of tendons occurred during the first testing of RPH-PF. A flag-shape hysteretic response was observed with negligible residual displacements for this column. This made the tendon replacement much easier as the column was close to its original plumbed position.
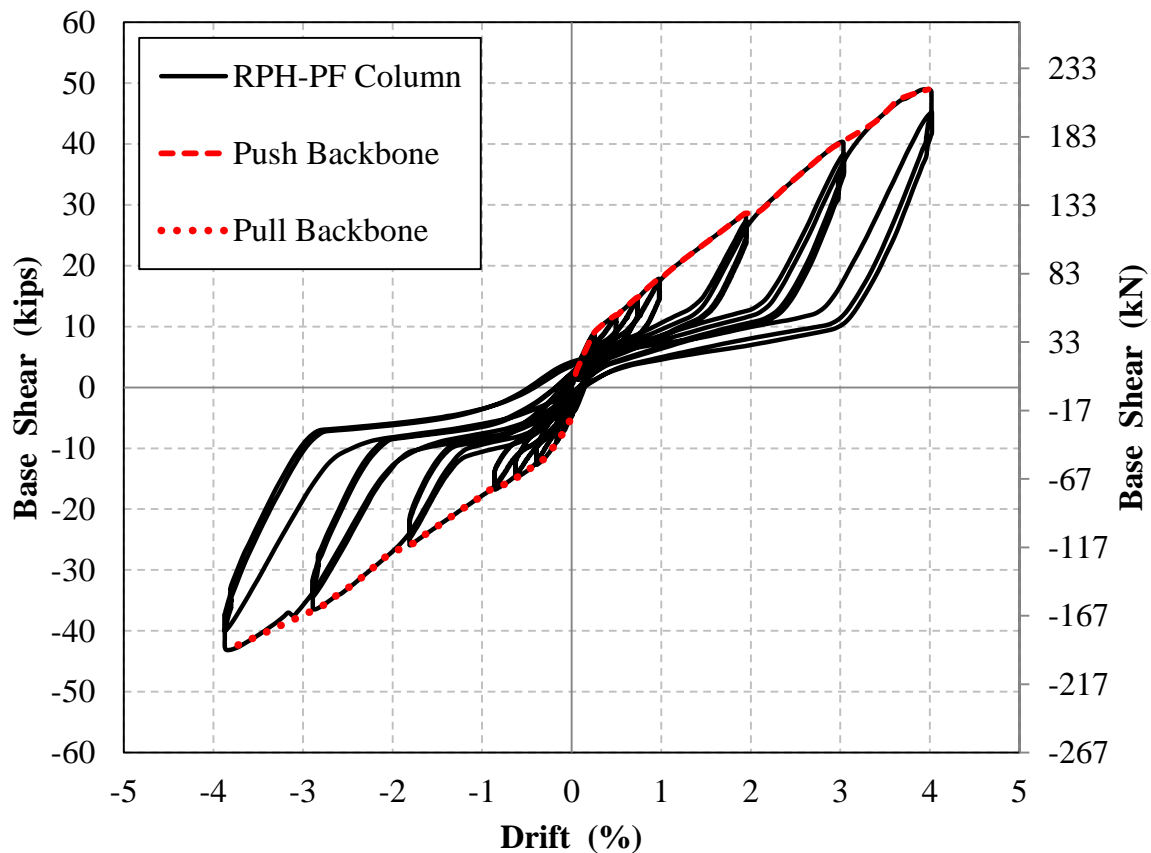
Figure 4.191. Measured RPH-PF Column Force-Drift Hysteretic and Envelope Responses

The average envelope of the push and pull directions can be seen in **Fig. 4.192**. No idealization was carried out for this test since the column did not fail and the tendons did not yield. It can also be observed that the force-displacement backbone did not plateau up to 4% drift. The overall stiffness of RPH-PF was lower than the CIP column. No soft start was observed in the force-displacement response indicating that the gap in the pipe-pin connection and the initial slippage of the tendons within the wedges were fully prevented.
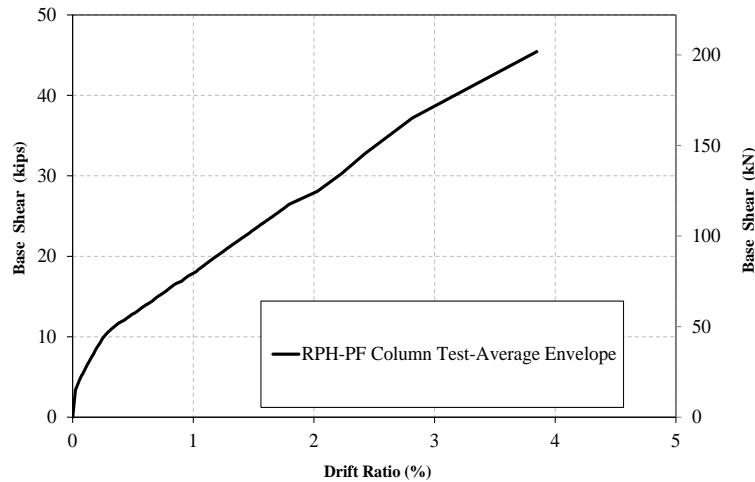
Figure 4.192. Measured RPH-PF Column Average Push/Pull Force-Drift Envelope

4.5.4.5 RPH-PF-R Force-Displacement Relationship

Figure 4.193 shows the measured lateral force-drift hysteretic and envelope responses from RPH-PF-R. A drop in lateral force capacity of over 15% occurred in the pull direction after two tendons were ruptured during the first cycle to 9.0% drift, ending the test. The maximum lateral load of 59.8 kips (266 kN) occurred in the pull direction at a drift ratio of 8.20%. The initial stiffness was higher in the push direction, but it was overall softer than the first test (RPH-PF). Tendons yielded in the push direction at a drift ratio of 4.25% and a lateral load of 45.8 kips (203.7 kN), and in the pull direction at a drift ratio of 4.23% and a lateral load of 49.5 kips (220.0 kN). The hysteretic response once again exhibited a flag-shape behavior, indicating negligible residual displacements even after large peak drifts.
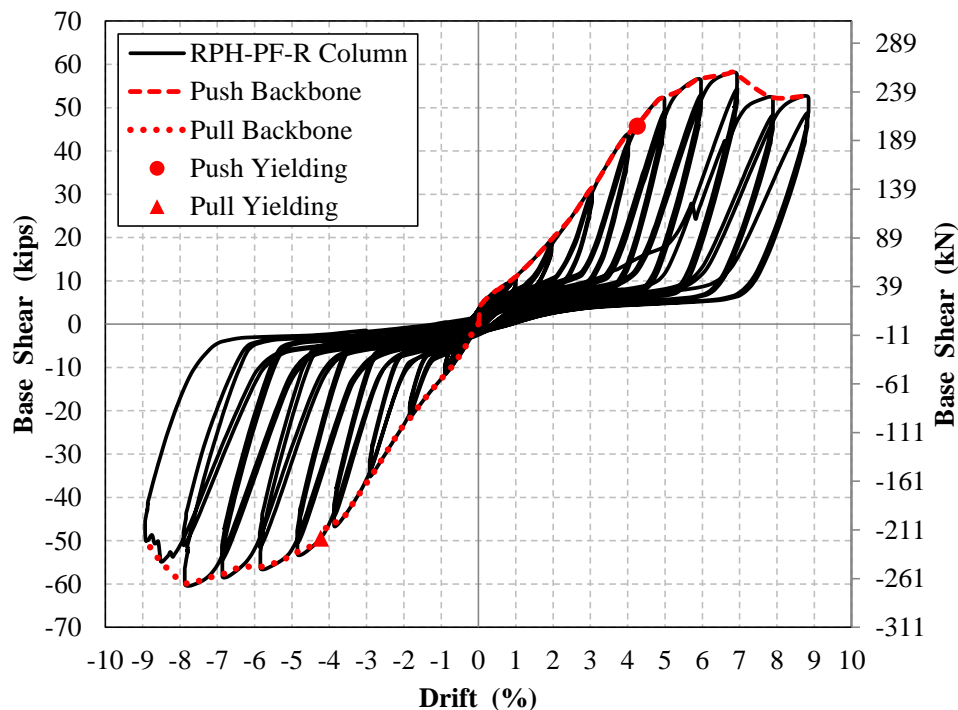
Figure 4.193. Measured RPH-PF-R Column Force-Drift Hysteretic and Envelope Responses

183

Figure 4.194 shows the average envelope of the push and pull directions for the RPH-PC-R column. The average yield drift ratio was 4.24% at a lateral load of 47.5 kips (211.3 kN). The effective yield drift was 4.93% at a lateral load of 55.23 kips (245.7 kN). The drift capacity of the column was 8.91% resulting in a displacement ductility capacity of 1.81 for RPH-PF-R. Novel columns often experience yielding at large drift ratios, reducing the displacement ductility. Therefore, the drift capacity is a better indicator of the column performacne. RPH-PF-R exhibited a similar drift capacity as CIP (8.91% vs 8.96%).

Figure 4.195 shows a comparison between the average backbones of RPH-PF, RPH-PF-R, and CIP. The effective stiffness of both RPH-PF and RPH-PF-R was much lower than that of CIP. Nevertheless, the initial stiffness, if calculated at 5 kips (22 kN), matched well in the repairable and CIP columns. There was a stiffness degradation between the first testing of RPH-PF and the repaired column, likely due to minor damage at the base of the column, including pullout of the shear studs in the steel baseplate.
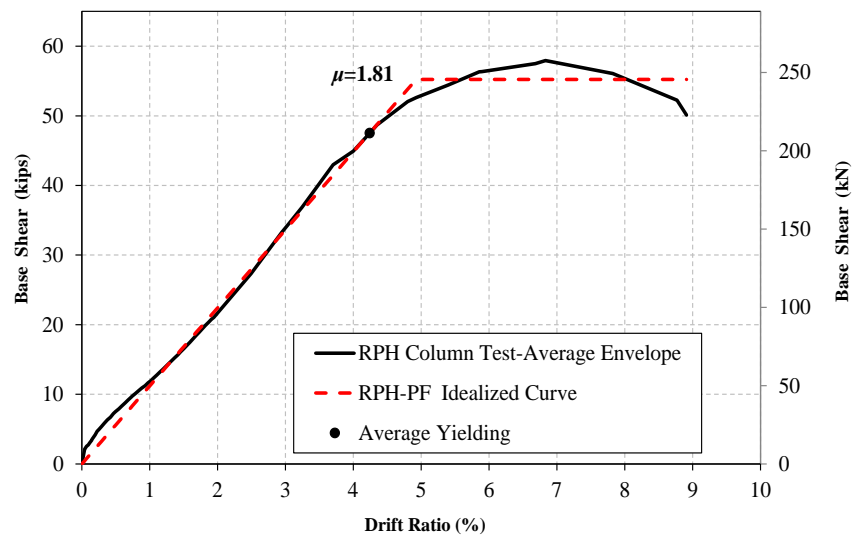
Figure 4.194. Measured RPH-PF-R Column Average Push/Pull Force-Drift Envelope and Idealized Curve
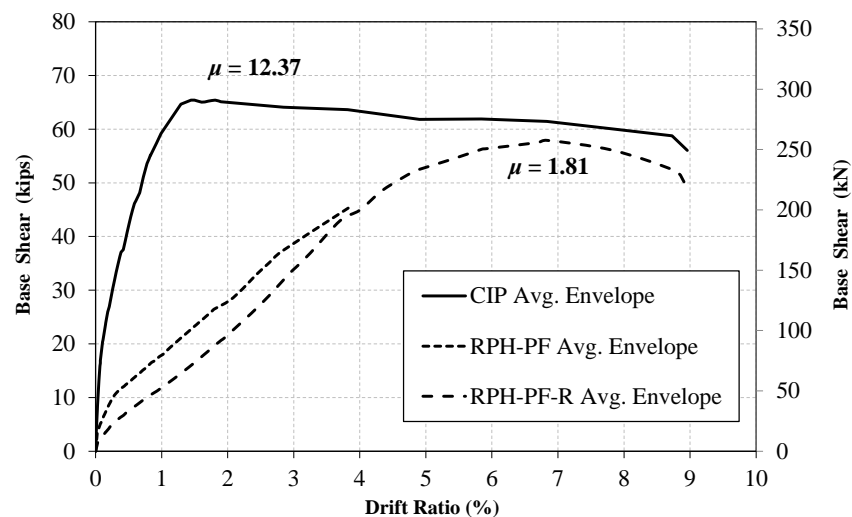
Figure 4.195. Measured Force-Drift Response of CIP, RPH-PF, and RPH-PF-R Columns

184

4.5.4.6 RPH-PF Strain Profiles

Forty-six steel strain gauges were installed on the RPH-PF column at five levels along the column height. Four of these levels also included strain gauges on the longitudinal bars within the neck section. The measured strain profiles for tendons corresponding to Bars/Tendons 1, 3, 8, and 10 are shown in **Fig. 4.196** to **4.199**. The bar/tendon number can be found in **Fig. 4.11**. Note that bar numbers are slightly different than those assigned to CIP and RPH-PC since four additional longitudinal bars/tendons were added to match the CIP lateral force capacity. However, the corresponding reinforcement positions approximately remained the same. The middle two levels of strain gauges for the main longitudinal reinforcement were placed on the tendon fuses. Approximately, the steel tendons were placed between the column height from 4 in. (102 mm) to 20 in. (508 mm). The strain profiles show the same patter in which the highest strains were at the center two levels (with tendons). This is due to much smaller tendon (fuse) area compared with the main No. 10 ($\varnothing$ 32-mm) column/footing dowels. Separate indicators of tendon and bar yielding were included in the graphs using red lines due to material differences. As can be noted, no tendon yielding was recorded during the first round of testing for RPH-PF although SG28 on Tendon 3 came very close to yielding at 4.0% drift. There was some minor yielding of Bar 3 below the footing surface.

The maximum compressive strains during each drift cycle were also recorded (**Fig. 4.200-4.203**). Limited correlation exists between the compressive strains and the height of the strain gauges; however, compressive strains at higher drifts for Bars/Tendons 3 and 8 seemed to be concentrated to the center two strain gauge levels, which were placed on the tendons. All compressive strain values remained below 500 $\mu\varepsilon$ except for the uppermost strain gauge on Bar 1 at 4.0% drift which seems to be an outlier and may be due to a strain gauge malfunction. The key observation is that the No. 10 (Ø32-mm) black steel bars serving as the column/footing dowels experienced minimal compressive strain demands up to 4% drift, which was the desired performance. In the previous column with stainless-steel BRR, these dowel bars bent at the same drift level.

Strain profiles for longitudinal No. 9 (Ø29-mm) conventional steel bars in the neck section were also developed to evaluate the neck section design (**Fig. 4.204-4.207**). The neck bars were numbered in the same way as the main column bars, with bars N1 and N2 corresponding to bars B1 and B2 and following in a clockwise direction. Note that the neck bar numbers vary slightly from those of RPH-PC due to a different bar size and layout used to accommodate the steel cup. Values for all bars were well below the yield point, indicating a successful linear-elastic design of the neck section.
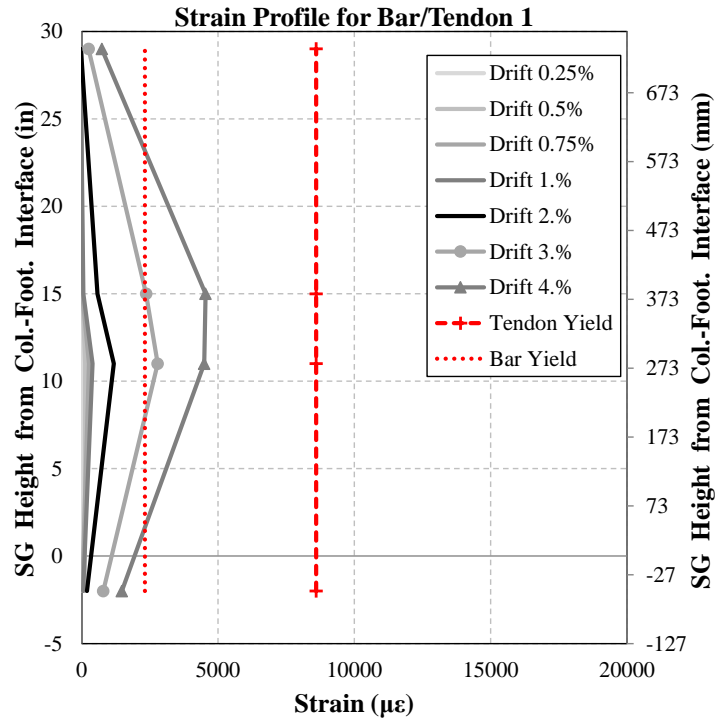
Figure 4.196. Measured Tensile Strain Profile for RPH-PF Column Bar/Tendon 1
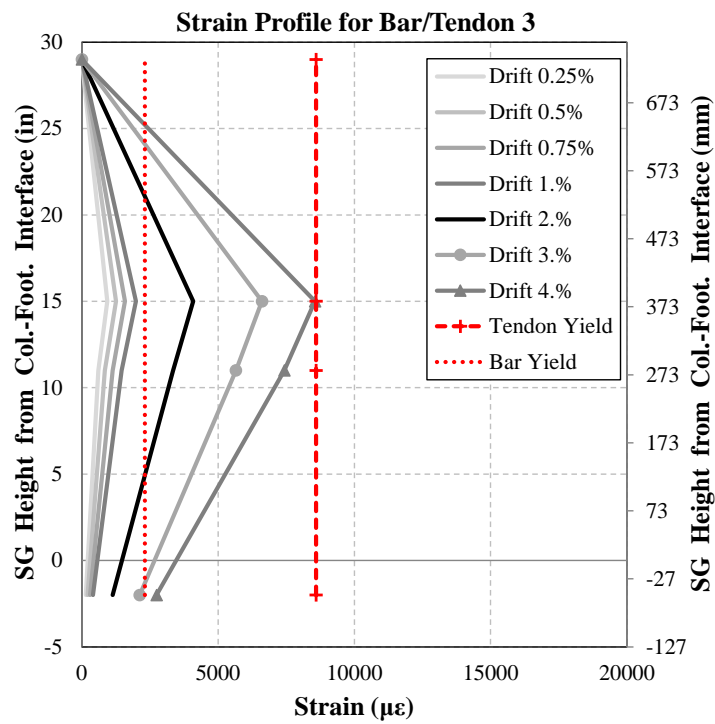
Figure 4.197. Measured Tensile Strain Profile for RPH-PF Column Bar/Tendon 3
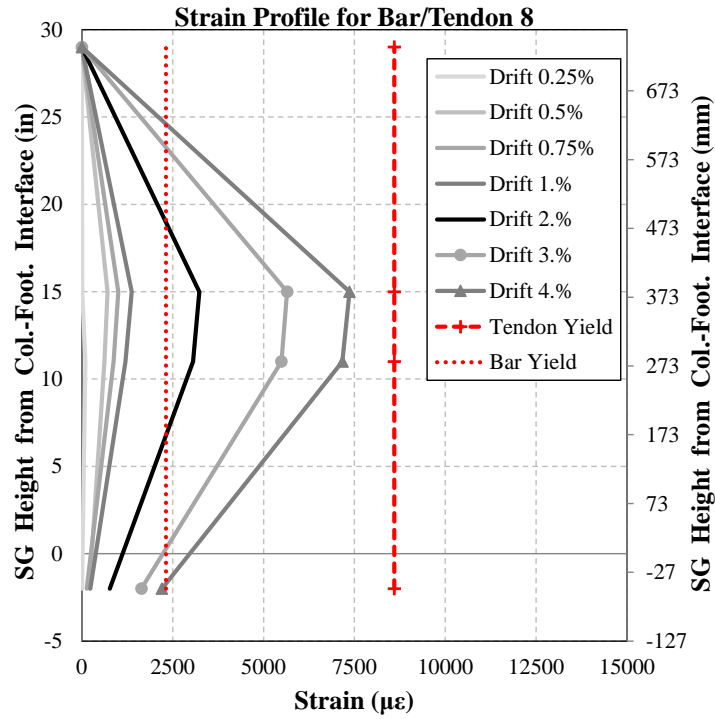
Figure 4.198. Measured Tensile Strain Profile for RPH-PF Column Bar/Tendon 8
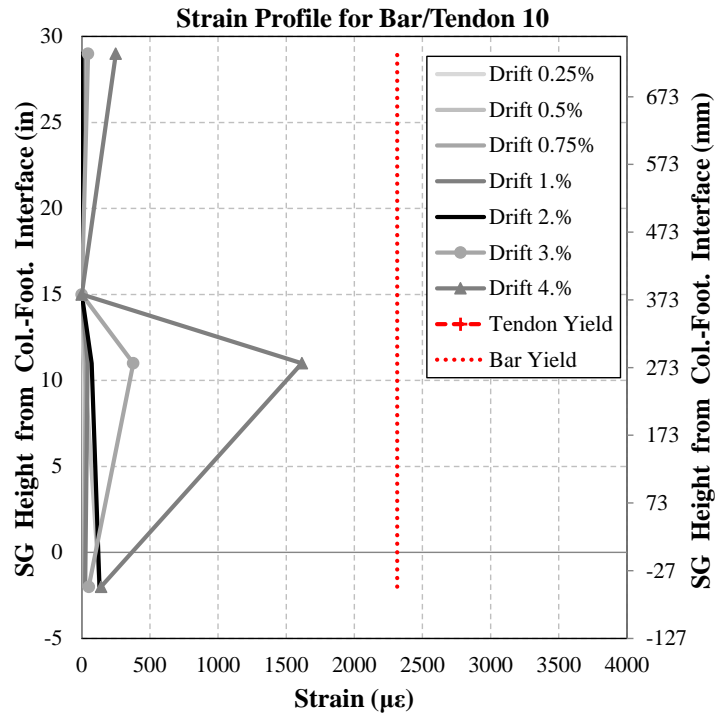
Figure 4.199. Measured Tensile Strain Profile for RPH-PF Column Bar/Tendon 10

187
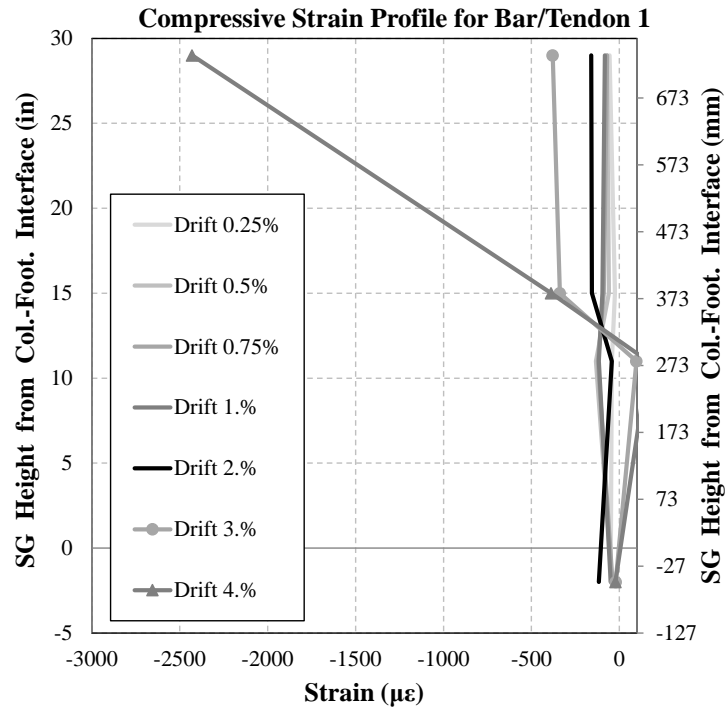
Figure 4.200. Measured Compressive Strain Profile for RPH-PF Column Bar/Tendon 1
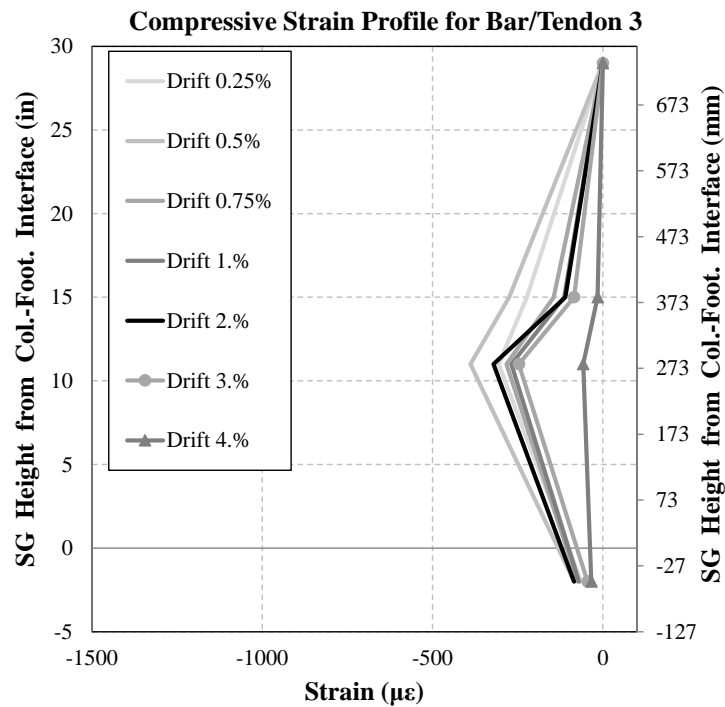
Figure 4.201. Measured Compressive Strain Profile for RPH-PF Column Bar/Tendon 2
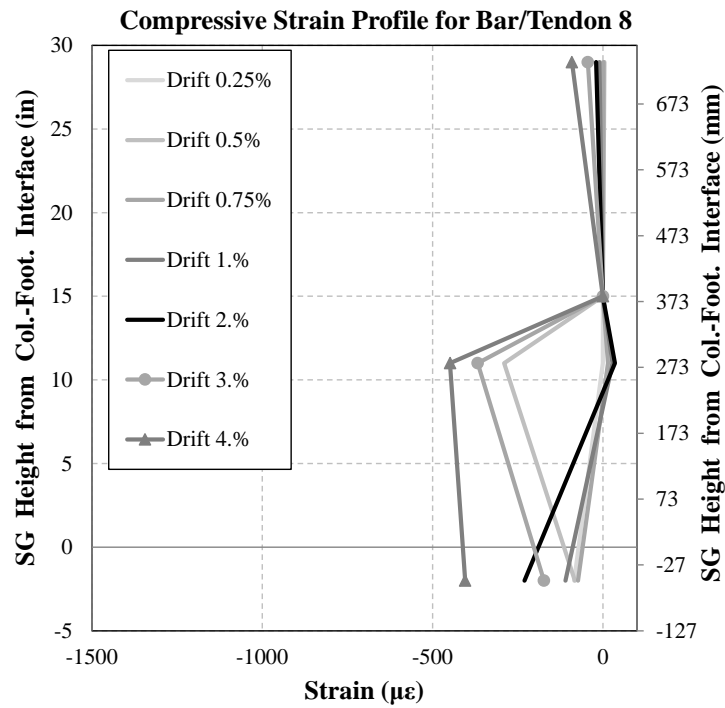
Figure 4.202. Measured Compressive Strain Profile for RPH-PF Column Bar/Tendon 8
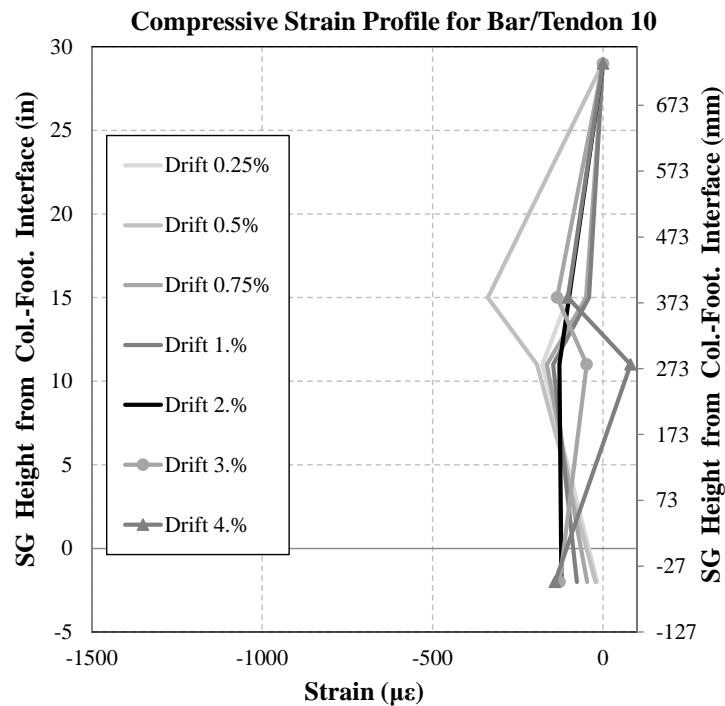
Figure 4.203. Measured Compressive Strain Profile for RPH-PF Column Bar/Tendon 10
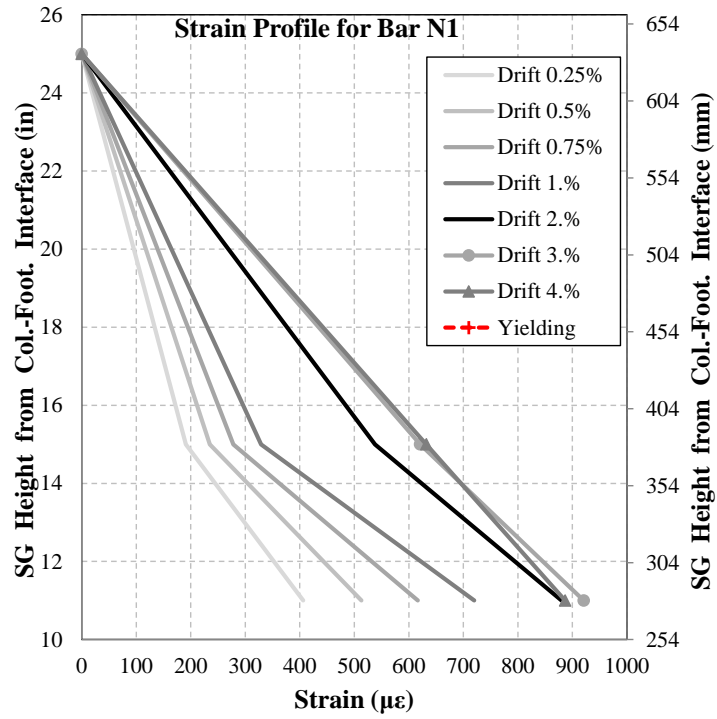
Figure 4.204. Measured Strain Profile for RPH-PF Column Neck Bar N1
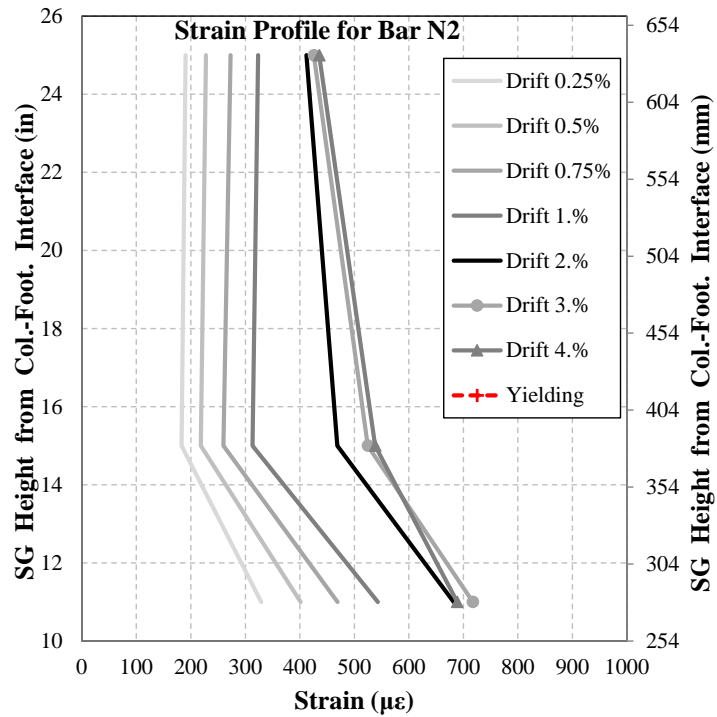
Figure 4.205. Measured Strain Profile for RPH-PF Column Neck Bar N2
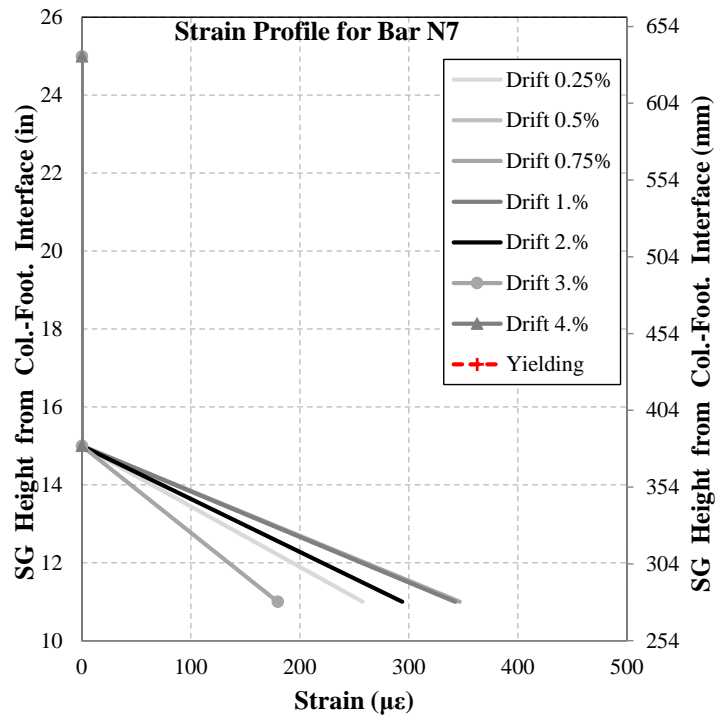
Figure 4.206. Measured Strain Profile for RPH-PF Column Neck Bar N7
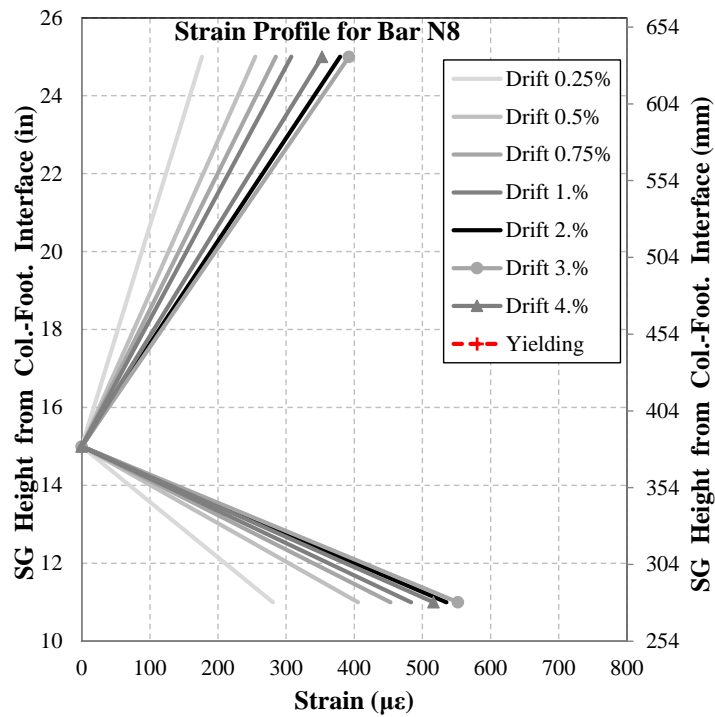
Figure 4.207. Measured Strain Profile for RPH-PC Column Neck Bar N8

Concrete strain gauges were installed along the perimeter of the base of the column, just inside of the transverse reinforcement, to measure the strains in the core UHPC. Concrete strain gauges were numbered following the same pattern as RPH-PC, with the first concrete strain gauge placed behind bar B1 following a clockwise pattern. **Figures 4.208** and **4.209** show the measured UHPC compressive and tensile strain profiles for RPH-PF with positive values representing tensile strains and negative values representing compressive strains.

In general, the maximum strains were concentrated near the north and south faces of the column. Strain gauges C1 on the north side and C6 on the south side experienced the highest compressive strains. Strain gauges C6 and C9 experienced the highest tensile strains. No UHPC strains exceeded 5000 $\mu\varepsilon$, which is the equivalent value for conventional concrete crushing. For UHPC, the crushing strain value is five times larger.

Figures 4.210-4.213 show the strain profiles along the east and west faces of the column during both push and pull cycles. Overall, it can be observed that during push cycles the gauges on the north side experienced tensile strains while the gauges on the south experienced compressive strains. The opposite behavior was seen during pull cycles. Overall, the UHPC strain data does not indicate any damage of UHPC within the core.
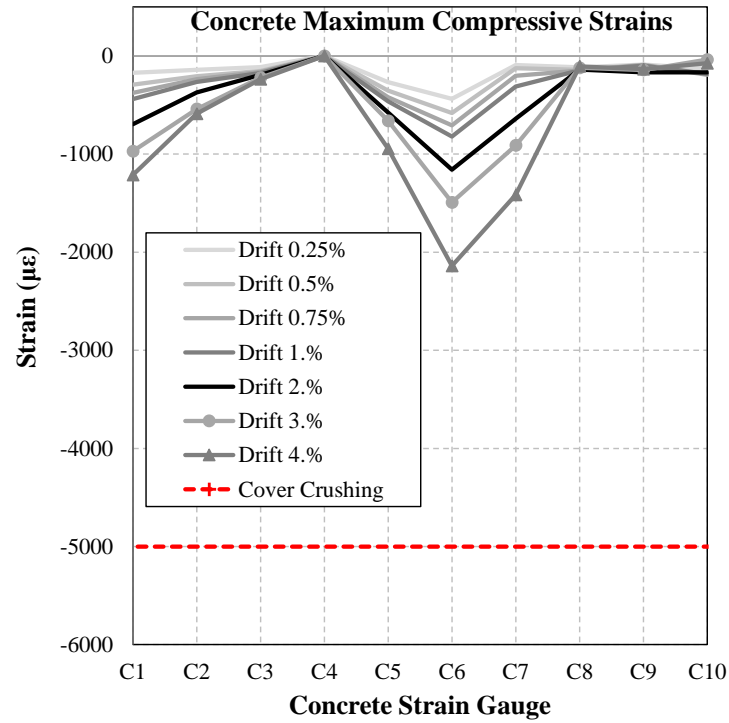
Figure 4.208. Measured UHPC Compressive Strain Profile for RPH-PF
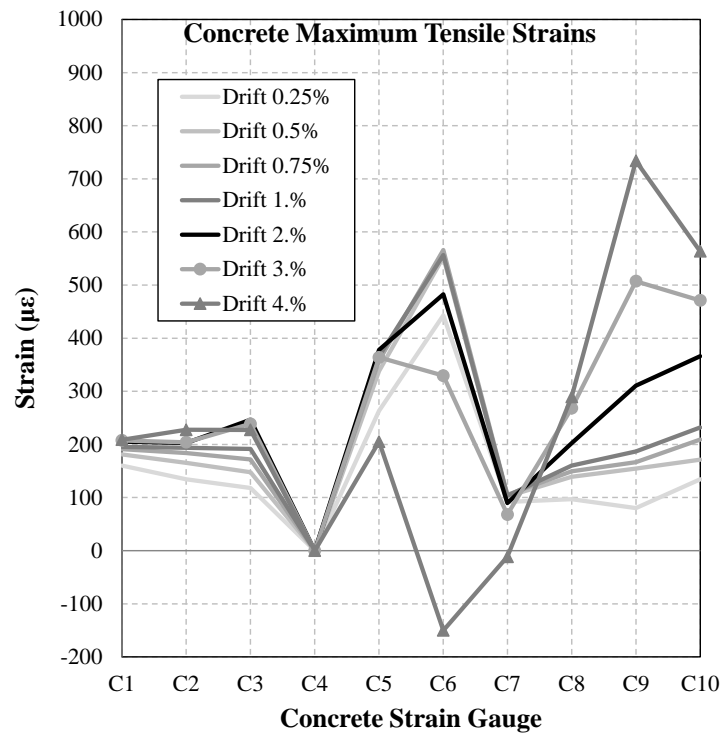
Figure 4.209. Measured UHPC Tensile Strain Profile for RPH-PF

193
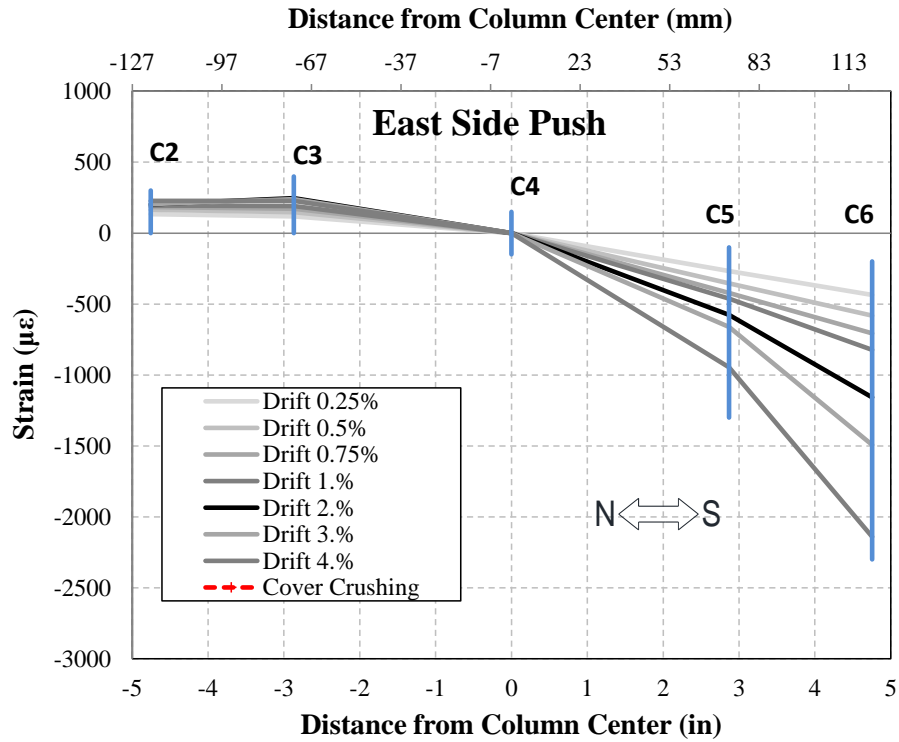
Figure 4.210. Measured UHPC Strain Profile for RPH-PF East Face During Push Cycles
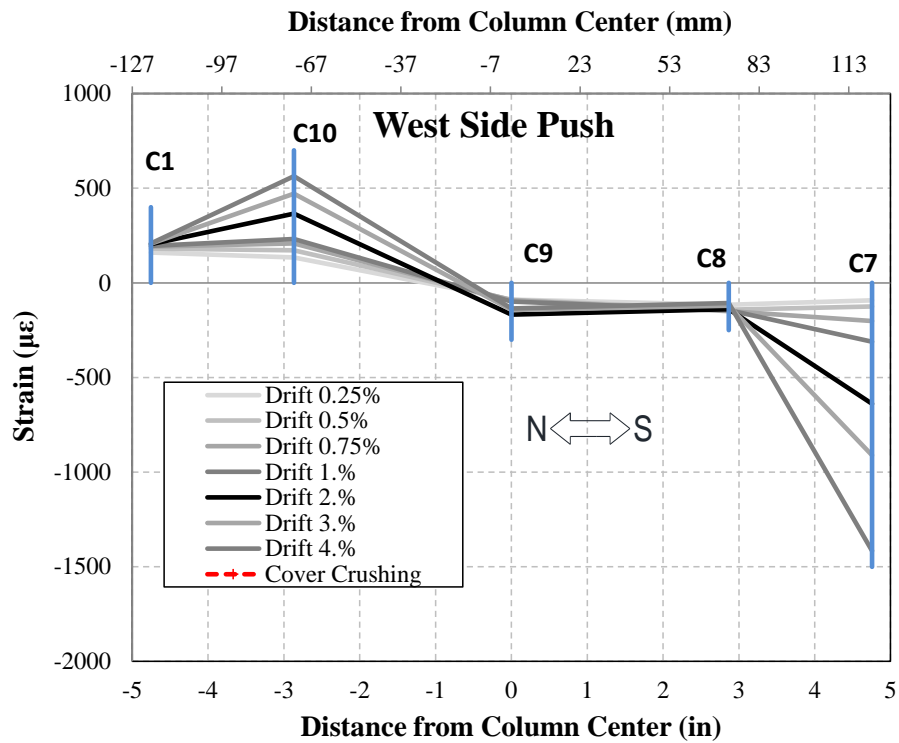
Figure 4.211. Measured UHPC Strain Profile for RPH-PF West Face During Push Cycles

194
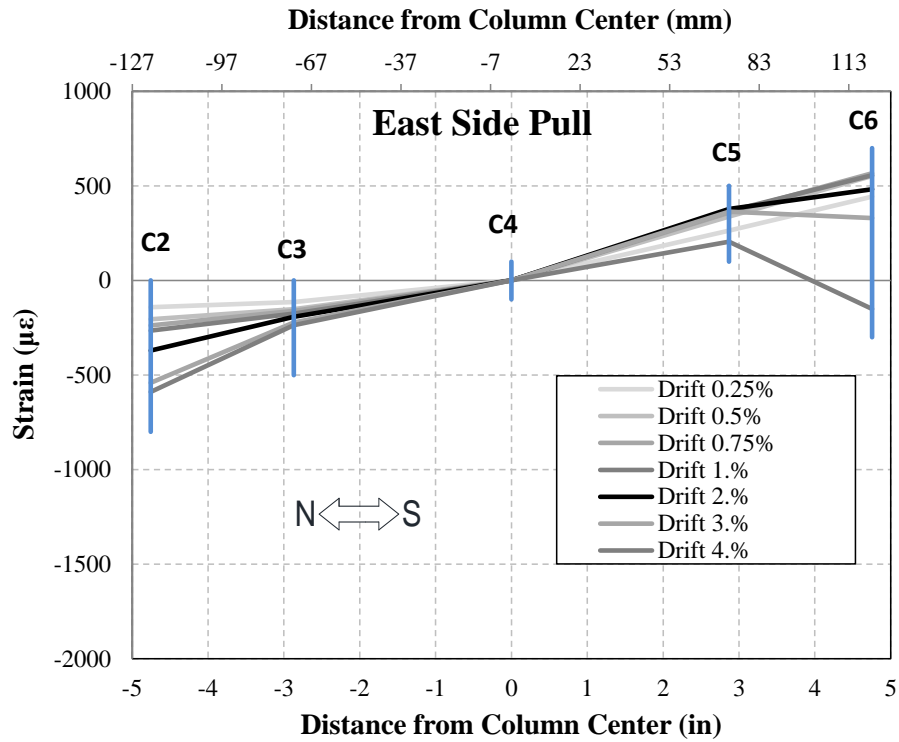
Figure 4.212. Measured UHPC Strain Profile for RPH-PF East Face During Pull Cycles
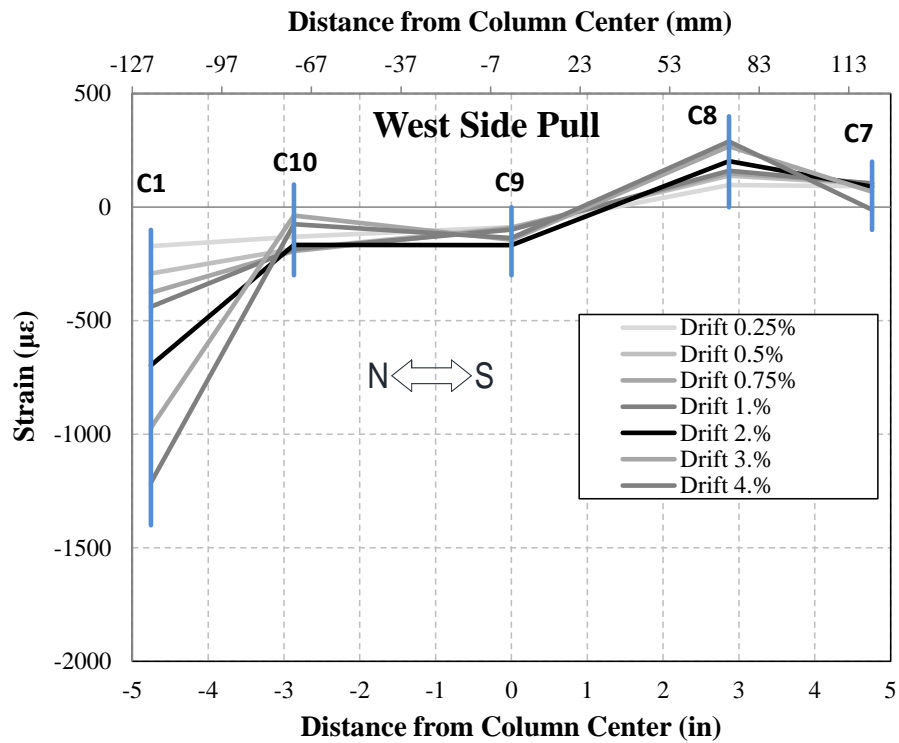
Figure 4.213. Measured UHPC Strain Profile for RPH-PF West Face During Pull Cycles

4.5.4.7 RPH-PF-R Strain Profiles

Figures 4.214-4.217 show the measured strain profiles for Bars/Tendons 1, 3, 8, and 10 in RPH-PF-R. Strain gauges in the middle two levels were replaced on the new tendon fuses used for the repair. The tensile strains were again concentrated in the tendons at the center two strain gauge levels. Yielding occurred in all four instrumented tendons at high drift ratios while some minor yielding of column/footing steel dowel bars was also observed at high drift ratios. Overall, tendons significantly yielded and ruptured while column/footing steel dowel bars slightly yielded at tendon rupture indicating a successful design of tendon fuses in this column.

Compressive strain profiles were also recorded for RPH-PC-R as shown in **Fig. 4.218-4.221**. Compressive strains were all relatively low when compared with the maximum tensile values in the same bars. Compressive strains seemed to be concentrated within the tendons at higher drift ratios, likely as they buckled before compressive strains caused the wedges to release and allow the tendons to snap back to straight position. Furthermore, column/footing dowel bars experienced minimal compressive strains which was desired in preventing buckling/bending of these bars for quick fuse replacement.

Neck bar strain gauge profiles for RPH-PC-R are shown in **Fig. 4.222-4.225**. The center strain gauge on Bar N7 indicated some minor yielding; however, the linear-elastic design of the neck section was overall valid even at the tendon rupture.

Figures 4.226-4.227 show the measured UHPC compressive and tensile strain profiles for RPH-PF-R with positive values representing tensile strains and negative values representing compressive strains. Strains did not exceed the strain capacity of the conventional concrete, indicating successful use of UHPC. Note UHPC has significantly higher compressive strain capacity. Strain gauges C1 and C6 again read the highest compressive strain values while gauges C6 and C9 read the highest tensile strain values. **Figures 4.228-4.231** show the strain profiles along the east and west faces of the column during both push and pull cycles. Strain gauges on the north side experienced tensile strains and gauges on the south experienced compressive strains during push cycles, while the opposite is true during pull cycles.

196
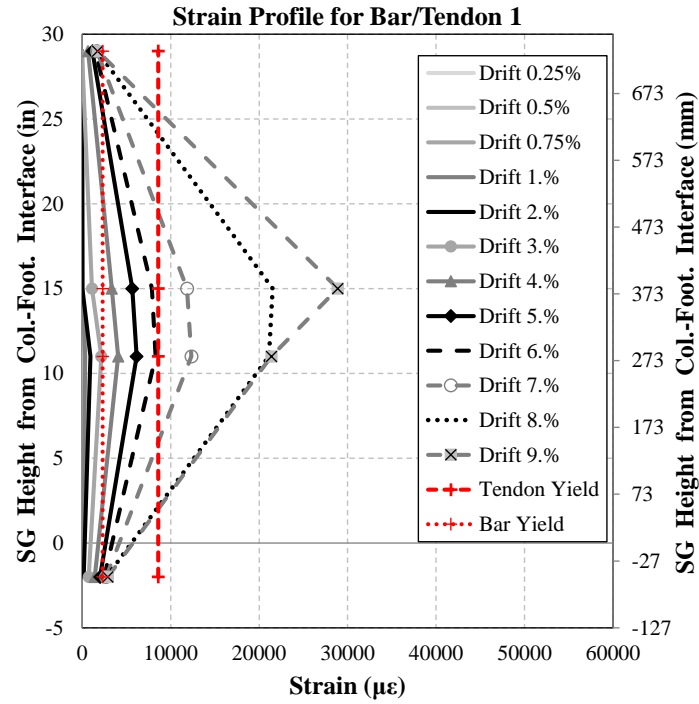
Figure 4.214. Measured Strain Profile for RPH-PF-R Column Bar/Tendon 1
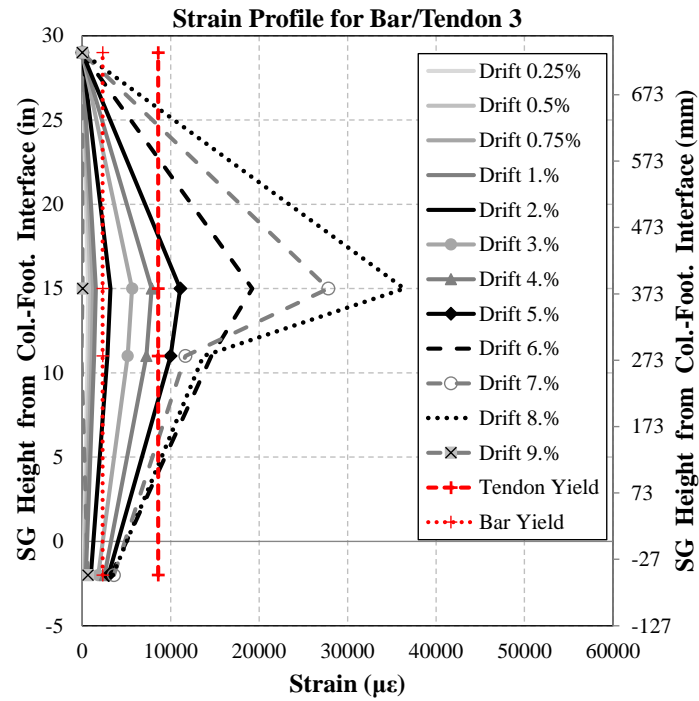
Figure 4.215. Measured Strain Profile for RPH-PF-R Column Bar/Tendon 3
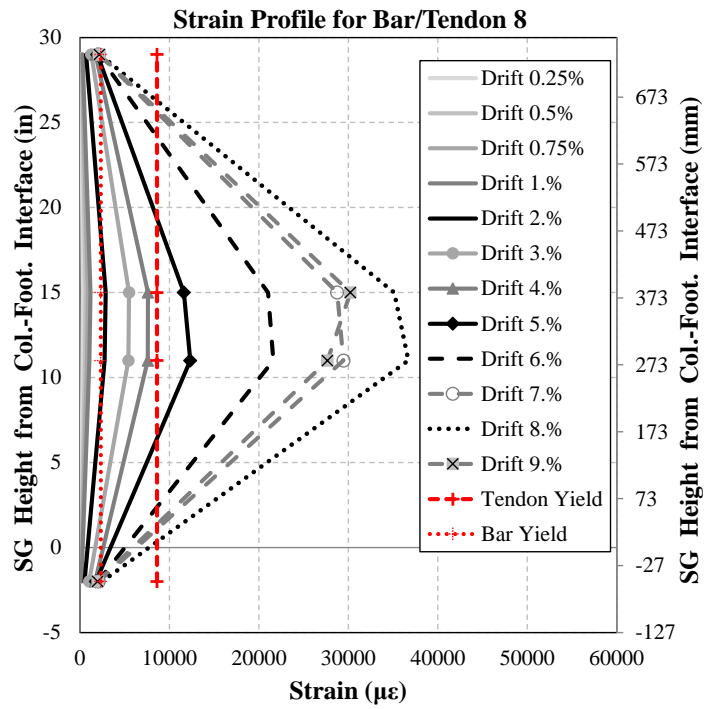
Figure 4.216. Measured Strain Profile for RPH-PF-R Column Bar/Tendon 8
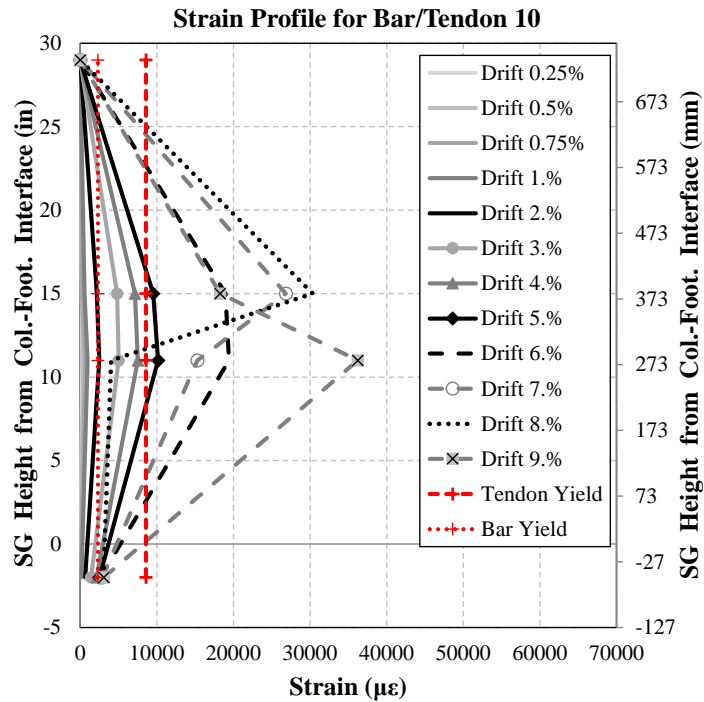
Figure 4.217. Measured Strain Profile for RPH-PF-R Column Bar/Tendon 10
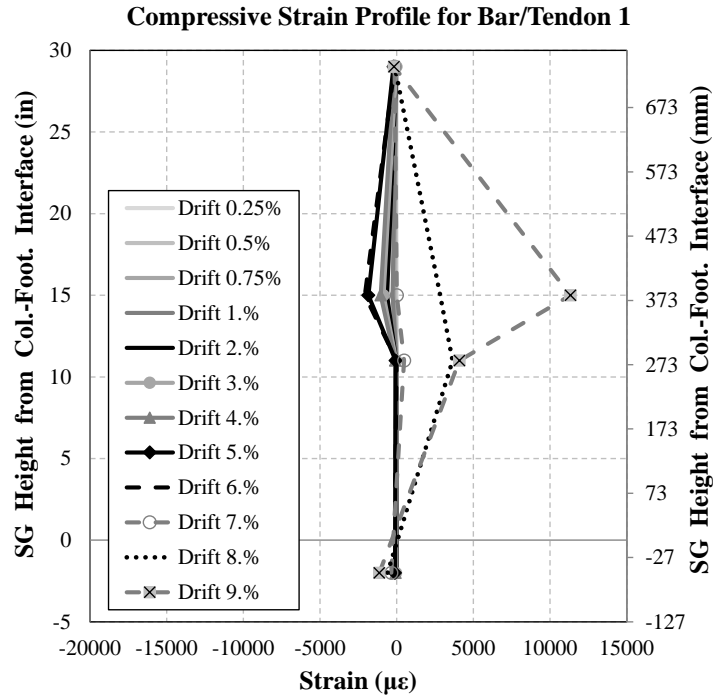
Figure 4.218. Measured Compressive Strain Profile for RPH-PF-R Column Bar/Tendon 1
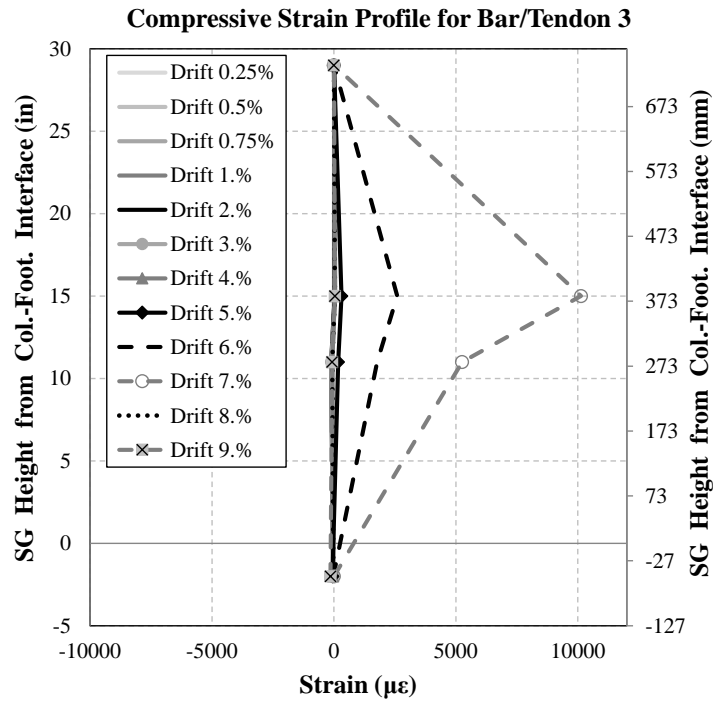
Figure 4.219. Measured Compressive Strain Profile for RPH-PC-R Column Bar/Tendon 3
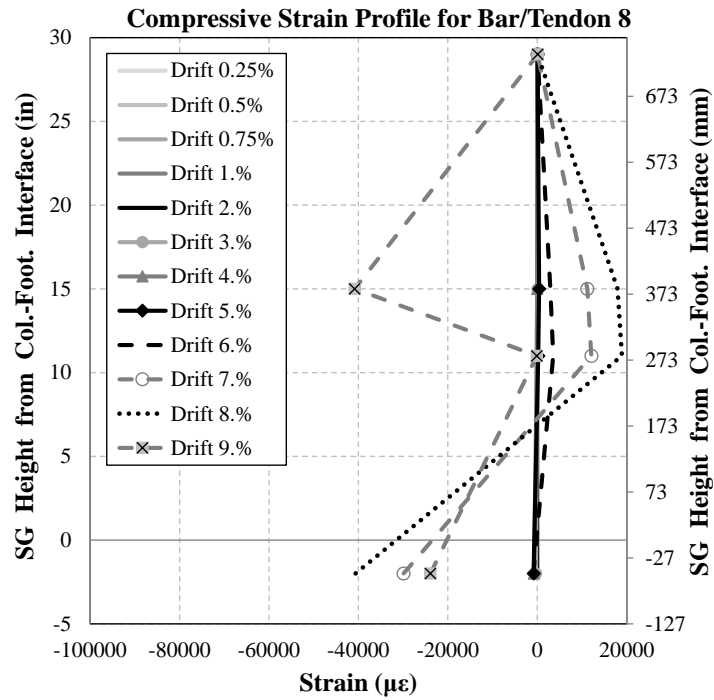
Figure 4.220. Measured Compressive Strain Profile for RPH-PF-R Column Bar/Tendon 8
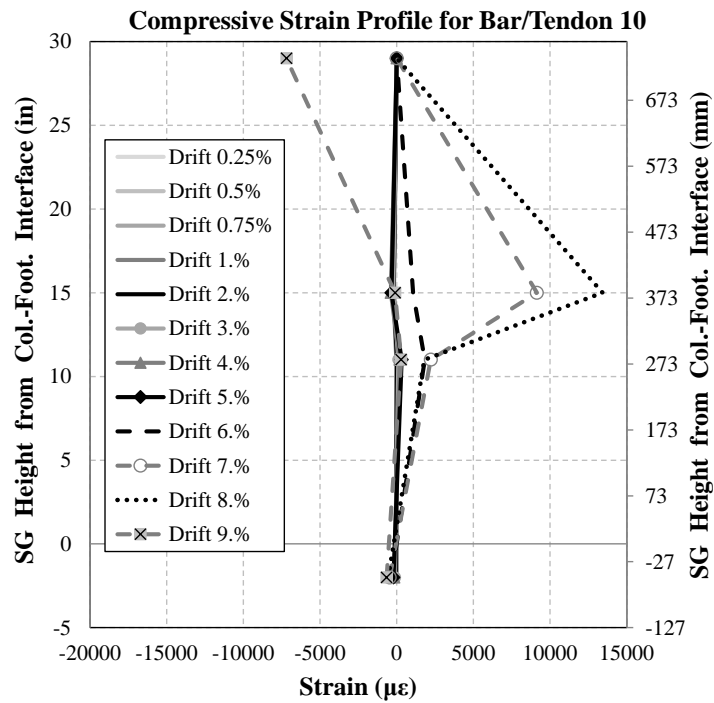
Figure 4.221. Measured Compressive Strain Profile for RPH-PC-R Column Bar/Tendon 10
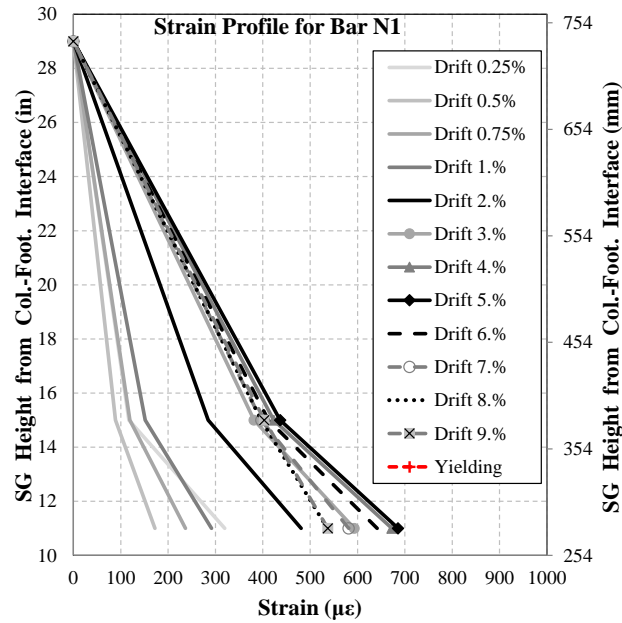
Figure 4.222. Measured Strain Profile for RPH-PF-R Column Neck Bar N1
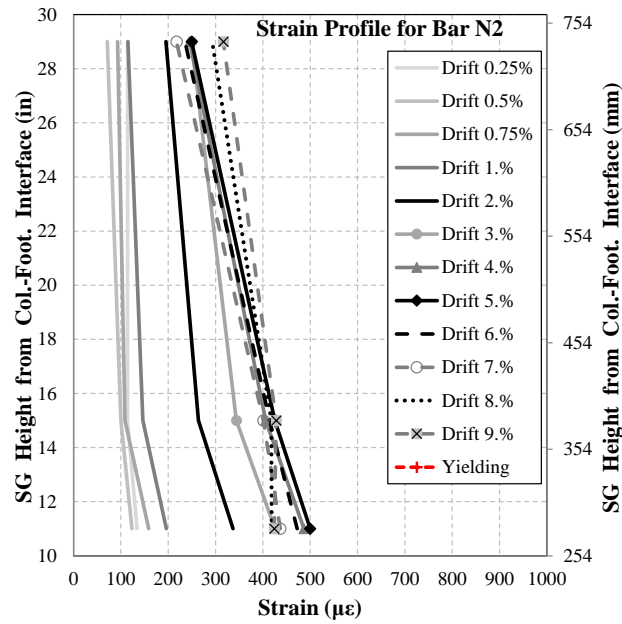
Figure 4.223. Measured Strain Profile for RPH-PF-R Column Neck Bar N2
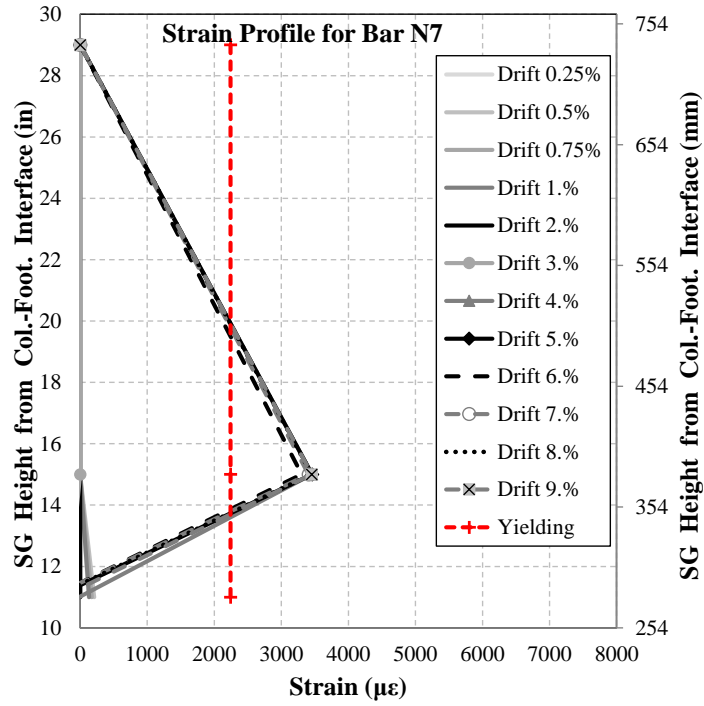
Figure 4.224. Measured Strain Profile for RPH-PF-R Column Neck Bar N7
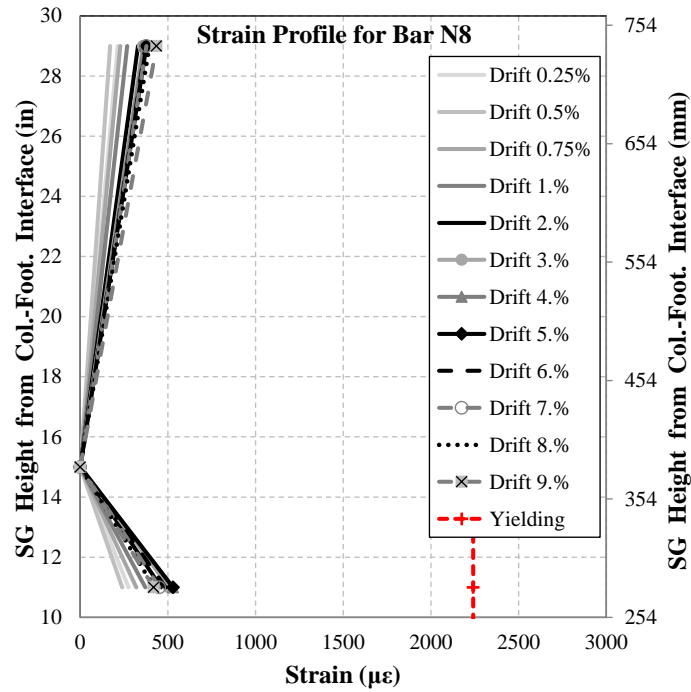
Figure 4.225. Measured Strain Profile for RPH-PF-R Column Neck Bar N8
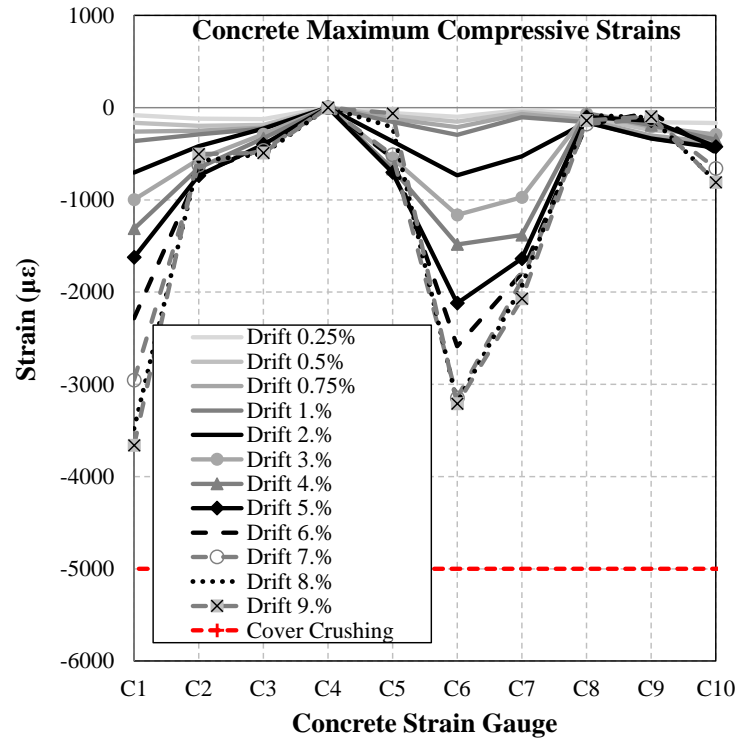
Figure 4.226. Measured UHPC Compressive Strain Profile for RPH-PF-R
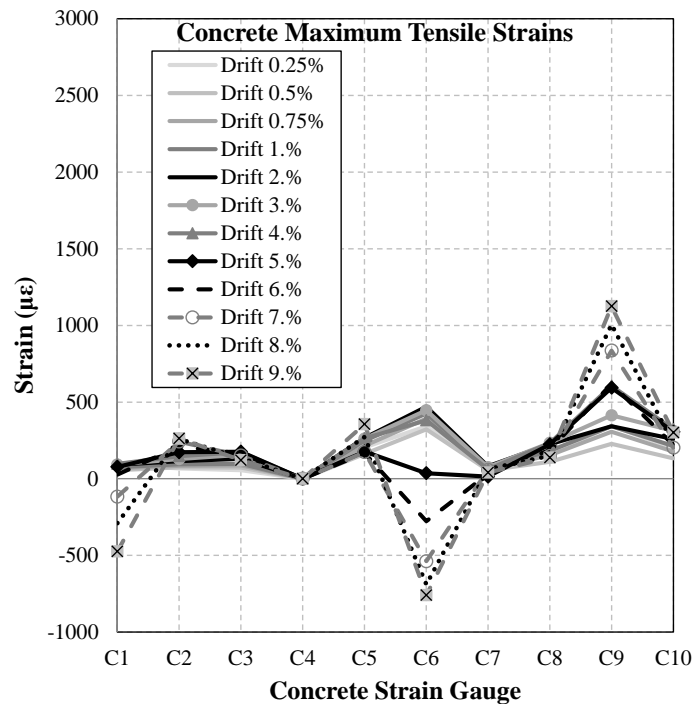
Figure 4.227. Measured UHPC Tensile Strain Profile for RPH-PF-R

Figure 4.228. Measured UHPC Strain Profile for RPH-PF-R East Face During Push Cycles

Figure 4.229. Measured UHPC Strain Profile for RPH-PF-R West Face During Push Cycles
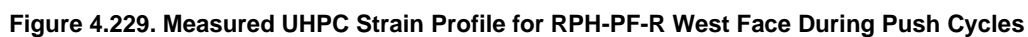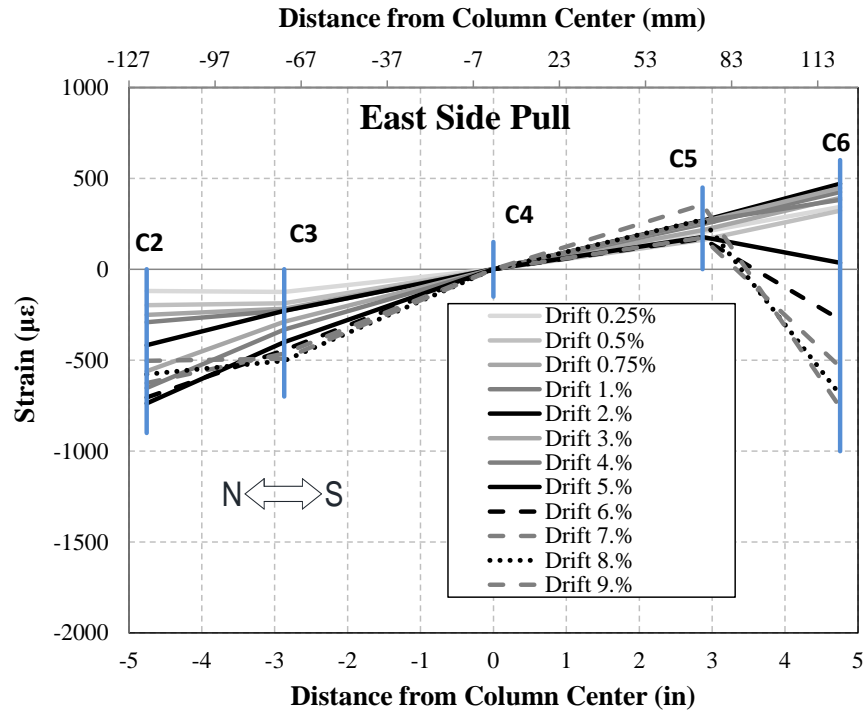
Figure 4.230. Measured UHPC Strain Profile for RPH-PF-R East Face During Pull Cycles
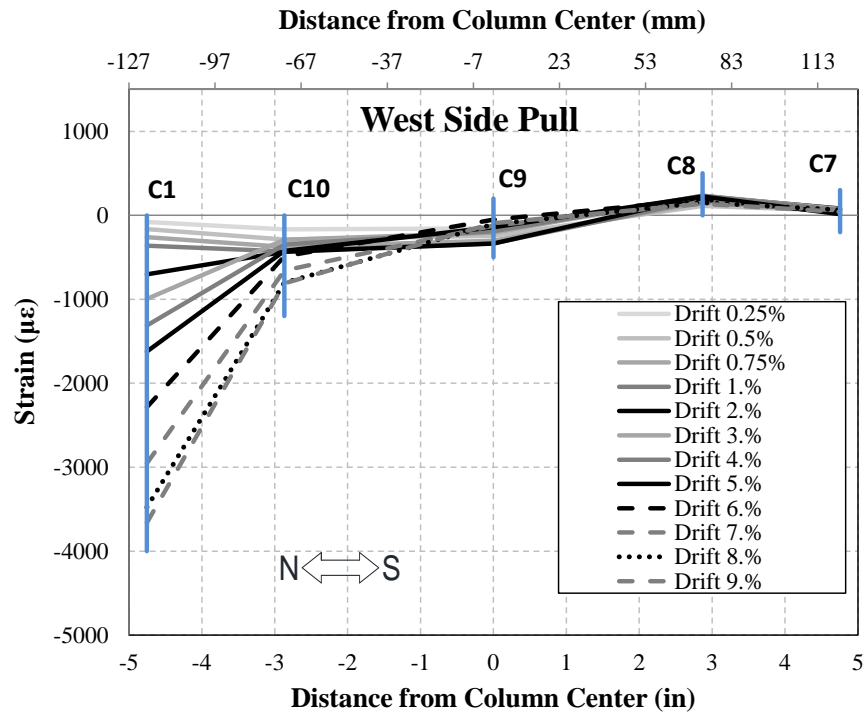
Figure 4.231. Measured UHPC Strain Profile for RPH-PF-R West Face During Pull Cycles

4.5.4.8 RPH-PF Measured Rotation and Curvature

Rotations and curvatures were recorded and determined in the same manner as RPH-PC and CIP. **Figure 4.232** shows the measured curvature profile for RPH-PF from drift ratios of 0.25% to 4.0%. The highest curvature was concentrated at the base of the column due to the rocking at the column base (steel baseplate). Limited curvatures occurred at the upper three levels. Measured curvature was also symmetric at both sides of the column.
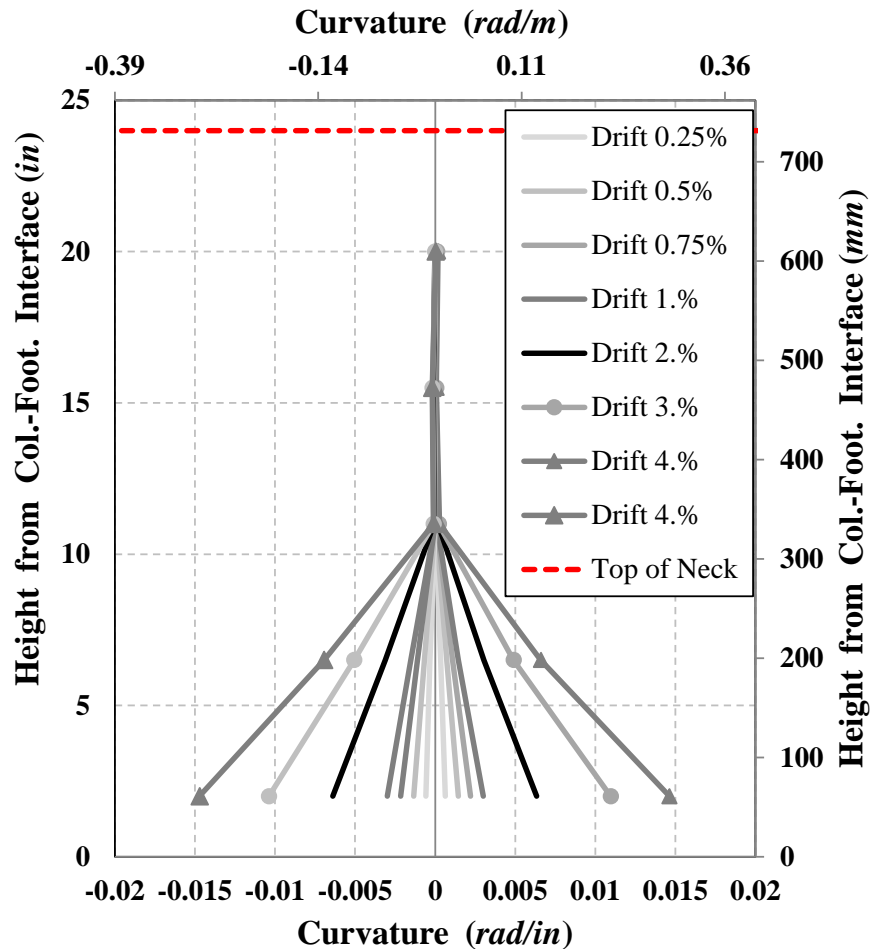
Figure 4.232. Measured Curvature Profile for RPH-PF Column

4.5.4.9 RPH-PF-R Measured Rotation and Curvature

Figure 4.233 shows the measured curvature profile for the RPH-PF-R column from drift ratios of 0.25% to 4.0%. The highest curvature was concentrated at the base of the column. The curvature profiles of RPH-PC and RPH-PF-R were overall similar in shape.
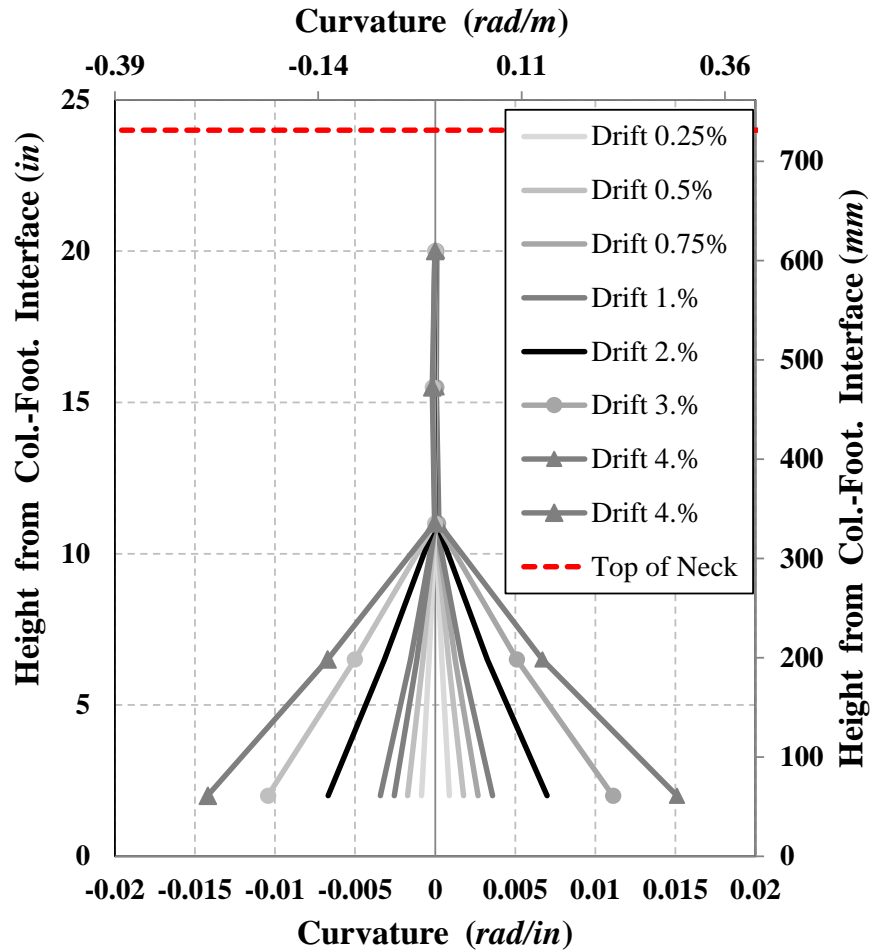
Figure 4.233. Measured Curvature Profile for RPH-PF-R Column

4.5.4.10 RHP-PF Energy Dissipation

The cumulative energy dissipation for RPH-PF is shown in **Fig. 4.234** for drift ratios of 0.25% until the end of the test at 4.0%. The dissipated energy is low until 0.5% drift ratio. RPH-PF dissipated a total of 216 kip-in. (24.4 kN-m) energy before the test was stopped at 4.0% drift ratio.
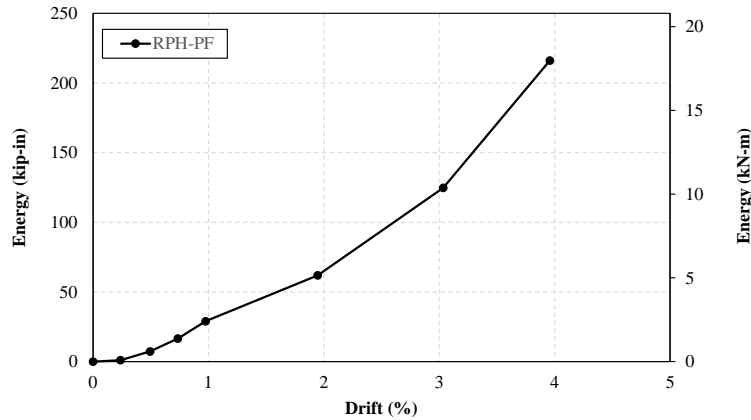
Figure 4.234. Measured Energy Dissipation for RPH-PF Column

4.5.4.11 RPH-PF-R Energy Dissipation

Figure 4.235 shows the cumulative energy dissipation for the RPH-PF-R column. The dissipated energy is low up to 1.0% drift ratio. RPH-PF-R dissipated a total of 1,094 kip-in. (123.6kN-m) energy at 10.0% drift ratio.
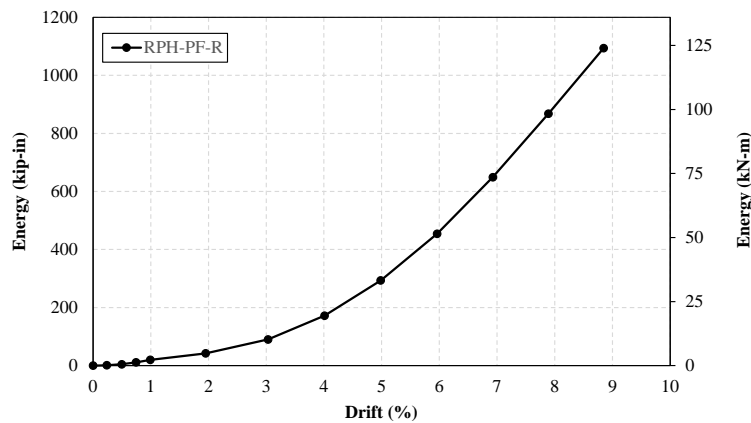
Figure 4.235. Measured Energy Dissipation for RPH-PF-R Column

4.5.5 RPH-NP Column Results

The performance of the RPH-NP repairable precast column is presented in this section.

4.5.5.1 RPH-NP Observed Damage

The testing of RPH-NP also followed the same cyclic loading protocol as the other columns. In the first round of experiment, the test was stopped at 4.0% drift to perform the repair.

A summary of the observed damage is presented in **Table 4.10** and **Fig. 4.236-4.249** show the damage of RPH-NP at each drift cycle. No damage was observed in the column until 0.75% drift ratio at which a crack was seen in the footing socket grout and at the column base (**Fig. 4.240**). Some flexural cracks were observed when the column was pulled to 0.75% and pushed to 2.0% drift (**Fig. 4.241** and **4.244**). Vertical cracks also occurred at the column base when pulled to 2.0% drift (**Fig. 4.245**). Minor spalling occurred at 3.0% while the crack due to uplift on the opposite end of the column widened (**Fig. 4.246**). Even though the neck bars of RPH-NP extended into the lower portion of the column inside the footing socket, the column acted as a rocking column. The rocking face uplifting gap continued to widen until the test was stopped at a drift ratio of 4.0% to replace the tendon fuses (**Fig. 4.248**).

Table 4.10. Summary of Damage in RPH-PC

Drift Ratio, %	Observed Damage
+0.25	• No noticeable damage
-0.25	• No noticeable damage
+0.50	• No noticeable damage
-0.50	• No noticeable damage
+0.75	• Cracking and minor uplift at column base
-0.75	• Cracking in upper layer of footing socket grout • Flexural cracking in column neck section
+1.00	• No further damage
-1.00	• No further damage
+2.00	• Further flexural cracks in neck
-2.00	• Vertical cracks near column base
+3.00	• Minor spalling at column base
-3.00	• Crack at column base widens
+4.00	• Flexural cracks above neck section on south face • Crack at column base widens
-4.00	• Crack at column base widens

Note: Positive drifts were based on displacements away from the reaction blocks (north to south)

a) North-West Side   b) South-East Side

Figure 4.236. RPH-NP Column Plastic Hinge Damage, Second Push of 0.25% Drift Cycle

a) North-West Side   b) South-East Side

Figure 4.237. RPH-NP Column Plastic Hinge Damage, Second Pull of 0.25% Drift Cycle

a) North-West Side   b) South-East Side
Figure 4.238. RPH-NP Column Plastic Hinge Damage, Second Push of 0.50% Drift Cycle

a) North-West Side   b) South-East Side
Figure 4.239. RPH-NP Column Plastic Hinge Damage, Second Pull of 0.50% Drift Cycle

a) North-West Side   b) South-East Side
Figure 4.240. RPH-NP Column Plastic Hinge Damage, Second Push of 0.75% Drift Cycle
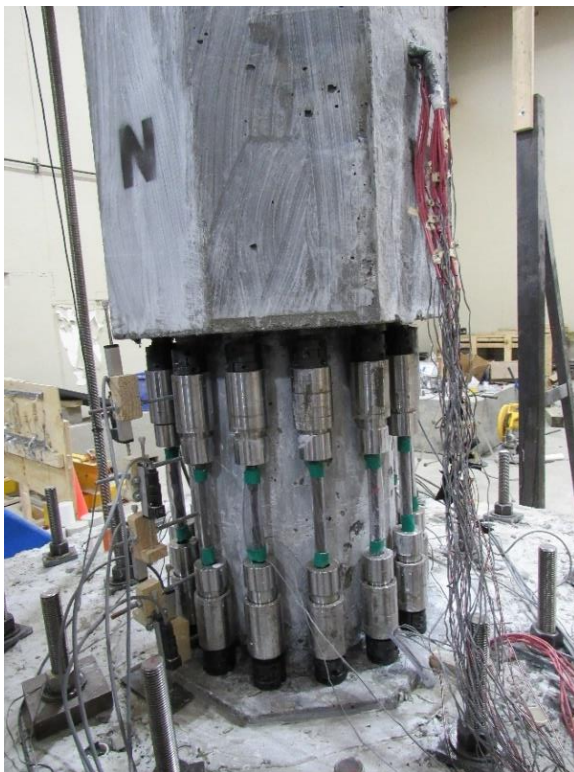
a) North-West Side   b) South-East Side
Figure 4.241. RPH-NP Column Plastic Hinge Damage, Second Pull of 0.75% Drift Cycle

212

a) North-West Side   b) South-East Side
Figure 4.242. RPH-NP Column Plastic Hinge Damage, Second Push of 1.0% Drift Cycle
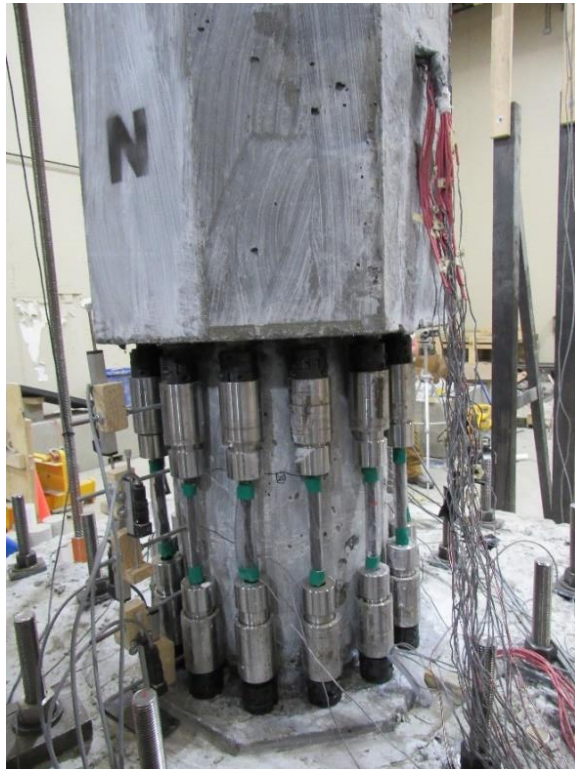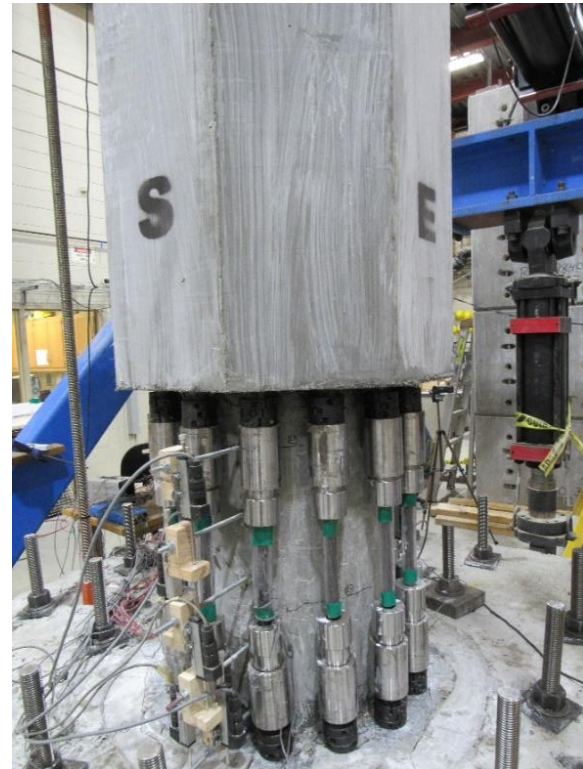
a) North-West Side   b) South-East Side
Figure 4.243. RPH-NP Column Plastic Hinge Damage, Second Pull of 1.0% Drift Cycle

213
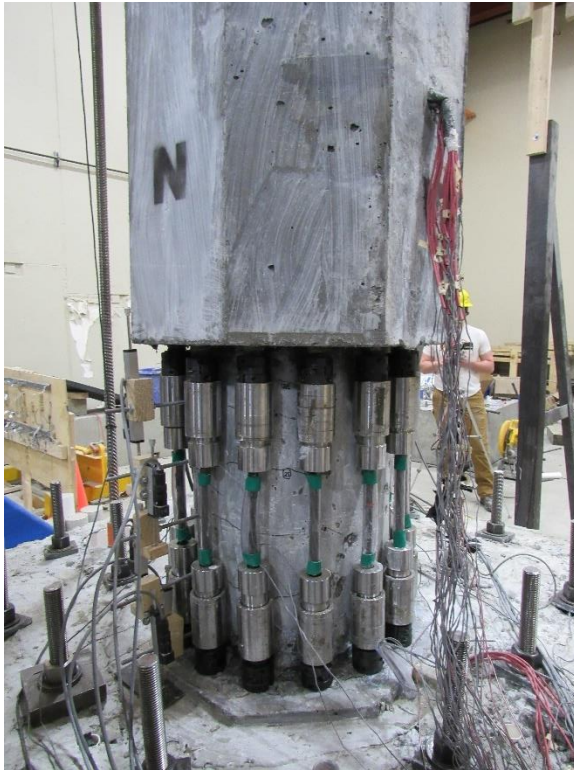
a) North-West Side   b) South-East Side
Figure 4.244. RPH-NP Column Plastic Hinge Damage, Second Push of 2.0% Drift Cycle

a) North-West Side   b) South-East Side
Figure 4.245. RPH-NP Column Plastic Hinge Damage, Second Pull of 2.0% Drift Cycle
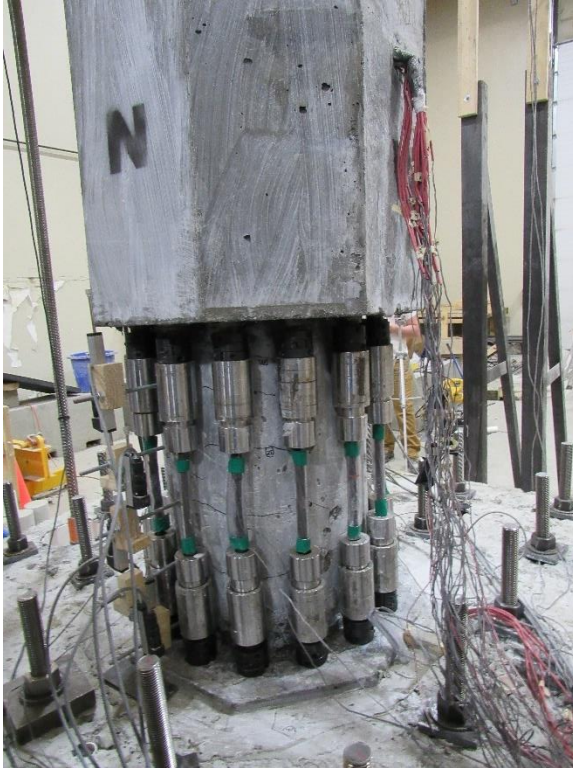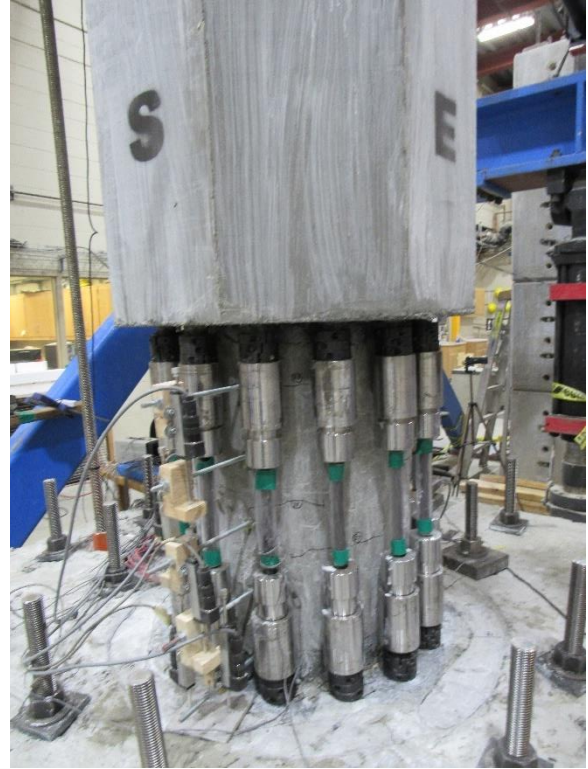
a) North-West Side   b) South-East Side

Figure 4.246. RPH-NP Column Plastic Hinge Damage, Second Push of 3.0% Drift Cycle

a) North-West Side   b) South-East Side

Figure 4.247. RPH-NP Column Plastic Hinge Damage, Second Pull of 3.0% Drift Cycle

a) North-West Side   b) South-East Side

Figure 4.248. RPH-NP Column Plastic Hinge Damage, Second Push of 4.0% Drift Cycle

a) North-West Side   b) South-East Side

Figure 4.249. RPH-NP Column Plastic Hinge Damage, Second Pull of 4.0% Drift Cycle

4.5.5.2 Repair of RPH-NP Column

Testing of RPH-NP was stopped after two cycles of 4.0% drift ratio to remove and replace the exposed tendon fuses. The clamping collars were removed before the couplers could be unscrewed. The wedges had once again become set between the tendons and female portion of the couplers and had to be removed in the same manner as RPH-PF by cutting the tendons and striking the cut end against the lab strong floor. No damage to the wedges or couplers occurred during any of the column tests or repair.

Tendons in the same length as the previous tests were cut and assembled with the prestressing wedges and male portion of the couplers. The new tendon fuses were then installed into the column. The clamping collars were not placed for the second set of testing since no damage or buckling of the column/footing dowel bars was observed. **Figure 4.250** shows the RPH-NP-R column conditions prior to retesting.

a) North-East Side   b) South-East Side
Figure 4.250. RPH-NP-R Column Plastic Hinge Damage before Retesting

4.5.5.3 RPH-NP-R Observed Damage

No change in testing protocol was made for the RPH-NP-R column compared with others. The column was tested to failure and the observed damage was documented in **Table. 4.11**. **Figures 4.251-4.272** show the column observed damage at different drifts. New cracks were marked in red for the second round of testing.

No further damage was noticed until 2.0% drift when some vertical cracks were found on the neck section (**Fig. 4.259**). At 4.0% drift, further vertical and flexural cracks were observed (**Fig. 4.263-4.264**). Yielding of the extreme tendon fuses on both the north and south faces occurred during 5.0% drift ratio (**Fig. 4.265-4.266**) and the gap at the base of the column continued to widen exceeding 0.5 in. (13mm). This gap exceeded 1.0 in. (25 mm) at 7.0% drift ratio (**Fig. 4.269**). During the first pull at 7.0% drift ratio, a loud pop was heard which was attributed to the fracture of one of the neck longitudinal bars on the south side (bars inside the neck not the exposed tendons, **Fig. 4.270**). Two more neck bars fractured during the first push to 8.0% drift ratio (**Fig. 4.271**), resulting in a large drop in the lateral force resistance and the test was stopped. No rupture of the tendon fuses was observed in the RPH-NP-R column.

Unlike RPH-PC-R and RPH-PF-R, the RPH-NP-R column was not designed for deconstruction and could not be disassembled due to the column socket connection. While at least three longitudinal bars ruptured within the neck section, visible damage remained minor with only flexural cracks and minor spalling at the column base throughout the test.

Table 4.11. Summary of Damage in RPH-PC-R

Drift Ratio, %	Observed Damage
Beginning of Test	• Minor concrete spalling at column base • Minor flexural cracks above and on neck section
+0.25	• No further damage
-0.25	• No further damage
+0.50	• No further damage
-0.50	• No further damage
+0.75	• No further damage
-0.75	• No further damage
+1.00	• No further damage
-1.00	• No further damage
+2.00	• Small vertical crack on neck section on North face
-2.00	• Vertical crack above neck section on South face
+3.00	• No further damage
-3.00	• No further damage
+4.00	• Vertical crack above and on neck section on North face • Minor flexural cracks throughout column
-4.00	• Further vertical cracks above and on neck section on South face • Minor flexural cracks throughout column
+5.00	• Yielding of tendon on North side • Crack/uplift at column base exceeds 0.5 in. (13 mm)
-5.00	• Yielding of tendon on South side
+6.00	• Column uplift worsens
-6.00	• Column uplift worsens
+7.00	• Crack/uplift at column base exceeds 1 in. (25 mm)
-7.00	• Rupture of two neck bars on the South side
+8.00	• Rupture of additional neck bar on the North side • Some tendon buckling noticeable before wedge pops
-8.00	• Further minor spalling at column base

Note: Positive drifts were based on displacements away from the reaction blocks (north to south)

a) North-West Side   b) South-East Side
Figure 4.251. RPH-NP-R Column Plastic Hinge Damage, Second Push of 0.25% Drift Cycle
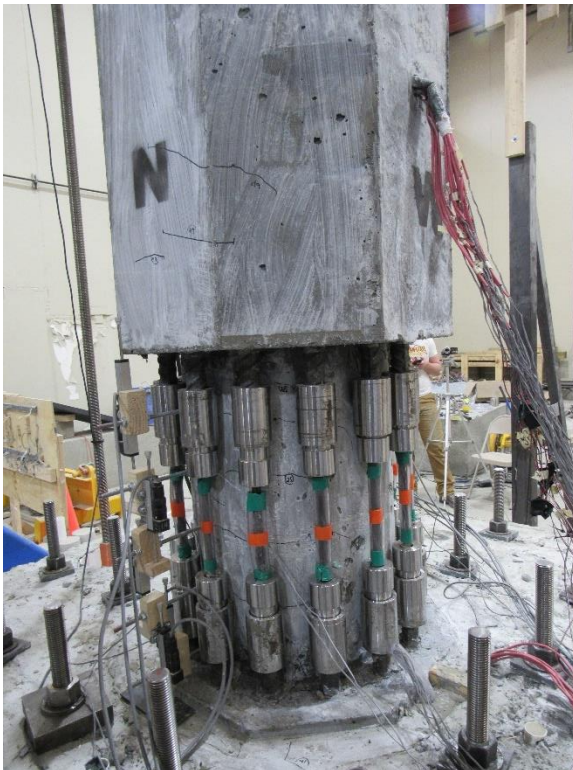
a) North-West Side   b) South-East Side
Figure 4.252. RPH-NP-R Column Plastic Hinge Damage, Second Pull of 0.25% Drift Cycle

a) North-West Side　　　　　　　　　　　　b) South-East Side

Figure 4.253. RPH-NP-R Column Plastic Hinge Damage, Second Push of 0.50% Drift Cycle
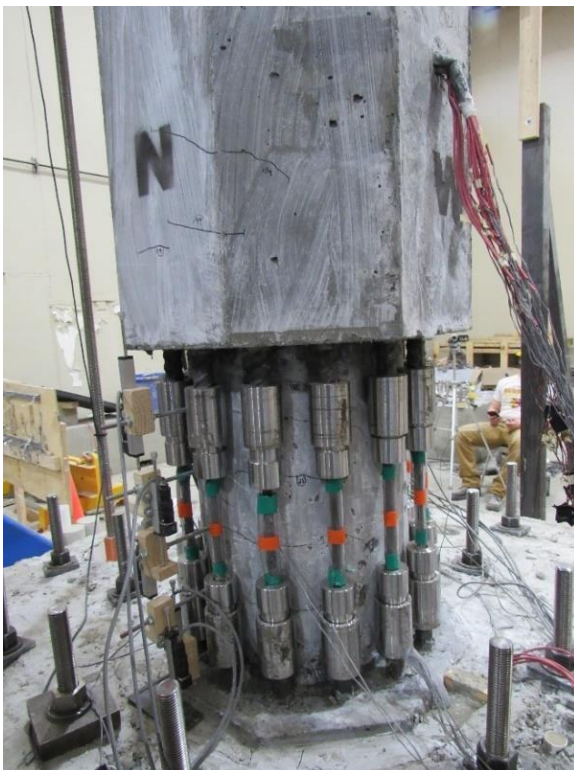
a) North-West Side　　　　　　　　　　　　b) South-East Side

Figure 4.254. RPH-NP-R Column Plastic Hinge Damage, Second Pull of 0.50% Drift Cycle
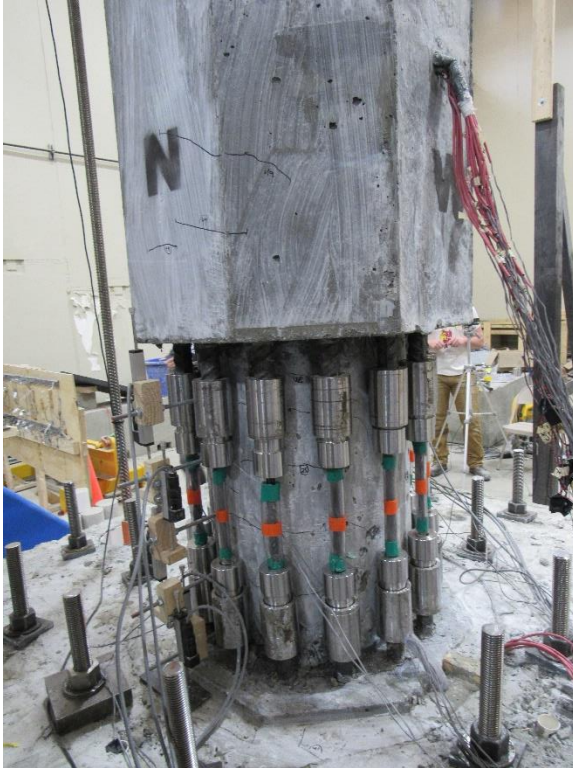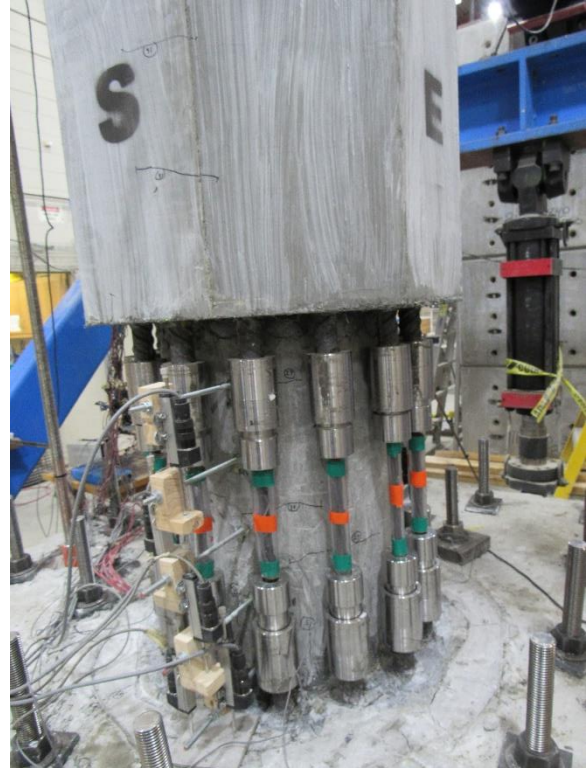
a) North-West Side   b) South-East Side
Figure 4.255. RPH-NP-R Column Plastic Hinge Damage, Second Push of 0.75% Drift Cycle
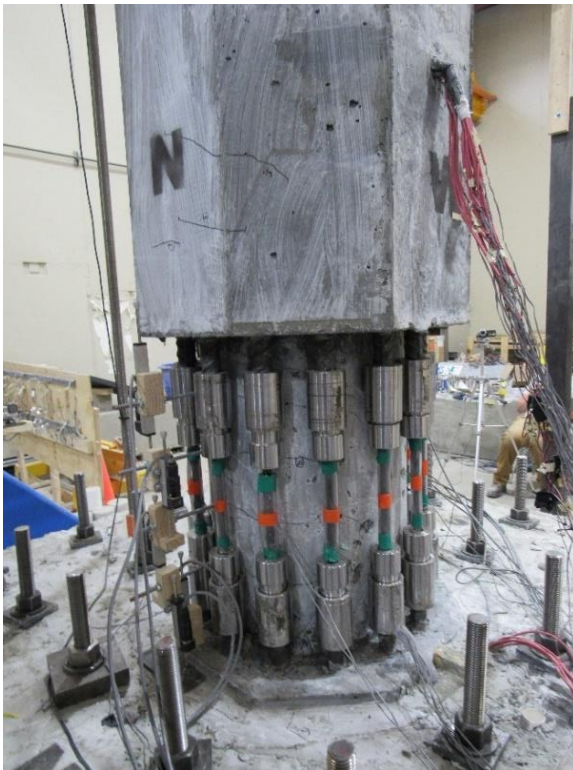
a) North-West Side   b) South-East Side
Figure 4.256. RPH-NP-R Column Plastic Hinge Damage, Second Pull of 0.75% Drift Cycle

221
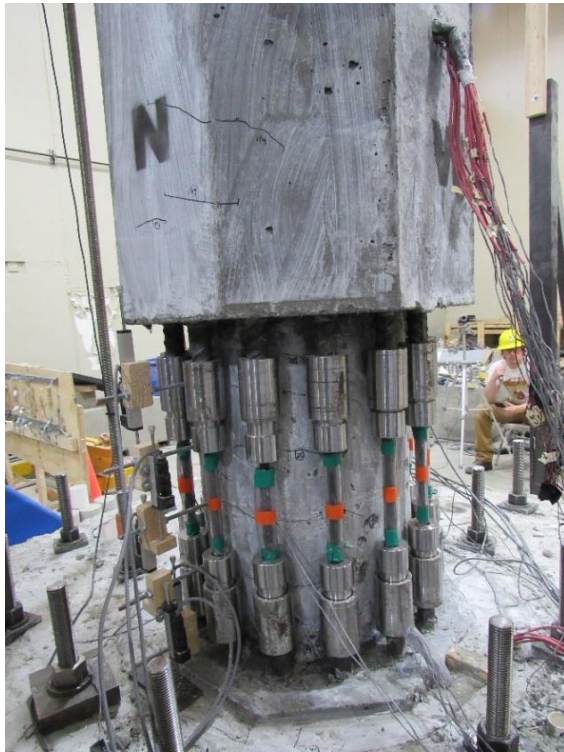
a) North-West Side   b) South-East Side
Figure 4.257. RPH-NP-R Column Plastic Hinge Damage, Second Push of 1.0% Drift Cycle

a) North-West Side   b) South-East Side
Figure 4.258. RPH-NP-R Column Plastic Hinge Damage, Second Pull of 1.0% Drift Cycle

a) North-West Side   b) South-East Side

Figure 4.259. RPH-NP-R Column Plastic Hinge Damage, Second Push of 2.0% Drift Cycle

a) North-West Side   b) South-East Side

Figure 4.260. RPH-NP-R Column Plastic Hinge Damage, Second Pull of 2.0% Drift Cycle

a) North-West Side

b) South-East Side

Figure 4.261. RPH-NP-R Column Plastic Hinge Damage, Second Push of 3.0% Drift Cycle

a) North-West Side

b) South-East Side

Figure 4.262. RPH-NP-R Column Plastic Hinge Damage, Second Pull of 3.0% Drift Cycle
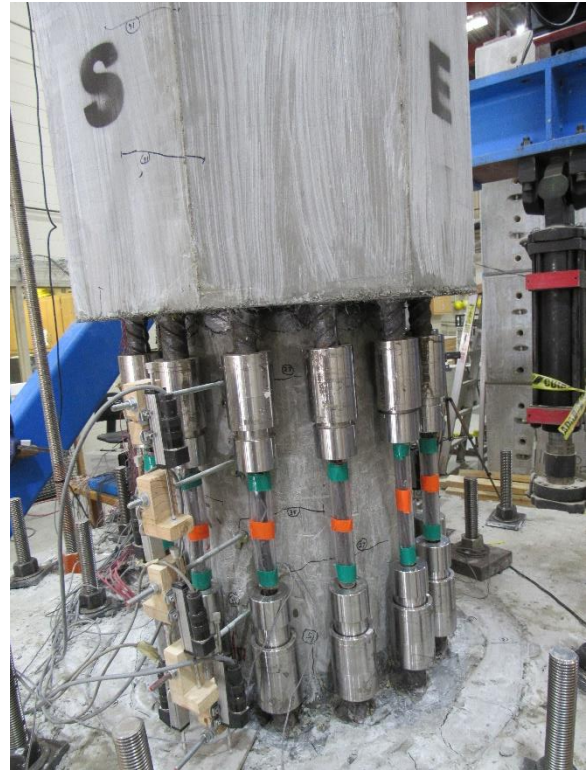
a) North-West Side   b) South-East Side

Figure 4.263. RPH-NP-R Column Plastic Hinge Damage, Second Push of 4.0% Drift Cycle

a) North-West Side   b) South-East Side

Figure 4.264. RPH-NP-R Column Plastic Hinge Damage, Second Pull of 4.0% Drift Cycle

a) North-West Side   b) South-East Side

Figure 4.265. RPH-NP-R Column Plastic Hinge Damage, Second Push of 5.0% Drift Cycle

a) North-West Side   b) South-East Side

Figure 4.266. RPH-NP-R Column Plastic Hinge Damage, Second Pull of 5.0% Drift Cycle

a) North-West Side   b) South-East Side

Figure 4.267. RPH-NP-R Column Plastic Hinge Damage, Second Push of 6.0% Drift Cycle

a) North-West Side   b) South-East Side

Figure 4.268. RPH-NP-R Column Plastic Hinge Damage, Second Pull of 6.0% Drift Cycle

a) North-West Side
b) South-East Side
Figure 4.269. RPH-NP-R Column Plastic Hinge Damage, Second Push of 7.0% Drift Cycle

a) North-West Side
b) South-East Side
Figure 4.270. RPH-NP-R Column Plastic Hinge Damage, Second Pull of 7.0% Drift Cycle

a) North-West Side

b) South-East Side

Figure 4.271. RPH-NP-R Column Plastic Hinge Damage, Second Push of 8.0% Drift Cycle

a) North-West Side

b) South-East Side

Figure 4.272. RPH-NP-R Column Plastic Hinge Damage, Second Pull of 8.0% Drift Cycle

4.5.5.4 RPH-NP Force-Displacement Relationship

Figure 4.273 shows the measured force-drift hysteresis and envelope for RPH-NP. This test was stopped at 4.0% drift to replace the tendon fuses. The maximum lateral load of 85.09 kips (378 kN) occurred in the push direction when the test was stopped at 3.90% drift. The column had a slightly higher lateral load capacity in the push direction but showed a similar stiffness in both directions. No yielding of tendon fuses occurred during the testing of RPH-NP. The hysteresis of RPH-NP was slightly fatter than that of RPH-PF mainly due to the yielding of neck longitudinal bars. Furthermore, residual displacements were larger than those of RPH-PF despite the use of 15 post-tensioning tendons as the recentering mechanism. **Figure 4.274** shows the average envelope of the push and pull directions for RPH-NP. No idealization was carried out since the tendons did not yield and the column did not fail.
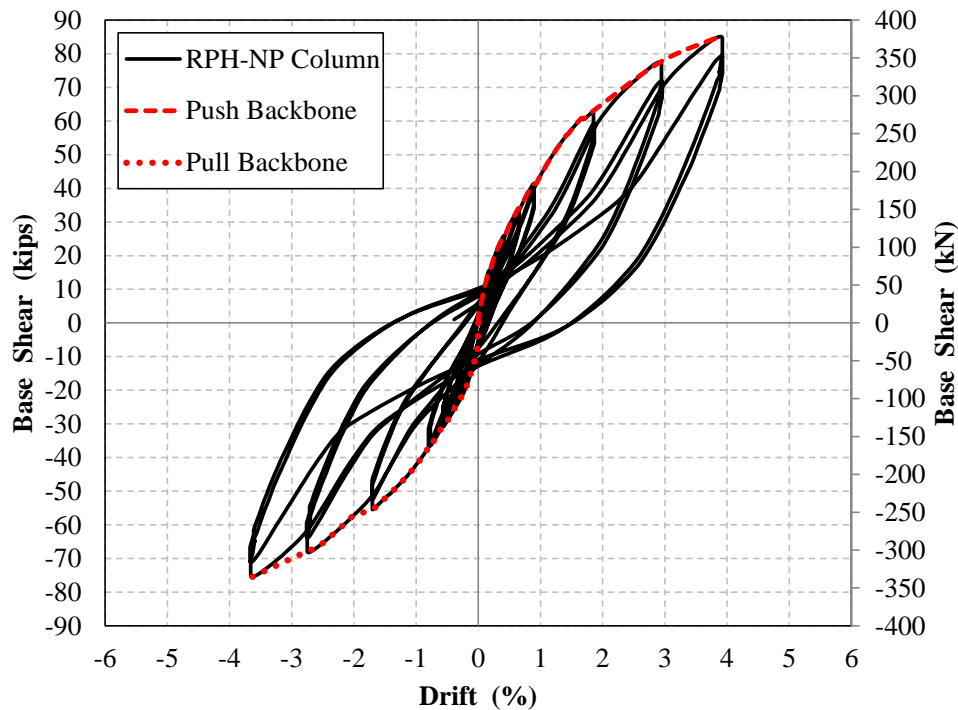
Figure 4.273. Measured RPH-NP Column Force-Drift Hysteretic and Envelope Responses
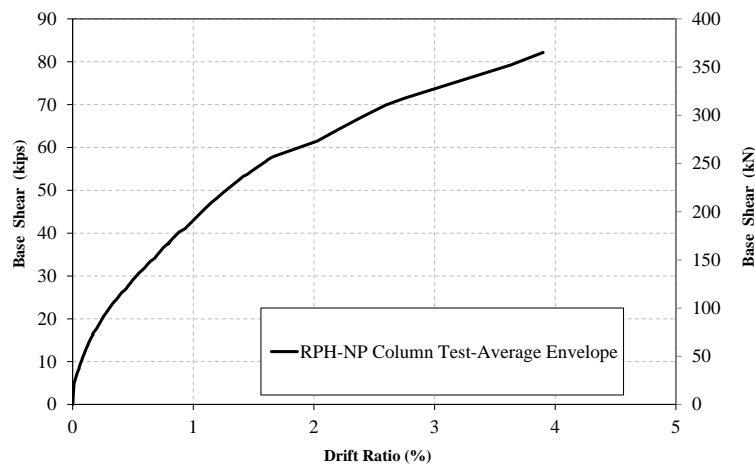
Figure 4.274. Measured RPH-NP Column Average Push/Pull Force-Drift Envelope

4.5.5.5 RPH-NP-R Force-Displacement Relationship

Figure 4.275 shows the measured lateral force-drift hysteretic and envelope for RPH-NP-R. A strength degradation of over 15% occurred in the pull direction after two neck bars ruptured during the 7.0% drift ratio cycle. The test was stopped at 8.0% drift ratio after an additional neck bar ruptured during the first push cycle.

The maximum lateral load of 86.9 kips (387 kN) occurred in the pull direction at a drift ratio of 5.78%. The column had similar overall stiffness in both directions. The tendon fuses yielded in the push direction at a drift ratio of 4.99% and a load of 81.0 kips (360 kN), and in the pull direction at a drift ratio of 4.44% and a lateral load of 76.7 kips (341 kN). No yielding of the 15 post-tensioning tendons (the tendons at the center of the column) occurred during the test. The hysteresis again indicated some residual displacements after large drift cycles mainly due to the yielding of the neck bars. However, the final two loops after which the three neck bars ruptured were flag shaped with smaller residual displacements than previous cycles, indicating that the post-tensioning tendons were more efficient in recentering the column after the loss of neck bars. Furthermore, the rebar hinge incorporated at the base of the neck section increased the column lateral strength by 45% compared with RPH-PF.
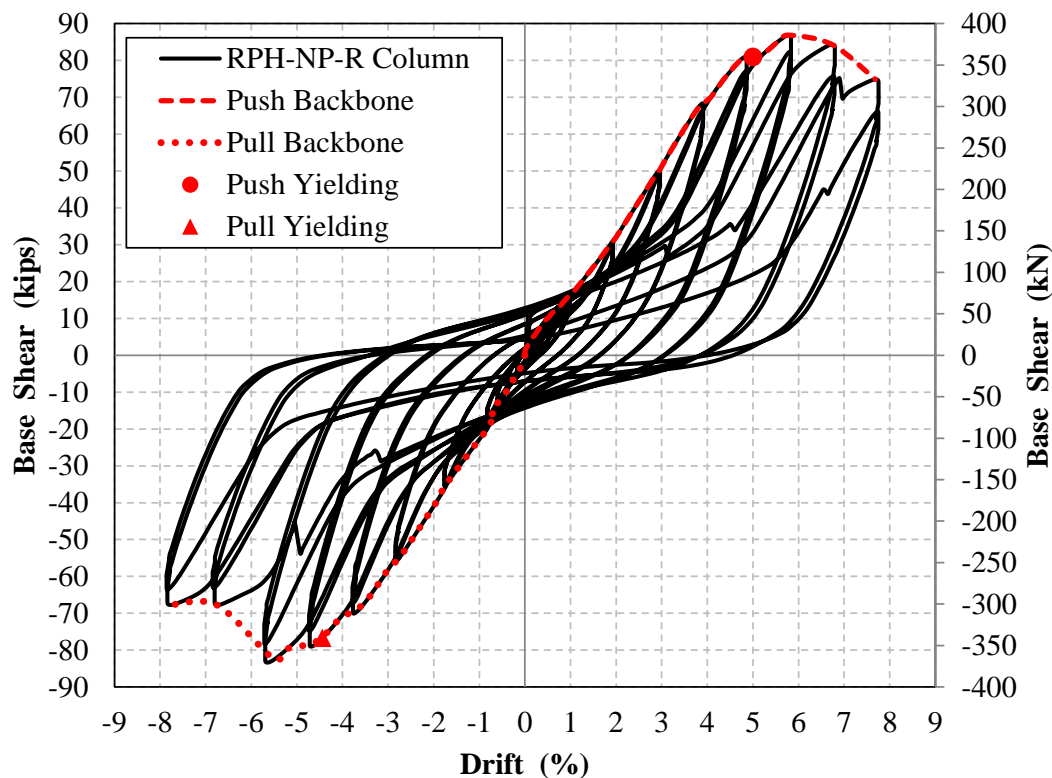
Figure 4.275. Measured RPH-NP-R Column Force-Drift Hysteretic and Envelope Responses

Figure 4.276 shows the average envelope of the push and pull directions for the RPH-NP-R column. The average yield drift ratio was 4.72% at a lateral load of 79.1 kips (351 kN). The idealized curve is also included in the figure. The effective yield was also at 4.72% drift ratio and 79.1 kips (351 kN). The drift capacity of the column was 7.68%. The resulting displacement ductility capacity was 1.63 for the RPH-NP-R column which is not a good measure of column performance since the tendons yielded at such high drifts. RPH-PC-R column exhibited a slightly lower drift capacity compared with the CIP column (7.68 vs 8.96%).
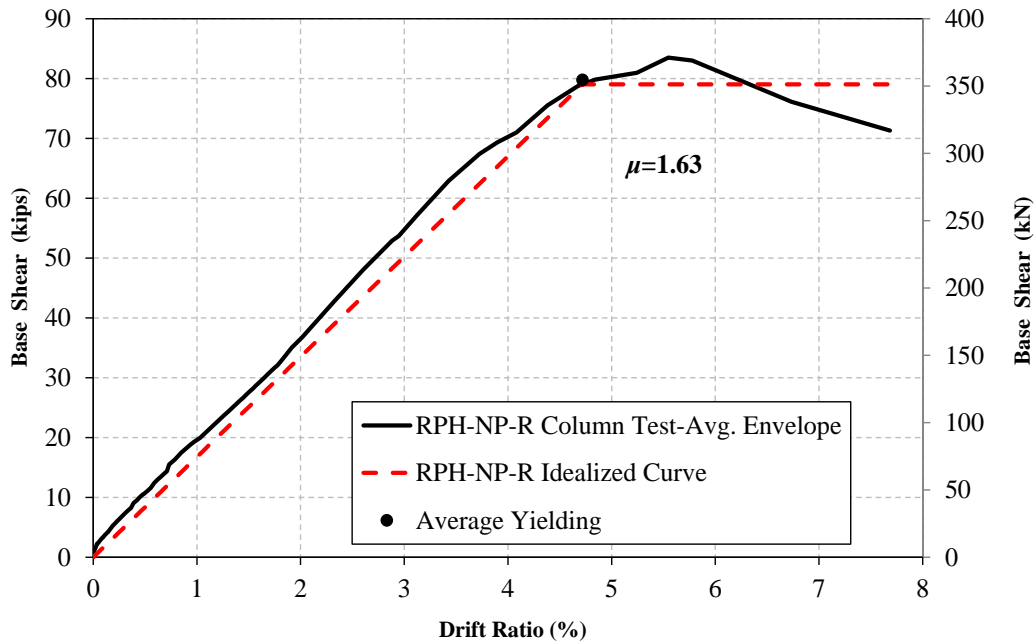
Figure 4.276. Measured RPH-NP-R Column Average Push/Pull Force-Drift Envelope and Idealized Curve

Figure 4.277 compared the average backbones of RPH-NP, RPH-NP-R, and CIP. The initial stiffness of RPH-NP was slightly lower than that of CIP but there was a significant stiffness degradation in the column retesting (RPH-NP-R), likely due to the UHPC cracking and uplift at the base of the column. It would be desirable for the stiffness of a repaired column to remain the same as in retesting.
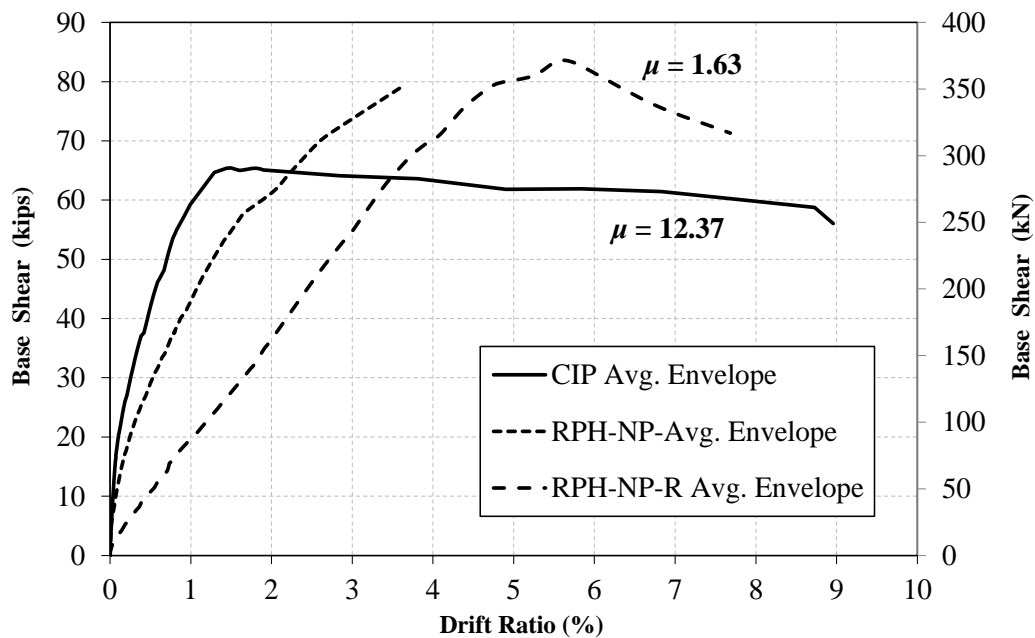
Figure 4.277. Measured Force-Drift Response of CIP, RPH-NP, and RPH-NP-R Columns

232

4.5.5.6 RPH-NP Strain Profiles

Forty-six steel strain gauges were installed on the RPH-NP column at five levels along the column height. Furthermore, five strain gauges were placed on the post-tensioning tendons. **Figures 4.278-4.281** show the measured strain profiles for Bars/Tendons 1, 3, 8, and 10. The strains were mainly concentrated at the center two levels, which were placed on the tendon fuses. No yielding of the tendon fuses occurred during the first testing of RPH-NP. Furthermore, minor yielding occurred in three steel bars below the footing surface.

Compressive strains were also plotted (**Fig. 4.282-4.285**). Tendons 3 and 10 experienced some minor compressive strains at higher drift ratios while strain gauges on Tendons 1 and 8 recorded limited compressive strains. The outer two levels of strain gauges placed on all four steel bars also experienced limited compressive strains.

Strain profiles along the No. 9 (12-Ø29 mm) conventional steel bars in the neck section were also generated to validate the neck section design (**Fig. 4.286-4.289**). The numbering system for the neck bars was the same as that used in RPH-PF. Most of the strains were concentrated at the lower strain gauge levels near the base of the neck section. While the data indicates no yielding of the steel bars in the neck, it is evident that significant yielding occurred at the column-footing interface where the rebar hinge was incorporated since neck longitudinal bars fractured at this level. No strain gauges were installed at this level.

Concrete strain gauges were installed in the same pattern as the other two repairable columns to compare the measured concrete strains at the base of the neck section. **Figures 4.290** and **4.291** show the measured concrete compressive and tensile strain profiles for RPH-NP with positive values representing tensile strains and negative values representing compressive strains.

The maximum strains were recorded in strain gauges C1 on the north face and C7 on the south face. Gauge C7 recorded compressive strains above the strain capacity of the unconfined cover concrete, but still well below the capacity of the confined concrete. **Figures 4.292-4.295** show the strain profiles along the east and west faces of the column during both push and pull cycles. Overall, it can be observed that during push cycles the gauges on the north side experienced tensile strains while the gauges on the south experienced compressive strains while the opposite is true during pull cycles.
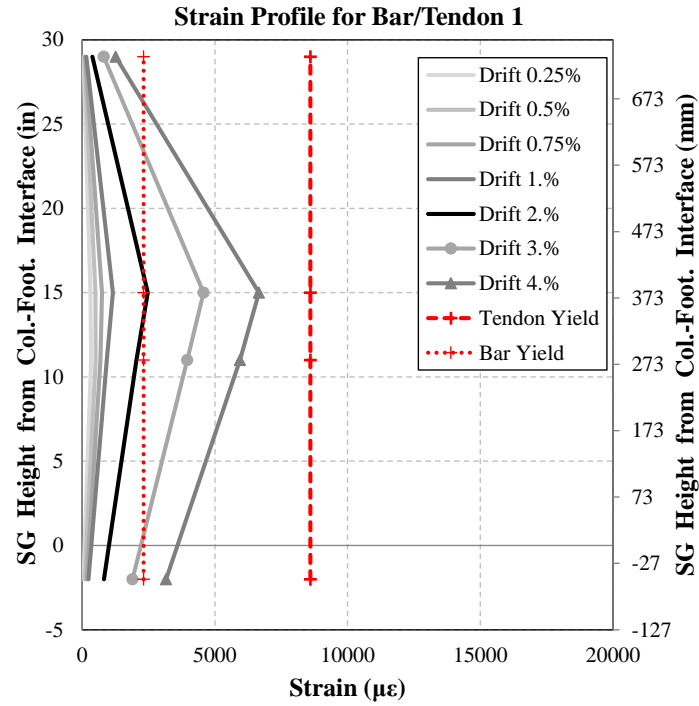
Figure 4.278. Measured Tensile Strain Profile for RPH-NP Column Bar/Tendon 1
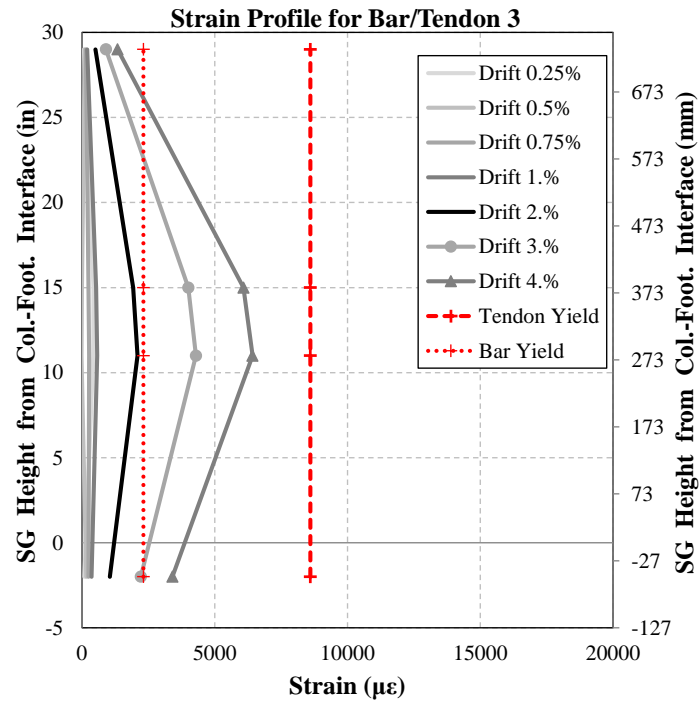
Figure 4.279 Measured Tensile Strain Profile for RPH-NP Column Bar/Tendon 3
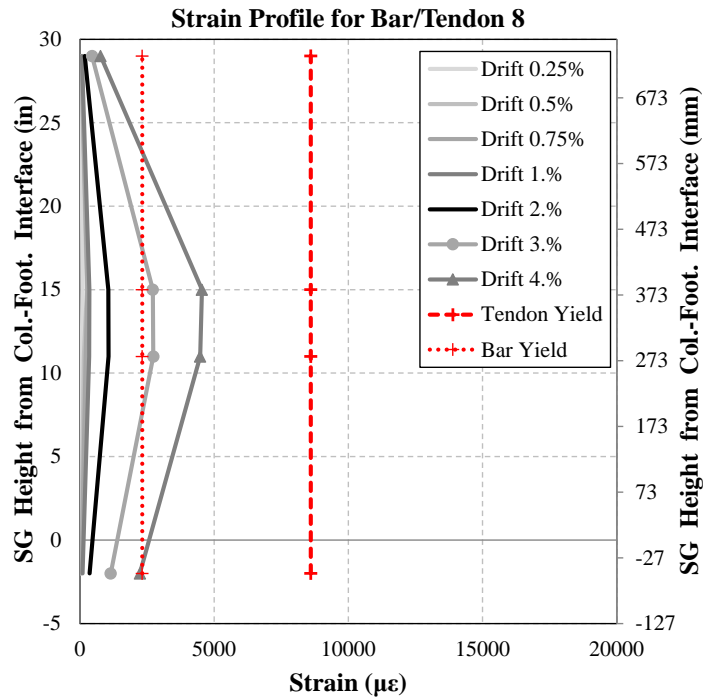
Figure 4.280. Measured Tensile Strain Profile for RPH-NP Column Bar/Tendon 8
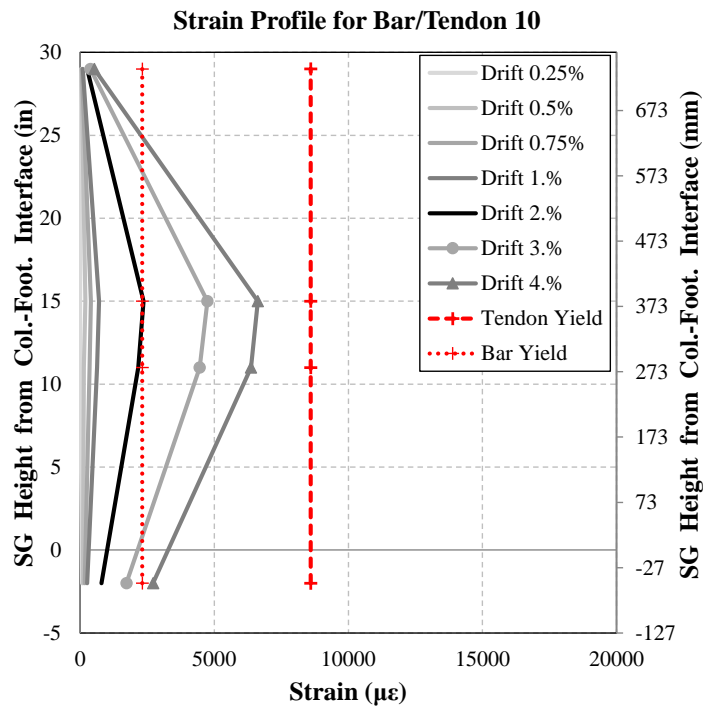
Figure 4.281. Measured Tensile Strain Profile for RPH-NP Column Bar/Tendon 10
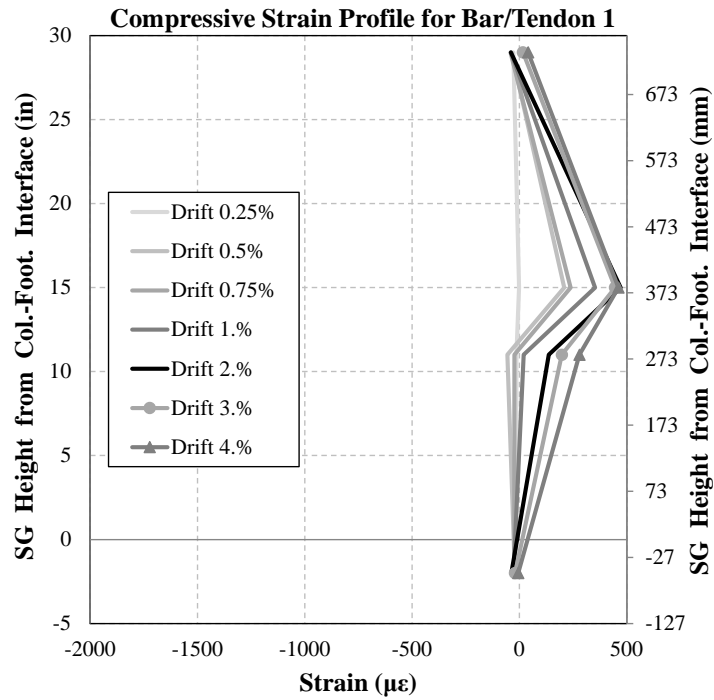
Figure 4.282. Measured Compressive Strain Profile for RPH-NP Column Bar/Tendon 1
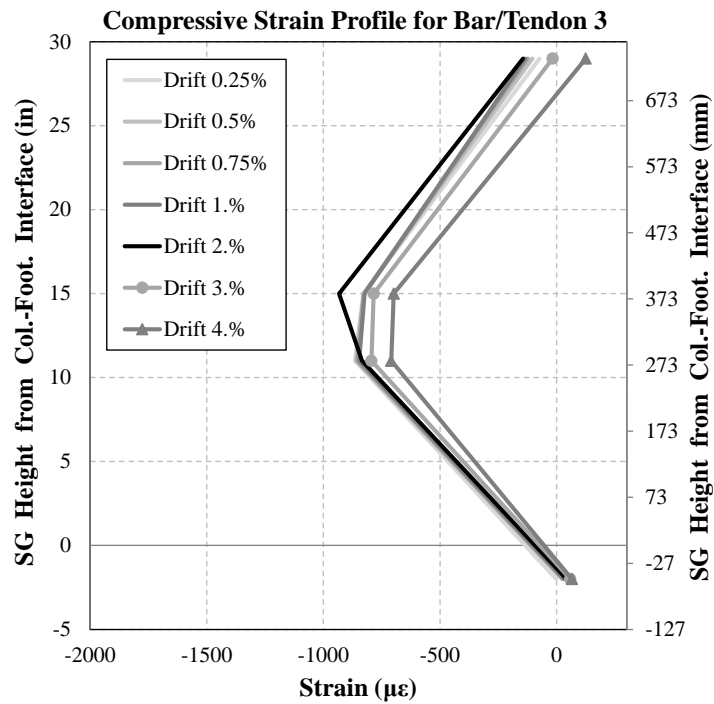
Figure 4.283. Measured Compressive Strain Profile for RPH-NP Column Bar/Tendon 3

236
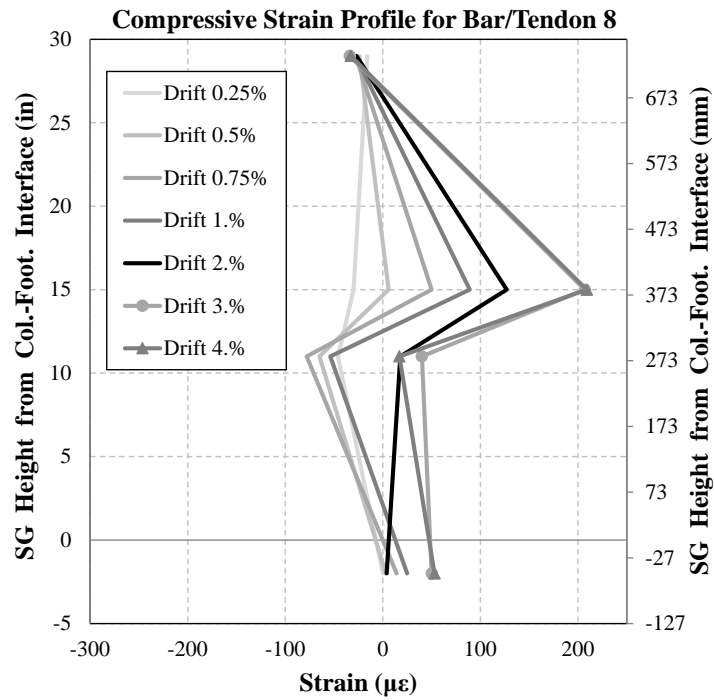
Figure 4.284. Measured Compressive Strain Profile for RPH-NP Column Bar/Tendon 8
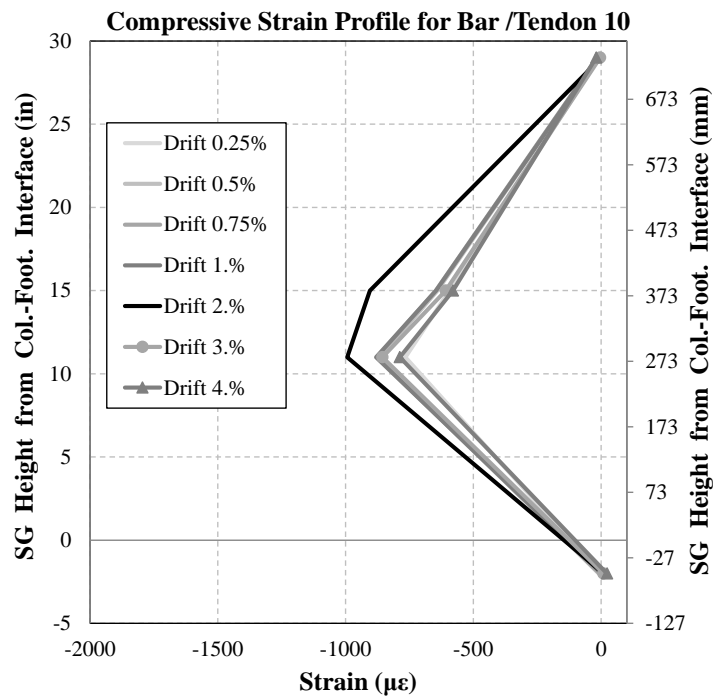
Figure 4.285. Measured Compressive Strain Profile for RPH-NP Column Bar/Tendon 10

237
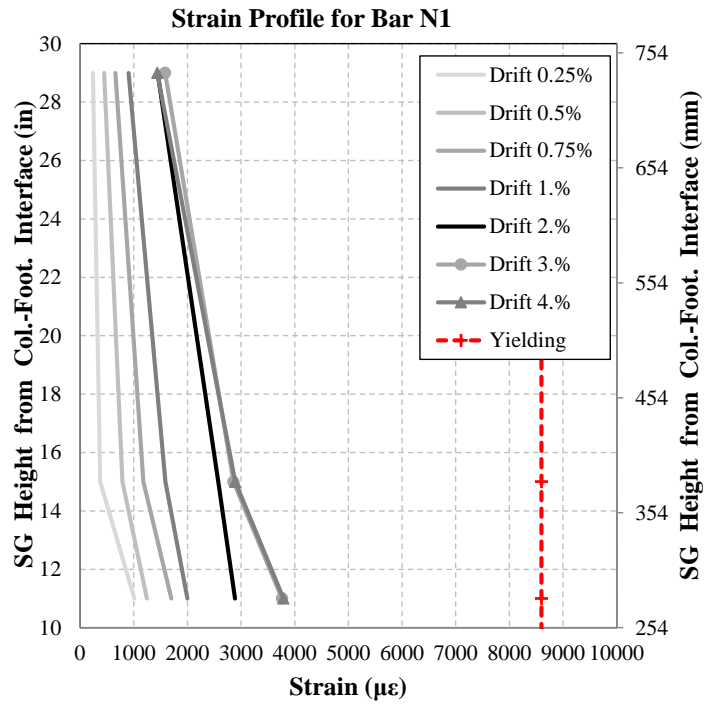
Figure 4.286. Measured Strain Profile for RPH-NP Column Neck Bar N1
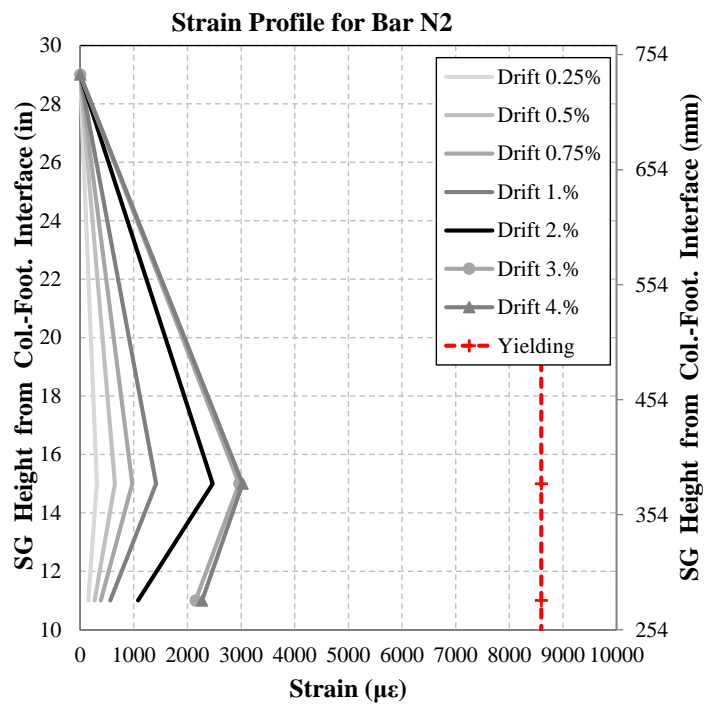
Figure 4.287. Measured Strain Profile for RPH-NP Column Neck Bar N2
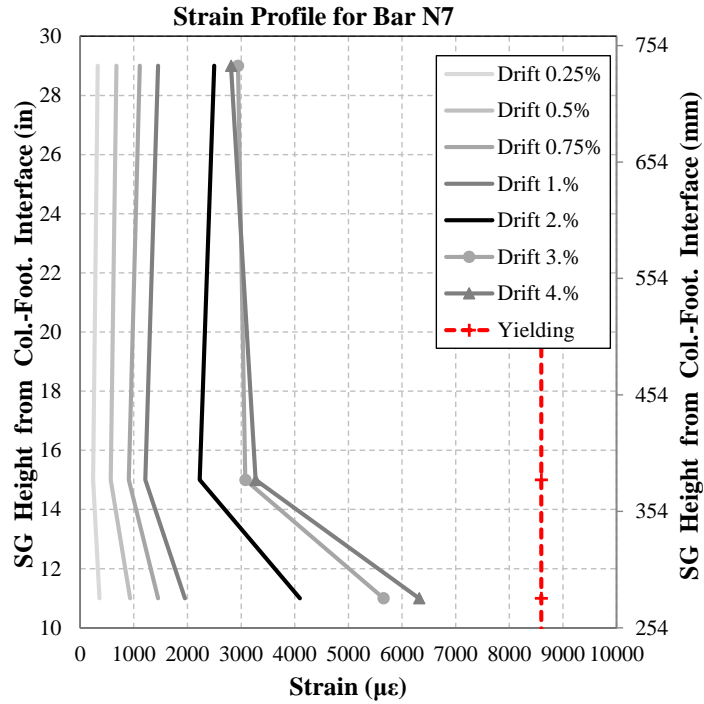
Figure 4.288. Measured Strain Profile for RPH-NP Column Neck Bar N7
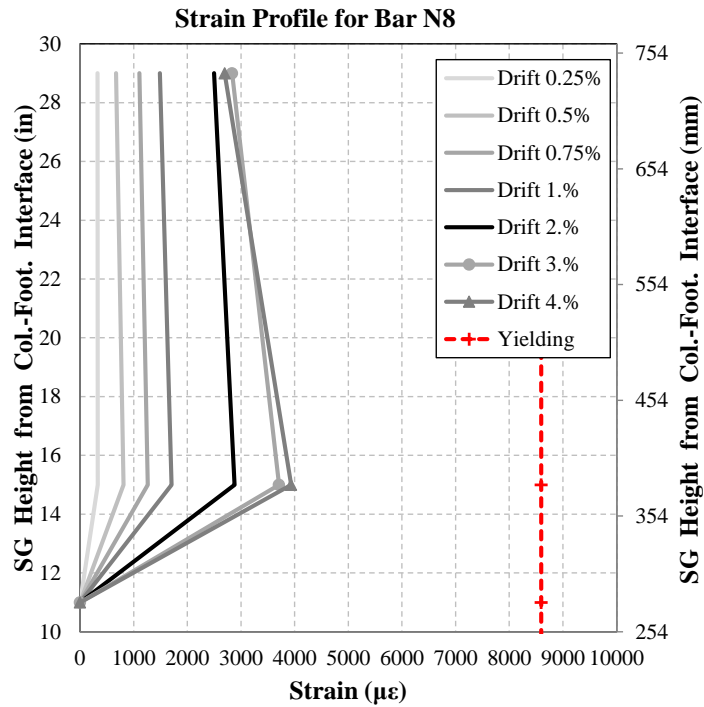
Figure 4.289. Measured Strain Profile for RPH-NP Column Neck Bar N8

239
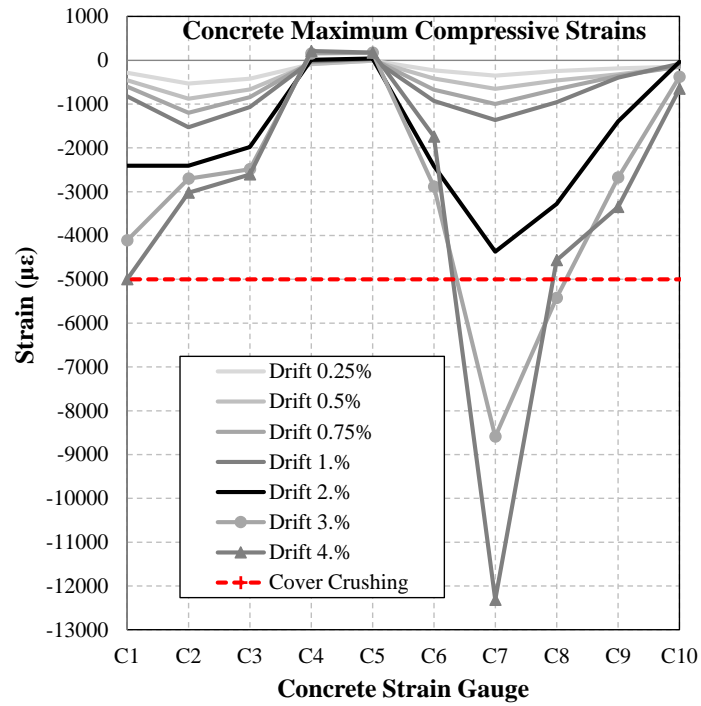
Figure 4.290. Measured UHPC Compressive Strain Profile for RPH-NP
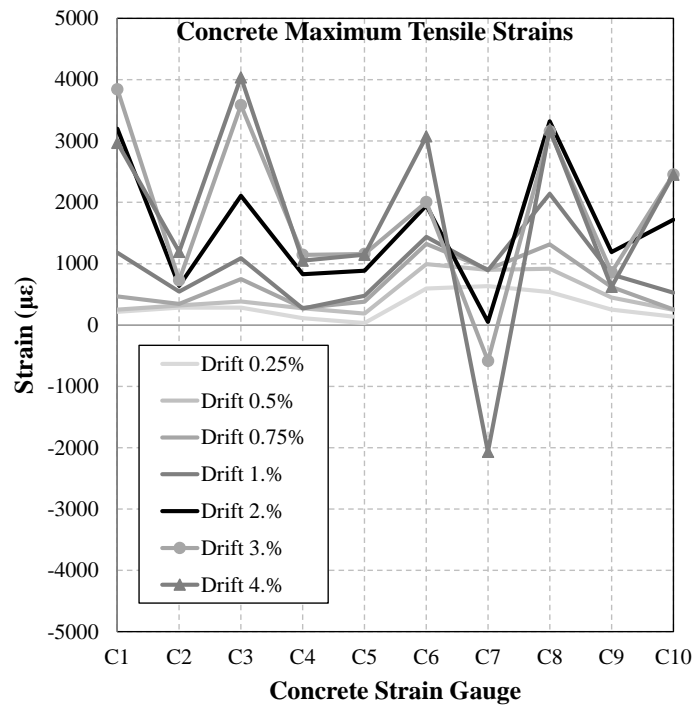
Figure 4.291. Measured UHPC Tensile Strain Profile for RPH-NP
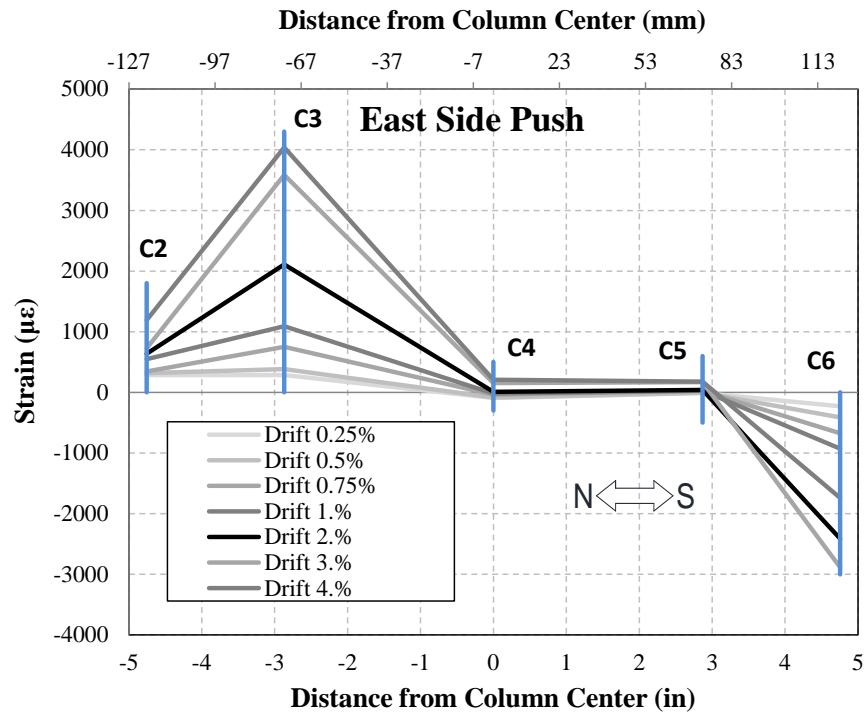
Figure 4.292. Measured UHPC Strain Profile for RPH-NP East Face During Push Cycles
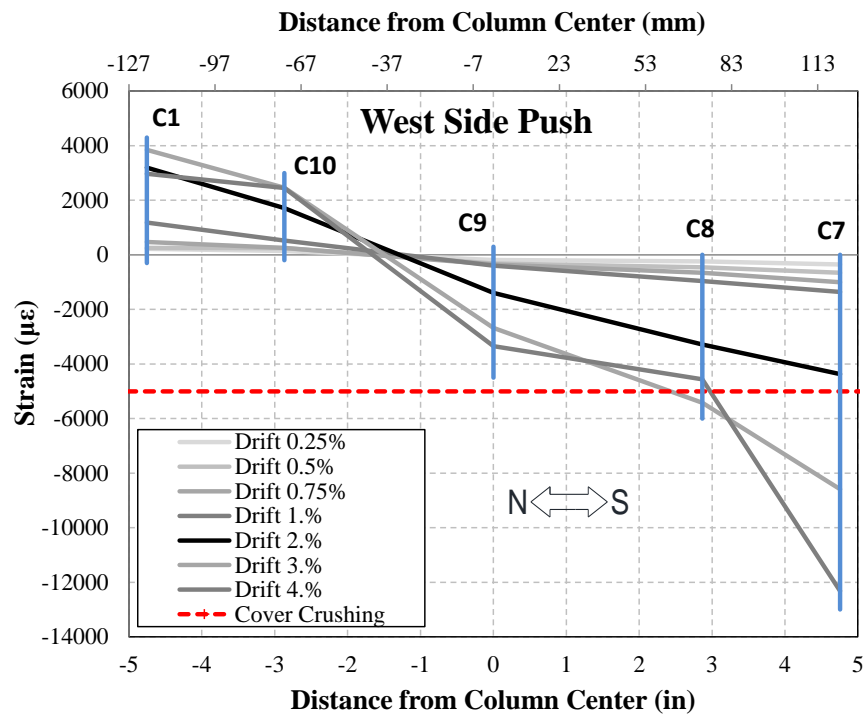
Figure 4.293. Measured UHPC Strain Profile for RPH-NP West Face During Push Cycles
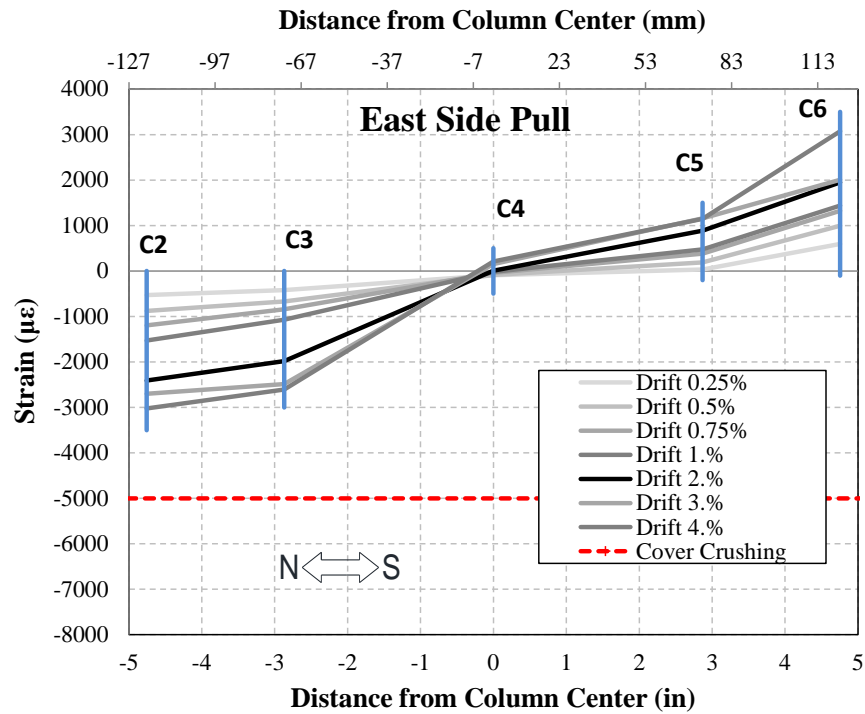
Figure 4.294. Measured UHPC Strain Profile for RPH-NP East Face During Pull Cycles
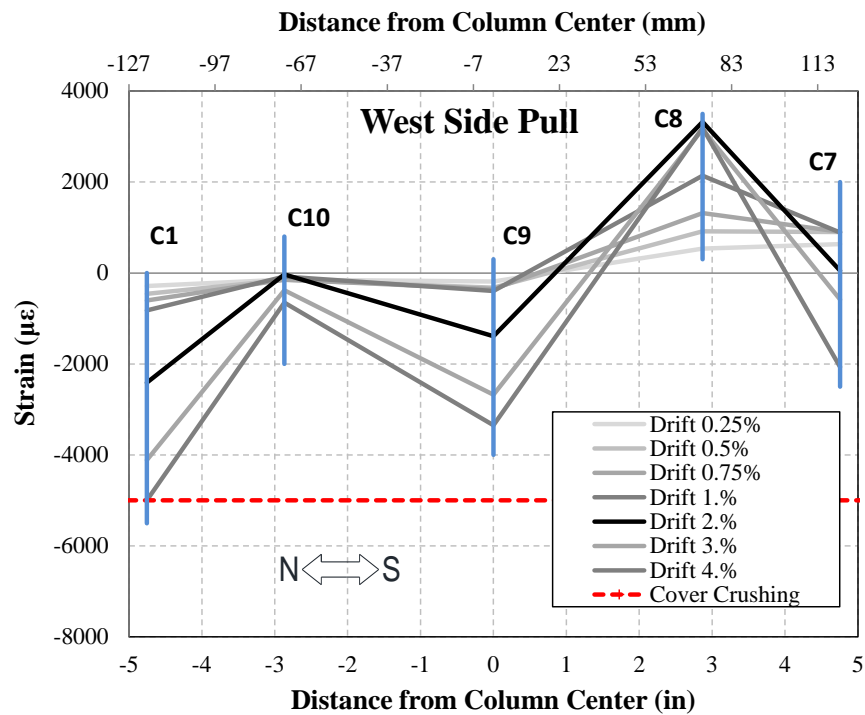
Figure 4.295. Measured UHPC Strain Profile for RPH-NP West Face During Pull Cycles

Tensile strains within the post-tensioning tendons used in RPH-NP were recorded to ensure that the tendons never yielded and were designed successfully (**Fig 4.296**). The average tendon tensile strain after all post-tensioning losses was 1625 $\mu\varepsilon$ while this value dropped slightly to 1567 $\mu\varepsilon$ after the column axial load was applied. It may be noted that all sensors were zeroed at the beginning of the test, thus the recorded strain values as shown in the figure must all be added to the initial strain value after post-tensioning losses at the plant to obtain the actual tendon strains. Through this method, the maximum recorded tendon strain was 2516 $\mu\varepsilon$, only 30% of the specified yield strain of the tendons which was 8596 $\mu\varepsilon$. Tendon strains were all relatively close together and increased uniformly up to the end of the test at 4% drift.
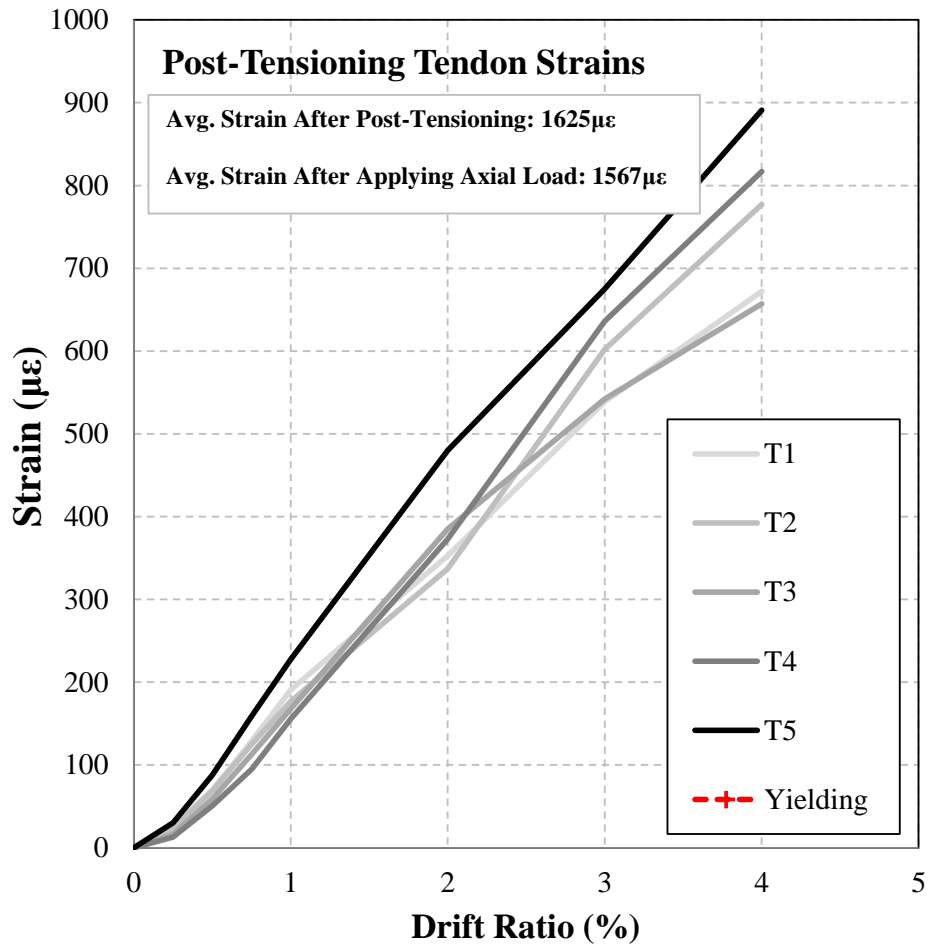
Figure 4.296. Measured Post-Tensioning Tendon Strain Profile for RPH-NP

4.5.5.7 RPH-NP-R Strain Profiles

Strain gauges in the center two levels were replaced along with new tendon fuses before testing of RPH-NP-R. The measured strain profiles of Bars/Tendons 1, 3, 8, and 10 are shown in **Fig. 4.297-4.300**. Higher strains were concentrated at the center two strain gauges placed on the tendon fuses. The tendons yielded at higher drift ratios. Furthermore, the footing dowel bars at the bottom end of the tendons yielded at 4.0% drift ratio.

Compressive strain profiles for RPH-NP-R are displayed in **Fig. 4.301-4.304**. The compressive strains were concentrated at the center two levels, which were on the tendon fuses while limited compressive strains were recorded at the outer two strain gauge levels which were placed on the main longitudinal bars.

The strain gauge profiles for the neck steel bars are shown in **Fig. 4.305-4.308**. Higher tensile strains were recorded at the lower strain gauge levels closer to the rebar hinge. Same as RPH-NP, no yielding at the gauges were recorded. Nevertheless, three bars of the rebar hinge connection close to the column-footing interface ruptured at high drifts. The design of the neck section for the other two repairable columns was found viable. However, an alternative detailing such as bar debonding may be considered for RPH-NP if the owner specifies no internal damage to the neck reinforcement.

Figures 4.309 and **4.310** shows the measured UHPC compressive and tensile strain profiles. As an alternative graph to the previous ones, **Fig. 4.311-4.314** show the strain profiles along the east and west faces of the column during both push and pull cycles. Same as the steel gauges, a positive value represents a tensile strain, and a negative sign means it is in compression. The highest compressive strains were recorded in strain gauges C1 on the north face and C7 and C8 on the south face. Gauges C7 and C8 exceeded the cover crushing strain of a normal concrete (not UHPC) but not that of the core UHPC. Compressive values of RPH-NP were higher than those of RPH-PF likely due to a higher strength of the RPH-NP column (45% higher in lateral strength).
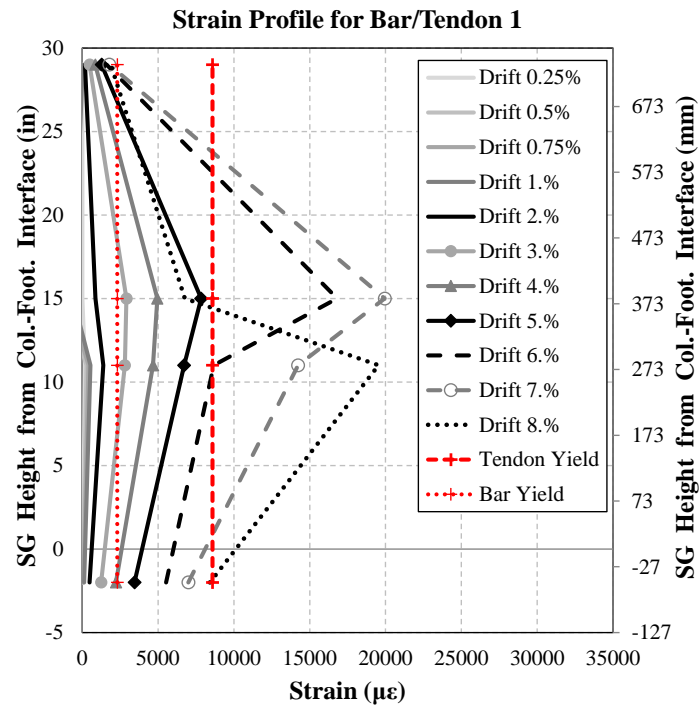
Figure 4.297. Measured Tensile Strain Profile for RPH-NP-R Column Bar/Tendon 1
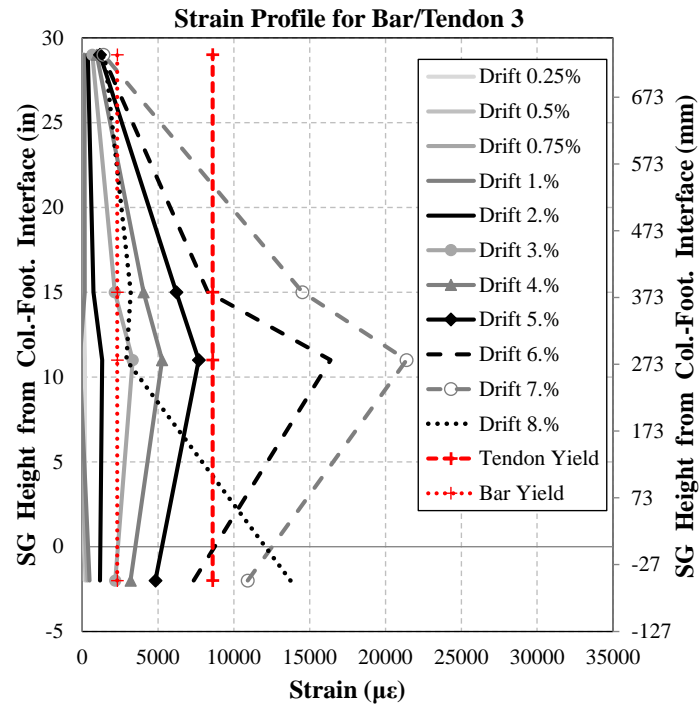
Figure 4.298. Measured Tensile Strain Profile for RPH-NP-R Column Bar/Tendon 3
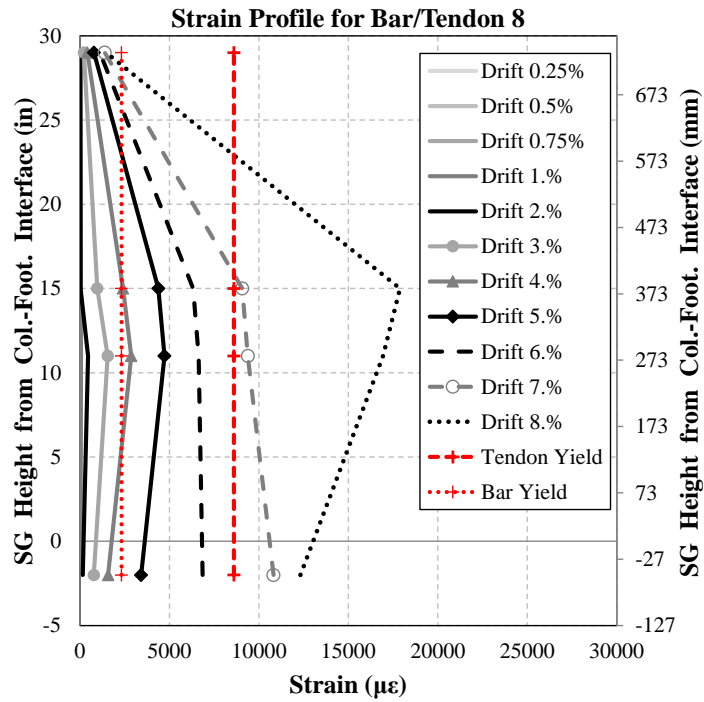
Figure 4.299. Measured Tensile Strain Profile for RPH-NP-R Column Bar/Tendon 8
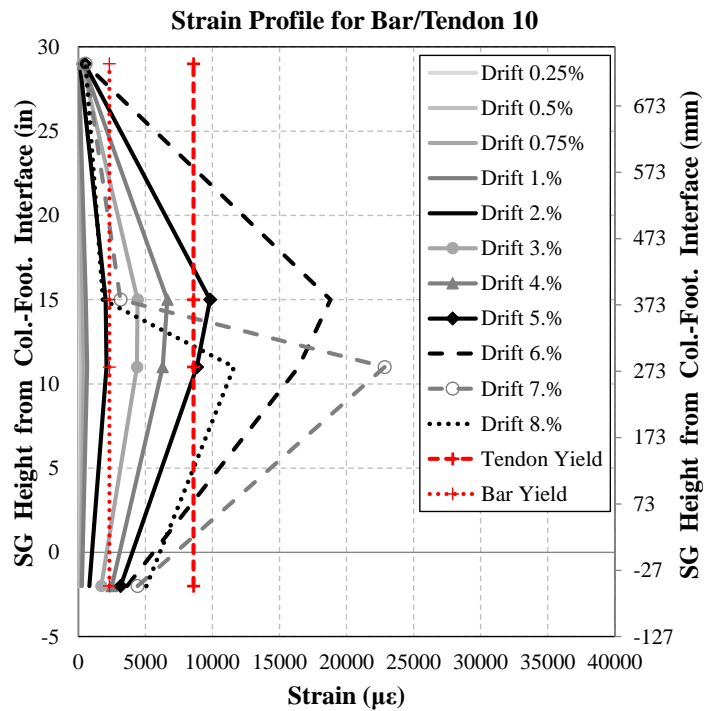
Figure 4.300. Measured Tensile Strain Profile for RPH-NP-R Column Bar/Tendon 10
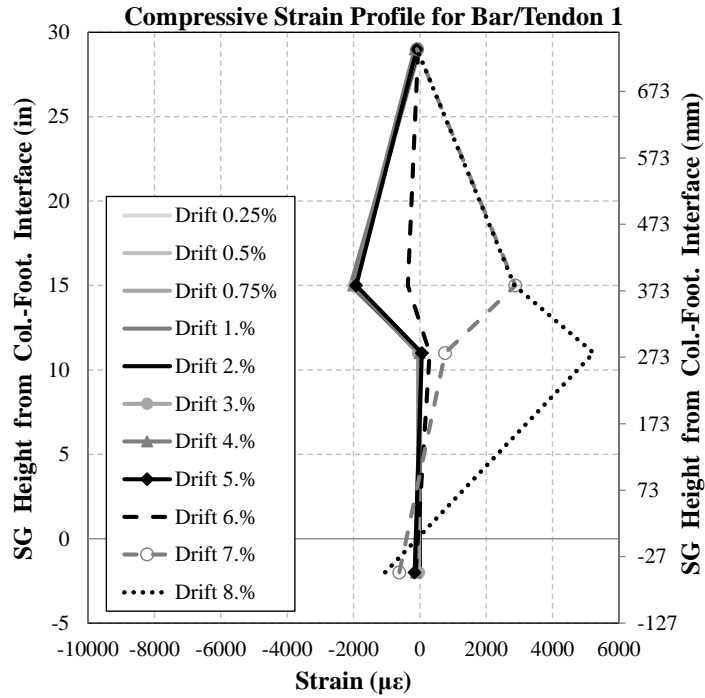
Figure 4.301. Measured Compressive Strain Profile for RPH-NP-R Column Bar/Tendon 1
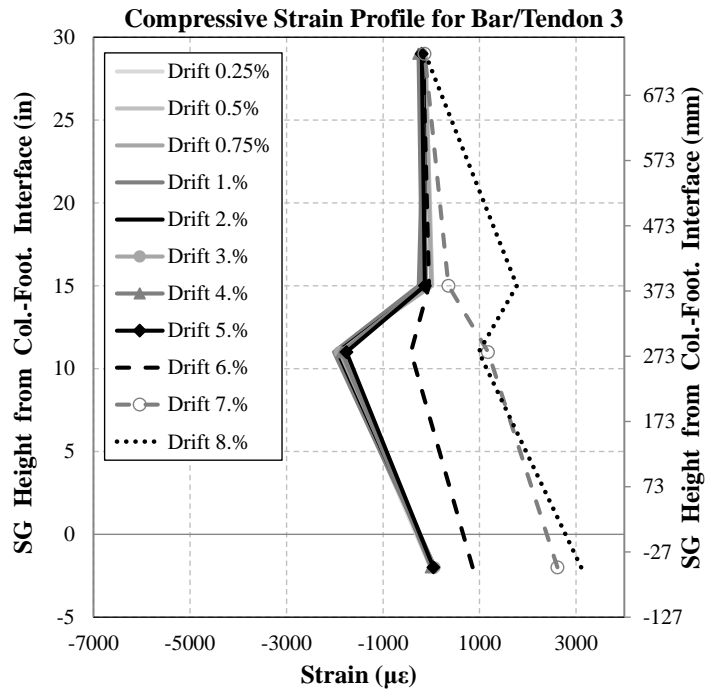
Figure 4.302. Measured Compressive Strain Profile for RPH-NP-R Column Bar/Tendon 3

247
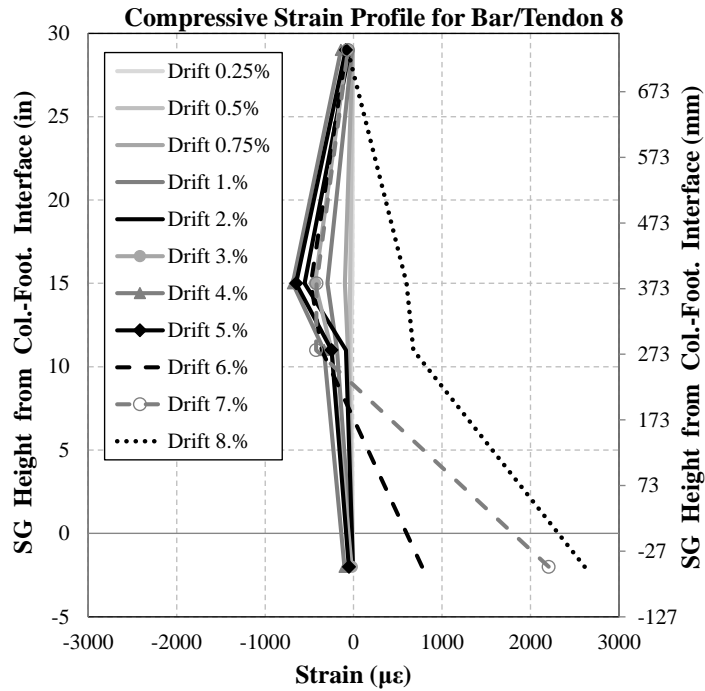
Figure 4.303. Measured Compressive Strain Profile for RPH-NP-R Column Bar/Tendon 8
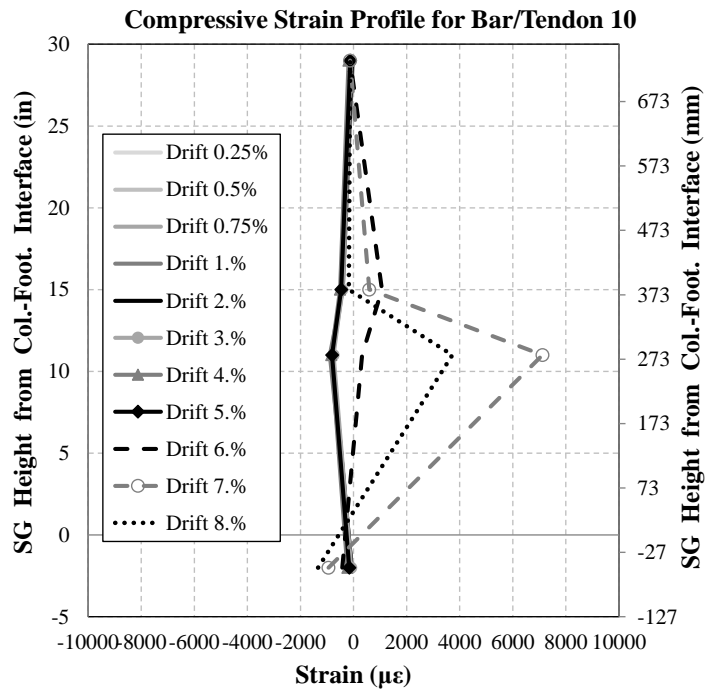
Figure 4.304. Measured Compressive Strain Profile for RPH-NP-R Column Bar/Tendon 10
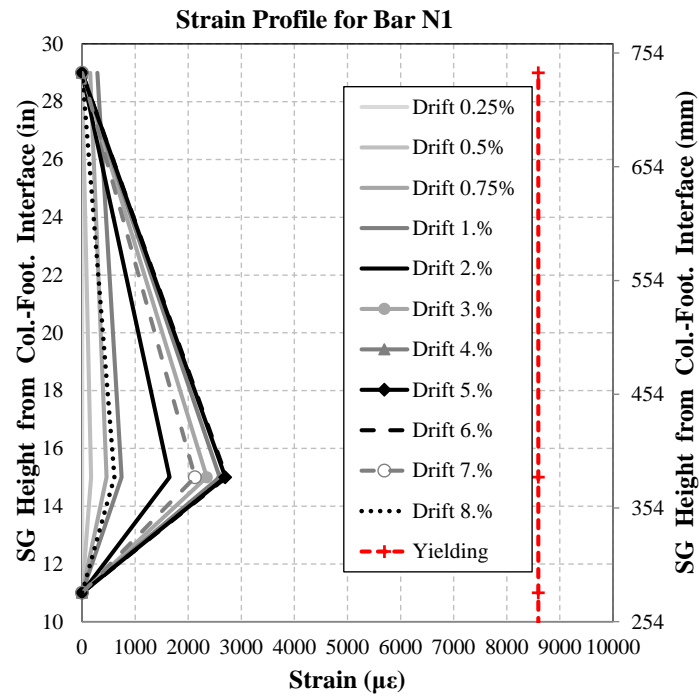
Figure 4.305. Measured Strain Profile for RPH-NP-R Column Neck Bar N1
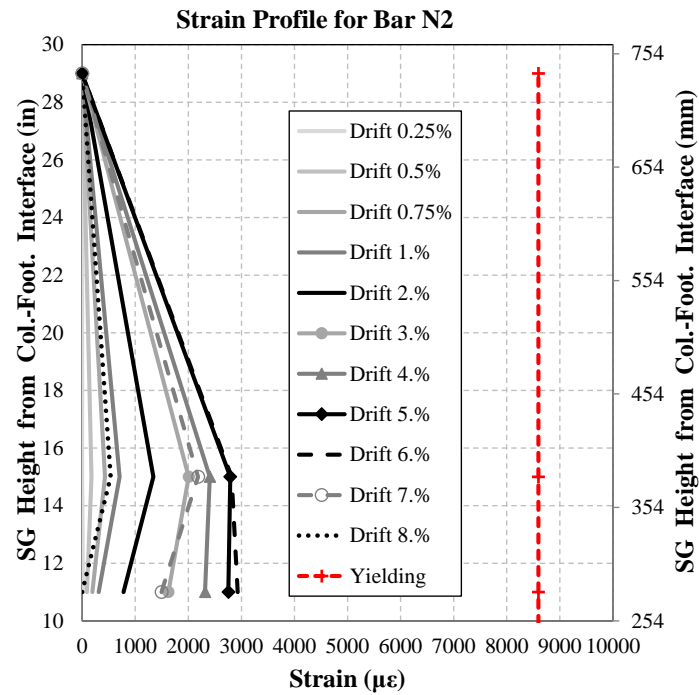
Figure 4.306. Measured Strain Profile for RPH-NP-R Column Neck Bar N2
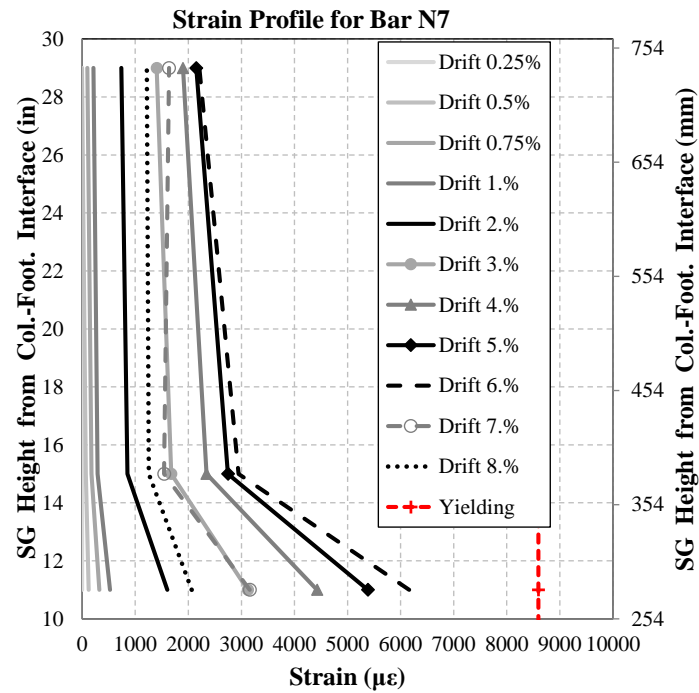
Figure 4.307. Measured Strain Profile for RPH-NP-R Column Neck Bar N7
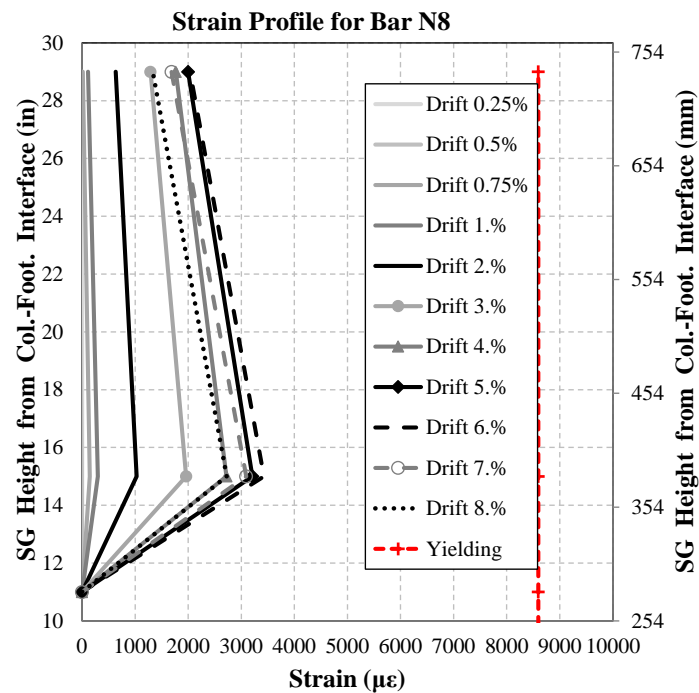
Figure 4.308. Measured Strain Profile for RPH-NP-R Column Neck Bar N8
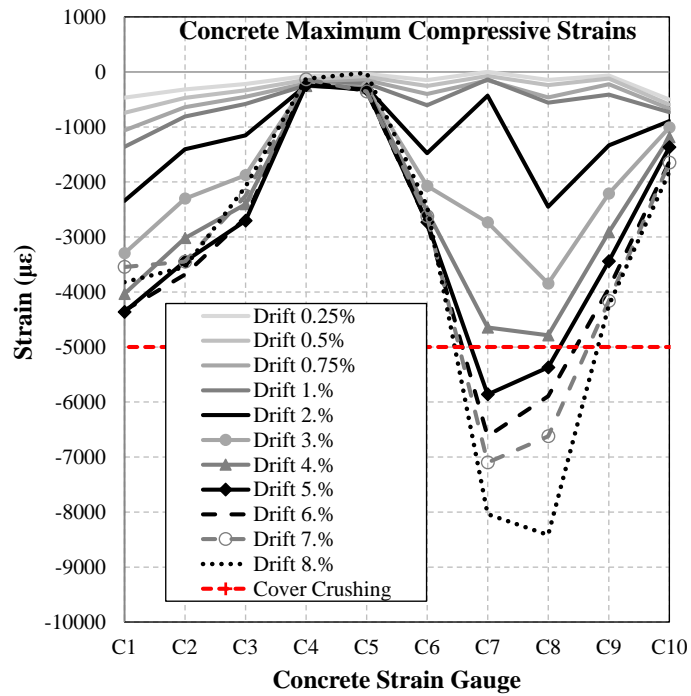
Figure 4.309. Measured UHPC Compressive Strain Profile for RPH-NP-R
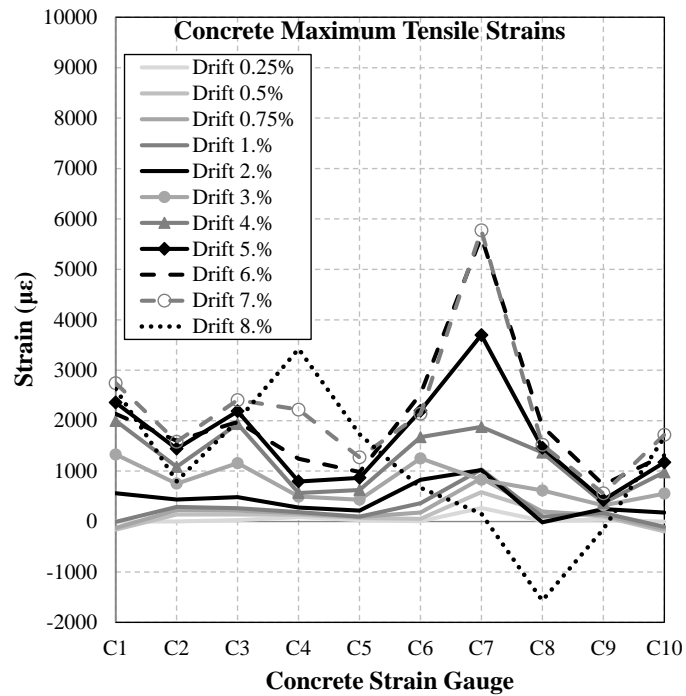
Figure 4.310. Measured UHPC Tensile Strain Profile for RPH-NP-R
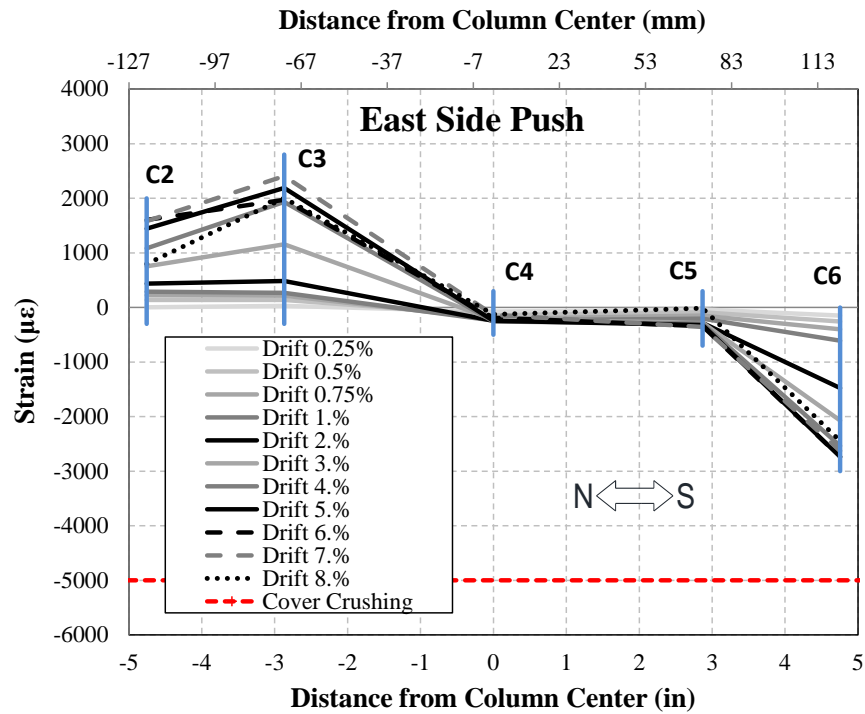
Figure 4.311. Measured UHPC Strain Profile for RPH-NP-R East Face During Push Cycles
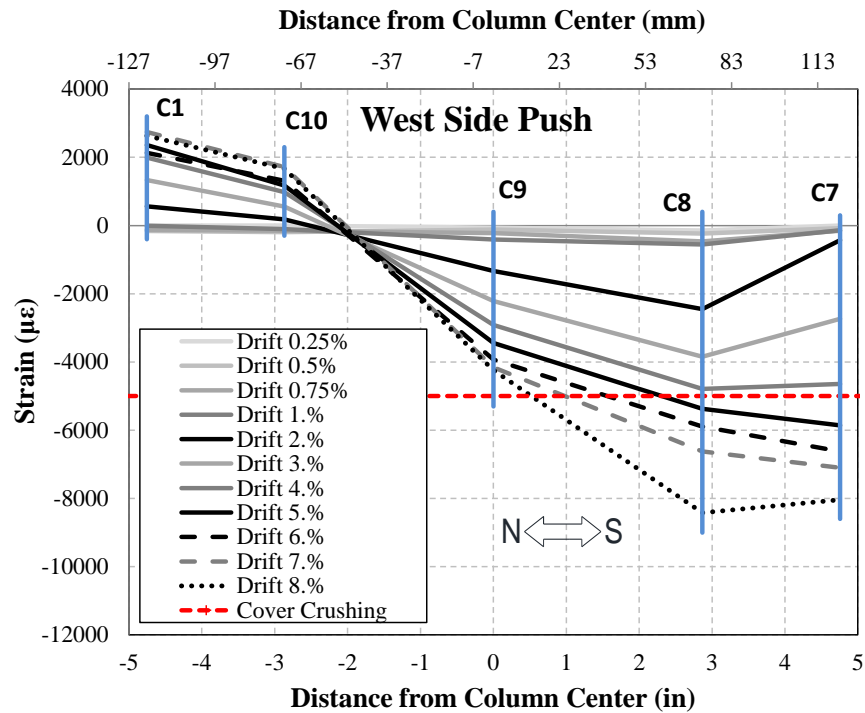
Figure 4.312. Measured UHPC Strain Profile for RPH-NP-R West Face During Push Cycles

252
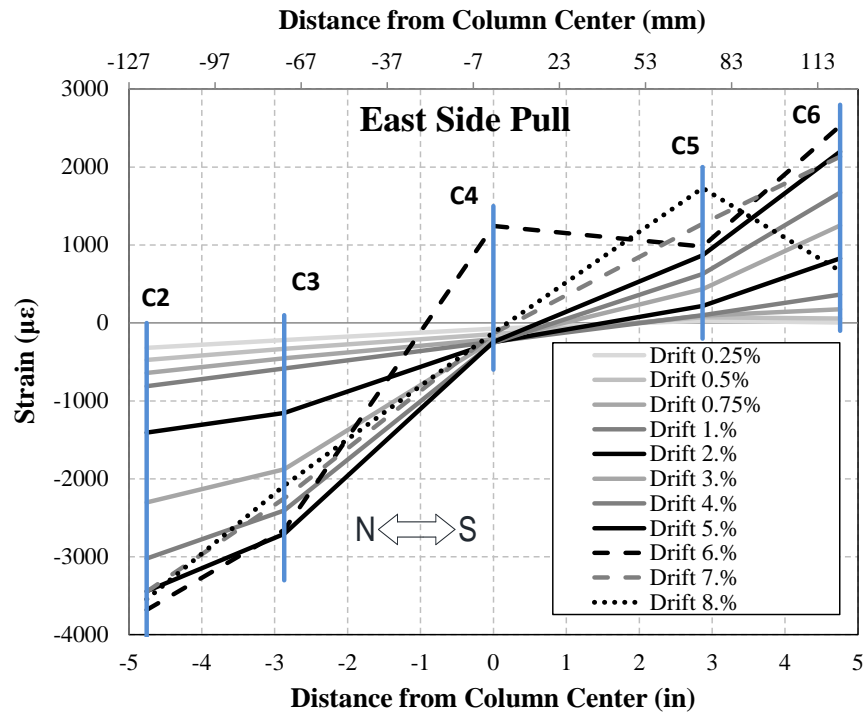
Figure 4.313. Measured UHPC Strain Profile for RPH-NP-R East Face During Pull Cycles
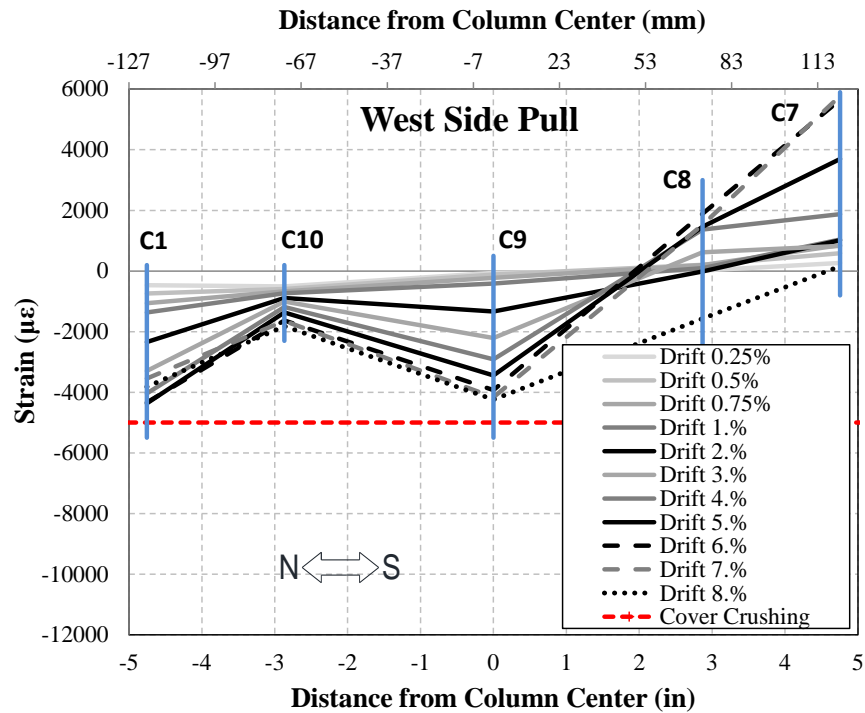
Figure 4.314. Measured UHPC Strain Profile for RPH-NP-R West Face During Pull Cycles

Figure 4.315 shows the measured tensile strains in the post-tensioning tendons at the center of the RPH-NP-R column. The average tendon stress after all losses and applying the axial load was 1501 $\mu\varepsilon$. Assuming this strain as the initial value prior to the column testing, the maximum recorded tendon strain was 3115 $\mu\varepsilon$, which is only 36% of the tendon specified yield of 8596 $\mu\varepsilon$. The strains of all tendons were close up to 1% drift ratio and increased afterwards linearly up to the end of the test at 8% drift. Overall, the post-tension tendons of the rocking system did not yield validating the design of this rocking column discussed in **Sec. 4.3.4**.
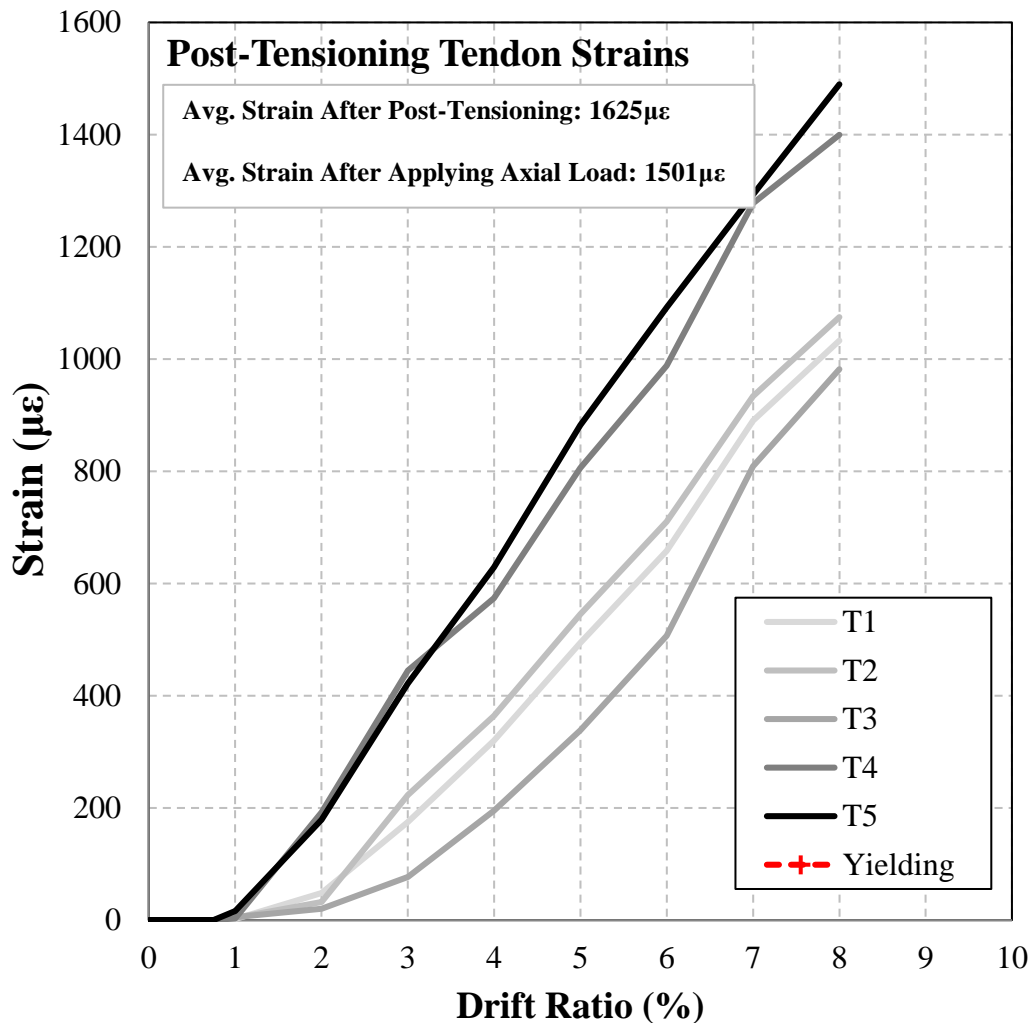
Figure 4.315. Measured Post-Tensioning Tendon Strain Profile for RPH-NP-R

4.5.5.8 RPH-NP Measured Rotation and Curvature

Rotations and curvatures were recorded and calculated in the same waw as the previous columns. **Figure 4.316** shows the measured curvature profile for RPH-NP from drift ratios of 0.25% to 4.0%. The highest curvatures were recorded at the base of the column while the upper three levels experienced a limited curvature due to the incorporation of the rebar hinge which allowed uplift and rotation at the base. The base of the north side also seemed to experience a higher curvature than the south side.
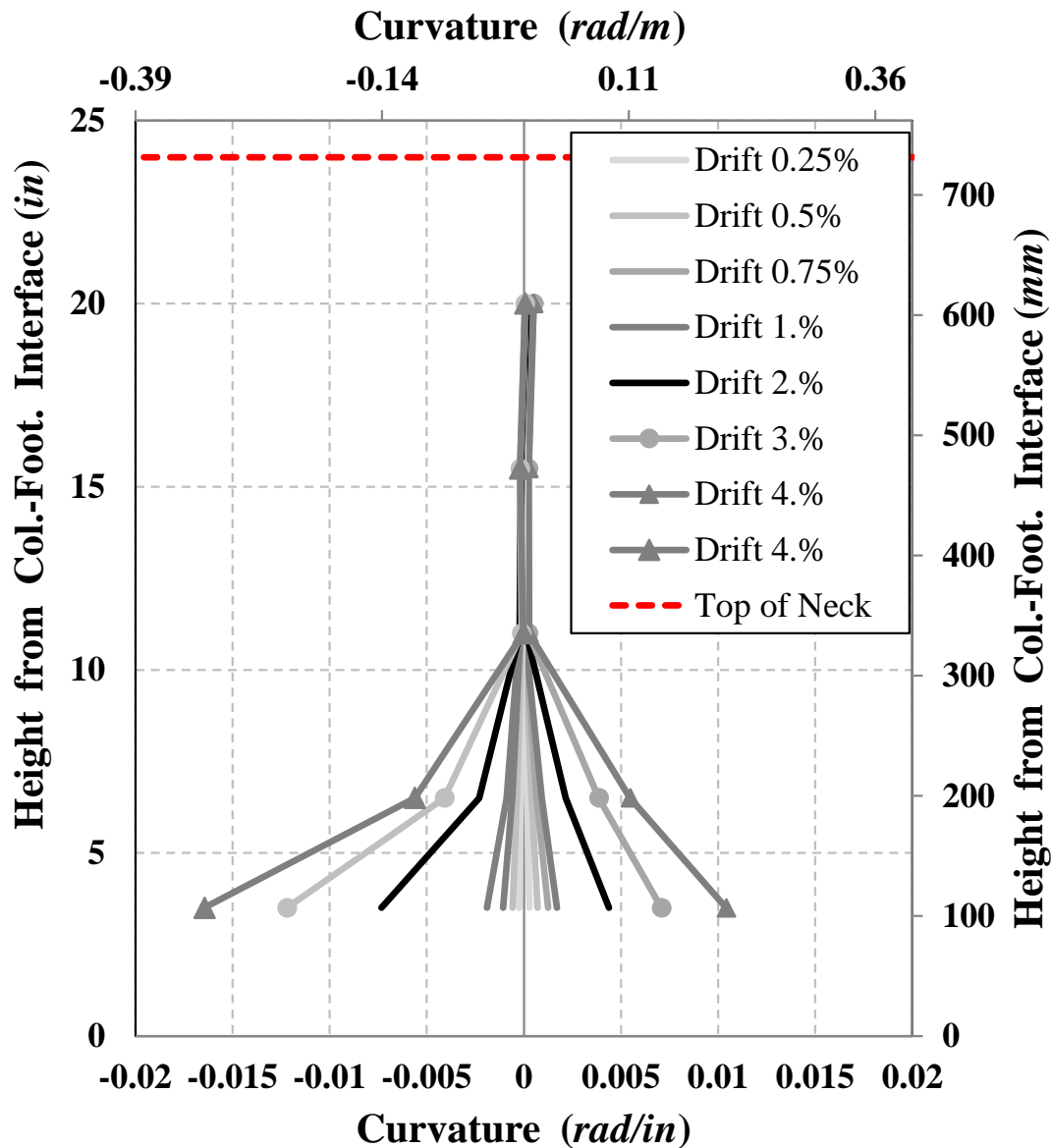
Figure 4.316. Measured Curvature Profile for RPH-NP Column

4.5.5.9 RPH-NP-R Measured Rotation and Curvature

Figure 4.317 shows the measured curvature profile for the RPH-NP-R column from drift ratios of 0.25% to 4.0%. The highest curvatures were at the base of the column while both the north and south faces of the column experienced similar amounts of curvature. The overall shape is similar to that of RPH-PF, RPH-PF-R, and RPH-NP.
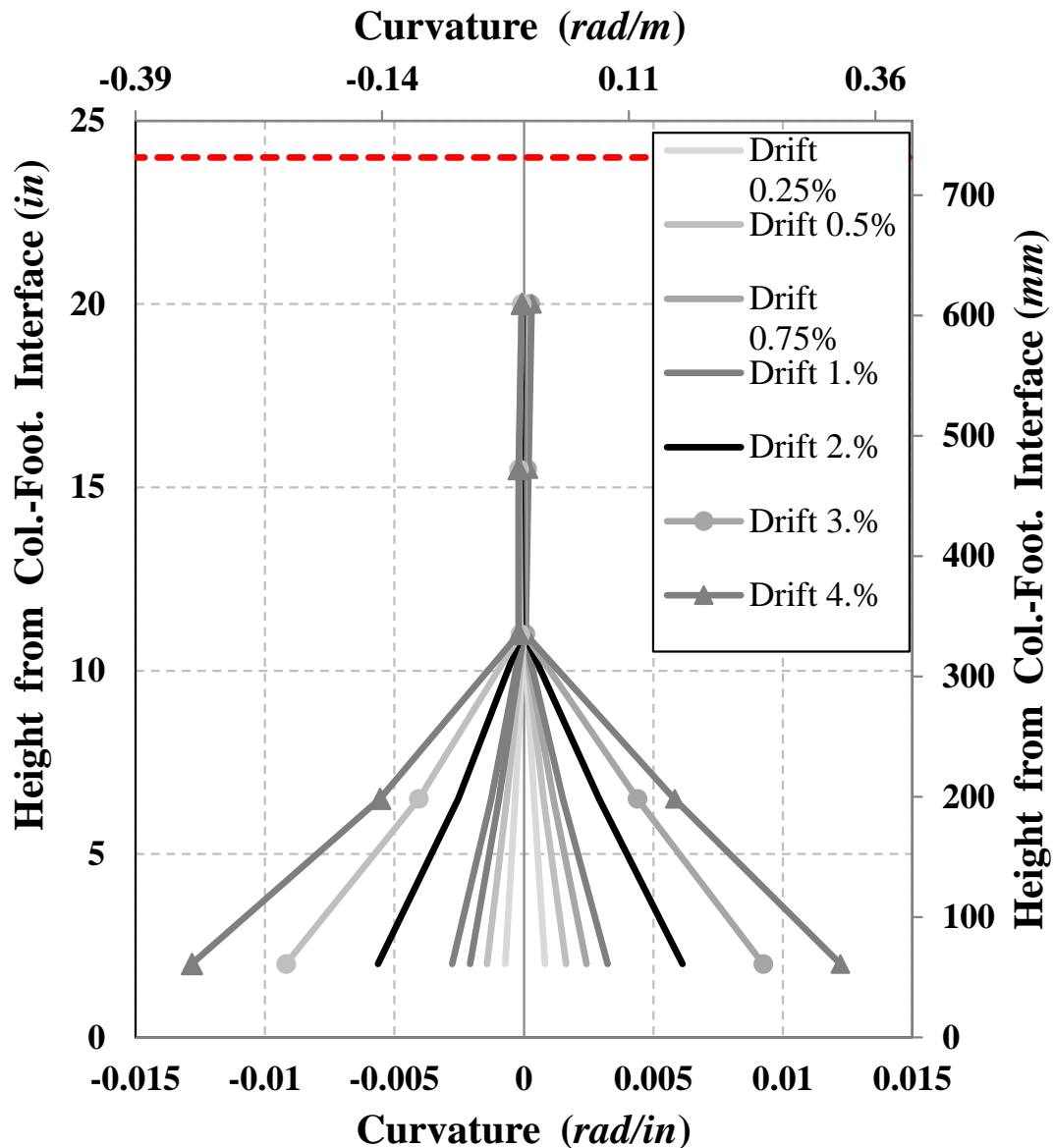
Figure 4.317. Measured Curvature Profile for RPH-NP-R Column

4.5.5.10 RHP-NP Energy Dissipation

Figure 4.318 shows the cumulative energy dissipation for RPH-NP. The dissipated energy begins to pick up at 0.5% drift possibly due to the cracking of UHPC and the yielding of the rebar hinge close to the column-footing interface. RPH-NP dissipated a total of 577 kip-in. (65.2 kN-m) before the test was stopped at 4.0% drift for the fuse replacement.
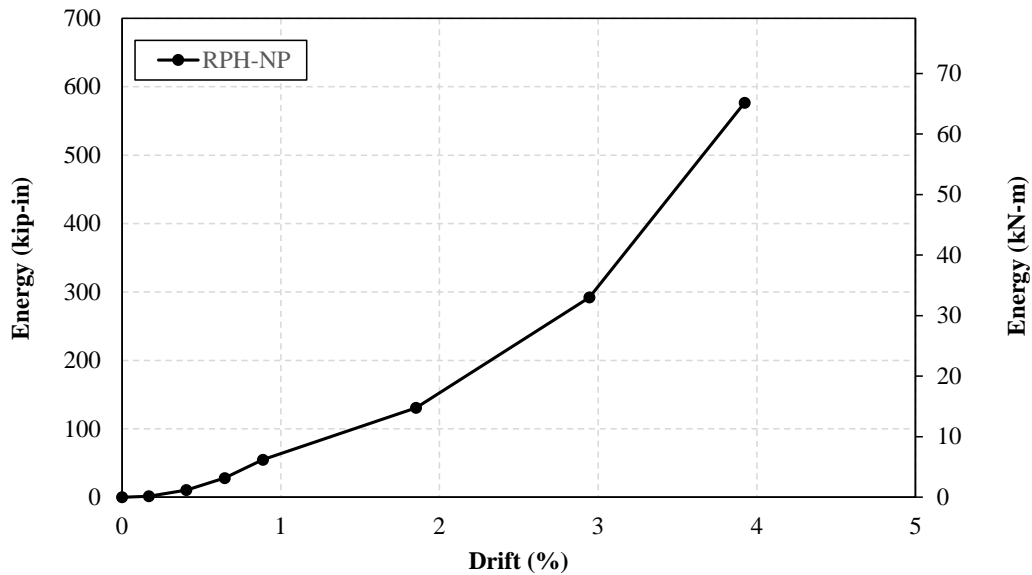
Figure 4.318. Measured Energy Dissipation for RPH-NP Column

4.5.5.11 RPH-NP-R Energy Dissipation

The cumulative energy dissipation for the RPH-NP-R column is shown in **Fig. 4.319**. RPH-NP-R dissipated a total of 2,600 kip-in. (294 kN-m) energy at 8.0% drift ratio.
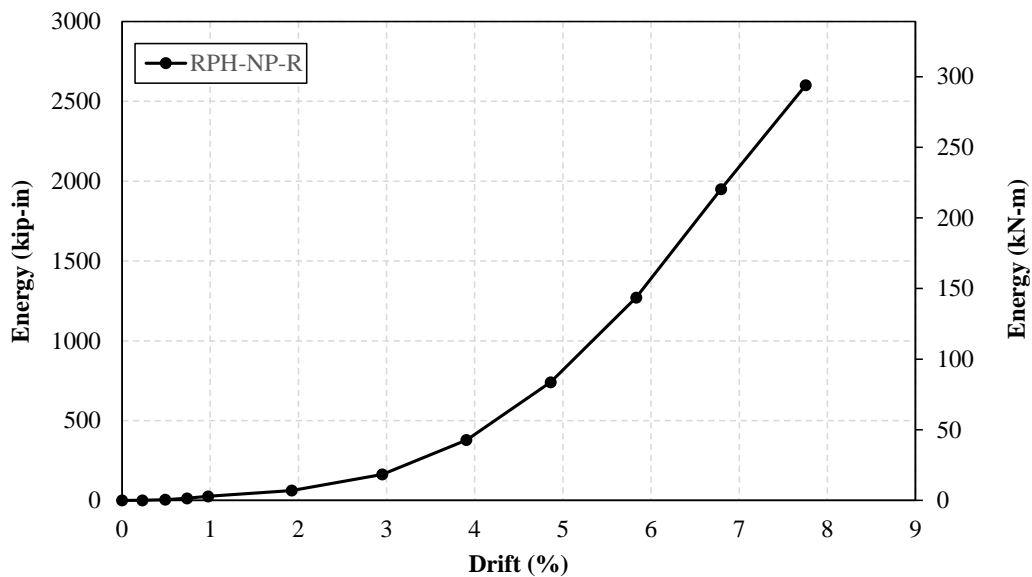
Figure 4.319. Measured Energy Dissipation for RPH-NP-R Column

4.6 Repairable Column Evaluation

The previous sections presented the results for each of the column testing individually. The following section evaluates the performance of the repairable precast columns in comparison with the reference CIP column. Specifically, the column damages, the force-displacement relationships, the strain profiles, and the energy dissipation of the four columns are compared.

4.6.1 Observed Damage

Figure 4.320 shows the damage of the plastic hinge region for CIP, RPH-PC, RPH-PF, and RPH-NP after the second pull of the 2.0% drift cycle. CIP and RPH-PC experienced more flexural cracks while no visible damage can be observed on RPH-PF and RPH-NP. CIP was a conventional column thus the observed damage was typical. SCC was used in RPH-PC thus some cracks were expected. At the rocking face of RPH-PC, some spalling was observed mainly due to the use of the steel shims placed between the column and the steel baseplate at the rocking interface. Nevertheless, the apparent damage of RPH-PF and RPH-NP cast with UHPC was minimal at 2% drift ratios.

Figure 4.321 shows the damage of the four columns at 4% drift ratio, just prior to the repair (for the precast columns not CIP). CIP experienced a significant spalling. RPH-PC exhibited both flexural and shear cracks above the neck section, a minor buckling of BRR, and spalling of SCC at the column base. Nevertheless, RPH-PF showed no damage and RPH-NP exhibited minor flexural cracks in the neck section.

Figure 4.322 shows the plastic hinge damage of CIP, RPH-PC-R, RPH-PF-R, and RPH-NP-R at their failure. CIP exhibited extensive damage such as concrete crushing, and buckling and fracture of the longitudinal bars. Several cracks, spalling of SCC, and a Z-shape buckling of BRR were observed for RPH-PC-R. Nevertheless, the UHPC damage was minimal in RPH-PF-R and RPH-NP-R. RPH-PF-R had only a few cracks at the base of the column. RPH-NP-R had a few more flexural cracks than RPH-PF-R both on and above the neck section.

In terms of reparability, CIP could not be repaired at 10% drift due to the extent of the damage. The repair of RPH-PC was difficult due to the bending of column/footing dowel bars, the Z-shape deformation of BRR, and large residual displacements seen at high drifts. RPH-PF had insignificant residual displacements with no column/footing dowels bent thus it is very easy to repair. In fact, this column was repaired and prepared for retesting in less than two hours. The repair of RPH-NP was also simple and quick at 4% drift ratio; however, the repair might be slightly more challenging at very large drifts due to moderate level residual displacements. Nevertheless, at any residual displacements, the tendons can be cut to the appropriate lengths and installed. This is a significant enhancement of the repairability compared with RPH-PC where BRR lengths cannot be easily adjusted onsite (a portable heading machine is needed to head the ends of BRR onsite) and there is a small tolerance to install each BRR. Furthermore, tightening the coupler of the tendon-to-bars using simple tools (pipe wrenches) can generate a significant tensile force in tendons (e.g., 10 kips (44.5 kN) in RPH-PF) thus such fuses may serve as both the column longitudinal reinforcement and a recentering mechanism. This is a novel hybrid rocking connection in which post-tensioning is outside the column and fully accessible. This is a significant enhancement of durability compared to conventional rocking systems since post-tensioning of rocking columns in all past studies were internal with no to minimal accessibility for the inspection and maintenance. UHPC showed a superior performance compared with conventional concrete and SCC and is thus recommended for such repairable columns.

In summary, the use of external fuses made with tendons are recommended in repairable columns. UHPC should be used to minimize concrete damages.

a) CIP (Sjurseth et al., 2022)

b) RPH-PC

c) RPH-PF

d) RPH-NP

Figure 4.320. CIP, RPH-PC, RPH-PF, and RPH-NP Plastic Hinge Damage after 2% Drift Cycle

a) CIP (Sjurseth et al. 2022)

b) RPH-PC

c) RPH-PF

d) RPH-NP

Figure 4.321. CIP, RPH-PC-R, RPH-PF-R, and RPH-NP-R Plastic Hinge Damage at 4%

a) CIP at 10% Drift (Sjurseth et al. 2022)

b) RPH-PC-R at 10% Drift

c) RPH-PF-R at 9% Drift

d) RPH-NP-R at 8% Drift

Figure 4.322. CIP, RPH-PC-R, RPH-PF-R, and RPH-NP-R Plastic Hinge Damage at Failure State

4.6.2 Force-Displacement Relationships

Figures 4.323-4.325 show the lateral force-drift hysteretic curves for the three repairable columns including their repaired testing superimposed on the CIP response. RPH-PC and RPH-PC-R exhibited a lower initial stiffness compared with that of CIP, but similar force and displacement capacities were achieved. Note that RPH-PC did not fail but the test was stopped at 10% drift, where the CIP column failed. Even though no specific self-centering mechanism was used, RPH-PC and its repaired version, both with stainless-steel BRR, showed a moderate-level reduction (e.g., 44% at the last cycle) in residual displacements compared with CIP. However, the residual displacement reduction at high drifts was not sufficient to allow an easy BRR replacement. The column/footing dowels were also bent limiting the repair-by-replacement technique. Therefore, this column needs an alternative BRR such as SMA to minimize the dowel damage and the residual displacement. The incorporation of tendon fuses might be another alternative.

RPH-PF and RPH-PF-R had a significantly lower initial stiffness, a slightly lower lateral strength, and a similar displacement capacity compared with CIP. Both RPH-PF and RPH-PF-R exhibited insignificant residual displacements throughout the entire testing allowing a simple and fast replacement of tendon fuses. The strong recentering behavior of this column proves that the external tendons can simultaneously serve as the column longitudinal reinforcement and rocking reinforcement. Therefore, RPH-PF detailing is a new generation of hybrid rocking columns in which rocking reinforcement is fully accessible. Note that exposing the tendons may cause durability issues. All exposed reinforcement should be protected against weather conditions. For example, stainless steel bars must be used as column/footing dowels, and stainless steel, galvanized, or epoxy-coated tendons (such as those used in cable-stayed bridges) should be incorporated as tendon fuses.

In RPH-NP and RPH-NP-R, the initial stiffness most closely matched that of CIP. Furthermore, this repairable column showed a 37% higher lateral strength, but a 14% lower displacement capacity compared with CIP. Despite the use of an established rocking system (internal post-tensioning) as well as the external tendon fuses, this column did not show insignificant residual displacements mainly due to the rebar hinge connection at the column base. Nevertheless, the repair at 4% drift ratio was relatively easy and fast since the new tendons were cut in length and installed even when the column had a residual drift ratio of 1.5%.

Figure 4.326 shows the average pushover envelopes for CIP and all repairable columns. The displacement ductility capacities of the three repaired precast columns were all significantly lower than that of CIP due to the reduced stiffness and delayed yielding. However, for novel columns, the drift capacity is often a better indicator of the column performance than the displacement ductility capacity. CIP failed by the longitudinal bar fracture at 8.96%. RPH-PC-R did not fail, since the test was stopped, but the column drift capacity was assumed to be 9.8%. RPH-PF-R failed by the tendon rupture at 8.9% drift ratio. RPH-NP-R failed by the neck bar rupture at 7.7% drift ratio. Therefore, the displacement capacity of RPH-PC-R was 9% higher than that of CIP and the displacement capacities of RPH-PF-R and RPH-NP-R were 0.6% and 14% lower than that of CIP, respectively. **Figure 4.326** also includes the design level drift demand based on the AASHTO spectrum for Downtown Los Angeles, CA using the period of the CIP reference column. While all repairable columns were pushed well past the drift demand before repair and retesting, it may be noted that their reduced stiffness increases their period and thus likely increases their drift demand under the same design level earthquake. Further study such as shake table testing is needed to better understand the dynamic behavior of the proposed repairable columns.

Overall, all precast columns were repairable, especially those with tendon fuses, and were retested after being pushed well past the displacement demand of the CIP column with minimal damage.
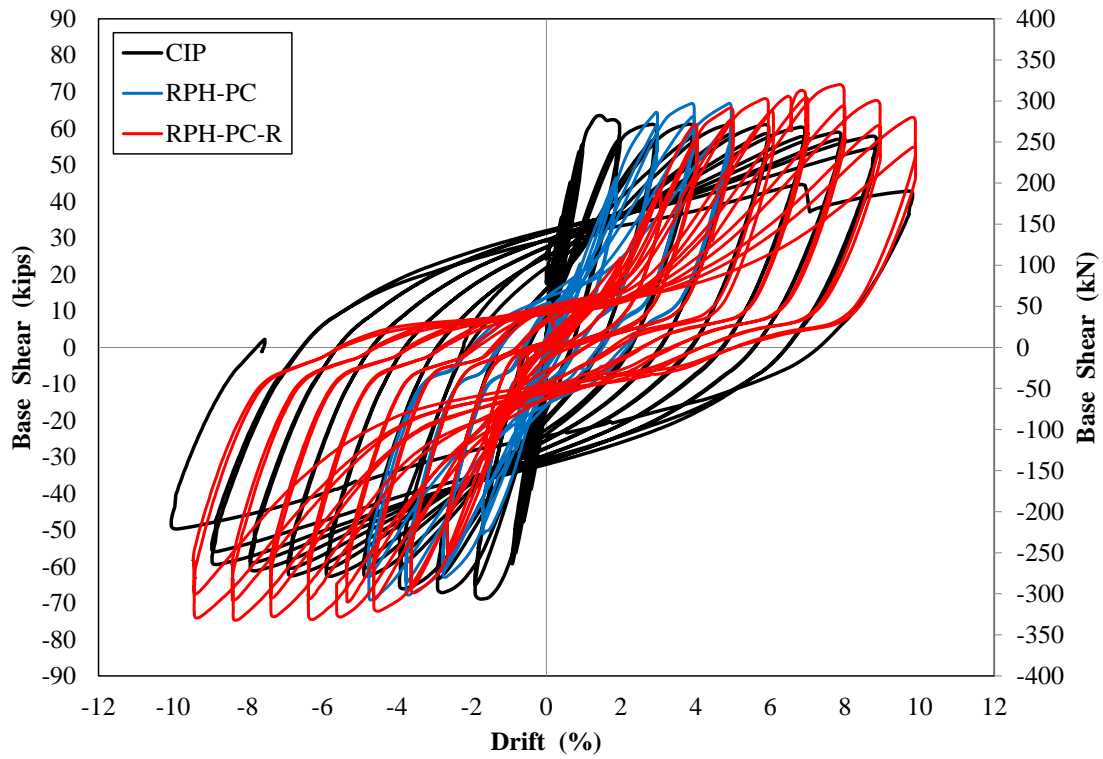
Figure 4.323. Measured CIP, RPH-PC, and RPH-PC-R Force-Drift Hysteretic Responses
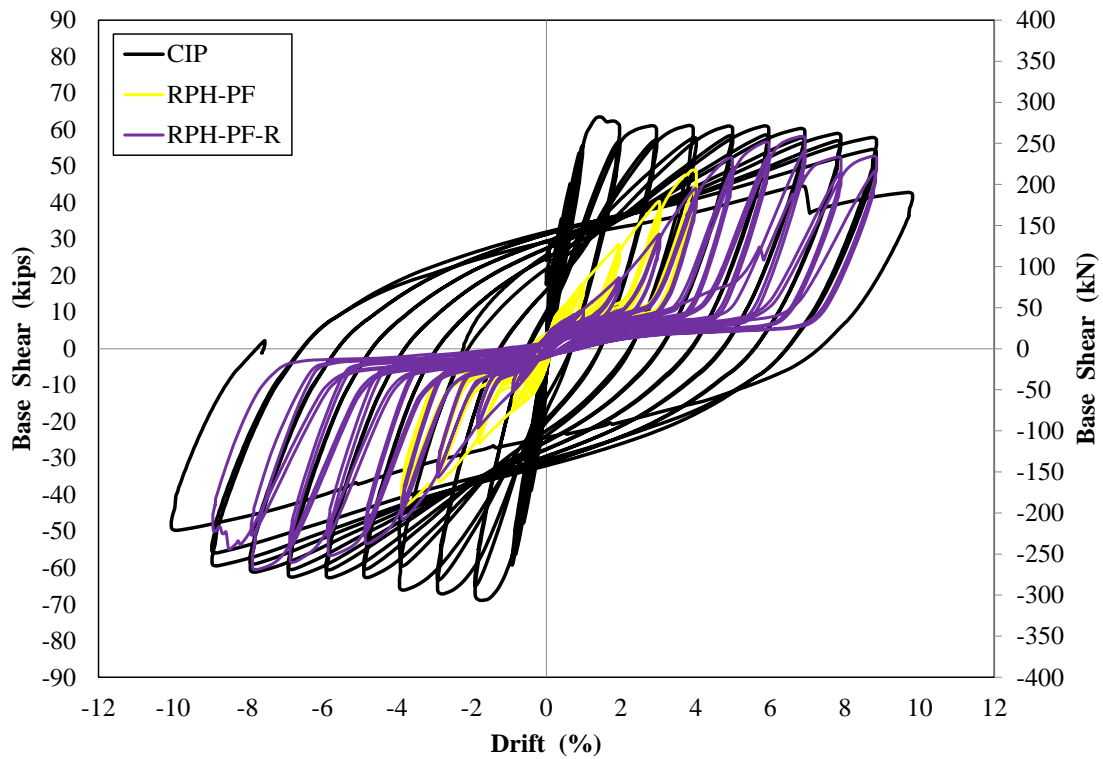
Figure 4.324. Measured CIP, RPH-PF, and RPH-PF-R Force-Drift Hysteretic Responses

263
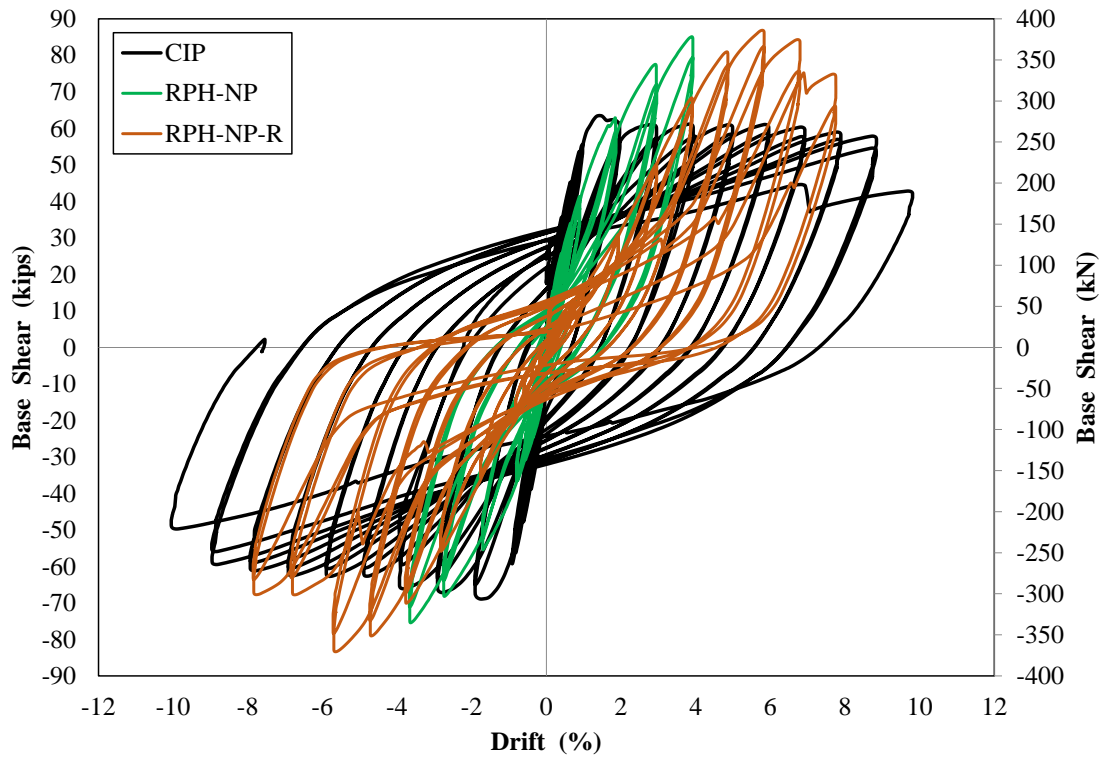
Figure 4.325. Measured CIP, RPH-NP, and RPH-NP-R Force-Drift Hysteretic Responses
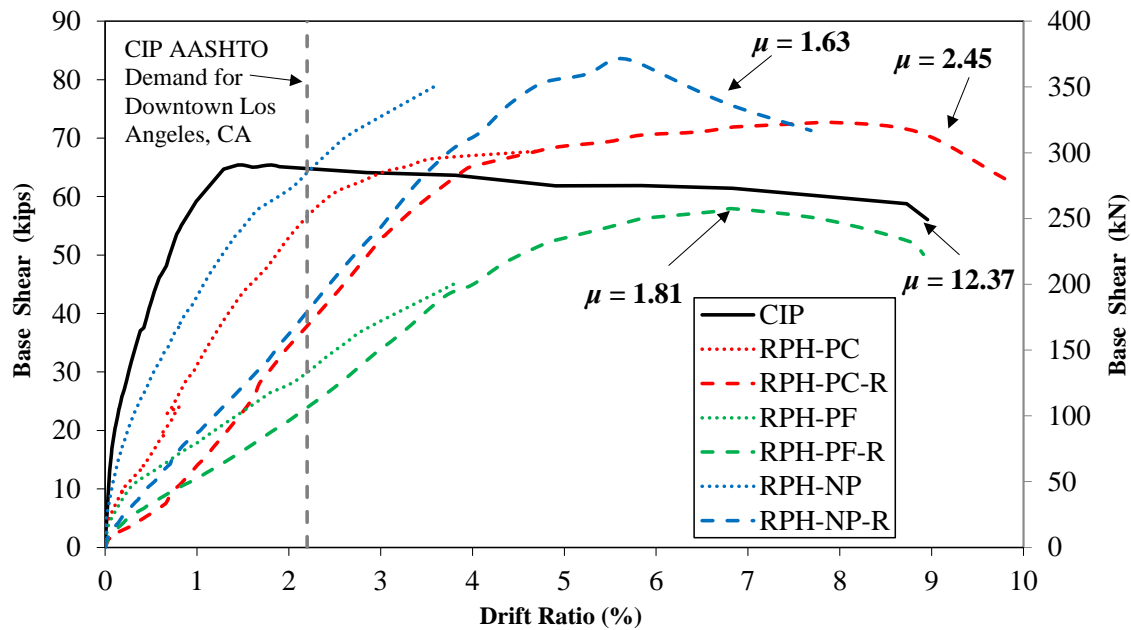
Figure 4.326. Measured CIP and Repairable Column Pushover Envelopes

4.6.3 Residual Displacements

To better comment on the self-centering capability of the proposed repairable columns, the hysteretic responses for the CIP column and the three repaired columns, RPH-PC-R, RPH-PF-R, and RPH-NP-R, at the 8.0% drift cycle were superimposed (**Fig. 4.327**). The graph indicates a similar or higher lateral strength for repairable columns compared with CIP. A flag-shape behavior can be seen for the repairable columns and is overall similar between the three specimens with RPH-PF with smallest residual displacements. This graph indicates that the proposed repairable columns exhibited a similar hysteretic behavior with moderate (in RPH-PC and RPH-NP) to high (in RPH-PF) self-centering capabilities.

Figure 3.328 shows the measured residual vs peak drift relationships for the CIP and repairable columns. All columns had a negligible residual displacement up to a 1% drift. Furthermore, RPH-PC and RPH-PF exhibited insignificant residual drifts up to 4.0% peak drift. The residual-peak drift relationships for RPH-PF-R and RPH-NP-R closely match those of their initial testing while RPH-PC-R experienced smaller residual drifts compared with its initial testing (RPH-PC). After their initial plateaus, it can be seen that the residual-peak drift response for RPH-PC-R and RPH-NP-R follows the same slope as CIP, while the response for RPH-PF-R increases at a much smaller rate.

Residual drifts less than 1% may be assumed insignificant after an earthquake (NCHRP 864). Overall, RPH-PF-R experienced the smallest residual drifts among all columns and stayed below the "1% residual drift" limit. Self-centering is a key parameter in the reparability of the proposed precast columns since a close-to-plumb position allows for the quick and easy replacement of the fuses.
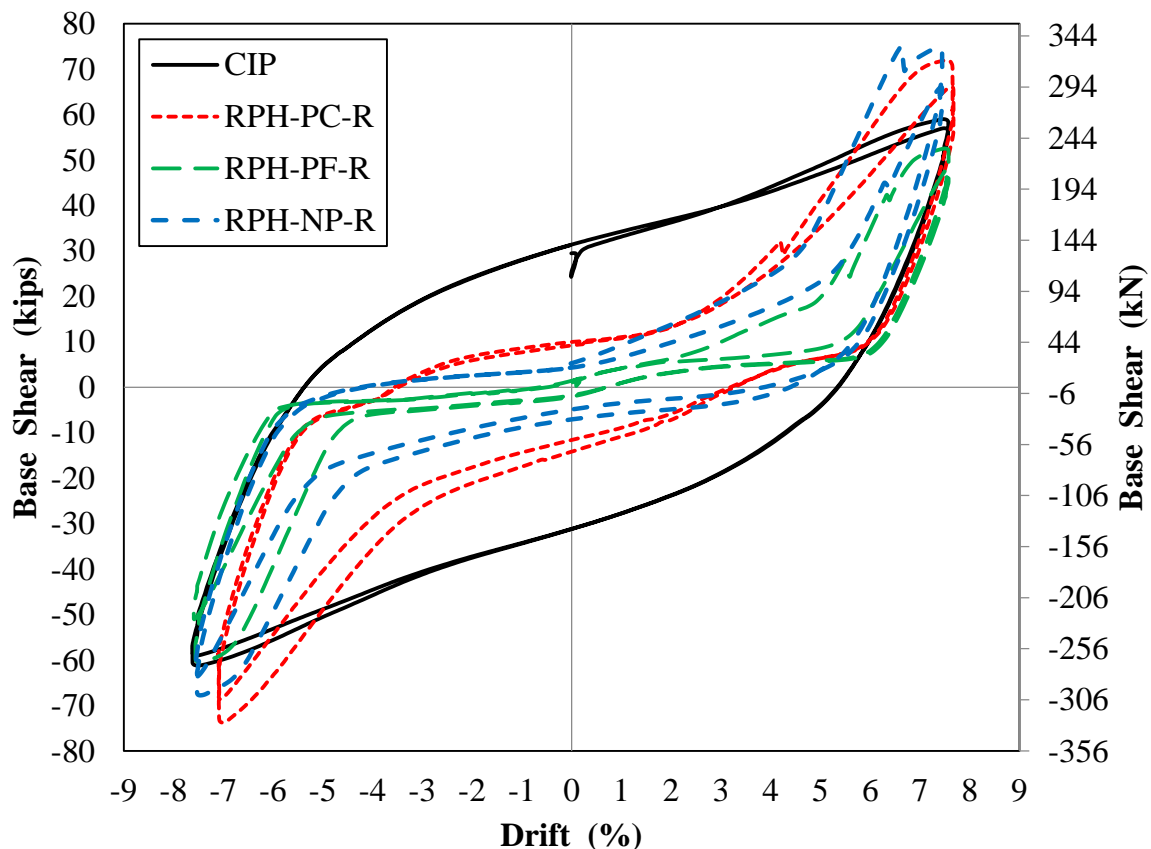
Figure 4.327. Measured CIP and Repairable Column Hysteretic Loops at 8.0% Drift Ratio
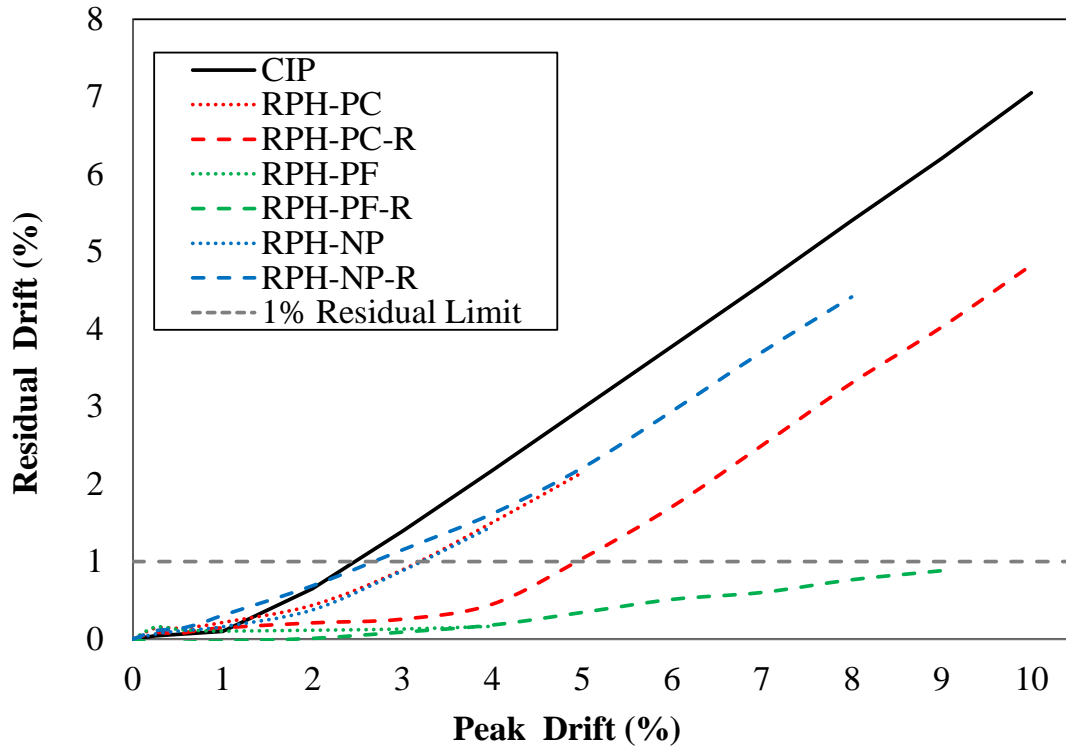
Figure 4.328. Measured CIP and Repairable Column Residual Drifts

4.6.4 Strain Profiles

Figures 4.329 to **4.332** show the maximum measured tensile strains at each strain gauge level for CIP and the three repairable columns. The center two levels of strain gauges were placed on the dog-bone BRR bars of RPH-PC and RPH-PC-R and on the tendon fuses of RPH-PF, RPH-PF-R, RPH-NP, and RPH-NP-R. The outer two levels were placed on the main longitudinal reinforcement for all repairable columns, the column/footing dowels. All repairable columns showed the highest strains at their fuses which indicate a successful design of the fuse using either the reduced bar diameter in BRR or small-size tendons. Furthermore, the strains of column/footing dowels in the two tendon fuse columns (RPH-PF and RPH-NP) were insignificant and much lower than those of CIP and RPH-PC-R. Overall, all fuses (either stainless steel BRR or steel tendon) were indeed the weak link in the system with a significant yielding compared with the column/footing dowel bars. Therefore, the design of these fuses, especially the tendon fuses, was successful.
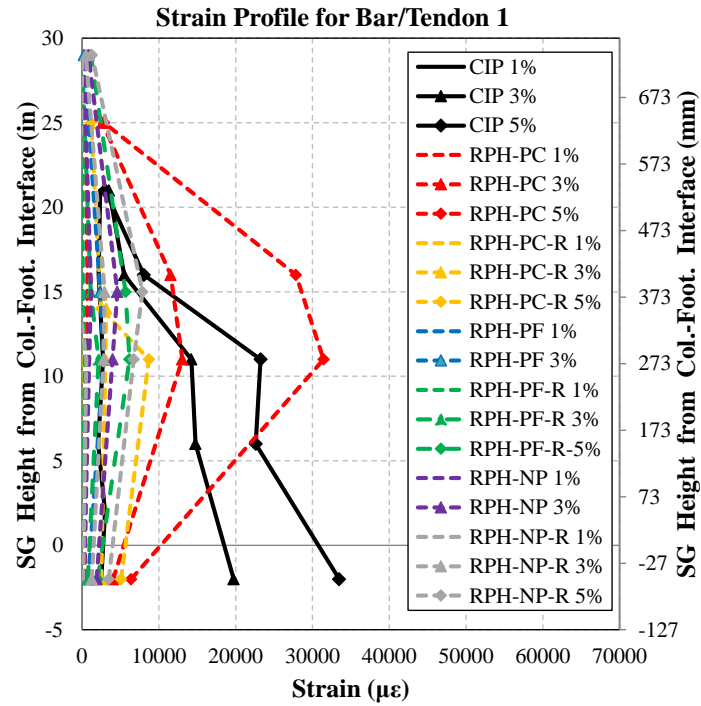
Figure 4.329. Measured CIP and Repairable Column Tensile Strain Profile for Bar/Tendon 1
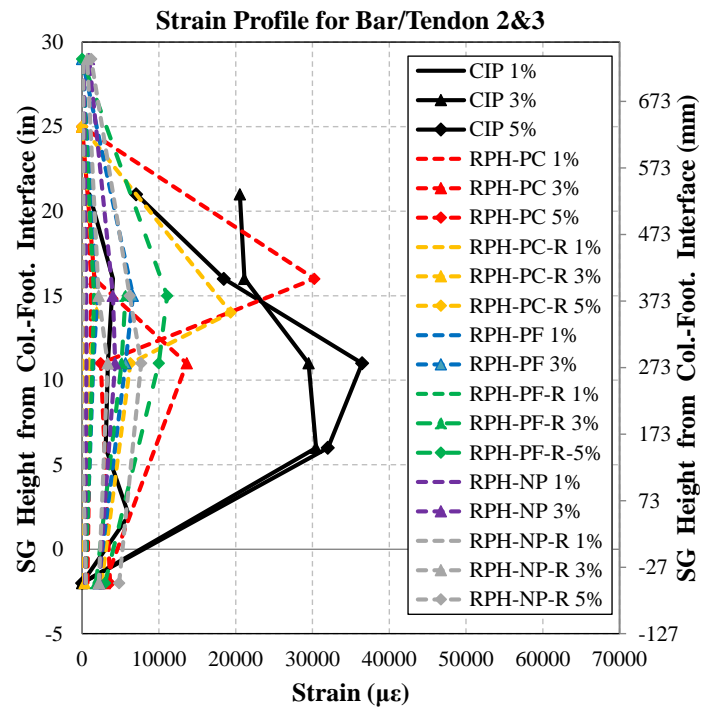
Figure 4.330. Measured CIP and Repairable Column Tensile Strain Profile for Bar/Tendon 2&3
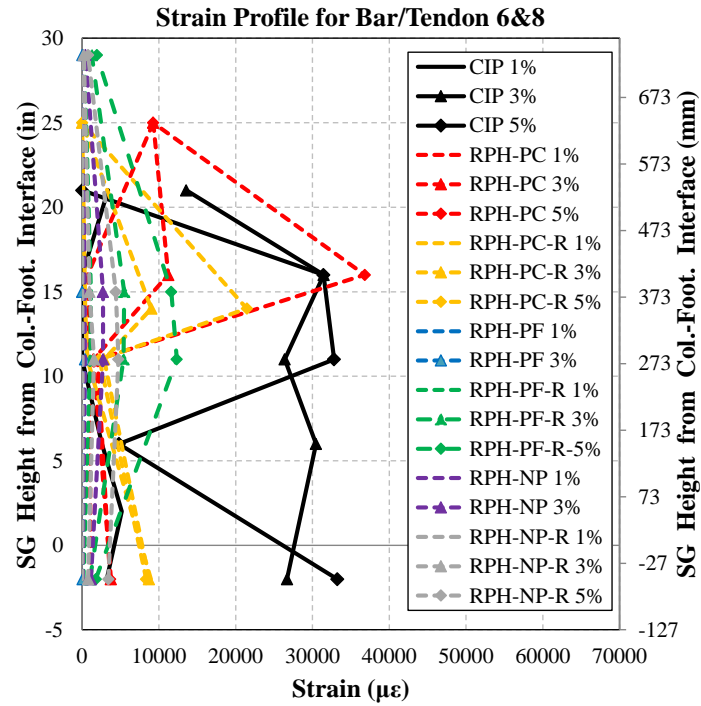
Figure 4.331. Measured CIP and Repairable Column Tensile Strain Profile for Bar/Tendon 6&8
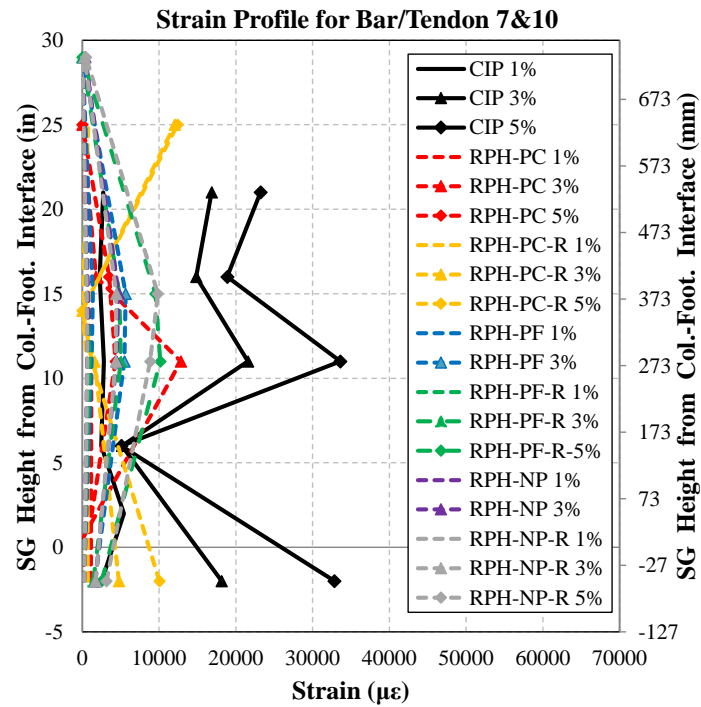
Figure 4.332. Measured CIP and Repairable Column Tensile Strain Profile for Bar/Tendon 7&10

268

4.6.5 Energy Dissipation

Figure 4.333 shows the cumulative energy dissipation of CIP and the repairable columns. All the repairable columns exhibited significantly lower energy dissipation than CIP. At the same drift level, the second test of each precast column also exhibited a lower energy dissipation than the original specimen mainly due to the accumulation of damage. RPH-PF and RPH-PF-R experienced the lowest energy dissipation among all columns due to the flag shaped hysteresis caused by the recentering of the tendon fuses. Furthermore, RPH-NP and RPH-NP-R, which used both tendon fuses and post-tensioned tendons, exhibited a large energy dissipation than other precast column due to the yielding of the longitudinal reinforcement of the rebar hinge connection incorporated at the column base.
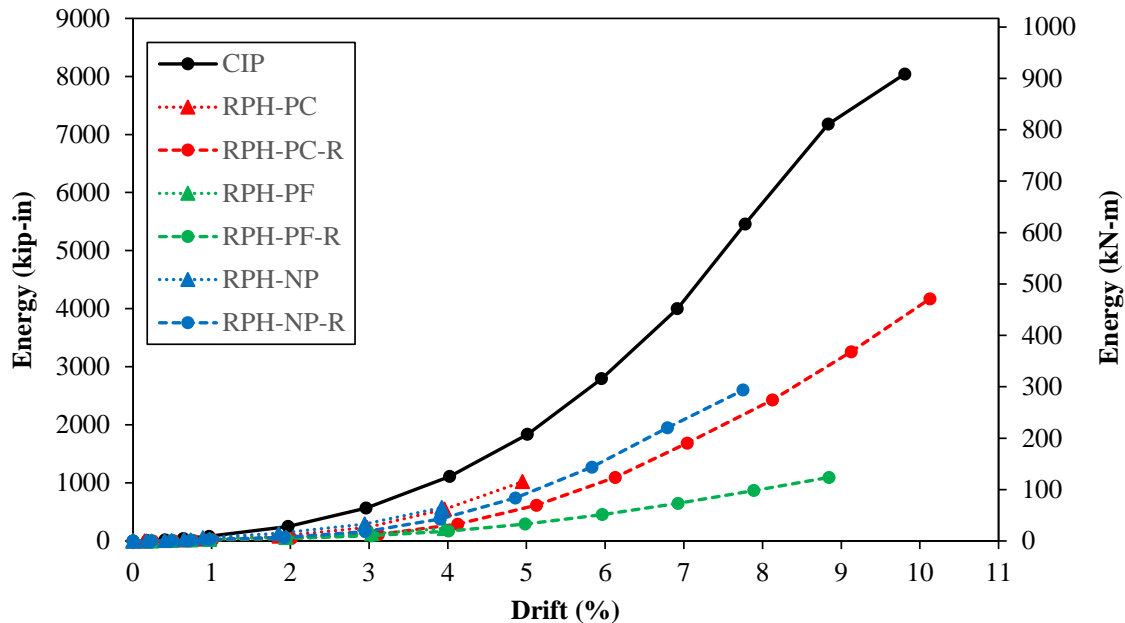
Figure 4.333. Energy Dissipation for CIP and Repairable Columns

4.7 Summary and Conclusions

One CIP and three repairable columns, all at 50%-scale, were tested under a cyclic loading protocol to failure. The precast columns were tested twice to practice repair-by-replacement technique. The first round of testing of the precast columns was ended at either 4% or 5% drift ratio to replace the exposed fuses. The external detachable fuses were made of either buckling restrained reinforcement (BRR) or steel tendons. A summary of the experimental findings is as follows:

- The mode of failure for CIP was the longitudinal bar rupture.
- RPH-PC-R did not fail at 10% drift ratio, but the test was stopped to prevent setup damage.
- The mode of failure for RPH-PF-R was tendon rupture while the mode of failure for RPH-NP-R was rupture of the neck bars at the rebar hinge connection.
- The drift ratio capacities for CIP, RPH-PC-R, RPH-PF-R, and RPH-NP-R were 8.96%, 9.8%, 8.9%, and 7.7%, respectively.
- The Z-shape buckling of stainless steel BRR used in the RPH-PC column made the repair by replacement very difficult. Furthermore, the column/footing dowels were bent, and the column had some residual displacements which made the placement of new BRR difficult. Nevertheless, the incorporation of the steel tendons as the tension-only fuses eliminated any column/footing dowel damage and further helped with the recentering of the columns. No to small residual

269

displacements are desired in the proposed columns since the column would be close to its original position easing the fuse replacement.

- All repairable columns showed smaller residual displacements compared with CIP. However, the residual displacement of RPH-PF was insignificant throughout the entire testing.
- A tendon fuse can double serve as typical longitudinal reinforcement and self-centering reinforcement with an additional benefit of accessibility for inspection since they are exposed.
- Use of UHPC greatly reduced apparent cracking and spalling, even at the fuse failure.
- All three repairable columns were successfully repaired after the initial testing and the repaired specimens were pushed well past the displacement demand for the corresponding CIP column. However, the repair of the column with stainless-steel BRR was difficult due to a Z-shape buckling at high drifts.

Overall, the study has proved that the repair-by-replacement of exposed bars is a feasible technique. The repairable columns with exposed tendon fuses and UHPC were found to be the most feasible alternative(s) and are recommended for future investigations and field deployments.

4.8 References

AASHTO SGS (2011) "AASHTO Guide Specifications for Seismic Bridge Design," Washington, D.C., American Association of State Highway and Transportation Officials.

ACI 374.2R-13 (2013). "Guide for Testing Reinforced Concrete Structural Elements Under Slowly Applied Simulated Seismic Loads." American Concrete Institute (ACI) Committee 374, Farmington Hills, MI, 2013.

ASTM A416/A416 M (2006). "Standard Specification for Steel Strand, Uncoated Seven-Wire for Prestressed Concrete." West Conshohocken, PA, 5 pp.

ASTM A706 (2016). "Standard Specification for Low-Alloy Steel Deformed and Plain Bars for Concrete Reinforcement." West Conshohocken, PA, 6 pp.

ASTM A760/A760M (2010). "Standard Specification for Corrugated Steel Pipe, Metallic-Coated for Sewers and Drains." West Conshohocken, PA, 15 pp.

ASTM A955/A955M (2019). "Standard Specification for Deformed and Plain Stainless Steel Bars for Concrete Reinforcement." West Conshohocken, PA, 15 pp.

ASTM E8 (2012). "Standard Test Methods for Tension Testing of Metallic Materials." ASTM International, West Conshohocken, PA.

ASTM C109/C109M-11b. (2011). "Standard Test Method for Compressive Strength of Hydraulic Cement Mortars (Using 2-in. or [50-mm] Cube Specimens)," West Conshohocken, PA.

ASTM C39/C39M-12. (2012). "Standard Test Method for Compressive Strength of Cylindrical Concrete Specimens," West Conshohocken, PA.

ASTM E8 (2012). "Standard Test Methods for Tension Testing of Metallic Materials." ASTM International, West Conshohocken, PA.

Boudaqa, A., Tazarv, M., and Tuhin, I. (2017). "Ductility without Confinement - A New Design and Construction Approach for RC Bridge Columns," International Journal of Bridge Engineering, Special Issue, pp. 53-77.

Caltrans. (2019). "Caltrans Seismic Design Criteria (SDC), Version 2.0" Sacramento, CA.: California Department of Transportation, 250 pp.

OpenSees. (2016). "Open System for Earthquake Engineering Simulations," Version 2.4.1, Berkeley, CA, Available online: http://opensees.berkeley.edu.

Saiidi, M.S., Tazarv, M., Varela, S., Bennion, S., Marsh, M.L., Ghorbani, I., Murphy, T.M. (2017). "Seismic Evaluation of Bridge Columns with Energy Dissipating Mechanisms, Volume 1: Research Overview and Volume 2: Guidelines," National Academies of Sciences, Engineering, and Medicine, NCHRP Report No. 864, Washington, DC: The National Academies Press, 344 pp.

Saiidi, M.S., Mehraein, M., Shrestha, G., Jordan, E., Itani, A., Tazarv, M., Sanders, D., Murphy, T.M., Reno, M.L., and Pohll, M.N. (2020). "Proposed AASHTO Seismic Specifications for ABC Column Connections," National Academies of Sciences, Engineering, and Medicine, NCHRP Report No. 935, Washington, DC: The National Academies Press, 354 pp.

Sjurseth, T., Greeneway, E., Hart, K., LaVoy, M., Tazarv, M., and Wehbe, N. (2022). "Mechanically Spliced Precast Bridge Columns," North Dakota State University - Upper Great Plains Transportation Institute, Fargo: Mountain-Plains Consortium (MPC), MPC Report No. 22-451, 359 pp.

Krawinkler, H. and Moncarz, P.D. (1982). Similitude Requirements for Dynamic Models." ACI Special Publication, Vol. 73, pp. 1-22.

LaVoy, M.R. (2020). "Seismic Performance of Mechanically Spliced Bridge Columns Through Analytical Studies." MS Thesis, South Dakota State University, 106 pp.

Zaghi, A.E. and Saiidi, M.S., (2010). "Seismic Performance of Pipe-pin Two-way Hinges in Concrete Bridge Columns," Journal of Earthquake Engineering, Vol. 14, No. 8, pp. 1253-1302.

CHAPTER 5. ANALYTICAL INVESTIGATION ON REPAIRABLE PRECAST BRIDGE COLUMNS

5.1 Introduction

The previous chapter discussed the experimental results for three repairable precast and one reference cast-in-place column. An analytical study was performed in this chapter to simulate the response of the column test specimens. All analyses were performed in OpenSees (2016).

Several studies have successfully modelled the behavior of conventional bridge columns (e.g., Tazarv and Saiidi, 2016; LaVoy, 2020; Sjurseth et al., 2022). Nevertheless, the repairable columns of the present study are relatively new, and models should be developed to estimate their responses. Boudaqa et al. (2017) proposed a finite element modeling method to simulate the behavior of precast bridge columns incorporating pipe-pin connections and steel BRR in the plastic hinge region (**Fig. 5.1**). Conventional bridge columns are often modeled using a single beam-column element. However, the inclusion of exposed reinforcement and a pipe-pin connection requires additional efforts. Tension-only and compression-only reinforcement of the different repairable column detailing also need to be included in the simulations. In Boudaqa's work, the neck and column sections were modeled using a beam-column element and the exposed tension-compression BRR were modeled using truss elements. Lateral springs were included to simulate the pipe-pin connection. The remaining non-reduced diameter portion of BRR was modeled using rigid-link elements on either side of the BRR trusses which were then connected to the main column element using concrete elastic elements. The modelling method by Boudaqa et al. (2017) was adopted in the present study, was further refined to accommodate different repairable alternatives, and validated using test data discussed in the previous chapter. The analytical work is discussed herein.
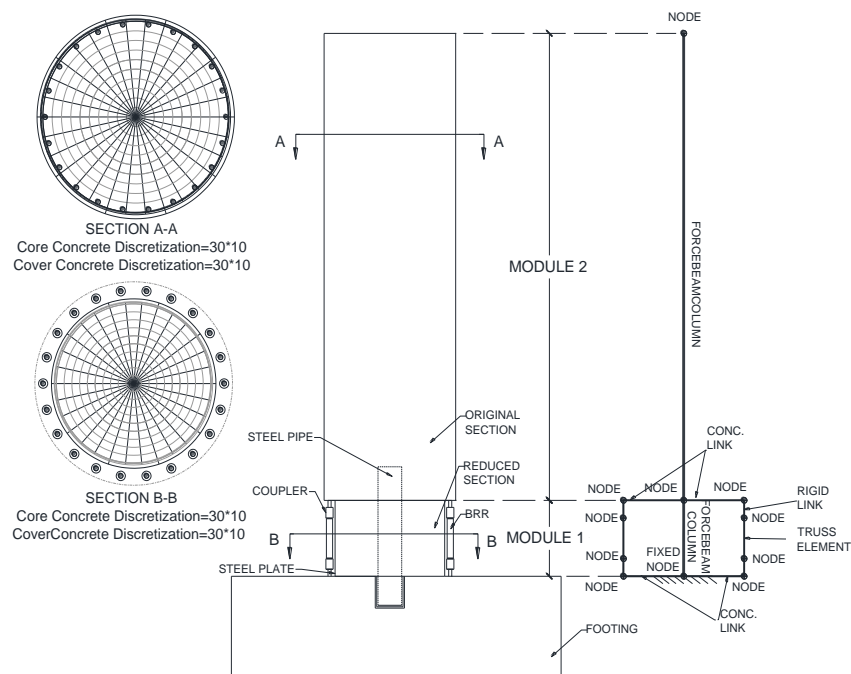
Figure 5.1. Finite Element Modeling Method for Repairable Precast Bridge Columns (Boudaqa et al., 2017)

5.2 Analysis of Column Test Specimens

The following section discusses the modeling method used for the reference cast-in-place column as well as the three repairable precast columns.

5.2.1 Modeling Methods

A three-dimensional finite element model utilizing six degrees of freedom (DOFs) and a fiber-section was used to analyze the CIP, RPH-PC, RPH-PF, and RPH-NP columns.

5.2.1.1 CIP Column Model

The cast-in-place column tested by Sjurseth et al. (2022) was modeled using a single "forceBeamColumn" element as shown in **Fig. 5.2**. Five integration points with the same cross section were used along the length of the column model. The measured mechanical properties (**Ch. 4**) were used for steel and concrete. Cover and core concrete were modeled with "Concrete01" and were discretized into 10×4 and 50×50 fibers, respectively. The material model proposed by Mander et al. (1988) was used for the confined (core) concrete. The longitudinal bars were modeled using "reinforcingSteel". The P-Δ and bond-slip effects were included in the analysis based on the study by Tazarv and Saiidi (2014). A summary of the material properties used in the CIP analytical model are presented in **Table 5.1**.
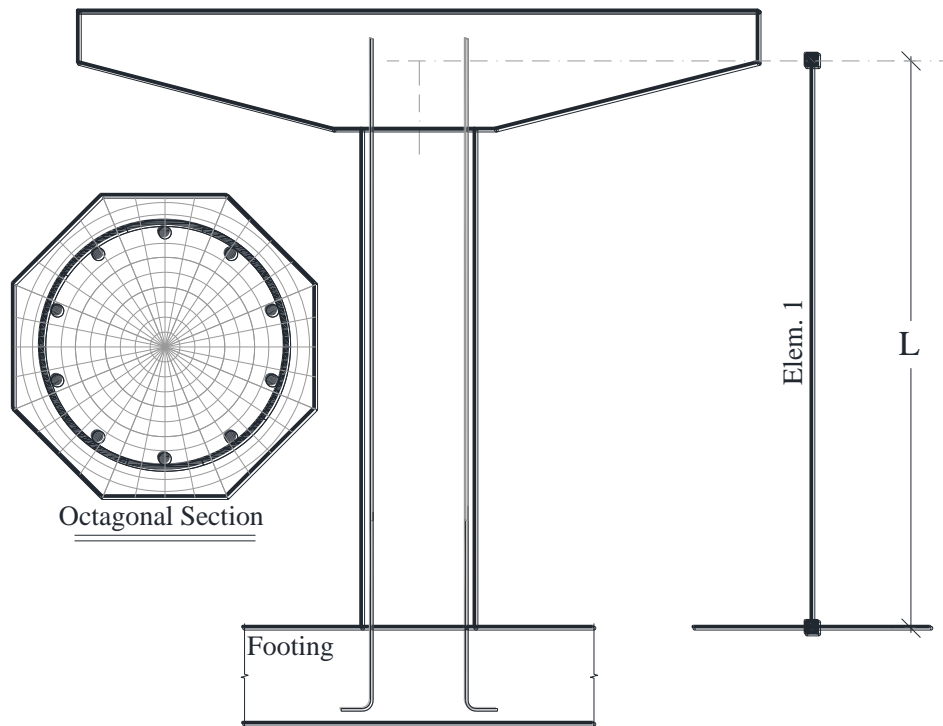
Figure 5.2. Analytical Modeling Method for Cast-in-Place Column (Sjurseth et al., 2022)

273

Table 5.1. Sectional Fiber Material Properties Used in CIP from Sjurseth et al. (2022)

Concrete Fibers	
Application: Unconfined concrete	Application: Confined concrete (based on Mander's model)
Type: Concrete01	Type: Concrete01
f'_{cc} = -4300 psi (29.6MPa)	f'_{cc} = -7930 psi (54.7 MPa)
ε_{cc} = -0.002 in/in	ε_{cc} = -0.0104 in/in
f'_{cu} = -0.0 psi (0 MPa)	f'_{cu} = -6950 psi (47.9 MPa)
ε_{cu} = -0.005 in/in	ε_{cu} = -0.0341 in/in
Steel Fibers	
Application: Bars at the base including bond-slip effects	Application: Bars above the base
Type: ReinforcingSteel	Type: ReinforcingSteel
f_y = 69.3 ksi (477.8 MPa)	f_y = 69.3 ksi (477.8 MPa)
f_{su} = 97.4 ksi (671.5 MPa)	f_{su} = 97.4 ksi (671.5 MPa)
E_s = 10640 ksi (20000 MPa)	E_s = 29000 ksi (20000 MPa)
E_{sh} = 840 ksi (5880 MPa)	E_{sh} = 853 ksi (5880 MPa)
ε_{sh} = 0.009 in/in	ε_{sh} = 0.005 in/in
ε_{su} = 0.126 in/in	ε_{su} = 0.12 in/in

5.2.1.2 RPH-PC Column Model

Figure 5.3 shows the analytical model for the RPH-PC column. Similar to CIP, an octagonal cross section with side dimensions of 24 in. (610 mm) and a height of 8 ft (2.44 m) were used in all the repairable column models. The columns were reinforced longitudinally with 10 – No. 10 (32-mm) bars in the main cross section (above the neck) and transversely with No. 4 (13-mm) hoops spaced at 2 in. (51 mm) in both the main cross section and the reduced neck section in the lower 24 in. (0.61 m) of the column. The cross section of the reduced neck was circular with a diameter of 16.5 in. (419 mm) and was reinforced longitudinally with 14 – No. 8 (25-mm) bars. Two "forceBeamColumn" elements each with five integration points were used to model the neck and main column members.

The bottom of the column model was fixed (both in translation and rotation DOFs) despite the actual column using a pipe-pin connection. A fixed connection was needed in the analytical model for the stability purposes. Note that the pipe-pin connection allowed rotation but did not act entirely as a true pin since the concrete at the base of the column on the north and south sides was in contact with the footing during cycles at each pull and push, respectively, causing rocking of the column. The 14 – No. 8 (25-mm) bars in the column neck did not extend into the footing and thus experienced limited tensile stresses but did add to the column stiffness as they sustained compressive stresses as the column rocked. To approximate this behavior, the neck bars were modeled using the "hysteretic" material model following the longitudinal bar properties in compression but with negligible tensile strength. No bond slip was included in the model since the neck bars did not extend into the footing. The P-Δ effects were included.

The BRR elements were simulated using ten "truss" elements spread radially around the center two "forceBeamColumn" elements. The truss elements had the length and diameter of the "dog-bone" portion of the BRR (including half of the fillet on either side). Two analytical models were created for RPH-PC to match the two separate tests with the first utilizing the long (colored in yellow) BRR with a dog-bone length of 11.25 in. (273 mm) and the second with the short (colored in green) BRR with a dog-bone length of 6.125 in. (143 mm). While the model proposed by Boudaqa et al. (2017) used "rigidLink" elements at both ends of the truss to approximate the remaining exposed length of the bars in the neck section (the length associated with the BRR none reduced sections and the column/footing dowels), it was determined that only the fuse overall length (L_f in **Fig. 5.3**) affects the model behavior, thus the additional bars were removed from the model.

The truss elements were connected to the column section using ten "elasticBeamColumn" elements. The core concrete properties were used to determine the modulus of elasticity used in the beam-column elements while it was found that the cross section used to determine the area and moment of inertia could best be approximated using a rectangle with a width equal to one-tenth of the circumference of the column core and an arbitrary height. The height used was 3.5 in. (89 mm) and was determined based on the approximate length of the spalled section on the south column face directly above the entry point of the longitudinal bars into the column octagonal cross section.

The core and cover of the column octagonal cross section were modeled using "Concrete01" and were discretized into 30×10 and 10×4 fibers, respectively. The core and cover of the neck section also used "Concrete01" and were discretized into 30×10 and 10×10 fibers, respectively. The stainless-steel fibers of the BRR core in the "truss" elements utilized a "Steel02" material model. Only measured material properties were included in the model. Table 5.2 presents a summary of the material properties and models used in the RPH-PC analysis.
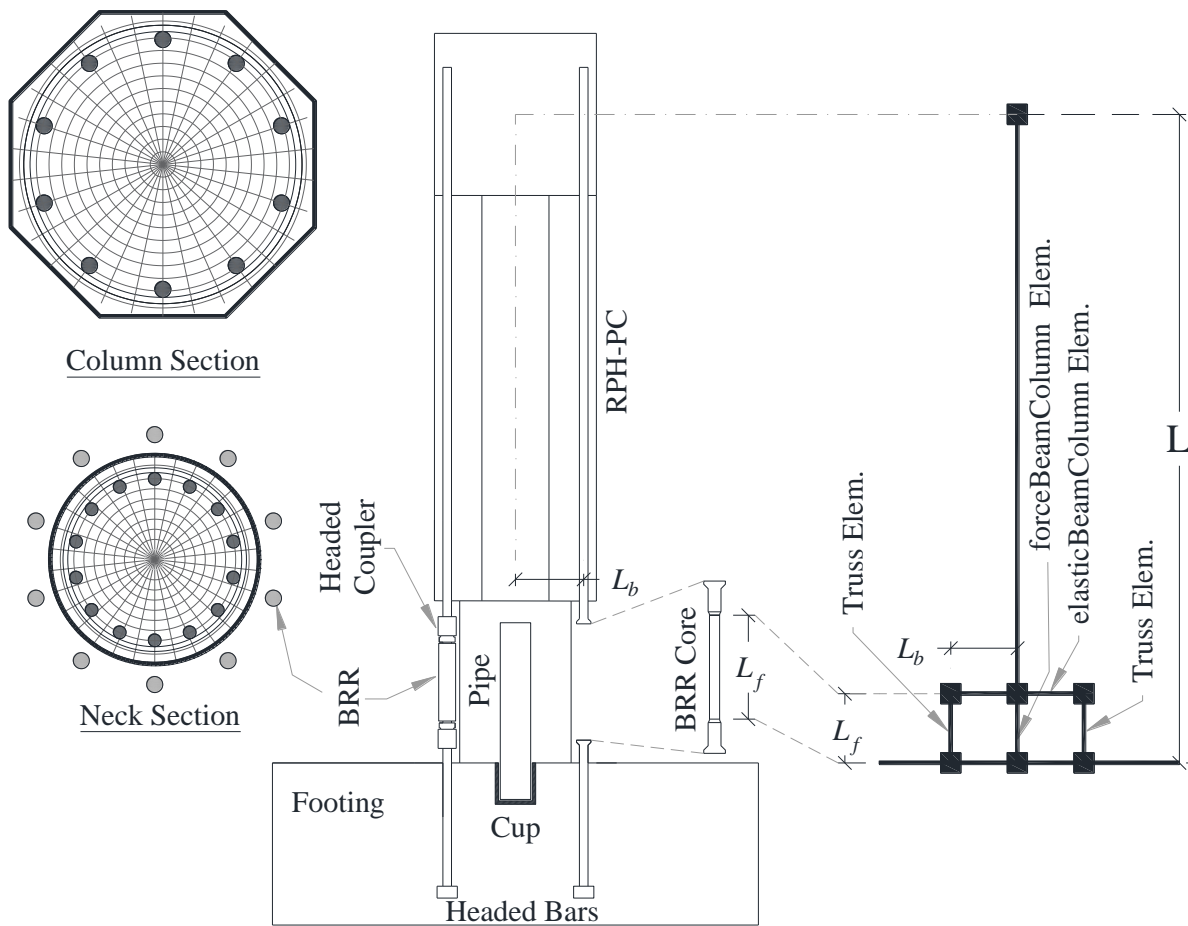
Figure 5.3. Analytical Modeling Method for RPH-PC

275

Table 5.2. Sectional Fiber Material Properties Used in RPH-PC

Concrete Fibers	
Application: Unconfined SCC Type: Concrete01 f'_{cc} = -10136 psi (69.9 MPa) ε_{cc} = -0.002 in/in f'_{cu} = -6082 psi (41.9 MPa) ε_{cu} = -0.005 in/in	Application: Confined SCC in column octagonal section (based on Mander's model) Type: Concrete01 f'_{cc} = -14494 psi (99.9 MPa) ε_{cc} = -0.00555 in/in f'_{cu} = -10136 psi (69.9 MPa) ε_{cu} = -0.0157 in/in
	Application: Confined SCC in circular neck section (based on Mander's model) Type: Concrete01 f'_{cc} = -16049 psi (110.7 MPa) ε_{cc} = -0.007 in/in f'_{cu} = -12143 psi (83.7 MPa) ε_{cu} = -0.0198 in/in

Steel Fibers	
Application: main longitudinal bars including BRR (symmetric material in tension/compression) Type: Steel02 f_y = 100 ksi (689.7 MPa) E_s = 29000 ksi (20000 MPa) B_s = 0.002843 R_0 = 2.3 cR_1 = 0.925 cR_2 = 0.15	Application: neck longitudinal bars (compression only, tension ignored) Type: Hysteretic f_y = -69.3 ksi (477.9 MPa) ε_y = -0.00239 in/in f_2 = -69.3 ksi (477.9 MPa) ε_2 = -0.0115 in/in f_u = -97.4 ksi (671.7 MPa) ε_u = -0.12 in/in

The stress-strain data for the BRR truss elements within the model was monitored to determine the failure point while column tip displacement and lateral base shear were also recorded. The failure point of the analytical model was determined when one of the following two limit states occurred:

1) The extreme BRR on the tension side reached their ultimate tensile strain,
2) The column lateral load resistance dropped below 85% of the lateral strength after the peak load.

It should be noted that the failure of the extreme concrete fiber at the compression side was not considered when determining the failure point of the analytical model since concrete crushed at the base of the column during the physical testing of RPH-PC but had minimal effects on the lateral strength of the column.

5.2.1.3 RPH-PF Column Model

Figure 5.4 shows the analytical model for RPH-PF. The same cross section as RPH-PC was used for RPH-PF. However, the number of column longitudinal bars was increased from 10 to 14. Further, No. 10 (32-mm) back steel bars were used as the longitudinal reinforcement. Double hoops with a size of No. 4 (13 mm) were utilized with a spacing of 2 in. (51 mm). The neck and column were again modeled with two "forceBeamColumn" elements while the tendon fuses were modeled with "truss" elements. The neck bar orientation was changed to include 12 – No. 9 (29 mm) black steel bars (to accommodate the lateral bolts used in the pipe-pin connection to eliminate any lateral gap in the connection).

The neck longitudinal bars were modeled using a "hysteretic" material model to include only their compressive strength and ignore the tensile strength since the neck bars were not extended into the column footing. The length of the truss elements was 15 in. (381 mm), which was the exposed portion of the tendons between two couplers (L_f shown in the figure). The material used for the fuses was switched from "steel02" as in RPH-PC to "hysteretic" to only simulate the tensile behavior (cables do not have any compressive strength). A summary of the material properties and models used for RPH-PF is presented in **Table 5.3**. UHPC was modeled using the "Concrete01" material and its confined properties were estimated using the Mander's model. It is understood that such material model and mechanical properties are not valid for UHPC. However, this one done since UHPC of RPH-PF in both tests had insignificant damage and the measured stains of core UHPC was less than 4000 $\mu\varepsilon$ (0.004 mm/mm). Furthermore, for UHPC, steel confinement models and material models (e.g., in OpenSees) are yet to be developed.
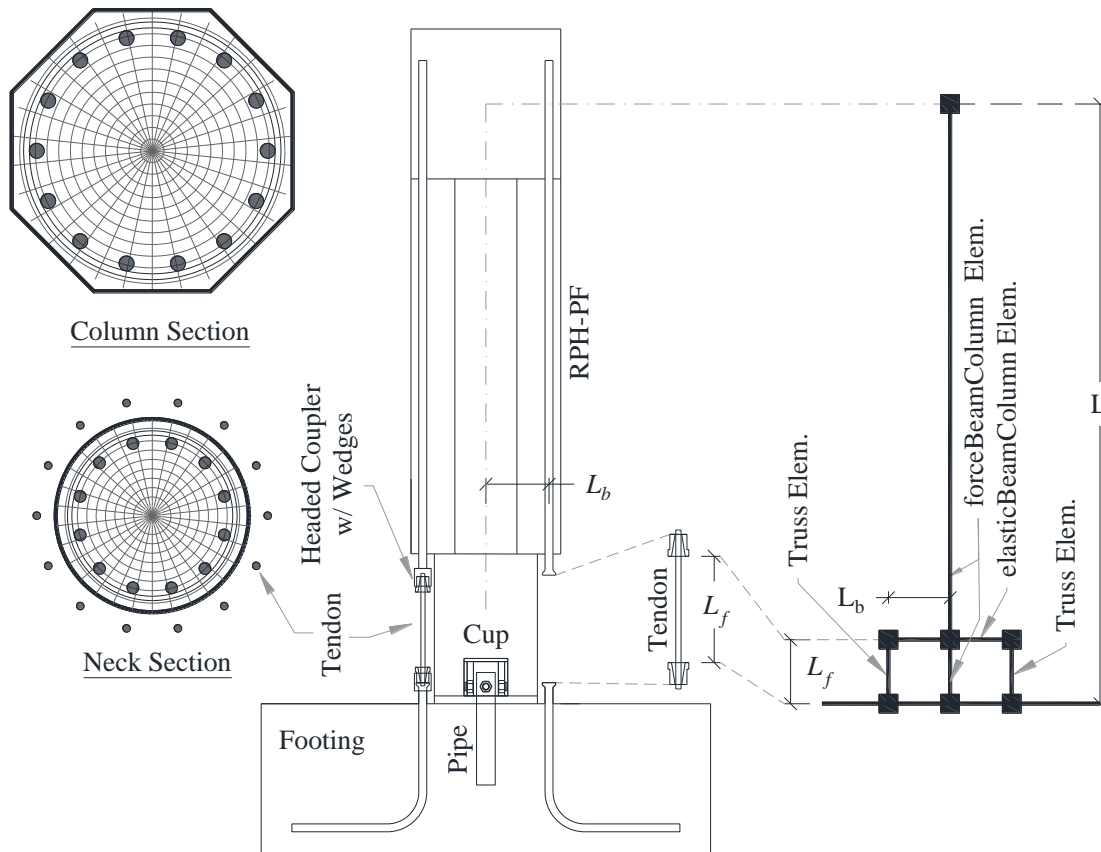
Figure 5.4. Analytical Modeling Method for RPH-PF

Table 5.3. Sectional Fiber Material Properties Used in RPH-PF

Concrete Fibers	
Application: Unconfined UHPC Type: Concrete01 f'_{cc} = -14533psi (100 MPa) ε_{cc} = -0.0027 in/in f'_{cu} = -7267 psi (50 MPa) ε_{cu} = -0.005 in/in	Application: Confined UHPC in column octagonal section (based on Mander's model) Type: Concrete01 f'_{cc} = -18574 psi (128 MPa) ε_{cc} = -0.0048 in/in f'_{cu} = -8974 psi (61.9 MPa) ε_{cu} = -0.0148 in/in
	Application: Confined UHPC in circular neck section (based on Mander's model) Type: Concrete01 f'_{cc} = -21142 psi (146 MPa) ε_{cc} = -0.0065 in/in f'_{cu} = -13140 psi (90.6 MPa) ε_{cu} = -0.0205 in/in
Steel Fibers	
Application: Column longitudinal bars Type: ReinforcingSteel (symmetric) f_y = 67.1 ksi (462.6 MPa) f_{su} = 105.5 ksi (727.4 MPa) E_s = 29000 ksi (20000 MPa) E_{sh} = 1125 ksi (7756 MPa) ε_{sh} = 0.00557 in/in ε_{su} = 0.117 in/in	Application: Neck longitudinal bars Type: Hysteretic (in compression only) f_y = -69.3 ksi (477.9 MPa) ε_y = -0.00239 in/in f_2 = -69.3 ksi (477.9 MPa) ε_2 = -0.0115 in/in f_u = -97.4 ksi (671.7 MPa) ε_u = -0.12 in/in
	Application: Fuse tendons Type: Hysteretic (in tension only) f_y = 284 ksi (1958 MPa) ε_y = 0.01 in/in f_2 = 306 ksi (2110 MPa) ε_2 = 0.0275 in/in f_u = 306.5 ksi (2113 MPa) ε_u = 0.062 in/in

The lateral base shear, column tip displacement, and stress-strain data for the tendon fuses were measured in the analytical model. Failure was defined as one of the following two limit states:

1) The extreme tendons on the tension side reached their ultimate tensile strain,
2) The column lateral load resistance dropped below 85% of the peak lateral load.

5.2.1.4 RPH-NP Column Model

Figure 5.5 shows the analytical model developed for RPH-NP. Most of material and modeling methods including the column and neck cross sections were the same as those used in RPH-PF. However, some modifications were made to include the specific detailing of this test specimen. Since the neck bars of RPH-NP were extended into the footing, the neck bar material model was changed to "ReinforcingSteel" simulating a symmetric behavior. Furthermore, the distribution radius of the neck bar at the column-footing interface was reduced to 3 in. (76 mm) simulating the rebar hinge. Bond-slip effects of the neck bars were modeled using the technique proposed by Tazarv and Saiidi (2014).

The post-tensioning tendons of RPH-NP (at the column center) was modeled using a "corotTruss" element which stretched between nodes 1 and 3 at the bottom and top of the column, respectively. The total combined area of the 15 – 0.5 in. (13-mm) diameter strands was used as the area of this element. Furthermore, this element utilized an "InitStressMaterial", which was stressed to the initial average stress of the tendons after all post-tensioning losses. A "Steel01" material model was considered for the post-tensioning tendons. **Table 5.4** presents a summary of the material models used for RPH-NP. Failure was again defined as either rupture of the tendon fuses or a 15% drop in the lateral force resistance.
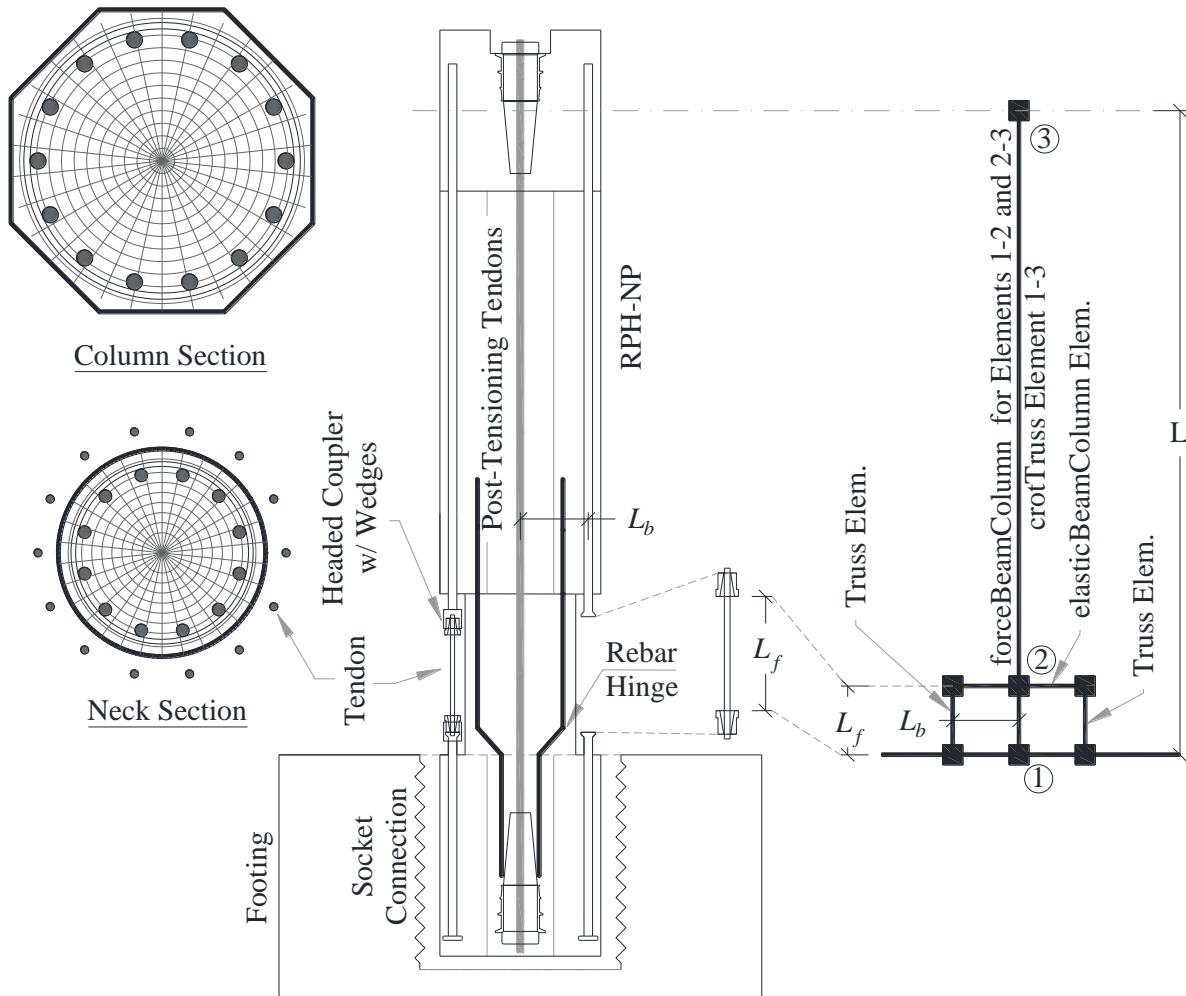
Figure 5.5 Analytical Modeling Method for RPH-NP

Table 5.4. Sectional Fiber Material Properties Used in RPH-NP

Concrete Fibers	
Application: Unconfined UHPC Type: Concrete01 f'_{cc} = -15144 psi (104 MPa) ε_{cc} = -0.0025 in/in f'_{cu} = -7572 psi (52.2 MPa) ε_{cu} = -0.005 in/in	Application: Confined UHPC in column octagonal sections (based on Mander's model) Type: Concrete01 f'_{cc} = -19196 psi (132MPa) ε_{cc} = -0.0047 in/in f'_{cu} = -8650 psi (59.6 MPa) ε_{cu} = -0.0144 in/in
	Application: Confined UHPC in circular neck section (based on Mander's model) Type: Concrete01 f'_{cc} = -21780 psi (150.17 MPa) ε_{cc} = -0.0064 in/in f'_{cu} = -13050 psi (90.0 MPa) ε_{cu} = -0.02 in/in

Steel Fibers	
Application: Column longitudinal bars Type: ReinforcingSteel f_y = 67.1 ksi (462.6 MPa) f_{su} = 105.5 ksi (727.4 MPa) E_s = 29000 ksi (20000 MPa) E_{sh} = 1125 ksi (7756 MPa) ε_{sh} = 0.00557 in/in ε_{su} = 0.117 in/in	Application: Neck longitudinal bars Type: ReinforcingSteel f_y = 65.05 ksi (462.6 MPa) f_{su} = 101.8 ksi (727.4 MPa) E_s = 29000 ksi (20000 MPa) E_{sh} = 1127 ksi (7756 MPa) ε_{sh} = 0.00416 in/in ε_{su} = 0.1113 in/in
Application: Post-Tensioning tendons Type: InitStressMaterial and Steel01 f_{init} = 47.12 ksi (324.9 MPa) f_y = 245 ksi (1689 MPa) E_s = 28500 ksi (196500 MPa) B_s = 0.040	Application: Fuse tendons Type: Hysteretic (in tension only) f_y = 284 ksi (1958 MPa) ε_y = 0.01 in/in f_2 = 306 ksi (2110 MPa) ε_2 = 0.0275 in/in f_u = 306.5 ksi (2113 MPa) ε_u = 0.062 in/in

The stress-strain data for the tendon fuses of the model was monitored to determine a failure point while column tip displacement and lateral forces were also recorded. The failure point of the analytical model was determined when one of the following two limit states occurred:
1) The extreme tendon fuses on the tension side reached their ultimate tensile strain,
2) The column lateral load resistance dropped below 85% of the peak lateral strength.

Failure of the extreme UHPC fiber at the compression side was not considered when determining the failure point of the analytical model since the actual column did not fail by UHPC failure.

5.2.2 Calculated Force-Displacement Relationships

The following section presents the pushover response of each of the column models and compares them with the physical test data. Full cyclic responses will be determined in future studies.

5.2.2.1 CIP Column Model Response

Figure 5.6 shows the calculated and measured force-displacement relationships for the CIP column. The initial stiffness of the calculated and measured pushover curves matched well. Furthermore, there was only a 5.4% difference between the calculated (61.9 kips or 276 kN) and measured (65.4 kips or 291 kN) lateral strength of the column. The calculated drift capacity of CIP was 7.64%, which was 14.7% lower than the measured drift capacity of 8.96%. A drop in the calculated lateral force can be seen between drifts of 1% and 3%; however, the calculated and measured forces match well beyond 3% drift. The model predicted that CIP failed by bar fracture, which was also observed in the column testing.
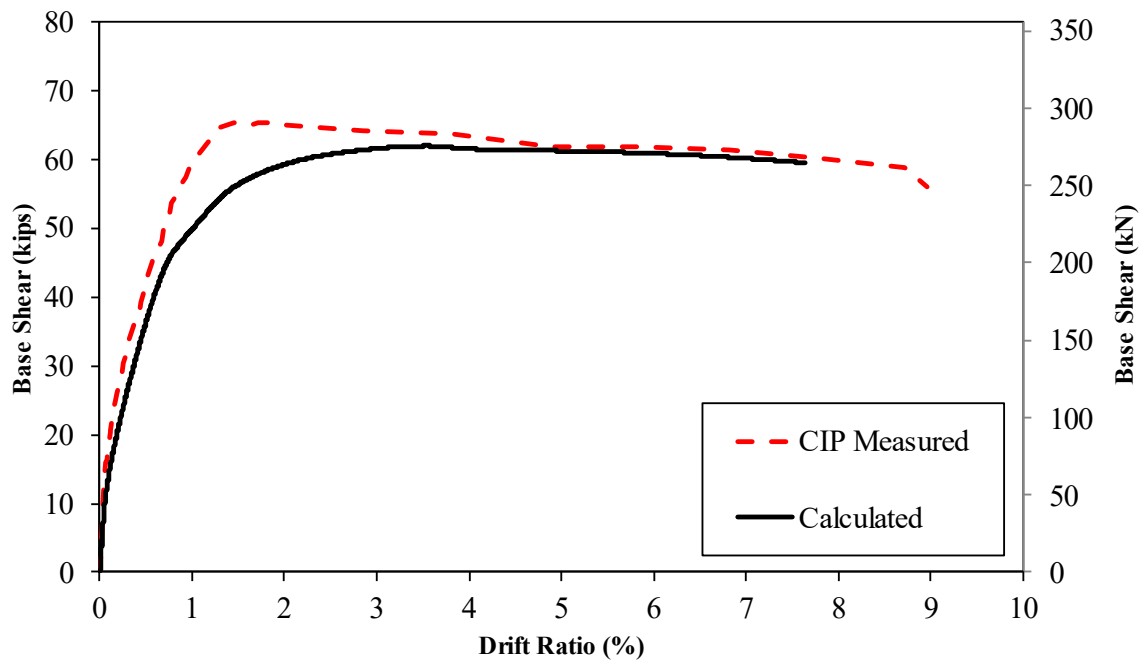
Figure 5.6. Calculated and Measured Force-Drift Relationships for CIP (Sjurseth et al. 2022)

5.2.2.2 RPH-PC Column Model Response

Figure 5.7 shows the calculated and measured force-drift relationships for RPH-PC with the long BRR (L_f of 11.25 in (286 mm) used in the first test). The initial calculated stiffness is slightly higher than the measured stiffness. The calculated peak lateral force was 64.0 kips (285 kN) while the measured lateral strength was 5.6% higher (67.8 kips or 302 kN). The first test of RPH-PC was stopped at a drift ratio of 5% to perform the fuse replacement. Nevertheless, the analytical model predicts that the failure is at 13.2% drift ratio due to a strength degradation. Overall, the analytical model for RPH-PC using the long fuses reasonably reproduced the behavior of RPH-PC up to 5% drift.

Figure 5.8 shows the calculated and measured force-drift relationships for RPH-PC-R with the short BRR (L_f of 6.125 in. or 156 mm). It is evident that the measured initial stiffness is significantly lower than the calculated initial stiffness. It was expected that a reduction of the BRR dog-bone length would increase the overall stiffness and decrease the displacement capacity. Nevertheless, a significant spalling of concrete at the base of the column and on the south face right above the neck in the first test led to this reduced stiffness in the second test. The calculated peak lateral force was 65.8 kips (293 kN) while the measured peak lateral force was 72.7 kips (322 kN), a 9.5% difference. Furthermore, the calculated lateral force reached its peak at a drift ratio of 4% and plateaued afterwards while the measured peak lateral force was around 8% drift ratio. The calculated drift capacity of RPH-PC-R was 8.69% while the measured drift capacity for this column was at 9.80% drift, a 11.3% difference.

The analytical model for RPH-PC-R predicts a failure due to the bar rupture; however, the physical test was stopped at 10% drift cycle. In the end, it is evident that the changes in the cross section between the two tests due to crushing of SCC and Z-shape buckling of BRR changed the measured responses between the two tests making it difficult to fully simulate such changes. Overall, the model predicted the initial stiffness of the first test and the failure of the second test with a reasonable accuracy. More advanced modeling methods are needed to included material degradation between the tests of RPH-PC.
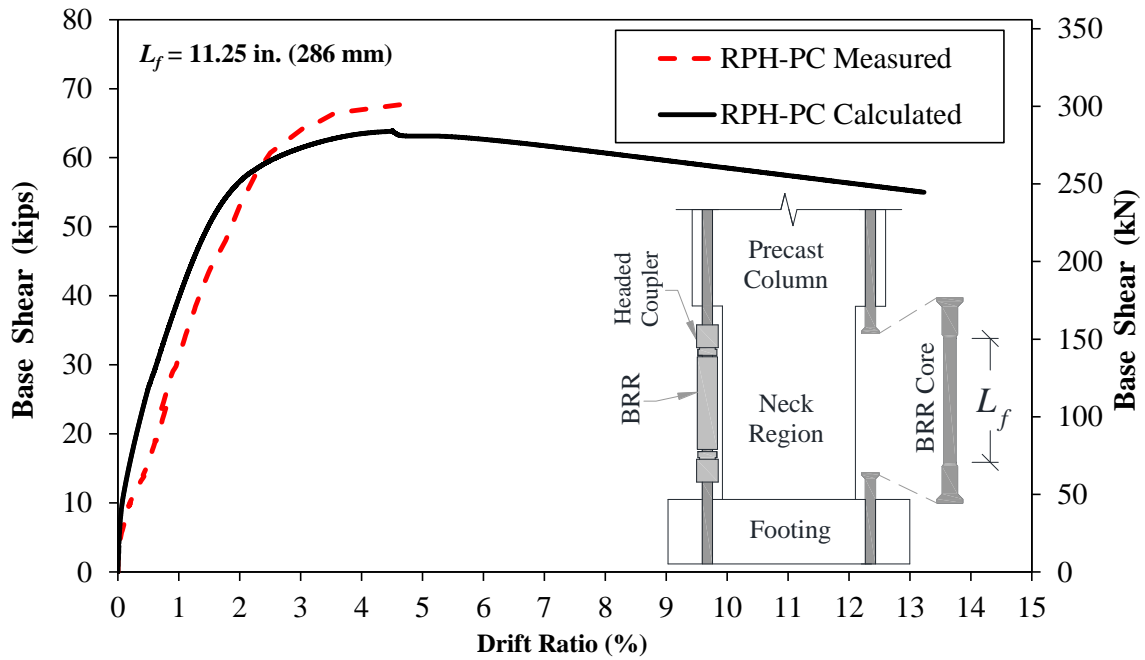
Figure 5.7. Calculated and Measured Force-Drift Relationships for RPH-PC (Long Fuse)
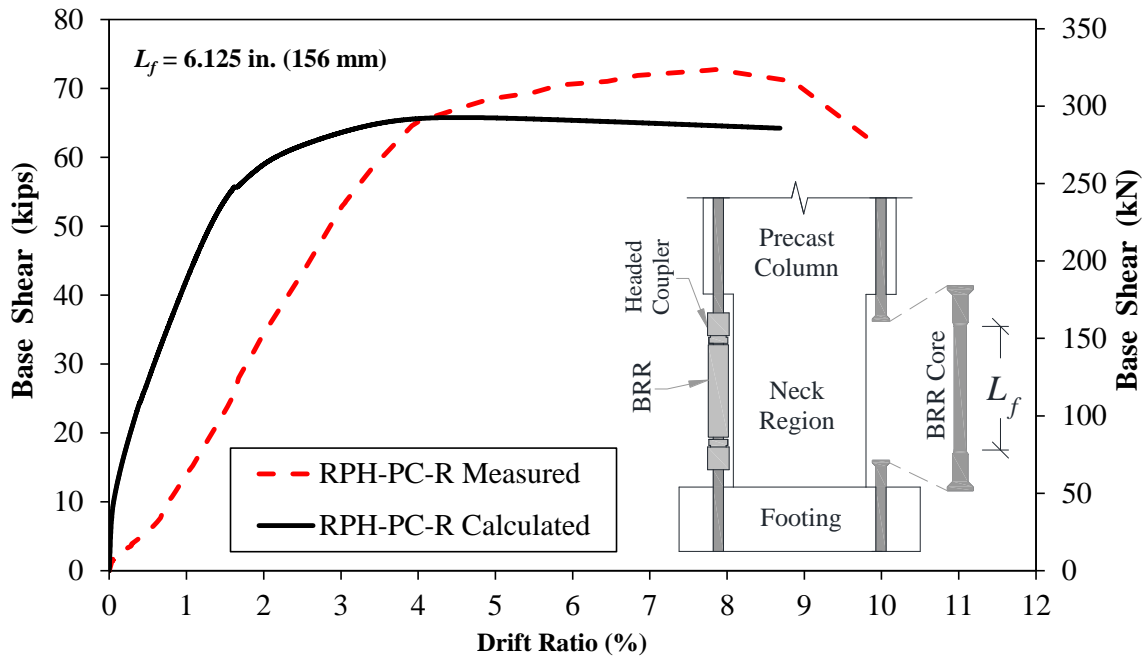
Figure 5.8. Calculated and Measured Force-Drift Relationships for RPH-PC-R (Short Fuse)

5.2.2.3 RPH-PF Column Model Response

Figure 5.9 shows the calculated and measured force-drift relationships for both RPH-PF and RPH-PF-R. The same analytical model was used for both columns since no change to the fuse properties and geometries was made. The average fuse length (L_f) was 13 in. (330 mm) but differed slightly between tendons due to a minor slipping of some wedges during installation and a minor difference in the column/footing dowel lengths. The calculated and measured initial stiffnesses were similar up to 5 kips (22 kN) after which the stiffness of the test specimens softened. The calculated peak lateral force was 56.8 kips (253 kN) while the measured lateral strength was slightly higher at 57.9 kips (258 kN), a 1.9% difference. The analytical model predicted the failure drift at 8.03% due to the rupture of the tendon fuses. RPH-PF-R failed at 8.91% drift ratio in the test, which is 9.9% higher than the calculated failure drift. Overall, the analytical model reproduced the behavior of the RPH-PF and RPH-PF-R columns with a reasonable accuracy.

Figure 5.9. Calculated and Measured Force-Drift Relationships for RPH-PF and RPH-PF-R

5.2.2.4 RPH-NP Column Model Response

The calculated and measured force-drift relationships for both RPH-NP and RPH-NP-R are shown in **Fig. 5.10**. Similar to RPH-PF, no change was made to the fuse properties and geometries between the two tests thus the same model was utilized for both columns. The average fuse length (L_f) was again 13 in. (330 mm) with a slight difference between tendons. It can be seen that the measured initial stiffness of the RPH-NP column matched well that of the analysis. The initial stiffness of RPH-NP-R was degraded between the two tests, mainly due to the UHPC and neck bar damage, which was not included in the analysis. The calculated peak lateral force was 83.0 kips (369 kN) while the measured lateral strength was 83.5 kips (371 kN), only a 0.6% difference.

While the calculated stiffness and lateral load capacity of RPH-PF matched those of the testing, the calculated drift capacity was 9.59%, which was 25% higher than the measured drift capacity of 7.68%. The model predicts that the column fails by a tendon fuse rupture; however, the actual column failed by the strength degradation caused by the bar fracture in the rebar hinge connection. This is likely due to the large cracking of UHPC at the column-footing interface resulting in a high strain concentration at the rebar hinge, which would be very hard to simulate in software that assumes plane sections remain plane.

Figure 5.10. Calculated and Measured Force-Drift Relationships for RPH-NP and RPH-NP-R

5.3 Summary and Conclusions

This chapter presented the analytical modeling methods that were developed for the three repairable precast columns tested in this project. The models were able to replicate the force-displacement relationship of the columns with a reasonable accuracy. Further analyses are needed to include the material degradation between two tests. Cyclic and dynamic models are yet to be developed.

5.4 References

AASHTO SGS. (2011). "AASHTO Guide Specifications for LRFD Seismic Bridge Design," Washington, DC: American Association of State Highway and Transportation Officials.

Boudaqa, A., Tazarv, M., and Tuhin, I. (2017). "Ductility without Confinement - A New Design and Construction Approach for RC Bridge Columns," International Journal of Bridge Engineering, Special Issue, pp. 53-77.

LaVoy, M.R. (2020). "Seismic Performance of Mechanically Spliced Bridge Columns through Analytical Studies." MS Thesis, South Dakota State University, 106 pp.

Mander, J.B., Priestley, M.J.N., Park, R. (1988). "Theoretical Stress-Strain Model for Confined Concrete," Journal of Structural Engineering, ASCE, Vol. 114, No. 8, pp. 1804-1826.

OpenSees. (2016). "Open System for Earthquake Engineering Simulations," Version 2.4.1, Berkeley, CA, Available online: http://opensees.berkeley.edu.

Sjurseth, T., Greeneway, E., Hart, K., LaVoy, M., Tazarv, M., and Wehbe, N. (2022). "Mechanically Spliced Precast Bridge Columns," North Dakota State University - Upper Great Plains Transportation Institute, Fargo: Mountain-Plains Consortium (MPC), MPC Report No. 22-451, 359 pp.

Tazarv, M. and Saiidi, M.S. (2014) "Next Generation of Bridge Columns for Accelerated Bridge Construction in High Seismic Zones," Center for Civil Engineering Earthquake Research, Department of Civil and Environmental Engineering, University of Nevada, Reno, Nevada, Report No. CCEER-14-06, 400 pp.

Tazarv, M. and Saiidi, M.S. (2016). "Seismic Design of Bridge Columns Incorporating Mechanical Bar Splices in Plastic Hinge Regions," Engineering Structures, DOI: 10.1016/j.engstruct.2016.06.041, Vol 124, pp. 507-520.

CHAPTER 6. PARAMETRIC STUDY ON REPAIRABLE PRECAST BRIDGE COLUMNS

6.1 Introduction

The experimental study presented in **Ch. 3** proved the feasibility of three repairable precast bridge column alternatives through cyclic testing of 50%-scale specimens. The post-test analytical study presented in the previous chapter offered modeling methods for these repairable bridge columns. The current chapter discusses a parametric study which was performed to investigate the seismic performance of full-scale repairable bridge columns with different variables. OpenSees (2016) was used in the parametric study.

6.2 Analytical Bridge Columns

Conventional bridge columns are monolithically cast with their footings (and the cap beams). Current pushover and dynamic modeling methods for cast-in-place (CIP) columns usually incorporate a single distributed or lumped plasticity element with a constant cross section. A previous study at SDSU (Sjurseth et al., 2022) explored the effects of three critical parameters on the behavior of full-scale CIP columns: aspect ratio (AR), axial load index (ALI), and displacement ductility capacity (μ or D). The aspect ratio refers to the column length divided by the column diameter or side dimension. The axial load index is the ratio of the column axial load to the product of the column cross sectional area and concrete strength. The displacement ductility capacity is the ratio of the column tip displacement to the effective yield displacement. Nine CIP columns with three ARs (of 4, 6, and 8) and three ALIs (of 5%, 10%, and 15%), all with a displacement ductility capacity of 7, were adopted from Sjurseth et al. (2022) and were included herein as the reference models. Only the CIP columns with the highest ductility were included since any repairable column matching or exceeding its corresponding CIP column's displacement capacity will of the interest.

For repairable columns, four key variables were included in the parametric study including (a) three column aspect ratios (4, 6, and 8), (b) three column axial load indices (5%, 10%, and 15%), (c) three fuse types (stainless steel bars, shape memory alloy bars, and steel tendons), and (d) three fuse lengths of $0.25L_p$, $0.5L_p$, and $0.75L_p$, where L_p is the analytical plastic hinge length of a corresponding CIP calculated according to AASHTO SGS (2011). A total of 81 repairable precast bridge columns were included in the study.

6.2.1 Modeling Methods

The full-scale CIP columns were circular with a diameter of 4 ft (1.22 m). Since three ARs of 4, 6, and 8 were chosen and the column diameter was fixed, the column heights were then 16 ft (4.88 m), 24 ft (7.32 m), and 32 ft (9.75 m). All circular CIP columns had 18, No.10 (32-mm) longitudinal reinforcing black-steel bars resulting in a longitudinal reinforcement ratio of 1.26%. Transverse reinforcement of the CIP columns varied from No. 5 (Ø16-mm) to No. 7 (Ø22-mm) hoops with a minimum spacing of 4.5 in. (114 mm) to achieve the CIP target displacement ductility of 7. ASTM A706 Grade 60 (414-MPa) reinforcing steel bars were used in the CIP columns as the longitudinal and transverse reinforcement. A concrete compressive strength of 5 ksi (34.47 MPa) and a clear cover of 2 in. (51 mm) were used in all models.

The modeling methods for CIP (**Fig. 6.1**) remain the same as those discussed in **Ch. 5**.
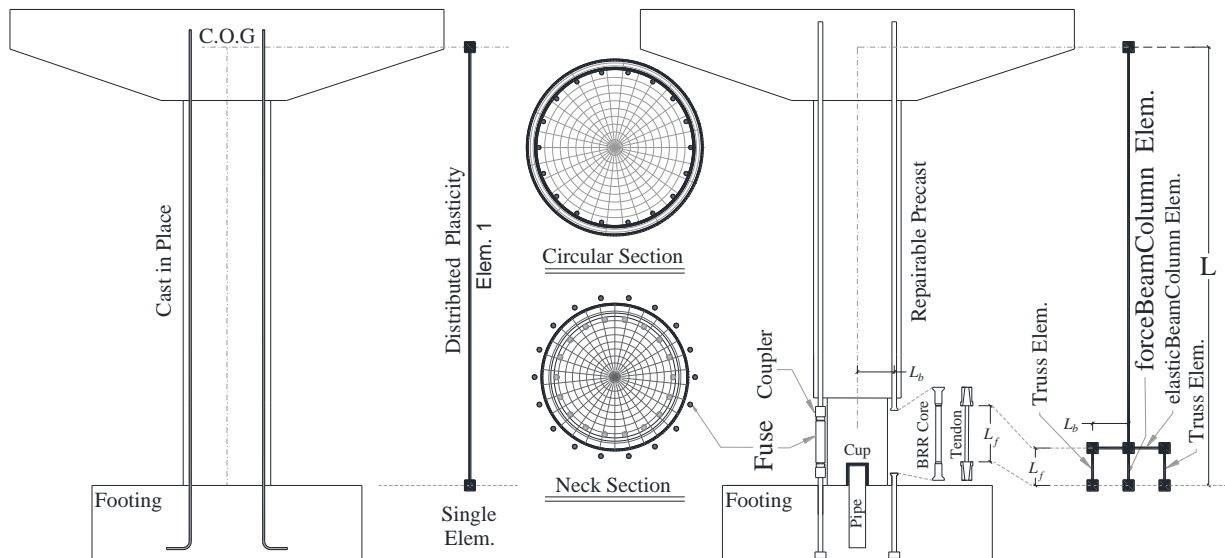
Figure 6.1. Full-Scale Cast-in-Place and Repairable Bridge Column Models

The cross section of repairable precast bridge columns with headed couplers (RPH) was changed from octagonal used in the test specimens to circular to match that of the CIP columns. The circular column sections had a diameter of 48 in. (1.22 m) and were longitudinally reinforced with 18, No. 11 (Ø36-mm) black-steel bars. Note that the RPH column main bars were oversized compared with CIP to shift the damage to the fuses. The diameter of the column was reduced to 40 in. (1.02 m) at the base of the column as the neck region. The circular neck section was longitudinally reinforced with 22, No. 8 (Ø25-mm) black-steel bars. Three fuse types were incorporated in the RPH columns: BRR with stainless-steel core, BRR with SMA core, and steel tendons. In the exposed fuses, the diameter of the longitudinal bars was reduced from No. 11 to No. 10 (Ø36-mm) when the stainless steel and SMA bars were incorporated. However, 0.7-in. (18-mm) diameter seven-wire strands were used as the tendon fuses. This size is the largest commercially available for seven-wire steel strands. The same transverse reinforcement of CIP was used in its corresponding RPH columns. Similar to CIP, ASTM A706 Grade 60 (414-MPa) reinforcing steel bars were used in RPH as longitudinal and transverse reinforcement. A concrete compressive strength of 5 ksi (34.47 MPa) and a clear cover of 2 in. (51 mm) were used in all models.

The modeling methods discussed in **Ch. 5** for the half-scale RPH columns were adopted herein to analyze full-scale RPH columns. As shown in the previous chapter, a repairable bridge column with exposed fuses must incorporate different modeling techniques, such as using "truss" elements for the fuses, for a successful simulation. A three-dimensional finite element model with six degrees of freedom (DOFs) and two cross sections was developed for all RPH columns (**Fig. 6.1**). Both column and neck sections were modeled with "forceBeamColumn" elements while the exposed reinforcement were modeled with "truss" elements. The truss elements were connected to the main column section using "elasticBeamColumn" elements. "steel02" and "hysteretic" material models were used for stainless steel and tendon reinforcement, respectively, while a "selfCentering" material model was used to represent SMA fuses. The modeling methods and material properties for SMA were taken from Tazarv and Saiidi (2015) while ASTM A416 values were used for steel tendons. Due to a lack of design values for stainless steel bars, the tensile test results from **Ch. 4** were used for the stainless-steel RPH columns. **Table 6.1** summarizes the material properties used in the analyses.

Table 6.1. Sectional Fiber Material Properties Used in RHP Parametric Study

Concrete Fibers	
Application: Unconfined Concrete Type: Concrete01 f'_{cc} = -5000 psi (34.5 MPa) ε_{cc} = -0.002 in/in f'_{cu} = -2500 psi (17.2 MPa) ε_{cu} = -0.005 in/in	Application: Confined concrete in column circular sections (based on Mander's model) Type: Concrete01 f'_{cc} = -6008 psi (41.4 MPa) ε_{cc} = -0.00402 in/in f'_{cu} = -4419 psi (30.5 MPa) ε_{cu} = -0.0127 in/in
	Application: Confined concrete in circular neck section (based on Mander's model) Type: Concrete01 f'_{cc} = -6217 psi (42.9 MPa) ε_{cc} = -0.0044 in/in f'_{cu} = -4683 psi (32.3 MPa) ε_{cu} = -0.0143 in/in

Reinforcement Fibers	
Application: Column longitudinal bars with a symmetric tension/compression. For neck bars, only the compressive properties were used. Type: ReinforcingSteel (for column bars) or Hysteretic (for neck bars) f_y = 68.0 ksi (468.9 MPa) f_{su} = 95.0 ksi (655 MPa) E_s = 29000 ksi (200000 MPa) E_{sh} = 1247 ksi (8598 MPa) ε_{sh} = 0.0115 in/in ε_{su} = 0.12 in/in	Application: Stainless-Steel BRR Fuses with a symmetric tension/compression. Type: Steel02 f_y = 100 ksi (689.7 MPa) E_s = 29000 ksi (20000 MPa) B_s = 0.002843 R_0 = 2.3 cR_1 = 0.925 cR_2 = 0.15
Application: Shape Memory Alloy BRR Fuses with a symmetric tension/compression Type: SelfCentering k_1 = 5500 ksi (37921 MPa) k_2 = 250 ksi (174 MPa) f_y = 55 ksi (379 MPa) Beta = 0.65 ε_r = 0.06 in/in Alpha = 0.3	Application: Tendon fuses with a tension-only properties Type: Hysteretic (in tension only) f_y = 243 ksi (1675 MPa) ε_y = 0.00853 in/in f_2 = 270 ksi (1861 MPa) ε_2 = 0.02746 in/in f_u = 275 ksi (1896 MPa) ε_u = 0.062 in/in

A naming convention for the precast columns was considered including five terms. The first term is RPH referring to the repairable precast bridge column with headed couplers. The second component specifies the type of fuse materials (SS for stainless steel BRR, SMA for SMA BRR, tendon for tendon fuses). The third and fourth components refer to AR and ALI of the columns. The last term of the naming system refers to the length of the fuse used in the model.

6.2.2 Force-Displacement Relationships

Overall, 90 pushover analyses were performed including 81 on RPH and 9 on CIP. **Table 6.2** presents a summary of the parametric results for all RPH columns, which includes the drift capacity, the displacement ductility capacity, and the mode of failure per analysis. Failure was defined as either the rupture of the fuse reinforcement in tension or a 15% drop in the lateral load carrying capacity of the column with respect to the column lateral strength. It was observed that the fuse rupture was the predominant mode of failure for the RPH columns with low aspect ratios while the columns with high aspect ratios were mostly failed by the strength degradation. Furthermore, a longer fuse length resulted in a failure mostly controlled by the strength degradation. The SS-fuse columns tended to exhibit the highest displacement capacity followed by the columns with SMA fuse columns and the tendon fuse columns. This was due to a higher strain capacity of SS compared with SMA and tendons (**Table 6.1**).

Figures 6.2 through **6.10** show the force-displacement relationships for all 81 RPH columns. Each graph includes the pushover results for RPH columns with the same aspect ratio and axial load index. Furthermore, the pushover response for a corresponding CIP column was included in each figure for completeness.

In general, stainless-steel fuse columns most closely matched the force capacity of its corresponding CIP column and showed the highest displacement capacities. This is because the stress-strain behavior SS is closer to ASTM A706 black-steel bars than other materials.

The SMA columns yielded at a much lower force due to a low yield strength of these materials. However, the low aspect ratio SMA-fuse columns reached the force capacity of the CIP columns due to the secondary post-yield stiffness of SMA (the third branch of SMA stress-strain behavior controlled by Alpha). However, at high aspect ratios, the SMA fuse columns failed by the strength degradation and did not reach the lateral strength of CIP.

The tendon fuse columns had much lower force capacities than the other RPH columns due to smaller reinforcement areas (0.7 in. (Ø18-mm) diameter tendons vs. No. 10 (Ø36-mm) bars used in SS and SMA BRR fuse) despite the Grade 270 (1862-MPa) tendons had a much higher yield strength than SS and SMA. Furthermore, the tendon fuse columns exhibited the lowest displacement capacities among all RPH columns due to a lower strain capacity of the steel tendons (e.g., 6.2% in steel tendon vs 16% in SS).

The stainless-steel fuse columns had the highest displacement capacity with only a fuse length of 0.25 times the plastic hinge length of the CIP column (L_p) to surpass the CIP displacement capacity. The SMA fuse columns generally needed a fuse length of $0.5L_p$ to reach the CIP displacement capacities. The steel tendon fuse columns needed a fuse length of $0.75L_p$ to match the CIP displacement capacity.

Overall, the parametric study indicates that all three material types (SS, SMA, tendon) can be used as external fuses. The designer has the option to match the force and/or displacement capacity of RPH with its corresponding CIP column. The forces can be adjusted by the number or diameter of the fuses. Further, the displacement capacity can be adjusted by changing the fuse length. For example, a designer can increase the number of the 0.7-in. (Ø18-mm) diameter steel tendons with a fuse length of $0.75L_p$ to match the CIP force and displacement capacities.

More research is needed on the initial stiffness degradation which was observed between retesting of RPH columns (**Ch. 4**) and how the lower initial stiffness of these columns affects their dynamic behavior.

Table 6.2. Summary of Parametric Study on Repairable Bridge Columns

Column I.D.	Fuse Material	Aspect Ratio	Axial Load Index (%)	Ultimate Drift Ratio (Ductility) Failure Mode		
				$0.25L_p$	$0.5L_p$	$0.75L_p$
RPH-SS-AR4-ALI5			5	5.76% (3.75) Fuse Rupture	9.56% (6.08) Fuse Rupture	13.5% (8.59) Fuse Rupture
RPH-SS-AR4-ALI10		4	10	5.83% (4.18) Fuse Rupture	9.75% (6.78) Fuse Rupture	9.43% (6.46) Fuse Rupture
RPH-SS-AR4-ALI15			15	6.01% (4.47) Fuse Rupture	7.46% (5.55) Strength Loss	6.73% (4.79) Strength Loss
RPH-SS-AR6-ALI5	Stainless Steel (SS)		5	7.08% (3.89) Fuse Rupture	11.5% (6.48) Strength Loss	10.5% (5.84) Strength Loss
RPH-SS-AR6-ALI10		6	10	7.35% (4.68) Strength Loss	6.98% (4.35) Strength Loss	6.62% (4.0) Strength Loss
RPH-SS-AR6-ALI15			15	5.42% (3.61) Strength Loss	5.25% (3.38) Strength Loss	5.16% (3.20) Strength Loss
RPH-SS-AR8-ALI5			5	8.62% (4.27) Fuse Rupture	8.8% (4.37) Strength Loss	8.22% (4.01) Strength Loss
RPH-SS-AR8-ALI10		8	10	6.00% (3.39) Strength Loss	5.70% (3.15) Strength Loss	5.7% (3.08) Strength Loss
RPH-SS-AR8-ALI15			15	4.76% (2.88) Strength Loss	4.46% (2.57) Strength Loss	4.69% (2.63) Strength Loss
RPH-SMA-AR4-ALI5			5	4.07% (7.21) Fuse Rupture	6.10% (9.76) Fuse Rupture	8.45% (12.00) Fuse Rupture
RPH-SMA-AR4-ALI10		4	10	4.23% (8.57) Fuse Rupture	6.61% (12.25) Fuse Rupture	8.95% (15.76) Fuse Rupture
RPH-SMA-AR4-ALI15			15	4.35% (9.34) Fuse Rupture	6.87% (14.12) Fuse Rupture	5.44% (10.67) Strength Loss
RPH-SMA-AR6-ALI5	Shape Memory Alloy (SMA)		5	5.10% (7.23) Fuse Rupture	7.90% (10.29) Fuse Rupture	10.7% (13.26) Fuse Rupture
RPH-SMA-AR6-ALI10		6	10	5.24% (8.83) Fuse Rupture	8.31% (13.87) Fuse Rupture	5.36% (8.38) Strength Loss
RPH-SMA-AR6-ALI15			815	5.39% (9.91) Fuse Rupture	4.01% (7.07) Strength Loss	4.08% (6.70) Strength Loss
RPH-SMA-AR8-ALI5			5	6.12% (7.58) Fuse Rupture	9.51% (11.54) Fuse Rupture	6.88% (8.19) Strength Loss
RPH-SMA-AR8-ALI10		8	10	6.27% (9.70) Fuse Rupture	4.26% (6.34) Strength Loss	4.36% (6.12) Strength Loss
RPH-SMA-AR8-ALI15			15	1.65% (2.89) Strength Loss	3.36% (5.23) Strength Loss	3.66% (5.43) Strength Loss
RPH-Tendon-AR4-ALI5			5	2.34% (2.26) Fuse Rupture	3.73% (3.07) Fuse Rupture	5.10% (3.70) Fuse Rupture
RPH-Tendon-AR4-ALI10		4	10	2.47% (2.49) Fuse Rupture	3.98% (3.45) Fuse Rupture	5.29% (4.05) Strength Loss
RPH-Tendon-AR4-ALI15			15	2.58% (2.58) Fuse Rupture	4.0% (3.34) Strength Loss	4.01% (2.88) Strength Loss
RPH-Tendon-AR6-ALI5	Steel Tendon (Tension Only)		5	2.96% (2.35) Fuse Rupture	4.73% (3.27) Fuse Rupture	6.42% (4.02) Strength Loss
RPH-Tendon-AR6-ALI10		6	10	3.11% (2.64) Fuse Rupture	3.99% (2.86) Strength Loss	4.19% (2.59) Strength Loss
RPH-Tendon-AR6-ALI15			15	3.20% (2.61) Strength Loss	3.11% (2.12) Strength Loss	3.41% (1.99) Strength Loss
RPH-Tendon-AR8-ALI5			5	2.64% (1.89) Strength Loss	5.30% (3.28) Strength Loss	5.36% (2.88) Strength Loss
RPH-Tendon-AR8-ALI10		8	10	3.40% (2.43) Strength Loss	3.50% (2.10) Strength Loss	3.79% (1.96) Strength Loss
RPH-Tendon-AR8-ALI15			15	2.59% (1.80) Strength Loss	2.90% (1.68) Strength Loss	3.19% (1.57) Strength Loss
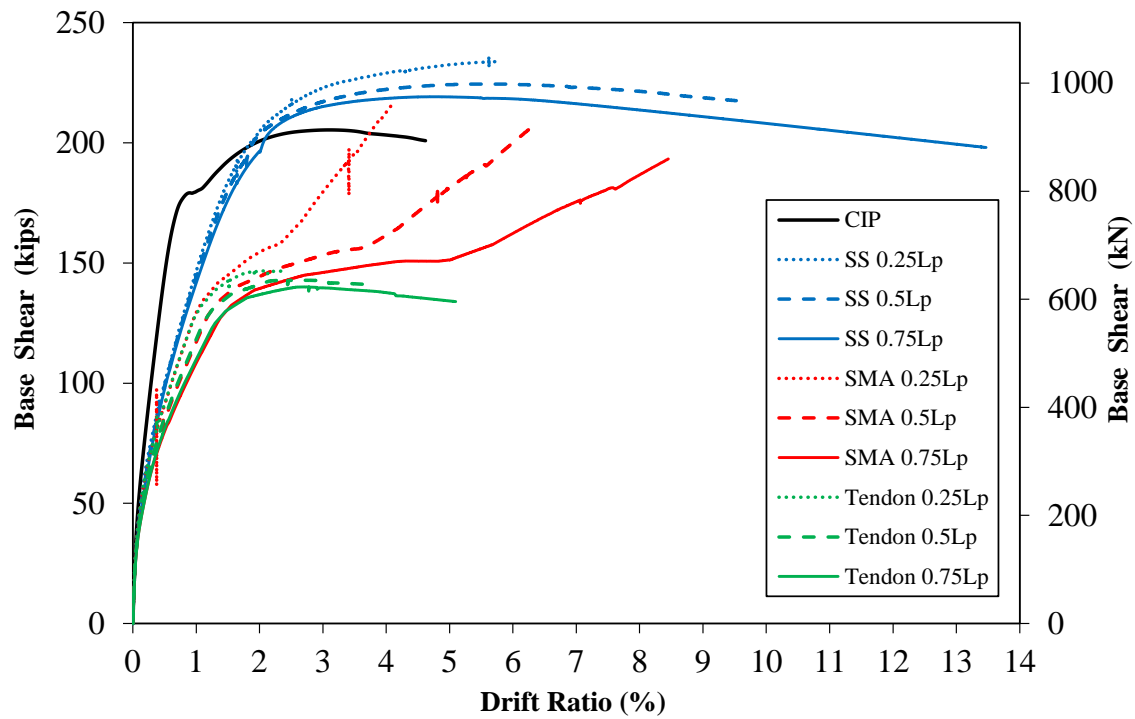
Figure 6.2. Pushover Analysis for RPH-AR4-ALI5
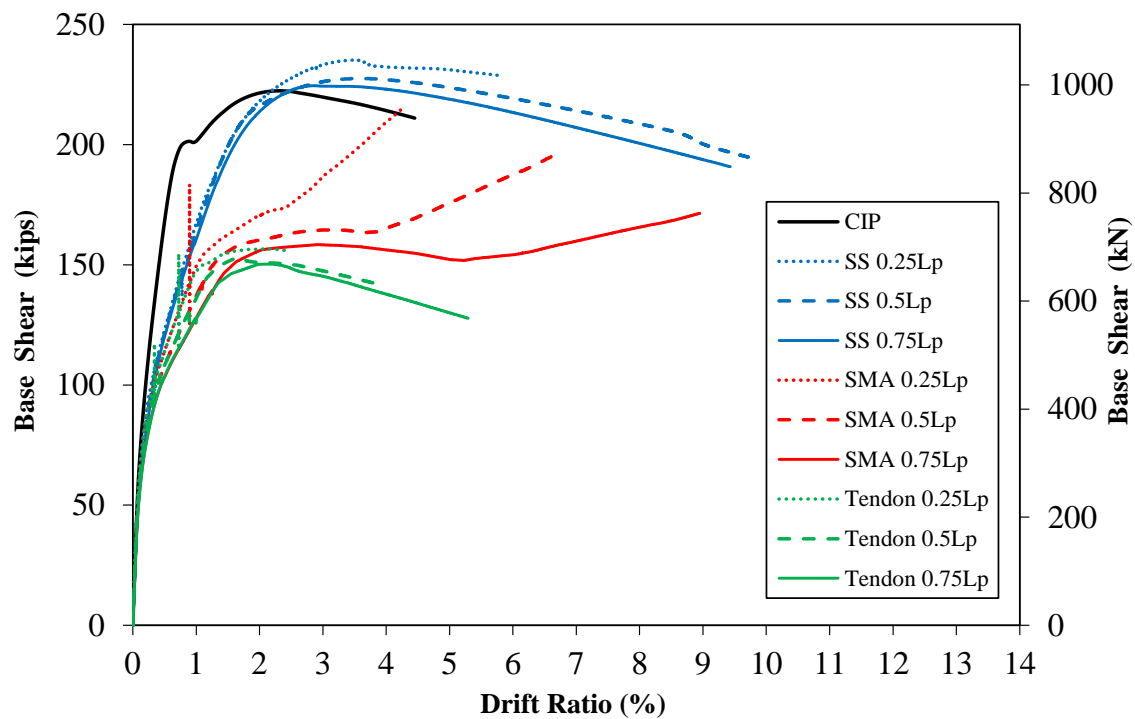
Figure 6.3. Pushover Analysis for RPH-AR4-ALI10
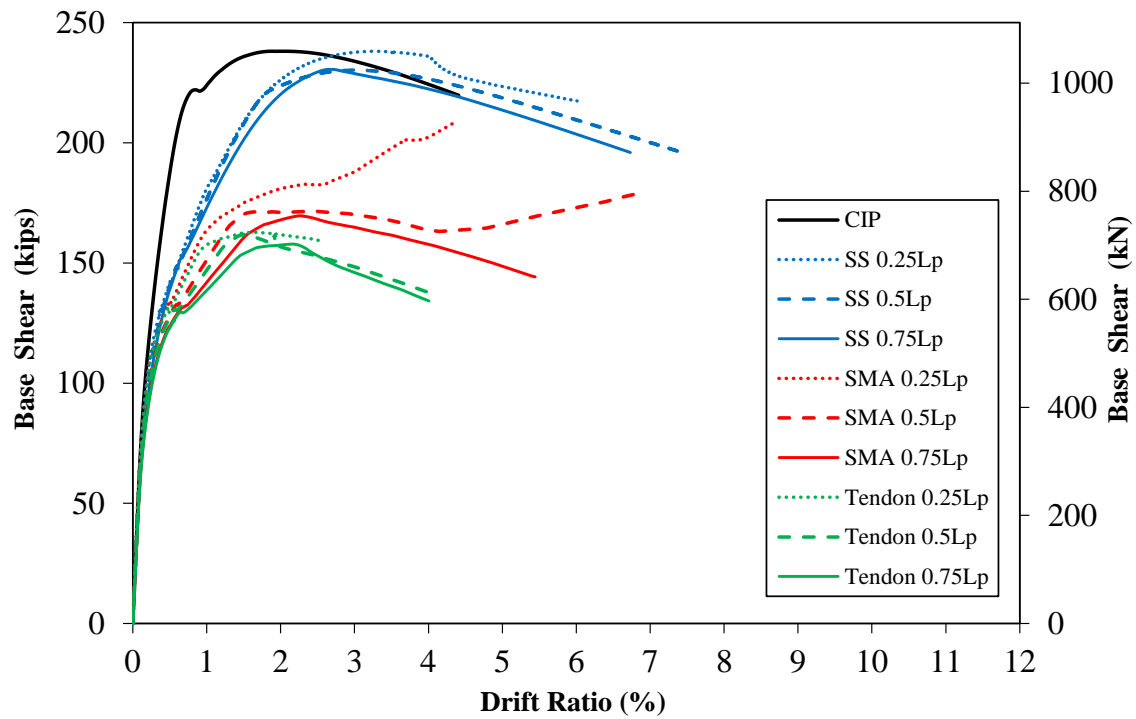
Figure 6.4. Pushover Analysis for RPH-AR4-ALI15
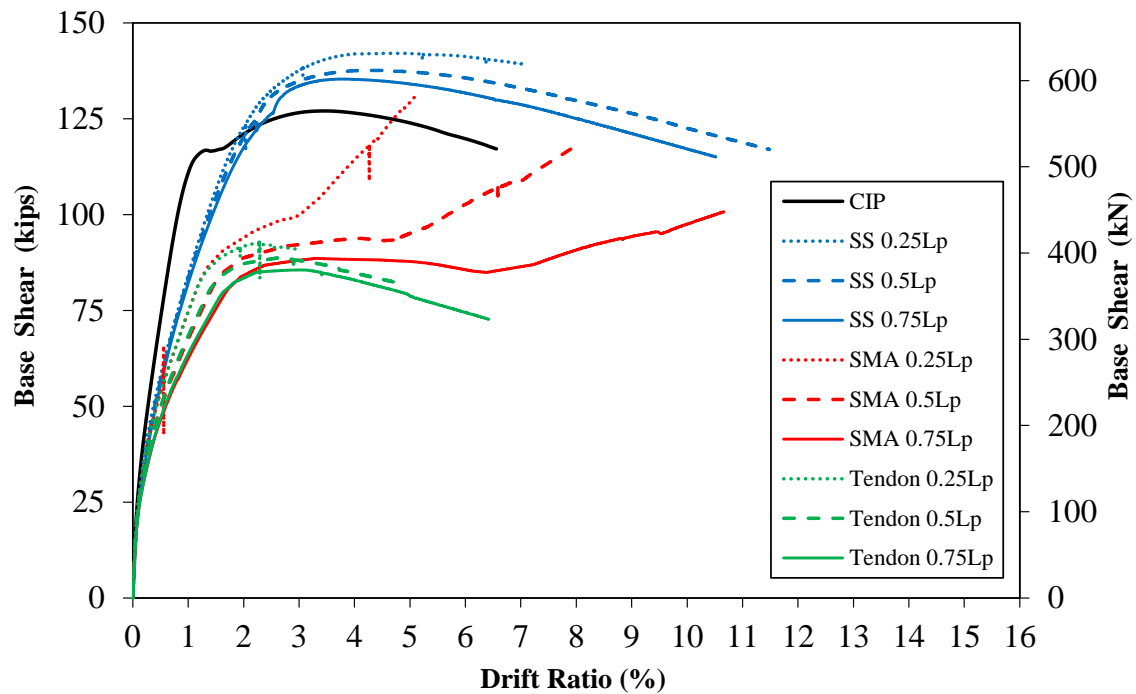
Figure 6.5. Pushover Analysis for RPH-AR6-ALI5

Figure 6.6. Pushover Analysis for RPH-AR6-ALI10

Figure 6.7. Pushover Analysis for RPH-AR6-ALI15

294
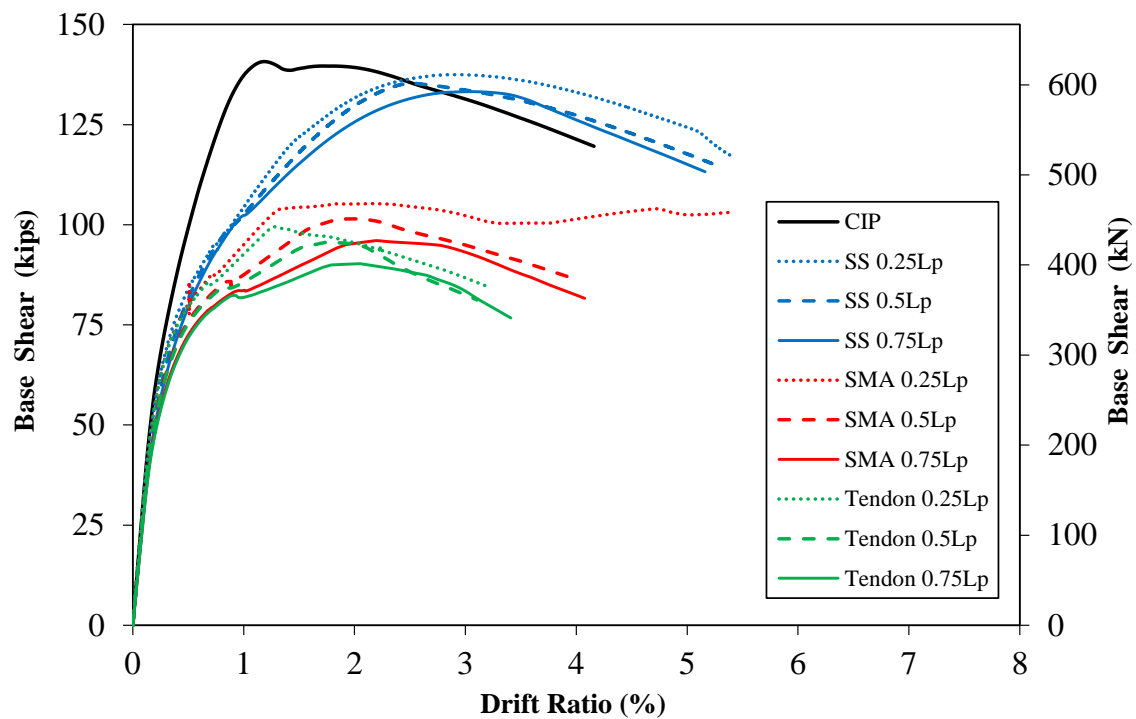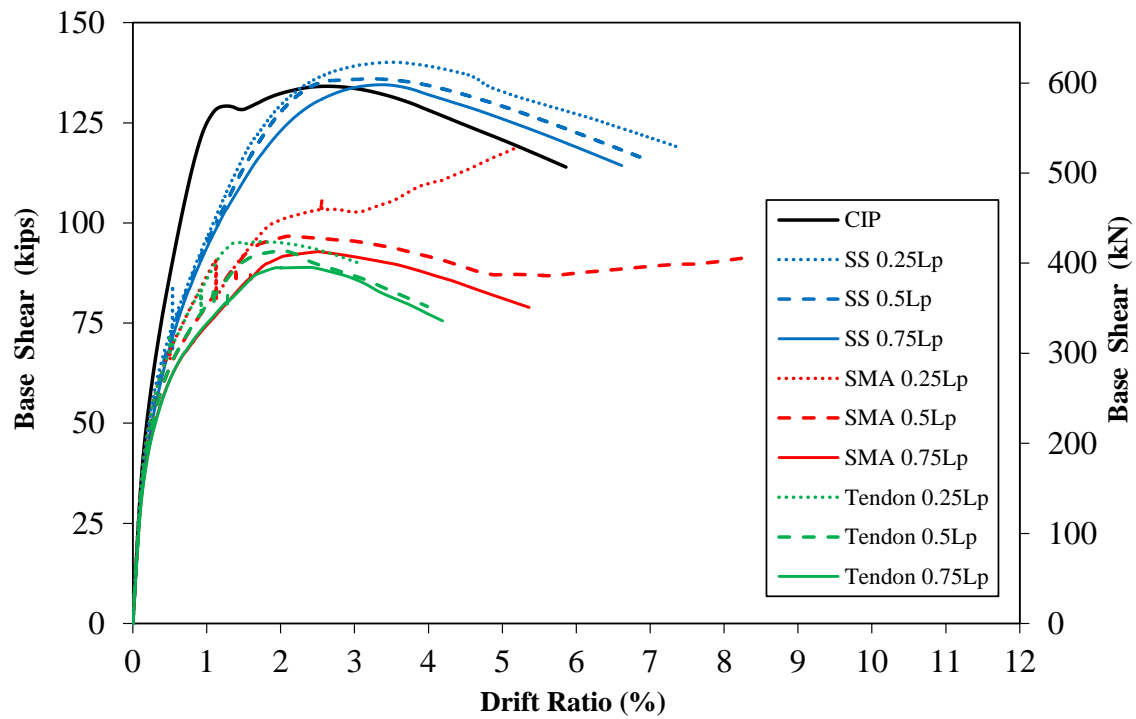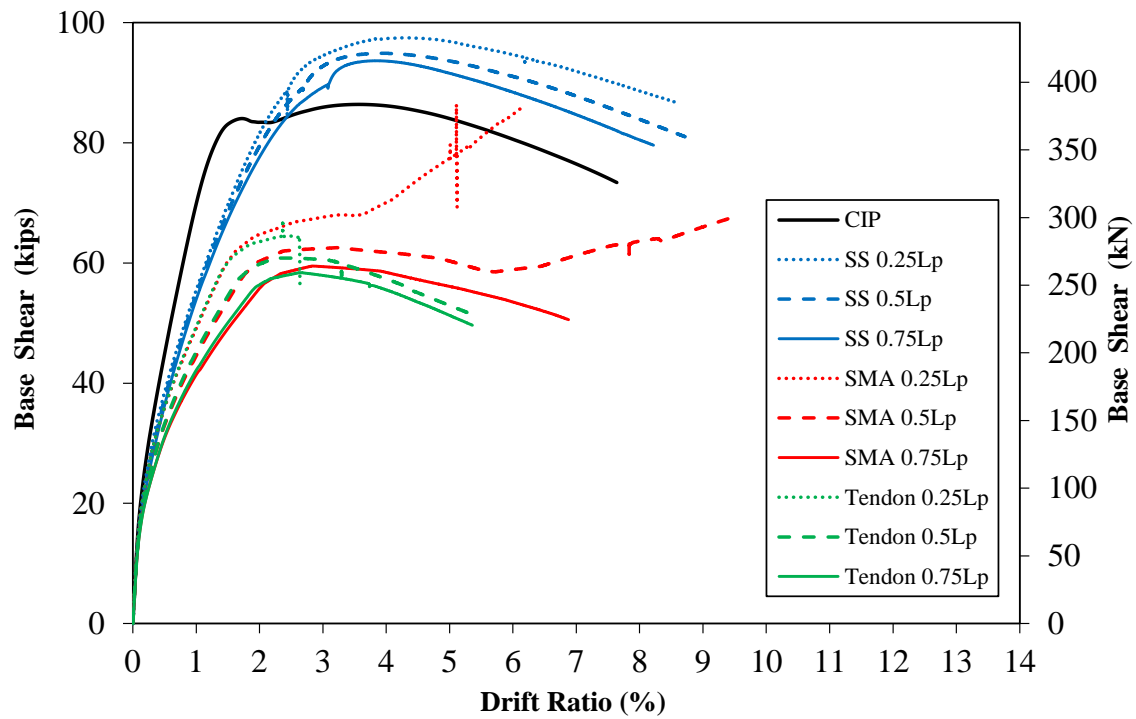
Figure 6.8. Pushover Analysis for RPH-AR8-ALI5
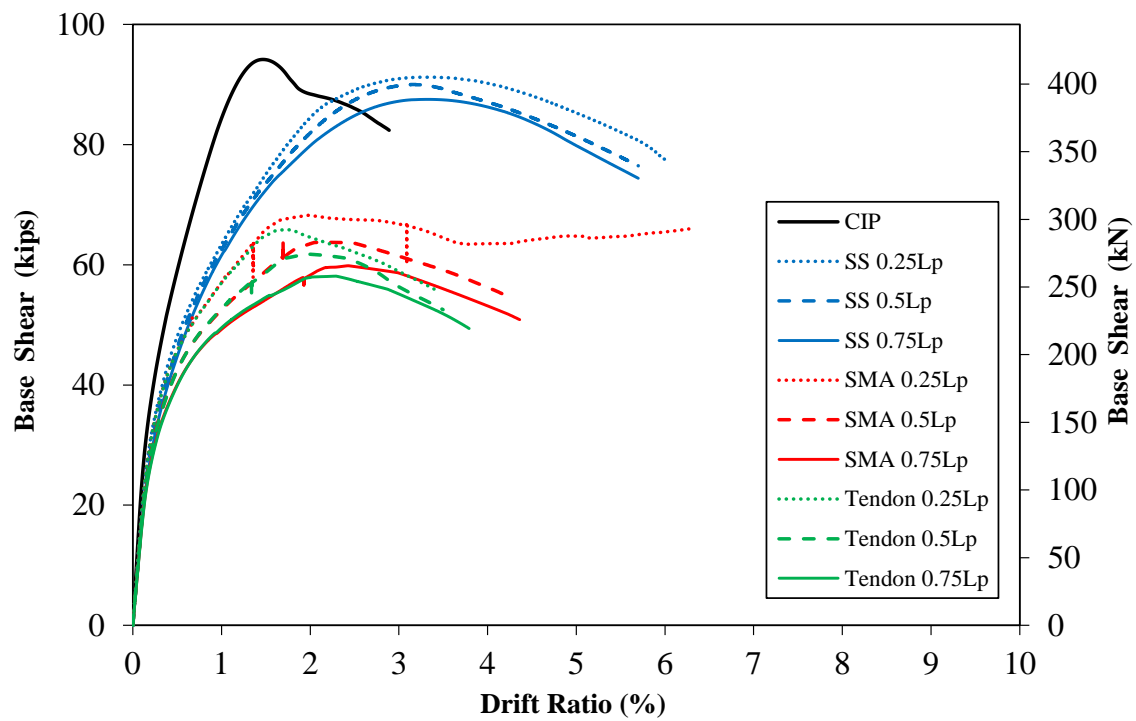
Figure 6.9. Pushover Analysis for RPH-AR8-ALI10

295
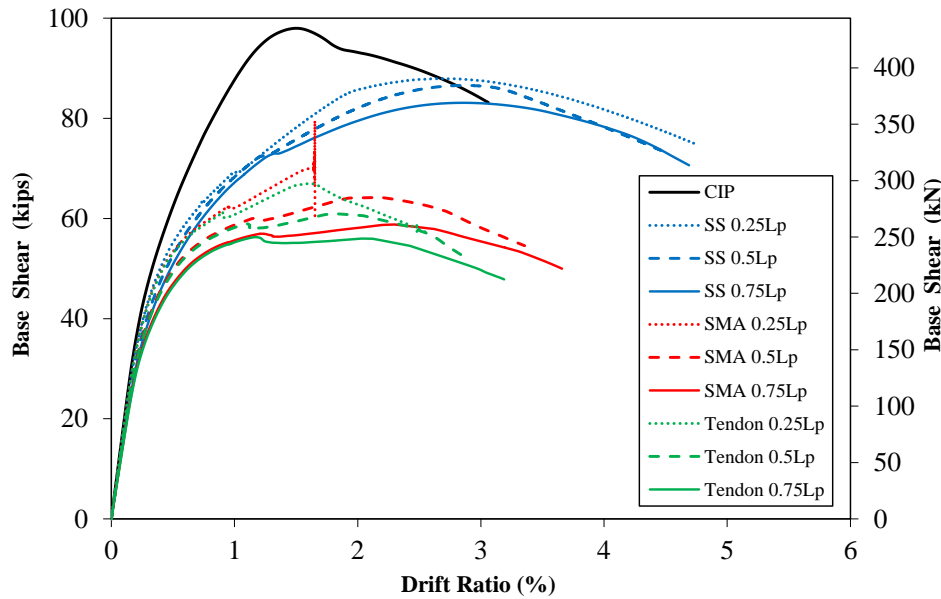
Figure 6.10. Pushover Analysis for RPH-AR8-ALI15

6.3 Summary and Conclusions

This chapter presented the findings of a parametric study on 81 full-scale repairable precast bridge columns using exposed, replaceable reinforcement in the plastic hinge region. The study explored the effect of different design parameters on the overall column performance including aspect ratio, axial load index, fuse reinforcement material, and fuse length. The displacement capacities of the columns and their failure modes were estimated.

Overall, the parametric study indicates that RPH columns incorporating any of three fuse material types (SS, SMA, tendon) can potentially match and even surpass the seismic performance of their corresponding CIP columns. Nevertheless, different stress and strain capacities of the different materials may require fuse length adjustment and/or number of reinforcement modification to match the CIP capacities.

6.4 References

AASHTO SGS. (2011). "AASHTO Guide Specifications for LRFD Seismic Bridge Design," Washington, DC: American Association of State Highway and Transportation Officials.

ASTM A416/A416 M (2006). "Standard Specification for Steel Strand, Uncoated Seven-Wire for Prestressed Concrete." West Conshohocken, PA, 5 pp.

Sjurseth, T., Greeneway, E., Hart, K., LaVoy, M., Tazarv, M., and Wehbe, N. (2022). "Mechanically Spliced Precast Bridge Columns," North Dakota State University - Upper Great Plains Transportation Institute, Fargo: Mountain-Plains Consortium (MPC), MPC Report No. 22-451, 359 pp.

Tazarv, M., and Saiidi, M.S. (2015). "Reinforcing NiTi Superelastic SMA for Concrete Structures." Journal of Structural Engineering, ASCE, Vol. 141. No. 8, 10 pp.

CHAPTER 7. DESIGN AND CONSTRUCTION RECOMMENDATIONS FOR REPAIRABLE PRECAST BRIDGE COLUMNS

7.1 Introduction

The testing and analytical modeling of three repairable precast bridge columns with exposed replaceable reinforcement was discussed in the previous chapters. Pipe-pin, inverted pipe-pin, and grouted socket connections were used in the column models. Furthermore, buckling restrained reinforcement (BRR) and steel tendons were used as the exposed fuses in the neck section of the columns. The present chapter offers general design and construction guidelines based on the findings of the experimental and analytical studies to facilitate the use of proposed repairable columns.

7.2 Recommendations

The following recommendations are made for the design and construction of repairable precast bridge columns. The text starting with "R" indicates the recommendation and the text starting with "C" is the commentary for that recommendation.

R.1 – The design of a repairable precast column follows current bridge standards with modifications included in this document.

C.1 – The bridge components should be designed following current AASHTO bridge codes (AASHTO LRFD and AASHTO SGS). The general geometry and reinforcement of a repairable column may follow those of its reference conventional cast-in-place (CIP) model with the modifications specified herein.

R.2 – A repairable column may utilize a pipe-pin connection at either end in a way that the pipe is underneath its housing socket. A type of accelerated bridge construction (ABC) connection may also be incorporated in a repairable column.

C.2 – Two general details are allowed for repairable columns as shown in **Fig. 7.1**. The key parameters of a repairable column are shown in **Fig. 7.2**. In one connection, pipe-pin may be used to allow deconstruction after an event or the bridge service life. In a pipe-pin connection, the pipe must be embedded underneath of its the housing socket (cup) for an improved durability. Only stainless-steel or corrosion-resistant steel is allowed in pipe-pin components. Different ABC connections should be allowed when connecting the repairable precast column to its adjoining members. Suitable options are grout-filled duct connections and socket/pocket connections.

The shear pipe/shaft and steel cup of a pipe-pin connection should be designed according to recommendations by Zaghi and Saiidi (2010). All shear pin components should remain linear elastic at the column failure. This can be achieved by including a minimum amplification factor of 1.25 to the column plastic shear and moment when designing the pipe-pin components. ABC connections should be designed based on the recommendations of NCHRP Report 935 (Saiidi et al., 2020).

a) Pipe-pin Connection   b) Sample of ABC Connection
Figure 7.1. Connection Details for Repairable Precast Bridge Columns

Figure 7.2. A Typical Detailing for Repairable Precast Bridge Columns
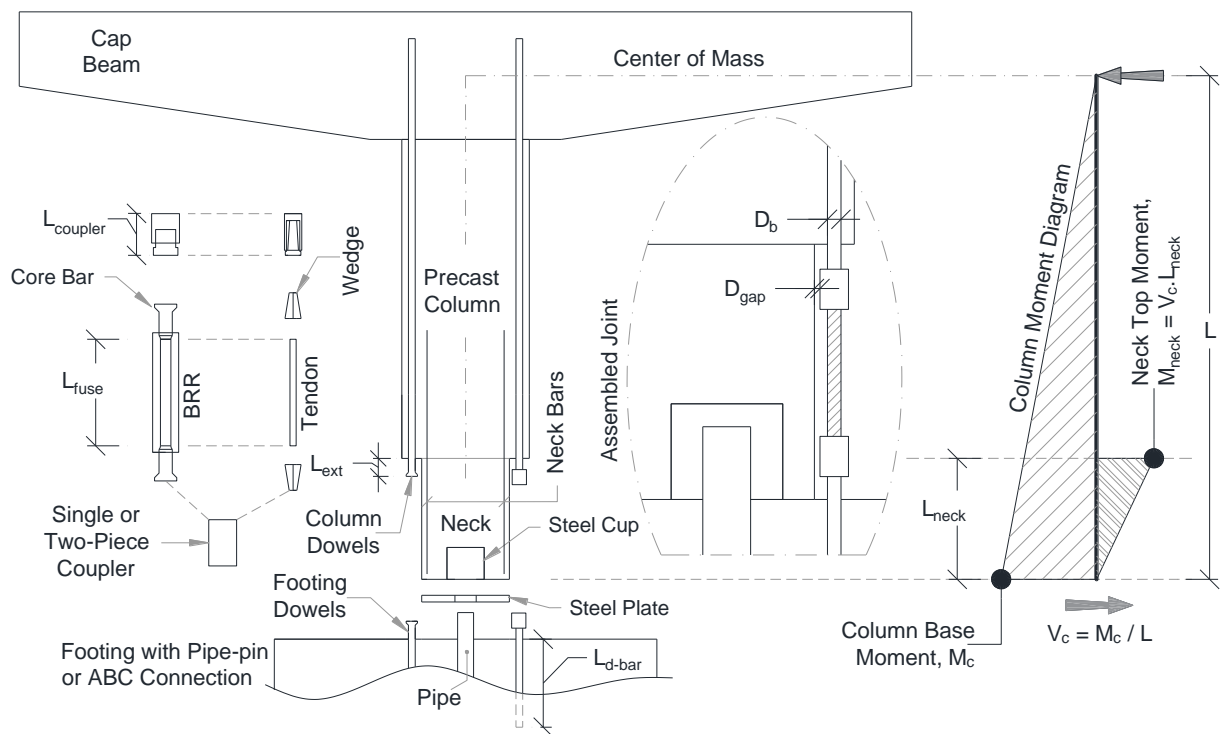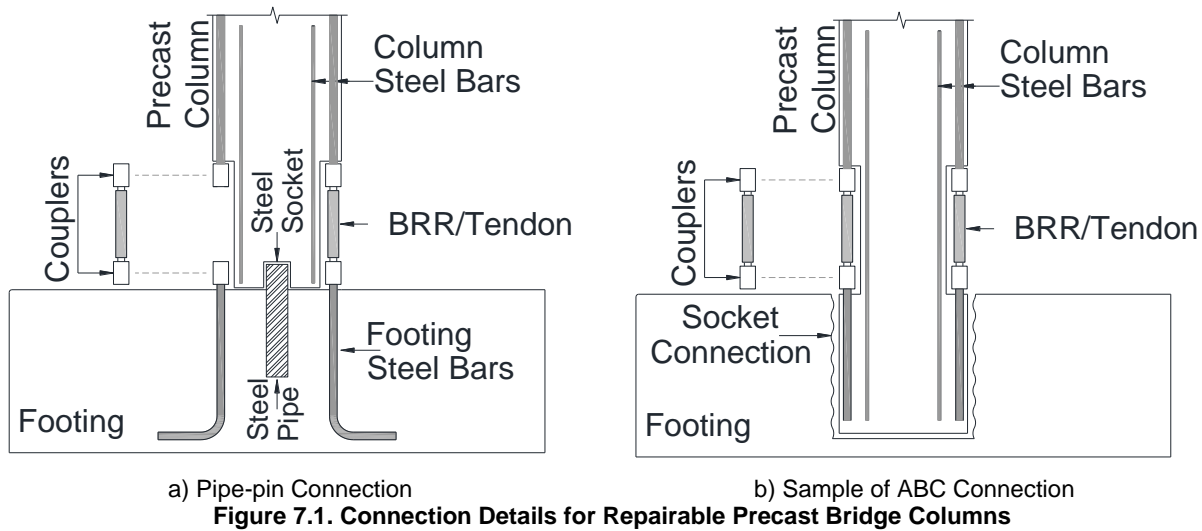
R.3 – The detachable external fuses must be detailed resulting in none to minimal damage to other components of a repairable column.

C.3 – The best detachable external fuse is a tension-only member such as cables (tendons). Cables with different materials including black steel, stainless steel, shape memory allow, and galvanized steel exit in the market. However, the cable should be made with low- to no-corrosion materials.

Buckling restrained reinforcement (BRR) is not recommended for use in repairable columns due to a Z-shape deformation outside of BRR bending column-footing dowels. However, the use of SMA BRR may

be allowed since SMA might minimize bending of the column-footing dowels. Further testing is required to validate SMA BRR.

R.4 – The gap between the face of the coupler and the face of the column neck (D_{gap}) should be at least 0.5 in. (13 mm).

C.4 – The gap between the face of the coupler and the face of the neck (D_{gap}) should be sufficiently large to allow for the neck section formwork to fit between the couplers. Furthermore, this gap should allow the coupler assembly and installation. Therefore, the diameter of the neck section is controlled by the location of the column longitudinal bars and D_{gap}. As an initial trial, the diameter of the neck section might be assumed as the column diameter (or the side dimension) less three times the coupler diameter.

R.5 – For a repairable precast column to meet the displacement capacity of its corresponding CIP column, the fuse length (L_{fuse}) should be at least $0.5L_p$ when using SMA BRR, and $0.75L_p$ when utilizing low-strain capacity tension-only fuses (e.g., conventional Grade 270 steel tendons commonly used in precast industry). L_p is the analytical plastic hinge length of the corresponding CIP column calculated per AASHTO SGS.

C.5 – Different materials have different stress-strain behavior. The displacement capacity of a repairable precast column depends on the fuse length and the strain capacity of the fuse material. The same displacement capacity as CIP may be achieved in a repairable precast column by altering the fuse length or fuse materials.

Furthermore, it is possible to change the number or size of fuses compared with those of the CIP longitudinal bars to match the CIP lateral strength.

R.6 – Internal longitudinal reinforcement of the neck section shall be designed to resist at least 1.25 the plastic shear and moment of the repairable precast column.

C.6 – As shown in **Fig.7.2**, a secondary moment at the top of the neck is produced caused by the column baseshear. The neck should be stronger than the column by at least 25% to achieve a linear-elastic behavior with a minimal damage. Therefore, the design moment for the neck is $M_{neck} = 1.25 \ V_c \ . \ L_{neck}$, where V_c is the column baseshear calculated as M_c / L_{column}, M_c is the column base moment, L_{column} is the column length, and L_{neck} is the neck length.

R.7 – The extension of the column/footing dowel bars beyond the column/footing (L_{ext}) should not be less than the physical length of the coupler.

C.7 – The column/footing dowel bar extension should be sufficiently large to allow the coupler to freely slide up/down to insert the fuse. This is to provide a large tolerance for fuse installation.

Furthermore, the use of clamping collars (or split nuts) is recommended when tension-compression BRR fuses are used since they limit the column/footing dowel bar bending. For tension-only fuses, clamping collars might not be used since minimal compressive forces will be transferred to the column/footing dowel bars.

R.8 – Bar debonding should be considered for all column longitudinal bars right above the neck section. Any neck longitudinal bars going into the column adjoining member must be debonded. Alternatively, the neck bars can stop at the column-adjoining member interface.

C.8 – Bar debonding spreads the yielding and delays fracture. The minimum debonding length can be six bar diameters. Debonding may be performed by wrapping the bars with two layers of duct tape.

R.9 – Internal post-tensioning as that typically used in rocking columns is not required for of repairable precast columns.

C.9 – No obvious benefit was seen when a reparable column was post-tensioned with internal tendons. However, if a designer prefers adding a rocking detailing to a repairable precast column shown in Fig. 7.1, the design of such rocking column should follow the recommendations in NCHRP Report 864 (Saiidi et al., 2017).

7.3 Conclusions

This chapter discusses general design and construction guidelines for repairable precast bridge columns. These guidelines are to ensure that the repairable columns are geometrically feasible and exhibit a damage that is limited to the exposed replaceable fuses.

7.4 References

AASHTO LRFD. (2017). "AASHTO LRFD Bridge Design Specifications, 8th Edition," Washington, D.C., American Association of State Highway and Transportation Officials.

AASHTO SGS. (2011) "AASHTO Guide Specifications for Seismic Bridge Design," Washington, D.C., American Association of State Highway and Transportation Officials.

Zaghi, A.E. and Saiidi, M.S., (2010). "Seismic Performance of Pipe-pin Two-way Hinges in Concrete Bridge Columns," Journal of Earthquake Engineering, Vol. 14. No. 8, pp.1253-1302.

Saiidi, M.S., Tazarv, M., Varela, S., Bennion, S., Marsh, M.L., Ghorbani, I., Murphy, T.M. (2017). "Seismic Evaluation of Bridge Columns with Energy Dissipating Mechanisms, Volume 1: Research Overview and Volume 2: Guidelines," National Academies of Sciences, Engineering, and Medicine, NCHRP Report No. 864, Washington, DC: The National Academies Press, 344 pp.

Saiidi, M.S., Mehraein, M., Shrestha, G., Jordan, E., Itani, A., Tazarv, M., Sanders, D., Murphy, T.M., Reno, M.L., and Pohll, M.N. (2020). "Proposed AASHTO Seismic Specifications for ABC Column Connections," National Academies of Sciences, Engineering, and Medicine, NCHRP Report No. 935, Washington, DC: The National Academies Press, 354 pp.

CHAPTER 8. SUMMARY AND CONCLUSIONS

8.1 Summary

Bridges designed with current seismic codes exhibit large displacement capacities, and the bridge total collapse is prevented. However, damage of ductile members is allowed at this performance level. In reinforced concrete bridges excited by ground shaking, columns are the target ductile members in which concrete cover, core, and reinforcement may damage, and the column may not return to its original position. Minor damages are usually repaired but excessive damages such as core crushing, bar buckling, and/or bar fracture are hard to repair and will usually result in the column or bridge replacement. According to FHWA, approximately 25% of the US bridges require rehabilitation, repair, or total replacement. Furthermore, within the next 50 years, many bridges located in the 16 seismic prone states of the nation will experience large earthquakes that may cause significant damage. Induced seismic activities in formerly non-seismic states such as Oklahoma may also damage bridges with poor seismic detailing. Even though current practice is successful in attaining the no-collapse objective, a new design paradigm is needed to minimize bridge damage incorporating low- to no-damage techniques. The benefit can be enhanced if those low-damage technologies are combined with precast techniques to accelerate bridge construction.

The main goal of the present study was to develop a new generation of bridge columns which are fully precast, low damage, and repairable through component replacement. To achieve the project objectives, 20 repairable precast detailing alternatives were developed then ranked using a 13-parameter rubric including design and construction considerations. Subsequently, top three candidates were selected, designed at 50% scale, and prepared for testing. The three precast columns incorporated different exposed fuses such as stainless-steel bars restrained against buckling and steel tendons, which are tension-only members. Advanced materials such as ultra-high performance concrete (UHPC) and self-centering mechanisms were utilized to reduce the column damage and residual displacements. A reference cast-in-place column (CIP) was included for comparison. The repairable precast bridge columns were tested twice under a slow cyclic loading. The columns were repaired only by replacing the exposed fuses and retested under the same loading. Analytical modeling method were developed for repairable columns. Subsequently, a parametric study was conducted to better understand the behavior of repairable columns using different fuse materials. Finally, design and construction guidelines were proposed to facilitate the use of this new technology.

8.2 Conclusions

The following conclusions were drawn based on the experimental and analytical investigations:

- The NCHRP 13-parameter rating system was found viable in identifying the best repairable bridge column detailing alternatives for testing. This rating system may be used for the development and evaluation of any new repairable column alternatives.

- CIP failed by the longitudinal bar fracture after extensive concrete spalling. The lateral strength of CIP was 65.4 kips (291 kN) with a drift capacity of 8.96%.

- Testing of RPH-PC-R was stopped at 10% drift to avoid setup damage, which was right before reaching the 15%-drop-in-force limit (as the failure point). SCC spalling was observed above the neck section mainly caused by compressive forces of BRR pressing clamping collars to SCC.

Furthermore, a Z-shape bending of BRR was seen, which limited their replacement. The lateral strength of RPH-PC-R was 74.7 kips (332.3 kN), which was 14.2% higher than that of CIP. The drift capacity of RPH-PC-R was 9.80%, which was 9.3% higher than that of CIP.

- RPH-PF-R failed by the rupture of multiple tendon fuses with minimal UHPC damage. The lateral load capacity of RPH-PF-R was 59.8 kips (266 kN), which was 8.6% less than that of CIP. The drift capacity was 8.91%, which was very close to that of CIP.

- RPH-NP-R failed by the strength degradation mainly due to the rupture of neck bars at the rebar hinge. Minor UHPC spalling at the base of the column was observed. The lateral load capacity of RPH-NP-R was 86.9 kips (387 kN), which was 32.9% higher than that of CIP. The drift capacity of this column was 7.68%, which was 14.3% less than the CIP drift capacity.

- The Z-shape buckling of stainless-steel BRR used in the RPH-PC column made the repair by replacement very difficult. Furthermore, the column/footing dowels of RPH-PC were bent, and the column had some residual displacements which further complicated the placement of new BRR. Nevertheless, the incorporation of the steel tendons as the tension-only fuses in RPH-PF and PPH-NP eliminated any column/footing dowel damage and further helped with the recentering of the columns. Tendon fuse replacement was relatively quick and simple.

- No to minimal residual displacements are desired in any repairable column since the column should be close to its original position easing the fuse replacement. All repairable columns showed smaller residual displacements compared with CIP. However, the residual displacement of RPH-PF was insignificant throughout the entire testing.

- A tendon fuse can double serve both as typical longitudinal reinforcement and self-centering reinforcement with an additional benefit of accessibility for inspection since they are exposed.

- Use of UHPC greatly reduced apparent cracking and spalling, even at the fuse failure.

- The pushover analysis by Sjurseth et al. (2022) correctly predicted the CIP mode of failure as the longitudinal bar rupture. The calculated peak lateral force was 61.9 kips (276 kN), which was 5.4% lower than the measured strength. The calculated drift capacity for CIP was 7.64%, which was 14.7% lower than that measured for CIP.

- The calculated and measured initial stiffness of RPH-PC matched well. The calculated peak lateral strength of the column with long stainless-steel BRR was 64.0 kips (285 kN) with a drift capacity of 13.2%. However, calculated peak lateral load for the column with short BRR was 65.8 kips (293 kN), which was 9.5% lower than that in the actual test. The calculated drift capacity for RPH-PC-R was 8.69%.

- The pushover model for RPH-PF-R predicted a peak lateral load of 56.8 kips (253 kN), which was 1.9% lower than the measured peak strength. The analysis predicted a failure due to the tendon fuse rupture at 8.03%, which was 9.9% lower than the actual drift capacity.

- The pushover analysis for RPH-NP-R predicted a failure by tendon fuse rupture while the neck bars at the rebar hinge fractured in the column test. The calculated drift capacity, which was at 9.59% drift, was 25% higher than that of the test. The calculated peak lateral load was 83.0 kips (369 kN), which was only 0.6% higher than the measured lateral strength.

- Overall, the proposed modeling methods for repairable columns can predict the column force-displacement relationship with a reasonable accuracy.

- Based on the 90 pushover parametric analyses, for a repairable column to surpass the displacement capacity of its corresponding CIP, the fuse length should be at least 25%, 50%, and

75% of the CIP analytical plastic hinge length using stainless-steel BRR, shape memory alloy BRR, and steel tendon fuse, respectively.

Overall, the proposed detailing alternatives for the three repairable columns were feasible since all columns were successfully repaired by fuse replacement and were retested. However, the repair-by-fuse-replacement is simple and easy if tension-only members are used as the external fuses. Furthermore, the three repairable columns exhibited comparable seismic performance compared with CIP with smaller residual displacements. Nevertheless, all repairable columns had lower initial stiffness compared with CIP and exhibited stiffness degradation between the two tests.

As future studies, multi-column bent system and shake table testing are recommended to better understand the capacity and demand of repairable columns before field deployment. Specifically, the effects of lower initial stiffness on the dynamic performance and system behavior should be understood. The stiffness degradation between multiple tests (not only two tests) should be investigated.

REFERENCES

AASHTO LRFD. (2017). "AASHTO LRFD Bridge Design Specifications, 8th Edition," Washington, D.C., American Association of State Highway and Transportation Officials.

AASHTO SGS. (2011) "AASHTO Guide Specifications for Seismic Bridge Design," Washington, D.C., American Association of State Highway and Transportation Officials.

ACI 374.2R-13 (2013). "Guide for Testing Reinforced Concrete Structural Elements Under Slowly Applied Simulated Seismic Loads." American Concrete Institute (ACI) Committee 374, Farmington Hills, MI, 2013.

Alian Amiri, S.M. (2020). "Performance of Reinforced Concrete Bridge Columns with Various Reinforcement Details Subject to Long-duration Earthquakes." PhD Dissertation, University of Nevada, Reno, 289 pp.

ASTM A416/A416M. (2006). "Standard Specification for Steel Strand, Uncoated Seven-Wire for Prestressed Concrete." West Conshohocken, PA, 5 pp.

ASTM A706. (2016). "Standard Specification for Low-Alloy Steel Deformed and Plain Bars for Concrete Reinforcement." West Conshohocken, PA, 6 pp.

ASTM A760/A760M. (2010). "Standard Specification for Corrugated Steel Pipe, Metallic-Coated for Sewers and Drains." West Conshohocken, PA, 15 pp.

ASTM A955/A955M. (2019). "Standard Specification for Deformed and Plain Stainless Steel Bars for Concrete Reinforcement." West Conshohocken, PA, 15 pp.

ASTM C109/C109M-11b. (2011). "Standard Test Method for Compressive Strength of Hydraulic Cement Mortars (Using 2-in. or [50-mm] Cube Specimens)," West Conshohocken, PA.

ASTM C39/C39M-12. (2012). "Standard Test Method for Compressive Strength of Cylindrical Concrete Specimens," West Conshohocken, PA.

ASTM E8. (2012). "Standard Test Methods for Tension Testing of Metallic Materials." ASTM International, West Conshohocken, PA.

Boudaqa, A., Tazarv, M., and Tuhin, I. (2017). "Ductility without Confinement - A New Design and Construction Approach for RC Bridge Columns," International Journal of Bridge Engineering, Special Issue, pp. 53-77.

Caltrans. (2019). "Caltrans Seismic Design Criteria (SDC), Version 2.0" Sacramento, CA.: California Department of Transportation, 250 pp.

Cruz Noguez, C.A., and Saiidi, M.S. (2012). "Shake-table Studies of a Four-span Bridge Model with Advanced Materials." Journal of Structural Engineering, Vol. 138, No. 2, pp.183-192.

Davis, P.M., Janes, T.M, Haraldsson, O.S, Eberhard, M.O., and Stanton, J.F. (2012). "Unbonded Pretensioned Columns for Accelerated Bridge Construction in Seismic Regions." Journal of Bridge Engineering, ASCE, Vol. 22, No. 5: 04017003.

ElGawady, M.A., and Sha'lan, A. (2011). "Seismic Behavior of Self-centering Precast Segmental Bridge Bents." Journal of Bridge Engineering, Vol. 16, No. 3, pp. 328-339.

Finnsson, G. (2013). "Unbonded Pre-tensioned Bridge Columns with Hybrid Fiber-reinforced Concrete Shells." University of Washington.

Guo, T., Cao, Z., Xu, Z. and Lu, S., (2016). "Cyclic Load Tests on Self-centering Concrete Pier with External Dissipators and Enhanced durability." Journal of Structural Engineering, Vol. 142, No. 1, 04015088.

Han, Q., Jia, Z., Xu, K., Zhou, Y. and Du, X. (2019). "Hysteretic Behavior Investigation of Self-centering Double-column Rocking Piers for Seismic Resilience." Engineering Structures, Vol. 188, pp. 218-232.

Ibrahim, A.M., Wu, Z., Fahmy, M.F. and Kamal, D. (2016). "Experimental Study on Cyclic Response of Concrete Bridge Columns Reinforced by Steel and Basalt FRP Reinforcements." Journal of Composites for Construction Vol. 20, No. 3, p.04015062.

Ichikawa, S., Matsuzaki, H., Moustafa, A., ElGawady, M.A. and Kawashima, K. (2016). "Seismic-resistant Bridge Columns with Ultrahigh-performance Concrete Segments." Journal of Bridge Engineering, Vol. 21, No. 9, p.04016049.

Jia, J., Zhang, K., Saiidi, M.S., Guo, Y., Wu, S., Bi, K. and Du, X. (2020). "Seismic Evaluation of Precast Bridge Columns with Built-in Elastomeric Pads." Soil Dynamics and Earthquake Engineering, Vol. 128, p.105868.

Krawinkler, H. and Moncarz, P.D. (1982). Similitude Requirements for Dynamic Models." ACI Special Publication, Vol. 73, pp. 1-22.

LaVoy, M.R. (2020). "Seismic Performance of Mechanically Spliced Bridge Columns Through Analytical Studies." MS Thesis, South Dakota State University, 106 pp.

Mander, J.B., Priestley, M.J.N., Park, R. (1988). "Theoretical Stress-Strain Model for Confined Concrete," Journal of Structural Engineering, ASCE, Vol. 114, No. 8, pp. 1804-1826.

Mashal, M. and Palermo, A. (2019). "Low-damage Seismic Design for Accelerated Bridge Construction." Journal of Bridge Engineering, Vol. 24, No. 2, p.04019066.

Motaref, S., Saiidi, M.S. and Sanders, D. (2014). "Shake Table Studies of Energy-dissipating Segmental Bridge Columns." Journal of Bridge Engineering, Vol. 19, No 2, pp. 186-199.

Nakashoji, B. and Saiidi, M. (2014). "Seismic Performance of Square Nickel-Titanium Reinforced ECC Columns with Headed Couplers." Rep. No. CCEER-14-05, Center for Civil Engineering Earthquake Research, Dept. of Civil and Environmental Engineering, Univ. of Nevada, Reno, NV.

OpenSees. (2016). "Open System for Earthquake Engineering Simulations," Version 2.4.1, Berkeley, CA, Available online: http://opensees.berkeley.edu.

Panagiotou, M., Trono, W., Jen, G., Kumar, P., and Ostertag, C.P. (2015). "Experimental Seismic Response of Hybrid Fiber-reinforced Concrete Bridge Columns with Novel Longitudinal Reinforcement Detailing." Journal of Bridge Engineering, Vol. 20, No. 7, p.04014090.

Pantelides, C.P., and Thapa, D. (2021). "Self-centering Bridge Bent for Accelerated Bridge Construction." MPC-21-436. North Dakota State University - Upper Great Plains Transportation Institute, Fargo: Mountain-Plains Consortium.

Saiidi, M.S., Tazarv, M., Varela, S., Bennion, S., Marsh, M.L., Ghorbani, I., Murphy, T.M. (2017). "Seismic Evaluation of Bridge Columns with Energy Dissipating Mechanisms, Volume 1: Research Overview and Volume 2: Guidelines," National Academies of Sciences, Engineering, and Medicine, NCHRP Report No. 864, Washington, DC: The National Academies Press, 344 pp.

Saiidi, M.S., Mehraein, M., Shrestha, G., Jordan, E., Itani, A., Tazarv, M., Sanders, D., Murphy, T.M., Reno, M.L., and Pohll, M.N. (2020). "Proposed AASHTO Seismic Specifications for ABC Column Connections," National Academies of Sciences, Engineering, and Medicine, NCHRP Report No. 935, Washington, DC: The National Academies Press, 354 pp.

Sjurseth, T., Greeneway, E., Hart, K., LaVoy, M., Tazarv, M., and Wehbe, N. (2022). "Mechanically Spliced Precast Bridge Columns," North Dakota State University - Upper Great Plains Transportation Institute, Fargo: Mountain-Plains Consortium (MPC), MPC Report No. 22-451, 359 pp.

Tazarv, M., Boudaqa, A., and Tuhin, I. (2020). "Repairable Precast Moment-Resisting Buildings: Part I— Experimental Investigations." ACI Structural Journal, Vol. 117, No. 6, pp. 147-160.

Tazarv, M., and Saiidi, M.S. (2014) "Next Generation of Bridge Columns for Accelerated Bridge Construction in High Seismic Zones," Center for Civil Engineering Earthquake Research, Department of Civil and Environmental Engineering, University of Nevada, Reno, Nevada, Report No. CCEER-14-06, 400 pp.

Tazarv, M., and Saiid, M.S. (2016). "Low-damage Precast Columns for Accelerated Bridge Construction in High Seismic Zones." Journal of Bridge Engineering, Vol. 21, No. 3, p.04015056.

Tazarv, M., and Saiidi, M.S. (2016). "Seismic Design of Bridge Columns Incorporating Mechanical Bar Splices in Plastic Hinge Regions," Engineering Structures, DOI: 10.1016/j.engstruct.2016.06.041, Vol 124, pp. 507-520.

Terzic, V., and Stojadinovic, B. (2010). "Post-earthquake Traffic Capacity of Modern Bridges in California." California. Dept. of Transportation. Division of Research and Innovation Report No. CA/PEER/2010-103.

Varela, S., and Saiidi, M.S. (2019). "Experimental Study on Seismically Resilient Two-span Bridge Models Designed for Disassembly." Journal of Earthquake Engineering, Vol. 23, No. 1, pp.72-111.

Wang, J., Wang, Z., Tang, Y., Liu, T. and Zhang, J. (2018). "Cyclic Loading Test of Self-centering Precast Segmental Unbonded Posttensioned UHPFRC Bridge Columns." Bulletin of Earthquake Engineering, Vol. 16, No. 11, pp. 5227-5255.

White, S., and Palermo, A. (2016). "Quasi-static Testing of Posttensioned Nonemulative Column-footing Connections for Bridge Piers." Journal of Bridge Engineering, Vol. 21, No. 6, p.04016025.

Zaghi, A.E., and Saiidi, M.S. (2010). "Seismic Performance of Pipe-pin Two-way Hinges in Concrete Bridge Columns," Journal of Earthquake Engineering, Vol. 14, No. 8, pp. 1253-1302.

Zhang, R., Meng, Q., Shui, Q., He, W., Chen, K., Liang, M. and Sun, Z. (2019). "Cyclic Response of RC Composite Bridge Columns with Precast PP-ECC Jackets in the Region of Plastic Hinges." Composite Structures, Vol. 221, p.110844.

APPENDIX A. LIFE CYCLE COST ANALYSIS

A1. Introduction

A life-cycle-cost analysis (LCCA) was performed to further evaluate the cost of repairable bents over bridge service life. LCCA was performed before the experimental study presented in Ch. 4 using data available at the time. LCCA is included in this report for completeness.

The following equation (Khatami et al., 2016) can be used to perform LLCA:

$$LCC = C_c + [C_{IN} + C_M + C_M^u] + C_{sf} + C_{sf}^u \qquad \text{(Eq. A.1)}$$

where, C_C is the initial construction cost, C_{IN} is the inspection cost, C_M is the maintenance cost, C_M^u is the indirect cost due to maintenance activities, C_{sf} is the direct cost due to extreme events, and C_{sf}^u is the indirect cost due to extreme events.

A2. Bridge Models and Seismic Analysis

NCHRP 864 (Saiidi et al., 2017) includes initial and event-based repair cost analyses for a five-span reinforced concrete bridge located near Olympia, Washington with a site class E. This cast-in-place (CIP) bridge was selected as the baseline for LCCA.

The key structural details are shown in **Fig. A.1** and **Fig. A.2**. The original bridge was designed according to MCEER/ATC 49 (ATC 49, 2003) and has four bents with clear heights of 30, 45, 50, and 45 ft. The bridge has no skew and is supported on seat-type abutments. The superstructure is a cast-in-place box girder that is integral with the bents. All the columns are round with a diameter of 4 ft, and there are two columns per bent. Each bent is supported by a 22 ft by 46 ft pile cap 5 ft deep, with 2-ft diameter, cast-in-place concrete piles with steel casing. The concrete has a specified compressive strength of 4 ksi and the reinforcing steel is Grade 60. The longitudinal and transverse reinforcement in the columns of each bent is summarized in **Table A.1**.

Table A.1. Reinforcement for CIP Bridge Columns

Bent	Longitudinal reinforcement	Transverse reinforcement ratio
1	28-#11 (2.4%)	1.3%
2, 3, 4	20-#10 (1.4%)	0.9%

First an elastic model of the bridge was built in SAP2000 (2016) to perform a response spectrum analysis. The uniformly distributed dead load assigned to the superstructure was 13 kip/ft, which consisted of 11.7 kip/ft from the dead load of components (box girder self-weight plus barriers) and 1.3 kip/ft from the dead load of wearing surfaces (asphalt concrete pavement plus a utility line). Modal spectral analysis was performed to determine the seismic displacement demand on each of the bents of the reference CIP bridge. This analysis was based on the design acceleration spectrum for the bridge given by the AASHTO SGS (2011) and shown in **Fig. A.3**. Twelve vibration modes were included in the analysis to guarantee a modal participating mass of 99% in total. The response was obtained using the complete quadratic modal combination method (CQC).
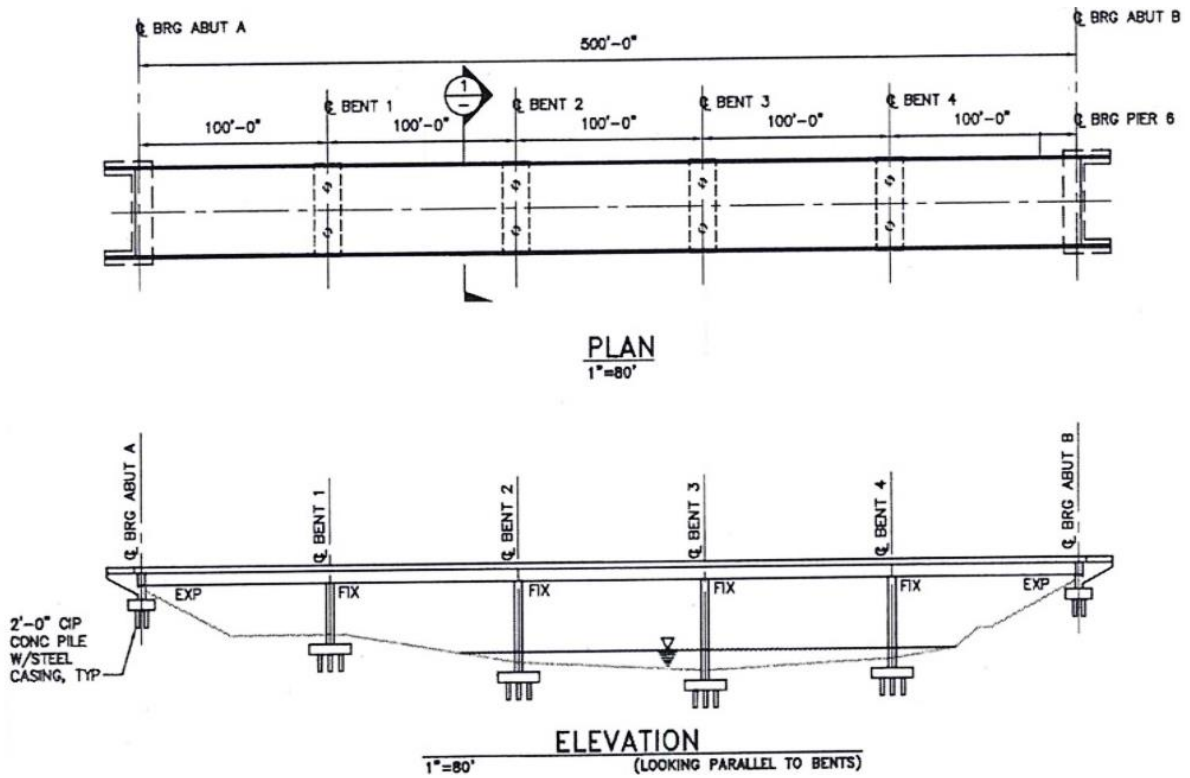
Figure A.1. Bridge Plan and Elevation Views
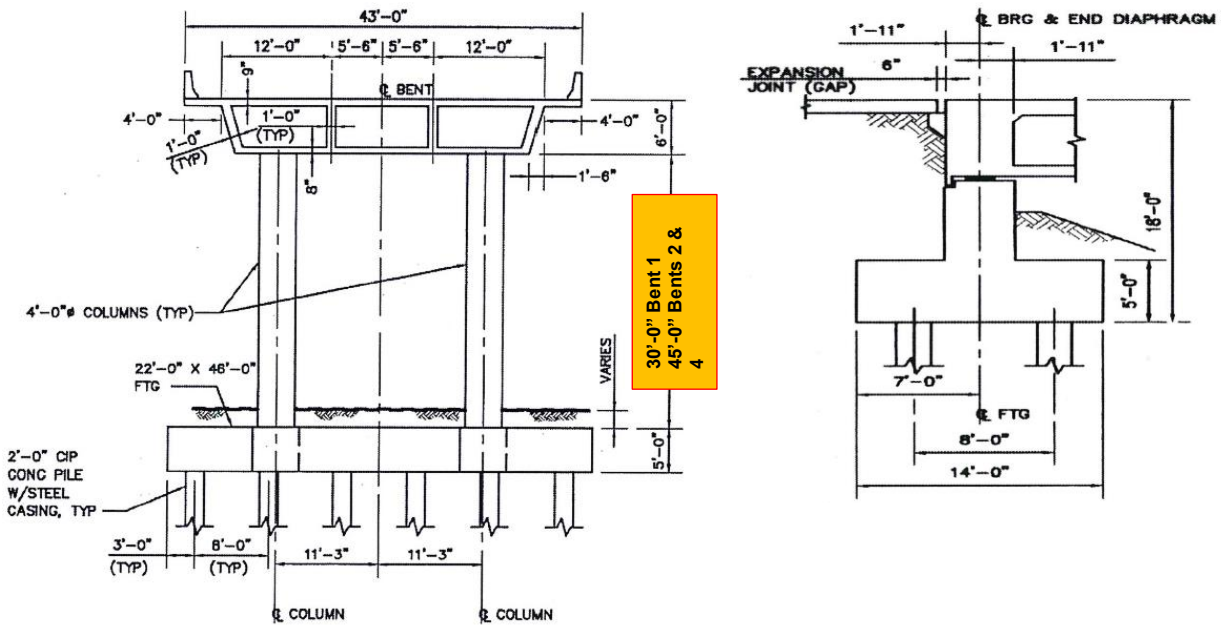
Figure A.2. Bent Section and Abutment Detail

A-2
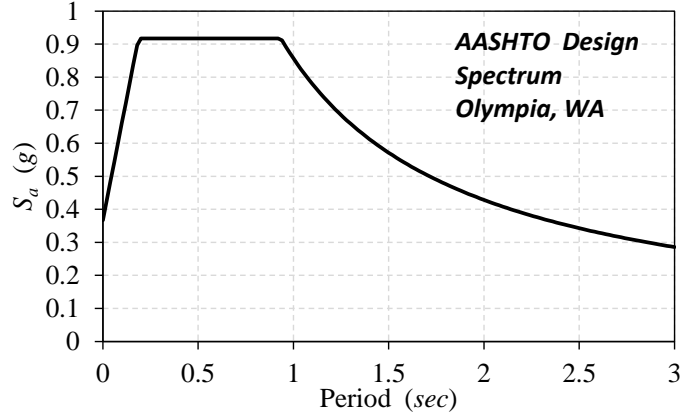
Figure A.3. Design Response Spectrum

Two-dimensional nonlinear models were developed in a finite-element software, OpenSees (2016), to assess the displacement capacity of each bent accounting for both material and geometric nonlinearities. The columns were modelled as force-based distributed plasticity frame elements with fiber sections connected by a rigid link element representing the cap-beam. The fiber sections were built using appropriate constitutive stress-strain relationships for each material according to AASHTO SGS (2011). The axial reactions in each column from the dead load analysis in SAP 2000 (e.g., 750 kips at Bent 1) were assigned as gravity point loads at the top of each column. Each bent was subjected to an increasing lateral displacement until failure.

The force-drift pushover curves for each bent of the CIP bridge are shown in **Fig. A.4**. Each plot shows a dotted line representing a bilinear elastic-plastic idealization of the pushover curve calculated using equivalent energy principles (AASHTO SGS). The plots also include the point where the first yield in the reinforcement takes place and the point corresponding to the drift demand calculated in the SAP2000 model. The drift ratio demand (δ_D), the effective yield drift ratio (δ_{yi}), the displacement ductility capacity (μ_c), the displacement ductility demand (μ_d), the damage index (DI), and the expected damage state (DS) for each bent are listed in **Table A.2**. The damage index is a parameter developed by Vosooghi and Saiidi (2010) for CIP columns, and it measures how far into the 'inelastic' range each bent responds. The damage index is calculated as:

$$DI = \frac{\mu_d - 1}{\mu_c - 1}$$
(Eq. A.2)

The maximum damage index is one, which corresponds to failure. A zero damage index indicates that the bent drift and base shear are at the effective yield point. When the index is negative, the bent is in the elastic range. Vosooghi and Saiidi (2010) correlated different damage indexes with the expected damage states of CIP bridge columns, DS-1 to DS-5. Damage states DS-2, DS-3, DS-4, and DS-5 correspond approximately to damage indexes of 0.15, 0.35, 0.55, and 0.80, respectively. The damage states in **Table A.2** were defined for each bent according to these reference values.
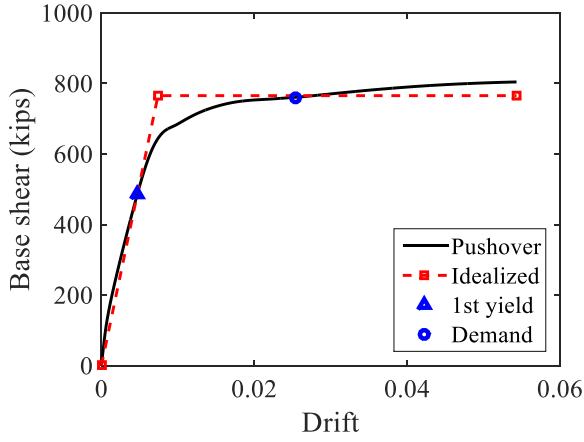
(a) Bent 1
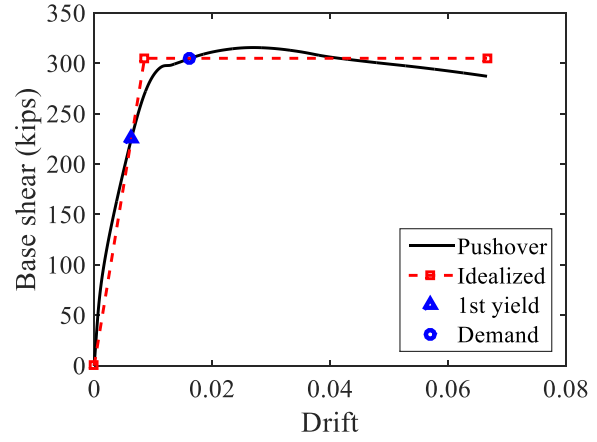
(b) Bent 2
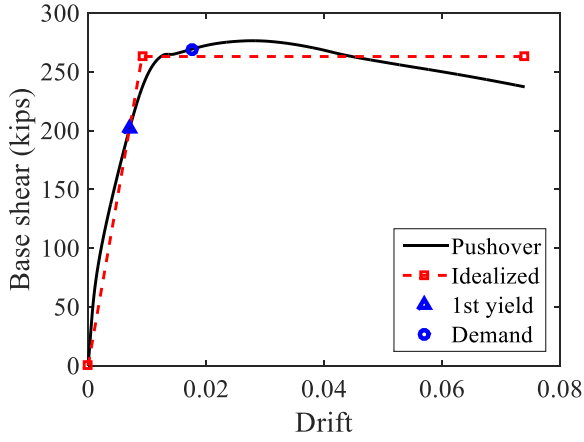
(c) Bent 3
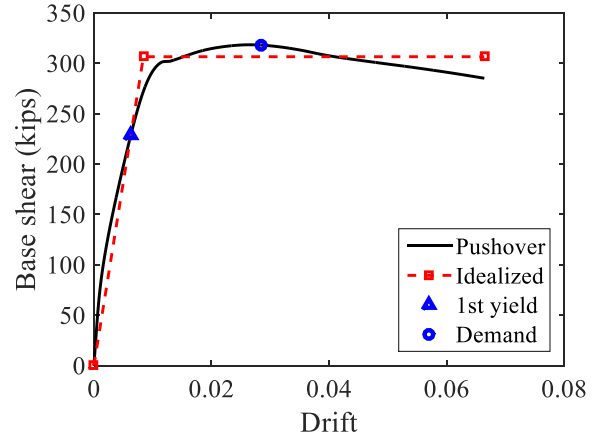
(d) Bent 4

Figure A.4. Pushover Curves for Each Bent of CIP Bridge

Table A.2. CIP Bridge Analysis Results and Damage State for each Bent

Parameter	Notation	Bent			
		1	2	3	4
Drift Ratio Demand	δ_D (%)	2.54	1.61	1.75	2.84
Effective Yield Drift Ratio	δ_{yi} (%)	0.74	0.85	0.91	0.84
Displacement Ductility Capacity	μ_c	7.3	7.8	8.1	7.9
Displacement Ductility Demand	μ_d	3.4	1.9	1.9	3.4
Damage Index	DI	0.38	0.13	0.13	0.35
Damage State	DS	3	2	2	3

A3. Cost Analysis

The initial cost of the CIP bridge was calculated based on the upper bound unit costs reported in Chapter 12 "Quantities, Costs and Specifications" of the Bridge Design Manual LRFD M 23-50 of the Washington Department of Transportation (2016). The cost breakdown is shown in **Table A.3** for a total initial cost of approximately 7.6 million dollars, not including labor, equipment, and design and consulting fees.

Table A.3. Initial Cost of CIP Bridge

Initial cost of RC Bridge

1. Substructure

LOCATION	ITEM	UNIT	UNIT COST	QTY	MEASUREMENT EA	COST
Abutment	Excavation Class A Incl Haul - Earth	CY	$30	2	681.48	$40,889
Abutment	Pile tip (CIP concrete with steel casing - short tip)	EACH	$250	24	1	$6,000
Abutment	Soil excavation for shaft including haul	CY	$600	24	5.82	$83,776
Abutment	Placing permanent casing for shaft	EACH	$3,000	24	1	$72,000
Abutment	Concrete class 4000P (CIP piling)	CY	$250	24	5.82	$34,907
Abutment	Concrete class 4000 (footings)	CY	$600	2	186.67	$224,000
Pier foundation	Excavation Class A Incl Haul - Earth	CY	$30	4	355.56	$42,667
Pier foundation	Cofferdam	SF	$30	4	1184	$142,080
Pier foundation	Pile tip (CIP concrete with steel casing - short tip)	EACH	$250	72	1	$18,000
Pier foundation	Soil excavation for shaft including haul	CY	$600	72	5.82	$251,327
Pier foundation	Placing permanent casing for shaft	EACH	$3,000	72	1	$216,000
Pier foundation	Concrete class 4000P (CIP piling)	CY	$250	72	5.82	$104,720
Pier foundation	Concrete class 4000 (footings)	CY	$600	4	195.56	$469,333
Bent 1 columns	Concrete class 4000	CY	$400	2	13.96	$11,170
Bent 1 columns	Longitudinal reinforcement - #11 Gr. 60	LBS	$1.30	56	212.52	$15,471
Bent 1 columns	Transverse reinforcement - #5@2.125" (assumed)	LBS	$1.30	2	1945.2	$5,057
Bent 2 columns	Concrete class 4000	CY	$400	2	20.94	$16,755
Bent 2 columns	Longitudinal reinforcement - #10 Gr. 60	LBS	$1.30	40	236.665	$12,307
Bent 2 columns	Transverse reinforcement - #5@3" (assumed)	LBS	$1.30	2	2132.2	$5,544
Bent 3 columns	Concrete class 4000	CY	$400	2	23.27	$18,617
Bent 3 columns	Longitudinal reinforcement - #10 Gr. 60	LBS	$1.30	40	258.18	$13,425
Bent 3 columns	Transverse reinforcement - #5@3" (assumed)	LBS	$1.30	2	2369.1	$6,160
Bent 4 columns	Concrete class 4000	CY	$400	2	20.94	$16,755
Bent 4 columns	Longitudinal reinforcement - #10 Gr. 60	LBS	$1.30	40	236.665	$12,307
Bent 4 columns	Transverse reinforcement - #5@3" (assumed)	LBS	$1.30	2	2132.2	$5,544

2. Superstructure

LOCATION	ITEM	UNIT	UNIT COST	QTY	MEASUREMENT EA	COST
Superstructure	RC box girder (water crossing w/piling)	SF	$250.00	1	21500	$5,375,000.00
Superstructure ends	Bridge approach slab	SF	$250.00	2	860	$430,000.00

TOTAL COST = $7,649,809

Based on the feedback from an expert contractor and expected level of damage using the estimated Damage Index (DI), NCHRP 864 estimated the repair cost of the CIP bridge at $248,000, as summarized in **Table A.4**. For expedited repair that require 24/7 work, the cost could increase by 40%, changing the repair cost to approximately $350,000.

Table A.4. Repair Cost of CIP Bridge at Design Level Earthquake

LOCATION	ITEM	UNIT	UNIT COST	QTY	MEASUREMENT EA	COST
Bent 1 plastic hinges	Epoxy injection in the cracks and mortar repair for spalled concrete	EACH	$13,000	4	1	$52,000
Bent 1 plastic hinges	FRP wrapping	EACH	$5,000	4	1	$20,000
Bent 2 plastic hinges	Epoxy injection in the cracks and mortar repair for spalled concrete	EACH	$13,000	4	1	$52,000
Bent 3 plastic hinges	Epoxy injection in the cracks and mortar repair for spalled concrete	EACH	$13,000	4	1	$52,000
Bent 4 plastic hinges	Epoxy injection in the cracks and mortar repair for spalled concrete	EACH	$13,000	4	1	$52,000
Bent 4 plastic hinges	FRP wrapping	EACH	$5,000	4	1	$20,000

TOTAL REPAIR COST = $248,000

A similar analysis should be performed on the bridge using the proposed repairable detailing for columns. Repairable detailing ALT-1 (**Fig. A.5**) was used at the ends of all columns of the reference CIP bridge. Except the columns, which are updated using the repairable detailing, it is assumed that all other

components of the bridge remain the same as the reference CIP bridge discussed above. The force capacity of a repairable column is at most the same as it corresponding reference CIP column thus the cap beam, footing, and pile design do not change.
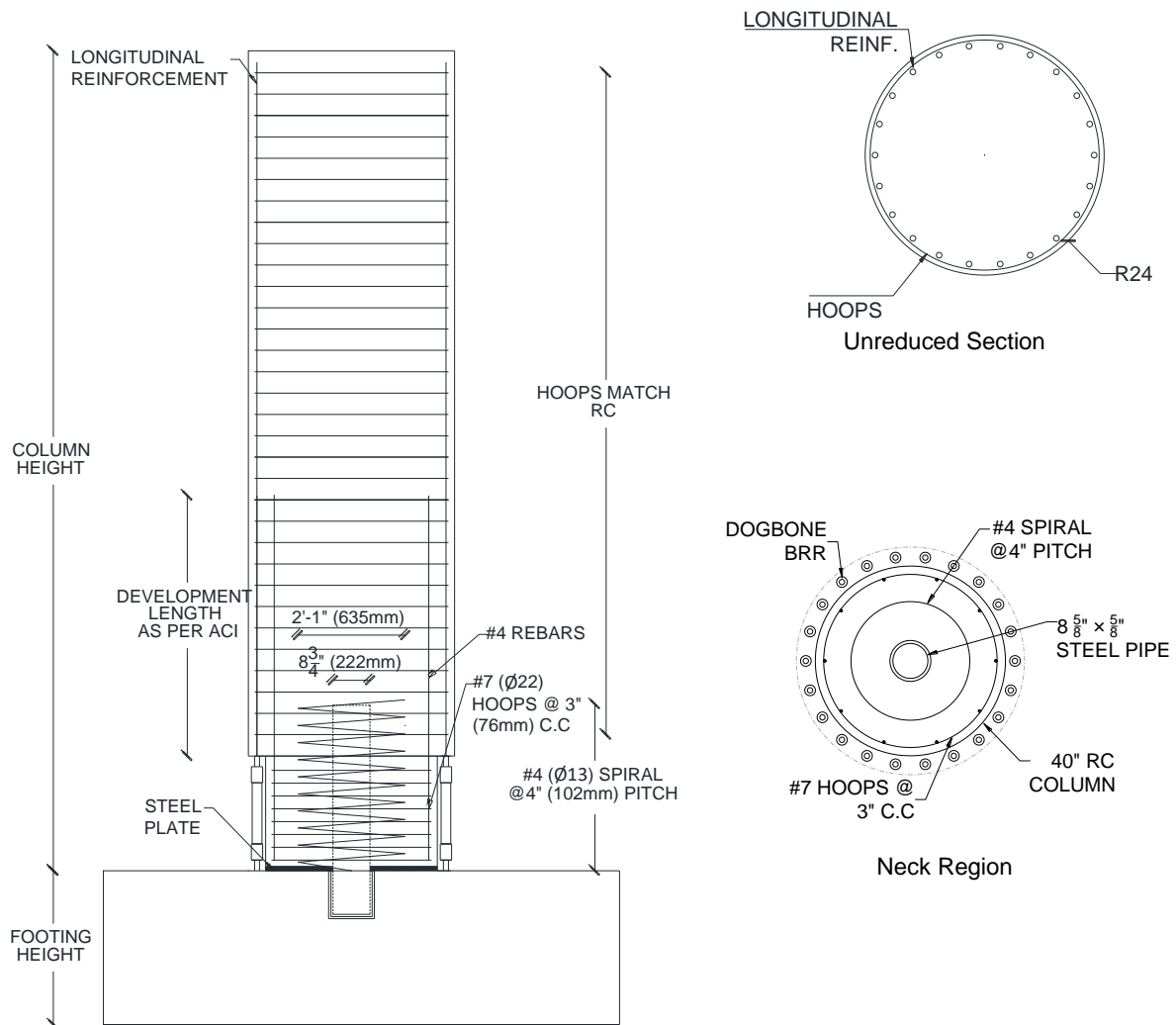
Figure A.5. Proposed Repairable Column Detailing with 4-ft Diameter

Several bridges have been constructed using ABC techniques. Many projects have reported 15% to 20% cost saving when substructure was precast (e.g., FHWA 2006; Youngblood and Noyer, 2012; Marsh et al., 2013). Furthermore, several months of time saving was reported. To estimate the initial cost of the repairable bridge; however, no cost saving was included for ABC. **Table A.5** presents a summary of the initial cost analysis for the repairable bridge. The column longitudinal bars were oversized and a dog-bone BRR was used to limit the damage to BRR. The cost of a 3-ft long BRR including machining, grouting, and confining steel tube was conservatively estimated as $100 per piece ($50 machining, $50 materials). The cost of steel pipe-pin was obtained from <https://www.speedymetals.com/>. Headed couplers are $15 per piece.

Table A.5. Initial Cost of Repairable Bridge

Initial cost of Repairable BRR Bridge

1. Substructure

LOCATION	ITEM	UNIT	UNIT COST	QTY	MEASUREMENT EA	COST
Abutment	Excavation Class A Incl Haul - Earth	CY	$30	2	681.48	$40,889
Abutment	Pile tip (CIP concrete with steel casing - short tip)	EACH	$250	24	1	$6,000
Abutment	Soil excavation for shaft including haul	CY	$600	24	5.82	$83,776
Abutment	Placing permanent casing for shaft	EACH	$3,000	24	1	$72,000
Abutment	Concrete class 4000P (CIP piling)	CY	$250	24	5.82	$34,907
Abutment	Concrete class 4000 (footings)	CY	$600	2	186.67	$224,000
Pier foundation	Excavation Class A Incl Haul - Earth	CY	$30	4	355.56	$42,667
Pier foundation	Cofferdam	SF	$30	4	1184	$142,080
Pier foundation	Pile tip (CIP concrete with steel casing - short tip)	EACH	$250	72	1	$18,000
Pier foundation	Soil excavation for shaft including haul	CY	$600	72	5.82	$251,327
Pier foundation	Placing permanent casing for shaft	EACH	$3,000	72	1	$216,000
Pier foundation	Concrete class 4000P (CIP piling)	CY	$250	72	5.82	$104,720
Pier foundation	Concrete class 4000 (footings)	CY	$600	4	195.56	$469,333
Bent 1 columns	Concrete class 4000	CY	$400	2	6.98	$5,585
Bent 1 columns	Longitudinal reinforcement - #14 Gr. 60	LBS	$1.30	56	248.625	$18,100
Bent 1 columns	Transverse reinforcement - #7@3"	LBS	$1.30	2	2774.1	$7,213
Bent 1 plastic hinges	Concrete class 4000	CY	$400	4	4.84	$7,742
Bent 1 plastic hinges	Longitudinal reinforcement - #11 BRR	EACH	$100	56	2.0	$11,200
Bent 1 plastic hinges	HRC Couplers	EACH	$15	56	4.0	$3,360
Bent 2 columns	Concrete class 4000	CY	$400	2	21.82	$17,453
Bent 2 columns	Longitudinal reinforcement - #11 Gr. 60	LBS	$1.30	40	252.3675	$13,123
Bent 2 columns	Transverse reinforcement - #7@3"	LBS	$1.30	2	2774.1	$7,213
Bent 2 plastic hinges	Concrete class 4000	CY	$400	4	4.84	$7,742
Bent 2 plastic hinges	Longitudinal reinforcement - #10 BRR	EACH	$100	40	2.0	$8,000
Bent 2 plastic hinges	HRC Couplers	EACH	$15	40	4.0	$2,400
Bent 3 columns	Concrete class 4000	CY	$400	2	16.29	$13,032
Bent 3 columns	Longitudinal reinforcement - #11 Gr. 60	LBS	$1.30	40	278.9325	$14,504
Bent 3 columns	Transverse reinforcement - #7@3"	LBS	$1.30	2	2774.1	$7,213
Bent 3 plastic hinges	Concrete class 4000	CY	$250	4	4.84	$4,838
Bent 3 plastic hinges	Longitudinal reinforcement - #10 BRR	EACH	$100	40	2.0	$8,000
Bent 2 plastic hinges	HRC Couplers	EACH	$15	40	4.0	$2,400
Bent 4 columns	Concrete class 4000	CY	$400	2	13.96	$11,170
Bent 4 columns	Longitudinal reinforcement - #11 Gr. 60	LBS	$1.30	40	252.3675	$13,123
Bent 4 columns	Transverse reinforcement - #7@3"	LBS	$1.30	2	2774.1	$7,213
Bent 4 plastic hinges	Concrete class 4000	CY	$250	4	4.84	$4,838
Bent 4 plastic hinges	Longitudinal reinforcement - #10 BRR	EACH	$100	40	2.0	$8,000
Bent 2 plastic hinges	HRC Couplers	EACH	$15	40	4.0	$2,400
Four Bents	Steel Plates at Column Ends	EACH	$200	4	4.0	$3,200
Four Bents	Steel Pipe-Pin	EACH	$1,206	4	4.0	$19,296

2. Superstructure

LOCATION	ITEM	UNIT	UNIT COST	QTY	MEASUREMENT EA	COST
Superstructure	RC box girder (water crossing w/piling)	SF	$250.00	1	21500	$5,375,000.00
Superstructure ends	Bridge approach slab	SF	$250.00	2	860	$430,000.00

TOTAL COST = $7,739,054

No test data is available for repairable bridge columns to directly verify analytical models. However, based on the repairable beam-column testing perform at SDSU by the PI, a model was developed in OpenSees. Detailed discussion of the modeling and results can be found in Boudaqa (2018). **Figure A.6** shows the pushover response of the repairable columns for each bent. Note only one-half length of a column of each bent (assuming that the inflection point is the mid-length of the column in the two-column bent, **Fig. A.2**) was modeled in a cantilever configuration to simplify the analysis. Therefore, lateral forces in each model are approximately 4 times smaller than those in the two-column bent, and the drift ratio of each model is the same as the bent.

A repairable column is softer than the CIP column thus a higher displacement demand is expected. No dynamic analysis has been performed on repairable columns to quantify the effect of the lower initial stiffness on the displacement demand. However, the work on buildings showed that a repairable building will experience on average 21% higher displacement demands compared with conventional CIP buildings due to the lower stiffness. For bridges, it is assumed that the displacement demand of a repairable column is 25% higher than its corresponding CIP column (further investigations are needed as planned in **Task 4**). The estimated displacement demands for the repairable columns (25% increase compared with the

CIP columns summarized in **Table A.2**) are marked with vertical lines in **Fig. A.6**. It can be seen that the repairable columns with a minimum fuse length of $0.5L_p$ (L_p is the CIP column plastic hinge length) have sufficient reserved capacity. Based on the beam-column testing and the analytical work, the expected damages at the design level earthquake for these repairable columns are a few minor cracks and yielding of BRR. Repairable bridge columns should be tested to prove this performance (**Task 3**). A repair cost analysis was performed at the design level earthquake as summarized in **Table A.6**. Cracks will be injected with epoxy and all BRR will be replaced.
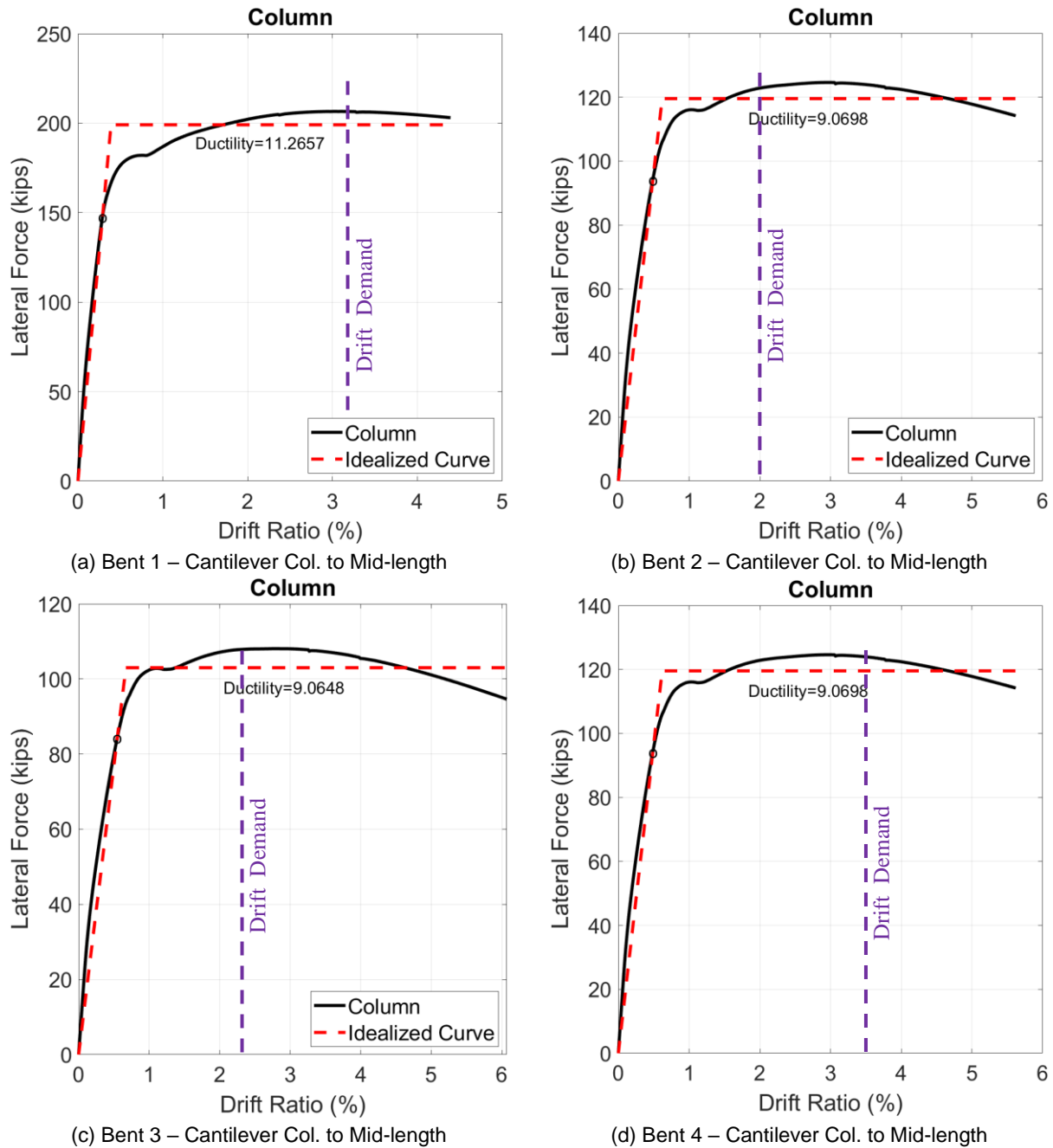

(a) Bent 1 – Cantilever Col. to Mid-length

(b) Bent 2 – Cantilever Col. to Mid-length

(c) Bent 3 – Cantilever Col. to Mid-length

(d) Bent 4 – Cantilever Col. to Mid-length

Figure A.6. Pushover Response of Repairable Columns

Table A.6. Repair Cost of Repairable Bridge at Design Level Earthquake

LOCATION	ITEM	UNIT	UNIT COST	QTY	MEASUREMENT EA	COST
Bent 1 plastic hinges	Epoxy injection in the cracks	EACH	$4,000	1	1	$4,000
Bent 1 plastic hinges	All BRR Replacement	EACH	$100	56	2	$11,200
Bent 2 plastic hinges	Epoxy injection in the cracks	EACH	$4,000	1	1	$4,000
Bent 2 plastic hinges	All BRR Replacement	EACH	$100	40	2	$8,000
Bent 3 plastic hinges	Epoxy injection in the cracks	EACH	$4,000	1	1	$4,000
Bent 3 plastic hinges	All BRR Replacement	EACH	$100	40	2	$8,000
Bent 4 plastic hinges	Epoxy injection in the cracks	EACH	$4,000	1	1	$4,000
Bent 4 plastic hinges	All BRR Replacement	EACH	$100	40	2	$8,000

TOTAL COST = $51,200

A3.1 Summary of Cost Analysis:

The initial cost of CIP bridge was $7,649,809 and the initial cost of the repairable bridge was $7,739,054 (1.2% increase). This does not include the 15-20% cost saving expected from the accelerated construction. The repair cost of the CIP bridge at the design level earthquake was $248,000 while the repair cost of the repairable bridge was $51,200 (only 20% of CIP).

A4. Life-Cycle Cost Analysis

Furthermore, LCCA was carried using BridgeLCC software (Ehlen, 2003), which was developed by NIST. For 2020, the US inflation rate was -0.5%, the real discount rate was 3%, and the nominal discount rate was 2.5% (FEMP, 2020). It is common to ignore the inflation rate in LCCA for bridges thus it was assumed zero. A screenshot of the software is shown below. It was assumed that an earthquake (design level) in the service year of 40 (out of 75) would occur thus a single repair cost was included for that year. Both CIP and repairable bridges approximately cost the same in 75 years of service.
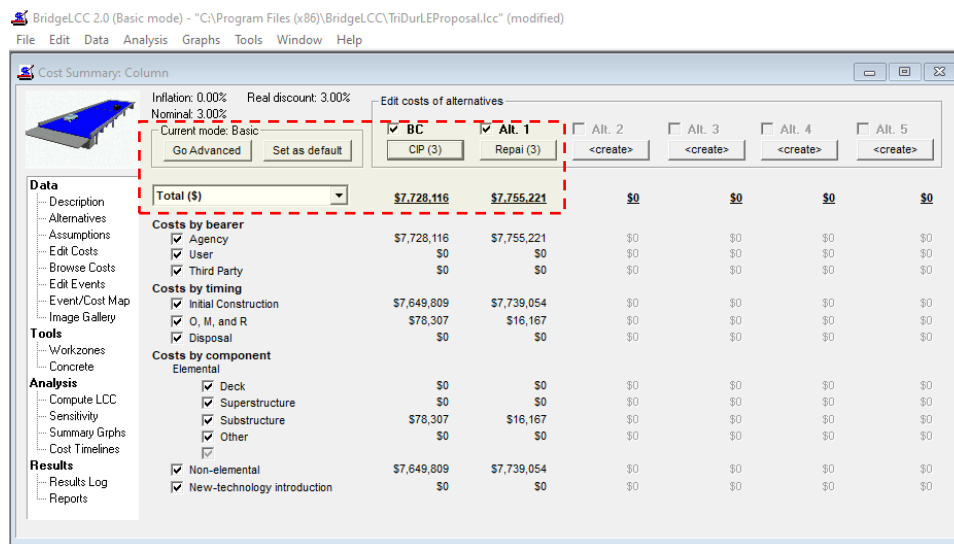

Figure A.7. LCCA Results

Overall, it is obvious that cost saving due to ABC (15-20%, which was not included) and significantly lower repair cost of the proposed detailing (80% cost saving) at the design level and stronger earthquakes make it a more appealing option. Furthermore, in earthquakes larger than the design, the CIP bridge may need total replacement due to the extent of damage to columns but the total replacement of the bridge using repairable detailing is unlikely. Even if in a rare event that the column needs to be replaced, it is feasible since the whole column can be disassembled (**Fig. A.5**) and the other components of the bridge can be preserved (e.g., jack up the superstructure, change the damaged column with new one, remove the jack).

A5. References

AASHTO SGS. (2011). "AASHTO Guide Specifications for LRFD Seismic Bridge Design, 2nd Edition," American Association of State Highway and Transportation Officials.

Boudaqa, A. (2018). "Repairable Precast Buildings and Bridges." PhD Dissertation, South Dakota State University, 278 pp., https://openprairie.sdstate.edu/etd/2467/.

Ehlen, M. (2003). BridgeLCC 2.0 Users Manual (Life-Cycle Costing Software for the Preliminary Design of Bridges). National Institute of Standards and Technology, Maryland.

FHWA. (2006). "Prefabricated Bridge Elements and Systems Cost Study: Accelerated Bridge Construction Success Stories," https://www.fhwa.dot.gov/bridge/prefab/successstories/091104/01.cfm.

FEMP. (2020). "2020 DISCOUNT RATES", https://www.energy.gov/sites/prod/files/2020/04/f74/2020discountrates.pdf.

Khatami, D., B. Shafei, and O. Smadi. (2016). "Management of Bridges Under Aging Mechanisms and Extreme Events: Risk-Based Approach." Transportation Research Record: Journal of the Transportation Research Board, No. 2550, pp. 89-95.

Marsh, M.L., Stringer, S.J., Stanton, J.F., Eberhard, M.O., Haraldsson, O., Tran, H.V., Khaleghi, B., Schultz, E. and Seguirant, S. (2013). "Precast Bent System for High Seismic Regions." Federal Highway Administration Report No. FHWA-HIF-13-037, 240 pp.

MCEER/ATC (2003). "Recommended LRFD Guidelines for the Seismic Design of Highway Bridges," MCEER/ATC-49, MCEER/ATC Joint Venture, NCHRP 12-49 Project Team.

OpenSees (2016). <http://opensees.berkeley.edu/index.php>, OpenSees 2.5.0.

SAP2000. (2016). "SAP2000 Nonlinear Version 18", Computers and Structures, Inc. Berkeley, CA.

Saiidi, M.S., Tazarv, M., Varela, S., Bennion, S., Marsh, M.L., Ghorbani, I., Murphy, T.M. (2017). "Seismic Evaluation of Bridge Columns with Energy Dissipating Mechanisms, Volume 1: Research Overview and Volume 2: Guidelines," National Academies of Sciences, Engineering, and Medicine, NCHRP Report No. 864, Washington, DC: The National Academies Press, 344 pp.

Vosooghi, A. and Saiidi, M.S. (2010). "Post-Earthquake Evaluation and Emergency Repair of Damaged RC Bridge Columns Using CFRP Materials," Center for Civil Engineering Earthquake Research, Department of Civil and Environmental Engineering, University of Nevada, Reno, Nevada, Report No. CCEER-10-05, 679 pp.

Washington Department of Transportation. (2016). "Bridge Design Manual LRFD M 23-50.16," Olympia, Washington

White, S. and Palermo, A., (2016). "Quasi-static testing of posttensioned nonemulative column-footing connections for bridge piers." Journal of Bridge Engineering, 21(6), p.04016025.

Youngblood, M., and Noyer, S. (2012). "Precast Concrete Bridge Substructure Components." 98th Road School. https://docs.lib.purdue.edu/cgi/viewcontent.cgi?article=1215&context=roadschool.